Automatica.it 2024

Bolzano, September 11-13

Free University of Bozen-Bolzano

Preface

This volume contains the extended abstracts submitted to and presented at Automatica.it 2024 held on September 11-13, 2024 in Bolzano, Italy.

Automatica.it represents the annual conference of the Società Italiana Docenti e Ricercatori in Automatica (SIDRA), which is coordinating the Italian national activities in the field of systems and control engineering (disciplinary scientific sector IINF-04/A).

Bolzano, 10.09.2024

Conference chairs:

Angelika Peer
Karl von Ellenrieder

Programme at a glance

Wednesday, September 11th

8:30-9:00
Registration (Room: Foyer)

9:00-9:30
Welcome (Room: D0.01)

9:30 - 11:00
Session 1A:
Robotics
(Room: D0.01)

9:30 - 11:00
Session 1B:
Vehicles
(Room: D1.02)

11:00 - 11:30
Coffee break (Room: Foyer)

11:30 - 13:00
Session 2A: Applications
(Room: D0.01)

11:30 - 13:00
Session 2B:
Robotics
(Room: D1.02)

13:00 - 14:30
Lunch (Room: Foyer)

14:30 - 16:00
Session 3A:
Control theory
(Room: D0.01)

14:30 - 16:00
Session 3B:
DAuSy session
(Room: D1.02)

16:00 - 16:30
Coffee break (Room: Foyer)

16:30 - 18:30
Session 4A: Optimization
(Room: D0.01)

16:30 - 18:30
Session 4B:
Control of energy systems
(Room: D1.02)

18:30 - 20:00
Cocktail event (Room: Foyer)

Thursday, September 12th

8:30-9:00
Registration (Room: Foyer)

9:00 - 10:30
Session 5A:
Machine learning & control
(Room: D0.01)

9:00 - 10:30
Session 5B:
Vehicles
(Room: D1.02)

9:00 - 10:30
Session 5C:
Path planning
(Room: D1.03)

10:30 - 11:00
Coffee break (Room: Foyer)

11:00 - 12:30
Session 6A:
Modelling and estimation
(Room: D0.01)

11:00 - 12:30
Session 6B:
Control theory
(Room: D1.02)

11:00 - 12:30
Session 6C:
Control of actuators
(Room: D1.03)

12:30 - 14:00
Lunch (Room: Foyer)

14:00 - 15:30
Session 7A:
Energy management in vehicles
(Room: D0.01)

14:00 - 15:30
Session 7B:
Computer vision and control
(Room: D1.02)

14:00 - 14:45
Session 7C: Education
(Room: D1.03)

14:45 - 15:30
Session 7D: Applications
(Room: D1.03)

15:30 - 16:00
Coffee break (Room: Foyer)

16:00 - 18:00
Round table: Facts and myths in machine-learning-based control
(Room: D0.01)

20:00 - 23:00
Social dinner

Friday, September 13th

8:30-9:00
Registration (Room: Foyer)

9:00-10:00
PhD award session
(Room: D0.01)

10:00-11:00
Assembly SIDRA
(Room: D0.01)

11:00-11:30
Coffee break (Room: Foyer)

11:30-13:00
Assembly SIDRA
(Room: D0.01)

13:00-14:30
Lunch (Room: Foyer)

Floor maps

GROUND FLOOR

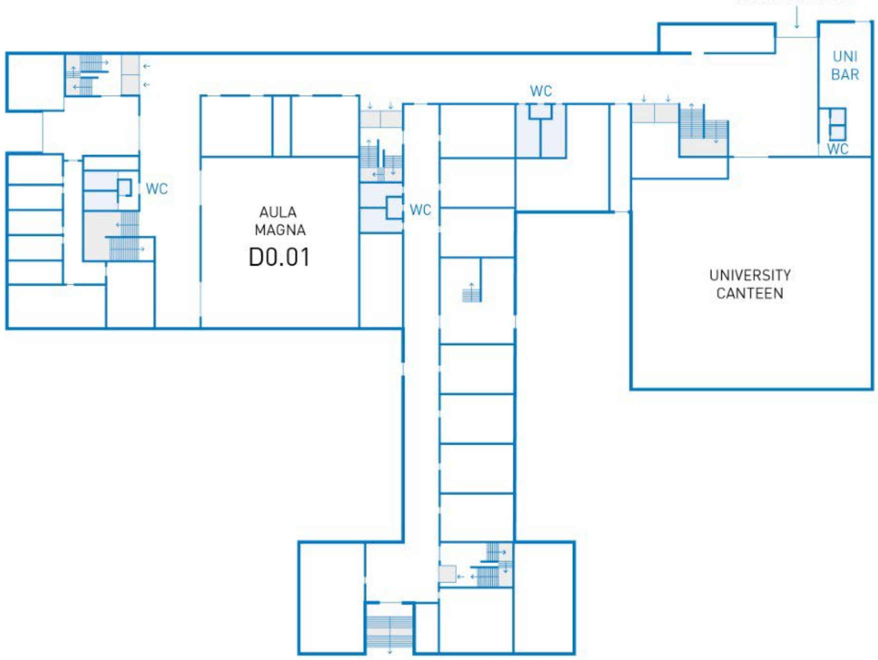

FIRST FLOOR

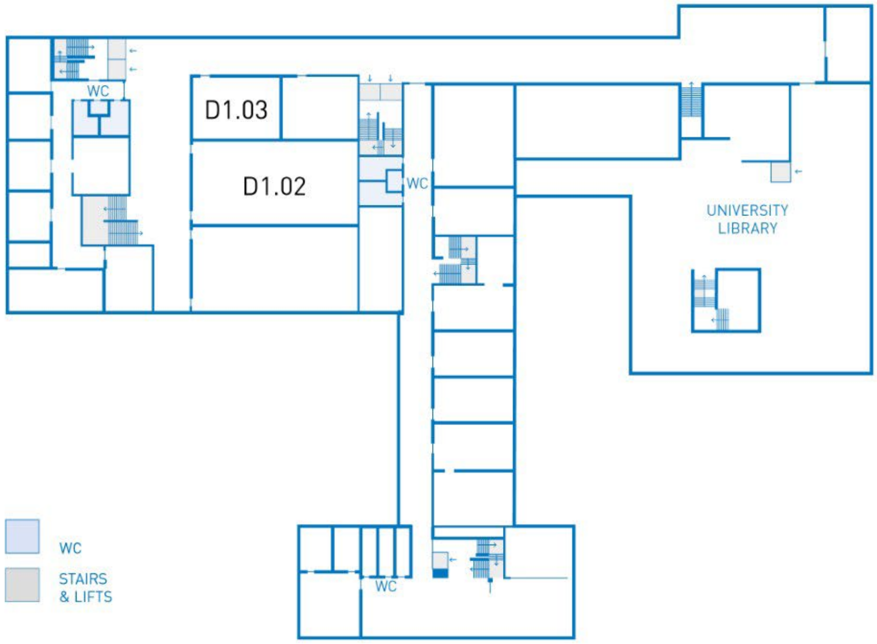

Social Dinner

The social dinner will take place at **Restaurant Fink** (https://www.gasthausfink.it/) in the city centre, Mustergasse 9 / Via della Mostra 9, Bolzano. Start: 8 p.m.

Detailed Technical Programme

Wednesday, September 11th

08:30-09:00	Session: Registration
09:00-09:30	Session: Welcome (chairs: Angelika Peer, Karl Dietrich von Ellenrieder)
09:30-11:00	**Session 1A: Robotics (chairs: Maria Pozzi, Marco Camurri)**
09:30-09:45	Dario Calogero Guastella. Experimental Investigation of Multi-Agent Systems with Micro-robots
09:45-10:00	Davide Tebaldi, Giovanni Braglia and Luigi Biagiotti. A Spatial Sampling Algorithm for Encoding Geometric Information in Demonstrated Trajectories
10:00-10:15	Maria Pozzi, Valerio Bo, Enrico Turco, Leonardo Franco, Gionata Salvietti, Monica Malvezzi and Domenico Prattichizzo. Soft Robotic Hands: Embracing Interaction with the Surrounding Environment
10:15-10:30	Martina Lippi, Michael Welle, Alessandro Marino, Andrea Gasparri and Danica Kragic. Visual Action Planning with Multiple Heterogeneous Agents
10:30-10:45	Alessandra Elisa Sindi Morando, Alessandro Bozzi, Simone Graffione, Enrico Zero and Roberto Sacile. Distributed Nonlinear Rolling Horizon Techniques Applied to Air-Ground Cooperation
10:45-11:00	Andrea Usai and Alessandro Rizzo. Artificial fear for the control of autonomous robots
09:30-11:00	**Session 1B: Vehicles (chairs: Karl Dietrich von Ellenrieder and Michele Pagone)**
09:30-09:45	Michele Pagone, Stefano Favelli, Raffaele Manca, Gabriel Jenner de Faria Orsi, Angelo Bonfitto, Carlo Novara and Andrea Tonoli. A Nonlinear MPC-based Adaptive Cruise Control for Electric Automotive Vehicles
09:45-10:00	Ivo Batkovic, Ankit Gupta, Mario Zanon and Paolo Falcone. Experimental Validation of Safe MPC for Autonomous Driving in Uncertain Environments
10:00-10:15	Mattia Laurini, Irene Saccani, Stefano Ardizzoni, Luca Consolini and Marco Locatelli. A Dynamic Programming approach for road traffic estimation
10:15-10:30	Bhaskar Varma and Karl Von Ellenrieder. Trajectory optimization of multi robot systems using opinion dynamics
10:30-10:45	Massimo Canale, Francesco Cerrito, Alessandro Fasiello and Valentino Razza. Enhancing Reinforcement Learning for Automated Driving through Virtual Lane Logic
10:45-11:00	Davide Tebaldi and Roberto Zanasi. Systematic Modeling of a Steering Vehicle Differential Using Power-Oriented Graphs
11:00-11:30	**Coffee break**
11:30-13:00	**Session 2A: Applications (chairs: Dario Calogero Guastella and Riccardo Caponetto)**
11:30-11:45	Michele Coco, Martina Mammarella, Cesare Donati, Federica Paganelli and Francesco Evangelisti. Huber-based Unscented Kalman Smoother with application to Earth observation missions
11:45-12:00	Federico Baldisseri, Danilo Menegatti and Andrea Wrona. Deep Deterministic Policy Gradient Control of Type 1 Diabetes

12:00-12:15	Chiara Cimolato, Massimo Bellato, Gianluca Selvaggio, Luca Marchetti, Giulia Giordano and Luca Schenato. Model Driven Design of Bacterial Communication Inhibition: from Quorum Sensing to Quorum Quenching
12:15-12:30	Maria Gabriella Xibilia, Luca Patanè, Francesca Sapuppo, Riccardo Caponetto, Marco Calapristi, Antonino Maio, Salvatore Graziani and Carlo Trigona. A Multiphysics Framework for Bacterial Cellulose Sensor Modeling
12:30-12:45	Alessandro Borri, Pasquale Palumbo and Federico Papa. Tumour growth control: analysis of alternative approaches
12:45-13:00	Gabriel Ferreira, Fabrizio Dabbene, Chiara Ravazzi and Giuseppe Calafiore. Joint Optimization for OFDMA Heterogeneous Networks with stochastic channel-gains
11:30-13:00	**Session 2B: Robotics (chairs: Dario Sanalitro and Tommaso Lisini)**
11:30-11:45	Tommaso Lisini Baldi, Enrico Turco, Chiara Castellani, Valerio Bo and Domenico Prattichizzo. Reducing Cognitive Load through a Data-Driven Shared Control Approach for Teleoperating Robot Swarms
11:45-12:00	Dario Sanalitro and Maide Bucolo. Hybrid Brain Computer Interface for Robot Control
12:00-12:15	Isacco Zappa, Andrea Maria Zanchettin and Paolo Rocco. Cobots Understanding Skills Programmed by Demonstration
12:15-12:30	Nicole D'Aurizio, Tommaso Lisini and Domenico Prattichizzo. Human Augmentation: Controlling Supernumerary Robotic Limbs via Body Redundancy
12:30-12:45	Bernardo Brogi, Giovanni Cortigiani, Nicole D'Aurizio, Alberto Villani, Domenico Prattichizzo and Tommaso Lisini. The Avatarm: Interacting in the Physical Metaverse via Robotics, Diminished Reality, and Haptics
12:45-13:00	Amir Jaberi, Seyed Mohsen Hosseini, Oliver Kutz and Angelika Peer. Robust Optimal Planning of Human-Robot Collaborative Operations
13:15-14:30	**Session : Lunch**
14:30-16:00	**Session 3A: Control theory (chairs: Carlo Famoso and Alessandro Baldini)**
14:30-14:45	Mirko Mazzoleni, Luca Maurelli, Simone Formentin and Fabio Previdi. A comparison of indirect and direct filter designs from data for LTI systems: the effect of unknown noise covariance matrices
14:45-15:00	Folco Giorgetti, Francesco Ferrante and Mario L. Fravolini. Anti-Windup-Like Compensator Design for Continuous-Time Systems affected by Unknown Nonlinearities and Input Saturation
15:00-15:15	Simone Betteti, Giacomo Baggio and Sandro Zampieri. Design and Stability of Dynamical Memory Networks: From Hopfield to Firing Rate Models
15:15-15:30	Arturo Buscarino, Carlo Famoso and Luigi Fortuna. Analysis and control of synaptic complex networks operating at high dimensionality
15:30-15:45	Alessandro Baldini, Riccardo Felicetti, Alessandro Freddi, Sauro Longhi and Andrea Monteriù. Observer-based residual generator for fault detection and isolation of convex sets
15:45-16:00	Riccardo Caponetto, Giovanni Dongola, Salvatore Graziani, Luca Patanè, Francesca Sapuppo and Maria Gabriella Xibilia. Hardware In the Loop simulation of PIλDμ controller
14:30-16:00	**Session 3B: DAuSy session (chairs: Raffaele Carli, Mariagrazia Dotoli)**
	Nadia Naz. Analysis of dosimetric parameters of linear accelerator

	Zohreh Shahrouei and Elio Usai. Management and automation systems for energy management in buildings and industrial processes
	Pietro Maria Marvulli, Domenico Buongiorno, Raffaele Carli, Mariagrazia Dotoli and Vitoantonio Bevilacqua. Autonomous Intelligent System for Predicting Response to TACE in Treating Hepatocellular Carcinoma
	Claudia Delprete, Domenico Buongiorno, Raffaele Carli, Mariagrazia Dotoli and Vitoantonio Bevilacqua. Autonomous Intelligent Systems for Polyp Detection and Segmentation in Colonoscopy
	Gabriele Gemignani, Margherita Bongiorni and Lorenzo Pollini. An Energy-aware Decision-making scheme for Mobile Robots on a Graph Map based on Deep Reinforcement Learning
	Valeriana Mancazzo, Elena Sibilano, Antonio Brunetti, Raffaele Carli, Mariagrazia Dotoli and Vitoantonio Bevilacqua. Intelligent Systems for Predicting Disability Progression in Multiple Sclerosis Using Motor Evoked Potentials and Digital Twin Technology
	Francesco Campregher and Antonio Visioli. Advanced control strategies with applications to sustainable bioprocesses
	Mahsa Ghavami, Davide Liuzza, Elisa Mostacciuolo, Luigi Iannelli and Francesco Vasca. A mixed-integer charging schedule for electric vehicles with request-dependent pricing
	Vittoria Socci and Chiara Mocenni. An Agent-Based Model to foster Citizens’ Sustainable Behavior in the Italian City of Siena
	Mohamed Mahmoud Abdelwahab Mohamed, Giulio Giacomuzzo, Alberto Dalla Libera and Ruggero Carli. Adaptive Robust Controller for handling Unknown Uncertainty of Robotic Manipulators
	Michela Prunella, Nicola Altini, Paolo Scarabaggio, Raffaele Carli, Mariagrazia Dotoli and Vitoantonio Bevilacqua. A quantitative systems biology approach to characterize advanced gastric cancer response
	Angelo Accetta, Maurizio Cirrinzione, Silvia Di Girolamo, Filippo D'Ippolito, Marcello Pucci and Antonino Sferlazza. Robust Nonlinear Control for Induction Motor Drives Based on Adaptive Disturbance Compensation
	Simone Gentile, Danilo Menegatti, Andrea Wrona, Antonio Di Paola and Alessandro Giuseppi. Deep Reinforcement Learning Platooning Control of Non-Cooperative Autonomous Vehicles in a Mixed Traffic Environment
	Denis Tognolo, Francesco Visentin and Riccardo Muradore. Vision-based Autonomous Navigation in Agricultural Rows
	Pierluigi Francesco De Paola, Jared Miller, Alessandro Borri, Alessia Paglialonga and Fabrizio Dabbene. A control system framework for counterfactuals: an optimization-based approach
	Amarnath Venkatachalam, Lucia Valentina Gambuzza, Carlo Famoso, Ludovico Minati, Giovanni Russo and Mattia Frasca. Recovering the governing equations of nonlinear dynamical systems by sparse identification from experimental data
	Sebastiano Taddei, Mattia Piccinini, Edoardo Pagot and Francesco Biral. Artificial Racing Coach: teaching humans how to maximize a racing vehicle's performance and drive at its limits
	Daniel-Costel Bouleanu, Costin Badica and Giancarlo Fortino. Multi-agent Systems Methodologies and Frameworks for Edge-AI in Smart Environments

	Mojtaba Porghoveh, Raffaele Carli and Mariagrazia Dotoli. Drone as a Service in Logistics: a Review of Optimization and Control Techniques
	Sara Gomiero and Karl Dietrich von Ellenrieder. Chattering-free Sliding Mode Control for Position and Attitude Tracking of a Quadrotor with a Cable-Suspended Load
	Mohammad Jeddi and Paolo Falcone. Safety-driven mixed model and learning-based motion planning and control of autonomous systems
	Alessandro Di Biase, Renat Kermenov, Sauro Longhi and Andrea Bonci. Human-robot co-transport of flexible materials using deformation constraints
	Giulia D'Addato, Daniele Fontanelli and Luigi Palopoli. Socially-Aware Opinion-Based Navigation with Oval Limit Cycles for Human-Robot Interaction
	Pietro Bonsanto, Mattia Mattioni, Alessio Iovine, Elena De Santis and Maria Domenica Di Benedetto. Mesoscopic digital control for Practical String Stability of vehicular platoons
	Alessandro Giuseppi, Antonio Di Paola, Alessandro Santopaolo, Syed Saad Saif, Federico Fiorini and Antonio Pietrabissa. ARIES: An Intelligent System for Landslide and Wildfire Risk Management
	Giorgio Manca, Mario Sassano and Sergio Galeani. Enhancing Extended Kalman Filters Performance through Covariance Estimation
	Sajjad Miralizadeh Jalalat, Alberto Cavallo and Antonio Russo. Safe Reinforcement Learning-Based Voltage Control in Nonlinear Power Systems
	Marco Perin, Angelo Cenedese and Francesco Bullo. Adaptive Deep Learning Controller for Nonlinear Systems with Contraction Theory
	Paul Christian Tesso Woafo. A novel multiobjective optimal LQ control strategy for energy harvesting in vehicle suspension systems
	Anna Tagliaferri, Bajramshahe Shkodra, Martina Aurora Costa Angeli, Mattia Petrelli, Antonio Altana, Pietro Ibba, Paolo Lugli and Luisa Petti. Improved stability of carbon-nanotube electrolyte-gated field-effect transistor-based sensors
	Lucrezia Manieri, Alessandro Falsone and Maria Prandini. A dual bisection approach to economic dispatch of generators with prohibited operating zones
16:00-16:30	**Coffee break**
16:30-18:30	**Session 4A: Optimization (chairs: Laura Giarré and Enrico Bertolazzi)**
16:30-16:45	Seyed Mohsen Hosseini and Angelika Peer. An Adaptive Heuristic Approach to Wood Sawing Optimization
16:45-17:00	Alessandro Del Duca and Fredy Ruiz. Distributed stochastic optimization with uncertain coupling constraint
17:00-17:15	Enrico Bertolazzi and Francesco Biral. Solve Optimal Control Problems with an hybrid Indirect/Direct method
17:15-17:30	Vito Cerone, Sophie M. Fosson, Simone Pirrera and Diego Regruto Tomalino. A control theory approach to convex optimization with inequality constraints
17:30-17:45	Mattia Alborghetti, Giulio Montecchio, Lorenzo Jr. Sabug, Lorenzo Fagiano and Fredy Ruiz. Feedback Control of the Exploitation-Exploration Trade-off in Set Membership Global Optimization

17:45-18:00	Renato Quartullo, Gianni Bianchini, Andrea Garulli and Antonello Giannitrapani. Robust Variable-Horizon MPC with Adaptive Terminal Constraints
18:00-18:15	Lorenzo Calogero, Michele Pagone and Alessandro Rizzo. Pseudo-Transient Continuation for Enhanced Quadratic Programming and Optimal Control
16:30-18:30	**Session 4B: Control of energy systems (chairs: Alessio La Bella and Giulio Ferro)**
16:30-16:45	Marco Capelletti and Giuseppe De Nicolao. Forecasting Wind Power: A Comparative Study of Parametric and Non-parametric Approaches Using Real-World Data
16:45-17:00	Luca Schenato, Jiali Wang and Yang Tang. Humans-in-the-Building: Getting Rid of Thermostats in Comfort-Based Energy Management Control Systems
17:00-17:15	Yassine Ennassiri, Giulio Ferro, Loredana Magistri and Michela Robba. Optimal scheduling and real-time control of a microgrid with an electrolyzer and a fuel cell systems using a reference governor approach
17:15-17:30	Sofia Trombini and Lorenzo Fagiano. On the kite-platform interactions in offshore Airborne Wind Energy Systems: Frequency analysis and control approach
17:30-17:45	Nicola Mignoni, Juan Martinez-Piazuelo, Raffaele Carli, Carlos Ocampo-Martinez, Nicanor Quijano and Mariagrazia Dotoli. A Game-Theoretical Control Framework for Transactive Energy Trading in Energy Communities
17:45-18:00	Giuseppe Olivieri, Gaetano Volpe, Agostino Marcello Mangini and Maria Pia Fanti. A User Based HVAC System Management Through Blockchain Technology and Model Predictive Control
18:00-18:15	Laura Boca de Giuli, Alessio La Bella and Riccardo Scattolini. Modeling and Predictive Control of District Heating Systems via Physics-Informed Recurrent Neural Networks
18:15-18:30	Lucrezia Manieri, Alessandro Falsone and Maria Prandini. A dual bisection approach to economic dispatch of generators with prohibited operating zones
18:30-20:00	**Cocktail event**

Thursday, September 12th

09:00-10:30	**Session 5A: Machine learning and control (chairs: Ciro Natale and Gabriele Costante)**
09:00-09:15	Marco Calapristi, Luca Patanè, Francesca Sapuppo, Riccardo Caponetto and Maria Gabriella Xibilia. Symbolic regression for industrial applications: an NN-based approach
09:15-09:30	Paolo Scarabaggio, Nicola Mignoni, Raffaele Carli and Mariagrazia Dotoli. On the Existence of Equilibria in Learning-Based Games
09:30-09:45	Sampath Kumar Mulagaleti and Andrea Del Prete. Sample Efficient Certification of Discrete-Time Barrier Functions
09:45-10:00	Diego Deplano, Mauro Franceschelli and Alessandro Giua. Stability of Nonexpansive Monotone Systems and Application to Recurrent Neural Networks
10:00-10:15	Irene Schimperna and Lalo Magni. Stability and constraint satisfaction in Recurrent Neural Network based Model Predictive Control
09:00-10:30	**Session 5B: Vehicles (chairs: Gaetano Volpe and Agostino Marcello Mangini)**
09:00-09:15	Elisa Gaetan, Laura Giarré and Paolo Falcone. Scenario-Based Model Predictive Control for vehicle interactions in Highway setting

09:15-09:30	Erica Salvato, Lorenzo Elia, Gianfranco Fenu and Thomas Parisini. Stop-and-Go Traffic Wave Attenuation: A Shared Control Approach
09:30-09:45	Stefano Ardizzoni, Mattia Laurini, Rafael Praxedes, Luca Consolini and Marco Locatelli. Identification of Cyclists' Route Choice Criteria
09:45-10:00	Francesco Paparella, Giuseppe Olivieri, Gaetano Volpe, Agostino Marcello Mangini and Maria Pia Fanti. A Deep Reinforcement Learning Approach for Route Planning of Autonomous Vehicles
10:00-10:15	Antonio Furchì, Martina Lippi, Renzo Fabrizio Carpio and Andrea Gasparri. Route Optimization in Precision Agriculture Settings: a Multi-Steiner TSP Formulation
10:15-10:30	Diego Deplano, Carla Seatzu and Mauro Franceschelli. A Distributed Online Heuristic for a Large-scale Workforce Task Assignment and Multi-Vehicle Routing Problem
09:00-10:30	**Session 5C: Path planning (chairs: Mattia Piccinini and Nicola Mimmo)**
09:00-09:15	Mattia Piccinini, Simon Gottschalk, Matthias Gerdts and Francesco Biral. Neural Motion Primitives for Online Time-Optimal Vehicle Trajectory Planning
09:15-09:30	Filip Dyba and Marco Frego. Following Zero-curvature Paths Using the Non-orthogonal Bishop Parametrization
09:30-09:45	Giordana Bucchioni, Michele Pagone and Carlo Novara. Autonomous Lunar Rendezvous Trajectory Planning and Control Using Nonlinear MPC and Pontryagin's Principle
09:45-10:00	Mattia Piazza, Enrico Bertolazzi and Marco Frego. Efficient Path Planning Solutions for the Three Point Dubins Problem using Non-Smooth Optimization
10:00-10:15	Nicola Mimmo, Marco Frego and Angelika Peer. Tracking of Clothoids via Internal Model Principle
10:15-10:30	Stefano Ardizzoni, Luca Consolini, Mattia Laurini and Marco Locatelli. Time-optimal speed planning under jerk constraints
10:30-11:00	**Coffee break**
11:00-12:30	**Session 6A: Modelling and estimation (chairs: Simone Guarino and Diego Deplano)**
11:00-11:15	Vito Cerone, Sophie M. Fosson, Diego Regruto and Francesco Ripa. A Lasso approach to secure state estimation for cyber-physical systems
11:15-11:30	Camilla Fioravanti, Stefano Panzieri and Gabriele Oliva. Negativizability: a Useful Property for Distributed State Estimation and Control in Cyber-Physical Systems
11:30-11:45	Rami Katz, Giulia Giordano and Dmitry Batenkov. Data-driven delay estimation in reaction-diffusion systems
11:45-12:00	Matteo Scandella, Alessio Moreschini and Thomas Parisini. Nonlinear Data-Driven Moment Matching using RKHS
12:00-12:15	Simone Guarino, Ernesto del Prete, Luca Faramondi, Francesco Flammini and Roberto Setola. Two novel Frameworks for Cyber-Physical Anomaly Detection in Industrial Control Systems
11:00-12:30	**Session 6B: Control theory (chairs: Lorenzo Zino and Mattia Laurini)**
11:00-11:15	Matteo Aicardi, Alessandro Bozzi, Simone Graffione, Roberto Sacile and Enrico Zero. Distributed Control of a System of Systems via Consensus Alternating Direction Method of Multipliers: a Quadruple Tank Application
11:15-11:30	Andres Felipe Cordoba Pacheco and Fredy Ruiz. Data-Driven Controller Tuning for MIMO Systems: A Set-Membership Approach

11:30-11:45	Marino Pavone, Nicola Epicoco, Giordano Pola and Andrea Manno. Modelling Sensors Degradation for Water Quality Monitoring
11:45-12:00	Lorenzo Zino, Daniele Vilone, Francesca Giardini and Ming Cao. An opinion dynamics model for collective risk perception
12:00-12:15	Giulia Di Credico, Luca Consolini, Mattia Laurini, Marco Locatelli, Marco Milanesi, Michele Schiavo and Antonio Visioli. PK-PD model identification with a Branch and Bound algorithm
12:15-12:30	Anton Proskurnikov. Multidimensional Opinion Dynamics with General Confidence Sets
11:00-12:30	**Session 6C: Control of actuators (chairs: Paolo Roberto Massenio and Francesco Ferracuti)**
11:00-11:15	Paolo Roberto Massenio, Giovanni Soleti, Carmen Perri, Gianluca Rizzello and David Naso. Control and Driving Technologies for Soft Robots based on Dielectric Elastomer Actuators
11:15-11:30	Gionata Cimini, Riccardo Felicetti, Francesco Ferracuti, Luca Cavanini and Andrea Monteriù. Adaptive Reference Governor for DC-DC Converters based on Model Predictive Control
11:30-11:45	Davide Tebaldi and Roberto Zanasi. Model-Based Optimal Control of Modular Multilevel Converters Using Ideal Capacitor Voltages Reference
11:45-12:00	Beatrice Zambotti, Yassine Ariba, Frederic Gouaisbaut and Luca Zaccarian. Modeling and control of an impacting electromagnetic actuator via hybrid Lyapunov techniques
12:00-12:15	Augusto Bozza, Graziana Cavone, Raffaele Carli and Mariagrazia Dotoli. PWM-Based Energy-Efficient Adaptive Control for Multi-Chamber Hydraulic Servo Actuators
12:30-14:00	**Session : Lunch**
14:00-15:30	**Session 7A: Energy management in vehicles (chairs: Maria Gabriella Xibilia and Luca Patanè)**
14:00-14:15	Stefano Radrizzani, Giorgio Riva, Giulio Panzani, Matteo Corno and Sergio M. Savaresi. Exploiting the potential of hybrid batteries in racing: optimal sizing and energy management
14:15-14:30	Alessio La Bella, Gian Paolo Incremona, Aline Cristiane Buzzi and Patrizio Colaneri. Energy Management System Based on Model Predictive Control for Battery-Powered Trains Under Catenary-Free Conditions
14:30-14:45	Luca Ambrosino, Giuseppe Calafiore, Khai Manh Nguyen, Riadh Zorgati, Doanh Nguyen-Ngoc and Laurent El Ghaoui. Optimizing electric vehicles charging through smart energy allocation and cost-saving
14:45-15:00	Luca Patanè, Francesca Sapuppo, Marco Calapristi, Antonino Maio, Antonino Comi, Giuseppe Napoli, Riccardo Caponetto and Maria Gabriella Xibilia. Predictive Models for Vehicle-to-Grid Available Aggregated Capacity Prediction
15:00-15:15	Valerio Brunacci, Alberto Dionigi, Alessio De Angelis and Gabriele Costante. Infrastructure-less UWB-based Relative Localization: an Active Approach
14:00-15:30	**Session 7B: Computer vision and control (chairs: Nicole D'Aurizio and Marco Costanzo)**
14:00-14:15	Mohammadamin Rezaei Naghadehi, Gioacchino Manfredi, Vito Andrea Racanelli, Luca De Cicco and Saverio Mascolo. Decentralized Control of UAV Swarms for Bandwidth-aware Video Surveillance using NMPC
14:15-14:30	Giovanni Cortigiani, Bernardo Brogi, Alberto Villani, Nicole D'Aurizio, Domenico Prattichizzo and Tommaso Lisini. Online Minimization of Robot Obstruction in Eye-to-Hand Camera View
14:30-14:45	Marco Costanzo, Giuseppe De Maria and Ciro Natale. Homography-Based Sampled-Data Visual Servoing

14:45-15:00	Francesco Crocetti, Marco Legittimo, Giuseeppe Mollica, Mario Luca Fravolini, Gabriele Costante and Paolo Valigi. Deep Learning-Based Feature Extraction for Robust Visual SLAM in Challenging Indoor Environments
15:00-15:15	Ashutosh Arora and Tanvi Saxena. Real-Time Hand Pose Extraction for Human-Computer Interaction Using Computer Vision
14:00-14:45	**Session 7C: Education (chairs: Cristiano Maria Verrelli and Laura Screpanti)**
14:00-14:15	Cristiano Maria Verrelli. Recent Developments in Dynamical-System Analysis (Self-Similarity and Time-Harmonic Structures) and Educational Activities (Kids in Control)
14:15-14:30	Laura Screpanti, Martina Morano and David Scaradozzi. System identification at university with blended learning techniques and advanced assessment strategies
14:30-14:45	Laura Screpanti, David Scaradozzi, Damiano Varagnolo and Adriano Fagiolini. Innovative Solutions for Collaborative Teaching in Automatic Control: Insights from IFAC TC 9.4
14:45-15:30	**Session 7D: Applications (chairs: Enrico Zero and Camilla Fioravanti)**
14:45-15:00	Enrico Zero, Alessandro Bozzi, Simone Graffione and Roberto Sacile. EEG Data-Driven Control and Risk Prediction in Roundabout Maneuvers
15:00-15:15	Camilla Fioravanti, Luca Faramondi, Gabriele Oliva and Roberto Setola. A Lightweight Encryption Approach for Data Confidentiality in Critical Infrastructures
15:15-15:30	Giordana Bucchioni and Lorenzo Pollini. MUSAPOEM: Multi Satellite Proximity Operations for Rendezvous and Docking Missions in Earth and Moon Orbits
15:30-16:00	**Coffee break**
16:00-18:00	Round table: Facts and myths in machine-learning-based control (chairs: Karl Dietrich von Ellenrieder, Angelika Peer) Participants of round table: • Alessandro Chiuso - Università di Padova • Simone Formentin - Politecnico di Milano • Matteo Saveriano - University of Trento • Mario Zanon - IMT School for Advanced Studies Lucca
20:00-23:00	**Social dinner**

Friday, September 13th

09:00-10:00	PhD award session (chairs: Simona Sacone and Alberto Leva)
10:00-11:00	Assembly SIDRA (chair: Sauro Longhi)
11:00-11:30	**Coffee break**
11:30-13:00	Assembly SIDRA (chair: Sauro Longhi)
13:00-14:30	**Lunch**

Session 1A: Robotics

Experimental Investigation of Multi-Agent Systems with Micro-robots

Dario Calogero Guastella

Dep. of Electrical Electronic and Computer Engineering
University of Catania, 95125, Catania, Italy

Abstract: Many relevant problems in multi-agent systems (MAS) such as formation control and coordination can be addressed with different solutions, including either centralized or distributed approaches, protocols based on either absolute or relative information, and many others. However, most of the related works address these topics only at a theoretical level, without investigating the practical applicability of the proposed control strategies. The aim of this paper is to showcase our recent works on the implementation of multi-agent systems control with an experimental setup based on a set of commercially available micro-robots and a vision-based position tracking system. With such a setup we were able to test and characterize face-to-face interaction dynamics and synchronization of moving chaotic oscillators in a real yet controllable multi-agent robotic implementation.

Keywords: Face-to-face interaction dynamics; Distributed Control; Synchronization; Chaotic oscillators; Time-varying networks

---

1. INTRODUCTION

In this paper we present our recent investigations on multi-agent robotic systems (Tomaselli et al., 2023, 2024) via an experimental setup that we have realized using a team of Elisa-3 robots [1]. Elisa-3 robots are small differential-drive robots, particularly suited for research applications in the field of cooperative robotics and multi-agent systems. Our objective is to provide a proof-of-concept illustrating the practical utility of theoretical models in a real-world setting, encompassing factors typically overlooked in numerical simulations, such as parameter mismatches, noise, message loss, and deviations from predetermined movements. Uncertainty in both sensing and actuation plays a major role when moving from simulated to real-world implementation, as environment changes (e.g., lighting conditions, wheel-floor friction, etc.) or robot changes (e.g., battery level, wheels alignment, etc.) may affect the overall system's behavior. Concerning robot communication, percentage of lost messages varies from 1% up to 63% when the time interval devoted to message exchange is 1000 ms and 350 ms.

2. FACE-TO-FACE INTERACTION DYNAMICS

In Tomaselli et al. (2023) we propose a robotic implementation of the attractiveness-based model for face-to-face interaction networks introduced in Starnini et al. (2013). The model is based on simple mechanisms that govern the interactions among the units and enable the formation of dynamic groups, as observed in empirical data sets of human gatherings.

We find that, under a variety of different experimental conditions, the multi-robot system displays a distribution of the contact duration and of the time interval between consecutive contacts similar to the theoretical model. Interestingly, the same features in the face-to-face interactions also emerge when the multi-robot team is operated in challenging conditions. For instance, this is the case when a very short time is allocated to receive messages from other robots, causing the loss of many interactions that still do not hamper the emergence of the face-to-face dynamics. Altogether these findings demonstrate the robustness of the attractiveness-based algorithm towards physical implementations. Fig. 1 includes five snapshots of an experiment, qualitatively showing the dynamical evolution of the formation of groups in the system.

3. SYNCHRONIZATION OF MOBILE CHAOTIC ROBOTS

Synchronization of chaotic oscillators associated to mobile agents has been investigated in Tomaselli et al. (2024). In these experiments we use 6 Elisa-3 robots moving in an arena of size $L_{y_1} \times L_{y_2}$ as shown in Fig. 2. The size of the arena is varied in order to change the agent density $\rho = N/(L_{y_1} L_{y_2})$. An IR and an RGB camera are positioned above the arena, to capture the whole area where the robots move. In our model we associate to each unit $i = 1, \ldots, N$ a dynamical state $\mathbf{x}_i(t) \in \mathbb{R}^n$. The evolution of these variables is governed by a chaotic dynamics given by the following system of coupled Rössler oscillators (Rössler, 1976):

$$\begin{cases} \dot{x}_{i,1} = -x_{i,2} - x_{i,3} \\ \dot{x}_{i,2} = x_{i,1} + a x_{i,2} + \sigma \displaystyle\sum_{j=1}^{N} \mathcal{A}_{ij}(t)(x_{j,2} - x_{i,2}) \\ \dot{x}_{i,3} = b + x_{i,3}(x_{i,1} - c) \end{cases} \tag{1}$$

with $i = 1, \ldots, N$. The parameters a, b, and c are set to $a = 0.2$, $b = 0.2$, $c = 7$, such that the uncoupled dynamics is chaotic. When coupled through a network with static links, this system has a master stability function of type II, which means that synchronization may be achieved for any network with large enough coupling (Huang et al., 2009). In the considered model, the evolution of the dynamical variables of the oscillators is influenced by the agent motion through the matrix $\mathcal{A}(t)$.

We exploit the robots' onboard IR transceivers to enable local communication among them and realize a fully decentralized and distributed control law for synchronization. Here, synchronous dynamics emerge under given condi-

---

[1] https://www.gctronic.com/doc/index.php/Elisa-3

Fig. 1. Dynamical evolution of group formation in an experiment made with 6 Elisa-3 robots. The units lighting up with red (green) light are interacting (communicating) each other, while no light indicates that the robot is performing a random walk. (a) The robots form a group of two units that are engaged into a face-to-face interaction. (b) A third robot is communicating with one of the two units of the group. (c) The group is now formed by three interacting units. (d) Another robot in the area is communicating with units in the group. (e) The previous group breaks apart and a new group of two units forms, while the other two robots, belonging to the previous group, move away from the area of the meeting.

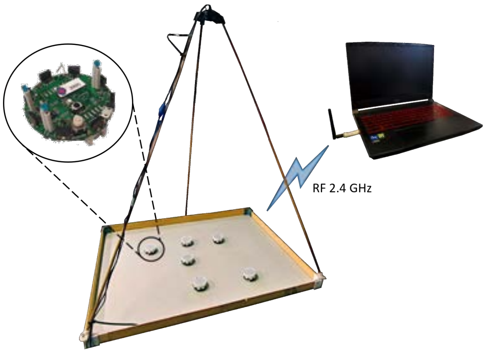

Fig. 2. Experimental setup with 6 Elisa-3 robots in a 80 × 60 cm arena.

tions on the characteristic parameters of agent motion, such as their density and speed, and on the system dynamics, such as the coupling gain. The underlying network of interactions can be characterized in terms of a time-varying structure where motion inherits the main topological features of the graph (Ghosh et al., 2022). We contrast our results with a theoretical analysis based on the system master stability function (Frasca et al., 2008) and show that the mismatches and non-idealities of the system do not hamper synchronization of all units. In particular, we find that a regime of robust synchronization emerges also in the presence of a significant portion of lost messages in the local communication among robots.

The team of 6 Elisa-3 robots is shown in Fig. 3(a), where different colors reflect different values of the chaotic state variable. In Fig. 3(b) the time evolution of the state variables $x_{i,1}(t)$ is reported. In this case the coupling strength is fixed to $\sigma = 2$. After a transient, the state variables converge to a common trajectory exhibiting a small synchronization error.

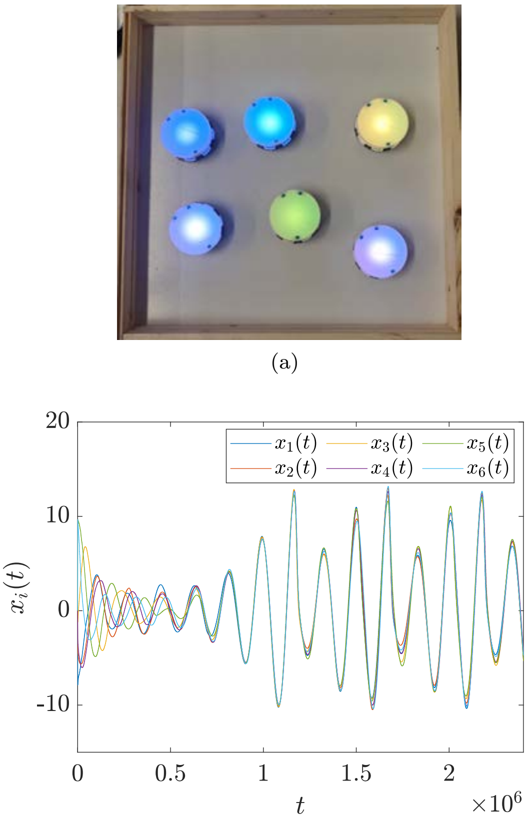

(a)

(b)

Fig. 3. (a) Picture of the team of 6 Elisa-3 robots used to study synchronization in coupled chaotic oscillators associated to mobile agents. (b) State variables of the oscillators showing the emergence of synchronization as the result of time-varying interactions.

ACKNOWLEDGEMENTS

This work was partially supported by University of Catania, through the PIA.CE.RI. framework, starting grant for RTDb. D.C. Guastella acknowledges support by the project PON R&I REACT-EU.

REFERENCES

Frasca, M., Buscarino, A., Rizzo, A., Fortuna, L., and Boccaletti, S. (2008). Synchronization of moving chaotic agents. *Physical Review Letters*, 100(4), 044102.

Ghosh, D., Frasca, M., Rizzo, A., Majhi, S., Rakshit, S., Alfaro-Bittner, K., and Boccaletti, S. (2022). The synchronized dynamics of time-varying networks. *Physics Reports*, 949, 1–63.

Huang, L., Chen, Q., Lai, Y.C., and Pecora, L.M. (2009). Generic behavior of master-stability functions in coupled nonlinear dynamical systems. *Physical Review E*, 80(3), 036204.

Rössler, O.E. (1976). An equation for continuous chaos. *Physics Letters A*, 57(5), 397–398.

Starnini, M., Baronchelli, A., and Pastor-Satorras, R. (2013). Modeling human dynamics of face-to-face interaction networks. *Physical Review Letters*, 110(16), 168701.

Tomaselli, C., Guastella, D.C., Muscato, G., Frasca, M., and Gambuzza, L.V. (2023). A multi-robot system for the study of face-to-face interaction dynamics. *IEEE Robotics and Automation Letters*, 8(10), 6715–6722.

Tomaselli, C., Guastella, D.C., Muscato, G., Minati, L., Frasca, M., and Gambuzza, L.V. (2024). Synchronization of moving chaotic robots. *IEEE Robotics and Automation Letters*, 9(7), 6496–6503.

A Spatial Sampling Algorithm for Encoding Geometric Information in Demonstrated Trajectories

Davide Tebaldi, Giovanni Braglia and Luigi Biagiotti

***Abstract*—This extended abstract addresses the proposal of a new spatial sampling algorithm for encoding geometric information through arc-length parametrization in demonstrated trajectories.**

I. INTRODUCTION

A wide variety of applications utilize Dynamic Movement Primitives (DMP) as a core for a Learning by Demonstration (LbD) framework to effectively reproduce the reference trajectories in both space and time [1], [2]:

$$\tau \dot{z}(t) = \alpha[\beta(g - y(t)) - z(t)] + f(s(t)), \tag{1}$$

$$\tau \dot{y}(t) = z(t), \tag{2}$$

$$\tau \dot{s}(t) = -\delta s(t), \tag{3}$$

In particular, one can set the Canonical System (CS) to ensure that the output of the DMP accurately reproduces the reference trajectory, including its time dependency [3]. This means that, if the user stops while recording the reference trajectory, this information will also be included in the parameterization of the desired trajectory. In the classical formulation of DMP, the duration of this pausing phase can be shortened or extended by appropriately adjusting a proper parameter τ. However, it will persist while reproducing the desired trajectory [4]. This issue becomes especially significant in applications where recording solely the traveled space is necessary, i.e., encoding a desired path irrespective of velocity and acceleration profiles. In [5], the reference trajectory is recorded in two steps by teaching the path and the velocity profiles separately. Another example of an application based on the demonstrated geometric path can be found in [6]. In this work, the authors introduce a varying scaling factor of the time in the DMP formulation, modulated by the tangent component of an external force. However, when the velocity along the curve slows down to zero during the demonstration, the tangent vector to the curve tends to zero as well. In instances where the velocity during the demonstration is exactly zero, the tangent direction is undefined, requiring special treatment in such cases. To fix the above-mentioned issues, we propose to parameterize the forcing term $f^{\star}(s)$ starting from an expression of the learned trajectory, which is a function of a curvilinear abscissa, i.e., the length along the curve, rather than time. This can be achieved by considering a novel sampling algorithm for the sequence of demonstrated positions, named "spatial sampling", that records the points when they are at a prescribed distance Δ.

II. SPATIAL SAMPLING ALGORITHM

The proposed procedure is based on two steps:

1) Starting from the sequence of samples obtained by recording the demonstrated trajectory $\boldsymbol{y}_r(t) = [y_{r_x}(t),\, y_{r_y}(t),\, y_{r_z}(t)]^T$ with constant period T,

$$\boldsymbol{y}_{T,k} = \boldsymbol{y}_r(t_k) = \boldsymbol{y}_r(kT) \quad k = 0, \ldots, N,$$

a continuous-time function $\boldsymbol{y}_L(t)$ is built by applying a First-Order Hold (FOH) on it [7]. In this way, the function $\boldsymbol{y}_L(t)$ linearly interpolates the samples obtained from $\boldsymbol{y}_r(t)$, and if the sampling period T is small enough one can assume that $\boldsymbol{y}_L(t) \simeq \boldsymbol{y}_r(t)$.

2) In the second step of this procedure, a new sequence $\boldsymbol{y}_{\Delta,k}$ is obtained by imposing that $\boldsymbol{y}_{\Delta,0} = \boldsymbol{y}_L(0)$ and then, for $k > 0$, $\boldsymbol{y}_{\Delta,k} = \boldsymbol{y}_L(t_{\Delta_k})$, where t_{Δ_k} is the time value that guarantees

$$\|\boldsymbol{y}_{\Delta,k} - \boldsymbol{y}_{\Delta,k-1}\| = \Delta, \text{ for } k = 1, \ldots, M. \tag{4}$$

The free parameter Δ defines the geometric distance between consecutive samples.

Because of the condition (4), the total distance between the first point $\boldsymbol{y}_{\Delta,0}$ and the generic k-th point $\boldsymbol{y}_{\Delta,k}$, $k > 0$, is simply given by $k\Delta$. This distance approximates the length of the curve $\boldsymbol{y}_L(t)$ at the time instant t_{Δ_k}, with a precision that depends on the value of Δ. Therefore, for Δ small enough, the new sampling mechanism induces a mapping between the length $s_k = k\Delta$ and the position along the approximating linear curve $\boldsymbol{y}_L$, i.e.

$$\boldsymbol{y}_{\Delta,k} = \boldsymbol{y}_L(t_{\Delta_k}) \text{ with } t_{\Delta_k} = \gamma^{-1}(s_k) \tag{5}$$

where $s = \gamma(t)$ is the particular timing law imposed during the demonstration of the trajectory which describes how the robot moves along the imposed geometric path, being variable s the arc-length parameterization of the curve. In conclusion, given the analytical expression of the trajectory parameterized with respect to the curvilinear abscissa $\hat{\boldsymbol{y}}_r(s) \approx \hat{\boldsymbol{y}}_L(s) = \boldsymbol{y}_L(\gamma^{-1}(s))$, the sequence $\boldsymbol{y}_{\Delta,k}$

The authors are with the Department of Engineering "Enzo Ferrari", University of Modena and Reggio Emilia, Modena, Italy. `davide.tebaldi@unimore.it, giovanni.braglia@unimore.it, luigi.biagiotti@unimore.it`

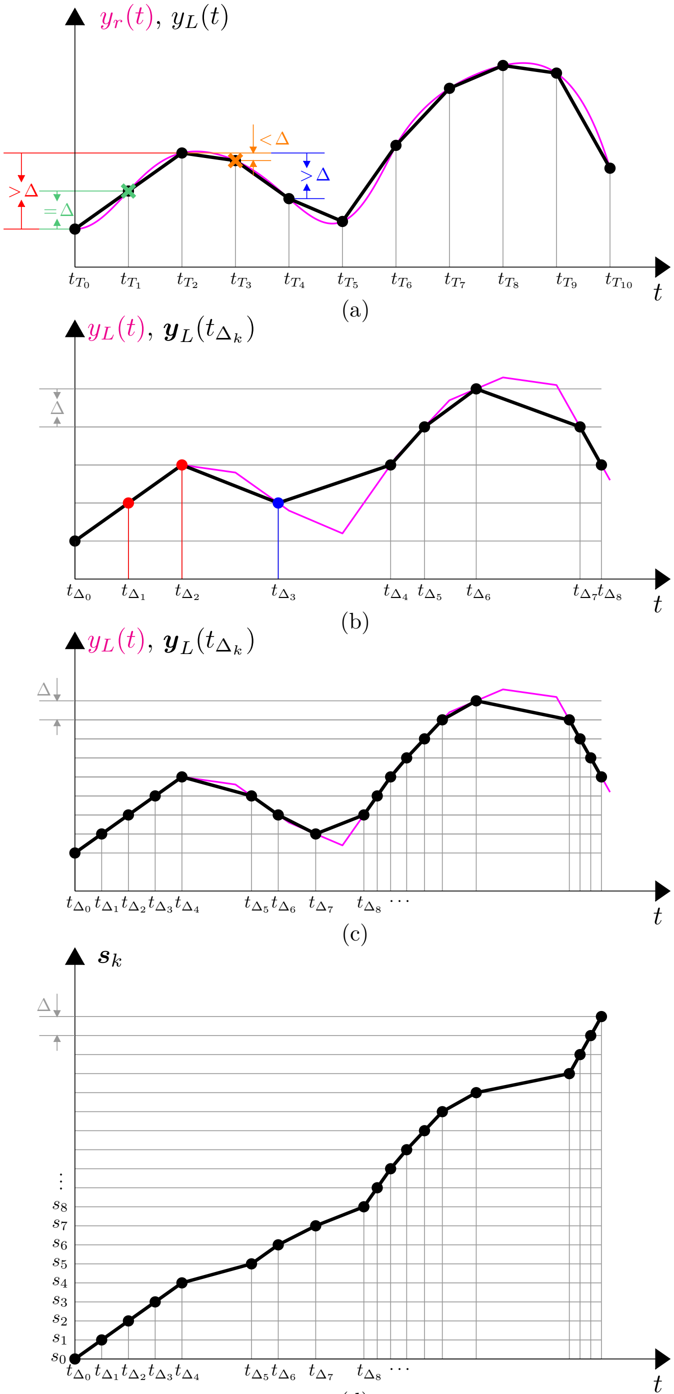

(d)

Figure 1: Sketch displaying the operation of the Spatial Sampling algorithm in a one-dimensional scenario: reference trajectory $y_L(\boldsymbol{t}_T)$ sampled with constant period T and interpolating linear curve $y_L(t)$ (a), sequence of spatially sampled points $\boldsymbol{y}_{\Delta,k} = \boldsymbol{y}_L(t_{\Delta_k})$ with $\Delta = \bar{\Delta}$ (b) and $\Delta = \bar{\Delta}/2$ (c), and samples of the function $s_k = \gamma(t_{\Delta_k})$ for $\Delta = \bar{\Delta}/2$ (d).

can be viewed as the result of a sampling operation with a constant spatial period Δ. Interestingly,

$$\left\|\frac{d\hat{\boldsymbol{y}}_r(s)}{ds}\right\|_{s=s_k} \approx \frac{\|\boldsymbol{y}_{\Delta,k+1} - \boldsymbol{y}_{\Delta,k}\|}{\|s_{k+1} - s_k\|} = \frac{\Delta}{\Delta} = 1. \tag{6}$$

Consequently, this derivative will always be different from zero, and the tangent direction will always be well-defined. The operation of the algorithm is graphically depicted in Fig. 1 for a one-dimensional case study. Initially, by sampling the reference trajectory $y_L(\boldsymbol{t}_T)$ at a constant time interval T, we derive the linear interpolation function $y_L(t)$. The geometric distance Δ_k between adjacent points is obviously varying. Subsequently, in Fig. 1b and Fig. 1c, the curve $y_L(t)$ is re-sampled using two different spatial intervals Δ. It is evident that smaller values of Δ result in a more accurate approximation of the original curve. In Fig. 1d, the samples of the timing-law $s = \gamma(t)$ imposed during the demonstration of the trajectory and obtained with the same spatial period Δ of case (c) are also presented. These illustrate how the length along the geometric path changes with time throughout the demonstration.

Remark 1: The computation of the parametric function $\boldsymbol{y}^\star(s)$ based on the pair $(\boldsymbol{s}_k,\ \boldsymbol{y}_{\Delta,k})$, $k = 0, \ldots, M$ defines the concept of *Geometric* DMP (GDMP) [8]. This type of DMP solely derives from the geometric path of the demonstrated trajectory and can be linked to any phase variable $s(t)$.

III. CONCLUSIONS

In this extended abstract, a new spatial sampling algorithm for encoding geometric information in demonstrated trajectories is presented. This algorithm decouples the demonstrated curve from its timing law thus allowing to generate an arc-length parameterized geometric path, and enables the concept of geometric dynamic movement primitives which is described in [8].

REFERENCES

[1] S. Calinon, F. Guenter and A. Billard, “On Learning, Representing, and Generalizing a Task in a Humanoid Robot”, IEEE Transactions on Systems, Man, and Cybernetics, Part B (Cybernetics), vol. 37, no. 2, pp. 286-298, April 2007.

[2] A. Jan Ijspeert, J. Nakanishi, H. Hoffmann, P. Pastor and S. Schaal, “Dynamical Movement Primitives: Learning Attractor Models for Motor Behaviors”, Neural Computation, vol. 25, no. 2, pp. 328-373, 2013.

[3] A. J. Ijspeert, J. Nakanishi and S. Schaal, “Movement imitation with nonlinear dynamical systems in humanoid robots”, 2002 IEEE International Conference on Robotics and Automation, Washington, DC, USA, 2002,

[4] S. Sanchez Restrepo, G. Raiola, P. Chevalier, X. Lamy and D. Sidobre, “Iterative virtual guides programming for human-robot comanipulation”, 2017 IEEE International Conference on Advanced Intelligent Mechatronics (AIM), Munich, Germany.

[5] A. Sidiropoulos and Z. Doulgeri, “A Reversible Dynamic Movement Primitive formulation”, 2021 IEEE International Conference on Robotics and Automation (ICRA), Xi’an, China, 2021.

[6] B. Nemec, M. Simonič, T. Petrič and A. Ude, “Incremental Policy Refinement by Recursive Regression and Kinesthetic Guidance”, 2019 19th International Conference on Advanced Robotics (ICAR), Belo Horizonte, Brazil, 2019.

[7] L. Biagiotti and C. Melchiorri, “Online trajectory planning and filtering for robotic applications via B-spline smoothing filters”, 2013 IEEE/RSJ International Conference on Intelligent Robots and Systems, Tokyo, Japan, 2013.

[8] G. Braglia, D. Tebaldi, and L. Biagiotti, “Phase-free Dynamic Movement Primitives Applied to Kinesthetic Guidance in Robotic Co-manipulation Tasks”, arXiv, https://arxiv.org/abs/2401.08238.

Soft Robotic Hands:
Embracing the Interaction with the Surrounding Environment

Maria Pozzi[1,2], Valerio Bo[1,2], Enrico Turco[1,2], Leonardo Franco[1],
Gionata Salvietti[1], Monica Malvezzi[1] and Domenico Prattichizzo[1,2]

***Abstract*— The advent of soft robotics has greatly changed researchers' perspectives on robotic manipulation. The philosophy of embedding the robot intelligence at the design level has led to new prototypes of robotic hands that show capabilities inconceivable with their rigid counterparts. This contribution outlines on-going research efforts on how to unlock new grasping skills in soft-rigid grippers exploiting the interaction with the environment.**

I. INTRODUCTION

Endowing robots with manipulation skills requires controlling the motion and forces transmitted at the contact points between the robotic gripper and the grasped object. While rigid robotic grippers are typically controlled to avoid the interaction with the environment over which the target objects are lying, soft hands can safely and deliberately enter in contact with the surrounding environment. It has been shown that the purposeful exploitation of environmental constraints generates robust grasps, even in the presence of perception uncertainties [1]–[3]. This abstract presents three different approaches to the exploitation of environmental constraints. The first focuses on the direct exploitation of rigid constraints present in the environment (e.g., tables, walls) using state-of-the-art soft anthropomorphic hands (Fig. 1a). The second explores the possibility of embedding softness directly in the environment to allow even rigid grippers to safely interact with it (Fig. 1b). The third proposes adding rigid "embedded constraints" directly in the hand structure, to facilitate the exploitation of environmental constraints (Fig. 1c).

II. EXPLOITING ENVIRONMENTAL CONSTRAINTS WITH STATE-OF-THE-ART SOFT ROBOTIC HANDS

In [2], [3], methods to execute grasping strategies that exploit environmental constraints with state-of-the-art robotic hands have been proposed. The main idea is to first align the hand over the object using a model-based approach, and then exploit the surface over which the object is lying either by dragging the object over it (Slide-to-edge grasp), or by caging the object (Surface-constrained grasp, Fig. 1a). In [2], we proposed to exploit the compliance of soft hands to establish large contact areas with the objects and generate enough friction forces to slide the object to the edge of a table. Two different strategies were developed and tested. The first performed a single motion to drag the object towards the edge of the table and grasp it. The second included two subsequent motions: dragging and then grasping from the edge. Both strategies relied on visual and force sensing data. Results suggested that the two strategies can be seen as complementary, where one fails the other one succeeds and vice-versa. In [3], a model-based approach to plan top-grasps with soft hands was proposed. The so-called "closure signature" was used to model closure motions of soft hands by associating to them a preferred grasping direction. This direction can be aligned to a suitable direction over the object to achieve successful surface-constrained grasps. The resulting grasp planner was tested with multiple experimental trials with two different robotic hands and achieved a remarkable grasp success rate with a variety of objects.


(a) (b) (c)

Fig. 1: (a) Soft hand over a rigid environment [3], (b) rigid gripper over a soft environment [4], and (c) soft-rigid gripper over a rigid environment [5].

III. EMBEDDING SOFTNESS IN THE ENVIRONMENT FOR SAFE INTERACTION WITH RIGID GRIPPERS

In [4], [6], we proposed to exploit soft inclusions in the environment to perform robust grasps with rigid grippers (Fig. 1b). This was achieved by introducing a grasping strategy that exploited the *SoftPad*, a matrix of silicone pneumatic modules connected to pressure sensors that, when placed beneath an object, can be used to estimate object pose, shape, and center of mass based on pressure variations. Given the estimated center of mass, a planner computes the center and the direction of grasp that can be used by a robotic gripper to pick the object up. Thanks to the SoftPad, grasps can be performed without the need of a camera to locate the object and without prior knowledge of its mass distribution or its shape. Additionally, the gripper can safely interact with the soft surface, coping with uncertainties on the object pose and achieving more robust grasps thanks to environmental

---

[1] Dept. of Information Engineering and Mathematics, University of Siena, Italy ({name.surname}@unisi.it).

[2] Humanoids & Human Centered Mechatronics Research Line, Istituto Italiano di Tecnologia, Genoa, Italy

*We acknowledge the support of the European Union by the Next Generation EU project ECS00000017 "Ecosistema dell'Innovazione" Tuscany Health Ecosystem (THE, PNRR: Spoke 9).

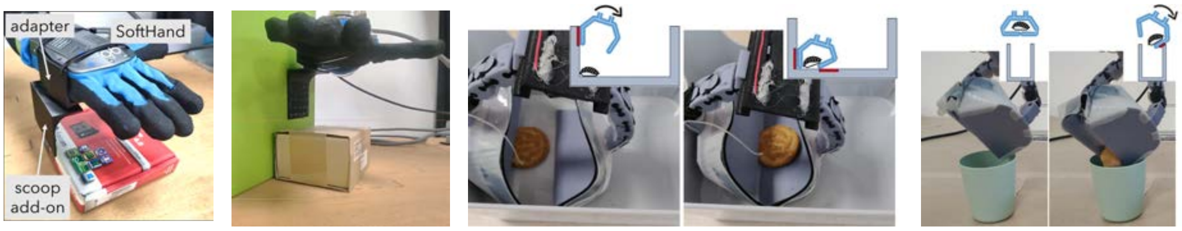

(a) (b) (c) (d)

Fig. 2: Promising features of scoop-shaped embedded constraints: (a, b) applicability to commercial hands to perform new grasping strategies; (c, d) versatility for unstructured environments: (c) pick and (d) place of food items in narrow containers.

constraints exploitation strategies. Our approach went beyond classical vision-based object detection strategies, as it allows to estimate not only the pose and shape of the object but also its center of mass. In addition, there is no need to add force sensors to the robot, as the sensorized modules can detect the contact between the gripper and the SoftPad. To test the proposed grasping strategy we chose different objects to show the potentialities of the grasp planning algorithm based on the SoftPad pressure readings.

IV. SOFT-RIGID GRIPPER WITH EMBEDDED CONSTRAINTS

Salvietti et al. [7], proposed the idea of embedding rigid constraints in the hand structure and developed the Soft ScoopGripper (Fig. 1c), a non-anthropomorphic gripper featuring two soft fingers and a scoop-shaped structure attached to the palm through a flexible hinge. Then, we started investigating grasp planning strategies to exploit embedded constraints [5], [8], as well as methods to automatically design them [9], [10].

From the planning point of view, we developed model-based and data-driven techniques for implementing the *scoop grasp*, in which the scoop is used to separate the target object from the contacting surfaces (e.g., table, wall) so that it can be enveloped with the soft fingers. First, we proposed to compute pre-grasp poses for the Soft ScoopGripper solving an optimization problem aimed at maximizing the grasp quality and the contact area between the scoop and the object [5]. Then, we developed a fast and data-efficient Learning from Demonstrations (LfD) method to learn grasping strategies from human demonstrations [8].

Regarding the design of embedded constraints, we introduced data-driven approaches for the automated design of scoop-shaped structures, including methods to find optimal size and placement of the add-ons to implement novel grasping strategies with commercial robotic hands [9] (Fig. 2a, 2b), and to optimize the material distribution [10].

Recently, also motivated by 2023 IEEE Robosoft Competition ("food handling for trays preparation"), we developed a novel gripper, the Double-Scoop Gripper, specifically designed for food handling. Thanks to the presence of two scoop-shaped structures, the new gripper can effectively exploit the edges of narrow containers to pick and place food items (Fig. 2c, 2d) [11].

V. CONCLUSIONS AND FUTURE WORK

This abstract summarizes recent research efforts towards the exploitation of environmental constraints with soft, rigid, and soft-rigid grippers. Indeed, the use of embedded soft-rigid constraints opened up several possibilities from the design and grasp planning points of view, unlocking new capabilities both in off-the-shelf general-purpose devices and in specialized grippers (Fig. 2). Future work will focus on applications in cluttered environments.

REFERENCES

[1] R. Deimel et al., "Exploitation of environmental constraints in human and robotic grasping," in *Robotics Research*. Springer, 2016, pp. 393–409.

[2] J. Bimbo, E. Turco, M. Ardahani, M. Pozzi, et al., "Exploiting robot hand compliance and environmental constraints for edge grasps," *Frontiers in Robotics and AI*, 2019.

[3] M. Pozzi, S. Marullo, G. Salvietti, J. Bimbo, M. Malvezzi, and D. Prattichizzo, "Hand closure model for planning top grasps with soft robotic hands," *The International Journal of Robotics Research*, vol. 39, no. 14, pp. 1706–1723, 2020.

[4] C. Gaudeni, M. Pozzi et al., "Grasping with the softpad, a soft sensorized surface for exploiting environmental constraints with rigid grippers," *IEEE RA-L*, 2020.

[5] E. Turco, V. Bo, M. Pozzi, A. Rizzo, and D. Prattichizzo, "Grasp planning with a soft reconfigurable gripper exploiting embedded and environmental constraints," *IEEE Robotics and Automation Letters*, vol. 6, no. 3, pp. 5215–5222, 2021.

[6] M. Pozzi, C. Gaudeni, Z. Iqbal, D. Prattichizzo, and M. Malvezzi, "Modeling a sensorized soft layer for adding compliance to the environment in robotic manipulation," in *Advances in Italian Mechanism Science: Proceedings of the 3rd International Conference of IFToMM Italy 3*. Springer, 2021, pp. 370–377.

[7] G. Salvietti, Z. Iqbal, M. Malvezzi, T. Eslami, and D. Prattichizzo, "Soft hands with embodied constraints: the soft scoopgripper," in *2019 International Conference on Robotics and Automation (ICRA)*. IEEE, 2019, pp. 2758–2764.

[8] E. Turco, V. Bo, M. Tavassoli, M. Pozzi, and D. Prattichizzo, "Learning grasping strategies for a soft non-anthropomorphic hand from human demonstrations," in *2022 31st IEEE International Conference on Robot and Human Interactive Communication (RO-MAN)*. IEEE, 2022, pp. 934–941.

[9] V. Bo, E. Turco, M. Pozzi, et al., "Automated design of embedded constraints for soft hands enabling new grasp strategies," *IEEE RA-L*, 2022.

[10] V. Bo, E. Turco, M. Pozzi, M. Malvezzi, and D. Prattichizzo, "A data-driven topology optimization framework for designing robotic grippers," in *2023 IEEE International Conference on Soft Robotics (RoboSoft)*. IEEE, 2023, pp. 1–6.

[11] L. Franco, E. Turco, V. Bo, M. Pozzi, M. Malvezzi, D. Prattichizzo, and G. Salvietti, "The double-scoop gripper: A tendon-driven soft-rigid end-effector for food handling exploiting constraints in narrow spaces," in *2024 IEEE International Conference on Robotics and Automation (ICRA)*, 2024, pp. 4170–4176.

Visual Action Planning with Multiple Heterogeneous Agents

Martina Lippi*[1], Michael C. Welle*[2], Alessandro Marino[3], Andrea Gasparri[1], Danica Kragic[2]

***Abstract*— Visual planning methods are promising to handle complex settings where extracting the system state is challenging. None of the existing works tackles the case of multiple heterogeneous agents, characterized by different capabilities and/or embodiment. We propose a centralized method to realize visual action planning in multi-agent systems (MASs) by exploiting a roadmap built in a low-dimensional latent space and used for planning. To enable MASs, we infer possible parallel actions from a dataset composed of tuples associated with individual actions. Next, we evaluate the feasibility and cost of them based on the capabilities of the MAS and endow the roadmap with this information. The approach is validated in a simulated burger cooking task and a real-world box packing task.**

I. INTRODUCTION

Planning from raw observation [1], like images, has proven very relevant in complex scenarios, such as when the scenes are highly dynamic and unstructured, as it eliminates the necessity to explicitly identify the system state. Moreover, the use of raw observations paves the way for realizing visual action planning, i.e., for generating *visual* plans, along with action plans, which allow to reach desired observations given start ones. The availability of visual plans also enhances the comprehension of the robot's plan by humans. Several prior works in the literature have investigated visual action planning methods, e.g. [2], [3]. However, all the above methods only consider a single agent. In many scenarios, the availability of multiple *heterogeneous* agents - meaning agents that have different capabilities and/or embodiment - is beneficial, if not essential, to successfully accomplish a given task. Although many works exist on multi-agent planning and allocation problems [4], these *i)* do not provide visual information and *ii)* often require extensive data regarding the actions to execute, which might not be easily retrieved.

Contribution: Differently from the literature, we propose a method to realize visual action planning with *multiple heterogeneous* agents by relying on *partial* data only. By building on our Latent Space Roadmap (LSR) framework [5] for single agents, the proposed method is able to identify visual and action plans, with possibly parallel actions, given start and goal observations, and determine the optimal assignment of actions to the available agents, taking into account their capabilities. Details on the method can be found in [6].

II. PRELIMINARIES

Dataset: Let $\mathcal{O}$ and $\mathcal{U}$ be the spaces of all possible system observations and actions, respectively. Similar to [5], we assume the availability of a dataset $\mathcal{T}_o$ composed of tuples (O_i, O_j, ρ), where $O_i, O_j \in \mathcal{O}$ are two observations, and $\rho = (b, u)$ represents the action information between them. Specifically, $b \in \{0, 1\}$ is a binary variable denoting whether an action occurred ($b = 1$) or not ($b = 0$) between O_i and O_j, and $u \in \mathcal{U}$, represents the respective action when $b = 1$, i.e., it is an atomic operation executed by one agent. *No-action* tuples (with $b = 0$) capture possible task-irrelevant factors of variation in the observations, e.g., varying light conditions.

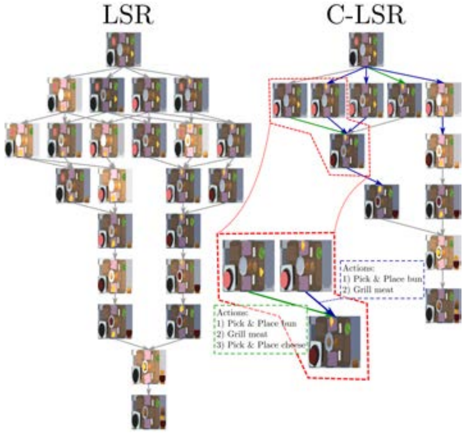

Fig. 1: Example of VAPs obtained with an LSR (left) with one agent, and with a C-LSR (right) with a MAS.

LSR framework: Given start O_s and goal O_g observations, the objective of visual action planning is to define the sequences of actions to reach the goal and of respective observations. In a single-agent scenario, a *sequential* Visual Action Plan (VAP) is defined as $P^{seq} = (P_o^{seq}, P_u^{seq})$, where the visual plan $P_o^{seq} = (O_s = O_1, \cdots, O_N = O_g)$ contains observations of the intermediate states from start to goal, and the sequential action plan $P_u^{seq} = (u_1, ..., u_{N-1})$ provides the respective actions u_i to transition from O_i to O_{i+1}, $\forall i$. The LSR framework [5] allows to realize sequential visual action planning in single agent scenarios. Briefly, this is based on mapping the high dimensional observations in a lower dimensional *structured* latent space $\mathcal{Z}$ and then build a roadmap in this space to perform planning. Based on the dataset $\mathcal{T}_o$, the latent space $\mathcal{Z}$ is obtained by resorting to an encoder-decoder architecture with a contrastive loss: observations of no-action tuples (with $b = 0$) are attracted, and observations of action tuples (with $b = 1$) are repelled, thus clustering together the same underlying states in $\mathcal{Z}$. Next, a directed graph $\mathcal{G} = \{\mathcal{V}, \mathcal{E}\}$, called LSR, is built in $\mathcal{Z}$ where each node in $\mathcal{V}$ is associated with a cluster of latent states, and each edge $e = (i, j)$ in $\mathcal{E}$ is associated with a possible action u_e to transition from node i to node j (inferred from $\mathcal{T}_o$). Given the latent encodings of O_s and O_g, the LSR is used to find plans in the latent space, which are then used to generate the VAP P^{seq}.

---

*These authors contributed equally (in alphabetical order).

[1] Roma Tre University, Italy, [2] KTH Royal Institute of Technology, Sweden, [3] University of Cassino and Southern Lazio, Italy

III. PROBLEM SETTING AND SOLUTION OVERVIEW

Setting: Let $\mathcal{A} = \{a_1, ..., a_{n_a}\}$ be the set of n_a available agents. For each agent a_i, we define *i)* the set $\mathcal{S}_i^a$ of available skills, e.g., tools or sensors, *ii)* the average normalized workload $w_{i,j} \in [0, 1]$ for performing the action u_j, $\forall u_j \in \mathcal{U}$, which can depend on physical or cognitive properties, and *iii)* a reachability function $r_i(x) \in [0, 1]$, assessing the ease of reaching (and operating in) a specific pose x. For each action $u_j \in \mathcal{U}$, we identify *i)* the set $\mathcal{S}_j^u$ of skills, e.g., tools or sensors, required to perform the action, and *ii)* the set $\mathcal{P}_j$ of relevant poses for the action which must be traversed to execute it. We define that an agent a_i possesses the *capability* to carry out an action u_j if it/they has/have all the necessary skills for executing the action, i.e., $\mathcal{S}_j^u \subseteq \mathcal{S}_i^a$, and can reach all the respective relevant poses, i.e., $r_i(x_j) > 0$, $\forall x_j \in \mathcal{P}_j$. In general, there exist actions that can be potentially executed concurrently (if the MAS has the needed capabilities). To identify them, we introduce the following condition.

Condition 1: Multiple actions $\{u_1, ..., u_p\}$ can be executed in parallel if executing them in arbitrary order from a certain state results in the same final state.

The rationale behind Condition 1 is that, if the execution order does not matter, then, no precedence constraints (i.e., expressing actions that must be executed before/after others) between the actions exist and these can be carried out concurrently. Let $\overline{\mathcal{U}}_k$ represent a collection of *assignment* couples (a_i, u_j), denoting that the agent a_i has to execute action u_j. We can define a *parallel* VAP as $P^{par} = (P_o^{par}, P_u^{par})$ where the action plan is $P_u^{par} = (\overline{\mathcal{U}}_1, ..., \overline{\mathcal{U}}_{N-1})$, while the visual plan $P_o^{par} = (O_s = O_1, \cdots, O_N = O_g)$ collects the observations obtained by applying all the actions in $\overline{\mathcal{U}}_i$.

Objective: We aim to generate parallel VAPs such that *i)* they provide visual and action plans to reach the goal state, *ii)* the assignment couples are *valid*, i.e., the assigned actions align with the capabilities of the respective agents, and *iii)* the overall workload and reachability indices are optimized.

Overview: To achieve this, our core idea is to infer all the possible actions that can be executed in parallel by exploiting the dataset $\mathcal{T}_o$ and the respective LSR framework, and subsequently build a new roadmap in the latent space that incorporates these actions by considering agent capabilities and action requirements. We resort to Condition 1 to identify potential parallel actions and define a Parallel LSR (P-LSR). This represents a directed graph $G^{par} = (\mathcal{V}, \mathcal{E}^{par})$ where the set of edges encodes potentially parallel actions that are executable by a multi-agent system, *regardless* of the number of agents and their individual capabilities. Hence, each edge $e = (i, j)$ in the set $\mathcal{E}^{par}$ is associated with a set of actions $\mathcal{U}_e$, all of which must be executed to transition from node i to node j. The set of nodes coincides with the LSR one.

Next, we build a *capability* LSR, denoted as C-LSR, that takes into account the agents capabilities and the actions requirements. This is defined as a directed graph $G^c = (\mathcal{V}, \mathcal{E}^c)$ where the set of edges encodes possible assignment couples by considering the agents at hand. Specifically, each edge $e = (i, j)$ in the set $\mathcal{E}^c$ is associated with a set $\overline{\mathcal{U}}_e$ of *valid* assignment couples and with a *cost* c_e, quantifying the effectiveness of the multi-agent system to perform the actions in $\overline{\mathcal{U}}_e$. The set of nodes remains unchanged with respect to the LSR. This graph is used online to generate parallel VAPs given start and goal observations. Fig. 1 depicts an example of plans obtained using the LSR (left) and the C-LSR (right) in a burger cooking task, showing how the parallelism of multiple agents is exploited in the C-LSR.

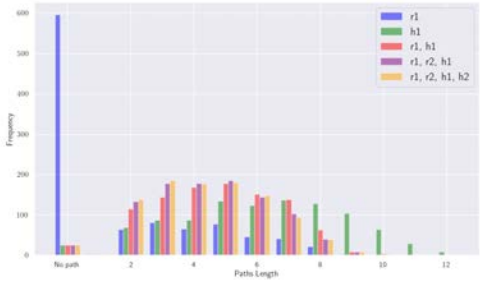

Fig. 2: Histograms of the path lengths N with different agents.

IV. VALIDATION RESULTS

We validate the framework on a simulated burger cooking task involving different objects, i.e., meat patty, cheese, lettuce, and the top and bottom parts of the bun, requiring different manipulation skills, i.e., gripping, cutting, and grilling skills. A team composed of maximum two robots r_1 and r_2, and two humans h_1 and h_2 is considered. Robots only have gripping and cutting skills, while humans possess all skills but require higher workload compared to the robots. We select 1000 different start and goal observations from a novel dataset and evaluate the respective parallel VAPs. The following sets of agents are analyzed: $\{r_1\}$, $\{h_1\}$, $\{r_1, h_1\}$, $\{r_1, r_2, h_1\}$, and $\{r_1, r_2, h_1, h_2\}$. In all cases, all actions selected as potential parallel actions are correctly combined and we obtain a percentage of correct individual transitions in the paths equal to $\approx 97\%$, and, except for $\mathcal{A} = \{r_1\}$, a percentage of full correct paths of $\approx 82\%$. Figure 2 reports the histograms of the path lengths N with the different agents. When only r_1 is included (in blue), no paths are found $597/1000$ times since the robot does not possess the grilling skill. In contrast, when only h_1 is included (in green), a path is obtained in the majority of cases, with average and maximum path lengths equal to ≈ 6.3 and 12, respectively. When adding a robot (in red), the path lengths significantly reduce achieving average equal to ≈ 4.8 and maximum equal to 10. Additional improvements are observed when expanding the set of agents further. Experimental results on a real-world box packing task are shown in the video at the link: https://newline.dia.uniroma3.it/videos/multi-LSR.mp4.

REFERENCES

[1] A. Wang et al., “Learning robotic manipulation through visual planning and acting,” in *Robotics: Science and Syst.*, 2019.

[2] R. Hoque et al., “Visuospatial foresight for physical sequential fabric manipulation,” *Autonomous Robots*, vol. 46, no. 1, 2022.

[3] H. Wu et al., “Transporters with visual foresight for solving unseen rearrangement tasks,” in *IEEE/RSJ Int. Conf. Intell. Robots Syst.*, 2022.

[4] A. Khamis et al., “Multi-robot task allocation: A review of the state-of-the-art,” *Cooperative robots and sensor networks*, 2015.

[5] M. Lippi et al., “Enabling visual action planning for object manipulation through latent space roadmap,” *IEEE Trans. Robot.*, vol. 39, 2023.

[6] M. Lippi et al., “Visual action planning with multiple heterogeneous agents,” *RO-MAN*, 2024. https://arxiv.org/abs/2403.16781.

Distributed Nonlinear Rolling Horizon Techniques Applied to Air-Ground Cooperation

Alessandra Elisa Sindi Morando [*] [†], Alessandro Bozzi [*], Simone Graffione [*], Enrico Zero [*], and Roberto Sacile[*]
[*] Department of Informatics, Bio-engineering, Robotics and Systems Engineering (DIBRIS), University of Genoa.
[†] Heudiasyc (Heuristics and Diagnosis of Complex Systems) CNRS laboratory of the Université de Technologie de Compiègne

I. INTRODUCTION

This work proposes a distributed estimation-control scheme for the control of two robots. As shown in Fig. 1, a steering car, defined as the leader, has to follow a desired trajectory while maintaining a safety distance from some static obstacles. From above, a quadcopter must follow the ground vehicle to maintain the formation. This topic is of interest because it is a common problem when dealing with multi-robot systems, which are used nowadays in different fields [1]. In addition, hybrid systems such as air-ground cooperation can tackle complex tasks by overcoming the limitations of homogeneous teams through the use of different capabilities.

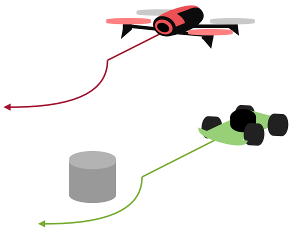

Fig. 1. In this paper, the problem of formation and trajctory-tracking of air-ground unmanned vehicles is addressed.

To solve this problem, a Nonlinear Model Predictive Controller (NMPC) and a Nonlinear Moving Horizon Estimator (NMHE) have been combined. To the authors' knowledge, while various works have demonstrated the robustness and accuracy of this type of scheme in different applications [2], none has used NMPC-NMHE for this type of heterogeneous system. Unlike classical control techniques, the presented scheme can handle noisy, partial, and missing measurements of the agents' state.

II. METHODS

A. Two Agents' Models

In order to describe the Unmanned Ground Vehicle (UGV) and the Unmanned Aerial Vehicle (UAV), the Ackermann model [3]

$$\begin{cases} \dot{x}(t) &= v(t)\cos(\psi(t)) \\ \dot{y}(t) &= v(t)\sin(\psi(t)) \\ \dot{\psi}(t) &= (v(t)/L)\tan(w_1(t)) \\ \dot{v}(t) &= w_2(t) \end{cases} \tag{1}$$

and the dynamic model obtained by the Euler-Lagrange approach in [4]

$$\begin{cases} \ddot{x}(t) &= -(u_1(t)/M)\sin(\theta(t)) \\ \ddot{y}(t) &= (u_1(t)/M)\cos(\theta(t))\sin(\phi(t)) \\ \ddot{z}(t) &= (u_1(t)/M)\cos(\theta(t))\cos(\phi(t)) - g \\ \ddot{\theta}(t) &= u_2(t) \\ \ddot{\phi}(t) &= u_3(t) \\ \ddot{\psi}(t) &= u_4(t) \end{cases} \tag{2}$$

are used. Both models are in continuous time, but discrete time models can be obtained using either the trapezoidal rule (as done for the drone) or the 4th order Runge-Kutta method (used here for the UGV).

B. NMHEs

The NMPC assumes that the entire state of the system is measurable, which is not always the case in practice. Therefore, a separate NMHE has been defined for both unmanned vehicles (UVs). The formulation is the same for both agents and is as follows

$$\min \quad \sum_{i=1}^{H_e} \|\boldsymbol{y}(k-i) - h(\hat{\boldsymbol{x}}(k-i), \boldsymbol{u}(k-i))\|^2_{\mathcal{V}} \tag{3a}$$

$$\text{s.t.} \quad \hat{\boldsymbol{x}}(k-i+1) = f(\hat{\boldsymbol{x}}(k-i), \boldsymbol{u}(k-i)) \tag{3b}$$

$$\boldsymbol{x}_{UV}^{min} \leq \hat{\boldsymbol{x}}(k-i) \leq \boldsymbol{x}_{UV}^{MAX} \tag{3c}$$

In short, $\boldsymbol{y}$ and $\boldsymbol{u}$ are the past noisy measurements and control inputs in the last H_e time instants (the "*prediction horizon*"). In a multiple shot fashion, the decision variables of the minimisation problem are the estimated states $\hat{\boldsymbol{x}}$ over the prediction horizon. The functions f and h are the nonlinear discrete time evolution and measurement models. The problem is therefore to minimise the deviations from the predicted past measurements and the collected values, subject to evolution constraints and state bounds. A classical choice for the deviation weights, when the measurement noise is zero mean and Gaussian, is

$$\nu(t) \sim \mathcal{N}(0_{n_y \times 1}, \Sigma_\nu) \quad \Sigma_\nu = \text{diag}(\sigma_1^2 \quad \cdots \quad \sigma_{n_y}^2) \tag{4a}$$

$$\mathcal{V} = \left(\sqrt{\Sigma_\nu}\right)^{-1} = \text{diag}(1/\sigma_1 \quad \cdots \quad 1/\sigma_{n_y}) \tag{4b}$$

C. NMPCs

Once the current state of both the UGV $\hat{\boldsymbol{x}}_{UGV}(k)$ and the UAV $\hat{\boldsymbol{x}}_{UAV}(k)$ are estimated, the control action can be computed in a distributed manner. The formulations of the two NMPCs are slightly different. Focus first on the leader. In absence of obstacles, the steering car's NMPC is defined as follows

$$\begin{aligned} \min \quad & \sum_{i=1}^{H_p} \|\boldsymbol{x}_{UGV}(k+i|k) - \boldsymbol{r}_{UGV}(k+i)\|^2_{\mathcal{Q}_{UGV}} \\ & + \sum_{i=0}^{H_u-1} \|\boldsymbol{u}_{UGV}(k+i|k)\|^2_{\mathcal{R}} + \\ & + \sum_{i=0}^{H_u-1} \|\Delta\boldsymbol{u}_{UGV}(k+i|k)\|^2_{\mathcal{R}_\Delta} \end{aligned} \tag{5a}$$

$$\text{s.t.} \quad \boldsymbol{x}_{UGV}(k|k) = \hat{\boldsymbol{x}}_{UGV}(k) \tag{5b}$$

$$\begin{aligned} & \boldsymbol{x}_{UGV}(k+i+1|k) = \\ & \quad f_{UGV}(\boldsymbol{x}_{UGV}(k+i|k), \boldsymbol{u}_{UGV}(k+i|k)) \end{aligned} \tag{5c}$$

$$0 \leq \boldsymbol{e}_{xy}(k+H_p|k)^T \boldsymbol{e}_{xy}(k+H_p|k) \leq (d_{Safe} + \varepsilon)^2 \tag{5d}$$

$$x_{UGV}^{min} \leq \boldsymbol{x}_{UGV}(k+i|k) \leq x_{UGV}^{MAX} \tag{5e}$$

$$u_{UGV}^{min} \leq \boldsymbol{u}_{UGV}(k+i|k) \leq u_{UGV}^{MAX} \tag{5f}$$

Again, the decision variables are both the state and the control trajectories over the prediction horizon H_p. The objective function simultaneously penalises the tracking errors, the control input and its variations. While the other constraints are trivial, (5d) are terminal-region constraints to force the vehicle to be sufficiently close to the reference signal at the end of the prediction horizon. If an obstacle is detected (assuming a sensor such as LIDAR is on board), the following inequality constraints are added to (5) in a switching control fashion.

$$d_{Obs}(k+i|k)^T d_{Obs}(k+i|k) \geq (d_{Safe} + \varepsilon)^2 \tag{6}$$

One of the main advantages of the MPC is that it can generate trajectories that can be transmitted to other followers. Following this insight and assuming that the ground robot is moving slowly, this last communicates its one-step state prediction to the drone. This last information is used in the aerial vehicle controller formulation

$$\begin{aligned}
\min \quad & \sum_{i=1}^{H_p} \|\boldsymbol{x}_{UAV}(k+i|k) - \boldsymbol{r}_{UAV}(k)\|^2_{\mathcal{Q}_{UAV}} && \text{(7a)}\\
\text{s.t.} \quad & \boldsymbol{x}_{UAV}(k|k) = \hat{\boldsymbol{x}}_{UAV}(k) && \text{(7b)}\\
& \boldsymbol{x}_{UAV}(k+i+1|k) = && \\
& \quad f_{UAV}(\boldsymbol{x}_{UAV}(k+i|k), \boldsymbol{u}_{UAV}(k+i|k)) && \text{(7c)}\\
& x_{UAV}^{min} \leq \boldsymbol{x}_{UAV}(k+i|k) \leq x_{UAV}^{MAX} && \text{(7d)}
\end{aligned}$$

as a constant reference over the prediction horizon

$$\begin{aligned}
\boldsymbol{r}_{UAV}(k) = \big[& x(k+1|k) \quad 0 \quad y(k+1|k) \quad 0 \\
& z_{Ref}(k) \quad 0 \quad 0 \quad 0 \\
& 0 \quad 0 \quad \psi(k+1|k) \quad 0 \big]^T
\end{aligned} \tag{8}$$

III. RESULTS

To validate the proposed solution, some simulations were carried out in MATLAB/Simulink. To efficiently solve the nonlinear optimisation problems, the internal point optimiser provided by the CasADi [5] framework is used. The parameters of the agents were chosen from the datasheets of two commercially available robots, the JetRacer racing car and the Parrot Bebop 2.0 drone. On the other hand, the measurement noise has been modelled according to the specifications of the Optitrack motion capture system. Different reference trajectories, numbers of obstacles and positions of obstacles were tested: Fig. 2 and 3 are two scenarios taken by sample. Thanks to the reliable estimates from NMHE and the accurate predictions from NMPC, the ground car can avoid detected obstacles while keeping the tracking errors of both robots within a few centimeters.

IV. CONCLUSION

The strengths of the presented distributed NMPC-NMHE compared to classical control techniques are obvious. The results obtained in simulation are promising and encourage to continue in this direction. The main idea is to implement the whole architecture and embed it in real robots. In addition to the classic problems associated with distributed control algorithms, such as communication between agents, the major difficulty is the computational load required to solve non-linear optimisation problems in real time.

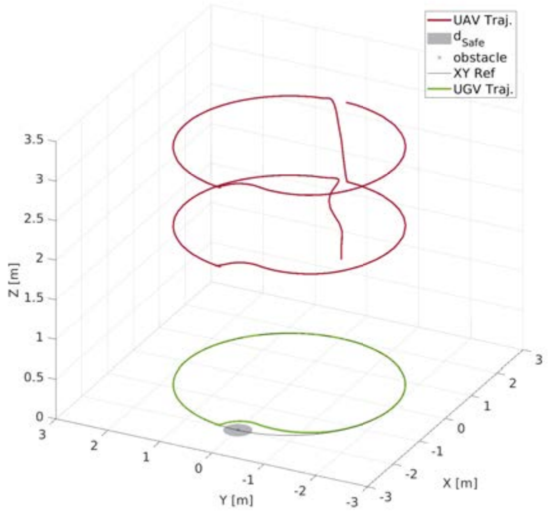

Fig. 2. A case study with a circular reference and an increasing desired height with one obstacle on the UGV way.

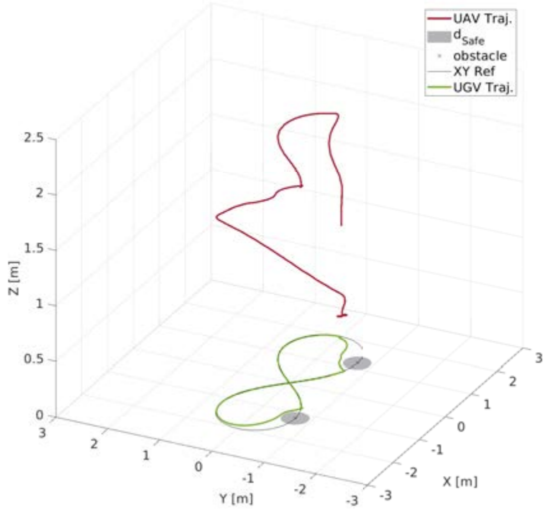

Fig. 3. Another case study with a eight-shaped reference and a decreasing desired height, with two obstacles this time.

REFERENCES

[1] A. Schweim, M. Zager, M. Schweim, A. Fay, and J. Horn, “Unmanned vehicles on the rise: a review on projects of cooperating robot teams,” *at - Automatisierungstechnik*, vol. 72, no. 1, pp. 3–14, Jan. 2024.

[2] L. Biegler, “A perspective on nonlinear model predictive control,” *Korean Journal of Chemical Engineering*, vol. 38, 06 2021.

[3] C. Frank, *Modern Robotics-Mechanics, Planning, and Control*. Cambridge University Press, 2017.

[4] P. Castillo, R. Lozano, and A. E. Dzul, *Modelling and control of mini-flying machines*, ser. Advances in industrial control. London ; New York: Springer, 2005, oCLC: ocm61141310.

[5] J. A. E. Andersson, J. Gillis, G. Horn, J. B. Rawlings, and M. Diehl, “CasADi – A software framework for nonlinear optimization and optimal control,” *Mathematical Programming Computation*, vol. 11, no. 1, pp. 1–36, 2019.

Artificial fear for the control of autonomous robots

Andrea Usai and Alessandro Rizzo

Abstract—**We present a neuro-inspired control framework for autonomous robots that integrates an artificial emotion of fear, drawing inspiration from LeDoux's dual-pathway hypothesis. To replicate the "Low Road" pathway, our system comprises proxies for the thalamus, implemented as a nonlinear filter; the amygdala, modeled as a Soft Actor-Critic (SAC) reinforcement learning agent; the brainstem, orchestrated through a Nonlinear Model Predictive Controller (NMPC). The NMPC's parameters are adjusted by the amygdala, enabling it to generate control inputs to actuate the robot. Our preliminary results demonstrate that the robot exhibits a better adaptive behavior than a standard NMPC in both static and dynamic environments with obstacles characterized by different hazard levels.**

I. INTRODUCTION AND METHODOLOGY

Survival and self-preservation are crucial for developing intelligent robots that can adapt to dynamic and unknown environments [1]. Implementing artificial emotions, among which fear has been mostly pursued, can help robots to better evaluate and respond to unexpected and potentially dangerous situations [2]. While most approaches incorporate emotions as adaptive mechanisms to enhance human-robot interaction in social contexts [3], few efforts use artificial emotions for autonomous robot control. Here, we take inspiration from neuroscientific evidence to propose a novel implementation of an artificial fear mechanism in robotics, to enhance robot's self-preservation. The *Dual-pathway hypothesis* is a neuroscientific model developed by Joseph LeDoux [4], which describes how the brain interprets the fear of external stimuli and how this influences the resulting behaviour. LeDoux suggests the presence of two afferent neural pathways involving the amygdala, which work together to mediate the conditioned fear response: the *Low Road* and the *High Road.* The Low Road enacts instinctive and fast reactions to stimuli, whereas the High Road mediates these stimuli with contextual information, past experience and reasoning ability. Based on this model, we present a new fear-based control architecture to enhance robot's self-preservation. At present, the model only reproduces the Low Road, comprising the amygdala, the thalamus and the brainstem-musculoskeletal system connection (see Fig. 1(a)). Each component is modeled based on its primary functions within the pathway. A brief explanation of each component is provided below:

1) Thalamus: It collects, selects, and fuses different types of environmental stimuli and transmits them as raw information to the amygdala. We model it as a filtering function $\Phi(\mathbf{x}_k, \mathbf{x}_k^{\text{env}})$, which takes in input the robot state vector $\mathbf{x}_k$ and the available environment information $\mathbf{x}_k^{\text{env}}$ at the discrete time k to create an observation vector $\boldsymbol{s}_k = \Phi(\mathbf{x}_k, \mathbf{x}_k^{\text{env}}) = [\varphi_k^{(1)}, \varphi_k^{(2)}, \dots, \varphi_k^{(p)}]^T$ composed of the $p \in \mathbb{N}$ main features $\varphi_k^{(p)}$ that can help the amygdala to assess the situation the robot is facing (e.g. obstacles distances and velocities, etc).

2) Amygdala: It evaluates the raw signals coming from the thalamus to identify potential threats by associating them to a negative or positive consequence. This association is achieved by a punishment/reward mechanism that serves to determine the emotional valence of the stimulus [5]. Therefore, we design an artificial fear emotion $\mathcal{F}_k$ whose discrete time behaviour is described by $\mathcal{F}_k = \sigma(\boldsymbol{w}^T \mathbf{s}_k)$ where $\mathbf{s}_k$ is the observation state extracted by the thalamus, $\boldsymbol{w}^T$ is a vector of manually tuned weights and $\sigma(\cdot)$ is a sigmoid function. The amygdala augments the observation vector of the thalamus with the current fear value $\mathcal{F}_k$. At each time k, such an augmented observation vector $\widetilde{\boldsymbol{s}}_k = [\varphi_k^{(1)}, \varphi_k^{(2)}, \dots, \varphi_k^{(p)}, \mathcal{F}_k]^T$ is used by the amygdala to derive a vector of optimal parameter matrices $\boldsymbol{a}_k^* = \left[Q_k, R_k, \alpha_k, \beta_k\right]^*$ for the NMPC. The latter, which emulates the brainstem, exploits such parameter matrices to actuate the robot motion (i.e., the muscoloskeletal system). Such vector is selected over a continuous action space through a reinforcement learning approach based on a Soft Actor-Critic agent. The action selection is guided by a reward function defined as $R(\widetilde{\boldsymbol{s}}_k, \boldsymbol{a}_k) = R_F + R_I + R_G$ where R_F promotes actions that reduce fear, R_I penalizes actions leading to infeasible states for the NMPC and R_G promotes actions guiding the robot to its goal in the shortest possible time.

3) NMPC: As stated above, it receives its parameters from the amygdala, which accounts for the level of fear and other exogenous information. Here, we consider a mobile robot model as a unicycle (Fig. 1(b)), with discrete-time kinematics

$$\begin{bmatrix} x_{k+1} \\ y_{k+1} \\ \theta_{k+1} \end{bmatrix} = \begin{bmatrix} x_k \\ y_k \\ \theta_k \end{bmatrix} + T_s \begin{bmatrix} \cos\theta_k & 0 \\ \sin\theta_k & 0 \\ 0 & 1 \end{bmatrix} \begin{bmatrix} v_k \\ \omega_k \end{bmatrix} = f_d(\mathbf{x}_k, \mathbf{u}_k) \quad (1)$$

where $\mathbf{x}_k = \begin{bmatrix} x_k & y_k & \theta_k \end{bmatrix}^T$ and $\mathbf{u}_k = \begin{bmatrix} v_k & \omega_k \end{bmatrix}^T$ are the state vector and the control input vector at discrete time instant k, respectively. At each time step k, the amygdala provides parameter matrices Q_k, R_k, α_k and β_k to the NMPC, which computes the optimal control input sequence $\mathbf{u}^*(\cdot|k)$ over the prediction horizon $N \in \mathbb{N}$ by solving the following

---

The authors are with the Department of Electronics and Telecommunications, Politecnico di Torino, Torino, Italy. Email: {`andrea.usai`, `alessandro.rizzo`}@`polito.it`. This study was carried out within the FAIR - Future Artificial Intelligence Research and received funding from the European Union Next- GenerationEU (PIANO NAZIONALE DI RIPRESA E RESILIENZA (PNRR) – MISSIONE 4 COMPONENTE 2, INVESTIMENTO 1.3 – D.D. 1555 11/10/2022, PE00000013). This manuscript reflects only the authors' views and opinions, neither the European Union nor the European Commission can be considered responsible for them.

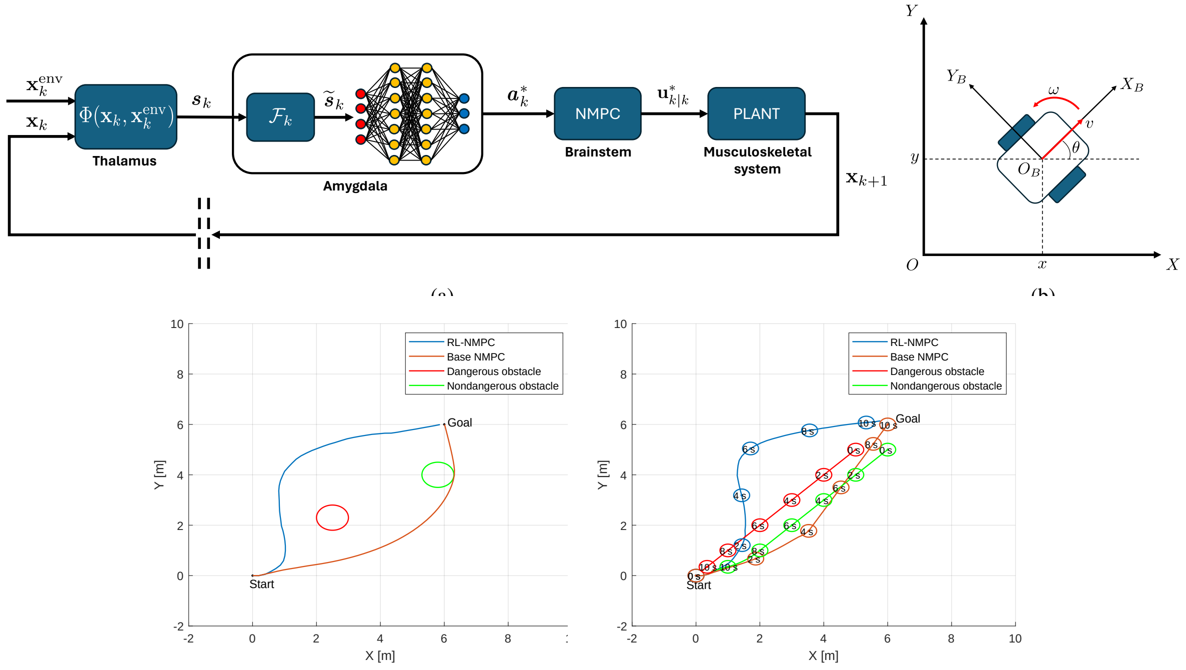

(c)

(d)

Fig. 1: a) Fear-based control architecture based on the Low Road - b) Coordinate systems of the mobile robot: $[x_k, y_k]$ and θ_k are the position and the orientation of the robot in the inertial frame $\{O, X, Y\}$, v_k and ω_k are the linear and angular velocity of the robot in the body frame $\{O_B, X_B, Y_B\}$, respectively - c) Comparison of RL-NMPC with a base NMPC in a static environment- d) Comparison of RL-NMPC with a base NMPC in a dynamic environment.

optimization problem:

$$\begin{aligned} \min_{\mathbf{u}(\cdot|k)} \quad & \sum_{i=0}^{N-1} \ell(\mathbf{x}_{k+i|k}, \mathbf{u}_{k+i|k}, Q_k, R_k) + B(\mathbf{x}_{k+i|k}, \alpha_k, \beta_k) \\ \text{s.t.} \quad & \mathbf{x}_{k|k} = \mathbf{x}_k, \\ & \mathbf{x}_{k+i+1|k} = f_d(\mathbf{x}_{k+i|k}, \mathbf{u}_{k+i|k}), \quad \forall i = 0, \dots, N-1, \\ & \mathbf{u}_{k+i|k} \in \mathbb{U}, \quad \mathbf{x}_{k+i+1|k} \in \mathbb{X}, \quad \forall i = 0, \dots, N-1, \end{aligned} \tag{2}$$

where $\mathbb{U}$ is the set of feasible control inputs and $\mathbb{X}$ is the set of feasible states. The stage cost $\ell(\mathbf{x}_{k+i|k}, \mathbf{u}_{k+i|k}, Q_k, R_k) = \left\|\mathbf{x}_r - C\mathbf{x}_{k+i|k}\right\|_{Q_k}^2 + \left\|\mathbf{u}_{k+i|k}\right\|_{R_k}^2$ is intended to guide the robot toward the goal $\mathbf{x}_r$ while the term $B(\mathbf{x}_{k+i|k}, \alpha_{k_j}, \beta_{k_j}) = \sum_{j=1}^{n_{obs}} -\alpha_{k_j} log(\beta_{k_j} \left\|C\mathbf{x}_{k+i|k} - \mathbf{x}_{obs_j}\right\|^2)$ is a logarithmic penalty function designed to move the robot away from the *j-th* harmful environmental obstacle in position $\mathbf{x}_{obs_j}$. Indeed, to ensure a better adaptive behaviour, the amygdala is able to estimate different logarithmic penalty function parameters α_{k_j} and β_{k_j} according the dangerousness of the *j-th* obstacles. Finally, the term $C = diag([1, 1, 0])$ is a matrix that extracts the robot's position from the state vector $\mathbf{x}_{k+i|k}$,

II. RESULTS AND DISCUSSION

Our approach has been validated through MATLAB simulations (see Fig. 1(c) and Fig. 1(d)). Preliminary results indicate that the robot's behavioral response can be modulated according to the fear level, producing better adaptive behavioral response with respect a standard NMPC, in both static and dynamic environments with different type of hazardous obstacles. Furthermore, our proposed approach provides two key advantages compared to a conventional NMPC implementation. Firstly, it guarantees an automatic parameter tuning mechanism, which is particularly beneficial in scenarios where manual parameter tuning could be challenging due to the complexity of the environment the robot operates in. Secondly, as the robot learns how to reach the goal, our approach eliminates the need for terminal cost, terminal constraint and a long prediction horizon to ensure successful navigation leading to a significant reduction in NMPC execution time. Nevertheless, the reactive response of the *Low Road* must be complemented by the mediated response of the *High Road,* to be suitably implemented with slower but more articulated decision-making processes. To this aim, we are exploring large language models to interpret the robot operational scenario and provide contextual information to attain a trade-off between reactive responses and long-term strategic planning.

REFERENCES

[1] K. Man and A. Damasio, "Homeostasis and soft robotics in the design of feeling machines," *Nature Machine Intelligence*, vol. 1, no. 10, pp. 446–452, 2019.

[2] J.-M. Fellous, "From human emotions to robot emotions," *Architectures for Modeling Emotion: Cross-Disciplinary Foundations, American Association for Artificial Intelligence*, pp. 39–46, 2004.

[3] C. P. Lee-Johnson and D. A. Carnegie, "Mobile robot navigation modulated by artificial emotions," *IEEE Transactions on Systems, Man, and Cybernetics, Part B (Cybernetics)*, vol. 40, no. 2, pp. 469–480, 2009.

[4] J. E. LeDoux, "Sensory systems and emotion: A model of affective processing." *Integrative psychiatry*, 1986.

[5] E. T. Rolls, "Neurophysiology and functions of the primate amygdala." 1992.

Session 1B: Vehicles

A Nonlinear MPC-based Adaptive Cruise Control for Electric Automotive Vehicles

Michele Pagone, Stefano Favelli, Raffaele Manca, Gabriel Jenner de Faria Orsi, Angelo Bonfitto,
Carlo Novara, Andrea Tonoli

I. INTRODUCTION

Electric Vehicles (EVs) are emerging as a promising, cleaner and more sustainable solution future for transportation, aiming to combat climate change and reduce our dependence on fossil fuels. EVs powertrain plays the main role in determining the overall performance and efficiency of an electric vehicle. An EV powertrain is composed of several interconnected subsystems, including the electric motor, power electronics (usually a DC/AC converter), and the energy storage system (usually lithium-ion batteries) [1], [2]. Efficiently managing and optimizing these subsystems is vital to achieve superior vehicle performance, extended driving range, and enhanced energy efficiency. In recent years, substantial advancements have been made in powertrain control strategies and optimization techniques, owing to breakthroughs in technology, computing power, and an increasing understanding of EV dynamics. The implementation of sophisticated control algorithms, intelligent energy management systems, and real-time optimization has revolutionized the way electric vehicles perform on the road. In this work, the purpose is to leverage the nonlinear Model Predictive Control (MPC) framework in order to design an efficient Adaptive Cruise Control (ACC) which accounts for the EV powertrain dynamics, in order to optimally managing the energy consumption of the battery to increase its range, and, thus, the energetic efficiency of the powertrain as a whole. A classic car following scenarios is studied, simulating a realistic ACC case, with the ego vehicle being controlled by the MPC, and the reference being generated using a Constant Time Gap (CTG) policy. Finally, the MPC is used to generate the required torque for a complete high-fidelity model of the case study vehicle, a Fiat 500e.

II. ELECTRIC VEHICLE DYNAMICS

The vehicle dynamics accounts for both the longitudinal chassis dynamics and the internal dynamics of the powertrain battery. In the following, we present a simplified vehicle nonlinear dynamics to be accounted as the MPC prediction model, whereas, as plant, an high-fidelity Fiat 500e model is employed. The longitudinal dynamics can be described as the sum the inertial force and the resistance forces: i) forces due to road inclination F_{slope}, ii) aerodynamics drag $F_{aero}(v_{vh})$, and iii) rolling resistance $F_{roll}(v_{vh})$, such that

$$\dot{v}_{vh} = \frac{1}{M_{vh}}\left(\frac{T_{wh}}{r_{wh}} - F_{slope} - F_{aero}(v_{vh}) - F_{roll}(v_{vh})\right) \quad (1)$$

where M_{vh} is vehicle mass, T_{wh} is the equivalent wheel torque and r_{wh} is the wheel radius. Note that, $F_{roll}(v)$ and $F_{aero}(v)$ are linear and quadratic function of the vehicle velocity, respectively. Concerning the battery model, the dynamics is written is terms of the battery state of charge (SOC) time evolution, i.e. the variation of the ration between the current battery charge and the nominal battery capacity (see, e.g., [3]). The torque at wheels can be related to the torque delivered by the powertrain as

$$T_{EM} = T_{wh}/\eta_{tr}^{\mathrm{sign}(T_{wh})\tau_{gb}} \quad (2)$$

where τ_{gb} and η_{tr} are the gearbox ratio and efficiency, respectively. Since the power of the electric motor is $P_{EM} = T_{EM}\omega_{EM}$ – where ω_{EM} is the electric motor angular rate – the power of the battery can be directly related to P_{EM}, given the electric motor efficiency map, as

$$P_b = P_{EM}/\eta_{EM}^{\mathrm{sign}(P_{EM})}. \quad (3)$$

Hence, the EM dynamics is given by

$$\dot{SOC} = -\frac{I_b}{Q_{nom}\eta_b^{\mathrm{sign}(I_b)}} \quad (4)$$

where Q_{nom} is the nominal battery capacity, η_b is the Columbic efficiency,

$$I_b = (V_{oc} - \sqrt{V_{oc}^2 - 4R_oP_b})/2R_o \quad (5)$$

is the battery current, P_b is the power delivered by the battery, V_{oc} is the battery open-circuit voltage, and R_o is the output resistance. Note that V_{oc} and R_o depend on the SOC itself and their value as been obtained by piece-wise polynomial fitting. In the end, for control purposes, the state is$x = [x_{vh}, v_{vh}, SOC]^\top$ – being x_{vh} the vehicle position – and the input $u = a_{vh} \doteq \dfrac{T_{wh}}{M_{vh}r_{wh}}$.

M. Pagone and C. Novara are with the Department of Electronics and Telecommunications, Politecnico di Torino. S. Favelli, G. Jenner de Faria Orsi, A. Bonfitto and A. Tonoli are with the Department of Mechanical and Aerospace Engineering, Politecnico di Torino. The work is supported by MOST (Sustainable Mobility National Research Center) and funded by the European Union NextGenerationEU project (Piano Nazionale di Ripresa e Resilienza - Mission 4, Component 2, Investment 1.4 - D.D. 1033 17/06/2022 - CN00000023). The work reflects only the authors' views and opinions, neither the European Union nor the European Commission can be considered responsible for them. Corresponding author: `michele.pagone@polito.it`.

III. PROPOSED MPC FORMULATION

The vehicle longitudinal and battery dynamics can be viewed as an affine-in-the-input nonlinear system

$$\dot{x}(t) = f(x(t)) + u(t) \tag{6}$$

where $x(t) \in \mathcal{X} \subseteq \mathbb{R}^{n_x}$ is the state vector at time $t \in \mathbb{R}$, $u(t) \in \mathcal{U} \subseteq \mathbb{R}^{n_u}$ is the input vector (where $\mathcal{U} \ni 0$ is a convex, closed, and compact set). The measurements of the state vector are sampled with period $T_S > 0$. At each sampling time $t = t_k$, a prediction of the system state $\hat{x}(t)$ over the time interval $[t_k, t_k + T_p]$ is performed, where $T_p \geq T_S$ is the prediction horizon.

The nonlinear MPC optimal control problem is formulated as follows.

$$\begin{aligned} & u^* = \arg\min_{u} J\big(x(t), u(t)\big) \\ & \text{subject to:} \\ & \dot{\hat{x}}(\tau) = f(\hat{x}(\tau)) + \hat{u}(\tau), \quad \hat{x}(t_k) = x(t_k), \\ & \hat{x}(\tau) \in \mathcal{X} \subset \mathbb{R}^{n_x}, \ \hat{u}(\tau) \in \mathcal{U} \subset \mathbb{R}^{n_u}, \quad \forall \tau \in [t_k, t_k + T_p]. \end{aligned} \tag{7}$$

Hence, associating to each solution $\hat{x}$ of (7) the tracking error $\tilde{x}(\tau) = \hat{x}(\tau) - x_r$, we employ the following performance index

$$J = \int_{t_k}^{t_k+T_p} \big(\|\tilde{x}(\tau)\|^2_{\mathbf{Q}} + \|\hat{u}(\tau)\|^2_{\mathbf{R}}\big)\ \mathrm{d}\tau \ + \|\tilde{x}(t_k + T_p)\|^2_{\mathbf{P}}. \tag{8}$$

IV. NUMERICAL EXAMPLE

A CTG policy is employed as generator for the relative velocity to be followed by the ego vehicle:

$$\dot{v}_{CTG} = -\frac{\lambda}{h}(x_{vh}h + d_{ref} + \epsilon) - \frac{\dot{\epsilon}}{h} \tag{9}$$

where h is the time gap (in seconds), λ is design parameter, ϵ is the relative distance between the two cars, and d_{ref} is the default distance to be kept between the two vehicles. In the proposed scenario, saturation of maximum torque delivered to the wheels is accounted, as $|T_{wh}| \leq 250\,Nm$. Given a realistic driving cycle, whose motor torque is the one in Figure 1, the CTG-based MPC is able to cope with the given reference in order to enhance the efficiency of the vehicle powertrain, while closely following the reference prescribed by the CTG policy. The model has been sampled at $0.05\,s$, while the prediction time window is set as $T_p = 10T_s$. Concerning the MPC weighting matrices, $\mathbf{R} = 0.05$, $\mathbf{P} = \mathrm{diag}(0, 0, 10000)$, $\mathbf{R} = \mathrm{diag}(0, 0, 1)$. MPC results of the ACC scenario are plotted in Figures 2-3 From the simulations results, we can highlight how the MPC controller, combined to the CTG policy, provides a smoother torque/acceleration signal then the reference relevant to the driving cycler. In the ACC scenarios, the distance between the vehicles oscillated around the set distance, while avoiding collision along all the driving cycle. As future research lines, the MPC controller can be tested in a real vehicle. Also, an economic MPC for reference tracking [4] can be employed for obtaining still more powertrain efficiency.

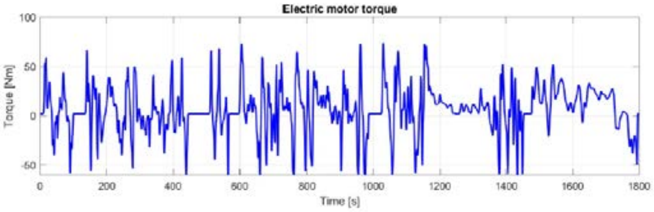

Fig. 1. Reference torque profile.

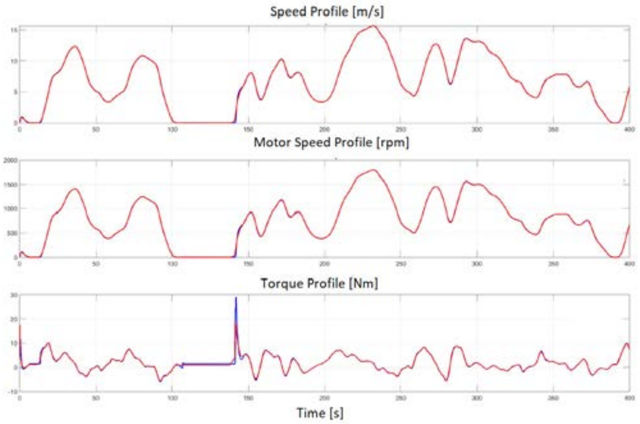

Fig. 2. MPC controlled and reference powertrain variables. The reference signals are drawn in red, the controlled ones in blue.

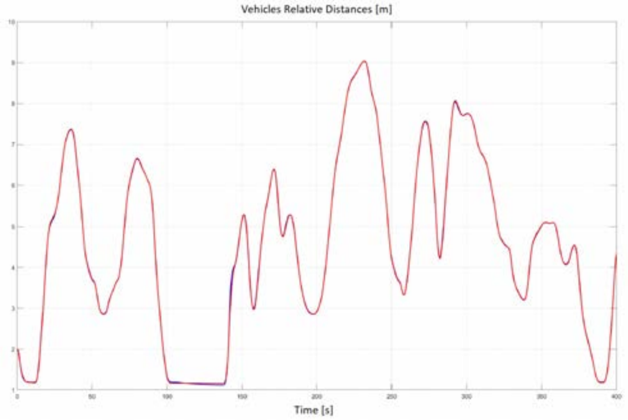

Fig. 3. Vehicle relative distance. The reference distance is drawn in red, the controlled ones in blue.

REFERENCES

[1] V. K. Kasimalla and V. Velisala, "A review on energy allocation of fuel cell/battery/ultracapacitor for hybrid electric vehicles," *International Journal of Energy Research*, vol. 42, no. 14, pp. 4263–4283, 2018.

[2] N. Sulaiman, M. Hannan, A. Mohamed, E. Majlan, and W. W. Daud, "A review on energy management system for fuel cell hybrid electric vehicle: Issues and challenges," *Renewable and Sustainable Energy Reviews*, vol. 52, pp. 802–814, 2015.

[3] S. Onori, L. Serrao, and G. Rizzoni, *Hybrid Electric Vehicles: Energy Management Strategies*, 1st ed. Springer, 2016.

[4] A. Ferramosca, D. Limon, and E. F. Camacho, "Economic MPC for a changing economic criterion for linear systems," *IEEE Transactions on Automatic Control*, vol. 59, no. 10, pp. 2657–2667, 2014.

Experimental Validation of Safe MPC for Autonomous Driving in Uncertain Environments

Ivo Batkovic[1,2], Ankit Gupta[2], Mario Zanon[3], and Paolo Falcone[1,4]

I. INTRODUCTION

Model Predictive Control (MPC) has been commonly used in autonomous driving. While it is well-known how to design an MPC controller such that closed-loop stability w.r.t. a reference trajectory (or path) is obtained and that constraint satisfaction holds at all times, the results in the literature rely on assumptions that are violated in practice. We address the problem of ensuring the safe operation of an autonomous vehicle in uncertain environments by relying on the Model Predictive Flexible trajectory Tracking Control (MPFTC) framework [1], [2], and we show in practice how a safe vehicle controller can be designed for urban autonomous driving settings.

II. PROBLEM FORMULATION

We consider a discrete-time nonlinear system defined by

$$\mathbf{x}_{k+1} = f(\mathbf{x}_k, \mathbf{u}_k), \tag{1}$$

where $\mathbf{x}_k \in \mathbb{R}^{n_\mathbf{x}}$ denotes the state and $\mathbf{u}_k \in \mathbb{R}^{n_\mathbf{u}}$ denotes the control input at time k. The system is subject to state and input constraints of two categories: a-priori known constraints $h(\mathbf{x}, \mathbf{u}) : \mathbb{R}^{n_\mathbf{x}} \times \mathbb{R}^{n_\mathbf{u}} \to \mathbb{R}^{n_h}$, which might be time-varying but which are fully known beforehand; and a-priori unknown constraints $g(\mathbf{x}, \mathbf{u}) : \mathbb{R}^{n_\mathbf{x}} \times \mathbb{R}^{n_\mathbf{u}} \to \mathbb{R}^{n_g}$, whose functional form is known a priori, but whose value is not. In both cases, the state and input must satisfy $h(\mathbf{x}, \mathbf{u}) \leq 0$, $g(\mathbf{x}, \mathbf{u}) \leq 0$ and all inequalities are defined element-wise. Examples of a-priori known constraints include engine torque limitations and braking force, while examples of a-priori unknown constraints include collision avoidance with other road users.

Due to the nature of the known and unknown constraints, we use $g_{n|k}(\mathbf{x}, \mathbf{u})$ to denote function g at time n, given the information available at time k. Moreover, we will denote by $g_n(\mathbf{x}, \mathbf{u}) := g_{n|\infty}(\mathbf{x}, \mathbf{u}) = g_{n|k}(\mathbf{x}, \mathbf{u})$, $\forall\, k \geq n$ the real constraint, since in general $g_{n|k}(\mathbf{x}, \mathbf{u}) \neq g_n(\mathbf{x}, \mathbf{u})$, $\forall\, k < n$. Note that instead for a-priori known constraints $h_{n|k}(\mathbf{x}, \mathbf{u}) := h_n(\mathbf{x}, \mathbf{u})$ holds $\forall\, k$ by definition. Throughout the remainder of the paper, we also apply the same notation to the predicted state and inputs, e.g., $\mathbf{x}_{n|k}$ and $\mathbf{u}_{n|k}$ denote the predicted state and input at time n given the current time k. In addition, we will use $\mathbb{I}_a^b := \{a, a+1, ..., b\}$ to denote a set of integers.

We consider the problem of tracking a user-defined parameterized reference $\mathbf{r}(\tau) := (\mathbf{r}^\mathbf{x}(\tau), \mathbf{r}^\mathbf{u}(\tau))$ as closely as possible. Parameter τ is a "fictitious time": if τ is selected to be time, its natural dynamics are given by $\tau_{k+1} = \tau_k + t_\mathrm{s}$, where t_s is the sampling time.

To ensure that requirements (a) and (b) are satisfied in the urban autonomous driving setting, we use the framework proposed in [1], where the dynamics of the reference trajectory are modified using the dynamics for τ given by

$$\tau_{k+1} = \tau_k + t_\mathrm{s} + v_k, \tag{2}$$

where v is an additional auxiliary control input, and τ comes as an auxiliary state. The Model Predictive Flexible trajectory Tracking Control (MPFTC) [1, Section V.A] can then be formulated as

$$\begin{aligned}
\min_{\substack{\mathbf{x},\mathbf{u}\\ \tau, v}} \; & \sum_{n=k}^{k+N-1} q_\mathbf{r}(\mathbf{x}_{n|k}, \mathbf{u}_{n|k}, \tau_{n|k}) + w v_{n|k}^2 && \text{(3a)}\\
& \qquad\qquad + p_\mathbf{r}(\mathbf{x}_{k+N|k}, \tau_{k+N|k}) \\
\text{s.t. } & \mathbf{x}_{k|k} = \mathbf{x}_k, \;\; \tau_{k|k} = \tau_k, && \text{(3b)}\\
& \mathbf{x}_{n+1|k} = f(\mathbf{x}_{n|k}, \mathbf{u}_{n|k}), \quad n \in \mathbb{I}_k^{k+M-1}, && \text{(3c)}\\
& \tau_{n+1|k} = \tau_{n|k} + t_\mathrm{s} + v_{n|k}, \quad n \in \mathbb{I}_k^{k+M-1}, && \text{(3d)}\\
& h_n(\mathbf{x}_{n|k}, \mathbf{u}_{n|k}) \leq 0, \quad n \in \mathbb{I}_k^{k+M-1}, && \text{(3e)}\\
& g_{n|k}(\mathbf{x}_{n|k}, \mathbf{u}_{n|k}) \leq 0, \quad n \in \mathbb{I}_k^{k+M-1}, && \text{(3f)}\\
& \mathbf{x}_{k+n|k} \in \mathcal{X}_\mathbf{r}^\mathrm{s}(\tau_{k+n|k}), \quad n \in \mathbb{I}_{k+N}^{k+M-1}, && \text{(3g)}\\
& \mathbf{x}_{k+M|k} \in \mathcal{X}_\mathrm{safe}(\tau_{k+M|k}) \subseteq \mathcal{X}_\mathbf{r}^\mathrm{s}(\tau_{k+M|k}). && \text{(3h)}
\end{aligned}$$

where k is the current time, N is the prediction horizon associated with a cost, $M \geq N$ is the full prediction horizon, $q_\mathbf{r}$ and $p_\mathbf{r}$ are cost functions that penalize deviations from the reference trajectory $\mathbf{r}(\tau) = (\mathbf{r}^\mathbf{x}(\tau), \mathbf{r}^\mathbf{u}(\tau))$, and $w > 0$ is associated with the cost of the auxiliary input $v_{n|k}$. The predicted state and control inputs are denoted by $\mathbf{x}_{n|k}$ and $\mathbf{u}_{n|k}$, respectively. Constraints (3g) and (3h) define a stabilizing set and a safe set, respectively. Note that Problem (3) can be seen as a two stage-problem, where the first stage $n \in \mathbb{I}_k^{k+N}$ defines the MPC problem, and the second stage $n \in \mathbb{I}_{k+N+1}^{k+M}$ defines the terminal set implicitly. This implicit terminal set formulation relates to the safety design which ensures that the state $\mathbf{x}_{k+N|k}$ is able to reach the safe set $\mathcal{X}_\mathrm{safe}(t_{k+M|k})$ in a finite amount of time $M - N \geq 0$ while satisfying the system dynamics and the a-priori known and unknown constraint. For

---

This work was partially supported by the Wallenberg Artificial Intelligence, Autonomous Systems and Software Program (WASP) funded by Knut and Alice Wallenberg Foundation.

[1] Ivo Batkovic and Paolo Falcone are with the Mechatronics group at the Department of Electrical Engineering, Chalmers University of Technology, Gothenburg, Sweden `{ivo.batkovic,falcone}@chalmers.se`

[2] Ivo Batkovic, and Ankit Gupta are with the research department at Zenseact AB `{ivo.batkovic,ankit.gupta}@zenseact.com`

[3] Mario Zanon is with the IMT School for Advanced Studies Lucca `mario.zanon@imtlucca.it`

[4] Paolo Falcone is with the Dipartimento di Ingegneria "Enzo Ferrari" Università di Modena e Reggio Emilia, Italy `falcone@unimore.it`

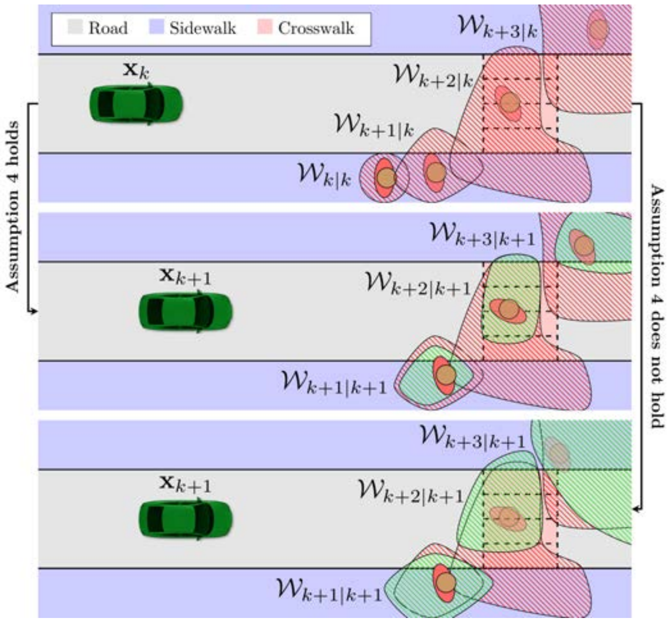

Figure. 1. The top panel shows an initial prediction for a pedestrian at time k, while the middle and bottom panels show different predictions at time $k+1$. The middle panel illustrates a model that satisfies (**??**), i.e., satisfying Assumption **??**, while the bottom panel does not satisfy (**??**), hence, Assumption **??** is also not satisfied.

a more detailed discussion related to the design of Problem (3), we refer the reader to [1].

Due to the lack of space, we will illustrate the main assumptions by means of some figures. The first assumption is that the pedestrian model is consistent, i.e., the predicted uncertainty cannot increase in future predictions, as illustrated in Figure 1. The second assumption is that we need to predict the presence of obstacles at the boundary of the sensor range in order to guarantee that in case an obstacle is indeed present the controller already accounted for that possibility. This is illustrated in Figure 2. Finally, as the uncertainty related to the presence of other road users cannot be controlled, it grows infinitely large. In order to deal with that issue, we postulate the existence of a safe set, i.e., a set in which all a-priori unknown constraints can be neglected, though possibly other a-priori known constraints might be introduced. A simple possibly oversimplistic example of such a set is the case in which the vehicle stops. For all details we refer teh interested reader to [2].

III. EXPERIMENTAL RESULTS

We deployed the safe MPC controller on a full-scale Volvo XC90 T6 petrol-turbo SUV at a closed test track in order to verify the performance in practice. The vehicle offers an actuation interface that accepts longitudinal acceleration requests and steering wheel angle setpoint requests.

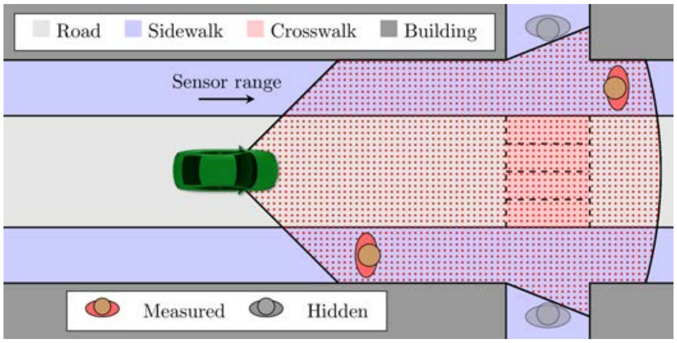

Figure. 2. Situation where the sensor range is not able to see pedestrians behind the corner of the building.

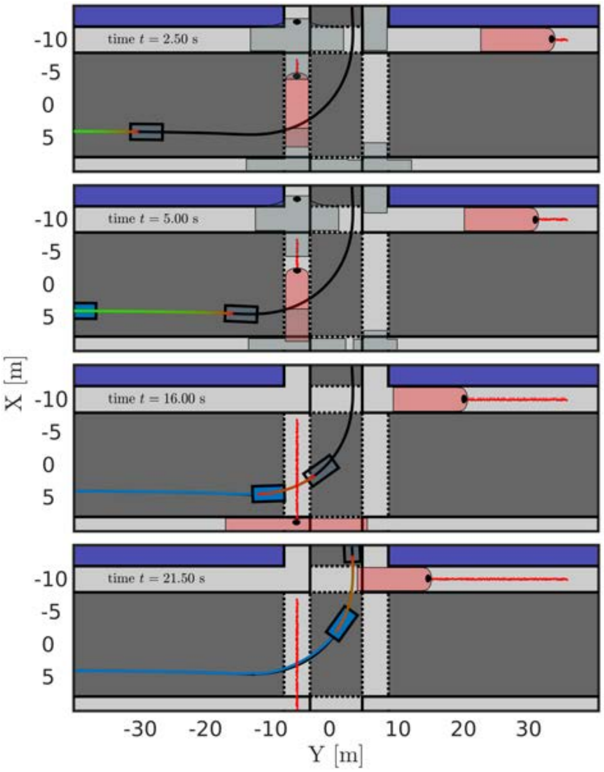

Figure. 3. The vehicle bounding box is illustrated by the blue box, while the predicted pedestrian motion is illustrated by the red regions for the real pedestrians and gray regions for the virtual pedestrians. The opaque box represents the terminal state, and the line connecting the vehicle bounding box and the opaque box illustrate the predicted open loop solution. The blue and red lines denote the traveled history of the vehicle and pedestrians, respectively

Due to the lack of space, we will limit ourselves to comment that the experimental results displayed in Figure 3 closely matched the simulation results and successfully avoided collisions with pedestrians. All details of the simulations and experiments can be found in [2], and a video is available at https://www.youtube.com/watch?v=nS8AFg21MTA&ab_channel=MechatronicsGroupatChalmersUniversity.

REFERENCES

[1] I. Batkovic, M. Ali, P. Falcone, and M. Zanon, “Safe trajectory tracking in uncertain environments,” *IEEE Transactions on Automatic Control*, pp. 1–14, 2022.

[2] I. Batkovic, M. Ali, P. Falcone, and M. Zanon, “Safe Trajectory Tracking in Uncertain Environments,” *IEEE Transaction on Automatic Control*, vol. 68, no. 7, pp. 4204–4217, 2023.

A Dynamic Programming approach for road traffic estimation

Mattia Laurini, Irene Saccani, Stefano Ardizzoni, Luca Consolini, and Marco Locatelli*

Many municipalities use systems to measure traffic flows at main roads and intersections. These systems employ various types of sensors, such as inductive loop detectors, video detection systems, microwave radar sensors, and LIDAR sensors. In this work, we focus on reconstructing the paths traveled by users based on available flow measurements. Specifically, we represent a road network as a directed graph and assume that several traffic flow measurements are available on all or some of the network's arcs. Users are divided into distinct groups, each taking a different route, with their flows modeled through independent Poisson processes. Our primary goal is to determine the routes taken by each user group and estimate the average rates of the corresponding Poisson processes.

Our research falls within the broader context of Network Tomography, first formulated by Vardi in 1996 (see [7]). The aim is to estimate the traffic demand of origin–destination (OD) pairs from the knowledge of traffic flows over certain network links. Ever since, this problem has been extensively studied, with numerous variations explored (see, e.g., [4]). Network Tomography is crucial not only in transportation networks but also in data communication networks. Many Network Tomography formulations assume limited available measurements and attempt to infer link characteristics and congestion within the network. Previous studies have addressed the problem of selecting minimal subsets of paths to monitor in order to infer the loss rates and latencies of other network paths (see, for instance [2]). Typically, traffic flows are assumed to be independent Poisson random processes, simplifying the problem formulation (see, e.g., Theorem 1.1 in Chapter 5 of [5]).

The main contribution of this work is given by the development of an approach for estimating traffic demands and road usage in a network, addressing the OD Tomography problem and identifying paths with non-zero flow. The novelty of such approach lies in the combination of Dynamic Programming, a technique from Computer Science and Control Theory, and Cumulant Generating Functions, a statistical tool. First, we define a partial order on the paths set and a monotone non-increasing function, deriving theoretical properties that support a Dynamic Programming procedure for efficiently solving the problem. By assuming known network topology, this method focuses on determining traffic demands and user paths, offering a detailed analysis of traffic behavior and network usage. The proposed Dynamic Programming algorithm operates by traversing possible paths and computing the necessary high-order cumulants to solve the estimation problem. Note that if paths connecting multiple OD pairs pass through the same measured arcs, only their aggregate contribution can be determined, not individual demands. This work also relates to studies using higher-order cumulants and heuristic procedures to reduce the number and order of computed cumulants, with the proposed method deterministically computing all necessary cumulants for solving the problem.

We tested our algorithm on two well-known benchmark networks, the NSFnet [1] and the Sioux Falls network [6], depicted in Figure 1 and 2, respectively, using synthetic data where true demands and paths were known. This allowed us to test the method in a setting in which the exact solution is known and compare the results obtained with our algorithm with the solutions of the synthetic

---

*All authors are with the Dipartimento di Ingegneria e Architettura, Università degli Studi di Parma, Parco Area delle Scienze, 181/A, 43124 Parma, Italy. E-mails: {`mattia.laurini`, `irene.saccani`, `stefano.ardizzoni`, `luca.consolini`, `marco.locatelli`}`@unipr.it`.

Project funded under the National Recovery and Resilience Plan (NRRP), Mission 4 Component 2 Investment 1.5 – Call for tender No. 3277 of 30/12/2021 of Italian Ministry of University and Research funded by the European Union – NextGenerationEU. Award Number: Project code ECS00000033, Concession Decree No. 1052 of 23/06/2022 adopted by the Italian Ministry of University and Research, CUP D93C22000460001, "Ecosystem for Sustainable Transition in Emilia-Romagna" (Ecosister).

tests. As expected, the error in estimating traffic demands decreases as measurements data sets increase. This improvement is due to the increased accuracy of estimating joint cumulants with more measurements. Despite the theoretical discussion, we acknowledge that in practical applications computing cumulants of orders higher than three can be numerically unstable and sensitive to noise and outliers (see, for instance, [3]). Future works aim at adapting the algorithm to balance the use of higher-order cumulants while avoiding their drawbacks, making the procedure more robust.

Figure 1: Graph of NSFnet.

Figure 2: Graph of Sioux Falls.

References

[1] L. H. Bonani. Modeling an optical network operating with hybrid-switching paradigms. *Journal of Microwaves, Optoelectronics and Electromagnetic Applications*, 15(4):275–291, December 2016.

[2] Y. Chen, D. Bindel, H. Song, and R. H. Katz. An algebraic approach to practical and scalable overlay network monitoring. In *ACM SIGCOMM Computer Communication Review*, volume 34, pages 55–66, August 2004.

[3] P. Filzmoser, R. Maronna, and M. Werner. Outlier identification in high dimensions. *Computational Statistics & Data Analysis*, 52:1694–1711, 2008.

[4] T. He, L. Ma, A. Swami, and D. Towsley. *Network Tomography: Identifiability, Measurement Design, and Network State Inference.* Cambridge University Press, 2021.

[5] H. M. Taylor and S. Karlin. *An Introduction To Stochastic Modeling.* Academic Press, third edition, 1998.

[6] Transportation Networks for Research Core Team. Transportation networks for research, https://github.com/bstabler/transportationnetworks, February 2024.

[7] Y. Vardi. Network tomography: Estimating source-destination traffic intensities from link data. *Journal of the American Statistical Association*, 91(433):365–377, 1996.

Trajectory optimization of multi robot systems using opinion dynamics

Bhaskar Varma, Karl D. von Ellenrieder

Facoltà di Ingegneria, Libera Universitá di Bolzano, 39100 Bolzano, BZ, Italia

Corresponding author: bhaskarvarma@ieee.org

Abstract

The paper proposes a decentralized optimization approach based on opinion dynamics, for decision making in multi robot systems, during trajectory planning in dynamic environments to avoid deadlocks and indecision's.

Keywords: trajectory planning, opinion dynamics, decision-making

---

1. Introduction

Multi robot trajectory planning has been gaining attention in recent years, due to its application in many fields. Consider a collection of multiple robots, connected vehicles, swarm of drones or even heterogeneous agents collaborating for a common goal. Tasks like path re-planning and trajectory optimization for a single robot, in a real time environment with dynamic obstacles, are challenging. Such tasks are even more complex when we consider multiple robots with different goals because often robots fall into indecision's resulting in deadlocks and collisions.

There are several centralized [1] architectures where the decision making is done by a single agent, or by a centralized system. But most of the centralized architectures neglect the feedback from different agents and merely work on priority-based algorithms, which are not efficient in the real world. On the other hand, decentralized [2] architectures, where each agent has equal decision power, provide more agility and overall safety for the systems working in environments with dynamic obstacles and disturbances. Although many methods have been proposed in the literature to ensure safe navigation of multi robot systems, preventing deadlocks in a decentralized fashion with global consensus still remains an open problem.

2. Opinion dynamics induced control

This is a recently developed method for decision making in multi agent systems, which is gaining interest as it makes use of cooperative feedback from all agents in the form of opinion [3] and attention dynamics. The theory behind this approach works on breaking indecision in large groups using bifurcation theory [4]. As shown in Figure 1, during trajectory planning every agent has multiple options while maneuvering for its task. Based on the option chosen by a single agent, we calculate the influence of it, on other agents in the form of opinion dynamics. An agent's opinion is influenced by the opinions of others only when it's attention [5] exceeds a critical level.

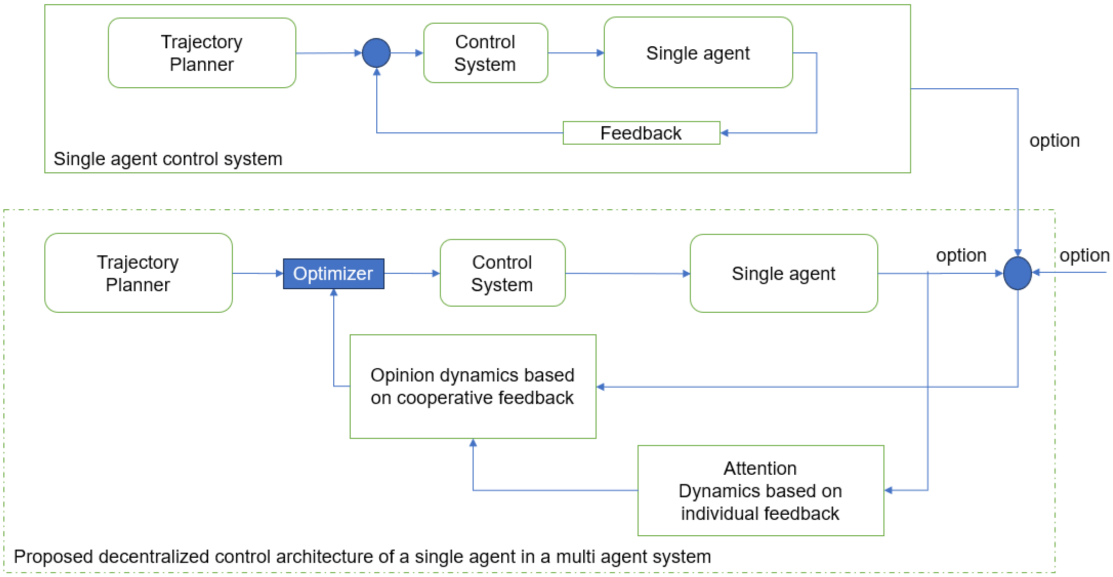

Figure 1: Hypothesized model

3. Remarks

This methodology, with application to ground vehicles for trajectory optimization, is further differentiated to optimize the longitudinal and lateral motion of the robot separately. The model provides an analytically tractable solution to the multi robot trajectory planning problem and also guarantees to break indecision in a collective manner with global consensus. Integrating it with suitable control method becomes crucial in yielding successful results.

References

[1] F. Matoui, B. Boussaid, B. Metoui, M. N. Abdelkrim, Contribution to the path planning of a multi-robot system: centralized architecture, Intelligent Service Robotics 13 (2020) 147–158.

[2] J. Salvado, M. Mansouri, F. Pecora, Dimopt: a distributed multi-robot trajectory optimization algorithm, in: 2022 IEEE/RSJ International Conference on Intelligent Robots and Systems (IROS), 2022, pp. 10110–10117. doi:10.1109/IROS47612.2022.9981345.

[3] N. E. Leonard, A. Bizyaeva, A. Franci, Fast and flexible multiagent decision-making, Annual Review of Control, Robotics, and Autonomous Systems 7 (2024).

[4] A. Franci, M. Golubitsky, I. Stewart, A. Bizyaeva, N. E. Leonard, Breaking indecision in multiagent, multioption dynamics, SIAM Journal on Applied Dynamical Systems 22 (2023) 1780–1817.

[5] A. Bizyaeva, A. Franci, N. E. Leonard, Nonlinear opinion dynamics with tunable sensitivity, IEEE Transactions on Automatic Control 68 (2022) 1415–1430.

Enhancing Reinforcement Learning for Automated Driving through Virtual Lane Logic*†

Alessandro Fasiello[1], Francesco Cerrito[1], Valentino Razza[2] and Massimo Canale[1]

[1]Department of Control and Computer Engineering, Politecnico di Torino, Torino, Italy.
[2]Department of Management and Production Engineering, Politecnico di Torino, Torino, Italy.

Abstract

This work investigates an alternative approach to current control systems for the Automated Driving (AD) of shuttle vehicles on dedicated roads. The proposed solution decouples the problem into two levels: a Deep Deterministic Policy Gradient (DDPG) Reinforcement Learning (RL) agent and a dedicated vehicle logic generating Virtual Lane (VL) data to eliminate redundancy and allow for smooth lane changes on curved roads. The training uses an environment defined through a model-based simulation, exploiting MatLab and Simulink tools, and has been conducted following a Curriculum Learning strategy. The performance of the introduced approach have been evaluated by testing the agent capabilities and exploring its behavior in the presence of external disturbances in the controlled states.

Introduction

Systems for Automated Driving (AD) leverage a great variety of cutting-edge technologies, such as Reinforcement Learning (RL), to perform the principal Dynamic Driving Tasks (DDTs) such as Adaptive Cruise Control (ACC), Lane Keeping (LK), and Lane Change (LC) [1].

Different RL implementations, methodologies, and paradigms can be found in literature: path, trajectory, and motion planning, optimization of actuation control, complex navigation and traffic decision-making, and lane position control are just a few examples outlined by [2] survey.

One of the most common driving scenarios in RL for AD literature is the racing one, where the need to run with the highest feasible speed while avoiding crashes is easily modeled by a reward function. These solutions exploit mainly a black-box approach, where the scenario readings given by the simulator is directly used as observation input by the agent without any pre-elaboration. As an example [3], and [4] present Deep Deterministic Policy Gradient (DDPG) agents for fast driving on the simulated racing circuit controlling acceleration, brake, and steering angle of the vehicle. The highway environment is another of the most important areas of application for AD, and the literature provides several examples of RL being used to directly control or support various subsystems for DDTs. In [5] a RL system for LK, comparing the performances of Deep Q-Network (DQN) and DDPG algorithms on a simulation system where the vehicle, initialized in a random heading angle and tracking error, is required to follow a highway-like road with constant curvature, controlling the steering angle.

The urban environment is the most complex, characterized by sharper curves and complex interactions with other actors on the road. This paper presents an RL-based AD approach. The approach exploits already available data from state-of-the-art lane boundary and road geometry recognition systems implemented on modern cars. This prevents a black-box solution that, starting from raw data like a camera image, directly computes the vehicle control input. The advantages are two-fold: the algorithm can focus on specific tasks while, on the other hand, the structure is kept simple. The work aims to present a new framework where a suitable Virtual Lane Logic (VLL) supports the learning of the RL agent and its control of the system, generating data for executing LC tasks smoothly and safely, even in the case of curved roads. This enhancement, while reducing the size of the needed observation input of the agent, allows the utilization in an urban environment of simpler neural networks (of dimension similar to the one used in the cited racing solutions) than the complex convolutional ones exploited in this scenario type.

Problem set-up

The goal of this work is to develop an AD solution for shuttle vehicles oriented to the fourth SAE level [6], capable of driving on dedicated roads. In this context, the proposed solution focuses on a low-complexity scenario where the shuttle operates in a restricted area without vulnerable road users. The vehicle can perform a complete range of maneuvers. In particular, it can start and stop at a pre-determined point and merge into and out of the main traffic lane. To meet all the application requirements, restrictions are placed on the vehicle's behavior, such as limiting the maximum speed to 50 km/h.

The proposed solution is developed and tested on a properly designed scenario. The shuttle route is placed in Torino, Italy, in a neighborhood of Politecnico area (see Fig. 1), with 12 strategic shuttle stop stations in an urban scenario. This road network is ideal for testing AD solutions thanks to the presence of vehicle-to-everything (V2X) facilities. In a V2X application framework, the infrastructure provides the vehicle with all information about speed limits and destination locations. The infrastructure also provides constraints on the required path length and the target lane for LC maneuvers.

The VLL can be suitably adapted to different scenario condi-

---

*This work is partly supported by the project Piano Nazionale di Ripresa e Resilienza (PNRR)-Next Generation Europe, which has funded by the European Union and the Italian Ministry of University and Research – DM 117/2023.

†Article accepted at "2024 Modeling, Estimation and Control Conference" (AACC, IFAC)

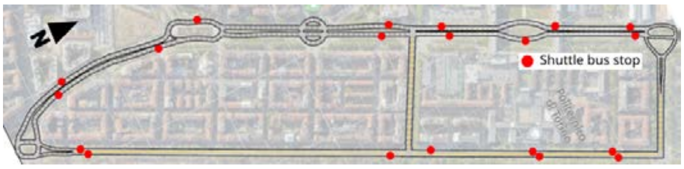

Figure 1: *Bird's eys view of the target circuit with interest map section of Torino, Italy, in the background.*

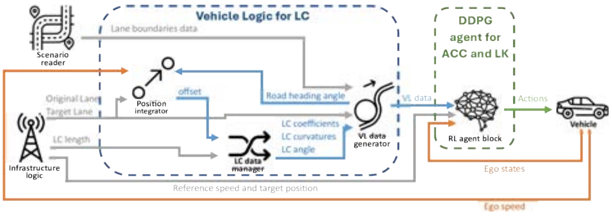

Figure 2: *Main flow of data inside the control architecture of the solution.*

tions and provided data. In the proposed solution, the agent receives the Virtual Lane (VL) data as input, as opposed to raw and redundant information produced by sensors. Thus, the VLL represents an intermediate layer capable of extending the usability of the trained networks to different data structures. The proposed framework separates the problems of planning and control. This increases the flexibility and explainability of the solution, enhancing the ability to understand the controller's behavior and intervene in case of evident biases. The core of the vehicle control is represented by a DDPG agent that interacts with the environment, as shown in Figure 2, receiving Observations and computing Actions. In coherence with SAE Level 4 application, the Agent acts on both the vehicle's longitudinal acceleration and steering speed. The Observation set is composed of 35 features mainly describing the vehicle state, the virtual lane, and the infrastructure information. Since DDPG is a deterministic agent, during learning, an Ornstein-Uhlenbeck noise structure is superimposed to the actions taken to allow for exploration.

Results

After suitable training a comprehensive simulation is carried out to evaluate the effectiveness of the proposed solution. The simulations have been performed in the MatLab and Simulink environments. The Automated Driving toolbox and the Vehicle Dynamics Blockset have been employed to simulate, respectively, the desired path and the vehicle dynamics.

In the graph illustrating the input control action (Figure 3), it is noticeable that both the vehicle's longitudinal acceleration and steering speed are consistently within the design limits. In addition, the vehicle can accurately track the VL with a maximum error of about 30 cm (Figure 3 A) while maintaining lateral acceleration (Figure 3 B) within the design comfort range ($|\dot{v_{lat}}| < 1.3 \mathrm{m/s}^2$). Satisfactory results are also obtained for the vehicle's steering angle (Figure 3 C) and speed (Figure 3 D). In particular, the latter shows how the shuttle accelerates smoothly, reaches and maintains the maximum allowed speed of 30 km/h, and finally slows down to stop at the target station.

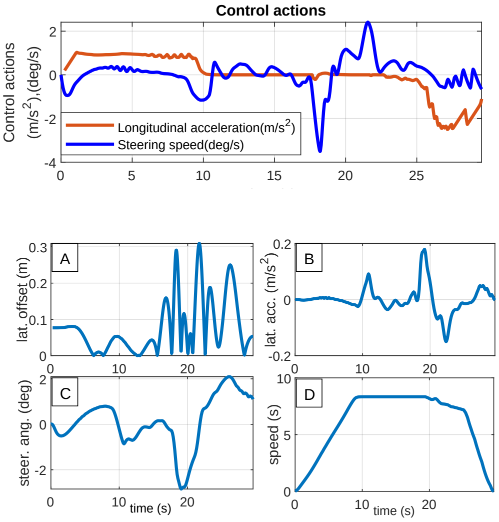

Figure 3: *Action signals and vehicle behavior during the route execution.*

Conclusion

This work presented a new framework for executing the main DDTs required in an AD SAE level 4 shuttle solution. It is based on the exploitation of an RL agent able to perform both ACC and LK, supported by a dedicated VLL that rapidly generates the virtual lane data, enabling the execution of LC maneuvers independently from the road geometry. The approach showed great potential, demonstrating a high ability to control the vehicle, meeting both comfort requirements and vehicle constraints, and overcoming potential disturbances.

The proposed VLL implementation has several advantages over standard RL methods. One of the main is the capability, thanks to VLL, of avoiding convolutional and recurrent neural networks. The proposed strategy exploits standard data already available from vehicle onboard safety systems, such as lane boundaries recognition, making it integrable with current technology. This streamlined approach not only makes the training process less complex but also enhances the adaptability of the trained actor, enabling it to handle unforeseen scenarios effectively through a strategic redesign of the VLL.

References

[1] D. Watzenig and M. Horn, *Automated driving: safer and more efficient future driving*. Springer, 2016.

[2] B. R. Kiran, I. Sobh, V. Talpaert, *et al.*, "Deep reinforcement learning for autonomous driving: A survey," *IEEE Transactions on Intelligent Transportation Systems*, vol. 23, no. 6, pp. 4909–4926, 2021.

[3] S. Wang, D. Jia, and X. Weng, "Deep reinforcement learning for autonomous driving," *arXiv preprint arXiv:1811.11329*, 2018.

[4] G. Hua, Z. Huang, J. Wang, J. Xie, and G. Shen, "Exploration strategy improved ddpg for lane keeping tasks in autonomous driving," in *Journal of Physics: Conference Series*, IOP Publishing, vol. 2347, 2022, p. 012 020.

[5] Q. Wang, W. Zhuang, L. Wang, and F. Ju, "Lane keeping assist for an autonomous vehicle based on deep reinforcement learning," SAE Technical Paper, Tech. Rep., 2020.

[6] SAE International, "Taxonomy and Definitions for Terms Related to Driving Automation Systems for On-Road Motor Vehicles (SAE J3016)," *https://www.sae.org/standards/content/j3016_202104/*, 2021.

Systematic Modeling of a Steering Vehicle Differential Using Power-Oriented Graphs

Davide Tebaldi and Roberto Zanasi

***Abstract*—This extended abstract addresses the modeling and simulation of a Steering Vehicle Differential for automotive applications.**

I. INTRODUCTION

One of the most important physical systems in the vehicle powertrain is the differential [1], [2], namely the element being responsible for properly distributing the engine motive torque among the vehicle wheels so as to increase the level of control on the vehicle itself. Different graphical formalisms, including Bond Graphs, Energetic Macroscopic Representation and Power-Oriented Graphs (POG) [3], are available in the literature for modeling physical systems in different energetic domains. In this extended abstract, the approach presented in [4], [5] based on the POG technique is used to model a steering vehicle differential. Next, the simulation results showing the clutches locking/unlocking states are presented.

II. MODELING

The differential in Fig. 1 can be modeled as follows:

$$\left\{\begin{array}{l} \mathbf{L}\,\dot{\mathbf{x}} = \mathbf{A}\,\mathbf{x} - \mathbf{S}^{\mathrm{T}}\mathbf{K}_s \mathrm{sign}(\mathbf{S}\mathbf{x}) + \mathbf{B}\,\boldsymbol{\tau} \\ \mathbf{y} = \mathbf{C}\,\mathbf{x} + \mathbf{D}\,\boldsymbol{\tau} \end{array}\right. , \quad \text{where}$$

$$\mathbf{L} = \begin{bmatrix} \mathbf{J} & \mathbf{0} \\ \mathbf{0} & \mathbf{K}^{-1} \end{bmatrix}, \ \mathbf{A} = \begin{bmatrix} -\mathbf{B}_\omega - \mathbf{B}_{\Delta\omega} - \mathbf{R}^{\mathrm{T}}\mathbf{B}_K\mathbf{R} & -\mathbf{R}^{\mathrm{T}} \\ \mathbf{R} & \mathbf{0} \end{bmatrix}, \ \mathbf{B} = \begin{bmatrix} \mathbf{I} \\ \mathbf{0} \end{bmatrix},$$

$$\mathbf{C} = \mathbf{B}^{\mathrm{T}}, \ \ \mathbf{D} = \mathbf{0}, \ \ \mathbf{S}^{\mathrm{T}} = \begin{bmatrix} \mathbf{S}_\omega^{\mathrm{T}} & \mathbf{0} \end{bmatrix}, \ \ \mathbf{x} = \begin{bmatrix} \boldsymbol{\omega} \\ \mathbf{F} \end{bmatrix},$$

$$\boldsymbol{\omega} = \overset{i}{\underset{\mathcal{N}_J}{[\![\, \omega_i \,]\!]}}, \ \boldsymbol{\tau} = \overset{i}{\underset{\mathcal{N}_J}{[\![\, \tau_i \,]\!]}}, \ \mathbf{J} = \overset{i}{\underset{\mathcal{N}_J}{[\![\, J_i \,]\!]}}, \ \mathbf{B}_\omega = \overset{i}{\underset{\mathcal{N}_J}{[\![\, b_i \,]\!]}},$$

$$\mathbf{F} = \overset{ij}{\underset{\mathcal{N}_K}{[\![\, F_{ij} \,]\!]}}, \ \ \mathbf{K} = \overset{ij}{\underset{\mathcal{N}_K}{[\![\, K_{ij} \,]\!]}}, \ \ \mathbf{B}_K = \overset{ij}{\underset{\mathcal{N}_K}{[\![\, d_{ij} \,]\!]}},$$

$$\left\{\begin{array}{ll} \mathcal{N}_J = \{s,\, d,\, p,\, a,\, b,\, c,\, e,\, f\}, & n_J = \dim(\mathcal{N}_J) = 8, \\ \mathcal{N}_K = \{sd,\, dc,\, pa,\, pb,\, ce,\, cf\}, & n_K = \dim(\mathcal{N}_K) = 6, \\ \mathcal{N}_B = \{da,\, db,\, ae,\, bf\}, & n_B = \dim(\mathcal{N}_B) = 4. \end{array}\right. \tag{1}$$

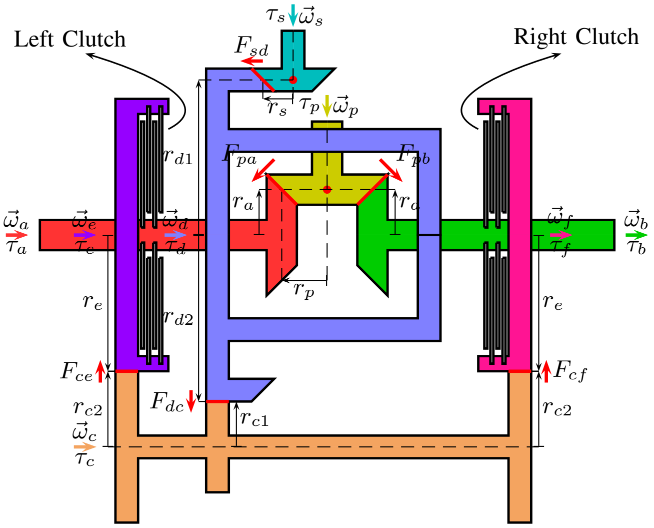

Fig. 1. Structure of the considered steering vehicle differential.

Model (1) is in a one-to-one correspondence with the POG block scheme of Fig. 2. The relative friction matrix $\mathbf{B}_{\Delta\omega}$ is:

$$\mathbf{B}_{\Delta\omega} = \begin{array}{c|cccccccc} & s & d & p & a & b & c & e & f \\ \hline s & 0 & 0 & 0 & 0 & 0 & 0 & 0 & 0 \\ d & 0 & b_{da}+b_{db} & 0 & -b_{da} & -b_{db} & 0 & 0 & 0 \\ p & 0 & 0 & 0 & 0 & 0 & 0 & 0 & 0 \\ a & 0 & -b_{da} & 0 & b_{ae}+b_{da} & 0 & 0 & -b_{ae} & 0 \\ b & 0 & -b_{db} & 0 & 0 & b_{bf}+b_{db} & 0 & 0 & -b_{bf} \\ c & 0 & 0 & 0 & 0 & 0 & 0 & 0 & 0 \\ e & 0 & 0 & 0 & -b_{ae} & 0 & 0 & b_{ae} & 0 \\ f & 0 & 0 & 0 & 0 & -b_{bf} & 0 & 0 & b_{bf} \end{array},$$

while the radii matrix $\mathbf{R}$ is given by:

$$\mathbf{R} = \begin{array}{c|cccccccc} & s & d & p & a & b & c & e & f \\ \hline sd & -r_s & -r_{d1} & 0 & 0 & 0 & 0 & 0 & 0 \\ dc & 0 & -r_{d2} & 0 & 0 & 0 & -r_{c1} & 0 & 0 \\ pa & 0 & r_a & -r_p & -r_a & 0 & 0 & 0 & 0 \\ pb & 0 & r_a & r_p & 0 & -r_a & 0 & 0 & 0 \\ ce & 0 & 0 & 0 & 0 & 0 & r_{c2} & r_e & 0 \\ cf & 0 & 0 & 0 & 0 & 0 & r_{c2} & 0 & r_e \end{array}.$$

The matrix $\mathbf{S}_\omega$ and the control matrix $\mathbf{K}_s$ are defined as:

$$\mathbf{S}_\omega = \begin{bmatrix} 0 & 0 & 0 & -1 & 0 & 0 & 1 & 0 \\ 0 & 0 & 0 & 0 & -1 & 0 & 0 & 1 \end{bmatrix}, \ \ \mathbf{K}_s = \begin{bmatrix} K_{ea} & 0 \\ 0 & K_{fb} \end{bmatrix}.$$

The authors are with the Department of Engineering "Enzo Ferrari", University of Modena and Reggio Emilia, Modena, Italy. `davide.tebaldi@unimore.it, roberto.zanasi@unimore.it`

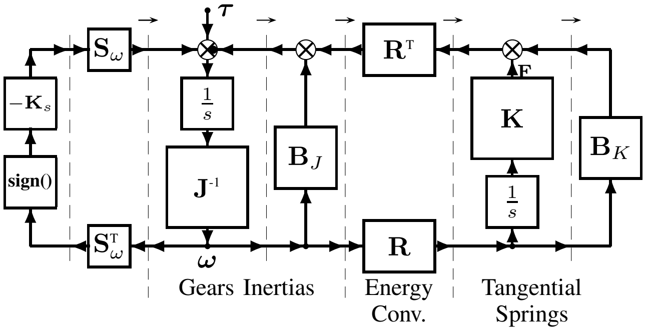

Fig. 2. Full POG scheme of the considered steering differential.

TABLE I
STEERING DIFFERENTIAL: SIMULATION PARAMETERS.

$r_a = 4.68$ cm	$r_{c1} = 3.6$ cm
$r_{c2} = 6.48$ cm	$r_{d1} = 16.2$ cm
$r_{d2} = 19.8$ cm	$r_e = 14.4$ cm
$r_p = 3.6$ cm	$r_s = 4.32$ cm
$b_{da} = b_{db} = 0.05$ Nm/rpm	$b_{ae} = b_{bf} = 0$ Nm/rpm
$J_i = 0.0658$ kg m^2 and $b_i = 0.05$ Nm/rpm, for $i \in \mathcal{N}_J$ in (1)	
$K_{ij} = 35 \cdot 10^3$ N/m and $d_{ij} = 160$ N s/m, for $i \in \mathcal{N}_K$ in (1)	

When $\mathbf{K} \to \infty$, it can be proven that the following reduced-order model can be obtained:

$$\mathbf{L}_1\,\dot{\mathbf{x}}_1 = \mathbf{A}_1\,\mathbf{x}_1 + \mathbf{B}_1\boldsymbol{\tau} - \mathbf{S}^{\mathrm{T}}\mathbf{K}_s\mathrm{sign}(\mathbf{S}\mathbf{x})\,,$$

where $\mathbf{L}_1 = \mathbf{Q}_1^{\mathrm{T}}\mathbf{J}\,\mathbf{Q}_1$, $\mathbf{A}_1 = -\mathbf{Q}_1^{\mathrm{T}}\mathbf{B}_J\mathbf{Q}_1$, $\mathbf{B}_1 = \mathbf{Q}_1^{\mathrm{T}}$ and $\mathbf{Q}_1$ is a properly defined transformation matrix [4], [5].

III. SIMULATIONS

The simulation of the steering differential of Fig. 1 is addressed in order to: 1) compare the results of the full and reduced-order models; 2) to verify the correctness of the clutches modeling. The simulation is performed using the system parameters in Table I, starting from zero initial conditions and applying an input torque $\tau_s = 100$ Nm. The simulation results are shown in Fig. 3, from which the good superposition between the characteristics obtained using the full and reduced-order models can be appreciated. At $t = 1.8$ s, the parameter K_{ea} of the control matrix $\mathbf{K}_s$ undergoes the transition $K_{ea} = 0 \to 10^4$, in order to simulate the locking of the left clutch shown in Fig. 1. At $t = 3.6$ s, the parameter K_{ea} of the control matrix $\mathbf{K}_s$ undergoes the transition $K_{ea} = 10^4 \to 0$, in order to simulate the unlocking of the left clutch shown in Fig. 1. From the center subplots, it can be seen that the involved angular velocities ω_a and ω_e are indeed kept equal to each other when the left clutch is locked. The locking and unlocking of the right clutch in Fig. 1, using the parameter K_{fb} of the control matrix $\mathbf{K}_s$, occur at $t = 5.4$ s and $t = 7.2$ s, respectively, and are shown in the lower subplots of Fig. 3. The same observations as those made for the left clutch locking/unlocking simulation also apply to the right clutch locking/unlocking simulation: indeed, the involved angular velocities ω_b and ω_f are kept equal to each other when the right clutch is locked. The obtained results show the correctness of the differential and clutches modeling.

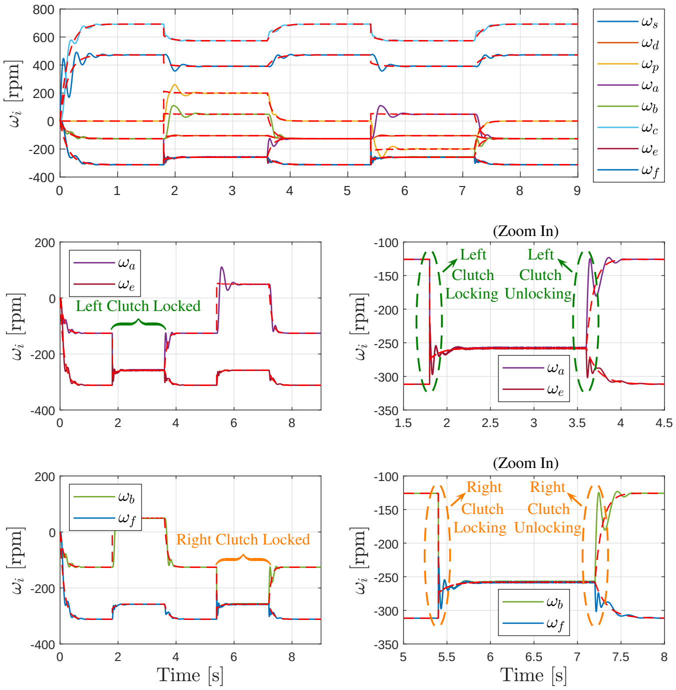

Fig. 3. Results of the simulation on the steering differential of Fig. 1 using the: full model (colored) and reduced-order model (red dashed).

IV. CONCLUSIONS

In this extended abstract, the systematic modeling and simulation of a steering vehicle differential using power-oriented graphs have been addressed. The two presented dynamic models of the steering differential exhibit a different degree of detail: a full model which also accounts for the gears elastic interaction and a reduced-rigid model neglecting it. Both dynamic models allow to effectively simulate the differential dynamics and the locking and unlocking of the differential clutches, and have been obtained applying a fully systematic procedure using the power-oriented graphs modeling technique. The simulation results have shown the good superposition between the results given by the full and reduced-order models of the considered steering differential.

REFERENCES

[1] W. Zhao, H. Zhang, "Coupling control strategy of force and displacement for electric differential power steering system of electric vehicle with motorized wheels", *IEEE Trans. Veh. Technol.*, vol. 67, no. 9, pp. 8118-8128, Sep. 2018.

[2] M. Gadola, D. Chindamo, "The mechanical limited-slip differential revisited: high-performance and racing car applications", *Int. Journal of Applied Engineering Research*, vol. 13, no. 2, pp. 1478-1495, 2018.

[3] R. Zanasi, G. H. Geitner, A. Bouscayrol, W. Lhomme, "Different energetic techniques for modelling traction drives", *Proceedings of 9th International Conference on Modeling and Simulation of Electric Machines, Converters and Systems (ELECTRIMACS)*, Québec, Canada, Jun. 8-11, 2008.

[4] R. Zanasi and D. Tebaldi, "Modeling of complex planetary gear sets using power-oriented graphs", *IEEE Trans. Veh. Technol.*, vol. 69, no. 12, pp. 14470-14483, Dec. 2020. 10.1109/TVT.2020.3040899

[5] D. Tebaldi, R. Zanasi, "Systematic modeling of complex time-variant gear systems using a power-oriented approach", *Control Engineering Practice*, vol. 132, Mar. 2023.

Session 2A: Applications

Huber-based Unscented Kalman Smoother with application to Earth observation missions

Michele Coco, Martina Mammarella, Cesare Donati, Federica Paganelli, Francesco Evangelisti

In the pathway towards fully autonomous spacecraft, space systems shall be designed to operate in an unpredictable and partially unknown environment. In this framework, the problem of sensor fusion is typically handled exploiting Kalman-like filtering techniques. A valid alternative when dealing with *non-Gaussian* probabilities are the so-called Particle Filters (see e.g., [1]), which use a set of samples to represent the posterior distribution of a stochastic process given the noisy and/or partial observations. The Unscented Kalman FIlter (UKF) belongs to the KFs family. However, it is based on a sigma-point method that shares some similarities with the PFs. Indeed, analogously to Kalman filters, the state distribution is represented by Gaussian random variables. However, UKF uses a minimal set of carefully chosen sample points (called sigma points), similar to PF samples, that properly capture the true mean and covariance of the states and are propagated through the nonlinearity.

To deal with non-Gaussian uncertainties and outliers, it is possible to extend the UKF scheme relying on the Huber method and obtaining Huber-based UKF (HUKF). Specifically, the Huber approach is a generalization of the maximum likelihood approach [2] and is based on the combination of minimum ℓ_1– and ℓ_2–norm estimators to improve robustness against deviations from the commonly assumed Gaussian probability density functions, thus making the HUKF able to solve non-Gaussian distribution problems efficiently. In detail, the standard cost function, defined as the sum of squared residuals e_i, is replaced by an indicator functional $J = \sum_{i=1}^{m} \rho(e_i)$, where $\rho(e_i)$ is a blend of the ℓ_1 and ℓ_2 norm functions, such that if $|e_i| \leq \gamma$ than $\rho(e_i) = \frac{1}{2}e_i^2$, otherwise $\rho(e_i) = \gamma|e_i| - \frac{1}{2}\gamma^2$. Here, the threshold parameter γ has a great impact on filtering precision and robustness. Hence, for $\gamma \to 0$, the robustness effect increases as more observations are treated as probable outliers, whereas for $\gamma \to \infty$ the Huber function behaves like a least square minimization algorithm and the HUKF as a standard UKF. While the HUKF is able to reduce the contribution of uncertain measurements in the computation of the estimator, on the other side this results in an increased variance of the estimator. Indeed, because the corresponding weighting function $\psi(e_i)$ is such that $\psi(e_i) = 1$ for $|e_i| \leq \gamma$ and $\psi(e_i) = \gamma/|e_i|$ otherwise, the measurement noise variance σ_i^2 is modified accordingly. Hence, as the residual e_i grows larger than γ so it does its variance as it takes into account the probability that the measurement is an outlier. Vice versa, for $e_i \leq \gamma$, the observation is expected to follow the assumed (Gaussian) distribution, and the variance remains unchanged.

In this abstract, we propose a Huber-based Unscented Kalman Smoother (HUKS), combining the benefits of a HUKF-based filtering techniques for nonlinear systems able to handle non-Gaussianity similarly to PFs with an optimal smoother for balancing the effects on the measurements variance. Specifically, we integrate an optimal smoother into the filtering scheme to incorporate also a memory characteristic, thus improving the state estimates and error covariances by harnessing information contained in the entire available data set. In this way, we obtain a forward Huber-based UKF that processes the measurements, followed by a backward smoothing step over past data and given future observations, which reduces the measurement variance. Indeed, in autonomous rendezvous and proximity operations scenarios, adaptive filtering can help mitigate numerical sensitivity and inconsistent filter performances [3]. In this context, applying smoothing enhances the filter's adaptability and improves state estimation accuracy [4]. Additionally, integrating the Huber approach addresses the limitations of assuming Gaussianity, which is critical given that typical sensor systems. Developing a HUKS can be a significant step towards understanding the benefits of integrating these solutions.

The efficacy of the proposed approach is validated in simulation for an Earth-observation scenario involving a small satellite equipped with commercial-off-the-shelf sensors. In particular, we assume that the GPS sensor has a probability p of providing accurate position measurements y, which adheres to the expected Gaussian distribution for the measurement noise, and a probability of $1 - p$ to fail, resulting in inaccurate measurements (outliers) that deviate from the expected distribution for measurement noise. Figure 1 highlights the impact of the parameter γ on the HUKF errors as the probability p varies. Specifically, we observe that lower values of γ result in reduced errors due to the filter's enhanced ability to reject outliers. However, this comes at the expense of an increment of the associated standard deviation. Conversely, higher values of γ lead to a higher likelihood of accepting outliers as valid measurements, resulting in increased errors, especially in cases where the probability of sensor failures is high. These trends are also confirmed by the RMSE reported in Table 1. Figure 2 compares the estimated positions using the Huber and the smoother for $p = 1$, i.e., no sensor failure, and $p = 0.5$. The Huber-based filters, i.e. HUKS and HUKF (first row), provide superior estimation accuracy compared to classical filters, such as UKS and UKF (second row). This improvement is

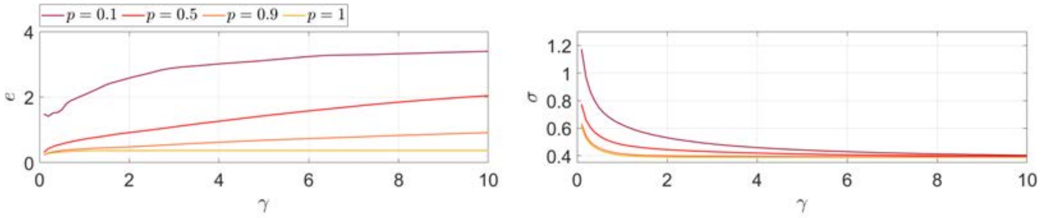

Figure 1: Position root mean square error e and standard deviation σ of the HUKF for different p, with respect to γ.

particularly evident when $p = 0.5$ (right column), as the higher probability of sensor failure leads to a greater number of outliers, which significantly degrade the predictions of UKF and UKS. As it can be noticed, the adoption of the Huber approach results in increased conservativeness and, consequently, higher standard deviations. However, we observe how the introduction of a smoother can mitigate this effect, thus compensating for the higher variances introduced by the Huber-based approaches. Last, Table 1 presents the RMSE and the average execution time for each tested filter. Specifically, we can observe that the small increase in computational time associated with the combinations of Huber-based and smoother techniques represents a trade-off for the improved robustness against outliers.

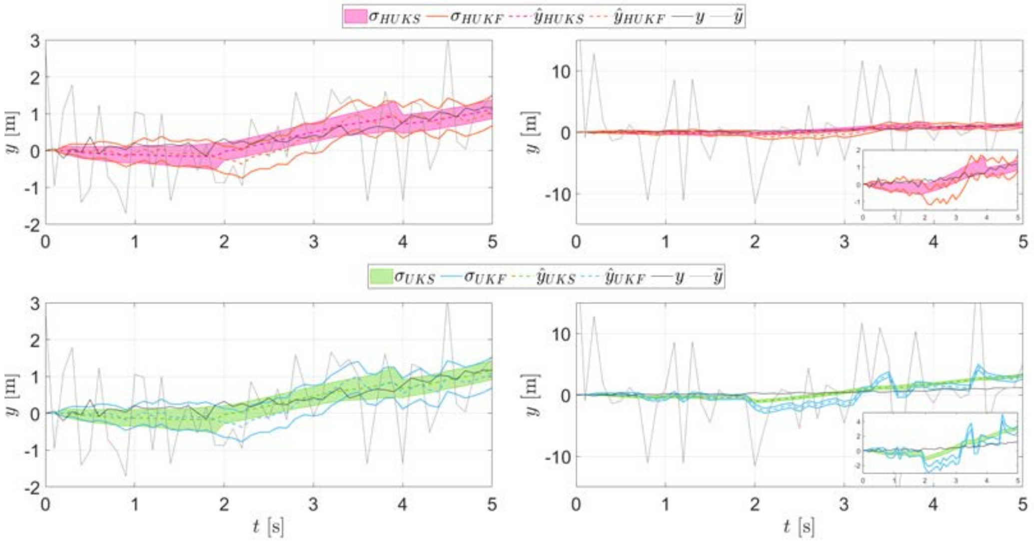

Figure 2: Comparison of position estimation and associated standard deviation for the different filters, with $\gamma = 1.345$ and $p = 1$ (left column) and $p = 0.5$ (right column).

UKF	UKS	HUKF	HUKS
0.3366	0.2992	0.3696	0.2946

(a)

UKF	UKS	HUKF	HUKS
2.3 ms	2.5 ms (+10%)	2.39 ms (+4%)	2.72 ms (+18%)

(b)

Table 1: (a) RMSE for $p = 1$ and (b) average execution time.

References

[1] Cesare Donati, Martina Mammarella, and Fabrizio Dabbene. Single-state weighted particle filter with application to earth observation missions. *IFAC-PapersOnLine*, 56(2):6024–6029, 2023.

[2] Peter J Huber. Robust estimation of a location parameter. In *Breakthroughs in statistics: Methodology and distribution*, pages 492–518. Springer, 1992.

[3] Joshua Sullivan and Simone D'Amico. Adaptive filtering for maneuver-free angles-only navigation in eccentric orbits. In *27th AAS/AIAA Space Flight Mechanics Conference*, 2017.

[4] Cory T Fraser and Steve Ulrich. Adaptive extended kalman filtering strategies for spacecraft formation relative navigation. *Acta Astronautica*, 178:700–721, 2021.

Deep Deterministic Policy Gradient Control of Type 1 Diabetes

Federico BALDISSERI*, Danilo MENEGATTI, and Andrea WRONA

Abstract— **This paper introduces a novel Reinforcement Learning-based controller for autonomous glycemic regulation in the treatment of type 1 diabetes, building on the Deep Deterministic Policy Gradient algorithm. The proposed control method is validated through in-vitro simulations on the Bergman glucoregulatory model, proving that it successfully preserves healthy values of blood glucose concentration, while overcoming both standard clinical practice and classical model-based control techniques in terms of both control effort and computational efficiency for real-time applications.**

Index Terms— **Deep Reinforcement Learning, Deep Deterministic Policy Gradient, Type 1 Diabetes.**

I. INTRODUCTION

Type 1 diabetes patients are completely dependent on external insulin administration. A safe and effective glucose regulation is of paramount importance since hyperglycemia can lead to cardiovascular diseases and blindness, while hypoglycemia can lead to coma and death [1]. Several classes of control algorithms have been used in academic literature, such as proportional integral derivative (PID) control and Model Predictive Control (MPC). Deep Reinforcement Learning can be enforced to develop fully automated algorithms that can provide personalized control under varying conditions, leveraging deep neural networks to automatically learn meaningful representations from high-dimensional and complex data, thus being more efficient in learning optimal control policies [2]. No work in academic literature has proposed data-driven insulin control strategy leveraging continuous action spaces, thus avoiding a quantization which usually yields information losses. This work overcomes the highlighted limitation in previous academic literature by applying a continuous control logic based on Deep Reinforcement Learning to the problem of autonomous insulin regulation for patients suffering from type 1 diabetes.

II. CONTROL METHODOLOGY

Deep Deterministic Policy Gradient (DDPG) is an advanced Deep Reinforcement Learning algorithm that is able to cope with continuous state and action spaces. It is an extension of the popular Deterministic Policy Gradient algorithm [3], combining deep neural networks with the principles of actor-critic methods. It uses neural networks as approximation functions to learn the optimal policy, while continuously evaluating the action quality during the training phase. In particular, the agent is denoted by four neural networks: the first two are the actor and critic networks, whereas the last two are the so-called target actor and target critic, copies of the first two with slowly updated parameters used to stabilize the learning phase. The DDPG methodology is outlined in Algorithm 1.

Algorithm 1 DDPG algorithm

```
Randomly initialize critic network $\mathcal{C}(s, a|\theta^{\mathcal{C}})$ and actor $\mathcal{A}(s|\theta^{\mathcal{A}})$ with weights $\theta^{\mathcal{C}}$ and $\theta^{\mathcal{A}}$
Initialize target network $\mathcal{C}'$ and $\mathcal{A}'$ with $\theta^{\mathcal{C}'} \leftarrow \theta^{\mathcal{C}}$ and $\theta^{\mathcal{A}'} \leftarrow \theta^{\mathcal{A}}$
Initialize replay buffer $R$
for $e = 1, 2, \dots, E$ do
    Define the random process noise $\mathcal{N}_e$ for action exploration
    Receive initial observation state $s_1$
    for $t = 1, 2, \dots, T$ do
        Select action $a_t = \mathcal{A}(s_t|\theta^{\mathcal{A}}) + \mathcal{N}_e$
        Execute $a_t = \mathcal{A}$ and observe $r_t$ and $s_{t+1}$
        Store transition $(s_t, a_t, r_t, s_{t+1})$ in $R$
        Sample $N$-transitions random minibatch from $R$
        Set $y_i = r_i + \gamma \mathcal{C}'(s_{i+1}, \mathcal{A}'(s_{i+1}|\theta^{\mathcal{A}'})|\theta^{\mathcal{C}'})$
        Update critic minimizing the loss:
            $L = \frac{1}{N} \sum_i (y_i - \mathcal{C}(s_i, a_i|\theta^{\mathcal{C}}))^2$
        Update actor policy using the policy gradient:
    $\nabla_{\theta^{\mathcal{A}}} J \approx \frac{1}{N} \sum_i \nabla_a \mathcal{C}(s, a|\theta^{\mathcal{C}})|_{s_i, \mathcal{A}(s_i)} \nabla_{\theta^{\mathcal{A}}} \mathcal{A}(s, |\theta^{\mathcal{A}})|_{s_i}$
        Update target networks, with $\tau \ll 1$:
            $\theta^{\mathcal{C}'} \leftarrow \tau \theta^{\mathcal{C}} + (1 - \tau)\theta^{\mathcal{C}'}$
            $\theta^{\mathcal{A}'} \leftarrow \tau \theta^{\mathcal{A}} + (1 - \tau)\theta^{\mathcal{A}'}$
    end for
end for
```

III. SYSTEM MATHEMATICAL MODELING

The Bergman Model is the simplest model that effectively describes the blood glucose-insulin regulatory system [4]. It is characterized by the following equations:

$$\dot{x} = \begin{bmatrix} -p_1 G - (G + G_b)X + d \\ -p_2 X + p_3 I \\ -nI + u \end{bmatrix}, \tag{1}$$

where G denotes the plasma glucose concentration, X the insulin's effect on net glucose disappearance, I the insulin concentration in plasma, u is the controlled insulin infusion rate, d the measurable meal disturbance, while $G_b, I_b, p_1, p_2, p_3, \delta$, and n are parameters of the model. A physiological constraint on the amount of injected insulin is imposed: $0 \leq u(t) \leq 4.27\ \mu\text{U/min}$. This system translates to the MDP framework in the following way: the state space is $\mathcal{S} = \{(\tilde{G}, d)\}$, the action space is $\mathcal{A} = \{u | u \in [0, 4.27]\ \mu\text{U/min}\}$, and the reward function is:

$$r(G) = \begin{cases} 1, & \text{if } 70 \leq G \leq 120, \\ 0.3, & \text{if } 120 < G \leq 160, \\ 0.1, & \text{if } 50 \leq G < 70 \\ -0.4 - \frac{(G-160)}{200}, & \text{if } 160 < G \leq 280, \\ -0.6 - \frac{(G-50)}{100}, & \text{if } 10 \leq G < 50, \\ -1, & \text{otherwise.} \end{cases} \tag{2}$$

All authors are with the Department of Computer, Control and Management Engineering "Antonio Ruberti", Sapienza University of Rome, Italy. Emails: {baldisseri, menegatti, wrona}@diag.uniroma1.it

*Corresponding author. Email: baldisseri@diag.uniroma1.it

TABLE I

KPIs COMPARISON OF THE USED CONTROL LOGICS

KPI	**CP**	**PID**	**NMPC**	**DDPG**
Minimum glycemic value [mg/dl]	71	51	75	75
Maximum glycemic value [mg/dl]	172	192	116	142
Time in hypoglycemia [min]	0	0	0	0
Time in hyperglycemia [min]	20	33	0	0
Total injected insulin [μU]	27.6	41.5	89.4	93.6
Computing time [sec]	1.7×10^{-6}	2.9×10^{-6}	2.4×10^{-2}	2.1×10^{-3}
Maximum control effort peak [μU]	0.69	0.19	4.68	0.94

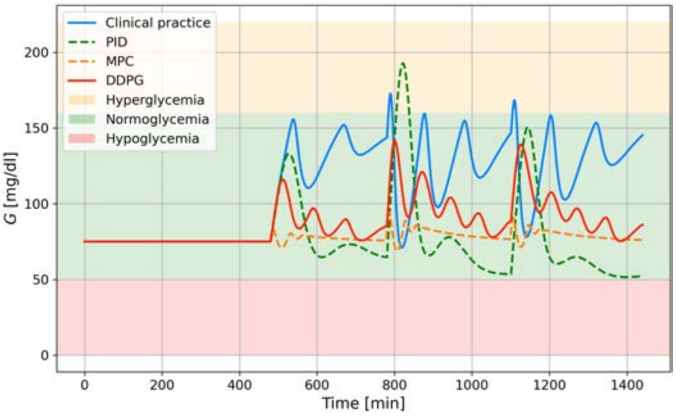

Fig. 1. Profile of the daily blood glucose concentration obtained with the analyzed control logics: clinical practice (blue), PID (green), MPC (yellow), and DDPG (red).

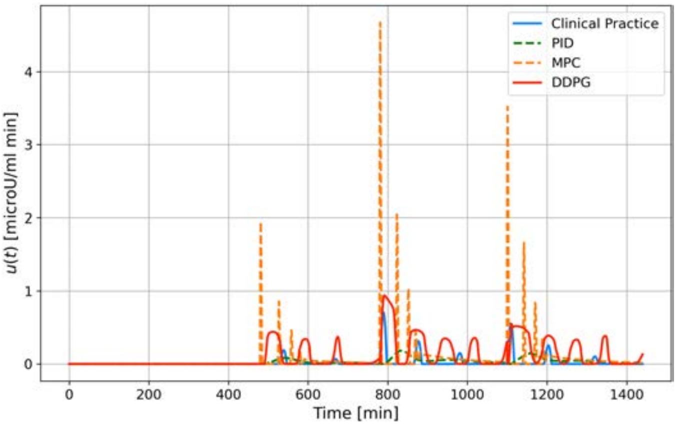

Fig. 2. Daily evolution of the control effort enforced by the analyzed control logics: clinical pratice (blue), PID (green), MPC (yellow), and DDPG (red).

IV. SIMULATIONS AND RESULTS

Disturbance is simulated by assuming that throughout a day three meals are consumed, cointaining 60, 110 and 90 grams of carbohydrates respectively. Both the actor and critic share the same neural architecture composed of three layers, the first two of 512 and 128 neurons with ReLU activation function, and the last one of one neuron only, with hyperbolic tangent activation function for the actor. The DDPG agent is trained for $E = 150$ episodes, each one lasting $T = 1440$ [min], thus for a total of 1440 steps (T/dt), converging to the maximum feasible value given the reward design illustrated in (2). Figures 1 and 2 illustrate respectively the daily profile of the blood glucose concentration and of the control effort enforced by the corresponding trained model, as well as by the other control logics illustrated in the following.

Benchmark comparisons are conducted with standard clinical practice (CP), Proportional Integral Derivative (PID) control, and Nonlinear Model Predictive Control (NMPC). With the first two methods, hyperglycemic episodes occur, in particular with PID since it tracks a reference by minimizing error without including bounds. The NMPC controller, analogously to the DDPG controller, effectively prevents both hyperglycemic and hypoglycemic episodes, the latter presents some advantages with respect to the former. First, performing inference with the DDPG controller is much faster (by an order of magnitude) than solving the NMPC optimization problem; although with the used sampling time such difference results negligible, it is expected that in future works, using more complex glucoregulatory models, the superior speed of the DDPG contorller makes it more suitable for real-time applications with respect to NMPC. Moreover, the peaks of the NMPC control effort reach much higher values with respect to the DDPG controller, reaching saturation at the maximum limit imposed by the physiological constraint on the amount of administrable insulin. The clinical relevance of lowering the maximum control effort peak consists of minimizing the discomfort of the patient, reducing the risk of hypoglycemia, and improving the overall glycemic control since rapid drops and increases in blood glucose concentration levels can be destabilizing. Table I synthesizes the Key Performance Indicators (KPIs) that are useful to compare the outcomes of the four presented control logics.

V. CONCLUSIONS

The proposed control logic shows superior performances with respect to the others in terms of insulin regulation, reducing control effort peaks and computation time. Future works shall tackle the limitations of this study: more complex glucoregulatory models may be used in order to describe more realistic scenarios in daily life of diabetic patients, with the introduction of additional disturbances such as stress and physical activity. Moreover, additional DRL algorithms, such as SAC, PPO and TD3 will be tested to compare performances, and domain randomization techniques will be employed to improve the generalization capabilities of the DRL agents.

REFERENCES

[1] M. A. Atkinson, G. S. Eisenbarth, and A. W. Michels, “Type 1 diabetes,” *The Lancet*, vol. 383, no. 9911, pp. 69–82, 2014.

[2] T. Zhu, K. Li, P. Herrero, and P. Georgiou, “Basal glucose control in type 1 diabetes using deep reinforcement learning: An in silico validation,” *IEEE Journal of Biomedical and Health Informatics*, vol. 25, no. 4, pp. 1223–1232, 2020.

[3] D. Silver, G. Lever, N. Heess, T. Degris, D. Wierstra, and M. Riedmiller, “Deterministic policy gradient algorithms,” in *International conference on machine learning*, pp. 387–395, Pmlr, 2014.

[4] A. G. Gallardo-Hernández, M. A. González-Olvera, M. Castellanos-Fuentes, J. Escobar, C. Revilla-Monsalve, A. L. Hernandez-Perez, and R. Leder, “Minimally-invasive and efficient method to accurately fit the bergman minimal model to diabetes type 2,” *Cellular and Molecular Bioengineering*, vol. 15, no. 3, pp. 267–279, 2022.

Model Driven Design of Bacterial Communication Inhibition: from Quorum Sensing to Quorum Quenching

C. Cimolato[1], M. Bellato[1,2], G. Selvaggio[3], L. Marchetti[3,4], G. Giordano[5] and L. Schenato[1]
[1] *Department of Information Engineering, University of Padua - Padua, Italy*
[2] *Department of Molecular Medicine, University of Padua - Padua, Italy*
[3] *Fondazione The Microsoft Research - University of Trento COSBI - Rovereto, Italy*
[4] *Department of Cellular, Computational and Integrative Biology (CIBIO), University of Trento - Trento, Italy*
[5] *Department of Industrial Engineering, University of Trento - Trento, Italy*

I. EXTENDED ABSTRACT

Antibiotic-resistant bacteria have emerged as a significant global threat to public health [1]. Both FAO and WHO ranked antimicrobial resistance (AMR) as one of the top ten global helath threats [1]. By 2002, AMR was already responsible for 60% of hospital infections [2], and it has since become one the leading causes of death worldwide, with 1.27 million deaths attributed to AMR in 2019 [3]. If current trends continue, AMR is projected to cause 10 million deaths each year by 2050 [3], [4]. The speed of onset and spreading of new AMR strains outclasses the development of new antibiotic molecules by the pharmaceutical industry. Therefore, new approaches need to be devised to counter AMR. Multiple synergistic mechanisms are involved in AMR, operating both at the single bacterium level, via expression of AMR-promoting genes, and at bacterial community level, where bacteria communicate to coordinate population-wide actions. One such communication system is Quorum Sensing (QS), which bacteria use to synchronize behaviors that promote AMR by means of diffusible signal molecules [5].

To face the challenge posed by AMR, exploring alternative treatments for bacterial infections is crucial [6]. In particular, Quorum Quenching (QQ), namely the inhibition of QS mechanisms, has been proposed as a promising approach for therapeutic strategies that consider QS as a possible target [2]: promising studies were aimed at discovering QS inhibitors and designing QQ synthetic circuits to treat bacterial infections by reducing the activation of antimicrobial resistance [7], [8]. Understanding how QS regulates gene expression is crucial to design effective QQ strategies that control the QS communication system.

Even though bacterial species differ in QS-associated genes and signal molecules, the overall mechanism is the same (Fig. 1): when the sensed bacterial population density is low, each cell produces low basal levels of signal molecules, which are also released out of the cell and gradually diffuse into the environment. As the cell population increases, the signal molecules accumulate inside and outside the cells. Inside the bacteria, these signaling molecules bind to a transcriptional regulator (*receptor*), and the resulting active complex induces the transcription of specific QS-regulated genes. In particular, the production of signal molecule synthases is up-regulated, which gives rise to a positive feedback loop that self-induces the synthesis of more signaling molecules (therefore called *autoinducers*).

Mathematical models and systems-and-control approaches are precious to enable a deeper understanding of the QS machinery through both theoretic analysis and computational studies, and also to design control strategies that either enhance Quorum Sensing (when it is desired to perform a prescribed functionality) or suppress it (to hinder the activity of pathogens).

1) Contributions: We present a systems-biology model that highlights the key structural features of QS. By analyzing two pivotal QS architectures, we gain insights into the interactions and cooperative behaviors of bacteria.

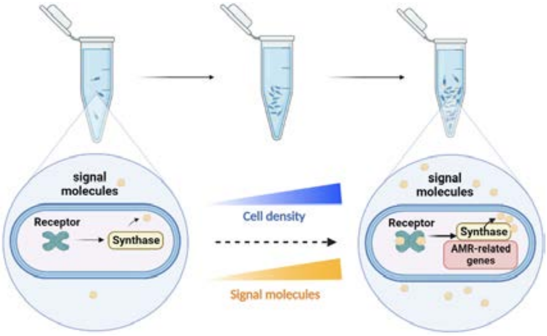

Fig. 1: Quorum sensing mechanism.

We mathematically model the following QS synthetic circuit architectures (see Fig. 2.1):

(i) The single-feedback QS architecture in which a single positive feedback loop autoinduces the synthesis of the signal molecule (model in [9]);
(ii) The double-feedback QS architecture which includes an additional positive feedback loop enhancing the synthesis of the signal molecule receptor (model in [9]).

We compare their equilibria and the asymptotic behavior of the system trajectories (Fig. 2.2). For both QS structures, our analysis reveals a bistable behavior, where crossing a threshold in the number of cells drives the system from a low stable equilibrium (associated with the OFF state of the related genes, at low cell numbers) to a high stable equilibrium (associated with the ON state and with the activation of AMR-related genes, at high cell numbers); the presence of hysteresis is shown to confer robustness to the QS mechanism, once it has been activated, with respect to disturbances and fluctuations in the number of cells.

By comparing the bifurcation diagrams for the two models in Fig. 2.2, we can observe that the presence of the second positive feedback definitely increases the range of hysteresis notably improving the robustness of the system with respect to fluctuations in the cell density. Moreover, the maximum steady- state concentration of synthase per cell is much larger in the double-feedback system, leading to a much higher stable equilibrium in the ON state.

We then perform an extensive sensitivity analysis on model parameters, not only to possibly generalize the model to further genetic contexts, but also to explore biological variability that can rise from external stimuli and environmental changes.

Finally, building upon the previous results, we investigate Quorum Quenching strategies for QS inhibition, to support a model-driven rational design of tools in synthetic biology; in particular, QQ can

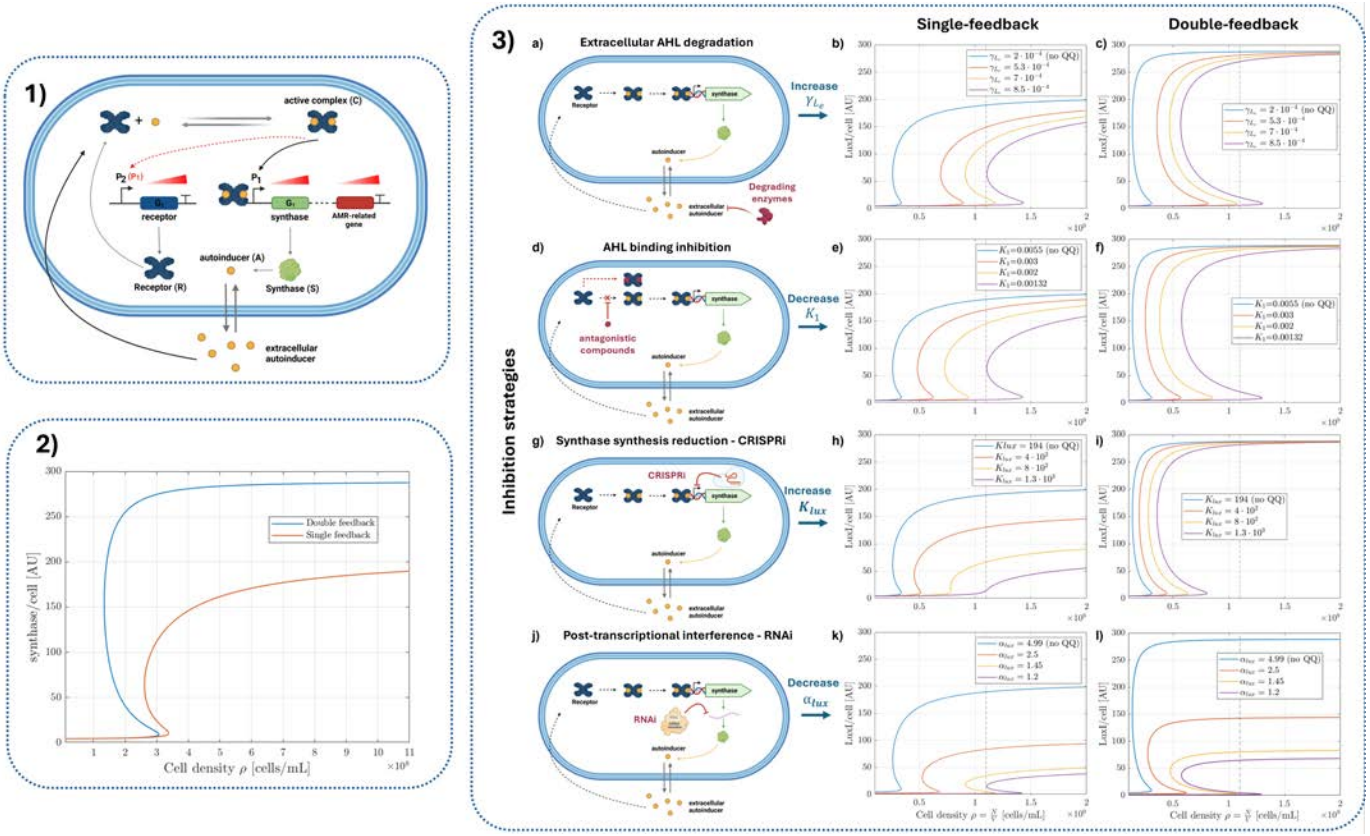

Fig. 2: **1)** Schematic of a generic QS network triggering AMR-related genes: the single positive feedback architecture, without the dashed red arrow, includes promoter P_2; the double positive feedback architecture, including the dashed red arrow, only has promoter P_1; **2)** Bifurcation diagrams of steady-state concentration of synthase per cell varying cell density for the single- and double-feedback QS systems; **3)** Effects on the synthase (called LuxI) bifurcation diagram of four different QS inhibition strategies: extracellular autoinducer (AHL) degradation (panels a-c), receptor sequestration (panels d-f), LuxI synthesis reduction with CRISPRi (panels g-i), post-transcriptional interference with RNAi (panels j-l). In each plot, the bifurcation diagrams are computed for increasing values of the inhibition strength. Dashed vertical lines correspond to the maximum cell density achievable for *E. coli* in a culture environment. In panels b, e, h and k the bifurcation diagrams are computed for the dynamics of the single-feedback Lux QS model, while the double-feedback Lux QS model dynamics are considered in panels c, f, i and l.

be achieved by degrading extracellular autoinducers, by sequestering the receptors to which autoinducers bind, or by reducing the production of autoinducer synthases by either CRISPRi or RNAi - at transcriptional or translational level, respectively (Fig. 2.3). We mathematically model four QQ techniques based on four mechanisms of different nature and prove that, in all cases, their impact on the QS system can be captured by varying specific model parameters. We then simulate and compare the steady-state behavior of the two synthetic QS systems in the presence of these four QQ strategies: the resulting effects on both systems prove their potential efficacy, and reveal critical thresholds that prevent the activation of QS communication by hampering bistability and making sure that the system exclusively admits the low equilibrium. To corroborate the effectiveness of these inhibition strategies, it is noteworthy that the parameters targeted by these QQ approaches are among the critical factors that most significantly influence the behavior of the system, as demostrated by the sensitivity analysis. Our study thus paves the way to devise and experimentally design QQ strategies that hinder the activation of the QS mechanism and of AMR-related genes in pathogens.

REFERENCES

[1] Wall, B. *et al.* Drivers, dynamics and epidemiology of antimicrobial resistance in animal production. *Food and Agriculture Organization of the United Nations* (2016).

[2] Williams, P. Quorum sensing: an emerging target for antibacterial chemotherapy? *Expert opinion on therapeutic targets* **6**, 257–274 (2002).

[3] Murray, C. J. L. *et al.* Global burden of bacterial antimicrobial resistance in 2019: a systematic analysis. *The Lancet* **399**, 629–655 (2022).

[4] Thompson, T. The staggering death toll of drug-resistant bacteria. *Nature* (2022).

[5] Miller, M. B. & Bassler, B. L. Quorum sensing in bacteria. *Annual Reviews in Microbiology* **55**, 165–199 (2001).

[6] Ghosh, C., Sarkar, P., Issa, R. & Haldar, J. Alternatives to conventional antibiotics in the era of antimicrobial resistance. *Trends in microbiology* **27**, 323–338 (2019).

[7] Saxena, P., Joshi, Y., Rawat, K. & Bisht, R. Biofilms: architecture, resistance, quorum sensing and control mechanisms. *Indian journal of microbiology* **59**, 3–12 (2019).

[8] Fleitas Martínez, O., Cardoso, M. H., Ribeiro, S. M. & Franco, O. L. Recent advances in anti-virulence therapeutic strategies with a focus on dismantling bacterial membrane microdomains, toxin neutralization, quorum-sensing interference and biofilm inhibition. *Frontiers in cellular and infection microbiology* **9**, 74 (2019).

[9] Cimolato, C. *et al.* Exploring alternative quorum sensing model structures and quorum quenching strategies. *bioRxiv* (2023).

A Multiphysics Framework for Bacterial Cellulose Sensor Modeling

Luca Patanè [*], Francesca Sapuppo[*], Marco Calapristi [*], Antonino Maio [*],
Riccardo Caponetto [*], Salvatore Graziani [†], Carlo Trigona [†], Maria Gabriella Xibilia [*][‡]
[*]*Dipartimento di Ingegneria*, *Università degli Studi di Messina*, Messina, Italy
[†]*Dipartimento di Ingegneria Elettrica Elettronica ed Informatica*, *Università degli Studi di Catania*, Catania, Italy

***Abstract*—Bacterial Cellulose (BC) is a promising biodegradable biopolymer synthesized by bacteria in a low energy consumption process based solely on renewable materials (a sucrose-based culture is required). BC-based composites exhibit excellent mechano-electrical transduction properties. However, there has been no systematic optimization of BC-based composites for the realization of transduction or low-cost electronics on BC. In this study, we propose different modeling paradigms categorized according to their basic principles: first principle white-box, grey-box, and black-box models. These paradigms have different levels of detail, interpretability and explainability, which are crucial for understanding model dynamics. The overall mltiphysics white-box model integrates electrical, mechanical and chemical effects into a unique solution, focusing on the coupling factors between the physics domains. In the case of grey-box models, reduced models are considered, while symbolic regression can be employed as enhanced black box models. The dynamic behavior of the BC model can be validated by data-driven characterization using experimental data.**

***Index Terms*—White-box model, grey-box model, black-box model, multiphysics, sensors, green chemistry, characterization, organic electronics**

I. INTRODUCTION

In December 2019, the EU introduced the European Green Deal to address environmental and climate challenges, aiming to make Europe the first carbon-neutral continent. This transformation requires €260 billion annually (1.5% of the EU's GDP) and €1,000 billion in green investments. Electronic waste has nearly doubled since 2010, reaching 62 million tons by 2022, with projections of 82 million tons by 2030. E-waste, often containing hazardous materials, poses significant environmental risks.

Polymers are used in sensors and electronic devices, with Ionic Electroactive Polymers (IEAPs) being popular for their flexibility. However, IEAPs are not environmentally friendly. Bio-derived polymers like cellulose offer greener alternatives. Bacterial Cellulose (BC) is a promising option, produced by bacteria and known for its strength, biocompatibility, biodegradability, and renewability. BC is used in electronics, actuators, and sensors [1], [2].

To design BC-based mechano-electrical transducers, understanding energy conversion phenomena is crucial. Current models for BC sensors are preliminary [3], and their behavior depends on various factors like signal amplitude, frequency, environmental conditions, geometry, fabrication, electrodes, and conditioning [4].

BC's similarities with IEAPs can aid in developing models for BC transducers. Existing IEAP models include black-box neural networks [5], gray-box models with fractional orders [6], and white-box finite element methods [7]. Relevant model parameters can be identified through experiments and optimization [8].

II. BACTERIAL CELLULOSE SENSOR GEOMETRY AND MANUFACTURING

The BC-based sensors were fabricated following the process in Figure 1, using CBP-GS010 films of BC, procured from Bio-Faber (Mesagne, Italy), with thickness $t_{BC} = 395m$, 1-Ethyl-3-Methylimidazolium tetrafluoroborate (EMIM-BF4), obtained from Alfa Aesar, Poly-(3,4-ethylene-dioxythiophene)-polystyrene-sulfonic acid (PEDOT-PSS), purchased from H.C. Starck (1.3 $wt\%$ dispersion in water, Baytron P AG).

BC served as a bulk material, while EMIM-BF4 was used as an ionic liquid (IL) to impregnate the BC. The impregnated BC was then coated on opposite sides with two films of PEDOT-PSS, which served as electrodes. The resulting BC/PEDOT sample can then be cut into strips of different sizes depending on the application. The BC strip, which acts as a sensor, is used in a cantilever configuration: it is pinned at one end and bends when a deformation occurs, generating an electrical signal at the electrodes.

III. MULTIPHYSICS WHITE-BOX MODEL

The BC-based transducer converts electrical energy into mechanical deformation and vice versa and acts as both an actuator and a sensor. As a sensor, when an external force (F) is applied to the tip, the mobile cations ($EMIM^+$) and anions ($BF4^-$) redistribute in the BC. An electrical potential is generated in the BC, which can be measured at the electrodes. The multiphysics model is described in the diagram in Figure 3. It includes four physics domains: Mechanical model for calculating the deformation of the structure; Chemical model for the definition of the ionic current and the study of the phenomenon linked to the transport of the IL; Electrical model for the study of the potential within the BC sensor. The coupling effects between the physics domains are here considered as the basis for the multiphysics modeling. Assumptions of isotropy, homogeneity, temporal invariance, and linearity for all materials are made.

Fig. 1. Fabrication process of the BC-based sensor

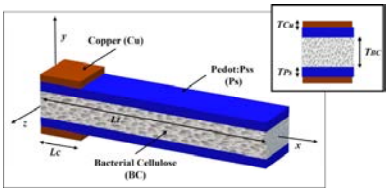

Fig. 2. Geometry of the BC-based sensor in the cantilever configuration.w is the width of the entire sample, L_c is the length of the clamped copper electrode, L_t is the total length of the sample, T_{BC}, T_{Ps}, T_{Cu} are the thickness of the BC, Pedot and copper electrodes respectively.

A. Finite Element Method Implementation

The white box model can be implemented using finite element method (FEM) models, which implement the solution of the partial differential equations in the time and space domain. In such a method, the differential equations are solved by dividing the spatial domain into smaller elements and approximating the solution within each element. The mesh of the spatial domain involves dividing the domain into finite elements and connecting nodes to represent the behavior and properties of the solution within each element.

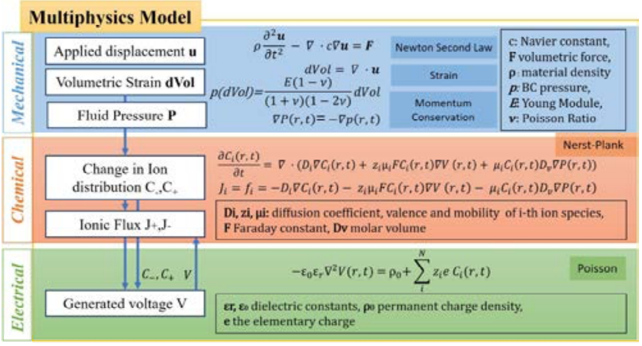

Fig. 3. Multi-Physics Diagram

The solution of such a model is therefore represented by the spatio-temporal mapping of the field variables such as the displacement (u), the cation and anion concentration (C_i), and the electric potential (V). The model parameters are determined by experiments or from the literature. Unknown parameters or additional scale factors can be determined by comparing the macroscopic model results with the experimentally measurable field quantities.

This work was funded by Progetto PRIN Green SENSing systems based on Bacterial Cellulose (SENS-BC), Italian Ministry of University and Research, CUP J53D23003460006

[‡] Corresponding Author

IV. GREY BOX MODELS

The grey box approach is based on a concise set of equations that describe well-understood phenomena. These equations are influenced by parameters obtained by analysing experimental data, especially with respect to the macroscopic properties of materials, which makes the grey-box approach sufficiently versatile for use in design applications. Various grey box models for IEAPs have been proposed in the literature [9]. Due to some similarities that can be observed between IEAPs and the behaviour of BC-based sensors, the model structure proposed in [9] for IEAPs is used here as a starting point and adapted to the specifics of BC-based sensors, whereby we consider the model to be linear to a first approximation. The model takes the displacement at the sensor tip as input and yields the current (under short circuit conditions) as output. Scaling of the sensor model depends on key geometric parameters of the sensor, including length, thickness, and width. A linear model for IEAPs sensors was suggested in [10] drawing from the Euler–Bernoulli theory of pinned beams and adapting piezoelectric coupling theory for BC-based sensors; the membrane was represented using a two-port equivalent circuit, with the introduction of a transformer to account for the piezoelectric effect, utilizing the d coupling coefficient. This model established a series of relationships between applied mechanical stimuli and resulting electrical reactions. We will particularly examine the relationship between the charge generated and the applied deformation among the proposed equations. We will focus on the dependence of the charge generated by an imposed deformation, where F is the applied force and δ is the deflection of the beam at the point of force application. In the case of deflection-to-current transduction, the relationship can be found if reciprocity of the piezoelectric effect for BC-based sensor is hypothesized:

$$\frac{i}{\delta} = s\frac{3\,d\,T_{BC}\,w\,Y}{4\,(L_t - L_c)} \tag{1}$$

where s is the Laplace operator, and d and Y are the complex functions to be identified by the identification process. The Euler-Bernoulli beam theory leads to the relationship between the applied force F and the deformation δ.

$$\delta = F\frac{4\,(L_t - L_c)}{Y\,w\,T_{BC}^3} \tag{2}$$

V. BLACK BOX MODELS

Considering the challenges in developing both first-principle and grey-box models due to their complexity, a purely data-driven black-box approach will also be employed. Black box models utilize universal approximators to fit experimental data and derive a macroscopic device description, resulting in simplified models with reduced computational demands. Typically, the design process for efficient and accurate black-box models is significantly shorter. The input-output relationship can be approximated using linear regression or machine learning methods. However, a key characteristic of black-box models is their lack of scalability, as they are tailored to the specific device from which the data were obtained, limiting their straightforward generalization to similar devices. In order to overcome such a limitation, our attention is directed towards an alternative approach to machine-learning models: symbolic regression. Symbolic regression (SR) [11] entails the simultaneous exploration for the optimal function form and parameter set tailored to the specific problem at hand. It serves as a potent regression method, particularly effective in scenarios where minimal a-priori knowledge of the data structure or distribution exists. SR enables the extraction of meaningful relationships from empirical data, thereby augmenting the predictive and generalization capabilities of our models.

VI. EXPERIMENTAL MODEL VALIDATION

The mechano-electric transduction properties of the BC-based sensor can be investigated by experiments for model validation. The experimental setup to be used to characterize the mechano-electric transduction properties of the BC/PEDOT device is shown in Figure 4. It allows experimentation with different ranges of maximum tip displacement and frequency for the model identification and is based on a shaker that is attached to the base of the sensor and generates a vibration. As shown in Figure 4.

The input voltage applied to motor controlling the oscillating platform and the shaker is shown in Figure 5. The displacement can measured by means of the laser proximity sensor. The data set ($300s$ sampled at $1kHz$) obtained by applying first a train of pulse, a frequency sweep signal depending on the experimental setup and then white noise signal. The persistence of excitation of the swept signal used to perform model identification has been verified.

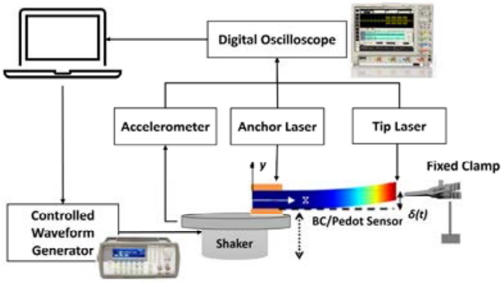

(a) Functional Schematic

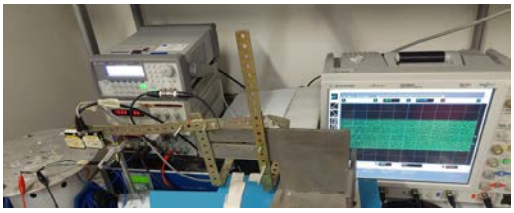

(b) Laboratory Equipment

Fig. 4. Experimental Setup with Shaker

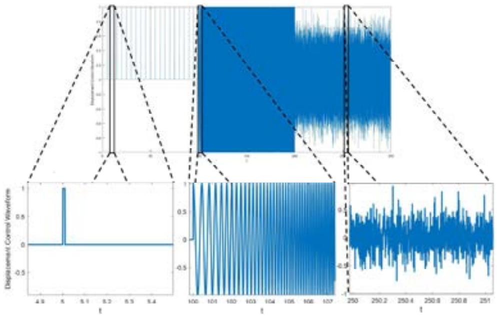

Fig. 5. Voltage waveform for the control of the oscillating platform and the shaker setup for system identification: pulse train, frequency sweep, white noise

VII. CONCLUSIONS

In the pursuit of advancing sensor modeling for BC, this study has presented a comprehensive multiphysics framework. Beginning with the description of BC geometry and manufacturing processes, we progressed to develop and validate a suite of predictive models. These models, ranging from transparent white box representations to physics-informed grey box models and enhanced black box models employing SR, collectively provide a holistic understanding of BC behavior. To date, the following steps have been completed: the theoretical multiphysics problem has been formulated and implemented in FEM, and the associated experimental setup has been established. Additionally, a preliminary study of the grey box and SR models has been conducted, pending a scientific experimental campaign to support the data-driven models. Through rigorous experimental validation, we will be able to demonstrate the efficacy of our multiphysics framework in accurately capturing the intricate dynamics of BC sensors across diverse conditions.

REFERENCES

[1] S.-S. Kim, J.-H. Jeon, C.-D. Kee, and I.-K. Oh, "Electro-active hybrid actuators based on freeze-dried bacterial cellulose and pedot:pss," *Smart Materials and Structures*, vol. 22, no. 8, p. 085026, jul 2013. [Online]. Available: https://dx.doi.org/10.1088/0964-1726/22/8/085026

[2] J. Huang, M. Zhao, Y. Hao, and Q. Wei, "Recent advances in functional bacterial cellulose for wearable physical sensing applications," *Advanced Materials Technologies*, vol. 7, no. 1, p. 2100617, 2022. [Online]. Available: https://onlinelibrary.wiley.com/doi/abs/10.1002/admt.202100617

[3] R. Caponetto, G. Di Pasquale, S. Graziani, A. Pollicino, F. Sapuppo, and C. Trigona, "Modeling of bacterial cellulose-based composite," *Electronics*, vol. 12, no. 21, 2023. [Online]. Available: https://www.mdpi.com/2079-9292/12/21/4530

[4] G. Di Pasquale, S. Graziani, A. Licciulli, R. Nisi, A. Pollicino, and C. Trigona, "Geometrical analysis of a bacterial cellulose-based sensing element," 06 2019, pp. 225–228.

[5] L. Yang, Y. Yang, and H. Wang, "Modeling and control of ionic polymer metal composite actuators: A review," *European Polymer Journal*, vol. 186, p. 111821, 2023.

[6] R. Caponetto, S. Graziani, F. Sapuppo, and V. Tomasello, "An Enhanced Fractional Order Model of Ionic Polymer-Metal Composites Actuator," *Advances in Mathematical Physics*, vol. 2013, pp. 1–6, August 2013.

[7] R. Caponetto, V. De Luca, G. Di Pasquale, S. Graziani, F. Sapuppo, and E. Umana, "A multiphysics frequency-dependent model of an ip^{2}c actuator," *IEEE Transactions on Instrumentation and Measurement*, vol. 63, no. 5, pp. 1347–1355, 2014.

[8] L. Patanè, F. Sapuppo, G. Calapristi, Di Pasquale, Marco, S. Graziani, A. Pollicino, C. Trigona, and M. G. Xibilia, "A multiphysics framework for bacterial cellulose sensor modeling," in *2024 IEEE International Conference on Metrology for eXtended Reality, Artificial Intelligence and Neural Engineering*, 2024.

[9] C. Bonomo, L. Fortuna, P. Giannone, S. Graziani, and S. Strazzeri, "A model for ionic polymer metal composites as sensors," *Smart Materials and Structures*, vol. 15, no. 3, p. 749, apr 2006. [Online]. Available: https://dx.doi.org/10.1088/0964-1726/15/3/010

[10] K. Newbury and D. Leo, "Electromechanical modeling and characterization of ionic polymer benders," *Journal of Intelligent Material Systems and Structures*, vol. 13, pp. 51–60, 01 2002.

[11] S.-M. Udrescu and M. Tegmark, "Ai feynman: A physics-inspired method for symbolic regression," *Science Advances*, vol. 6, no. 16, p. eaay2631, 2020.

Tumour growth control: analysis of alternative approaches

A. Borri(1), P. Palumbo(2), F. Papa(1)

(1) Institute for Systems Analysis and Computer Science, National Research Council
(2) University of Milano Bicocca, Department of Biotechnologies and Biosciences

Journal of Theoretical Biology, 562 (2023) 111420

Model-based control is gaining an increasing interest in the last decades, since it allows the design of very sophisticated feedback regulations accounting for the innate dynamics of the system under investigation. Within biomedical frameworks, minimal models are often exploited since they allow to catch the basic relationships among the involved variables without explicitly detailing all the physical/molecular mechanisms: they can be easily identified according to standard perturbation experiments, and allow the synthesis of affordable and readily implementable control laws. As far as tumour growth models are concerned, starting from the seminal paper [1] (proposing an Ordinary Differential Equation (ODE) model of the vascular growth of tumours characterized by low dimension and minimal number of parameters) several theoretical/experimental results have been achieved, dealing with model extensions (see [2, 3]) and closed-/open-loop anti-angiogenic drugging (see, e.g. [4-8), possibly combined with chemotherapy treatments (see, e.g. [9, 10]).

More recently, models of tumour growth have been proposed [11-13] as coming from the formalism of Chemical Reaction Network (CRN) [14]. The advantage of such an approach is that CRN can be straightforwardly modelled according to the stochastic framework implemented by the Chemical Master Equations (CME) [15], able to account for the inherent noise providing random fluctuations on the involved chemical players; the usual (ODE) models associated to CRNs may be thought of as a linear approximation of the average dynamics coming from the CME [16]. These ODE models can be fruitfully exploited in spite of the more complete CMEs whenever the chemical players copy number is very high, because of their superior computational manageability. In this work it is shown by realistic numerical simulations that the stochastic approach may be set aside for tumour growth control purposes, at least at the beginning of an exogenous drug administration therapy, because such therapies are supposed to start with a very large number of tumour cells. Instead, assuming to have successfully reduced the initial tumour mass, it could be interesting to approach the tumour eradication problem from a stochastic control perspective, dealing with a very low number of leftover tumour cells. In fact, this contribution starts from the qualitative analysis carried out in [15] for the ODE model associated to the CRN and further investigates tumour growth control techniques accounting for both fixed and state-dependent feedback control laws. The main results of this work show that constant administration therapies have several limitations. In particular, they cannot eradicate the tumour if its size is too large when the therapy starts. Conversely, a state-feedback control law can overcome the limitations of the constant therapy. Indeed, it is always possible to design a control scheme able to eradicate arbitrarily large tumours, allowing a high infusion rate only for a limited time period.

References

1) Hahnfeldt, P., Panigrahy, D., Folkman, J., Hlatky, L., 1999. Tumor development under angiogenic signaling. Cancer Res. 59 (19), 4770–4775.
2) d'Onofrio, A., Gandolfi, A., 2004. Tumour eradication by antiangiogenic therapy: Analysis and extensions of the model by Hahnfeldt et al. (1999). Math. Biosci. 191, 159–184.
3) d'Onofrio, A., Gandolfi, A., 2010. Chemotherapy of vascularised tumours: Role of vessel density and the effect of vascular ''pruning''. J. Theoret. Biol. 264, 253–265.
4) Cacace, F., Cusimano, V., Germani, A., Palumbo, P., 2018a. Optimal impulsive control with application to antiangiogenic tumor therapy. IEEE Trans. Control Syst. Technol. 1–12.
5) Cacace, F., Cusimano, V., Germani, A., Palumbo, P., Papa, P., 2018b. Closed-loop control of tumor growth by means of anti-angiogenic administration. Math. Biosci. Eng. 15 (4).
6) Drexler, D., Sápi, J., Kovács, L., 2017c. Optimal discrete time control of antiangiogenic tumor therapy. In: Proc. 20th IFAC World Congress. pp. 14046–14051.
7) Ledzewicz, U., Schättler, H., 2008. Optimal and suboptimal protocols for a class of mathematical models of tumor anti-angiogenesis. J. Theoret. Biol. 252 (2), 295–312.
8) Sápi, J., Drexler, D., Harmati, I., Sápi, Z., Kovács, L., 2016. Qualitative analysis of tumor growth model under antiangiogenic therapy–choosing the effective operating point and design parameters for controller design. Optim. Control Appl. Methods 37 (5), 848–866.
9) d'Onofrio, A., Ledzewicz, U., Maurer, H., Schättler, H., 2009. On optimal delivery of combination therapy for tumors. Math. Biosci. 222 (1), 13–26.
10) Ledzewicz, U., Maurer, H., Schaettler, H., 2011. Optimal and suboptimal protocols for a mathematical model for tumor anti-angiogenesis in combination with chemotherapy. Math. Biosci. Eng. 8 (2), 307–323.
11) Drexler, D.A., Ferenci, T., Lovrics, A., Kovács, L., 2019. Modeling of tumor growth incorporating the effect of pegylated liposomal doxorubicin. In: IEEE 23rd Int. Conf. on Intelligent Engineering Systems. pp. 369–374.
12) Drexler, D.A., Sápi, J., Kovács, L., 2017a. A minimal model of tumor growth with angiogenic inhibition using bevacizumab. In: Proceedings of the 2017 IEEE 15th International Symposium on Applied Machine Intelligence and Informatics. pp. 185–190.
13) Drexler, D.A., Sápi, J., Kovács, L., 2017b. Modeling of tumor growth incorporating the effects of necrosis and the effect of bevacizumab. Complexity 1–11.
14) Feinberg, M., 2019. Foundations of Chemical Reaction Network Theory. In: Applied Mathematical Sciences, Springer.
15) Borri, A., Palumbo, P., Papa, F., 2020. Deterministic vs stochastic formulations and qualitative analysis of a recent tumour growth model. IFAC-PapersOnLine 53 (2), 16418–16423. http://dx.doi.org/10.1016/j.ifacol.2020.12.724.
16) van Kampen, N.G., 2007. Stochastic Processes in Physics and Chemistry, third ed. Elsevier, The Nederlands.

Joint Optimization for OFDMA Heterogeneous Networks with stochastic channel-gains

Gabriel O. Ferreira [*], Chiara Ravazzi [*], Fabrizio Dabbene[*], Giuseppe C. Calafiore[†]
[*] IEIIT CNR Institute, Italy, [†] Politecnico di Torino, Italy
{chiara.ravazzi, fabrizio.dabbene, gabriel.oliveiraferreira}@ieiit.cnr.it, giuseppe.calafiore@polito.it

I. INTRODUCTION

The channel gains between user equipaments (UEs) and base stations (BSs) have a fundamental importance when optimizing mobile networks efficiency. In general, these parameters can be evaluated by means of site specific ray tracing solvers that simulate the radio waves propagation. These strategies (or any other relying on physics-based models) have the limitation of depending on how accurate the environment is described and reconstructed into the propagation solvers/models. However, even if the buildings geometry and electromagnetic properties of the construction materials are known, parameters such as motion of objects (people, cars, etc) make these quantities stochastic in practice. In real life situations the electromagnetic waves propagated by the antennas will suffer not only from shadowing, but also combined effects of reflection and diffraction. Consequently, the channel gain between a UE/BS pair is inherently a random quantity.

In this paper, we extend the work presented in [1] to the case where the channel gains are random variables. We propose a joint optimization algorithm that minimizes the BSs transmission powers in OFDMA heterogeneous networks, while respecting chance-constrained individual users quality of service (QoS) requirements. Unlike many works in the literature, our optimization problem does not rely on iterative/sequential procedures and does not require a known feasible initial solution, which in general leads to local optimal.

II. PROBLEM FORMULATION

The Mixed-Integer Geometric Programming (MIGP) (2) was introduce in [1]. We demonstrated that the MIGP is an upper-bound solution to a non-convex integer optimization problem, whose goal is to minimize transmission powers while respecting individual users' throughput constraints (measured in **bits/s**). B_j represents the bandwidth of BS j, the binary variable $z_{ij} = 1$ if a user i is connected to BS j and $z_{ij} = 0$ otherwise, $x_{ij} = e^{uij}$ represents the amount of bandwidth of BS j allocated to user i, P_j and $\hat{P}_j$ are the transmission powers of one resource block of BS j and its respective maximum physical limit, and $S_{ij}(P)$ is the SINR of user i connected to BS j, defined as

$$S_{ij}(P) \doteq \frac{P_j g_{ij}}{\eta^2 + \sum_{k \neq j} P_k g_{ik}}. \tag{1}$$

$$\min_{\bar{z}_{ij}, u_{ij}, q_j} \quad \sum_{j=1}^{N} e^{q_j} \tag{MIGP}$$

s.t.:

$$e^{u_{ij}} \leq 1, \quad i \in [n], j \in [N] \tag{2a}$$

$$\bar{z}_{ij} \in \{0,1\}, \quad i \in [n], \quad j \in [N], \tag{2b}$$

$$e^{q_j} \leq \hat{P}_j, \quad j \in [N], \tag{2c}$$

$$\sum_{j=1}^{N} \bar{z}_{ij} = N - 1, \quad i \in [n], \tag{2d}$$

$$\sum_{i=1}^{n} e^{u_{ij}} \leq 1, \quad j \in [N], \tag{2e}$$

$$\hat{f}_\ell(q_j, u_{ij}) \leq A_{ij}^{\ell} + M\bar{z}_{ij}, \qquad i \in [n], j \in [N], \ell \in [m], \tag{2f}$$

with $\bar{z}_{ij} = 1 - z_{ij}$, M being a sufficiently large constant

$$\hat{f}_\ell(q_j, u_{ij}) \doteq \log\left(\frac{\eta^2}{g_{ij}} e^{-q_j - \frac{u_{ij}}{b_\ell}} + \sum_{k \neq j} \frac{g_{ik}}{g_{ij}} e^{q_k - q_j - \frac{u_{ij}}{b_\ell}}\right),$$

$$A_{ij}^{\ell} \doteq \frac{\log\left(\frac{B_j a_\ell}{r_i}\right)}{b_\ell}.$$

η^2 is the noise power, g_{ij} is the channel gain between user i and BS j. For an OFDMA heterogeneous network composed of N BS and n users, the aforementioned optimization problem ensures that each user is connected to just one BS, a BS cannot provide more resources than available, and each user has an individual minimum throughput level r_i to be respected.

A. Stochastic MIGP

In real-world environments, the channel gains are random variables due to the combined effects of shadowing, multipath, diffraction, etc. In particular these quantities respect a log-normal distribution, i.e. the dB gains, defined as

$$g_{ij}^{(dB)} \doteq 10 \log_{10} g_{ij}, \quad i \in [n], j \in [N] \tag{3}$$

obey a Gaussian distribution, i.e. $g_{ij}^{(dB)} \sim \mathcal{N}(\tilde{\mu}_{ij}, \tilde{\sigma}_{ij}^2)$. We write this as $g_{ij} \sim \mathcal{LN}(\mu_{ij}, \sigma_{ij}^2)$. Furthermore, we can define the normalized gains as

$$\rho_{ij} \doteq \frac{10 \log_{10} g_{ij} - \tilde{\mu}_{ij}}{\tilde{\sigma}_{ij}} \sim \mathcal{N}(0,1), \quad i \in [n], j \in [N]. \tag{4}$$

From (4) and with $c = \frac{\log 10}{10}$, we have

$$g_{ij} = e^{c(\tilde{\mu}_{ij} + \rho_{ij}\tilde{\sigma}_{ij})}, \quad i \in [n], j \in [N]. \tag{5}$$

Since the channel gains are random variables and the users' throughput levels are highly dependent on them, constraint (2f) becomes stochastic, and must be respected with a probability $\mathbb{P}_i$ given by $1-\alpha_i$, leading to the following chance-constrained optimization problem

$$\begin{aligned} \min_{\bar{z}_{ij}, u_{ij}, q_j} \quad & \sum_{j=1}^{N} e^{q_j} && \text{(CC-MIGP)} \\ \text{s.t.: } & \text{(2a)} - \text{(2e)} && \text{(6a)} \\ & \mathbb{P}_i\left(\hat{f}_\ell(q_j, u_{ij}) \leq A^\ell_{ij} + M\bar{z}_{ij}\right) \geq 1 - \alpha_i \\ & \ell \in [m], i \in [n], j \in [N]. && \text{(6b)} \end{aligned}$$

Chance constrained optimization problems might be difficult to handle. Then we present a robust formulation based solution.

III. ROBUST MIGP

Proposition 1 (Box uncertainty): Let ρ_{ij}, $i \in [n]$, $j \in [N]$ be Gaussian random variables with zero mean and unitary standard deviation, as in (4). For each user, compute the quantities $[\underline{\rho}_{ij}, \overline{\rho}_{ij}]$ such that

$$\begin{cases} \mathbb{P}(\underline{\rho}_{ij} \leq \rho_{ij} \leq \overline{\rho}_{ij}) = \dfrac{\text{erf}\left[\frac{\overline{\rho}_{ij}}{\sqrt{2}}\right] - \text{erf}\left[\frac{\underline{\rho}_{ij}}{\sqrt{2}}\right]}{2} = \varphi_j, \quad j \in [N], \\ \prod_{j=1}^{N} \varphi_j = 1 - \alpha_i. \end{cases} \tag{7}$$

Then a robust optimization problem considering the uncertainty box can be derived such that its optimal solution is feasible to the CC-MIGP.

Theorem 1: For uncertainty boxes given by Proposition 1, the optimal solution $u^\star_{ij}, x^\star_{ij}, P^\star_j$ to

$$\begin{aligned} \min_{\bar{z}_{ij}, u_{ij}, q_j} \quad & \sum_{j=1}^{N} e^{q_j} && \text{(Robust-MIGP)} \\ \text{s.t.: } & \text{(2a)} - \text{(2e)} && \text{(8a)} \\ & \log(\eta^2 e^{\beta_{ij\ell}} + \sum_{k \neq j} e^{\zeta_{ik\ell}}) \leq A^\ell_{ij} + M\bar{z}_{ij}, \\ & \forall \rho_{ij} \in [\underline{\rho}_{ij}, \overline{\rho}_{ij}] \text{ and } \forall \rho_{ik} \in [\underline{\rho}_{ik}, \overline{\rho}_{ik}] \\ & \ell \in [m], i \in [n], j \in [N], && \text{(8b)} \end{aligned}$$

with

$$\beta_{ij\ell} = -c(\tilde{\mu}_{ij} + \underline{\rho}_{ij}\tilde{\sigma}_{ij}) - q_j - \frac{u_{ij}}{b_\ell},$$

$$\zeta_{ik\ell} = c(\tilde{\mu}_{ik} + \overline{\rho}_{ik}\tilde{\sigma}_{ik} - \tilde{\mu}_{ij} - \underline{\rho}_{ij}\tilde{\sigma}_{ij}) + q_k - q_j - \frac{u_{ij}}{b_\ell},$$

is always feasible to the chance constrained optimization problem in (6), i.e.

$$\text{Robust MIGP}(u^\star_{ij}, x^\star_{ij}, P^\star_j) \implies \text{Stochastic MIGP}.$$

IV. EXAMPLE

We estimate the channel gains from a neighbourhood in a large European city by reconstructing it (considering the urban environment characteristics previously mentioned) into a 3D ray tracing propagation software. Figure 1.(a) shows the channel gains expected values $\tilde{\mu}_{ij}$ and Figures 1.(b) and 1.(c) expose how the randomness in these quantities can lead to a different quality of signal and coverage.

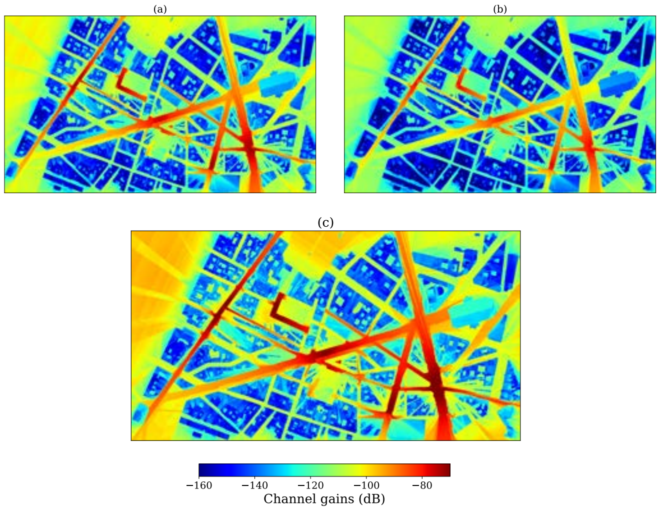

Fig. 1. Channel gains for $\sigma = 3$ and (a) $\tilde{\mu}_{ij}$, (b) $\tilde{\mu}_{ij} - 2\sigma$, and (c) $\tilde{\mu}_{ij} + 2\sigma$.

We illustrate the efficacy of our approach by applying it on a simulated heterogeneous wireless network composed of $N = 5$ BSs and $n = 130$ users. Our goal is to assign 120 users distributed over an area of 800m × 800m to a corresponding BS, respecting each throughput requirement and minimizing the total BSs transmission powers. The optimal values as a function of (a) standard deviation and (b) constraint probability are show in Figure 2.

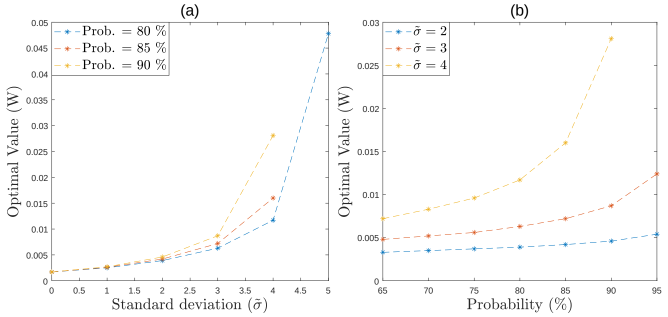

Fig. 2. Optimal value.

REFERENCES

[1] G. O. Ferreira, A. F. Zanella, S. Bakirtzis, C. Ravazzi, F. Dabbene, G. C. Calafiore, I. Wassel, J. Zhang, and M. Fiore, "A Joint Optimization Approach for Power-Efficient Heterogeneous OFDMA Radio Access Networks," 2024.

Session 2B: Robotics

Reducing Cognitive Load through a Data-Driven Shared Control Approach for Teleoperating Robot Swarms

T. Lisini Baldi[1,2], E. Turco[2], C. Castellani[2], V. Bo[2], C. Pacchierotti[3], and D. Prattichizzo[1,2]

***Abstract*— Multi-robot systems have gained increasing interest across various fields such as medicine, environmental monitoring, and more. Despite the evident advantages, the coordination of the swarm arises significant challenges for human operators, particularly concerning the cognitive burden needed for efficiently controlling the robots. In this study, we present a novel approach for enabling a human operator to effectively control the motion of multiple robots. Leveraging a shared control data-driven approach, we enable a single user to control the 9 degrees of freedom related to the pose and shape of a swarm. Subjective measures of cognitive load were assessed using a post-experiment questionnaire, comparing different levels of autonomy of the system. Results show substantial reductions in operator cognitive load when compared to conventional teleoperation techniques, accompanied by enhancements in task performance, including reduced completion times and fewer instances of contact with obstacles. This research underscores the efficacy of our approach in enhancing human-robot interaction and improving operational efficiency in multi-robot systems.**

I. INTRODUCTION

Multi-robot systems are emerging as an important area of research due to their potential to impact various fields, including search and rescue operations, environmental monitoring, medical robotics, and industrial automation.

While the advantages of multi-robot systems are evident, the complexity of coordinating multiple independent agents poses challenges for human operators. Controlling the motion of numerous robots simultaneously in an intuitive and effective manner requires sophisticated interfaces and algorithms. Ensuring seamless interaction between humans and multi-robot systems is crucial for maximizing their potential benefits while minimizing operational complexities, safety risks, human-robot trust, and the cognitive load imposed on users during control. [1].

Research has shown that enhancing robot autonomy decreases users' cognitive load [2], as cognitive burden correlates with the number of conceptual elements users must simultaneously manage to accomplish a specific task [3].

This work presents a data-driven shared-control method aiming to allocate the controlled DoFs of a multi-robot system between a human operator and an autonomous controller, seeking the best compromise between control effectiveness and cognitive load reduction. Utilizing statistical analysis on human demonstration data, shared control strategies are designed and tested in a human-subjects experiment where users navigate a simulated swarm in a narrow, tortuous environment.

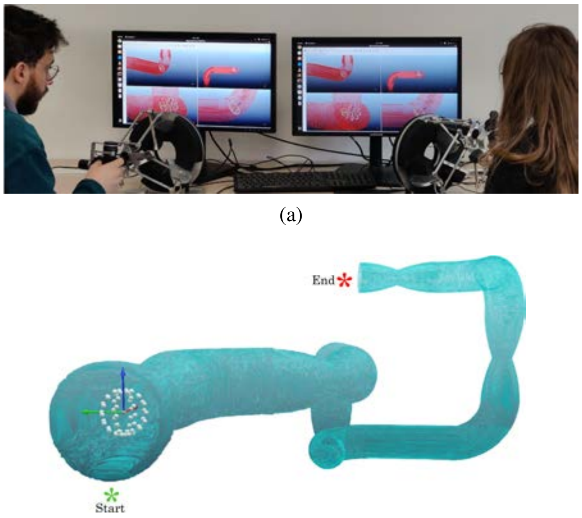

(a)

(b)

Fig. 1: In (a), two operators control the robotic swarm 9-DoF using two interfaces. In (b), the navigation path is shown, with green and red stars marking the start and end points.

II. SYSTEM OVERVIEW

The virtual environment is developed in CoppeliaSim. The swarm is composed of 64 agents initially arranged in a spherical formation with a depth sensor placed at its center. The target environment features straight and curved, deformed and non-deformed segments (Fig. 1b).

The pose and shape of the swarm can be controlled with 9-DoF, being the pose of the swarm centroid 6-DoF (i.e., position $\boldsymbol{p}$ and orientation $\boldsymbol{o}$) and 3 additional DoF (deformation $\boldsymbol{\delta}$) for modifying the shape along its three axes of symmetry.

A pair of Omega.7 (Force Dimension, CH) haptic interfaces is employed for the user to control the available DoF.

The system offers users haptic and visual feedback. Upon collision with the pipe wall, users receive vibrations on the haptic interfaces' handles along with visual cues.

III. DATA-DRIVEN SHARED CONTROL

A. Data collection from dual-user experiments

The data collection procedure involved 10 subjects (5 males and 5 females, average age 28 ± 3.1). Participants were randomly paired into 5 groups and instructed to collaboratively control the swarm along the pipe-like path (Fig. 1a).

They were asked to: *i*) navigate through the path as quickly as possible, *ii*) occupy with the robotic swarm the largest possible cross-sectional area within the path, and *iii*) minimize the number of collisions with the environment.

Each pair of users repeated the assigned task 6 times, switching control roles after three trials to experience both aspects of swarm control (pose and deformation). Performance

---

[3] Università degli Studi di Siena, Dip. di Ingegneria dell'Informazione e Scienze Matematiche, Siena, Italy. `{name.surname}@unisi.it`

[1] Istituto Italiano di Tecnologia, Genoa, Italy

[2] CNRS, Univ Rennes, Inria, IRISA – Rennes, France.

This work was supported by the European Union's Horizon Europe Research and Innovation Programme under Grant Agreement #101070066, project REGO, by the University of Siena curiosity driven (F-CUR) programme project "BRIOCHE: wearaBle sensoRImOtor interfaCes for Human augmentation, and by the European Union's FSE REACT-EU programme, PON Ricerca e Innovazione 2014-2020.

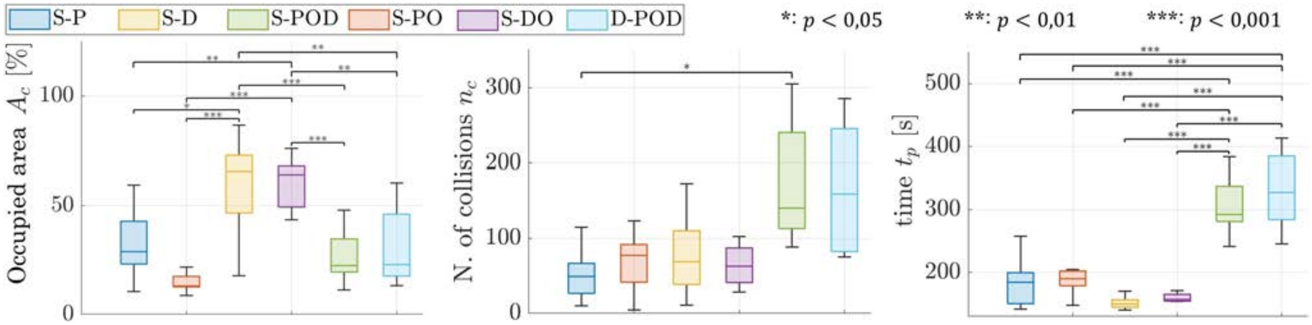

Fig. 2: Comparison of quantitative metrics for all tasks. Median and interquartile range of the six conditions are plotted. p-values, calculated using one-way repeated measures ANOVA, are shown above the bar charts.

in completing the task was evaluated using three metrics: (i) time to complete the path (t_p), (ii) percentage of the pipe cross-sectional area occupied by the swarm (A_c), and (iii) number of collisions (n_c). Cognitive load was assessed via NASA Task Load Index (NASA-TLX) questionnaire. Overall, 30 trials were conducted, capturing the users control inputs and the depth data from the sensor.

B. *Data analysis for variance estimation*

The goal of this analysis is to determine which DoF were most controlled during the trials. Initially, we classified data into different subsections based on point cloud similarities.

Signals were then normalized and time-aligned using Dynamic Time Warping algorithm. We evaluated inter-user variability among commanded positions, orientations, and deformations to identify trends in operator performance. A Pareto analysis was used to assess variance in dataset features, showing that deformation has the highest inter-user variability across all subsections, while position has the least.

C. *Shared-control algorithms for multi-robot control*

Based on this analysis, four shared control techniques were proposed, allocating DoF between a single user and an autonomous controller in different ways:

Single-Deformation (S-D): one user controls the swarm deformation (3-DoF, 65% of the total variance).

Single-Deformation-Orientation (S-DO): one user controls the deformation and orientation (6-DoF, 90% of the variance).

Single-Position (S-P): one user controls the swarm position (3-DoF, 10% of the total variance).

Single-Position-Orientation (S-PO): one user controls the swarm pose (6-DoF, 35% of the total variance).

For each strategy, the autonomous controller manages the remaining DoF using point cloud data as reference.

In addition, we consider two standard teleoperation conditions, where the human operator retains complete control i.e.,

Single-Position-Orientation-Deformation (S-POD): one user controls both the swarm pose and deformation (9-DoF).

Dual-Position-Orientation-Deformation (D-POD): one user controls the swarm pose (6-DoF), another user controls the swarm deformation (3-DoF). This modality was used in Sec. III-A for data collection.

IV. EXPERIMENTAL EVALUATION

The experimental evaluation included the same 10 subjects from the initial data collection phase. Each participant performed the task three times per control condition (S-D, S-DO, S-P, S-PO, S-POD), totaling 15 trials. After each task, participants completed a NASA-TLX questionnaire, and quantitative metrics were recorded.

	S-P	S-PO	S-D	S-DO	S-POD	D-PO	D-D
Overall Weighted Workload Score	41.58	52.83	**38.2**	**35.6**	72.07	70.25	58.8

TABLE I: NASA-TLX workload. D-POD modality was split into D-PO and D-D as users provided feedback for both pose and deformation.

Fig. 2 shows the results for the objective metrics. All four shared control techniques statistically outperform compared to single- (S-POD) and dual-user (D-POD) controls.

S-D and S-DO demonstrate high performance in maximizing the swarm's occupied area while notably reducing the task completion time, signifying their operational efficiency.

The S-P control strategy demonstrates good performance metrics in occupied areas and enhances user precision, resulting in significantly fewer collisions and shorter task completion times compared to standard S-POD and D-POD strategies. Conversely, S-PO yields lower performance but still outperforms S-POD and D-POD in completion time.

The NASA-TLX results align with the objective analysis. The subjective analysis indicates that our shared-control strategies significantly reduce cognitive load, resulting in decreased mental demand, effort, and frustration for users. Table I displays the total workload, indicating that deformation control strategies exhibited the lowest overall workloads, suggesting a better user experience.

V. CONCLUSION

In this work, we designed, implemented, and tested data-driven shared control strategies to reduce human cognitive burden during teleoperation of a robot swarm, while enhancing task performance. By analyzing user-controlled DoF, four shared control policies were designed with varying autonomy levels. Evaluation through a user study confirmed significant reductions in cognitive load and improved task performance when the DoFs to be controlled are shared between the user and the autonomous controller.

REFERENCES

[1] J. Pan *et al.*, "Exploring the effects of shared autonomy on cognitive load and trust in human-robot interaction," *arXiv preprint arXiv:2402.02758*, 2024.

[2] S. Baltrusch *et al.*, "What about the human in human robot collaboration? a literature review on hrc's effects on aspects of job quality," *Ergonomics*, vol. 65, no. 5, pp. 719–740, 2022.

[3] J. L. Plass *et al.*, "Cognitive load theory," 2010.

Hybrid Brain Computer Interface for Robot Control

D. Sanalitro[1], M. Bucolo[1] *Senior Member, IEEE*

I. INTRODUCTION

Brain-Computer Interface (BCI) systems have gained significant attention as a means of establishing direct communication between the human brain and external devices. Such direct communication provides novel ways of interacting with both healthy individuals, and more importantly, patients with disabilities resulting from spinal cord injuries, Amyotrophic Lateral Sclerosis (ALS), stroke, or other neurological conditions. Electroencephalographic (EEG) recordings of brain waves allow for this kind of connection to be established. In the robotics field, BCI applications have shown promise for intuitive and efficient control [1]. In this context, this paper presents a hybrid BCI approach for controlling a robotic system, combining Motor Imagery (MI) and Error-Related Negativity (ERN) paradigms. The proposed framework intends to use MI to empower users in actively controlling the robot and ERN for human visual feedback to empower users to provide feedback on the robot's state changes. In MI-based BCI systems, users imagine performing a specific movement without actual execution [2]. In particular, when subjects imagine left or right hand, arm, or foot movements, a lateralization can be seen in the data, particularly when the frequency EEG band [7-30 Hz] is considered [3]. By contrast, ERN is a type of error-related potential (ERP) present in the EEG signals when the user is aware of an erroneous behavior. They are characterized by an early negative voltage deflection over fronto-central regions, referred to as error-related negativity (N_E), followed by a positive deflection over parietal regions, referred to as error-positivity (P_E). Such peaks occur between 50 and 100 [ms] after the commission of a speeded motor response that the subject immediately realizes to be an error [4]. By combining these two distinct paradigms, i.e. MI and ERN, for active control and feedback retrieval, the BCI framework presented here becomes hybrid in nature. Separate and offline demonstrations, intended as a calibration stage, of the proposed BCI approach's feasibility have been made through simulations and experimental evaluations involving human participants and an Unmanned Aerial Vehicle (UAV). Such a calibration phase results essential as the initial step towards the implementation of active and closed-loop control for BCI systems.

II. SYSTEM ARCHITECTURE AND METHODOLOGY

This section proposes the overall intended control framework. In particular, in Fig. 1 we illustrate the active control branch and the ERN-based visual feedback. Both include an acquisition phase, a preprocessing phase, a feature extraction and a final classification which will be discussed in the following. To be noted, at the present moment, the proposed algorithms operate offline and can be seen as the first step of the BCI system, the calibration one.

A. Experimental Setup, Participants and Protocol

1) EEG Recording: The EEG signals were recorded in both cases by using a Biosemi ActiveTwo 64-channel montage based on the worldwide 10-10 system at 512 Hz sampling rates.

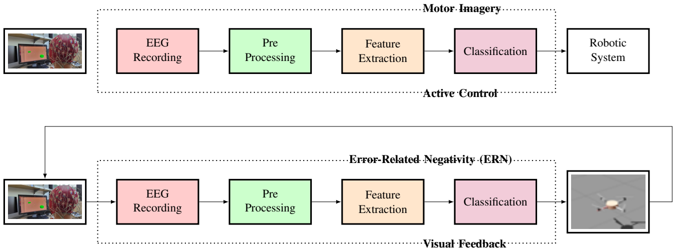

Fig. 1: System architectures overview: *1) Active Control*: from the signals acquisition to the robot control -: from the EEG recording to the ERN-Based Feedback

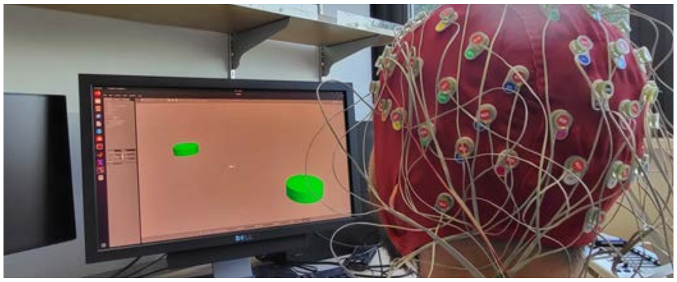

Fig. 2: Subject staring at the gazebo-based simulation showing a UAV performing forward and backward movements

2) Active Control: The study was conducted on 52 subjects and the data was taken from [5]. Before each trial began, the subject was instructed to wait two seconds for the monitor to display a blank screen with a fixation cross. Then, for three seconds, one of the two instructions, either imagining a left or right movement, was displayed. Subjects were asked to visualize moving their hand in response to the displayed instruction within this time interval.

3) ERN-Based Feedback: The user is asked to stare intently at a screen. At the beginning of each experiment, a robot takes off. Then, the trials start and a trajectory is designed to move the robot towards predefined waypoints, i.e x_{d_1} and x_{d_2}, multiples times resulting in a forward and backward behavior (see Fig. 2). Sometimes a wrong waypoint (x_w) is provided to elicit the ERN in the EEG signals. 28 waypoints were provided for each trial, 42% of them were not correct. Only a single user is participating in this experimental phase, with all experiments conducted in our lab. EEG data was recorded using ROS-Neuro [6] a framework designed for the integration of BCI technologies within robotic systems.

B. Control System Architecture

1) Active Control: In this step, MI control signals are decoded to extract the intended motion commands. EEGs capture the user's brain signals, which we then process and analyze to identify specific patterns associated with left or right motion intentions. Specifically, the process involves acquiring data, applying band pass filtering within the frequency range of [7-30] Hz to the EEG signals, extracting features such as Energy, Absolute Power, and Instantaneous Spectral Entropy, and utilizing a Convolutional Neural Network (CNN) to

---

[1] Department of Electrical Electronic and Computer Science Engineering, University of Catania, CT, Italy. `dario.sanalitro@unict.it` `maide.bucolo@unict.it`.

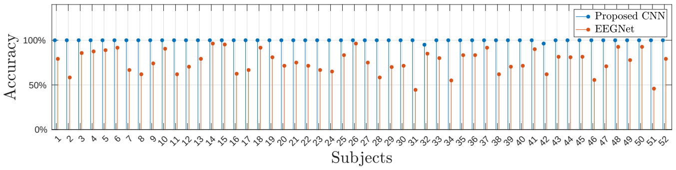

Fig. 3: *Active Control*: Accuracy comparison between the results of the proposed CNN and EEGNet during the test phase for the 52 subjects involved in the study.

classify and interpret the MI patterns. The outcome of this stage is a user model through which control inputs can be generated for the UAV, enabling the robot to online execute the desired movements.

2) ERN-Based Feedback: In this step, the brain signals are subjected to a filtering and an Artifact Subspace Reconstruction (ASR) employed to eliminate transient and high-amplitude artifacts that contaminate the EEG data. Then, Independent Component Analysis (ICA), a signal processing methodology useful to separate independent sources linearly mixed in several sensors, has been applied to identify independent components showing the ERN. A Linear Discriminant Analysis algorithm has been used to classify ERNs. Four statistical characteristics, i.e., mean, standard deviation, skewness and kurtosis have been used to train the classifier. In this case, the robot control is made possible via a state-of-the-art geometric controller implemented through telekyb3[1] , a free and open source software collection for UAVs. The UAV control inputs are computed through a geometric controller [7].

III. Results

1) Active Control: Our preliminary results, which pertain to the the calibration phase, are here described. In particular, we show two distinct learned models: i) a within subject model trained on each individual subject and ii) a cross-subject model trained on the entire set of 52 subjects. In particular, the latter highlights the CNN's capability to discriminate between classes despite the presentation of MI data, extremely subjective, from various individuals. TensorFlow, an open-source, end-to-end machine learning framework, and Python have been used for this offline study. 80% of the 40 recorded trials, for each subject, was given for the training phase and 20% was given for the test phase. The accuracy for the classification of three control inputs, i.e. left, right movement and resting state is then computed. Fig. 3 shows the results of our network for the withing subject models. In particular, we show the accuracy for each subject by employing EEGNet [8], a widely used CNN in the literature for MI classification, and the proposed CNN. As a result, just two of the 52 subjects (S32 and S42) demonstrated classification performances below 100%, specifically around 95%. Thus, the proposed CNN outperformed EEGNet for all the involved subjects. Moreover, we trained our model to generalize well across data from different individuals, rather than being tailored to a single subject. While not shown here, the results demonstrate that, even in this scenario, our network is capable of accurately classifying large datasets with an accuracy level exceeding 95%.

2) ERN-Based Feedback: Our initial findings are detailed here and are related to the offline stage, i.e. the calibration. EEGLAB [9] has been used to perform the pre-processing and the ICA decomposition. In all the recorded experiments, an ERN was present as a consequence of an erroneous robot behavior. The 18^{th} independent component of one of the performed experiments has been selected for visualization purposes. Fig. 4(a) shows the evolution over time of the EEG signals, showing a negative deflection (N_E) followed by a positive one (P_E) after the stimulus onset (RT) prominent over the central and prefrontal electrode position (see red areas of Fig. 4(b)). After the ERN identification phase, we performed the ERN classification in order to have a way of classifying ERNs when the online analysis is conducted. For this purpose, a linear classifier has been trained over 10 datasets and 280 trials. The reached accuracy was 70%. After this calibration stage, involving the offline ICA decomposition and the ERN classification, the retrieved outcomes will be used in the online phase for the robot control once the offline phase analyses will be consolidated.

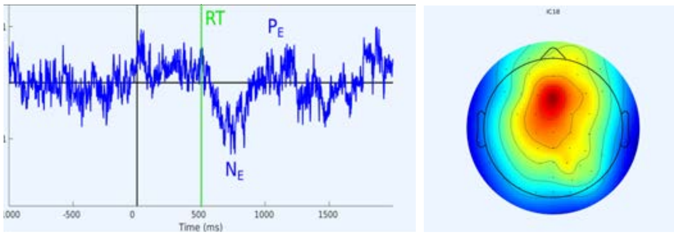

(a)

(b)

Fig. 4: *ERN-Based Feedback*: 18^{th} component time evolution for one trial along with the scalp map. The ERN deflection and a subsequent positive one are shown.

IV. Conclusions

This work presents a Hybrid BCI approach for controlling a robotic system, combining Motor Imagery (MI) and Error-Related Negativity (ERN) paradigms. We show the first step of the design of such BCI systems, i.e. the calibration phase. The goal of future research will be to incorporate such analyses in an online closed-loop system that will handle both MI and ERN, providing humans with brain actuated control frameworks able to both command external devices and provide feedback.

References

[1] J. Zhang and M. Wang, "A survey on robots controlled by motor imagery brain-computer interfaces," *Cogn Robot*, vol. 1, pp. 12–24, 2021.

[2] S. Cariello, D. Sanalitro, A. Micali, A. Buscarino, and M. Bucolo, "Brain–computer-interface-based smart-home interface by leveraging motor imagery signals," *Inventions*, vol. 8, no. 4, p. 91, 2023.

[3] R. Ortner, D.-C. Irimia, J. Scharinger, and C. Guger, "A motor imagery based brain-computer interface for stroke rehabilitation." *Annu. Rev. Cyberther. Telemed.*, vol. 181, pp. 319–323, 2012.

[4] P. Luu, D. M. Tucker, and S. Makeig, "Frontal midline theta and the error-related negativity: neurophysiological mechanisms of action regulation," *Clinical neurophysiology*, vol. 115, no. 8, pp. 1821–1835, 2004.

[5] H. Cho, M. Ahn, S. Ahn, M. Kwon, and S. C. Jun, "Eeg datasets for motor imagery brain–computer interface," *GigaScience*, vol. 6, no. 7, p. gix034, 2017.

[6] L. Tonin, G. Beraldo, S. Tortora, and E. Menegatti, "Ros-neuro: An open-source platform for neurorobotics," *Frontiers in Neurorobotics*, vol. 16, p. 886050, 2022.

[7] T. Lee, M. Leok, and N. H. McClamroch, "Geometric tracking control of a quadrotor uav on se (3)," in *49th IEEE conference on decision and control (CDC)*. IEEE, 2010, pp. 5420–5425.

[8] V. J. Lawhern, A. J. Solon, N. R. Waytowich, S. M. Gordon, C. P. Hung, and B. J. Lance, "Eegnet: a compact convolutional neural network for eeg-based brain–computer interfaces," *Journal of neural engineering*, vol. 15, no. 5, p. 056013, 2018.

[9] A. Delorme and S. Makeig, "Eeglab: an open source toolbox for analysis of single-trial eeg dynamics including independent component analysis," *Journal of neuroscience methods*, vol. 134, no. 1, pp. 9–21, 2004.

---

[1] https://git.openrobots.org/projects/telekyb3

Cobots Understanding Skills Programmed by Demonstration

Isacco Zappa[1], Andrea Maria Zanchettin[1] and Paolo Rocco[1]

***Abstract*— Traditional robot programming requires skilled operators, contrasting with small and medium-sized enterprises lacking robotics expertise. Programming by Demonstration offers a viable solution, allowing users to program a robot in a no-coding fashion. However, while the user demonstrates what a skill is about, the robot depicts it only as a sequence of movements. Therefore, the knowledge gathered from the demonstration can hardly be transferred to a different task. This abstract presents the outcomes of enriching Programming by Demonstration to encode the meaning of the skill being demonstrated. We enable the robot to understand the skill semantics in terms of preconditions and effects from a single demonstration. A symbolic planner can then use the taught skills as modular blocks to autonomously compute the sequence of actions required to solve a task. Finally, given the relevance of multi-robot systems on factory grounds, the abstract outlines the guidelines for extending the proposed teaching methodology to multi-agent systems.**

I. BACKGROUND

Despite the effort made by manufacturers in the development of intuitive programming interfaces, an expert operator is still required to program a collaborative robot. The problem becomes paramount for small and medium-sized enterprises, which usually lack such expertise in robotics.

Programming by Demonstration [1] provides the operator with a more accessible programming method that does not involve coding. The underlying concept is that the robot can learn how to execute a task from a demonstration. The demonstration spans from pure observations to kinesthetic demonstrations. The latter consists of the operator physically moving the robot along the execution of the skill. A key enabling technology is cobot's hand-guiding, which was devised by manufacturers to save movement waypoints and record trajectories easily. However, during the demonstration, the operator provides the robot with information about how to execute an action and the meaning of the action itself. Nevertheless, the robot still depicts the demonstration as a series of movements. Capturing the meaning of a skill from a demonstration can give the robot a certain level of autonomy, thus aiding the operator in deploying the cobot for a task.

II. SEMANTIC PROGRAMMING BY DEMONSTRATION

Semantics is the study of the meaning we give to the entities around us, their properties and relations, and how we structure this knowledge [2]. Semantics applied to robotics enable the robot to build abstractions from the raw data recorded by its sensor to represent the state of the environment as a list of first-order logic predicates. Providing the robot with the capability to build a semantic description of the scene enhances the interpretability of how the robot perceives the environment, resulting in more intuitive and meaningful interactions with the operator. An example of a state description with predicates can be seen in Figure 1.

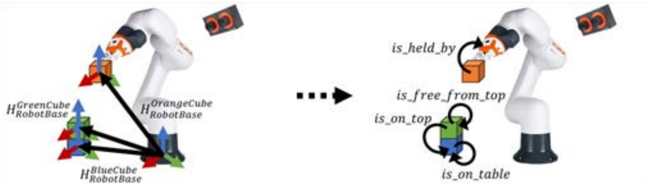

Fig. 1: Example of a semantic representation of the state of the environment built from sensor data.

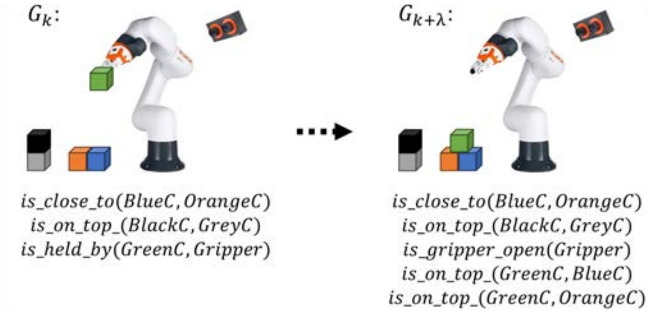

Fig. 2: Semantic representation of the state of the environment before and after the demonstration.

Recent work proposes to exploit this representation to extrapolate the meaning of the demonstrated skill in terms of its preconditions and effects [3]. The user starts recording a skill and defines the robot's movements by saving waypoints in the operational space. Upon the completion of the demonstration, the method compares the symbolic state before and after the recording to determine which predicates hold, are activated or deactivated. The method then autonomously computes the preconditions and effects of the demonstrated skill from these sets and formalizes the semantic skill model in Planning Domain Definition Language (PDDL) [4]. An example can be seen in Figure 2, with the resultant encoding of the skill in PDDL shown in Listing 1. However, the movement waypoints must be transformed into the most suitable reference frame to ensure skill adaptability across different environments. For instance, the waypoints of a *pick* skill should be described in the object reference frame to ensure a correct execution regardless of the object's initial position. The relevant reference frame for a skill is chosen between the entities being part of the two sets of predicates activated or deactivated by the skill. The choice is driven

---

[1] The authors are with Politecnico di Milano, Dipartimento di Elettronica, Informazione e Bioingegneria, Piazza L. Da Vinci 32, 20133, Milano, Italy. email: {`isacco.zappa, andreamaria.zanchettin, paolo.rocco`}`@polimi.it`

Listing 1: PDDL encoding of the demonstrated skill.

```
(:action skill_0
 :parameters (
 ?c1 ?c2 ?c3 - cube  ?g - gripper
 )
 :precondition (and
 (is_held_by ?c1 ?g) (is_close_to ?c2 ?c3)
 )
 :effect (and
 (is_gripper_open ?g) (is_on_top ?c1 ?c2)
 (is_on_top ?c1 ?c3) (not (is_held_by ?c1 ?g))
 )
)
```

by a decision tree that inputs the sets and outputs the most suitable object reference frame to describe the waypoints.

Semantic Programming by Demonstration allows the operator to teach the basic modular skills required for the task in a no-coding fashion. Then, after the goal is specified, a symbolic planner can use the PDDL skill models to compute and execute the sequence of skills that allows the robot to accomplish the task.

III. TEACHING SKILLS IN A MULTI-AGENT SCENARIO

A single robotic manipulator may not be appropriate for some tasks due to its limited workspace and intrinsic limitations. Indeed, it is expected to find multi-robot systems in factories when a production speed-up or robots with different capabilities are needed. Moreover, some tasks, such as screwing the cap of a bottle or lifting a tray from two handles, cannot be tackled by a single manipulator. Dual-arm robotic manipulators brought significant innovation to the field of industrial robotics. By emulating the human structure and coordinated movements, this type of robot shows a higher level of dexterity and adaptability to a broader range of skills. Dual-arm robots have gathered the interest of a niche in the industry, where high productivity in complex tasks is required, with precision and speed [5].

We focus on enabling a Multi-Agent (MA) system, such as a dual-arm robot, to learn the semantics of skills taught by demonstration. The challenges to be tackled are manifold. The basic formulation of PDDL is not appropriate for MA planning. Indeed, it is possible to define the entities in the scene to account for both the robot arms. However, the planner would still generate a sequential plan without actions scheduled in parallel, thus not exploiting the advantages of a dual-arm robot coordinated motion and task execution speed-up. Moreover, the robots must be provided with an understanding of space constraints and skills synergies to avoid unfeasible plans to be computed by the planner, such as in the examples depicted in Figure 3.

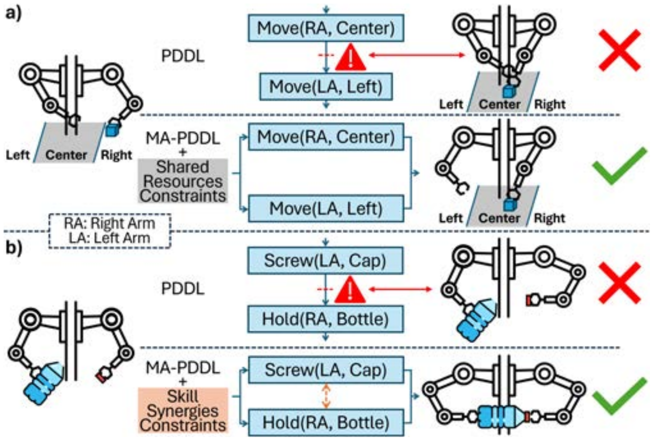

Fig. 3: Comparison between the baseline and the methodology extended to multi-agent system: a) scenario with shared resources and b) requirement of action synergies (i.e. close a bottle).

We address these issues by replacing the formalism employed to describe the skill semantics with MA-PDDL [6] and integrate a planning pipeline that can generate plans comprising of actions scheduled in parallel [7]. Then, we manually divide the workspace into areas and define movement skills that regulate the robots' access to them. The rules are implemented by including the availability of the target area in the skill preconditions. This way, the planner always schedules one robot at a time to act on shared portions of the workspace. Finally, we detect and encode concurrency constraints in the skills preconditions by checking during the demonstration which robots are concurrently modifying the environment. Therefore, the planner is constrained to schedule the synergetic skills in parallel.

We tested our framework on a dual-arm YuMi robot from ABB, asking ten candidates with limited robotic expertise to teach the skills required for a Tower of Hanoi task variant involving shared areas and coordinated motions. Results show that first-time users can effectively teach by demonstration the skills required to solve the task and that the parallel planning pipeline ensures an execution speed-up while accounting for the space constraints. The multi-agent extension guidelines, with their implementation on both hand-guiding teaching on a dual-arm robot and Virtual Reality teaching, and the experimental results are further outlined in a video available online[1].

REFERENCES

[1] A. Billard, S. Calinon, R. Dillmann, and S. Schaal, "Robot programming by demonstration," in *Springer handbook of robotics*. Springer, 2008, pp. 1371–1394.

[2] E. Tulving *et al.*, "Episodic and semantic memory," *Organization of memory*, vol. 1, no. 381-403, p. 1, 1972.

[3] A. M. Zanchettin, "Symbolic representation of what robots are taught in one demonstration," *Robotics and Autonomous Systems*, vol. 166, p. 104452, 2023.

[4] P. Haslum, N. Lipovetzky, D. Magazzeni, C. Muise, R. Brachman, F. Rossi, and P. Stone, *An introduction to the planning domain definition language*. Springer, 2019, vol. 13.

[5] C. Smith, Y. Karayiannidis, L. Nalpantidis, X. Gratal, P. Qi, D. V. Dimarogonas, and D. Kragic, "Dual arm manipulation—a survey," *Robotics and Autonomous systems*, vol. 60, no. 10, pp. 1340–1353, 2012.

[6] D. L. Kovács, "A multi-agent extension of pddl3. 1," 2012.

[7] D. Furelos-Blanco and A. Jonsson, "Solving multiagent planning problems with concurrent conditional effects," in *Proceedings of the AAAI Conference on Artificial Intelligence*, vol. 33, no. 01, 2019.

---

[1] `https://youtu.be/lDsZwaEpCjk`

Human Augmentation:
Controlling Supernumerary Robotic Limbs via Body Redundancy

Nicole D'Aurizio[1], Tommaso Lisini Baldi[1], and Domenico Prattichizzo[1]

***Abstract*—Supernumerary robotic limbs (SRLs) can restore lost motor functions and enhance human sensorimotor capabilities. An essential challenge is formulating intuitive augmentation policies for controlling SRLs without impeding natural limb functionality.**

This work introduces an innovative strategy utilizing the redundancy of the human kinematic chain for commanding SRLs having one degree of freedom. This concept is summarized in the definition of the Intrinsic Kinematic Null Space (IKNS). The newly developed procedure encompasses a real-time analysis of body motion and a subsequent computation of the control signal for SRLs based on the IKNS for single-arm tasks. What sets our approach apart is its explicit emphasis on incorporating user-specific biomechanical and physiological characteristics and constraints. This ensures an efficient and intuitive approach to commanding SRLs, tailored to the individual user's needs.

I. INTRODUCTION

Supernumerary robotic limbs (SRLs) offer the possibility to augment human capabilities in terms of perception and manipulation abilities [1], [2], allowing individuals to perform complex sensorimotor tasks by coordinating biological and artificial limbs. Differently from prostheses and exoskeletons, which are designed to empower human natural movements, SRLs represent additional degrees of freedom (DoFs) that need to be controlled independently from and simultaneously with biological limbs.

The cutting-edge component to implement the idea of augmentation is the design of wearable sensorimotor interfaces. From a broad perspective, these interfaces are meant for establishing a bidirectional connection between the human sensorimotor system and the robot's system of actuators and sensors. Through this connection, reciprocal awareness, trustworthiness, and mutual understanding are intended to be achieved, enhancing the overall integration between the user and the SRLs. For instance, by capturing signals from human body motion or muscle activation, sensorimotor interfaces can leverage the redundancy of the human sensorimotor system to map commands for the robot limbs.

Our work presents a novel methodology to extract a signal from the human kinematic redundancy for enabling the simultaneous control of natural and artificial limbs during task execution. By kinematic redundancy we refer to body motions that do not affect the action of the biological hands.

II. INTRINSIC KINEMATIC NULL SPACE

Considering a task to be accomplished and the kinematic space of the whole body, we can make a distinction between two types of null space:

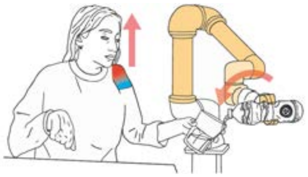

Fig. 1: An impaired subject exploiting the redundancy of the arm involved in the task to control the robotic extra-limb, while simultaneously holding the glass.

Extrinsic Kinematic Null Space (EKNS) that refers to velocities of joints which are not involved in such a task;

Intrinsic Kinematic Null Space (IKNS) that refers to velocities of joints directly employed in the task.

Taking advantage of movements in the IKNS lets the user operate a device using body parts already involved in the task, without compromising the use of free limbs which instead may be involved in further parallel tasks (see Fig. 1).

In this work, we focused our attention on exploiting motions in the IKNS in the specific use case of controlling a SRL while performing single-arm tasks, since we identified them as critical for impaired people and the most paradigmatic for presenting this innovative approach. We developed a user-centred, data-driven, systematic procedure to identify the IKNS. An overview of the method is shown in the block scheme depicted in Fig. 2a, while a through description is available in [3].

III. EXPERIMENTAL VALIDATION

Ten subjects per experiment participated in the experimental campaign. A flow diagram of the experimental procedure is in Fig. 2b.

Exp. 1*: Is it possible to use the IKNS to command an extra degree of freedom to execute dual tasks?*
Participants were asked to seat and move their upper limb to control the position and the radius of a virtual sphere. The goal was to overlap two spheres: one controlled by the user, and one considered the target. Two different conditions were tested. While in both conditions the radius was changed by exploiting the IKNS, in the first condition the position of the target was fixed while in the second condition the user had also to align with the position of the target by moving the hand. Results revealed that using the IKNS to control an additional degree of freedom in a dual task did not affect the performance of the primary task.

Exp. 2*: How is the user control ability affected by practice considering the difficulty of the task?*
Each user was asked to use their hand position to directly control the position of a cursor and match a target placed in one of the nine spatial positions around the rest position, which was a sphere located in front of their right shoulder. Targets were

---

[1] are with the Department of Information Engineering and Mathematics, University of Siena, Siena, Italy, and with the Department of Humanoids and Human Centered Mechatronics, Istituto Italiano di Tecnologia, Genova, Italy.

The research leading to these results has received funding from the European Union's Horizon Europe programme under grant agreement No. 101070292, project "HARIA- Human-Robot Sensorimotor Augmentation".

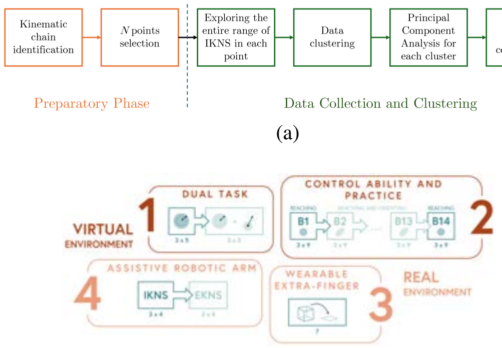

(a)

(b)

Fig. 2: In a) a flowchart reporting the phases for computing the control signal. In b) a flow diagram of the experimental procedure.

spherical or prolate spheroids. Users were asked to control simultaneously cursor position and orientation, exploiting the IKNS-based control signal to adjust the latter. The experiment was designed as a sequence of 14 blocks. Each block was made of 3 cycles, in each of which the user was asked to match 9 targets, that is, one per spatial position, for a total of 27 targets per block. In the first and the last blocks (B1 and B14) users were asked to control only the cursor position to establish a baseline for the users' control ability. Task performance was evaluated considering four metrics: *i)* reaching success rate, computed as the percentage of reached targets in the block, *ii)* holding success rate, computed as the percentage of targets held for at least 1 s in the block, *iii)* holding time, computed as the maximum time the cursor held the target matched within 10 s, and *iv)* angular error, computed as the difference between cursor and target orientation when the cursor position was within the spatial tolerance. An information theory-based approach based on [4] was adopted to devise a model of the participants' motor behaviour.

On average both success rates increased with block progression. Mean reaching success rate went from 50 ± 35% in B2 to 66 ± 32% in B13, while mean holding success rate started from 27 ± 31% in B2, and reached 37 ± 33% in B13. Mean holding time raised from 0.71 ± 0.50 s in B2 to 0.99 ± 0.44 s in B13. Mean angular error went from 10.28 ± 3.63 deg in B2 to 7.47 ± 3.43 deg in B13. No significant differences were found between B1 and B14 as regards reaching and holding success rates, while a statistically significant increase of 0.86 s in holding time was observed. These outcomes indicate not only that practice positively influenced users' control ability, but also a large inter-individual variability in task performance. As last measure of performance obtained from the Fitts' Law, we considered the throughput, which is defined as the ratio between the index of difficulty of the task and the movement time. The mean throughput across participants went from 0.81 ± 0.07 bit/s in B2 to 0.94 ± 0.11 bit/s in B13, confirming that participants improved their speed-accuracy trade-off with practice.

Exp. 3*: Is the IKNS-based control easy to learn for controlling a wearable extra-finger to accomplish common activities of daily living requiring simultaneous tasks?*
Subjects were asked to perform a repetitive pick-and-place task. They wore a robotic extra-finger on the right forearm and controlled the position of the opening/closing mechanism with the same arm using the IKNS to move a Rubik's Cube. The number of successfully reached target positions was used to estimate the learning curve describing the average improvement in performance. 8 users over 10 reached a speed of 30 pick-and-place motions in 3 minutes. On average, after 7 trials participants reached the plateau, meaning that asking them to perform further tasks would have led to limited improvement since their learning capacity was reduced. The slope of the learning curve demonstrates that with few trials users were able to take advantage of the IKNS-based control for accomplishing dual tasks with a wearable SRL.

Exp. 4*: How does user performance in accomplishing common activities of daily living that involve simultaneous tasks differ when using the IKNS-based control compared to an EKNS-based control?*
Participants were instructed to use a grounded supernumerary robotic arm to pour a glass of water. They were given two tasks to complete simultaneously: holding the glass under the bottle, and precisely controlling the robot to pour exactly 30 g of water. Subjects were asked to repeat the task under two experimental conditions, that is controlling the velocity of the joint using once the IKNS-based control signal extracted from the same arm holding the glass, and once using the EKNS-based control signal extracted from the dorsiflexion of their right foot. The deviation from the desired water quantity and the completion time were used as evaluation metrics. The mean difference of 1.51 g between using the IKNS-based control signal as opposed to using the EKNS-based control signal was not statistically significant, while there was a statistically significant time reduction of 2.91 s when commanding the robot with the EKNS approach.

IV. CONCLUSION

We developed and novel approach to control extra DoFs exploiting the human body kinematic redundancy and demonstrated the feasibility in controlling SRLs. Such an approach can be applied to more sophisticated assistive or augmentative robotic devices (as extra limbs/arm wearable or not) in everyday life situations, for both healthy and impaired people. The proposed method may be used, for instance, by impaired (including several impaired) patients to compensate for their disability using the same limb (the healthy one) both to accomplish a task and for controlling a robot in a cooperative way. In future studies we will evaluate the cognitive load needed for using such approach that might me too high for a frail person.

REFERENCES

[1] J. Eden *et al.*, "Principles of human movement augmentation and the challenges in making it a reality," *Nature Communications*, vol. 13, no. 1, p. 1345, 2022.
[2] D. Prattichizzo *et al.*, "Human augmentation by wearable supernumerary robotic limbs: review and perspectives," *Progress in Biomedical Engineering*, vol. 3, no. 4, p. 042005, 2021.
[3] T. Lisini Baldi *et al.*, "Exploiting body redundancy to control supernumerary robotic limbs in human augmentation," *The International Journal of Robotics Research*, 2024.
[4] P. M. Fitts, "The information capacity of the human motor system in controlling the amplitude of movement." *Journal of experimental psychology*, vol. 47, no. 6, p. 381, 1954.

Enabling Physical Interaction in the Metaverse through the Avatarm

B. Brogi[1], G. Cortigiani[1], N. D'Aurizio[1,2], A. Villani[1], D. Prattichizzo[1,2], T. Lisini Baldi[1,2]

Abstract— **The Metaverse is an immersive shared space that remote users can access through virtual and augmented reality interfaces, enabling their avatars to interact with each other and the surrounding. While digital objects can be manipulated, physical objects cannot be touched, grasped, or moved within the Metaverse due to the absence of appropriate interfaces. This work proposes a solution to overcome this limitation by introducing the "Physical Metaverse", a shared environment populated by "Avatarms": avatars equipped with robotic arms capable of performing physical manipulative tasks. These robotic arms remain hidden from the user's view through diminished reality techniques, enabling users to tangibly perceive the manipulated objects and gain a heightened sense of situational awareness.**

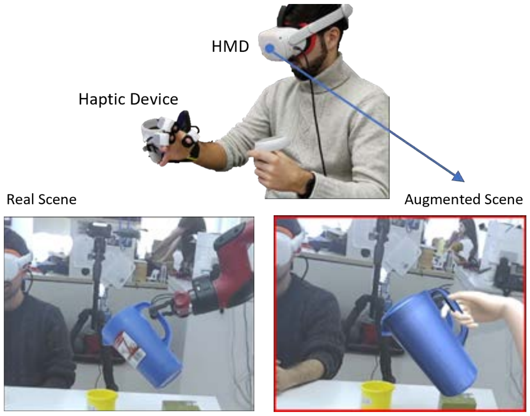

Fig. 1: Avatar representative scenario. On the left, the scene captured by the real camera; on the right, the scene as seen by the Avatar user.

I. INTRODUCTION

Human-robot collaboration has become very popular with the advent of domestic and assistive robotics, and it is interesting to note that digital environments gives the possibility to realize interfaces with the aim of helping people. Among various ways to utilize auxiliary robotics for wellness of persons, the metaverse offers captivating opportunities. The virtual spaces of the metaverse consist of computer-designed environments and digital twins of real objects and are populated by avatars, the graphical counterparts of the users. However, the key feature that is currently missing is the physical interaction with real remote objects. To overcome this limitation, this work presents the concept of a Physical Metaverse which will be enabled by a new interface enhancing the virtual avatar with manipulation capabilities that we will call the Avatarm.

II. AVATARM AND PHYSICAL METAVERSE

The Avatarm consists of a digital avatar augmented by a robotic arm that performs physical manipulation tasks while remaining entirely hidden in the metaverse. In this way, the users have the illusion that the avatar is directly manipulating objects without the mediation of a robot (Fig. 1). Moreover, the scenario represented in Fig. 2 will be instrumental in explaining the framework of the Physical Metaverse. Consider two people, Alice and Brad, having a conversation in the metaverse, sharing an augmented version of Alice's kitchen. They sit at the kitchen table, having tea from a distance. Alice's kitchen is equipped with a camera and a remotely controlled robotic arm, allowing Brad to interact with objects on the table. Both Alice and Brad view this shared environment through their head-mounted displays (HMDs). Alice's view is from a camera on her HMD, while Brad's view is from an additional camera in front of the table.

When Brad wants to pour tea or pass a biscuit, he uses his virtual hand to grasp the digital twin of the object. Simultaneously, the robotic arm manipulates the real object. Brad's virtual hand is controlled by his movements, and the robotic arm provides real-time feedback on its position and force through a wearable haptic interface. Furthermore, Brad receives haptic feedback when the robot approaches kinematic singularities. This feature is essential for giving Brad awareness of the space the robot can reach, as he cannot see it.

In the following sections, we will describe the main components of the Avatarm working framework: *i)* robot concealment, *ii)* robot motion control, *iii)* Avatarm hand with haptic feedback, and *iv)* situational awareness. The interestd reader is referred to [1] for technical details of the overall building blocks.

Robot Concealment

Differently from existing vision-based solutions, we propose a technique to determine the region to be removed using the robot's CAD model, which moves according to its kinematics. In the proposed framework, the real-time cancellation of the robotic arm is achieved through an ad-hoc virtual environment.

A digital camera in the virtual environment records the CAD model while it moves in front of a black panel. A region-based segmentation and binarization algorithm processes the frames from the virtual camera to estimate the pixels containing portions of the robot generating a binary mask. The image frames acquired by the real camera are projected onto a virtual panel. This panel is overlapped by a second virtual panel, which streams frames that are a combination of a background image (acquired before placing the robot) and the binary mask previously computed. Due to this panel overlapping, the robotic arm becomes transparent in the resulting frames by replacing the pixels within the mask with portions of the background image. The result is finally rendered in the user's HMD.

Robot Motion Control

To ensure realistic interaction, we implemented a closed-loop strategy to compute the joint velocities of the robot, considering the pose of the real object. Specifically, the pose of the center-of-mass of the object digital twin is used as reference for the

---

The research leading to these results has received funding from the European Union's Horizon Europe programme under grant agreement No. 101070292 of the project "HARIA - Human-Robot Sensorimotor Augmentation".

[1] are with the Department of Information Engineering and Mathematics, University of Siena, Italy. {surname}@diism.unisi.it

[2] are with the department of Humanoids and Human Centered Mechatronics, Istituto Italiano di Tecnologia, Genova, Italy.

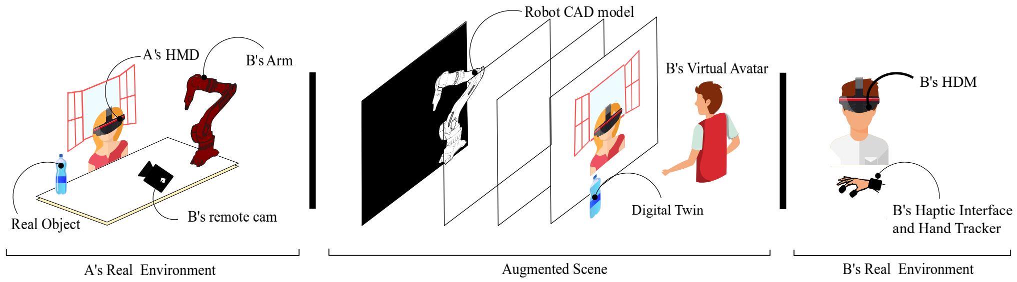

Fig. 2: Physical Metaverse framework. User (B) acts as the Avatar of the scene and can manipulate real objects in the remote environment of user (A) using the robot, which remains hidden from view inside the HMD.

pose of the end-effector, computing the manipulator's motion online based on user inputs.

Avatarm Hand

To prevent users from seeing the virtual hand penetrate objects during interaction, we superimposed a second virtual hand onto the avatar's original hand. This solution allows the user to command the gripper to close more than the object's size, ensuring it applies the necessary force to grasp the object while maintaining consistency in the virtual environment. Additionally, the squeezing forces were mapped from force sensors on the gripper to the user's fingertips using the backward mapping procedure described in [2] with a wearable haptic interface.

Situation Awareness

Since the robot is hidden from view in the Physical Metaverse, the user controlling the Avatar is unaware of the boundaries of the manipulator's reachable workspace. This means the user might try to move an object to a point the robot cannot reach, potentially causing system malfunctions. To address this, we informed the user of the distance to singular configurations through a vibrotactile signal provided via a haptic interface. To compute the manipulator's distance from singular configurations, we exploited the robot manipulability measure.

III. EXPERIMENTAL EVALUATION

To assess the feasibility of the Avatarm, three different experiments were designed. The first two experiments evaluated the capabilities of the algorithms for robot motion control and concealment, and for force feedback, respectively. The third experiment investigated the psychological sense of presence, co-presence, and social presence provided by the Avatarm.

The first experiment demonstrated that the gripper's positioning error was sufficiently small to perform daily activities effectively, such as pouring water or offering a glass. The average error in positioning the end-effector was less than $1.5\,\mathrm{cm}$, with minimal average misalignment between the desired and actual orientation (less than 1° on each axis). Regarding the concealment method, for each trial of the experiment, we recorded two videos simultaneously: one of the real environment (i.e., before hiding the robot) and one of the environment with the robot concealed. The analysis of the recorded videos revealed that the algorithm successfully removed $95.3\% \pm 3\%$ of the manipulator on average.

The second experiment simulated an interaction with a fragile object to assess the importance of haptic feedback. The haptic cue drastically reduced the occurrence of failures (i.e., object falls or breaks) and minimized the contact force impulse during pick-and-place tasks. Out of 100 pick-and-place trials (50 with haptic feedback and 50 without), participants achieved a statistically higher success rate when haptic feedback was provided ($62.0\% \pm 39.4\%$) compared to controlling the Avatarm without haptic feedback ($34.0\% \pm 25.0\%$).

Finally, the third experiment evaluated the effectiveness of the Avatarm in enhancing the sense of presence, co-presence, and social presence. The goal was to cooperate with a partner to stack up to nine cups of decreasing diameter, aiming to outperform other teams[1]. The experienced psychological sense of presence, co-presence, and social presence were used as metrics for evaluating the soundness of our framework. After the first three trials and at the end of the experiment (i.e., once for each role), team members were asked to complete an online survey to gather information on their experience. When using the Avatarm, participants took control of the task, giving them both the responsibility and the ability to determine the experimental outcome. This likely fostered a greater sense of cooperation, as their actions were more interdependent with those of their companion.

IV. CONCLUSIONS

This work introduces a novel framework for physical collaboration within the metaverse, built upon the Avatarm, an advanced avatar capable of interacting with physical objects. This framework creates a new form of extended remote physical environment shared among multiple users, which we term the 'Physical Metaverse'. However, experiments have revealed limitations in the framework. Rendering the scene in 2D diminishes the immersive experience, and the lack of three-dimensionality is a significant drawback. Additionally, the system uses a static background and does not account for dynamic changes in the environment, which is a crucial area for future improvement. Despite these challenges, continued development of the Avatarm holds the potential to revolutionize the XR experience, redefining how we interact with and perceive our surroundings in the metaverse by making it more tangible and physical.

REFERENCES

[1] B. Brogi *et al.*, "The avatarm: Interacting in the physical metaverse via robotics, diminished reality, and haptics," *IEEE Access*, vol. 12, pp. 90 750–90 767, 2024.

[2] G. Salvietti *et al.*, "Multicontact bilateral telemanipulation with kinematic asymmetries," *IEEE/ASME Transactions on Mechatronics*, vol. 22, no. 1, pp. 445–456, 2016.

---

[1] A video of the experiment is publicly available at `https://youtu.be/sO0WCDnuCjo`

Robust Optimal Planning of Human-Robot Collaborative Operations

Amir Jaberi, Seyed Mohsen Hosseini, Oliver Kutz, and Angelika Peer
Faculty of Engineering, Free University of Bozen-Bolzano, 39100, Bolzano, Italy

Abstract— **This study develops a robust optimization model for task planning of human-robot collaborative operations. Our primary objective is to minimize the total completion time of the tasks while taking into account feasibility and operational constraints. The proposed model provides robustness against the uncertainty of human behavior, while allowing the problem to remain deterministic and linear in nature. The level of conservativeness can be adjusted to provide a trade-off between optimality and robustness, such that over-conservatism is avoided in different operational scenarios. The performance and advantages of the model are discussed to highlight its capability to achieve an effective task plan, manage uncertainties, and fulfill constraints in a human-robot collaborative environment.**

I. INTRODUCTION

Human-Robot Collaboration (HRC) within industrial settings necessitates efficient planning and scheduling between humans and robots. This is crucial because factors such as safety concerns and human fatigue can cause execution times to exceed the nominal forecast times in the planning phase. By addressing these potential deviations, HRC systems can enhance overall performance and maintain operational reliability [1].

From this perspective, many HRC systems have developed planning approaches to identify feasible plans within predefined and dynamic constraints and rules. However, these sequences are not necessarily optimized for minimizing total completion time or other performance criteria. [2].

Most recent efforts focus on developing task planners to create feasible sequences that meet temporal and spatial constraints, and optimizing scheduling among human and robot. For example, the study in [3] proposed a dynamic optimization approach for HRC systems in collaborative manufacturing, minimizing execution time and considering safety criteria. They employed a timeline-based planning approach for scheduling. The work in [4] used Behavior Trees for adaptive task planning, and [5] introduced a Petri-Nets-based planning engine to minimize idle time in collaborative assembly.

This study contributes to optimal task planning in HRC systems by developing a robust optimization approach, addressing the challenges posed by task complexity and unpredictable human behavior.

II. THE PROPOSED ROBUST TASK PLANNING OPTIMIZATION APPROACH

We develop a robust optimization approach for HRC task planning. The details of the approach are provided in this section.

A. The Problem Definition

We consider a problem including several tasks to be completed collaboratively by human and robot in some sequences, such as assembling or disassembling a product in an industrial line. The objective is to minimize the total completion time of all operations performed by both human and a robot. Our approach considers constraints such as task precedence of operations, the possibility of assigning specific tasks to only humans or robot for particular operations, and the need to avoid overlapping assignments for tasks.

B. The Nominal Task Planning Optimization Approach

The optimization problem when all parameters are defined and referred to as *the nominal optimization problem*, can be formulated as follows:

$$\begin{aligned}
\text{minimize} \quad & \sum_{i=1}^{N}(p_i^H \cdot x_i^H + p_i^R \cdot x_i^R) \\
\text{subject to} \quad & x_i^H + x_i^R = 1, \quad \forall i && (1)\\
& x_i^H = 1, \quad \forall i \in H && (2)\\
& x_i^R = 1, \quad \forall i \in R && (3)\\
& t_i^c = t_i^s + p_i^H \cdot x_i^H + p_i^R \cdot x_i^R, \quad \forall i && (4)\\
& t_j^s \geq t_i^c \cdot S_{ij}, \quad \forall i, j && (5)\\
& x_i^H, x_i^R \in \{0, 1\}, \quad \forall i && (6)\\
& t_i^s \geq 0, \quad \forall i && (7)\\
& t_i^c \geq 0, \quad \forall i && (8)
\end{aligned}$$

where x_i^H and x_i^R are binary decision variables indicating if task i is assigned to the human or the robot, N is the total number of tasks or planning horizon, and t_i^s and t_i^c represent the start and completion times of task i. The parameters p_i^H and p_i^R are the processing times of task i by the human and the robot, respectively. S_{ik} is a binary variable indicating if task i precedes task k, and H and R are sets of tasks that can only be performed by humans and robots, respectively. The constraints ensure that each task is completed by either the human or the robot ($x_i^H + x_i^R = 1$), enforce the human-only ($x_i^H = 1$ for $i \in H$) and robot-only ($x_i^R = 1$ for $i \in R$) task assignments, and define the relationship between start and completion times ($t_i^c = t_i^s + p_i^H \cdot x_i^H + p_i^R \cdot x_i^R$). The non-overlapping constraint ($t_j^s \geq t_i^c$) ensures that tasks assigned to the same resource do not overlap in time, while the precedence constraint ($t_k^s \geq t_i^c \cdot S_{ik}$) ensures that tasks follow the required order. Finally, the non-negativity constraints ($t_i^s \geq 0$ and $t_i^c \geq 0$) ensure valid start and completion times.

C. The Robust Counterpart of the Problem

The nominal optimization problem defined in Section (II-B) aims to minimize the task completion time without taking into account the uncertainties of human behavior, such as the fact that a human worker might not perform the task exactly within the forecast time. This can provide solutions that are not only far from optimality but can be also infeasible in some cases because constraints, in particular the task precedence constraints in Eq. (5), can be easily violated. In order to tackle this, we developed a robust counterpart to the nominal problem based on the method developed by Bertsimas and Sim in [6].

Let p_i^H represent the nominal processing time for task i when performed by a human, and let the uncertain processing time be $\tilde{p}_i^H$, which can vary within $[p_i^H - \Delta p_i^H, p_i^H + \Delta p_i^H]$.

First, to properly use the method in [6], without loss of generality, we assume that the objective function is not subject to uncertainty and uncertainty only affects the constraints. To this aim, we introduce an auxiliary variable Z and define $Z \geq \sum_{i=1}^{N}(p_i^H \cdot x_i^H + p_i^R \cdot x_i^R)$ as a constraint and we change the optimization problem to minimize Z. In addition, in order to avoid nonlinearity in the problem, we need to transform the nonlinear precedence constraint $t_{s_j} \geq t_i^c \cdot S_{ij}$ (which with substituting t_i^c will be in a quadratic form) to a linear form. For this, we introduce a large constant M (big-M method) to enforce these constraints linearly. Let δ_{ij} be a binary variable that is 1 if task i precedes task j and 0 otherwise. This allows us to write the precedence constraint linearly as $t_j^s \geq t_i^s - M(1 - \delta_{ij})$. If $\delta_{ij} = 1$, this constraint reduces to $t_j^s \geq t_i^c$. If $\delta_{ij} = 0$, the constraint is not active because M is a sufficiently large number.

Thus, the robust counterpart of the nominal problem is formulated as follows:

$$\begin{aligned}
&\text{minimize} \quad Z \\
&\text{subject to (1)-(4), (6)-(8), and} \\
&Z \geq \sum_{i=1}^{N} \left(p_i^H \cdot x_i^H + p_i^R \cdot x_i^R\right) \\
&\qquad + \max_{\substack{S\cup\{t\} \\ S\subseteq J, |S| = \lfloor\Gamma\rfloor \\ t \in J\setminus S}} \sum_{i\in S} \Delta p_i^H \cdot x_i^H, \\
&t_j^s \geq t_i^c - M(1-\delta_{ij}) \\
&\qquad + \max_{\substack{S\cup\{t\} \\ S\subseteq J, |S| = \lfloor\Gamma\rfloor \\ t \in J\setminus S}} \sum_{i\in S} \Delta p_i^H \cdot x_i^H, \quad \forall i, j,
\end{aligned}$$

where Γ is a non-negative parameter called *the budget of uncertainty*, which ranges from $[0 \;\; N]$, indicating the number of parameters allowed to deviate from their forecast values. The two max terms in the constraints are *protection functions* that protect the constraint from being violated due to uncertainty.

This robust counterpart has an equivalent mixed-integer linear programming (MILP) formulation as follows [6]:

$$\begin{aligned}
&\text{minimize} \quad Z \\
&\text{subject to (1)-(4), (6)-(8), and} \\
&Z \geq \sum_{i=1}^{N} \left(p_i^H \cdot x_i^H + p_i^R \cdot x_i^R\right) + z_1 \cdot \Gamma + \sum_{i\in J} d_i, \\
&t_j^s \geq t_i^c - M(1-\delta_{ij}) + z_2 \cdot \Gamma + \sum_{i\in J} g_i, \quad \forall i, j, \\
&\quad z_1 + d_i \geq \Delta p_i^H \cdot y_i, \quad \forall i, j \in J, \\
&\quad -y_i \leq x_i \leq y_i, \quad \forall i, \\
&\quad l_i \leq x_i \leq u_i, \quad \forall i, \\
&\quad d_i \geq 0, \quad \forall i \in J, \\
&\quad y_i \geq 0, z_i \geq 0, \quad \forall i.
\end{aligned}$$

where z_1, z_2, d_i, g_i, and y_i are supporting variables for dual problem of the robust counterpart, l_i and u_i are lower and upper bounds that can be defined for each decision variable.

III. DISCUSSION AND CONCLUSION

A robust model was developed to optimize HRC task planning by minimizing completion times while satisfying constraints such as task precedence, the assignment of specific tasks to human and robot, and task overlapping avoidance. This deterministic robust approach handles uncertainties flexibly by adjusting the budget of uncertainty (Γ), and can balance optimality and robustness without heavily penalizing the objective function or constraints. The conservativeness of the solution is adjustable. For example, when $\Gamma = 0$, the model corresponds to the nominal optimization problem, and provides the lowest completion time but overly optimistic results (assumes no uncertainty). Conversely, when $\Gamma = N$, the model fully addresses uncertainty, giving the most conservative solution by considering the worst-case scenario for all uncertain parameters. However, by adjusting Γ within the range $[0, N]$, decision-makers can balance robustness and conservativeness, finding a tradeoff between time saving and constraint violation rates.

The model remains in MILP form which is manageable with commercial optimizers, making it applicable to industrial settings such as assembly and disassembly lines.

REFERENCES

[1] S. Pellegrinelli *et al.*, “Motion planning and scheduling for human and industrial-robot collaboration,” *CIRP Annals*, vol. 66, no. 1, pp. 1–4, 2017.

[2] M. Faroni *et al.*, “A layered control approach to human-aware task and motion planning for human-robot collaboration,” in *IEEE Int. Conference (RO-MAN)*, pp. 1204–1210, Aug 2020.

[3] M. Faroni *et al.*, “Optimal task and motion planning and execution for multiagent systems in dynamic environments,” *IEEE Trans. Cybern.*, vol. 54, pp. 3366–3377, June 2024.

[4] G. Kokotinis *et al.*, “A behavior trees-based architecture towards operation planning in hybrid manufacturing,” *Int. J. Comput. Integr. Manuf.*, vol. 37, pp. 1–26, 2023.

[5] A. Casalino *et al.*, “Optimal scheduling of human–robot collaborative assembly operations with time petri nets,” *IEEE Trans. Autom. Sci. Eng.*, vol. 18, pp. 70–84, Jan 2021.

[6] D. Bertsimas and M. Sim, “The price of robustness,” *Oper. Res.*, vol. 52, pp. 35–53, 2004.

Session 3A: Control theory

A comparison of indirect and direct filter designs from data for LTI systems: the effect of unknown noise covariance matrices

M. Mazzoleni *, **L. Maurelli** *, **S. Formentin** **, **F.Previdi** *

* *Department of Management, Information and Production engineering*
University of Bergamo, via Marconi 5, 24044 Dalmine (BG), Italy.
** *Dipartimento di Elettronica, Informazione e Biongegneria,*
Politecnico di Milano, via G. Ponzio 34/5, 20133 Milano, Italy

---

1. INTRODUCTION

Consider a discrete-time SISO LTI stochastic system:

$$\mathcal{S}\colon\quad \begin{aligned} \boldsymbol{x}_{k+1} &= \mathbf{A}\boldsymbol{x}_k + \mathbf{B}u_k + \boldsymbol{w}_k, && \text{(1a)}\\ y_k &= \mathbf{C}\boldsymbol{x}_k + \mathbf{D}u_k + v_k, && \text{(1b)}\\ \boldsymbol{z}_k &= \mathbf{F}\boldsymbol{x}_k + \mathbf{G}u_k, && \text{(1c)} \end{aligned}$$

Let WN denote a white noise stochastic process, with $\mathbf{A}, \mathbf{B}, \mathbf{C}, \mathbf{D}, \mathbf{F}, \mathbf{G}$ the system matrices with proper dimensions. The noises $\boldsymbol{w}_k \sim \text{WN}\left(\mathbf{0}_{n_x}, \mathbf{Q}\right), v_k \sim \text{WN}\left(0, R\right)$, with $\mathbf{Q} \in \mathbb{R}^{n_x \times n_x}, \mathbf{Q} \succeq 0$, and $R \in \mathbb{R}_{>0}$, are independent so that $\boldsymbol{w}_k \perp v_k \perp \boldsymbol{x}_0$. The notation $\mathbf{0}_{n_x} \in \mathbb{R}^{n_x}$ denotes the zero vector. The filtering problem for the system (1) consists in providing a possibly optimal estimate $\hat{\boldsymbol{z}}_k$ of $\boldsymbol{z}_k$ given a set of past measurements $\{u_\tau, y_\tau\}_{\tau=1}^{k}$ with $\tau \leq k$. When the system is not completely known, a two-steps rationale, that we denote as *model-based (indirect) filtering*, is commonly employed using a Kalman filter $\mathcal{K}(\hat{\mathcal{S}})$ for $\mathcal{S}$. The filtering performance of $\mathcal{K}(\hat{\mathcal{S}})$ degrades rapidly when the model $\hat{\mathcal{S}}$ is not well representative of the system $\mathcal{S}$ in (1), especially regarding the noise covariance matrices $\mathbf{Q}$ and R that often are *manually set.*

An alternative paradigm, denoted as *direct (data-driven) filtering*, has been studied in a parametric set membership (Milanese et al., 2010; Ruiz et al., 2010) and stochastic (Novara et al., 2012) frameworks. In this rationale, the aim is to directly identify a filter $\hat{\mathcal{D}}$ from data. To this end, consider noisy measurements $\boldsymbol{\ell}_k$ of $\boldsymbol{z}_k$ as

$$\boldsymbol{\ell}_k = \boldsymbol{z}_k + \boldsymbol{e}_k = \mathbf{F}\boldsymbol{x}_k + \mathbf{G}u_k + \boldsymbol{e}_k, \tag{2}$$

where $\boldsymbol{e}_k \sim \text{WN}\left(\mathbf{0}_{n_z}, \mathbf{\Sigma}\right)$ and $\mathbf{\Sigma} \in \mathbb{R}^{n_z \times n_z}, \mathbf{\Sigma} \succeq 0$ $\boldsymbol{e}_k \perp (\boldsymbol{w}_k, v_k, \boldsymbol{x}_0)$. Given a dataset of N observations $\{u_k, y_k, \boldsymbol{\ell}_k\}_{k=1}^{N}$, the direct data-driven design of filters for system (1) is a system identification problem where the inputs of the filter model are (u_k, y_k) and the output is $\boldsymbol{\ell}_k$. Notice that in the direct framework the *noise covariance matrices are implicitly learnt from data.* So, this work focuses on a comparison between the indirect and direct data-driven designs of full state filters for stochastic SISO LTI systems (1), studying the effect of noise covariance estimates on the state filtering.

2. PROBLEM STATEMENT

We start defining a set of assumptions common to both model-based and direct data-driven filter design rationales.

Assumption 1. (System order). The order n_x of (1) is known. In filtering applications, the user has often a physical knowledge of the system states, so this assumption is less critical than in identification problems.

Assumption 2. (Measured data). A set of N observations $\mathscr{D} \coloneqq \{u_\tau, y_\tau, \boldsymbol{\ell}_\tau\}_{\tau=1}^{N}$ has been collected from (1)-(2).

Assumption 3. (Observability). $(\mathbf{C}, \mathbf{A})$ is observable.

Under Assumptions 1-3, the problem of filter design for system (1) can be stated as follows.

Problem 1. (Full state filter design). Consider the case $\mathbf{F} = I_{n_x}$, $\mathbf{G} = 0$, so that $\boldsymbol{z}_k = \boldsymbol{x}_k$ and so $n_z = n_x$. Design a causal LTI filter using measurements in $\mathscr{D}$ that, given $\{u_\tau, y_\tau\}_{\tau=1}^{k}$, $\tau \leq k$, gives an estimate $\hat{\boldsymbol{z}}_k$ of $\boldsymbol{z}_k$.

3. INDIRECT FILTER DESIGN

Unbiased estimates of $(\hat{\mathbf{A}}, \hat{\mathbf{B}})$ are obtained in a least squares sense starting from a multi-targets regression relying on an instrumental variable $\boldsymbol{\xi}_k \coloneqq \left[\boldsymbol{\ell}_{k-1}^\top \; u_k\right]^\top \in \mathbb{R}^{n_x+1}$ so that

$$[\hat{\mathbf{A}}, \hat{\mathbf{B}}] = \left(\sum_{k=2}^{N} \boldsymbol{\ell}_{k+1}\, \boldsymbol{\xi}_k^\top\right) \cdot \left(\sum_{k=2}^{N} \boldsymbol{\varphi}_k\, \boldsymbol{\xi}_k^\top\right)^{-1}. \tag{3}$$

Unbiased estimates of $(\hat{\mathbf{C}}, \hat{\mathbf{D}})$ can be obtained in a least squares sense similarly to (3) as

$$[\hat{\mathbf{C}}, \hat{\mathbf{D}}] = \left(\sum_{k=2}^{N} y_k\, \boldsymbol{\xi}_k^\top\right) \cdot \left(\sum_{k=2}^{N} \boldsymbol{\varphi}_k\, \boldsymbol{\xi}_k^\top\right)^{-1}. \tag{4}$$

3.1 Estimation of $\mathbf{Q}$ *and* R

In this work we employ a specific one-step correlation approach known as the Autocovariance Least-Square (ALS) method for estimating the covariance matrices.

4. DIRECT FILTER DESIGN

The identification problem can be solved resorting to a PEM formulation

$$\widehat{\boldsymbol{\theta}}_{\text{D}} = \arg\min_{\boldsymbol{\theta}_{\text{D}}} \frac{1}{N} \sum_{k=1}^{N} \left\| \boldsymbol{\ell}_k - \widehat{\boldsymbol{\ell}}_{k|k-1}(\boldsymbol{\theta}_{\text{D}}) \right\|_2^2 \tag{5}$$

where $\widehat{\boldsymbol{\ell}}_{k|k-1}$ is the one-step prediction from model $\mathcal{D}(\boldsymbol{\theta}_{\text{D}})$.

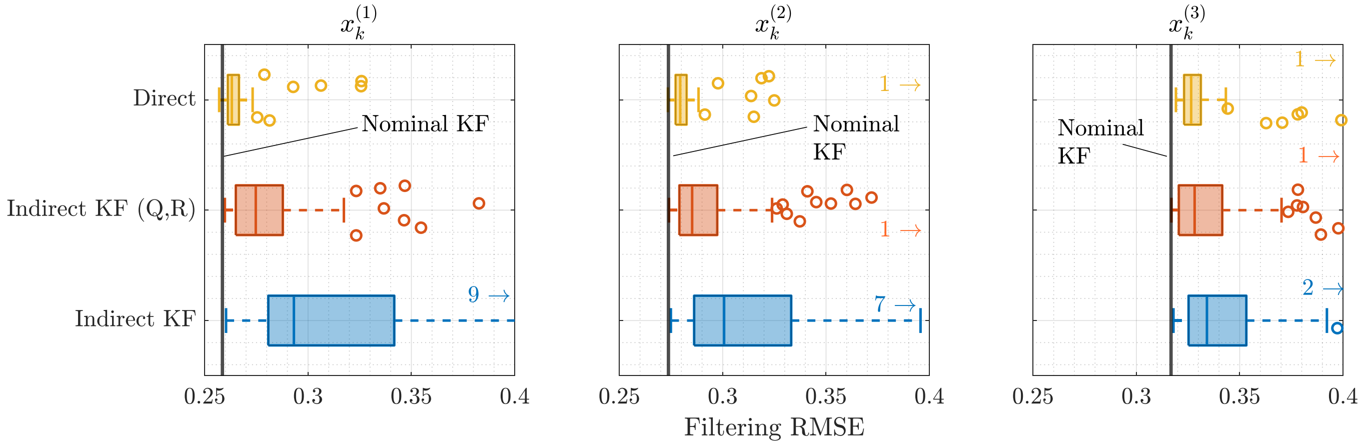

Fig. 1. Filtering root mean square error of the four approaches (the lower, the better). Each plot represents the filtering error of a single state of system (8). The vertical black line denotes the performance of the **Nominal KF** approach. The numbers close the plot border denote the number of outliers.

Assume that the system (1) is completely known. In this case, the Kalman filter recursions provide the best linear unbiased estimator, with minimum variance of the state prediction error. The steady-state expression of this optimal state filter is used to choose the structure of the data-driven filter.

The model $\mathcal{D}(\boldsymbol{\theta}_{\mathrm{D}})$ for the data-driven filter must be parametrized with both exogenous and noise models:

$$\boldsymbol{\ell}_k = G_u(z;\boldsymbol{\theta}_{\mathrm{D}})u_k + G_y(z;\boldsymbol{\theta}_{\mathrm{D}})y_k + H(z;\boldsymbol{\theta}_{\mathrm{D}})\rho_k \qquad (6)$$

where ρ_k is a white noise process and $G_u(z;\boldsymbol{\theta}_{\mathrm{D}}), G_u(z;\boldsymbol{\theta}_{\mathrm{D}})$, $H(z;\boldsymbol{\theta}_{\mathrm{D}}) \neq \mathbf{1}_{n_x}$ are $n_x \times 1$ transfer matrices that represent the parameterized models for the exogenous inputs u_k, y_k and noise ρ_k, respectively.

The state estimates provided by the direct data-driven approach can be computed by a *simulation* of the identified direct filter $\hat{\mathcal{D}}$ as

$$\hat{\boldsymbol{z}}_k^{\mathrm{D}} = G_u(z;\widehat{\boldsymbol{\theta}}_{\mathrm{D}})u_k + G_y(z;\widehat{\boldsymbol{\theta}}_{\mathrm{D}})y_k. \qquad (7)$$

5. NUMERICAL RESULTS

Consider a system (1) of order $n_x = 3$ sampled at $T_s = 0.01\,\mathrm{s}$ and measurements (2) with

$$\mathbf{A} = \begin{bmatrix} 0.610 & 0.084 & -0.536 \\ -0.139 & 0.270 & 0.763 \\ 0.124 & 0.279 & -0.245 \end{bmatrix}, \quad \mathbf{B} = \begin{bmatrix} -0.558 \\ -0.028 \\ -1.476 \end{bmatrix}, \qquad (8)$$
$$\mathbf{C} = [0.259\ \ -2.018\ \ 0.199], \quad \mathbf{D} = 0, \quad R = 1,$$
$$\mathbf{Q} = \mathrm{diag}\,(0.025, 0.05, 0.1), \quad \mathbf{\Sigma} = \mathrm{diag}\,(0.067, 0.1, 0.2),$$

where diag(·) indicates a diagonal matrix. We simulate $N = 1000$ data $\{y_k, \boldsymbol{\ell}_k\}$ from (8) using a white noise input $u_k \sim \mathrm{WN}(0,1)$. We compare the following four approaches:

1. **Nominal KF**: a Kalman Filter with all system $(\mathbf{A}, \mathbf{B}, \mathbf{C}, \mathbf{D})$ and covariance matrices $(\mathbf{Q}, R)$ *known*. This is the best possible linear filtering approach for systems of type (1).
2. **Indirect KF (Q,R)**: a Kalman Filter employing estimates of the system matrices (3) and (4), but with *known* covariance matrices $\mathbf{Q}, R$.
3. **Indirect KF**: a Kalman Filter employing estimates of the system matrices (3) and (4), and estimates of covariance matrices. This is the *typical situation in practical scenarios.*
4. **Direct filter**: a direct filter of a proper order and structure (6) is identified from the data.

We run $M_C = 100$ Monte-Carlo simulations, varying the realization of the noises $\boldsymbol{w}_k, v_k, \boldsymbol{e}_k$ at each run. For each run, the designed filters are evaluated on a test dataset (fixed for each simulation) of $N_{\text{test}} = 1000$ data generated with a white noise input $u_k^{\text{test}} \sim \mathrm{WN}(0,1)$. The test dataset is different from the identification one, both regarding the input and the realizations of the noises affecting the test data. Regarding the **Direct filter** approach, we choose a MIMO Box-Jenkins model structure, with 2 inputs (the input u_k and the output y_k of the system) and 3 outputs (the states measurements $\boldsymbol{\ell}_k$). The orders n_b, n_f, n_c, n_d are fixed for all the three outputs of the direct filter model. In particular, we set $n_b = n_f = n_c = n_d = n_x$. The adequacy of these setting is evaluated on the test dataset by residual correlation analysis of the one-step prediction error $\boldsymbol{\ell}_k - \widehat{\boldsymbol{\ell}}_{k|k-1}(\hat{\boldsymbol{\theta}}_{\mathrm{D}})$ of the direct filter model.

Figure 1 shows a comparison of the filtering performance of the four approaches, on the test dataset. The **Direct Filter** is superior to both the **Indirect KF (Q,R)** and **Indirect KF** approaches, as it *directly* (and implicitly) *optimizes for the unknown covariance and system matrices.* On the other side, the **Indirect KF (Q,R)** is sensitive to the estimation uncertainty of system matrices, and the **Indirect KF** approach is sensitive to the uncertainty in both system and noise covariance matrices.

REFERENCES

Milanese, M., Ruiz, F., and Taragna, M. (2010). Direct data-driven filter design for uncertain lti systems with bounded noise. *Automatica*, 46(11), 1773–1784. doi:10.1016/j.automatica.2010.07.006.

Novara, C., Milanese, M., Bitar, E., and Poolla, K. (2012). The filter design from data (fd2) problem: parametric-statistical approach. *International Journal of Robust and Nonlinear Control*, 22(16), 1853–1872. doi:10.1002/rnc.1791.

Ruiz, F., Novara, C., and Milanese, M. (2010). Direct design from data of optimal filters for lpv systems. *Systems & Control Letters*, 59(1), 1–8. doi:10.1016/j.sysconle.2009.10.008.

Anti-Windup-Like Compensator Design for Continuous-Time Systems affected by Unknown Nonlinearities and Input Saturation

Folco Giorgetti, Francesco Ferrante, and Mario L. Fravolini

***Abstract*— This paper addresses the stabilization of a particular class of continuous-time systems affected by unknown sector bound nonlinearities and input saturation. An observer is designed to provide an estimate of the unknown nonlinearity. Such an estimate is used by an additional compensation loop with the purpose of mitigating the effect of the nonlinearity and enlarge the basin of attraction of the system. Stability conditions are given as a set of matrix inequalities and quadratic Lyapunov functions are exploited. An optimal compensator design algorithm based on semidefinite programming is proposed.**

I. INTRODUCTION

A. Motivation and background

Most of real life systems are affected by nonlinear dynamics that characterize different phenomena such as saturation, backlash, friction, or hysteresis in actuators or sensors. For this reason, the study of systems affected by nonlinearities is of particular interest in the field of automatic control [5], [6]. A widely used strategy to mitigate the effects of nonlinearities like input saturation is to use anti-windup loops. This technique works by modifying the control signal to compensate for the effects of the input saturation on the controller, improving the performance and stability margins of the system. In the past years, this topic has been studied by many researchers, see [11], [10], [4], [7] and [8] just to mention a few. In this work, we focus our attention on a specific class of systems affected by an unknown sector bound nonlinearity and input saturation expressed by:

$$\begin{aligned} \dot{x}_p &= A_p x_p + G_p \phi(L_p x_p) + B_p \operatorname{sat}(u) \\ y_c &= C_p x_p \end{aligned} \tag{1}$$

where $x_p \in \mathbb{R}^{n_p}$ and $u \in \mathbb{R}^m$, are the state and input and $y_c \in \mathbb{R}^{n_c}$ is the measured output used for feedback control and sat indicates the standard symmetric decentralized nonlinearity with saturation levels $u_{01}, u_{02}, \ldots, u_{0i}$. Matrices A_p, B_p, G_p, C_p and L_p are real of appropriate dimensions and are assumed to be known. The nonlinearity $\phi : \mathbb{R}^b \to \mathbb{R}^b$ is unknown and it is assumed that its components are continuous and contained in a cone-bounded sector characterized by a symmetric positive definite matrix $\Omega \in \mathbb{R}^{n_c \times n_c}$. Namely

$$\phi^T(w)\Lambda(\phi - \Omega w) \leq 0, \quad \forall w \in \mathbb{R}^b, \phi(0) = 0; \tag{2}$$

where matrix $\Lambda \in \mathbb{R}^{n_c \times n_c}$ is any positive diagonal matrix. Our objective is to design an anti-windup-like compensator to mitigate the effect of the unknown state-dependent nonlinearity, using a strategy similar to that in [1]. The control and stabilization of similar systems is tackled in [2] through the synthesis of nonlinear state feedback controllers. In [2], the authors assume the nonlinearity and the state of the system to be known. In our case, however, the nonlinearity and the state are unknown. To deal with this problem, we use an observer that provides an estimate of the state and nonlinearity, based on the constructions in [3]. The estimate of the nonlinearity is used by an additional compensation loop with the objective of maximizing the estimate of the basin of attraction of the closed-loop system. For that purpose quadratic Lyapunov functions are exploited. The stability analysis is based on the application to our case of the sector conditions proposed in [2].

Notation: The symbols $\mathbb{R}$, $\mathbb{R}^n, \mathbb{R}^{n \times n}$ represent, respectively, the set of the real numbers, the n-dimensional Euclidean space, and the set of $n \times n$ real matrices. For a square matrix A, we use the notation $\operatorname{He}(A) = A + A^T$ and $\operatorname{trace}(A)$ is the trace of the matrix A. Symbol $*$ stands for a symmetric block in a symmetric matrix. The notation A_i stands for the $i-th$ row of matrix A. Given a symmetric matrix A, $A < 0$ ($A > 0$) means that A is negative (positive) definite.

II. PROBLEM SETTING AND KEY RESULTS

The system (1) is controlled by the following output feedback dynamic controller

$$\dot{x}_c = A_c x_c + B_c y_c, \quad u = C_c x_c + D_c y_c + v \tag{3}$$

where A_c, B_c, C_c, D_c are given and $v \in \mathbb{R}^{n_c}$ is an additional signal specifically designed to mitigate the effect of the unknown nonlinearity. Inspired by the work of [9] and [1] the signal v is chosen as $v := E\hat{\phi}$ where $\hat{\phi}$ is an estimate of ϕ that is provided by an estimator. We also assume to have an additional measured output $y = H_p x_p + D_p \phi(L_p x_p)$ used for the estimator design.

A. Outline of the proposed estimator

The observer is constructed based on a Luenberger-like structure and it is defined as follows:

$$\begin{aligned} \dot{\xi} &= A_l \xi + B_p \operatorname{sat}(u) + G_p y_m + F(y_l - \hat{y}_l) \\ \hat{y}_l &= H_l \xi \\ \hat{\phi} &= D^+ y - D^+ H_p \xi = y_m - H_m \xi \end{aligned} \tag{4}$$

where $A_l = A_p - B_p D^+ C_p$, D^+ is a left inverse matrix of D_p and $D^\perp$ is any full row rank matrix such that $D^\perp D_p = 0$, and $D^+ D_P = I_m$, $\begin{bmatrix} H_m \\ H_l \end{bmatrix} = U H_p$, $\begin{bmatrix} y_m \\ y_l \end{bmatrix} = U y$ where

---

The authors are with Department of Engineering, University of Perugia, 06125 Perugia, Italy
`folco.giorgetti@dottorandi.unipg.it`,
`{francesco.ferrante, mario.fravolini}@unipg.it`

$U = \begin{bmatrix} D^{+} \\ D^{\perp} \end{bmatrix}$. Defining the error $z = x_p - \xi$ and its dynamic the overall closed loop system is written as:

$$\begin{aligned} \dot{x} &= A_{cl}x + B_{cl}\psi(u) + G_{cl}\phi(L_p x_p) \\ \dot{z} &= (A_l - F_l H_l)z \\ u &= Kx + E(\phi(L_p x_p) + D^{+}Hz) \end{aligned} \tag{5}$$

where:

$$x := \begin{bmatrix} x_p \\ x_c \end{bmatrix}, B_{cl} := \begin{bmatrix} B_p \\ 0 \end{bmatrix}, G_{cl} := \begin{bmatrix} G_p \\ 0 \end{bmatrix}$$

$$K := [D_c C_p \quad Cc], A_{cl} := \begin{bmatrix} A_p + B_p D_c C_p & B_p C_c \\ B_c C_p & A_c \end{bmatrix}.$$

and $\psi(u) := \mathrm{sat}(u) - u \quad \forall u \in \mathbb{R}^m$. The problem we study in this work can be formalized as follows

Problem 1: Determine a compensator gain E, and an observer gain F and a region $S_0 \subset \mathbb{R}^{n \times n}$, (where $n := n_c + n_p + n_z$), as large as possible, such that the origin of the closed-loop system is asymptotically stable and S_0 is included in the basin of attraction of the origin.

B. Stability Analysis

Proposition 1: If there exist two symmetric positive definite matrices $W \in \mathbb{R}^{(n_c+n_p)\times(n_c+n_p)}$ and $Q \in \mathbb{R}^{n_c \times n_c}$, two positive diagonal matrices $\Delta \in \mathbb{R}^{n_c \times n_c}$ and $S \in \mathbb{R}^{m \times m}$ and matrices $X \in \mathbb{R}^{m \times n_c}$, $Z \in \mathbb{R}^{m \times (n_c+n_p)}$, $J_2 \in \mathbb{R}^{m \times n_c}$ and $E \in \mathbb{R}^{m \times m}$ satisfying

$$\begin{bmatrix} H_e(WA_{cl}^T) & B_{cl}ED^{+}H_p & N_{1,3} & B_{cl}S - WK^T - Z^T \\ * & H_e(A_l^T Q - H_l^T X) & 0 & H_p^T N^{+T} E^T + J_2^T \\ * & * & -2\Delta & -\Delta E^T \\ * & * & * & -2S \end{bmatrix} < 0 \tag{6}$$

where $N_{1,3} = B_{cl}E\Delta + G_{cl}\Delta + WL_{cl}^T\Omega$, and

$$\begin{bmatrix} W & 0 & Z_i^T \\ * & Q & J_{2i}^T \\ * & * & u_{0i}^2 \end{bmatrix} \geq 0, \; i = 1, \ldots, m \tag{7}$$

then, defining $P := W^{-1}$, the gains E, and F and the ellipsoid

$$\mathcal{E}(P, Q) = \left\{ (x, z) \in \mathbb{R}^n, \begin{bmatrix} x \\ z \end{bmatrix}^T \begin{bmatrix} P & 0 \\ 0 & Q \end{bmatrix} \begin{bmatrix} x \\ z \end{bmatrix} \leq 1 \right\}$$

are a solution to Problem 1.

Condition (6) is a bilinear matrix inequality (BMI). Therefore, directly exploiting such a condition is hard from a numerical standpoint. To overcome this drawback, next we propose set of sufficient LMI conditions that solve the Problem 1.

Proposition 2: If there exist three symmetric positive definite matrices $W \in \mathbb{R}^{n \times n}$, $P_2 \in \mathbb{R}^{n_c \times n_c}$ and $\overline{Q} \in \mathbb{R}^{n_c \times n_c}$, two positive diagonal matrices $\Delta \in \mathbb{R}^{n_c \times n_c}$ and $S \in \mathbb{R}^{m \times m}$ and matrices $M \in \mathbb{R}^{m \times p}$, $Z \in \mathbb{R}^{m \times n}$ and $\Sigma \in \mathbb{R}^{m \times m}$ satisfying

$$\begin{bmatrix} \mathrm{He}(WA_{cl}^{\top}) & B_{cl}\Sigma + G_{cl}\Delta + WL_{cl}^T\Omega & B_{cl}S - WK^T - Z^T & B_{cl}\Sigma \\ * & -2\Delta & -\Sigma^T & 0 \\ * & * & -2S & -\Sigma \\ * & * & * & -\overline{Q} \end{bmatrix} < 0 \tag{8}$$

and

$$\begin{bmatrix} W & Z_i^T \\ * & u_{0i}^2 \end{bmatrix} \geq 0, \; i = 1, \ldots, m \tag{9}$$

$$\begin{aligned} &He(M^T P_2) + \gamma I < 0 \\ &R^T \Delta^{-1} \overline{Q} \Delta^{-1} R - \gamma I < 0 \end{aligned} \tag{10}$$

where $R := D^{+}H_l$ and $M = A_l - FH_l$. Then: the gains E, and F and the ellipsoid

$$\mathcal{E}(P_1, P_2) := \left\{ (x, z) \in \mathbb{R}^n, \begin{bmatrix} x \\ z \end{bmatrix}^T \begin{bmatrix} P_1 & 0 \\ 0 & P_2 \end{bmatrix} \begin{bmatrix} x \\ z \end{bmatrix} \leq 1 \right\}$$

with $P_1 := W^{-1}$ are a solution to Problem 1

C. Optimal compensator design

To maximize the size of the basin of attraction of the closed loop-system we define an optimization problem subject to the following constraints

$$\begin{bmatrix} M_W & I_n \\ I_n & W \end{bmatrix} > 0, \; M_W = M_W^T > 0 \tag{11}$$

$$\Delta \geq c^{-1} I_p \tag{12}$$

$$\overline{Q} - \alpha I_p \leq 0. \tag{13}$$

A suboptimal solution to Problem 1 is obtained using the following two steps algorithm.

Algorithm 1

1. Solve

$$\min_{W,\Sigma,\Delta,P_2,S,\overline{Q},Z,M_W,\alpha} \mathrm{trace}(M_W) + \alpha \tag{14}$$

subject to LMIs: (8), (9), (11), (12), (13).
2. Using the matrix Q computed in step 1, solve:

$$\min_{M,P_2} \mathrm{trace}(P_2) \tag{15}$$

subject to (10).

REFERENCES

[1] S. Alsamadi, F. Ferrante, and S. Tarbouriech. Anti-windup-like compensator synthesis for discrete-time quantized control systems. In *Procedings of the 10th IFAC Symposium on Robust Control Design*, pages 43–48, 2022.

[2] E. B. Castelan, S. Tarbouriech, and I. Queinnec. Control design for a class of nonlinear continuous-time systems. *Automatica*, 44(8):2034–2039, 2008.

[3] M. Di Loreto and D. Eberard. Strong left inversion of linear systems and input reconstruction. *IEEE Transactions on Automatic Control*, 2022.

[4] S. Galeani, S. Tarbouriech, M. Turner, and L. Zaccarian. A tutorial on modern anti-windup design. *European Journal of Control*, 15(3-4):418–440, 2009.

[5] H. K. Khalil. *Control of nonlinear systems*. Prentice Hall, New York, NY, 2002.

[6] P. Kokotović and M. Arcak. Constructive nonlinear control: a historical perspective. *Automatica*, 37(5):637–662, 2001.

[7] J. Sofrony and M. Turner. Anti-windup design for systems with input quantization. In *Proceedings of the 54th IEEE Conference on Decision and Control*, pages 7586–7591, 2015.

[8] S. Tarbouriech, G. Garcia, J. M. G. da Silva Jr, and I. Queinnec. *Stability and stabilization of linear systems with saturating actuators*. 2011.

[9] S. Tarbouriech, C. Prieur, and J.M.G. da Silva. Stability analysis and stabilization of systems presenting nested saturations. *IEEE Transactions on Automatic Control*, 51(8):1364–1371, 2006.

[10] S. Tarbouriech, I. Queinnec, and C. Prieur. Nonstandard use of anti-windup loop for systems with input backlash. *IFAC Journal of Systems and Control*, 6:33–42, 2018.

[11] L. Zaccarian and A. R. Teel. *Modern anti-windup synthesis: control augmentation for actuator saturation*, volume 38. 2011.

Design and Stability of Dynamical Memory Networks: From Hopfield to Firing Rate Models

Simone Betteti, Giacomo Baggio, and Sandro Zampieri

I. DYNAMICAL SYSTEMS FOR MEMORY RETRIEVAL

The second half of the twentieth century marked a pioneering era in the characterization of brain functions through the use of dynamical models. This effort began with the abstraction by McCulloch and Pitts of a neuron as a computational unit [1], followed by the groundbreaking description by Hodgkin and Huxley of the neuron biochemical response [2]. Since then, characterizing neuronal properties through dynamical systems has become increasingly pervasive.

In the early 1980s, Hopfield's seminal work [3], [4] introduced the concept of attractor networks—dynamical systems of computational units (neurons) that encode specific patterns (memories) as equilibria of the system dynamics. These attractor networks are governed by the dynamics:

$$\dot{x} = -x + \mathcal{F}(x, W), \tag{1}$$

where $x \in \mathbb{R}^N$ denotes the activity of the neurons in the network, $W \in \mathbb{R}^{N\times N}$ is the symmetric synaptic matrix defining how the neurons in the network interact, and $\mathcal{F}\colon \mathbb{R}^N \to \mathbb{R}^N$ is a (nonlinear) synaptic field. The two main types of attractor networks are Hopfield networks and firing rate networks, in which the synaptic field $\mathcal{F}(\cdot)$ is described via a (typically nonlinear) activation function $\Phi\colon \mathbb{R}^N \to [a,b]^N$. In most cases, such activation function is taken to be diagonal, i.e. such that $\Phi_i(x) = \phi(x_i)$ for all $i = 1,\dots,N$ and $x \in \mathbb{R}^N$. The Hopfield and firing rate networks differ in terms of the choice and order of application of the activation function.

Hopfield networks are classically defined by the autonomous dynamics

$$\dot{x} = -x + W\Phi(x), \tag{H}$$

where the non-linearity is odd, non-decreasing and with asymptotic values $a = -1$ and $b = 1$. The specific choice of the activation function, as well as a biologically plausible construction of the synaptic matrix W, has allowed for an extensive analytical investigation of the retrieval properties and storage capacity of the model [6]. In particular, memory retrieval in these networks has been examined by applying LaSalle invariance principle to the "energy" function

$$E_{\mathrm{H}}(x) = -\frac{1}{2}\Phi(x)^\top W\Phi(x) + \sum_{i=1}^{N}\int_0^{\phi(x_i)} \phi^{-1}(s)\ \mathrm{d}s. \tag{2}$$

Despite its pioneering role in modeling memory dynamics, the Hopfield model lacks a clear biological interpretation, as it represents neurons as binary ± 1 states akin to spin magnets. The firing rate model of neural activity addresses exactly this issue, through the adoption of an activation function that is non-decreasing and with asymptotic values $a = 0$ (neuronal inactivation) and $b = 1$ (neural activation), and the following dynamics

$$\dot{x} = -x + \Phi(Wx). \tag{FR}$$

An important feature of the firing rate model (FR) is that it preserves positivity of trajectories; more precisely, it can be shown that the set $[0,1]^N$ is forward invariant for (FR).

Despite its biological relevance, a thorough study of the properties of the model (FR) seems to be missing. To the best of our knowledge, the design of the synaptic matrix W for assigning desired memories as equilibria of (FR) has been addressed only for a restrictive choice of model parameters in [5, Sec. 7.4]. Given the significance of the firing rate model in representing neural activities during memory retrieval, we present an in-depth and extensive treatment on the design of the synaptic matrix of (FR) to store prescribed memories and analyze the stability properties of such memories.

II. DESIGN OF THE SYNAPTIC MATRIX

In firing rate networks, memories are represented as vectors encoding the distributed activity of neurons. Let $N \in \mathbb{N}$ be the number of units in the network. We require that at each memory retrieval exactly qN, for $q \in (0,1)$, neurons are active, while all the others are inactive. The prototypical memory patterns, representing the vectors with the ideal neuronal activation during retrieval, are of the form $\xi^\mu \in \{0,1\}^N$, $\mu = 1,\dots,P$, and satisfy the following constraints

$$\begin{aligned} \mathbb{1}^\top \xi^\mu &= qN \quad \mu = 1,\dots,P \\ {\xi^\nu}^\top \xi^\mu &= q^2 N \quad \nu = 1,\dots,P, \ \ \nu \neq \mu. \end{aligned}$$

which are satisfied in expectation for memories with i.i.d. entries satisfying $\mathbb{P}[\xi_i^\mu = 1] = q$. Once the prototypical memory patterns are given, it is necessary to fix a diagonal activation function $\Phi(\cdot)$ (e.g. a sigmoid, a rectified tanh) and the values $x_0, x_1 \in \mathbb{R}$, with $x_0 < x_1$, representing the membrane voltages at neural inactivation and activation, respectively. When these two ingredients are given, we determine the average activation rates $y_0 = \phi(x_0)$ and $y_1 = \phi(x_1)$

The authors are with the Department of Information Engineering of the University of Padova. E-mails: `{bettetisim,baggio,zampi}@dei.unipd.it`

and define the synaptic map

$$\mathcal{W}\colon \{0,1\}^{N\times P} \to \mathbb{R}^{N\times N} \tag{3}$$
$$\{\xi^{\mu}\}_{\mu=1}^{P} \mapsto \frac{1}{q(1-q)\alpha N}\sum_{\mu=1}^{P}(\xi^{\mu}-q\mathbb{1})(\xi^{\mu}-q\mathbb{1})^{\top}+\frac{1}{\gamma N}\mathbb{1}\mathbb{1}^{\top},$$

where α, $\gamma \in \mathbb{R}$ are defined as

$$\alpha := \frac{y_1 - y_0}{x_1 - x_0}, \tag{4a}$$
$$\gamma := \frac{qy_1 + (1-q)y_0}{qx_1 + (1-q)x_0}. \tag{4b}$$

From a geometrical viewpoint, the parameter $\alpha > 0$ is the slope of the straight line intersecting the activation function at the coordinates x_0, x_1, while the parameter $\gamma \in \mathbb{R}$ is the slope of the line passing through the origin and intersecting the line $\alpha(x - x_0) + y_0$ at the coordinate $x_q = qx_1 + (1-q)x_0$.

Finally, we define the retrievable memories as $\bar{\xi}^{\mu} = \mathcal{E}(\xi^{\mu}) = (y_1 - y_0)\xi^{\mu} + y_0\mathbb{1}$, $\mu = 1, \dots, P$, which correspond to the vectors of activations that the firing rate network can actually retrieve. The following result shows how to map prototypical memory vectors to equilibria of the firing rate dynamics via a synaptic matrix of the form (3).

Theorem 1: (Assignment of memories through W). Consider the set of prototypical memory vectors $\{\xi^{\mu}\}_{\mu=1}^{P}$. If $W = \mathcal{W}(\xi^1, \dots \xi^P)$, then the vectors $\{\bar{\xi}^{\mu}\}_{\mu=1}^{P}$, with $\bar{\xi}^{\mu} = \mathcal{E}(\xi^{\mu})$, are equilibria of (FR).

III. STABILITY OF MEMORIES

Assigning a set of prototypical memories as equilibria is not enough for (FR) to function as a memory network; we also need these memories to be (locally) attractive points for the dynamics. To this end, we present a condition for the local asymptotic stability of retrievable memories and then expand on the topic by presenting a suitable "energy" function ensuring global convergence to equilibria.

Theorem 2: (Local stability of memories). Consider the set of prototypical memory vectors $\{\xi^{\mu}\}_{\mu=1}^{P}$, let W be as in Theorem 1, and define $\eta := \max\{\phi'(x_0), \phi'(x_1)\}$. If

$$\eta \max\{\alpha^{-1}, \gamma^{-1}\} < 1 \tag{5}$$

then the equilibria $\{\bar{\xi}^{\mu}\}_{\mu=1}^{P}$ of (FR), with $\bar{\xi}^{\mu} = \mathcal{E}(\xi^{\mu})$, are locally asymptotically stable.

It is worth pointing out that when $\gamma < 0$, i.e. when the system receives a global synaptic inhibition, the local stability condition (5) simplifies to

$$\eta < \alpha. \tag{6}$$

Similarly to the Hopfield model, it is possible to analyze the global behavior of trajectories of (FR) by means of a suitable "energy" function, namely

$$E_{\text{FR}}(x) = -\frac{1}{2}x^{\top}Wx + \sum_{i=1}^{N}\int_{0}^{x_i}\phi^{-1}(s)\ \mathrm{d}s. \tag{7}$$

It is easy to observe that (7) coincides with the energy of the Hopfield model (2) under the change of variable $y = \Phi(x)$. The following result, whose proof is based on LaSalle invariance principle, establishes that for any initial condition the trajectories of (FR) always converge to an equilibrium point (potentially a desired memory).

Theorem 3: (Global convergence to equilibria). Consider the function $E_{\text{FR}}(\cdot)$ in (7), a synaptic matrix W as in Theorem 1, and assume that $\phi(\cdot)$ is non-decreasing and differentiable. Then $\dot{E}_{\text{FR}} \leq 0$ along the flow of (FR) and the trajectories of (FR) converge to an equilibrium point of (FR).

In Fig. 1 we plot the energy function E_{FR} over the region of state space between two memories as γ varies. More precisely, we let $x_1, x_2 \in [0,1]$ be interpolation parameters and define the vector having components $v_i^{x_1,x_2} = \min\{1, x_1\xi_i^{\mu_1} + x_2\xi_i^{\mu_2}\}$, where ξ^{μ_1} and ξ^{μ_2} are two randomly chosen prototypical memories. Fig. 1 shows the energy over the mesh $\{v^{x_1,x_2} : \ x_1, x_2 \in [0,1]\}$ for $\gamma < 0$ and $\gamma > 0$ and a fixed sigmoidal activation function.

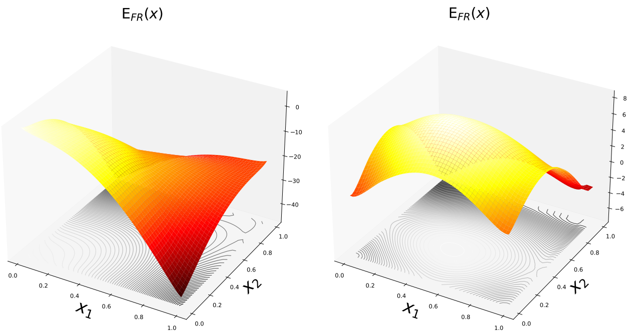

(a) $\gamma < 0$ (b) $\gamma > 0$

Fig. 1. Profile of the energy function (7) along two randomly chosen prototypical memories and two values of γ with opposite sign.

As observable from the figure, the case with $\gamma < 0$ favours attractiveness towards memories and repulsion from spurious attractors of the form $x = \zeta\mathbb{1}$, $\zeta \in \mathbb{R}$ (corresponding to the critical point close to the origin in Fig. 1). Conversely, when $\gamma > 0$, the basin of attraction of the memories is smaller and the spurious attractors gain stability. This numerical evidence seems to support the fact that global inhibition (encoded in the parameter γ) is crucial for the correct retrieval of memories in the brain.

REFERENCES

[1] W. McCulloch and W. Pitts, "A Logical Calculus of Ideas Immanent in Nervous Activity", *Bulletin of Mathematical Biophysics*, 1943.

[2] A. L. Hodgkin and A. F. Huxley, "A quantitative description of membrane current and its application to conduction and excitation in nerve", *The Journal of Physiology*, 1952.

[3] J. J. Hopfield, "Neural networks and physical systems with emergent collective computational abilities", *PNAS*, 1982, vol. 79, pp. 2554-2558.

[4] J. J. Hopfield, "Neurons with graded response have collective computational properties like those of two-state neurons", *PNAS*, 1984, vol. 81, pp. 3088-3092.

[5] L. F. Abbott and P. Dayan, "Theoretical neuroscience: computational and mathematical modeling of neural systems", *MIT press*, 2005.

[6] R. O. McEliece, E. Posner, E. U. Rodemich, and S. A. Venkatesh, "The capacity of the Hopfield associative memory", *IEEE Transactions on Information Theory*. 1987, 33(4), pp. 461-82.

Analysis and control of synaptic complex networks operating at high dimensionality

Arturo Buscarino, Carlo Famoso, Luigi Fortuna

Dipartimento di Ingegneria Elettrica Elettronica e Informatica, University of Catania, 95125 Catania, Italy

I. INTRODUCTION

The nervous systems of leaving beings are the most intricate automatic control systems. They are responsible for functions such as locomotion, coordination, processing, and memory. Neuro-engineering aims at merging artificial intelligence and automatic control engineering with biology, psychology, chemistry, physics, medicine, and other sciences, to understand, reproduce and mimic the abilities of nervous systems, their structure and functions. Central to any nervous system is the spiking neuron, which plays a fundamental role in neuronal dynamics by ensuring efficiency and low-power consumption. Spiking networks model neurons behavior through discrete-event action potentials (spikes), allowing neurons to communicate via brief, rapid, thus low-power, impulses rather than continuous signals. Mathematical models and simple logic rules can efficiently mimic these characteristics, garnering significant scientific interest. The features of spiking signals, characterized by slow–fast dynamics, reflect mechanisms of accumulation and rapid energy release.

Synaptic complex networks refer to the highly interconnected nature of synaptic connections within the brain, enabling a vast range of neural activities and computations. Studying these networks, especially at high dimensionality, allows to understand how they are essential for brain function, underpinning the communication and processing capabilities of neural circuits. They demonstrate robustness to faults and disturbances from the external environment. Analyzing and controlling these networks requires sophisticated approaches due to their complexity. Traditional tools and concepts from experimental computational neuroscience are insufficient, prompting the need for a new paradigm. This paradigm should reconsider spiking neuron models and their interconnection methods, aiming to closely mimic the behavior of biological neural networks.

Moreover, multidimensional analysis necessitates to ensure adequate representation and interpretation. Under this perspective, neural networks working at high dimensionality are more suitable to cope with real-world complexity.

These aspects are currently investigated within the PNRR project FAIR “Future Artificial Intelligence Research”. In particular, the research carried on by the authors of this communication is devoted to a twofold perspective on high dimensionality neural networks. On the one hand, the research aims at rethinking the concept of artificial neural networks for modeling complex dynamics by adopting a novel computational paradigm based on hypercomplex algebra. On the other hand, the possibility to represents higher order neuronal dynamics by recasting nonlinear models of neurons based on ordinary differential equations with matrix differential equations.

The contribution will span these two intercorrelated aspects. In section II we will introduce the evolution of the traditional neural network towards a hyper-complex topology. The concept of Hyper-neuron will be introduced in section III. Section IV will summarize the current results and the future developments.

II. HYPER-COMPLEX NETWORKS

Processing extensive sets of interconnected data represents a crucial field with numerous practical uses, wherein machine learning and deep learning are pivotal through specific types of artificial neural networks (ANNs) like convolutional neural networks (CNNs) and other deep networks. In the past, Multilayer Perceptron (MLP) was a prevalent artificial network architecture; however, its adequacy for processing multidimensional data is limited as it necessitates a high number of parameters. Research indicates that leveraging alternative algebras, like complex numbers and quaternions, can enhance network performance without increasing, in fact reducing, the parameters number.

A quaternion-valued multilayer perceptron (QMLP) is a MLP in which input, output, weights and biases are quaternions, and the activation functions are quaternion-valued [1]. There is an isomorphism between a hypercomplex algebra $\mathbb{H}$ and the vector space $\mathbb{R}^{1+3}$. However, the algorithm for processing quaternions in a hypercomplex neural network differs from the simple vector product in the space $\mathbb{R}^{1+3}$. These computational specifics, tied to the properties of the Hamilton product, underlie the exceptional performance of hypercomplex networks in processing highly correlated datasets. Therefore, starting from a quaternion-valued multilayer perceptron (QMLP), it is necessary to properly develop the basic building blocks of a backpropagation-based algorithm on QNN, including activation functions, and the forward, backward, and update phases. The backpropagation algorithm for QMLPs is dual to the one adopted for classic MLPs. It is important to note that all the parameters are quaternions and that the product between the gradient and the derivative is a component-wise product.

From an application viewpoint, QMLPs leverage the geometric and algebraic properties of hypercomplex numbers, offering potential for modeling three- and four-dimensional data. They find numerous promising applications in pattern recognition, classification, nonlinear filtering, advanced image processing, brain-computer interfaces, time-series prediction, bioinformatics, robotics, and other fields.

The current research has been oriented towards improving the learning capabilities of QNNs by defining an approach based on the parallel training of smaller-sized auxiliary QNNs capable of predicting the outcome of the learning process of a set of internal weights of the main network. This exploits the parallel capabilities of modern processors and microcontrollers, thus paving the way for real-time practical applications [2-3]. Considering the Levenberg-Marquardt learning algorithm and its parallel implementation using auxiliary networks, the number of epochs needed to model the dynamics of a fourth-order chaotic Chua’s circuit can be substantially reduced [4], as shown in Figure 1.

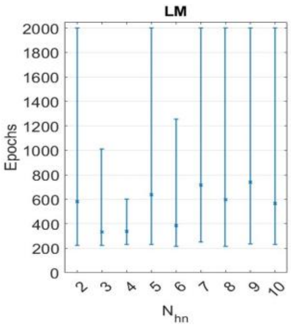

Figure 1 - Epoch comparison. N_{hn} is the number of adopted hidden neurons. Levenberg-Marquardt (left), and Levenberg-Marquardt with auxiliary networks (right).

III. FROM NEURON TO HYPERNEURON

Recent research has introduced the notion of hypersystems, building upon the concept of frequency transformation, which is an efficient method for designing high-order selective filters based on low-pass reference filters. While frequency transformation is suitable for linear systems [5], in the case of nonlinear systems, transformations in the time domain give rise to the concept of hypersystems [6].

Let us consider the dynamics of a generic nonlinear system:

$$\dot{x} = f(x,t)$$

where: $x \in R^{n\times 1}$, $f: R^{n\times 1} \to R^{n\times 1}$ and $t \in R^{+}$.

Let us now consider the dynamics of an hypersystem defined as:

$$\dot{X} = \dot{F}(X,t)$$

where $X \in R^{n\times(N\times N)}$, $F: R^{n\times(N\times N)} \to R^{n\times(N\times N)}$ and $t \in R^{+}$.

Hence, a hypersystem is derived from the scalar dynamics by substituting the state vector with a vector of *n* square matrices, each with dimensions *N*. Additionally, the scalar vector field *f* is replaced by a matrix field *F*. This implies that instead of *n* individual scalar state variables x_i belonging to the set of real numbers, the dynamics of the hypersystem is characterized by *n* square matrices X_i belonging to the set of $N\times N$ real matrices. The dynamical properties of an hypersystem have been shown to be highly correlated to the dynamical properties of the corresponding "*gene*" scalar system.

The formulation of the hyperneuron involves a larger number of initial conditions, compared to the scalar model, on which the dynamics of the system itself depends. Despite this, some models lend themselves very well to hyperdimensional implementation, showing peculiarities that go beyond what is shown in the scalar model. Furthermore, the growing computing power of embedded systems has allowed the implementation of some of these systems directly on microcontroller boards, giving rise to the silicon neuron paradigm. The algorithm to implement the hyperneuron on a microcontroller is essentially based on the Euler discretization, thus obtaining a discrete map.

Recent experimental results, obtained by implementing two hyperneurons starting from the Hindmarsh-Rose and Morris-Lecar models respectively, have demonstrated the validity of the model's hyper-dimensionality paradigm. In both cases it emerged that the hyperneuron, compared to its scalar representation, presents greater robustness with respect to noise or faults, as reported in Figure 2 for the Hindmarsh-Rose model [6], and it is also possible to observe richer dynamics (i.e. chaotic bursting), not observable in the scalar model. These results confirm that the hyperneuron structures are able to mimic behavior related to an increased level of complexity, but without complicating the formulation of the neuron models. Moreover, the intrinsic nature of hyperneurons to be ready for digital implementations make then suitable for the realization of spiking neural networks with tunable behavior with several ground-breaking applications, including control.

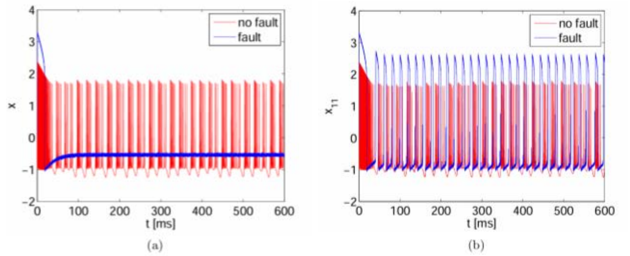

(a) (b)

Figure 2 - Experimental robustness of the hyperneuron with respect to a persistent noise: (a) scalar Hindmarsh-Rose, (b) hyper Hindmarsh-Rose

IV. CONCLUSIONS

The aim of this contribution is to illustrate the recent results obtained within the framework of the PNRR project FAIR at the University of Catania. The extension of multilayer perceptron to hypercomplex topology (QNNs), and its optimization, and models for the neuron dynamics based on nonlinear matrix differential equations, referred to as hyper-neurons, have provided innovative results that are the basis of a novel paradigm of high-dimensional neural networks.

The numerous promising applications of QNNs, ranging from modeling nonlinear dynamics to orbital planetary motion and vibrating systems, make them suitable tools dedicated to modeling nonlinear systems that present a considerable amount of correlated data. It has to be stressed the fact that, despite it is possible to consider quaternionic extension of other types of neural networks, including Hopfield nets with quaternion Hebbian rules [7], the project focuses on multilayer perceptrons and their hypercomplex generalization. The intrinsic robustness of hyper-neurons allows them to maintain spiking behavior even in the presence of faults and learning errors, making them suitable to be implemented in real devices for control, especially when information and data are uncertain and affected by noise.

REFERENCES

[1] Buscarino, A., Fortuna, L., Famoso, C., La Spina, G., Puglisi, G. (2023). Predicting Chaos in the Three-body Problem with Quaternion-valued Neural Networks. NONLINEAR PHENOMENA IN COMPLEX SYSTEMS, 26(3), 247-256.

[2] Buscarino, A., Famoso, C., Fortuna, L., Puglisi, G., Fast hypercomplex neural networks for modeling Venus planetary orbit. In 2023 30th IEEE International Conference on Electronics, Circuits and Systems (ICECS) (pp. 1-4). IEEE.

[3] Buscarino, A., Famoso, C., Fortuna, L., Puglisi, G., Hypercomplex Multilayer Perceptron for Planetary Orbits Prediction. In 2023 9th International Conference on Control, Decision and Information Technologies (CoDIT) (pp. 1427-1431). IEEE.

[4] Buscarino, A., Fortuna, L., Puglisi, G., Optimizing Multilayer Perceptrons to Approximate Nonlinear Quaternion Functions. In International Conference on Nonlinear Dynamics and Applications (pp. 441-450). Cham: Springer Nature Switzerland.

[5] Buscarino, A., Fortuna, L., Frasca, M., Xibilia, M. G. (2016). Invariance of characteristic values and L∞ norm under lossless positive real transformations. Journal of the Franklin Institute, 353(9), 2057-2073.

[6] Branciforte, M., Buscarino, A., Fortuna, L. (2022). A Hyperneuron Model Towards in Silico Implementation. International Journal of Bifurcation and Chaos, 32(13), 2250202.

[7] Isokawa, T., Nishimura, H., Kamiura, N, and Matsui Nobuyuki (2006). Fundamental properties of quaternionic Hopfield neural networks. Int. Joint Conference on Neural Networks, July 16-21, 2006.

Observer-based residual generator for fault detection and isolation of convex sets

Alessandro Baldini, Riccardo Felicetti, Alessandro Freddi, Sauro Longhi, and Andrea Monteriù

***Abstract*— In this paper, we formulate and solve a residual generation problem that incorporates elements from both set-based estimation and unknown input observers. The objective is to determine whether the unknown input variables (e.g., possible faults) lie in a generic convex set of the input (fault) space, without needing to estimate the exact value of these variables. This extended abstract is based on [1].**

I. INTRODUCTION

Unknown Input Observers (UIOs) assume a geometric structure for the unknown input to decouple its effects, and no bounds are needed for the unknown input. Conversely, given a system with bounded uncertainties, the set membership estimation returns a compact set of admissible values for the observed variable (e.g., the state) that are consistent with the (uncertain) model and measurements. Several set-membership state estimators have been developed using basic geometrical forms such as parallelotopes, ellipsoids, zonotopes, or intervals (see [2] and references therein). In the case of convex polytopic bounds, the uncertainty set is also a convex polytope, and the corresponding updating algorithms become computationally infeasible [3], as they suffer from an explosion in the number of vertices and facets. Zonotopic observers represent a compromise between exactness and computational load, however, the number of facets still increases in time, and reduction algorithms are necessary to keep them computationally feasible [4]. Instead, interval observers adopt simpler shapes to achieve computationally efficient set-based estimations, and they can be applied to linear time-varying discrete-time systems as well [2]. In this paper, we formulate and solve the problem of detecting if the unknown inputs lie in a convex set, without needing to estimate the exact value of these variables. Such region may represent a safety limit: as long as the fault does not assume critical values, estimating the exact magnitude of the fault may be unnecessary for Fault Detection and Isolation (FDI). To solve such residual generation problem, we present a set-based estimation approach for an unknown input (fault) employing classical point-wise observers. This approach offers two advantages with respect to traditional set-based estimation:

1) the solution is not limited to zonotopes and intervals but extends to convex (as well as non-convex) sets,
2) there is no need for approximations or reduction algorithms to manage the computational burden.

II. MAIN PROBLEM

The accessible state system

$$\Sigma : \qquad \dot{x}(t) = f(x(t), u(t)) + Pw(t) + Ed(t), \tag{1}$$

is considered as plant, where $x(t) \in \mathbb{R}^{n_x}$ is the state vector, $u(t) \in \mathbb{R}^{n_u}$ is the control input vector, $w(t) \in \mathbb{R}^{n_w}$ is the fault vector, and $d(t) \in \mathbb{R}^{n_d}$ is the process disturbance vector. Consider a pair of convex sets, here denoted as fault regions, defined as

$$\mathcal{W} = \{w : \; Aw \le b\}, \quad \mathcal{W}_\epsilon = \{w : \; Aw - b \le -\epsilon\bar{1}\}, \tag{2}$$

where $A = \mathbb{R}^{n_r \times n_w}$, $b \in \mathbb{R}^{n_r}$, and $\epsilon > 0$. We assume that $\{\} \subsetneq \mathcal{W}_\epsilon \subsetneq \mathcal{W}$.

Problem 1. *Consider the control system Σ and the fault region $\mathcal{W}$. Find an observer-based residual generator*

$$\dot{z}(t) = Lz(t) + g(x(t), u(t)) + q \tag{3a}$$

$$r(t) = h(z(t), x(t)) \tag{3b}$$

where $r(t) \in \mathbb{R}$ is the residual and $q \in \mathbb{R}^{n_r}$ is a design parameter, such that

1) *if $w(t) \in \mathcal{W}_\epsilon$ for $t \ge t_0$, then $r(t) > 0$ for $t \ge t_0' \ge t_0$,*
2) *if $w(t) \notin \mathcal{W}$ for $t \ge t_0$, then $r(t) = 0$ for $t \ge t_0' \ge t_0$.*

Proposition 1. *If*

$$\textit{rank}\begin{bmatrix} P & E \end{bmatrix} = \textit{rank}\begin{bmatrix} P & E \\ A & 0 \end{bmatrix} \tag{4}$$

there exists a residual generator which solves Problem 1.

A pseudocode solving Problem 1 is provided in Algorithm 1. In case of many fault regions $\mathcal{W}_1, \dots, \mathcal{W}_m$ a bank of residual generators can be built, where each residual component $r_i(t)$ is sensitive to the fault region $\mathcal{W}_i$ only and decoupled from the disturbance $d(t)$. The set of $r_i(t)$ can be considered a robust structured residual, and in case case of disjoint fault regions, also as a directional residual.

III. GEOMETRIC CONSIDERATIONS

Proposition 2. *Consider a fault region $\mathcal{W}$, and let a_i^T be the i-th row of A. Condition* (4) *is satisfied if and only if $a_i \in P^T(\ker(E^T))$ for $i = 1, \dots, n_r$.*

Roughly speaking, the condition $w(t) \in \mathcal{W}_\epsilon$ holds if the hyperplane $\bar{\mathcal{H}}_i = \{w : \; a_i^T w = 0\}$ satisfies $\bar{\mathcal{H}}_i^\perp \subset P^T(\ker(E^T))$, which limits the shape of $\mathcal{W}$.

This work was not supported by any organization.

All the authors are with the Department of Information Engineering, Università Politecnica delle Marche, Italy. `a.baldini@univpm.it`, `r.felicetti@univpm.it`, `a.freddi@univpm.it`, `s.longhi@univpm.it`, `a.monteriu@univpm.it`.

```
Algorithm 1 Fault detection residual generator design.
Require: $f(\cdot,\cdot)$, $P$, $E$ from $\Sigma$ in (1), $A$, $b$ of the faulty region $\mathcal{W}$ to detect.
Ensure: Condition (4).
    Find vectors $v_1, \dots, v_{n_r}$ satisfying the linear systems
        $\begin{bmatrix} P^T \\ E^T \end{bmatrix} v_i = \begin{bmatrix} a_i \\ 0 \end{bmatrix}$
    Choose $h_1, \dots, h_{n_r} > 0$;
    $M \leftarrow \begin{bmatrix} v_1 & \dots & v_{n_r} \end{bmatrix}^T$;
    $H \leftarrow diag(h_1, \dots, h_{n_r})$;
    $L \leftarrow -H$;
    $g(x,u) \leftarrow Mf(x,u) + HMx$;
    $h(z,x) \leftarrow \prod_{i=1}^{n_r} ramp(e_i^T(z - Mx))$;
    $q \leftarrow b - \frac{\epsilon}{2}\bar{1}$;
```

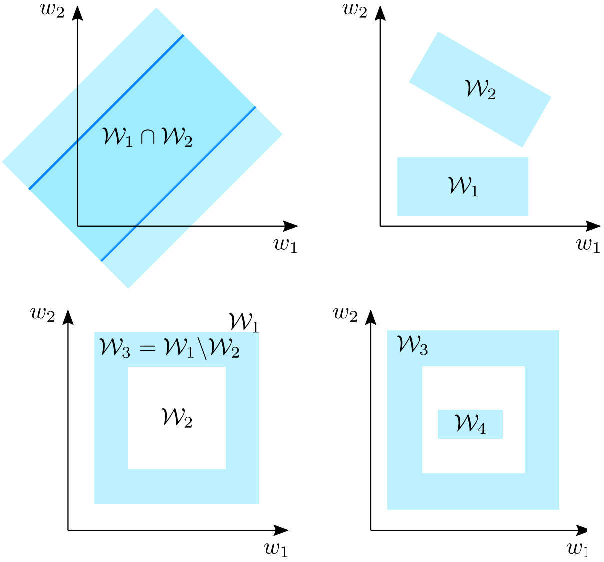

Fig. 1. Examples of fault regions obtained through set intersection and subtraction.

IV. APPLICATION TO FAULT DETECTION AND ISOLATION

Using intersection and set subtraction, it is possible to isolate non-convex regions. Figure 1 shows four bidimensional examples. Let $r_1(t)$ and $r_2(t)$ be two residuals for the isolation of $\mathcal{W}_1$ and $\mathcal{W}_2$, respectively. The isolation of $\mathcal{W}_1 \cap \mathcal{W}_2$, $\mathcal{W}_1 \cup \mathcal{W}_2$ and $\mathcal{W}_1 \backslash \mathcal{W}_2$ could be achieved through the decision rules

$$w(t) \in \mathcal{W}_{1,\epsilon} \cap \mathcal{W}_{2,\epsilon} \quad \text{if } r_1(t) > 0 \texttt{ and } r_2(t) > 0, \tag{5a}$$

$$w(t) \in \mathcal{W}_{1,\epsilon} \cup \mathcal{W}_{2,\epsilon} \quad \text{if } r_1(t) > 0 \texttt{ or } r_2(t) > 0, \tag{5b}$$

$$w(t) \in \mathcal{W}_{1,\epsilon} \backslash \mathcal{W}_{2,\epsilon} \quad \text{if } r_1(t) > 0 \texttt{ and } r_2(t) = 0. \tag{5c}$$

V. CASE STUDY: MULTIROTORS

Consider a multirotor model with n_a actuators under multiplicative actuator faults. Choosing proper body fixed coordinates and input transformation, the multirotor takes the structure (1), where $P^T = \begin{bmatrix} 0 & 0 & F_1^T & F_2^T \end{bmatrix} \in \mathbb{R}^{n_a \times 12}$ and $E^T = \begin{bmatrix} 0 & 0 & I & 0 \end{bmatrix} \in \mathbb{R}^{3 \times 12}$. According to Proposition (1), a fault region $\mathcal{W} = \{w : Aw \leq b\}$ can be isolated if

$$\text{rank} \begin{bmatrix} P & E \end{bmatrix} = \text{rank} \begin{bmatrix} F_1 & I \\ F_2 & 0 \end{bmatrix} = \begin{bmatrix} F_1 & I \\ F_2 & 0 \\ A & 0 \end{bmatrix} \tag{6}$$

holds. Geometrically, there exists a residual generator for $\{w : a_i^T w \leq b_i\}$ if $a_i \in P^T(\ker(E^T)) = Im(F_2^T)$.

Consider the special case of a quadrotor, with $n_a = 4$ and

$$F_1 = \begin{bmatrix} 0 & 0 & 0 & 0 \\ 0 & 0 & 0 & 0 \\ 1 & 1 & 1 & 1 \end{bmatrix}, \quad F_2 = \begin{bmatrix} l & 0 & -l & 0 \\ 0 & l & 0 & -l \\ \frac{c_T}{c_D} & -\frac{c_T}{c_D} & \frac{c_T}{c_D} & -\frac{c_T}{c_D} \end{bmatrix},$$

where c_T and c_D are the thrust and the drag coefficients. Due to the full rank of $\begin{bmatrix} F_1^T & F_2^T \end{bmatrix}$, it is possible to select fault regions $\mathcal{W}_1, \dots, \mathcal{W}_4$ such that in case of no faults $w(t) \notin \mathcal{W}_i$ for $i = 1, 2, 3, 4$, and in case of a fault (of prescribed magnitude) on the ith motor only, $w(t) \in \mathcal{W}_i$ and $w(t) \notin \mathcal{W}_j$ for $j \neq i$. A residual $r_i(t)$ is designed to trigger on $\mathcal{W}_i$, and the fault isolation for the ith motor is triggered when $r_i(t) > 0$. A simulation is carried out using Matlab Simulink, for a total time of 30 s and a sample time of 10^{-3} s. A low frequency external disturbance is injected in the linear acceleration. We inject a loss of effectiveness at 10 s, and a 50% of loss is accomplished at 15 s. The residual components r_i are instead reported in Figure 2. After the fault is injected, the residual $r_1(t)$ triggers when a sufficient fault magnitude (30%) is reached, while $r_j(t) = 0$ for $j \neq i$.

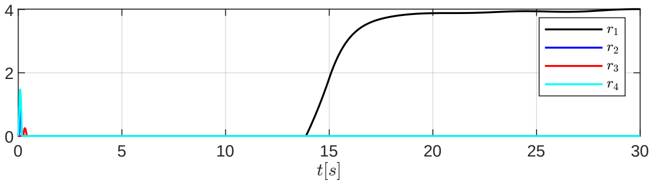

Fig. 2. Residual.

VI. CONCLUSIONS

The proposed solution offers a residual that indicates whether the unknown variables belong to a predefined region or not, making it well suited for FDI. Simulation results demonstrate the practical application of the proposed observer-based solution in a case study involving actuator FDI for an autonomous quadrotor vehicle. Future works involve addressing non-accessible state and the joint problem of both passive and active disturbance rejection.

REFERENCES

[1] A. Baldini, R. Felicetti, A. Freddi, L. Sauro, and A. Monteriù, "Observer-based residual generator for fault detection and isolation of convex sets," in *2024 IEEE 20th International Conference on Automation Science and Engineering*. IEEE, 2024.

[2] D. Efimov, W. Perruquetti, T. Raïssi, and A. Zolghadri, "Interval observers for time-varying discrete-time systems," *IEEE Transactions on Automatic Control*, vol. 58, no. 12, pp. 3218–3224, 2013.

[3] L. Chisci, A. Garulli, and G. Zappa, "Recursive state bounding by parallelotopes," *Automatica*, vol. 32, no. 7, pp. 1049–1055, 1996.

[4] C. Combastel, "A state bounding observer based on zonotopes," in *2003 European control conference (ECC)*. IEEE, 2003, pp. 2589–2594.

Hardware In the Loop simulation of $PI^{\lambda}D^{\mu}$ controller

R. Caponetto[1], G. Dongola[1], S. Graziani[2], L. Patenè[1], F. Sapuppo[1], and M.G. Xibilia[1]

[1]Università di Messina, Dipartimento di Ingegneria
[2]Università di Catania, DIEEI

July 5, 2024

The paper will show an application of the Hardware In the Loop (HIL) approach realized to verify the stability properties of the implemented fractional order $PI^{\lambda}D^{\mu}$ controller [1].

HIL simulation is a form of real-time simulation used for testing controller designs. It allows to evaluate how the designed controller reacts in real-time to realistic virtual stimuli and helps validate plant model and fine tune the controller.

In HIL simulation, a real-time computer is used as a virtual representation of the plant while a physical controller is used during the experiment. In our application an Arduino 2 has been used to implement the Grunwald-Letnikov approximation of the designed $PI^{\lambda}D^{\mu}$ controller.

A typical HIL simulation setup consists in: the computer that hosts the Matalb/Simulink© closed loop system, along with an interface, usually the ControlDesk© program, used to manage the virtual plant parameters; the target hardware that in our application is a DSpace© DS2201 Multi I/O Board and the controller hardware, the Arduiono 2, that runs software generated from the controller model, again developed in the Matalb/Simulink environment.

The interest toward fractional control is increasing [2], but commercial applications are far to be identified and realized. The HIL approach can help, in a realist way, in verifying the performance of the fractional controller, in terms of approximation, CPU speed, quantization and DAC-ACD effects, and at the same time allows to test its stability versus plant parameters variations.

The simulated closed loop system is proposed in [3] and is composed by a first order system with a delay and the fractional PID controller.

Figure 2 reports preliminary tests on a classical PI and PI^{λ} controller. In particular, in a-d for the PI controller, the Arduino schematic, the Dspace scheme, the step response, the control signal on Arduino and step response on

ControlDesk are shown, while in e-f for the PI^{λ}, the Arduino schematic with PI^{λ} controller and its step response and control, are depicted.

]

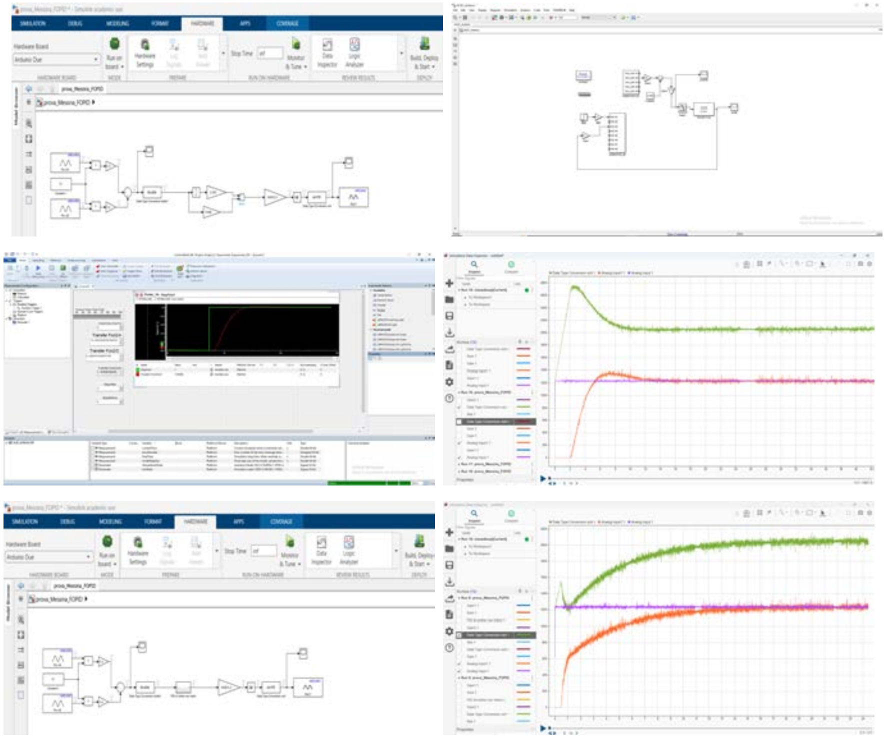

Figure 1: Preliminary tests on a classical PI and a PI^{λ} controller.

References

[1] Podlubny I.“Fractional-order systems and $PI^{\lambda}D^{\mu}$ controllers.”,*IEEE Transactions on Automatic Control* 44 (1), 1999.

[2] Efe M.O.“Fractional order systems in industrial automation A survey.”,*IEEE Transactions on Industrial Informatics* 7 (4), art. no. 6011685, 2011.

[3] Moreira W. E. M. Moreira and Garcia C.“ Performance comparison between IOPID and FOPID controllers in an industrial flow pilot plant. ”,*IFAC-PapersOnLine* Volume 54, Issue 4, pages 232-237 ISSN 2405-8963, 2021.

Session 3B: DAuSy

Analysis of Dosimetric Parameters of Linear Accelerator

Nadia Naz[1*], Saeed Ahmad Buzdar[2], Muhammad Asghar Gadhi[3] and Aasia Bibi[4]
[1]Department of Electrical and Information Engineering, University of Parma, 43121, Italy
[2]Institute of Physics, The Islamia University of Bahawalpur, Bahawalpur, 63100, Pakistan
[3]Department of Radiation Therapy, Bahawalpur Institute of Nuclear Medicine and Oncology (BINO), Pakistan Atomic Energy Commission (PAEC)
[4]Department of Biosciences, Biotechnology and Environment, University of Bari Aldo Moro, Via Edoardo Orabona, 70125 Bari, Italy

[*]Correspondence: naz203429@gmail.com

ABSTRACT

With the advancements in the radiation delivery techniques and modern Linac systems, the need for better quality control devices also arises. Different devices manufactured by companies are available at hospitals and some of these devices are found to be more accurate in one category then others. The main objective of this study to analyze the dosimetric parameters of linear accelerator was to use PTW QUICKCHECK device at radiotherapy department of BINO hospital, Bahawalpur and evaluate their performances in checking the beam uniformity and symmetry in daily QC and other required periodic QC tests. For Daily Quality Control PTW QUICKCHECK device was used daily in the morning checks for 50 days to monitor CAX, beam flatness, GT symmetry, LR symmetry, Beam Quality Factor for electron beam of 6, 9, 12, 15, 18, 22 MeV energies and photon beam of 6, 15 MV energies with 100 MU given to the QUICK CHECK device at dose rate of 300 MU/min. To ensure the stability of data monitored through QUICKCHECK repeatability and reproducibility tests were performed. PTW QUICKCHECK device can be easily setup on daily basis for daily checks. According to the results it is clear that PTW QUICKCHECK device is quite accurate with regard to symmetry measurements as all data is within tolerance range (3%). However, accuracy in flatness measurement shows uncertainties i.e for 6 MV 7.3%, for 15 MV 7.31%, for 6 MeV 16.12%, for 9 MeV 6.92%, for 12 MeV 5.92%, for 15 MeV 4.01%, for 18 MeV 4.01% and for 22 MeV 4.13% of data are within tolerance range.

For treatment delivery, CLINAC IX by VARIAN medical system was under operation at BINO hospital. The MV imager known as the Electronic Portal Imaging Device was placed for image purposes. Energy options of 6MV and 15 MV for photons and 6Mev, 9Mev, 12Mev, 15Mev, 18Mev and 22Mev were available for electrons.

The purpose of this research is to check the consistency of photon beam and electron beam in linear accelerator used for radiotherapy and also examine the dosimetric parameters of linear accelerator to be used in highly conformal radiation therapy. The deviation of flatness, symmetry, CAX and beam quality factor were compared with data taken from PTW QUICKCHECK device, also reproducibility and repeatability was determined.

Based on the result, this study suggest that linear accelerator is reliable dosimetric tool in radiotherapy. Linear accelerator can be used for dose assessment of absorbed dose levels as well as relative dosimetry when compared to absolute absorbed dose calibrated using QUICKCHECK device results. It does not depend on side orientation and also not affected by room light. PTW QUICKCHECK device can be easily set up on daily bases for daily checks.

Keywords: PTW QUICKCHECK device, Flatness, Symmetry, Central axis, dosimetry, Quality assurance, Linear accelerator

Bibliography

1. W. H. Organization, *Quality assurance in radiation therapy: guidelines based on a workshop in Schloss Reisensburg, Federal Republic of Germany, 3-7 December 1984*: World Health Organization, 2017.

2. P. J. Biggs, C. C. Ling, J. A. Purdy, and J. van de Geijn, "AAPM code of practice for radiotherapy accelerators: report of AAPM Radiation Therapy Task Group No. 45," *Medical Physics,* vol. 21, p. 1093, 2018.

3. T. Pawlicki, D. J. Scanderbeg, and G. Starkschall, *Hendee's radiation therapy physics*: John Wiley & Sons, 2016.

4. A. A. o. P. i. Medicine, "Protocol for clinical reference dosimetry of high- energy photon and electron beams," *Med Phys,* vol. 26, pp. 1847-1870, 2017.

5. E. E. Klein, J. Hanley, J. Bayouth, F. F. Yin, W. Simon, S. Dresser*, et al.*, "Task Group 142 report: Quality assurance of medical accelerators a," *Medical physics,* vol. 36, pp. 4197-4212, 2019.

6. R. C. S. d. Silva, "Analysis of the use of dosimetrically equivalent linear accelerators for Intensity Modulated Radiotherapy treatments," 2020.

7. M. S. Huq, "Absorbed dose determination in external beam radiotherapy: an international code of practice for dosimetry based on standards of absorbed dose to water," 2016.

8. F. M. Khan and J. P. Gibbons, *Khan's the physics of radiation therapy*: Lippincott Williams & Wilkins, 2018.

9. G. J. Kutcher, L. Coia, M. Gillin, W. F. Hanson, S. Leibel, R. J. Morton*, et al.*, "Comprehensive QA for radiation oncology: report of AAPM radiation therapy committee task group 40," vol. 21, pp. 581-581, 2016.

10. E. E. Klein, J. Hanley, and J. J. M. P. Bayouth, "Quality assurance of medical accelerators," vol. 36, p. 4112, 2019.

Management and automation systems for energy management in buildings and industrial processes

Zohreh Shahrouei [1*], Elio Usai[1]

University of Cagliari[1]

The building sector plays a crucial role in global decarbonization and energy efficiency efforts. According to the International Energy Agency's 2022 report, this sector is responsible for 27% of global energy-related emissions. Additionally, the significant energy savings potential in buildings has made optimal control in this area a popular research topic in recent years. [1]- [7]

This project focuses on the optimization and energy management of buildings, both residential and industrial, aiming to maintain thermal comfort while reducing energy consumption costs. The proposed approach incorporates renewable energy sources, such as solar panels, and includes battery energy storage and the use of the building structure as thermal storage.

Since the thermal comfort can strongly depend on the thermal behavior of the building, a first analysis will be devoted to design the building such that the variation of the internal temperature is significantly small with respect to the daily variation of weather conditions. The building is considered as a thermal storage unit, where the building behaves as a low-pass filter, whose characteristics depend on its thermal characteristics, such as thermal transmittance and capacity. In addition, a second approach involves controlling the building's temperature according to the user's preferences by adjusting the output air temperature and scheduling the operation times of a HVAC system, exploiting the thermal storage characteristics of the building to reduce the economic and environmental cost of the use of energy.

A grey-box model is suggested to estimate the building's thermal parameters through a physical thermal model. In this context, a physics-informed neural network can be applied to speed up computing time. The optimization problem can be framed as a constrained optimization problem or a multi-objective optimization problem, depending on the chosen scenario.

This study highlights the potential for significant energy savings and cost reductions through optimized energy management and control in the building sector, contributing to broader decarbonization efforts.

Keywords: Thermal comfort- Constrained optimization- Multi-objectives optimization- Energy management- Physics-informed neural network.

Reference:

[1] T. Xiao and F. You, “Building thermal modeling and model predictive control with physically consistent deep learning for decarbonization and energy optimization,” *Appl Energy*, vol. 342, Jul. 2023.

[2] C. Chen, J. Wang, Y. Heo, and S. Kishore, “MPC-based appliance scheduling for residential building energy management controller,” *IEEE Trans Smart Grid*, vol. 4, no. 3, pp. 1401–1410, 2013.

[3] Y. Chen, Q. Yang, Z. Chen, C. Yan, S. Zeng, and M. Dai, “Physics-informed neural networks for building thermal modeling and demand response control,” *Build Environ*, vol. 234, Apr. 2023.

[4] J. Arroyo, C. Manna, F. Spiessens, and L. Helsen, “Reinforced model predictive control (RL-MPC) for building energy management,” *Appl Energy*, vol. 309, Mar. 2022.

[5] J. Aguilar, A. Garces-Jimenez, M. D. R-Moreno, and R. García, “A systematic literature review on the use of artificial intelligence in energy self-management in smart buildings,” Nov. 01, 2021, *Elsevier Ltd*.

[6] Y. Balali, A. Chong, A. Busch, and S. O’Keefe, “Energy modelling and control of building heating and cooling systems with data-driven and hybrid models—A review,” Sep. 01, 2023, *Elsevier Ltd*.

[7] H. F. Scherer, M. Pasamontes, J. L. Guzmán, J. D. Álvarez, E. Camponogara, and J. E. Normey-Rico, “Efficient building energy management using distributed model predictive control,” *J Process Control*, vol. 24, no. 6, pp. 740–749, 2014.

Autonomous Intelligent System for Predicting Response to TACE in Treating Hepatocellular Carcinoma

Pietro Maria Marvulli*, Domenico Buongiorno*, Raffaele Carli*, Mariagrazia Dotoli* and Vitoantonio Bevilacqua*
*Department of Electrical and Information Engineering (DEI), Polytechnic University of Bari, 70126 Bari, Italy

***Abstract*—Predicting the response to Trans-Arterial Chemoembolization (TACE) is crucial to personalize the treatment of hepatocellular carcinoma, improving therapeutic efficacy and prognosis and reducing side effects. This study has the aim to design and develop an autonomous intelligent system to predict the response to TACE using advanced machine learning techniques. Pre-procedure CT and clinical data from 105 patients were employed and time-to-progression treatment was used to discriminate if a patient is responsive or non-responsive. Different machine learning models were tested with a narrow selection of both clinical and radiomics features as input to discover the most effective way to assist doctors in their clinical practice.**

I. INTRODUCTION

Hepatocellular carcinoma (HCC) is one of the most common causes of cancer-related deaths globally. Treating is intricate and varies with the tumor's stage. In surgically inoperable cases and in advanced stages, the clinical practice includes treatments that act on the vascular system of the carcinoma, mainly formed by arteries. Among these, one of the most used is the Trans-Arterial Chemoembolization (TACE) which consists in the insertion of a catheter for the injection of a chemotherapy drug into the artery through which the tumor feeds. This technique has a dual action, a pharmacological one due to the toxic effect of chemo drug and an embolizing one that physically blocks the blood supply to the tumor tissue. The goal of the treatment is the complete destruction of the tumor or size reduction to enable subsequent resection or transplantation. Since both HCC diagnosis and post-treatment control are based on CT, they can be exploited to predict whether or not a patient will respond to the healing effects of TACE. In fact, knowing in advance the optimal therapeutic path for a patient with HCC can increase the patient's overall survival and greatly reduce the risk of progression of the disease. In clinical practice, the prediction of the response to TACE treatment is entrusted to clinical scores that consider a few factors. In recent years, machine learning techniques have been applied to both clinical data and imaging to try to find new ways to predict the response by combining different types of features. However, current state-of-the-art methods have several limitations such as the lack of sufficient robustness and generalizability across different patient populations and clinical settings due to the heterogeneity of HCC and there is no comparison between different methodologies on the same dataset. This work aims to design and create an autonomous intelligent data-driven system to forecast the response to TACE by utilizing quantitative features derived from CT images and clinical information. In particular, starting from clinical data and features extracted from CT images, the most important features are selected through correlation analysis and statistical methods. The impact of different combinations of input features on different machine learning models is then investigated to find the best model in terms of accuracy and area under ROC curve (AUC) to determine whether a patient is responsive or non-responsive to treatment

II. MATERIALS AND METHODS

A. Dataset

The data obtained from the cancer imaging archive includes 105 HCC patients' pre and post-procedural CT scans and clinical information who were treated with TACE. Manual segmentation of the tumor on the venous phase was performed by three expert radiologists. Time to progression (TTP) information from the patient's clinical data was used to evaluate the TACE response. A 14-week TTP cutoff was taken to stratify the response of patients to the first TACE session as TACE-refractory or TACE-susceptible according to Moawad et al. [1]. Clinical data includes, in addition to demographic, lifestyle and comorbidity factors, specific information on cancer, treatment and radiological response criteria. After removing the features that did not have 50% of the values and patients who have missing values and the patients who lack clinical data, 89 patients were retained. Quantitative computational image analysis, termed radiomics, was used to extract various features from the region of interest of the lesion.

B. Radiomics features extraction

The features extracted from the images include first-order features, shape features and texture features. All these features were extracted both from the original image and from many filtered images. The filters used for the analysis was *Laplacian of Gaussian (LoG)*, *Wavelet*, *Square*, *SquareRoot*, *Logarithm*, *Exponential*, *Gradient* and *Local Binary Patterns (LBP)*. All the series were resampled to a spacing of 1 mm × 1 mm × 1 mm to avoid having results dependent on the CT acquisition setup. We used PyRadiomics library to extract all the 2016 features. Through a literature analysis, the most effective and useful methods for feature selection in similar studies were analyzed [2].

C. Feature selection

As a first step, a correlation analysis was performed. In particular, features with a Pearson coefficient greater than 0.85 were eliminated. The AUC obtained from two logistics regression models trained with each feature was the criterion for selecting which characteristic of a pair of correlation characteristics had to be maintained. Subsequently, the features maintained after correlation analysis were further selected through a least absolute shrinkage and selection operator (Lasso) analysis after which they were normalized with z-score normalization. Lasso automatically selects the relevant characteristics by regularizing the coefficients through a penalty term. This model is frequently used in machine learning to handle high dimensional data as it facilitates automatic feature selection with its application. A 10-fold cross-validation on a single Lasso model was performed to select the optimum value of this penalty term. The result is a model that is used to compute a score, called *RadScore*, calculated as:

$$RadScore = q + \sum_{i=1}^{N} c(i) * f(i) \tag{1}$$

where q is the intercept, $c(i)$ the coefficient of the retained feature $f(i)$. Clinical risk factors were selected by univariate and multivariate logistic regression analyses via a backward step-wise process. Factors with p-value < 0.1 in univariate logistic regression were included in multivariate analysis and those with p-value < 0.1 were identified as independent risk factors.

D. Machine Learning Models

Five machine learning models were trained to assess which is the best model and which is the best combination of features for predicting the effectiveness of treatment for each patient. The models are:

- Logistic Regression (LR)
- Support Vector Machines (SVM)
- Random Forest (RF)
- Extreme Gradient Boosting (XGB)
- Multi Layer Perceptron (MLP)

Every single model was tested with three different input sets: only radiomics features, radiomics features combined with clinical features and clinical features combined with $RadScore$. Every model was trained with 5-fold cross-validation and the performances were evaluated based on area under Receiver Operating Characteristic curve and accuracy.

III. RESULTS

After deleting correlated features and performing a Lasso analysis, only 12 of the 2016 extracted radiomics features were elected as significant for prediction while the only clinical feature that met the requirements was the variable *hepatitis* that indicates whether a patient does not have, has hepatitis B or C virus or both of them. In Table I all the results were shown for the aforementioned models.

In general, the clinical variable increases the performance of prediction when is taken into consideration by models. The results in terms of accuracy and AUC show how the RF model, analyzing 'hepatitis' and *RadScore* can effectively predicts patients' response to TACE. Comparing these models based on accuracy and AUC, some configurations lead to higher AUC but much worse accuracy indicating potential issues such as overfitting. The results show how RF manages both to achieve high accuracy in its predictions and to maintain a strong AUC, indicating its robustness in distinguishing between classes.

Input Features	**Model**	**Performance Test** **ACC**	 **AUC**
Clinic $\bigcup$ RadScore	LR	0.7284	0.8759
	SVM	0.7706	0.8465
	RF	**0.8266**	**0.8726**
	XGB	0.8386	0.86
	MLP	0.7824	0.8569
Radiomics Features	LR	0.7699	0.8357
	SVM	0.7922	0.8394
	RF	0.6895	0.7624
	XGB	0.6895	0.7529
	MLP	0.7582	0.8263
Radiomics Features $\bigcup$ Clinic	LR	0.781	0.8582
	SVM	0.7804	0.8462
	RF	0.7007	0.7542
	XGB	0.7007	0.7515
	MLP	0.7464	0.8201

TABLE I
COMPARISON OF MODEL PERFORMANCE ACROSS DIFFERENT INPUT FEATURES

IV. CONCLUSION AND FUTURE WORK

This work seeks to find an effective and robust way to predict whether a patient is responsive or non-responsive to Trans-Arterial Chemoembolization. Through radiomic analysis of pretreatment CT images and clinical data, we lead to build an autonomous intelligent system that involves a sought-after set of features. Among different machine learning models, the Random Forest model predicts with great accuracy the response using only hepatitis and *RadScore*. However, emerging deep learning models, particularly Convolutional Neural Networks (CNNs) and Transformers, present promising avenues to predict a treatment response from medical images. CNNs and Trasnformers can automate and enhance feature extraction from imaging data which are less interpretable than those extracted from radiomics analysis but can build robust and accurate models, more useful in clinical practice. Future works will focus on the combination of different methods to extract information from images to develop systems that could improve both the clinic decision-making process and the prognosis for patients.

REFERENCES

[1] A. Moawad, A. Morshid, A. Khalaf, M. Elmohr, J. Hazle, D. Fuentes, M. Badawy, A. Kaseb, M. Hassan, A. Mahvash, J. Szklaruk, A. Qayyum, A. Abusaif, W. Bennett, T. Nolan, B. Camp, and K. Elsayes, "Multimodality annotated hepatocellular carcinoma data set including pre- and post-tace with imaging segmentation," *Scientific Data*, vol. 10, no. 1, Dec. 2023, publisher Copyright: © 2023, The Author(s).

[2] Y. Wang, M. Li, Z. Zhang, M. Gao, and L. Zhao, "Application of radiomics in the efficacy evaluation of transarterial chemoembolization for hepatocellular carcinoma: A systematic review and meta-analysis," *Academic Radiology*, vol. 31, no. 1, pp. 273–285, 2024. [Online]. Available: https://www.sciencedirect.com/science/article/pii/S1076633223004002

A Comprehensive Review of Autonomous Intelligent Systems for Polyp Detection and Segmentation in Colonoscopy

Claudia Delprete*, Domenico Buongiorno*, Raffaele Carli*, Mariagrazia Dotoli*, and Vitoantonio Bevilacqua*
* Department of Electrical and Information Engineering (DEI), Polytechnic University of Bari, 70126 Bari, Italy.

Abstract—**Colorectal cancer is the third most frequently diagnosed cancer globally. Colonoscopy is crucial for screening, aiming to detect and treat malignant or pre-malignant polyps. However, the accuracy of this procedure is influenced by factors such as physician expertise, lighting variations, artifacts and differences in imaging modalities. This study conducts a comprehensive literature review on automatic polyp segmentation and detection methodologies, emphasizing unsupervised methods.**

I. INTRODUCTION

Colorectal cancer (CRC) is the third most frequently diagnosed cancer and its early detection significantly improve the survival rate. Colonoscopy is the gold standard procedure for diagnosis and removal of colorectal lesions.

The accuracy of detection and classification in colonoscopy procedures is influenced by several factors: the experience of the physician, the color variations in images/videos due to lighting conditions (Fig. 1 a), differences in polyp size and shape, indistinct boundaries, and multiple polyps (Fig. 1 b, d), as well as artifacts like specularity, floating objects, stool, bubbles, pixel saturation, and surgical instruments (Fig. 1 c). Differences in image centers and modalities (WLE, NBI, BLI, FICE, and LCI) (Fig. 1 e, f) also contribute to the complexity in the detection and classification of colorectal polyps.

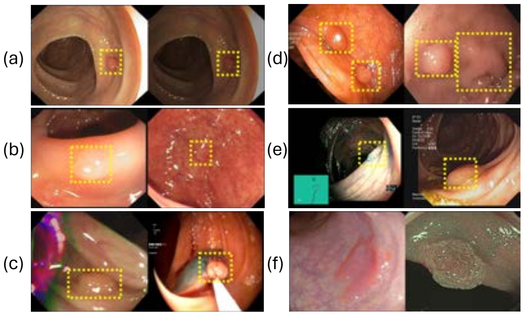

Fig. 1. Factors affecting the accuracy of polyp detection and classification in colonoscopy. Yellow bounding boxes are used to highlight the polyps.

Autonomous intelligent systems have the potential to improve endoscopic practice by enhancing inspection techniques, automatically detecting CRC lesions and facilitating real-time diagnosis through optical biopsy. Based on the level of supervision, Deep Learning (DL) methods used for polyp detection and segmentation can be classified into fully-supervised, semi-supervised, weakly-supervised and self-supervised approaches [1, 2]. Traditional methods are trained using fully-supervised approaches, where a model is trained using a dataset with pixel-level annotations, relying on extensive manual labeling to achieve high performance. While fully-supervised models can deliver high performance, they depend on large and balanced datasets with pixel-wise labels. Consequently, many researchers are turning to semi-supervised learning, which need limited labeled and unlabeled data. To reduce reliance on pixel-wise annotations, some have adopted weakly-supervised approaches using point, semantic label, scribble, and bounding-box. Additionally, some researchers are using unsupervised methods. Self-supervised learning is a subset of unsupervised learning. Both methods do not use labels in the training process, focusing on learning intrinsic patterns in unlabeled data. Unsupervised learning does not measure results against any pre-known ground truth and is used for tasks like clustering and anomaly detection, deriving utility from discovering hidden correlations. In contrast, self-supervised learning measures results against a ground truth derived from the data itself and uses a loss function to optimize model accuracy.

This work focuses on a literature review on unsupervised polyp segmentation and detection methods in colonoscopy images and videos.

II. METHODOLOGY

To provide a comprehensive overview of the research topic on DL applied to the analysis of gastrointestinal endoscopy images and videos, a set of related publications was selected. An initial group of articles was retrieved through an electronic search on the Scopus® . As a result of this process, 14 articles were included for the scope of this work and 4 surveys. Exclusion criteria were applied to omit papers addressing different topics, not utilizing deep learning techniques and employing supervised, semi-supervised and weakly-supervised methods. Additionally, the research involved identifying public datasets. Eleven open public datasets were identified, including 3 video-level datasets and 10 image-level datasets. Although 4 surveys were identified, they do not focus exclusively on unsupervised methods. Instead, they consider models used for detection and/or segmentation across all four levels of supervision. This highlights the need for a survey dedicated solely to unsupervised methods. In this work, the state-of-the-art models for unsupervised detection and segmentation of polyps were studied, identifying those capable of performing automatic segmentation and detection. Furthermore, the available public datasets relevant to this research area were analyzed.

III. DISCUSSION

In medical image analysis, various methods are employed to address the challenges of automatically detect and segment polyps in colonoscopy images and videos. This section delves into the polyp datasets description, the effectiveness of unsupervised methods, strategies to enhance model generalizability and the importance of addressing domain shifts through domain adaptation.

A. *Unsupervised Polyp Detection and Segmentation*

Advancements in Computer Vision and Machine Learning have improved medical image analysis, especially with DL models. These models require extensive labeled datasets and are prone to overfitting, leading to increased interest in unsupervised learning approaches.

Analyzing the identified papers, the unsupervised polyp detection and segmentation methods can be divided into two methodologies: reconstruction methods and self-supervised approaches [3–6].

Reconstruction-based methods detect and localize polyps by reconstructing a negative/polyp-free/healthy image and computing the difference between the test image and the reconstruction. Common architectures include Autoencoders (AEs) and Generative Adversarial Networks (GANs). During AE training the encoder compresses input images into a lower-dimensional latent space and the decoder reconstructs the images from this representation. The model is trained on negative images, minimizing the reconstruction error, which is the difference between the original and reconstructed image. During the inference phase with test images, the AE reconstructs the image. The differences between the original test image and its reconstruction highlight areas where the model failed to accurately recreate the image, indicating potential polyps. Polyp-ODD and MemMC-MAE are based AEs [3], achieving results on the order of 0.90 AUC (Area Under the Curve) for the detection task and 0.40 IoU (Intersection over Union) for the segmentation task. Another reconstruction-based method involves GANs that are trained adversarially, improving the generator's ability to create accurate reconstructions of negative images. The difference between the original and reconstructed images is used to detect polyps. For example, f-AnoGAN combines these differences with additional features learned by the discriminator. Areas with high reconstruction errors are segmented as polyps, as the GAN struggles to accurately reconstruct these regions. F-AnoGAN, ADGAN and AnoGAN are GAN-based methods [3]. These methods are used for polyp detection, achieving results on the order of 0.90 AUC. The segmentation performance has been evaluated qualitatively.

Self-Supervised Learning (SSL) methods is designed to learn useful representations from data without requiring manual annotation. The process starts with an unlabeled dataset, using a feature extractor to learn meaningful representations. The feature extractor is trained using a pretext task, designed to teach the model to understand the data better. Examples of pretext tasks include predicting the rotation of an image, inpainting missing parts of an image, solving jigsaw puzzles. Once the model has learned useful features from the pretext task, the acquired knowledge is then leveraged through transfer learning and domain adaptation, enhancing the model's performance on downstream tasks such as polyp detection and segmentation. Examples of SSL methods applied to medical image analysis include PMSCAL achieving an AUC value of 0.996 and IoU of 0.406, CDD [4] achieving an AUC of 0.972 and IoU of 0.372.

A challenge with unsupervised methods is learning effective image feature representations, which is crucial for detecting lesions in medical images due to their subtle differences from healthy tissues. These methods can overfit to negative training data, leading to ineffective representations and failures in lesion detection and segmentation. Although ImageNet-based pre-trained models are commonly used, they might not be ideal because the features learned from natural images do not align well with medical images. This representation challenge can be addressed using methods based on SSL and reconstruction techniques.

B. Enhancing Model Generalizability

Most datasets are imbalanced with more negative/healthy images than positive/diseases ones. Unsupervised methods offer advantages in this context. Firstly, acquiring the training set is simple since most screening datasets consist of standard images, removing the need to a large number of positive images for training. Secondly, these methods do not require a representative training set containing positive images. Fully-supervised DL models require numerous annotated pixel-level ground truths, which are resource-intensive and time-consuming to create. Unsupervised learning reduces reliance on the large annotated datasets and improves generalization to unseen data, addressing the issue of dataset imbalance and enhancing the model's ability to detect and classify polyps in diverse real-world medical images.

C. Addressing Domain Shifts with Domain Adaptation

DL models typically assume that training and test datasets share the same distribution and modality, which is often not the case in real-world scenarios. When the distribution of the test dataset differs from that of the training dataset, the model's performance significantly declines. To effectively apply DL in medical image analysis, addressing domain shift is crucial. Domain adaptation has emerged as a promising solution, aiming to reduce the distribution gap between different but related datasets. Enhancing the model's robustness and adaptability can be achieved by incorporating data from multiple centers and various imaging modalities, addressing limitations related to variations in imaging conditions and equipment.

D. Polyp Datasets

Colonoscopic datasets can be categorized into two types: image-level datasets and video-level datasets [1]. Image-level datasets consist of individual frames taken from colonoscopy videos. Video-level datasets comprise entire video sequences captured during colonoscopy, providing a comprehensive view of the procedure and enabling the analysis of temporal dynamics and polyp tracking.

IV. CONCLUSION

This study has presented a comprehensive literature review on automatic polyp segmentation and detection methodologies, with a particular focus on unsupervised methods. While significant progress has been made in this field, several challenges remain to be addressed. Future research should aim to optimize these methods for medical image analysis by incorporating domain-specific knowledge, enhancing the generalizability of models to diverse and unseen data and improving models robustness.

REFERENCES

[1] Z. Wu, F. Lv, C. Chen, A. Hao, and S. Li, "Colorectal polyp segmentation in the deep learning era: A comprehensive survey," *arXiv preprint arXiv:2401.11734*, 2024.

[2] V. Bevilacqua, "Three-dimensional virtual colonoscopy for automatic polyps detection by artificial neural network approach: New tests on an enlarged cohort of polyps," *Neurocomputing*, vol. 116, pp. 62–75, 2013, advanced Theory and Methodology in Intelligent Computing. [Online]. Available: https://www.sciencedirect.com/science/article/pii/S0925231212006819

[3] J. Guo, S. Lu, L. Jia, W. Zhang, and H. Li, "Encoder-decoder contrast for unsupervised anomaly detection in medical images," *IEEE Transactions on Medical Imaging*, 2023.

[4] Y. Tian, F. Liu, G. Pang, Y. Chen, Y. Liu, J. W. Verjans, R. Singh, and G. Carneiro, "Self-supervised pseudo multi-class pre-training for unsupervised anomaly detection and segmentation in medical images," *Medical image analysis*, vol. 90, p. 102930, 2023.

[5] Y. Tian, G. Pang, F. Liu, Y. Chen, S. H. Shin, J. W. Verjans, R. Singh, and G. Carneiro, "Constrained contrastive distribution learning for unsupervised anomaly detection and localisation in medical images," in *Medical Image Computing and Computer Assisted Intervention-MICCAI 2021*. Springer, 2021, pp. 128–140.

[6] E. Sanderson and B. J. Matuszewski, "A study on self-supervised pretraining for vision problems in gastrointestinal endoscopy," *IEEE Access*, 2024.

An Energy-aware Decision-making scheme for Mobile Robots on a Graph Map based on Deep Reinforcement Learning

Gemignani Gabriele, Margherita Bongiorni, Lorenzo Pollini

July 13, 2024

Sequential control of Autonomous Mobile Robots (AMRs) at different levels has been a standard area of application of Deep Reinforcement Learning (DRL) over the past decade. This latter machine learning technique is notably less prone to the so called *curse of dimensionality* [1], with respect to optimization-based strategies, namely it is particularly adapt to large and highly dynamic environments. Besides that, the intrinsic formulation of model-free DRL [2] often produce controllers which are quite robust to unknown, even stochastic, dynamics, a topic that was historically considered of fundamental importance by researchers of the field and thus studied in various forms.

One of the key properties, yet rarely examined, when it comes to robots' long-term independence is the energy-awareness. The used expression implies more than just finding a minimum-consumption solution; it rather refers to the capability of autonomously discerning whether the energy left is sufficient in relation to the job and, whenever the scenario permits that, taking an action in favour of a battery recharge. Implementing such behaviour in a brutal force fashion, namely imposing a Return-to-Home (RtH) if battery drops below a certain level, would turn out to be a safe but too conservative solution, especially when dealing with complex operational scenarios.

The present work presents a DRL framework for an energy-aware high-level decision-making in a graph environment. A graph is in fact an abstract concept that can be applied to a wide variety of fields, fully justifying its use in a high-level control problem. To the best of the author's knowledge, [3] was the only previous paper in which the energy-awareness feature was properly included in the DRL formulation. Here, we try to further optimize the agent's behaviour by reshaping the reward feedback, penalizing both low battery levels as well as unnecessary time-wasting recharges.

As applicative case, we imagined a scenario where an autonomous service robot must react to alarms due to failures in its area of interest; the robot must have onboard the necessary servicing tool by resorting to a tool change station, reach the area of the failure and fix it, while at the same time managing its battery status. Once trained the model via Double Deep Q Network (DDQN) with Prioritized Experience Replay (PER) for around $5e5$ epochs, Fig.1 depicts a typical mission route on an arbitrary defined map. A common pattern to most of the episodes is that the agent first seeks to reach the warehouse to pick the tool corresponding to the failure type and eventually recharges itself if it finds it necessary. This occurs almost in every circumstance, except in those lucky ones in which the UAV is initialized with the same tool requested by the target; only then the path to the failure location may be direct without intermediate stops, provided that the battery to do so is sufficient.

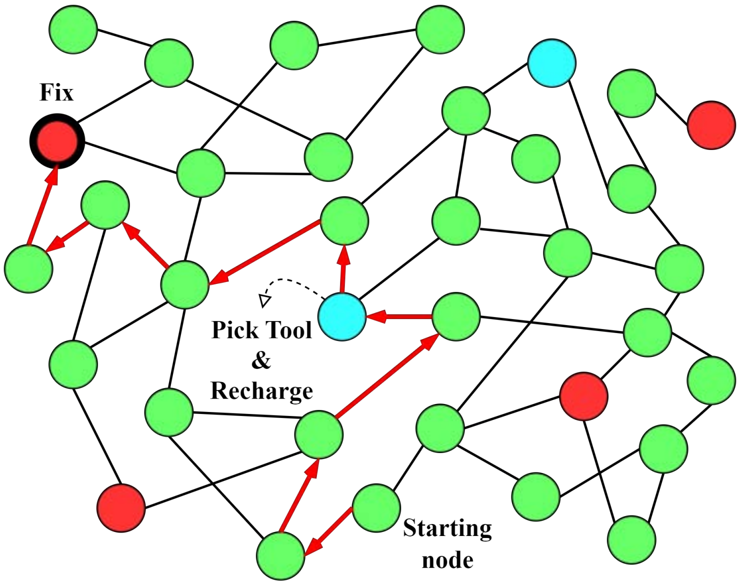

Figure 1: A graphical representation of the agent's optimal behaviour. The graph utilized as test-bed contains 35 nodes (green), among which 4 are targets (red) and 2 are warehouses (light blue). The active target is the one with the thicker black edge. All nodes are randomly positioned. Arcs are non-oriented and inserted without any logic. Moves along neighbouring nodes are indicated with red arrows.

As a last note, we remark that, although the proposed scenario is quite simple and a mixture of other "classical" techniques (e.g. shortest paths, decision trees etc.) might be employed to achieve a similar result, this experiment should be regarded as a proof of concept. We in fact identified this as a starting point for possible future contributions, for instance exploiting multiple intelligent agents communicating to cope with more challenging tasks and environments.

References

[1] Kai Arulkumaran et al. “Deep Reinforcement Learning: A Brief Survey”. In: *IEEE Signal Processing Magazine* 34.6 (Nov. 2017). Conference Name: IEEE Signal Processing Magazine, pp. 26–38. ISSN: 1558-0792. DOI: `10.1109/MSP.2017.2743240`. URL: `https://ieeexplore.ieee.org/abstract/document/8103164` (visited on 11/21/2023).

[2] Richard S Sutton and Andrew G Barto. *Reinforcement learning: An introduction*. MIT press, 2018.

[3] Omar Bouhamed et al. “A DDPG-based Approach for Energy-aware UAV Navigation in Obstacle-constrained Environment”. en. In: *2020 IEEE 6th World Forum on Internet of Things (WF-IoT)*. New Orleans, LA, USA: IEEE, June 2020, pp. 1–6. ISBN: 978-1-72815-503-6. DOI: `10.1109/WF-IoT48130.2020.9221115`. URL: `https://ieeexplore.ieee.org/document/9221115/` (visited on 04/18/2024).

Intelligent Systems for Predicting Disability Progression in Multiple Sclerosis Using Motor Evoked Potentials and Digital Twin Technology

Valeriana Mancazzo*, Elena Sibilano*, Antonio Brunetti*, Raffaele Carli*, Mariagrazia Dotoli* and Vitoantonio Bevilacqua*
* Department of Electrical and Information Engineering (DEI), Polytechnic University of Bari, 70126 Bari, Italy.

***Abstract*—Multiple Sclerosis (MS) is a chronic autoimmune disease that affects the central nervous system. Motor Evoked Potentials (MEPs) could provide insights into neural conduction and motor cortex functionality. Digital Twin (DT) has recently been proposed as a new paradigm that can implement individualized, innovative disease management through artificial intelligence models, dealing with the multidimensional complexity of several pathologies. This paper investigates a DT approach to predict motor disability progression in patients with MS by processing MEPs. Generative Artificial Intelligence (GAI) models have been deployed employing a Vision Transformer (ViT) for classification and a Class-Informed Variational Autoencoder (CI-VAE) for data augmentation. This approach utilizes a longitudinal dataset to forecast the progression of disability by evaluating variations in the Expanded Disability Status Scale (EDSS). DT driven by GAI for data management, analysis and modeling can be a promising paradigm for precision medicine.**

I. INTRODUCTION

Multiple Sclerosis (MS) is an inflammatory, immune-mediated and demyelinating disease of the central nervous system (CNS) characterized by a wide range of symptoms, disease courses and treatment responses. In fact, as the inflammatory and neurodegenerative process can involve a variety of different neuroanatomical locations in CNS, many functional neurological systems can be affected, ranging from visual, motor, cerebellar, sensory and cognitive problems. The prognosis is unpredictable and variable as a subset of patients show a benign course with minimal or none disability, while others may present progression and accumulation of significant disabilities leading to functional impairment. However considering that a reliable prediction of the disease course of MS is a requirement for individually tailored disease-modifying therapy, the monitoring and the prevention of progression become very crucial for patients.

Evoked Potentials (EPs) measurements provide an insight in neural conduction by stimulating a specific area of the nervous system and measuring the resulting signal at a determined area of the body. Specifically, Motor Evoked Potentials (MEPs) are acquired through the stimulation of the motor cortex (M1) using transcranial magnetic stimulation (TMS) while the electrodes are placed on hands and feet providing information on the signal conductivity from motor cortex to limbs. Therefore they can be a useful source of information of the patients' motor disability and be used for the prediction of disability progression.

In the literature, several prognostic models for multiple sclerosis already exist, but none of them adopt deep learning (DL) models to classify patients based on disability progression. Mainly, a machine learning analysis is performed, consisting of data preprocessing, extraction of the most relevant features, and subsequent classification or regression using models such as linear or logistic regression, support vector machines (SVMs) or Decision Trees [1]. In this paper, it will be used an innovative Digital Twin (DT) approach, whose concept was first introduced in 2002 when Michael Grieves delivered a presentation at the University of Michigan [2]. It was later brought into the medical field as a potential solution for precision medicine and was called Health Digital Twin (HDT). The HDT is a virtual mirror of patients that allow to simulate their state of health using data-driven analytical algorithms and theory-driven physical knowledge [3] and GAI has been recognized as a promising technology which can effectively assist the implementation of HDT.

This study aims to predict the progression of patients' motor disability based on MEPs by employing a DT approach that utilizes Deep Learning (DL) models, which serve as a support mechanism for the HDT implementation, encompassing data generation, model training, and classification processes.

II. MATERIALS AND METHODS

The publicly available longitudinal dataset [4] covers six years of follow-up and is characterized by full measurements timeseries (MEPs) recorded from the abductor pollicis brevis (APB) and the abductor hallucis (AH) muscles bilaterally. The dataset contains the Expanded Disability Status Scale (EDSS) measurements, which asses the level of disability of MS patients starting from 0 (absence of disability) to 10 (total disability). These values will be adopted for the determination of the two classes of patients upon an established condition. To predict the motor disability progression in patients, the change of EDSS values after two years from an initial baseline date T_0 is considered and only MEPs recorded during visits which are within an interval of ± 2 years from T_0 are included.

A. Analysis pipeline for Motor Evoked Potentials

MEPs were recorded from the APB and AH muscles bilaterally. Magnetic stimuli were delivered to the hand and leg areas of the motor cortex with a Magstim 2002 device (The Magstim Company Ltd., Whitland, UK). The signal is recorded for 100 milliseconds, starting from the moment of stimulation in the brain. The dataset contains measurements from two separate machines which have the same hardware but different acquisition rate (20 kHz for machine A, 19.2 kHz for machine B, respectively). For each limb, each excitation strength results in one timeseries and for each patient four distinct tests have been considered (APB-R, APB-L, AH-R, AH-L). An example of all the MEPs for a single visit is shown in Fig. 1. Only measurements acquired in visits 1 year before or after T_0 (date of the first EDSS of each patient) have been considered:

$$T_0 - 1\ year \leqslant VisitDate \leqslant T_0 + 1\ year$$

The signals have been resampled to 1920 points and MEPs with more than 100 ms of duration have been deleted. The "facilitated measures" in which the patient was asked to flex the limb to obtain a good measurement, have not been included. Finally, for each patient, only the three measurement with the maximum peak-to-peak amplitude for each type of test have been chosen. In the end, it has been created a dataset characterized by 333 patients, 982 visits and 11784 measures.

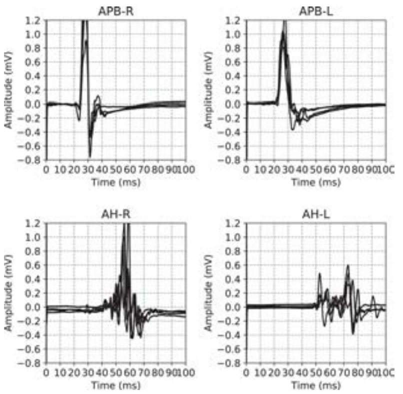

Fig. 1. Example of the MEP series recorded at a single visit. APB indicates that the signal is recorded from hands (R=Right and L=Left) while AH indicates the signal is recorded from feet.

B. ViT model for classification

Classification consists in the prediction of patients' motor disability progression after 2 years from the baseline date T_0. It has been considered the standard definition of disability progression, where the patient has progressed if $(EDSS_{T1} - EDSS_{T0} \geqslant 1)$ for $(EDSS_{T0} \leqslant 5.5)$ or if $(EDSS_{T1} - EDSS_{T0} \geqslant 0.5)$ for $(EDSS_{T0} > 5.5)$, where T_1 is the time of the EDSS measurement closest to the 2 year mark, between 1.5 and 3 years. In this way, the input is a collection of timeseries; the output is the presence (class Positive) or absence (class Negative) of disability progression. To classify input timeseries, we employed the Vision Transformer (ViT), a Generative Artificial Intelligence (GAI) model suited for sequence classification tasks. The dataset has been split into training (80 %) and test set (20 %) and k-fold cross validation has been applied ($k = 5$). For each fold, the model was trained over 200 epochs, and the Area Under the Curve (AUC) was computed for the train, validation and test set at each epoch. The highest validation AUC value across the 200 epochs was identified, and the corresponding model parameters were retained and used for the final performance metrics, i.e. AUC, accuracy, precision, recall, and F1-score, computed for each fold. The results from all folds were then averaged to obtain a robust estimate of the model's predictive capabilities and generalizability.

C. CI-VAE for data augmentation

The dataset provided for this study is characterized by a scarcity of data and class imbalance, in fact the Negative class is overestimated respect to the Positive class. These limitations can lead models to overfitting, expecially with complex DL architectures, and to poor performance on the minority class. To overcome these two issues, a Variational Autoencoder (VAE) with an additive classifier layer based on a Multilayer Perceptron (MLP) architecture has been implemented and called Class-Informed VAE (CI-VAE). The model is characterized by an encoder which transforms input data to a low-dimensional latent space representation z and a decoder that from z is able to reconstruct the original signals. In this way, the model is capable of synthesize new data, as shown in Fig. 2, as digital replica of the original ones which can be added to the previous dataset. The MLP layer takes z in input and classifies the input as Positive or Negative in order to enhance the linear separability between the two classes. After CI-VAE training, its parameters and weights are freezed in order to generate new signals starting from those targeted as Positives. In this way, the dataset input to the ViT is augmented and balancing between the two classes is achieved.

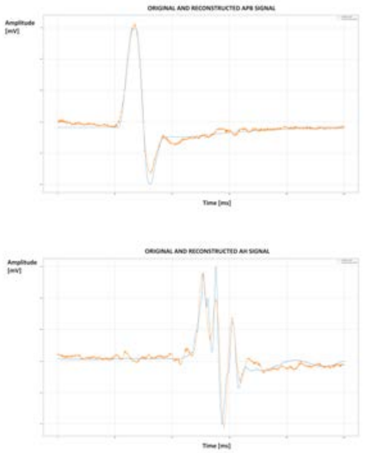

Fig. 2. Results of CI-VAE reconstruction of MEP signals recorded from hand (first figure above) and foot (second figure below). The blue signal is the original MEP; the orange signal is that reconstructed from CI-VAE.

III. CONCLUSIONS

In this paper, we emphasized the implementation of GAI-driven HDT for the construction of a predictive model for motor disability progression in MS. Specifically, GAI can generate diverse and highly realistic synthetic data and automatically extract the most relevant features for classification purposes. The aim was to refine the monitoring of the disease, improving the management of patients. These preliminary findings may have the potential application in the development of automated control systems designed for personalized therapeutic interventions and adaptable disease management in MS.

IV. ACKNOWLEDGEMENTS

The authors want to thank PNRR-D34H (Digital Driven Diagnostics, prognostics and therapeutics for Sustainable Health care) foundation with all its partners for the research enhancement activities on digital technologies in the healthcare sector. This work has been funded under the National Plan for Complementary Investments to the NRRP, project "D34H—Digital Driven Diagnostics, prognostics and therapeutics for sustainable Health care" (project code: PNC0000001), CUP: B53C22006170001, funded by the Italian Ministry of University and Research.

REFERENCES

[1] R. Seccia, S. Romano, M. Salvetti, A. Crisanti, L. Palagi, and F. Grassi, "Machine learning use for prognostic purposes in multiple sclerosis," *Life*, vol. 11, no. 2, p. 122, 2021.

[2] J. Chen, Y. Shi, C. Yi, H. Du, J. Kang, and D. Niyato, "Generative ai-driven human digital twin in iot-healthcare: A comprehensive survey," *arXiv preprint arXiv:2401.13699*, 2024.

[3] S. Cen, M. Gebregziabher, S. Moazami, C. J. Azevedo, and D. Pelletier, "Toward precision medicine using a "digital twin" approach: modeling the onset of disease-specific brain atrophy in individuals with multiple sclerosis," *Scientific Reports*, vol. 13, no. 1, p. 16279, 2023.

[4] J. Yperman, V. Popescu, B. Van Wijmeersch, T. Becker, and L. M. Peeters, "Motor evoked potentials for multiple sclerosis, a multiyear follow-up dataset," *Scientific Data*, vol. 9, no. 1, p. 207, 2022.

Advanced control strategies with applications to sustainable bioprocesses

Francesco Campregher, Antonio Visioli

DIMI, University of Brescia, Piazza del Mercato, 15 - 25121 Brescia
`francesco.campregher@unibs.it, antonio.visioli@unibs.it`

Water pollution and global warming are two critical issues plaguing our society. Microalgae offers a compelling solution [1] that can tackle both problems simultaneously. They consume nitrogen, phosphorus, and other harmful substances, as well as CO2 through their photosynthetic nature. Microalgae are cultivated in various bioreactors, such as tubular, raceway, and thin layer. The raceway bioreactor has proven to be the most suitable due to its higher biomass production rate, which leads to a greater volume of purified water and consumed CO2.

Fig. 1: Raceway bioreactor at Universidad de Almeria, Almeria

However, the system's nonlinear behavior and sensitivity to atmospheric conditions influence its effectiveness. To ensure this promising solution is efficient, it must be maintained in optimal operating conditions. Therefore, advanced control approaches are necessary to keep the system at its optimum operating point. In the literature, examples of control solutions exist for this problem mainly based on Proportional Integrative Derivative (PID) controllers [2,3,4].

We have chosen a model-based control algorithm to guarantee the process's optimality. By studying and developing accurate models of the system, we aim to precisely control and enhance its performance. At a low level, the raceway reactor is modeled as a MIMO system, as shown in Figure 2, where the controlled variables are the dissolved oxygen and pH. The control variables are CO2 injection and air injection in the medium. CO2 injection decreases the pH level which is increased by the microalgae photosynthetic process and provides nutrients to them, air injection reduces the dissolved oxygen in the medium increased by the microalgae photosynthetic process. Solar irradiance and medium temperature are measured disturbances.

Currently, we are developing a linear Model Predictive Control for the low-level pH control. We have designed the inputs for the MIMO system in such a way that the inputs are uncorrelated and respect the concept of persistent excitation. The reactor presents an integrator-like behavior for this reason a conventional open-loop identification framework is not feasible, therefore we have developed a closed-loop identification method, which preserves the uncorrelation characteristic of the input signals. We are identifying the bioreactor as a block-oriented model, such as the Wiener or Hammerstein models, taking advantage of the fact that the dynamic of the system in a day is almost linear.

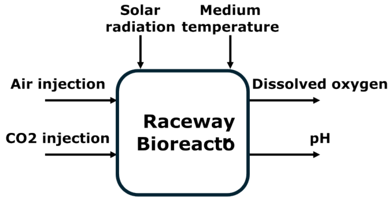

Fig. 2: Raceway reactor model

The ultimate goal of our project is to develop a comprehensive framework that not only enhances the efficiency of the microalgae process but also makes it cost-effective and sustainable thanks to the economic value of biomass. By optimizing the microalgae growth rate, we can maximize their water-purifying and CO2-consuming capabilities. The biomass's economic value is because it can be used as fertilizer, biofuel, and more.

References

1. Y. Wang, S.-H. Ho, C.-L. Cheng, W.-Q. Guo, D. Nagarajan, N.-Q. Ren, D.-J. Lee, J.-S. Chang, Perspectives on the feasibility of using microalgae for industrial wastewater treatment, Bioresource Technology 222 (2016) 485–497. `doi:https://doi.org/10.1016/j.biortech.2016.09.106`.
   URL https://www.sciencedirect.com/science/article/pii/S0960852416313736
2. A. Pawlowski, J. Guzmán, M. Berenguel, F. Acién, Control system for ph in raceway photobioreactors based on wiener models, IFAC-PapersOnLine 52 (1) (2019) 928–933, 12th IFAC Symposium on Dynamics and Control of Process Systems, including Biosystems DYCOPS 2019. `doi:https://doi.org/10.1016/j.ifacol.2019.06.181`.
   URL https://www.sciencedirect.com/science/article/pii/S2405896319302691
3. I. Fernández, J. Peña, J. Guzman, M. Berenguel, F. Acién, Modelling and control issues of ph in tubular photobioreactors, IFAC Proceedings Volumes 43 (6) (2010) 186–191, 11th IFAC Symposium on Computer Applications in Biotechnology. `doi:https://doi.org/10.3182/20100707-3-BE-2012.0046`.
   URL https://www.sciencedirect.com/science/article/pii/S1474667016303524
4. M. Caparroz, P. Otálora, J. L. Guzmán, M. Berenguel, F. G. Acién, Modelado y control del ph en la producción de microalgas en reactores raceway usando técnicas de adaptación de parámetros, Revista Iberoamericana de Automática e Informática industrial 20 (4) (2023) 379–388.

A mixed-integer charging schedule for electric vehicles with request-dependent pricing

1st Mahsa Ghavami
DAUSY
Politecnico di Bari
Bari, Italy
m.ghavami@phd.poliba.it

2nd Davide Liuzza
Dept. of Engineering
University of Sannio
Benevento, Italy
liuzza@unisannio.it

3rd Elisa Mostacciuolo
Dept. of Engineering
University of Sannio
Benevento, Italy
emostac@unisannio.it

4th Luigi Iannelli
Dept. of Engineering
University of Sannio
Benevento, Italy
luiannel@unisannio.it

5th Francesco Vasca
Dept. of Engineering
University of Sannio
Benevento, Italy
vasca@unisannio.it

I. EXTENDED ABSTRACT

Nowadays Electric Vehicles (EVs) have become much more popular thanks to the advancement in battery technology and the government's efforts to reduce carbon emissions. Due to the growing number of EVs and the limited charging resources like available electric power and chargers, it is essential to manage EVs charging demand from the grid. A demand response program is an effective method for demand-side management [1], whereby the charging cost of EVs decreases, and the grid reliability increases. For the demand-side management, authors in [2] have assumed that the electricity price depends on the amount and time of consumption. Then, the demand can be shifted from the on-peak hours to the off-peak. To model the charging control system, the study of multi-agent systems has attracted considerable attention. Authors in [1]–[6] have considered EVs as agents and designed a control method for the charging management system. The key assumption in these references is that there are enough chargers in one charging station. Therefore the sole problem is to schedule EVs. In case there are a limited number of chargers in one station and the number of EVs requesting the charge is more than the chargers installed in one station, there is a resource allocation problem that specifies whether one EV should be connected or not and how much charge it should receive in each time. For this problem, some binary variables should be defined to determine the status of connection of each EV to the chargers at each time. Authors in [6] have proposed a mixed-integer game formulation for the charging schedule of EVs. The proposed price scheme in [6] incorporates the Time-Of-Use(TOU) tariff and the total energy demand. For this price function, when the total number of EVs is more than the number of chargers, the price might not increase when the total number or request of EVs increases. However, in real-world booking systems, by increasing the request and the fixed limited resources, the price should increase. To this aim, in this paper, a new pricing policy has been designed that models the charging request of all EVs, including satisfied or dissatisfied EVs. In this paper, we have considered EVs as cooperative agents in the multi-agent system that they cooperatively aim to minimize the charging cost, battery degradation cost, and the cost of deviation from their desired state of charge. The charging cost depends on the new proposed charging price. Additionally, we have analyzed the effect of the new pricing scheme on peak shaving and the EVs charging satisfaction. The problem formulation has been described as follows. Let $\mathcal{N} := \{1, ..., N\}$ be a finite set of EVs and $t \in \mathcal{T} \subset \mathbb{N}$ be a generic discrete time-step over the finite time horizon $\mathcal{T} = \{1, ..., T\}$. For each EV $i \in \mathcal{N}$, the State Of Charge (SOC) of the battery at the time t is denoted by $x_i(t) \in [0, 1]$, where $x_i(t) = 1$ occurs when the battery is fully charged and $x_i(t) = 0$ when the battery is completely discharged. The dynamic of SOC is defined as follows

$$x_i(t+1) = x_i(t) + \frac{\mu_i}{\nu_i} u_i(t), \tag{1}$$

where $x_i(0) = x_i^0 \in [0, 1]$ is initial SOC, where $\mu_i \geq 0$ is the battery efficiency of the i-th EV, $\nu_i > 0$ is its battery capacity and $u_i(t) \in \mathbb{R}_+$ is the amount of electric power transferred to the i-th EV at time t. We assume that the i-th EV aims to reach the final SOC $x_i(T) = x_i^F$. we also consider the binary variable $\delta_i(t) \in \{0, 1\}$, $i \in \mathcal{N}$, where $\delta_i(t) = 1$ if at time t the i-th EV is connected to a charger and $\delta_i(t) = 0$ otherwise. When the EV is plugged in, the amount of power it receives can be positive. This condition is represented using the following logical constraints:

$$\delta_i(t) = 0 \Longrightarrow u_i(t) = 0, \;, \delta_i(t) = 1 \Longrightarrow u_i(t) \in [\underline{u}, \overline{u}], \tag{2}$$

where $\underline{u}, \overline{u} \in \mathbb{R}_+$, and $\overline{u} > \underline{u} \geq 0$. Another condition is that when the i-th EV is connected to the charging station then it remains connected for a time horizon of length $\ell_i \in \mathbb{N}$, $i \in \mathcal{N}$:

$$[\delta_i(t-1) = 0] \wedge [\delta_i(t) = 1] \Longrightarrow \delta_i(t+\ell) = 1. \tag{3}$$

Also, a single charging station with $\bar{c}$ chargers is considered:

$$\sum_{i \in \mathcal{N}} \delta_i(t) \leq \bar{c}. \tag{4}$$

The total energy demand from the grid can be expressed as

$$\mathcal{E}_d(t) = d(t) + \sum_{i \in \mathcal{N}} u_i(t), \tag{5}$$

The activities have been partially supported by the research project PSC Campania–Piano B, H-MOBILITY, CUP B32C18000250007.

where $d(t) \in \mathbb{R}_+$ is the total inelastic non-EVs lo the limitation of the grid capacity, we assume

$$0 \leq \mathcal{E}_d(t) \leq \bar{\mathcal{E}},$$

where $\bar{\mathcal{E}}$ is the maximum capacity of the grid. The charging schedule where all EVs aim to minimize is formulated as

$$\min_{u,\delta,x} \sum_{i=1}^{N} J_i(u_i, u_{-i}, x_i, x_{-i})$$
$$s.t. \quad (1)-(4),(6) \quad \forall i \in \mathcal{N}.$$

The cost function J_i is given as

$$J_i(u_i, u_{-i}, x_i, x_{-i}) = J_i^{\text{sat}} + \sum_{t\in\mathcal{T}} \Big(J_i^{\text{buy}}(t) + J_i^{\text{de}}$$

where $u_{-i} = \text{col}((u_j)_{j\in\mathcal{N}\setminus\{i\}})$ and $x_{-i} = \text{col}((x_{j})_{j\in}$ $i \in \mathcal{N}$. J_i^{sat} is the cost of deviation from the desired va and defined as

$$J_i^{\text{sat}} = \theta_i (x_i(T) - x_i^F)^2,$$

where $\theta_i \in \mathbb{R}_+$ shows the monetary value of the devia the final SOC from the desired SOC x_i^F. The term in (8) is the cost of purchasing electricity and is defin

$$J_i^{\text{buy}}(t) = p(t) u_i(t),$$

where the price per unitary energy $p(t) \in \mathbb{R}_+$ is defin

$$p(t) = h(t) + q_1 r(t) + q_2 \sum_{i\in\mathcal{N}} \eta_i(t)(x_i^F - x_i^0), \tag{11}$$

where q_1 is set based on the grid policy and $h(t)$ is the TOU pricing tariff. In this paper, we have defined q_2 to model the total EV demand in the price function. The variable $r(t)$ represents the effects of the total satisfied demand [3] and it can be defined as follows

$$r(t) = \frac{1}{\gamma(\bar{c}, \bar{\mathcal{E}})} \mathcal{E}_d(t) = \frac{1}{\gamma(\bar{c}, \bar{\mathcal{E}})} \left(d(t) + \sum_{i\in\mathcal{N}} u_i(t) \right). \tag{12}$$

$J_i^{\deg}(t)$ is the battery degradation cost and defined as

$$J_i^{\deg}(t) = a_i (u_i(t))^2 + b_i u_i(t), \tag{13}$$

where $a_i \in \mathbb{R}_+$ and $b_i \in \mathbb{R}_+$ are parameters of the b degradation cost. Figures 1-3 show the results of the res Figure 1 shows the effects of changing q_2 on the dissatisf of all EVs. By analyzing Fig. 1, we have chosen the a priate limitation of the parameter $q_2 \in [0, 0.1]$ in orde the dissatisfaction of EVs does not increase a lot. In F we have shown the sensitivity of the proposed price fu $p(t)$ to the selected limitation for q_2 obtained from ana Fig. 1. Figure 3 shows non-EV load (blue curve) and tot demand (red curve). As shown, by employing the pro system, EVs are encouraged to be charged when the no load is less.

REFERENCES

[1] Z. Zhou, F. Zhao, and J. Wang, "Agent-based electricity market sin with demand response from commercial buildings," in *IEEE Pov Energy Society General Meeting*, 2012, pp. 1–1.

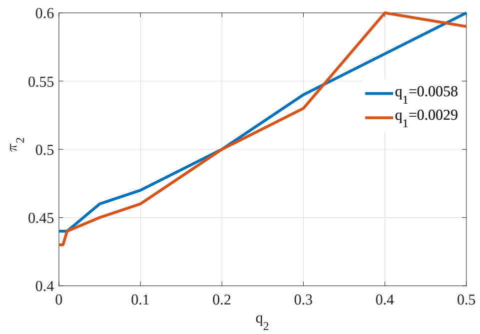

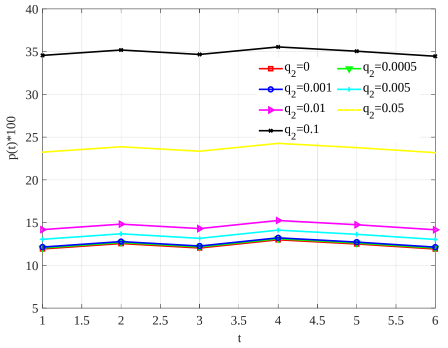

Fig. 2. The effect of q_2 on $p(t)$ for $q_1 = 0.0058$.

[2] A. Joshi, H. Kebriaei, V. Mariani, and L. Glielmo, "Decentralized control of residential energy storage system for community peak shaving: A constrained aggregative game," in *IEEE Madrid PowerTech*, 2021, pp. 1–6.

[3] Z. Ma, D. S. Callaway, and I. A. Hiskens, "Decentralized charging control of large populations of plug-in electric vehicles," *IEEE Transactions on Control Systems Technology*, vol. 21, no. 1, pp. 67–78, 2013.

[4] M. Ghavami, B. G. Bakhshayesh, M. Haeri, G. Como, and H. Kebriaei, "A consensus-based generalized multi-population aggregative game with application to charging coordination of electric vehicles," *IEEE Control Systems Letters*, vol. 7, pp. 3435–3440, 2023.

[5] H. R. Babaei Ghazvini, M. Ghavami, and M. Haeri, "Distributed nash equilibrium seeking of residential energy grids over unreliable communication networks using predictive control," *AUT Journal of Modeling and Simulation*, vol. 55, no. 1, pp. 139–154, 2023.

[6] C. Cenedese, F. Fabiani, M. Cucuzzella, J. M. A. Scherpen, M. Cao, and S. Grammatico, "Charging plug-in electric vehicles as a mixed-integer aggregative game," in *IEEE 58th Conference on Decision and Control*

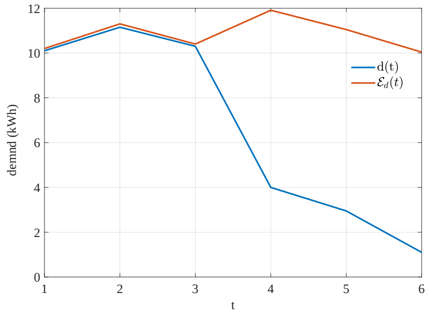

Fig. 3. Non-EV and total demand from the grid.

An Agent-Based Model to foster Citizens' Sustainable Behavior in the Italian City of Siena

Vittoria Socci,[1] Chiara Mocenni[1]

1. Department of Information Engineering and Mathematics, University of Siena, Via Roma, 56, 53100 Siena, Italy

Climate change is irreversibly having an increasing impact on the environment, people, and the economy worldwide [1]. Although not decisive without the synergistic actions of stakeholders and policymakers, the contribution of each individual in counteracting its effects is crucial, as everyday actions can shape a more resilient and sustainable future.

In [2] we propose a georeferenced agent-based model (ABM) for the Italian city of Siena whose agents are people who live in the historic center of the city and whose goal is to promote sustainable behaviors among them. The ABM is being developed using Netlogo and starting from a survey administered to 324 citizens, representing a sample of the considered population and consisting of the model agents. The answers concern the agents' georeferentiation and individual climate awareness evaluated in terms of their propensity to be cooperative toward sustainable actions, such as for example waste recycling, cleaning public spaces, and so on. This produces five behavioral traits, which correspond to five different types of evolutionary games, including Prisoner's Dilemma (PD), Stag-Hunt (SH), Hawk-Dove (HD) and fixed-strategy games, cooperative (A) or defective (D), and implying that the ABM's human decision-making (DM) is modeled using game theory [3]. Each agent, regardless of its behavioral propensity, chooses at each iteration between two fixed strategies: cooperation (sustainable actions) and defection (the opposite).

We obtain initial findings by analyzing the survey data set, which is then used to adjust the ABM, with respect to the analysis of climate awareness and the sample's composition. Our findings show significant and surprising differences across age, gender and educational level groups, discovering for instance that younger individuals are not the most aware. Concerning the sample composition, we find, as expected, a prevalence of PD players, followed by SH, HD, fixed cooperators, and finally full defectors.

Social interaction is a key element in human DM, as decisions depend on individual propensities and the choices of others [4]. In our work, this is considered by locating the ABM on a graph whose nodes are the 324 agents of the sample and whose connections represent their interactions. The ABM is initially developed to a theoretical case, called the Basic Model (BM), where the 324 agents have all the features obtained from the survey except for the geographical location on the map of Siena and they are positioned to form a 2-dimensional lattice, thus representing a city with a perfectly regular urban structure. Subsequently, the ABM is fully adapted to our case study, the so-called Siena model (SM), where the 324 agents are also georeferenced on the city map (Fig.1). In both model versions, we explore two graph scenarios: one with links representing geographical proximity connections, and another with a small-world (SW) topology, embedding agents' social networks of friendships into the DM.

The simulations of the ABM allow us to evaluate how cooperation among citizens towards sustainability spread in the Italian city of Siena. We find different levels of cooperation depending on the model version and the network topology, detecting significant variations not only between the geographical and SW networks but also between the Basic and Siena models. Notably, the geographical network appears less cooperative than the others, thus opening interesting questions on the effects of the urban structures of cities and their modeling.

A new, more extensive and structured survey is presently being distributed in a project supported by the municipal administration to extend the ABM to the entire population (approximately 10000 agents) living in Siena, including also temporary residents such as students, tourists, and visitors [5]. The ABM created with this new data collection will simulate the behavior of the entire population, not only to a sample, although representative, as in the previous case. The resulting agent-based model will be used to study measures to foster sustainable behaviors at the individual level, contributing to fighting climate

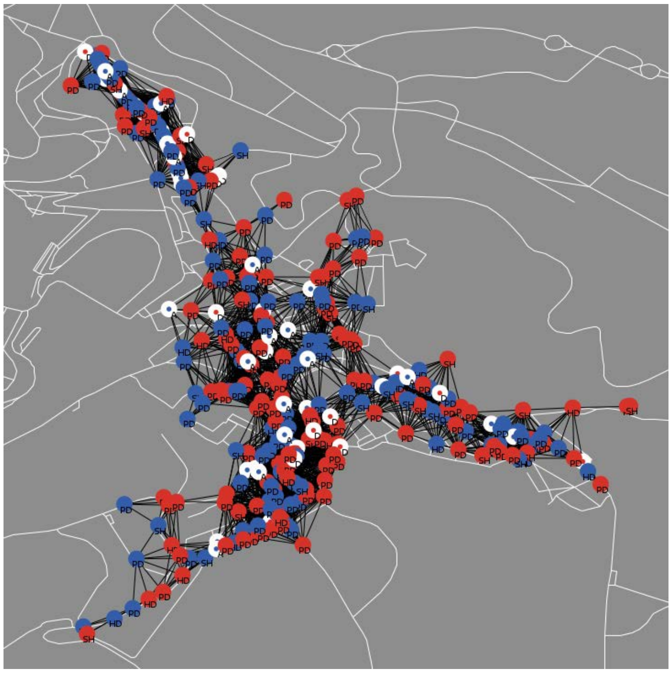

Figure 1: Siena Model (SM) visualization in the Netlogo world display at initial time t = 0. The white lines represent Siena's road network, while the black ones are the links of the model's graph. The five different games A, D, PD, SH and HD are represented by labels on the nodes, which are the 324 agents georeferenced on the Siena map.

change, developing and personalizing intervention strategies, and adapting sustainable policies based on the specific needs of citizens. The new data collection will also allow for the validation of the previous model.

Furthermore, the ABM will be placed in the context of distributed control by incorporating previously trained special agents acting as pinner nodes into the network [6]. Preliminary results show that these types of agents are the SH players rather than full cooperators, while the nodes to be acted upon, called pinned nodes, are PD players.

[1] Abbass K. *et al.*: A review of the global climate change impacts, adaptation, and sustainable mitigation measures. *Environ Sci Pollut Res* **29**, 42539–42559 (2022).
[2] Socci V. *et al.*: An Agent-Based Model to foster citizens' sustainable behavior in the Italian city of Siena, (2024). (Submitted to *EPJ B Topical Issue: Recent Advances in Complex Systems*).
[3] Adami C. *et al.*: Evolutionary game theory using agent-based methods. *Physics of life reviews* **19**, 1–26 (2016)
[4] Bianchi F. *et al.*: Agent-based models in sociology. Wiley Interdisciplinary Reviews: Computational Statistics **7**(4), 284–306 (2015)
[5] `mas.diism.unisi.it`
[6] Ancona C. *et al.*: Influencing opinions in a nonlinear pinning control model. *IEEE Control Systems Letters*, vol. 7, pp. 1945-1950 (2023).

Adaptive Robust Controller for handling Unknown Uncertainty of Robotic Manipulators

Mohamed Abdelwahab[1], Giulio Giacomuzzo[1], Alberto Dalla Libera[1], Ruggero Carli[1]

***Abstract*— The ability to achieve precise and smooth trajectory tracking is crucial for ensuring the successful execution of various tasks involving robotic manipulators. State-of-the-art techniques require accurate mathematical models of the robot dynamics, and robustness to model uncertainties is achieved by relying on precise bounds on the model mismatch. In this paper, we propose a novel adaptive robust feedback linearization scheme able to compensate for model uncertainties without any a-priori knowledge on them, and we provide a theoretical proof of convergence under mild assumptions. We evaluate the method on a simulated RR robot. First, we consider a nominal model with known model mismatch, which allows us to compare our strategy with state-of-the-art uncertainty-aware methods. Second, we implement the proposed control law in combination with a learned model, for which uncertainty bounds are not available. Results show that our method leads to performance comparable to uncertainty-aware methods while requiring less prior knowledge.**

I. INTRODUCTION

In modern industries, the demand for industrial robots spans various applications such as welding, spraying, assembly, handling, transportation, and precise manufacturing. As the complexity of tasks increases, the requirements for robotic controllers escalate. This paper addresses the trajectory tracking control problem for industrial robots, focusing on designing controllers capable of driving a robot to track a desired trajectory within a pre-assigned tolerance. Traditional approaches include PID control, feedback linearization, adaptive control, robust control, sliding mode control, neural network control, fuzzy control, iterative learning control, and reinforcement learning.

We focus on feedback linearization control, known for its remarkable performance with accurate system models. This method employs a cascade of loops: an outer loop eliminates the system's nonlinearities, and an inner loop stabilizes the dynamics using feedforward and PD control. Challenges arise with model mismatches, where traditional robust control methods require a priori uncertainty bounds.

II. PROBLEM FORMULATION

In this paper, we focus on a class of Lagrangian systems whose dynamics can be described by

$$M(q(t))\ddot{q}(t) + C(q(t),\dot{q}(t))\dot{q}(t) + g(q(t)) = \tau(t), \quad (1)$$

where

- $q = [q_1, \dots, q_N]^T$ denote the N-th dimensional vector of generalized coordinates; accordingly, $\dot{q} = [\dot{q}_1, \dots, \dot{q}_N]^T$ and $\ddot{q} = [\ddot{q}_1, \dots, \ddot{q}_N]^T$ are the vectors of the generalized velocities and accelerations, respectively;
- $M(q(t)) \in \mathbb{R}^{N\times N}$ represents the inertia matrix which is a definite positive matrix for any $q(t)$;
- $C(q(t),\dot{q}(t)) \in \mathbb{R}^{N\times N}$ depends on the Coriolis and centrifugal forces;
- $g(q(t)) \in \mathbb{R}^N$ describes the gravitational effects;
- $\tau = [\tau_1, \dots, \tau_N]^T$ represents the vector of the generalized torques applied to system.

We consider the problem of making the system positions, velocities and accelerations $(q(t), \dot{q}(t), \ddot{q}(t))$ to track a desired trajectory $\left(q^d(t), \dot{q}^d(t), \ddot{q}^d(t)\right)$.

Traditional control architectures assume perfect model knowledge. In practice, this assumption is rarely met, leading to unavoidable model uncertainty. Robust control strategies typically include a compensating term w, designed via the Lyapunov direct method, requiring knowledge of the uncertainty bounds.

III. ADAPTIVE ROBUST FEEDBACK LINEARIZATION CONTROL

The method we propose is a robust version of the feedback linearization strategy [1] of the form

$$\tau = \hat{M}(q)\left(\ddot{q}_d + K_P e + K_D \dot{e} + \rho\frac{z}{\|z\|}\right) + \hat{n}(q,\dot{q}), \quad (2)$$

with $z = D^T Q\xi$, and ρ is updated by:

$$\dot{\rho} = \begin{cases} k_\rho & \text{if} \quad \dot{V} \geq 0 \text{ and } \|z\| \geq \epsilon \\ 0 & \text{if} \quad \text{otherwise} \end{cases} \quad (3)$$

where $k_\rho > 0$ adjusts the increase rate of ρ. This update law ensures compensation for model uncertainties by increasing ρ when the Lyapunov function's derivative is non-negative[2]. The results presented are derived under the assumptions outlined in [2], accompanied with the corresponding proofs.

IV. NUMERICAL RESULTS

We evaluate the Adaptive Robust Feedback Linearization (ARFBL) on a simulated 2-DOF RR planar manipulator. We designed a trajectory tracking experiment, where the reference trajectory of the i-th joint, is defined by the sum of random sinusoidal trajectories.

In all experiments, the controller parameters in (2) and (3) are set with proportional and derivative gains as diagonal matrices defined as $K_P = k_p I$ and $K_D = k_d I$, with I being the identity matrix, $k_p = 100$, and $k_d = 2\sqrt{k_p}$. The parameter ϵ was set to 0.5, resulting in almost no chattering. The experiments used $K_\rho = 1000$ for the first experiment and $K_\rho = 500$ for the second experiment. In both numerical examples we compare the performance of the ARBFL only for joint 2, but similar results also hold for joint 1.

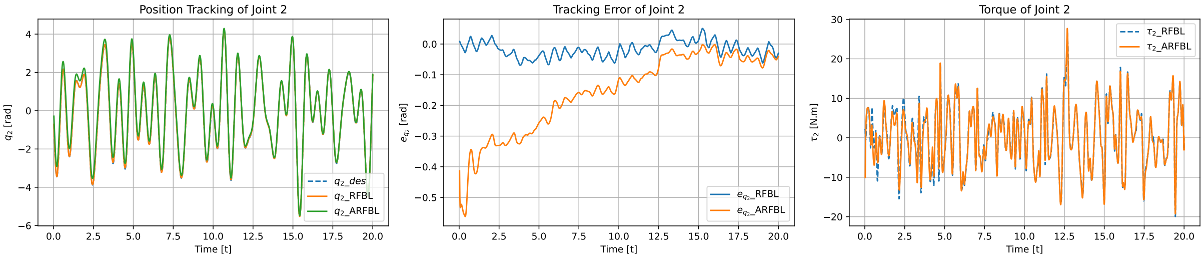

Fig. 1. Implementation results of ARFBL compared to RFBL

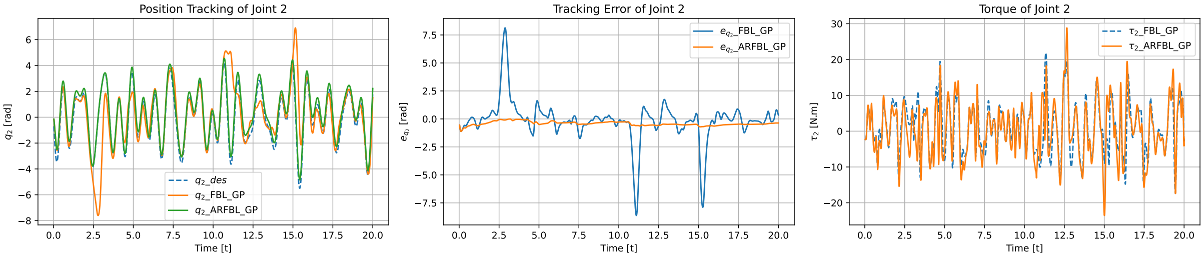

Fig. 2. Feedback linearization Vs. Adaptive robust feedback linearization using GP estimated dynamics

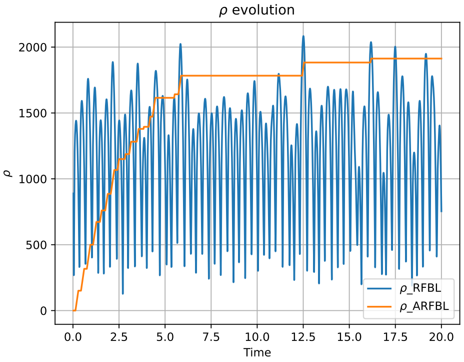

Fig. 3. ρ evolution of the proposed update method Vs True ρ from RFBL

A. *First Experiment: Perturbed dynamics*

In Fig. 1, we compare ARFBL with Robust Feedback Linearization (RFBL), showing ARFBL achieves similar tracking performance without requiring prior uncertainty knowledge, while in Fig. 3 we plot the evolution of ρ. Results show that the ARFBL scheme converges to the same error dynamics of the standard RBFL, despite being independent of a priori knowledge concerning the uncertainty bounds.

B. *Second Experiment: black-box dynamics*

In this experiment, we considered a black-box dynamics model based on GPR, for which it is not possible to derive the uncertainty bounds.

In Fig. (2), ARFBL significantly outperforms standard Feedback Linearization (FBL), maintaining lower tracking errors and smoother torque profiles. Additionally, in Fig. 4, we report the evolution of ρ. We observe that ρ increases in all input regions where the GP dynamics fail to cancel the non-linearity properly and stabilizes at a constant value upon the error's entrance into the boundary region.

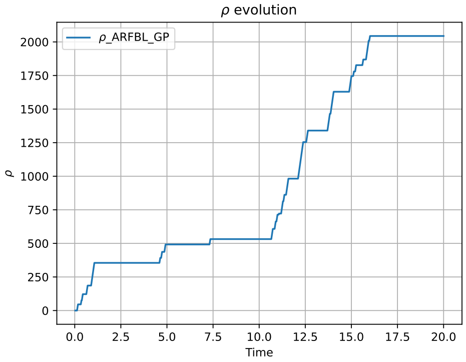

Fig. 4. ρ evolution using ARFBL when modeling dynamics using GPR

V. CONCLUSIONS

We introduce a novel adaptive robust feedback linearization scheme compensating for model uncertainties without prior bounds. Theoretical analysis and numerical experiments validate the proposed method's effectiveness in achieving robust trajectory tracking. Future work will extend the update law to allow ρ to decrease, aiming for dynamics closer to standard RFBL. The ARFBL strategy offers a promising approach for robust control in uncertain scenarios, enabling reliable trajectory tracking for complex robotic systems..

REFERENCES

[1] B. Siciliano, L. Sciavicco, L. Villani, and G. Oriolo, "Modelling, planning and control," *Advanced Textbooks in Control and Signal Processing. Springer,*, 2009.

[2] M. Abdelwahab, G. Giacomuzzo, A. D. Libera, and R. Carli, "Adaptive robust controller for handling unknown uncertainty of robotic manipulators," 2024.

A quantitative systems biology approach to characterize advanced gastric cancer response

Michela Prunella*, Nicola Altini*, Paolo Scarabaggio*, Raffaele Carli*,
Mariagrazia Dotoli*, and Vitoantonio Bevilacqua*
* Department of Electrical and Information Engineering (DEI), Polytechnic University of Bari, 70126 Bari, Italy.

I. INTRODUCTION

At the beginning of 2024, the U.S. Food & Drug Administration launched the *Project Optimus* [1] with the aim to improve the dose-optimization process, minimize toxicity, and improve benefits for patients in oncology drug development. One challenge is using mechanistic modeling approaches followed by quantitative analysis to provide clinical teams with safety and efficacy indicators of a treatment plan according to the specific patient conditions.

Oncology clinical trials have very strict eligibility criteria, that, although necessary to establish the intervention efficacy, permit to adequately represent only a subsample of the broader actual patient population. Moreover, elderly patients or those with a dismal prognosis usually do not meet the inclusion criteria. These aspects can limit the generalizability of the results in the real world, where an increased rate of adverse events is observed due to the higher variability of conditions in patients receiving treatment. As a consequence, the interruption of therapy is mandatory and patients experience both shorter survival and a poorer quality of life.

Here, we describe a quantitative method that integrates real-world data into mathematical disease modeling to address the above-mentioned issues. We have developed a simulation model that manages to reproduce the disease outcomes observed in a large study cohort of patients with gastric cancer, thus being able to support the decision-making of oncologists in the scheduling of treatment.

The tumor is a biological tissue with abnormal increased proliferative signaling and vigorous metabolism, in which angiogenesis assumes a catalytic role, since the tumor's ability to induce or access vasculature promotes the enlargement and cancerization of both the surrounding and distal tissues. Here, we utilize a mechanistic model to couple the dynamics of vessel networks, which are made of both mature and newly-formed vessels, with the tumor core development, in order to make predictive simulations and gain insights into the impact of drug scheduling.

In addition, compared with monotherapy, the combination of anti-tumor drugs enhances the therapeutic efficacy since they target synergistically such deregulated signaling pathways. More specifically, the order of administration of combined drugs should be optimized such that the action of one drug promotes the effectiveness of the subsequent therapies, by making the tumor tissue and its microenvironment more susceptible to the action of other drugs. In the last twenty years, evidence showed that anti-angiogenic therapies, by pursuing a vessel normalization process, can increase the efficacy of conventional therapies, i.e., cytotoxic drugs, if both are carefully scheduled [2].

II. MATERIALS AND METHODS

We used data from a large study, named KCSG-ST19-16 [3], that was conducted on a real-world cohort of 1021 patients suffering from gastric cancer. Data included baseline patient and tumor characteristics, treatment data, and tumor response. Among these, the Eastern Cooperative Oncology Group (ECOG) performance status is included, with integers ranging from 0, meaning a good health status, and 5, corresponding to death. This scoring system evaluates how a patient's disease affects their daily activities and is crucial for doctors in determining the appropriate treatment.

These patients received a second-line combination therapy consisting in Ramucirumab (*'R'*), which is an anti-angiogenic monoclonal antibody plus Paclitaxel (*'P'*), which is a chemotherapeutic agent with cytotoxic effect. The standard administration schedule [*'PR', 'P', 'PR'*] was implemented, as provided by the RAINBOW clinical trial [4], in which the three infusions were spaced 7 days apart with a washout period of 14 days before the second cycle. The response assessment occurred after three treatment cycles through a radiological evaluation of the disease burden. Tumor response was assessed by investigators using the Response Evaluation Criteria in Solid Tumors (version 1.1), thus reporting cases of complete response (CR), progressive disease (PD), partial response (PR), and stable disease (SD). The RAINBOW trial involved all patients with an ECOG score of 0 or 1, while the KCSG-ST19-16 contained 97 patients (9.2%) with a score of 2, 3, or 4, thus adding much variability in the patients' conditions. Patients with low ECOG have better prognosis and experience more frequently higher responses (i.e. CR, PR, SD), than those with high ECOG values, as shown in Figure 1a).

A. Mathematical model

The system of ordinary differential equations (ODEs) derives from the model proposed by Benzekry et al. [5]. The Eq.(1.a) describes the total tumor burden $x(t)$ over time as a function of the proliferative rate μ_C and the carrying capacity $s(t)$, which corresponds to the mature fraction of the vascular network. The second term of Eq. (1.a) describes the tumor reaction to cytotoxic drug concentration $C(t)$; the delayed effect of the drug with respect to the tumor cells exposure is taken into account with a transit compartment model that describes the cells undergoing progressive degrees of damage by passing through $n = 4$ different stages before death with $K_{transit}$ rate. The Eq. (1.b) describes the dynamic of the carrying capacity $s(t)$. This is obtained from the balance between the maturation λ of unstable vessels $u(t)$ and the natural death τ of stable vessels $s(t)$. The Eq. (1.c) models the pro-angiogenic effect γ on unstable vessels $u(t)$ provided by the tumor $x(t)$ and by subtracting the fraction of vessels $u(t)$ that become stable with a rate λ. This stimulatory effect is exerted by the fraction of active tumor cells $x_1(t)$. On the other hand, the tumor slightly inhibits new vessels formation to elude uncontrolled tumor growth; this was reflected in the term $-\delta x(t)^{\frac{2}{3}} s(t)$ in the original Benzekry model. We substituted it with the auxiliary equation (2), weighting the inhibitory effects on the residual life of tumor cells. The second term in Eq. (1.c) represents the effect of anti-angiogenic drug concentration $A(t)$, with $q(t)$ measuring the quality of vascolature and hence the distribution of the drugs to the target tissue, according to auxiliary equation (3).

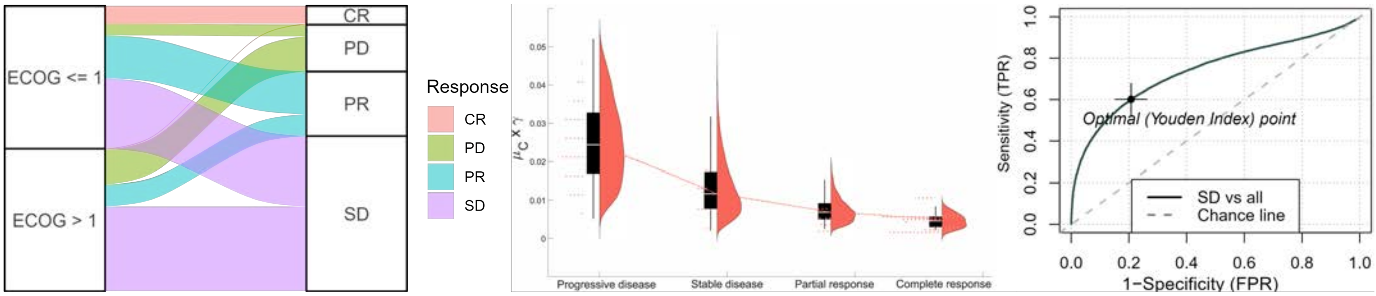

a) b) c)

Fig. 1. Distribution of virtual patients outcomes in the four response classes (i.e., CR: Complete Response, PD: Progressive Disease, PR: Partial Response, SD: Stable Disease) with respect to ECOG performance status (a). Distribution of $\mu_C \times \gamma$ among therapy response categories (b). SD vs all classification by ROC analysis (c).

The effective concentrations $C(t)$ and $A(t)$ of drugs follow distinct pharmacokinetic laws, while k_a and k_x are scale factors of drug effects.

$$\begin{cases} \dot{x}_t = \mu_C x(t)\left(1 - \dfrac{x(t)}{s(t)}\right) - k_x q(t) C(t) x(t) & \text{(1.a)} \\ \dot{s}_t = \lambda u(t) - \tau s(t) & \text{(1.b)} \\ \dot{u}_t = -\lambda u(t) + \gamma x(t) - \delta I(t) s(t) - k_a q(t) s(t) A(t) u(t) & \text{(1.c)} \end{cases}$$

$$I(t) = x(t) - 0.65 x_1(t) - 0.4 x_2(t) - 0.1 x_3(t) - 0.05 x_4(t) \quad (2)$$

$$q(t) = \frac{s(t)}{s(t) + u(t)} \quad (3)$$

The tumor burden $x(t)$ tends to the carrying capacity time-dependent variable, $s(t)$, which corresponds to the dynamics of the stable vessels, since these enable tumor nourishment.

B. *Parameter fitting procedure*

The procedure to fit parameters consists of two steps that were built using the SimBiology toolbox of MATLAB (Mathworks, Natick, MA, USA). Firstly, global sensitivity analysis has measured both the first- and total-order Sobol indices and has revealed how much both single and joint variations of the model parameters could explain the variance of the three state variables. Secondly, the optimal upper and lower bounds for parameters $\mu_C, \gamma, \tau, \lambda, K_{transit}$ are iteratively found by applying the Kolmogorov-Smirnov test. Hence, the multiparametric global sensitivity analysis is employed to find the parameter ranges that could reproduce the four treatment responses at the simulation time with the same distribution as the KCSG-ST19-16 study. In this work, the distinction of patients into low-ECOG class, ($ECOG \leq 1$), and high-ECOG class, ($ECOG > 1$), was used to set up the simulation initial conditions, corresponding to different regions of the mathematical model. Patients with unfavorable conditions are represented within the high-ECOG class, where $s(0) \geq x(0)$: in this case, the tumor growth is sustained in its growth by a large carrying capacity and doctors would choose a reduced dose to limit the toxic side effects. Conversely, patients with more favorable conditions, which are represented within the low-ECOG class, have an initial condition where $s(0) \leq x(0)$. Disease trajectories were analyzed under the application of the standard therapy schedule, that administers cytotoxic and anti-angiogenic drugs, which are defined as $C(t)$ and $A(t)$ in Eq. (1.a) and Eq. (1.c), respectively. A reduced dosage to a fraction of patients belonging to the high-ECOG class is applied to comply with the KCSG-ST19-16 cases history.

III. RESULTS AND DISCUSSION

The calibration phase identified distinct plausible ranges of values for each of the model parameters describing the pathobiology of the disease, that are: μ_C, λ, γ, τ, $K_{transit}$. Different simulations were run over those ranges to study how these parameters affect the distribution of outcomes, i.e. the evolution of the state variables $x(t), s(t), u(t)$.

Notably, the two classes of patients describe different culprits of disease. For instance, the μ_c parameter is a proxy measures of the intrinsic ability of the tumor to escape the programmed death, whilst the γ parameter measures the stem of new vessels induced by tumor cells. We found that their interaction, $\mu_c \times \gamma$, is an interpretable biomarker. The higher median of the distribution (i.e. more aggressive tumor) suggests lower responses, as shown in Figure 1b. Moreover, ROC analysis in Figure 1c reveals unique optimal cut-off values for $\mu_c \times \gamma$, as determined by the Youden's J statistics. An overall accuracy of 0.9421, 0.7393, 0.8762, and 0.8692 is reached in discriminating the SD, PR, CR, and PD response class in a one versus all classification, respectively. Future works will be done towards the exploration of new scheduling strategies for administering C(t) and A(t) with the aim to gather efficacy indicators of such alternative treatment plans on different subgroups of patients.

REFERENCES

[1] S. Rodney and U. Banerji, "Optimizing the fda's project optimus: Opportunities and challenges," *Nature Reviews Clinical Oncology*, vol. 21, no. 3, pp. 165–166, 2024.

[2] R. K. Jain, "Normalization of tumor vasculature: An emerging concept in antiangiogenic therapy," *Science*, vol. 307, pp. 58 – 62, 2005.

[3] H. S. Han and B. J. K. et. al., "Ramucirumab plus paclitaxel as second-line treatment in patients with advanced gastric or gastroesophageal junction adenocarcinoma: a nationwide real-world outcomes in korea study (kcsg-st19-16)," *Therapeutic Advances in Medical Oncology*, vol. 13, 2021.

[4] H. Wilke and K. M. et. al., "Ramucirumab plus paclitaxel versus placebo plus paclitaxel in patients with previously treated advanced gastric or gastro-oesophageal junction adenocarcinoma (rainbow): a double-blind, randomised phase 3 trial." *The Lancet. Oncology*, vol. 15 11, pp. 1224–35, 2014.

[5] S. Benzekry and G. C. et. al., "A new mathematical model for optimizing the combination between antiangiogenic and cytotoxic drugs in oncology," *Comptes Rendus Mathematique*, vol. 350, pp. 23–28, 2012.

Robust Nonlinear Control for Induction Motor Drives Based on Adaptive Disturbance Compensation

Angelo Accetta[1], Maurizio Cirrincione[2], Silvia Di Girolamo[3], Filippo D'Ippolito[3], Marcello Pucci[1], and Antonino Sferlazza[3].

[1] Institute for Marine Engineering (INM), National Research Council of Italy (CNR). (angelo.accetta@cnr.it, marcello.pucci@cnr.it)
[2] School of Engineering and Physics, University of the South Pacific, Laucala Campus. (cirrincionem@usp.ac.fj)
[3] Department of Engineering, University of Palermo. (silvia.digirolamo01@unipa.it, filippo.dippolito@unipa.it, antonino.sferlazza@unipa.it)

This paper deals with the theoretical development and experimental application of a new version of Active Disturbance Rejection Control (ADRC) to Induction Motor (IM) drives. The ADRC method is a robust adaptive extension of the input-output feedback linearization control. It performs the exact linearization of the IM model by a suitable nonlinear state transformation based on the online estimation of the corrective term by the so-called Extended State Observers (ESO). Consequently, any unmodeled dynamics or uncertainty in the parameters are properly addressed. It should be remarked, however, that parameter variations and errors in estimating the total disturbance cannot be included in the endogenous disturbance and cannot be estimated by the ESO, so these problems may deteriorate the performance of the ADRC method. In this paper, a new control structure is proposed where, in place of an ESO, a high-gain Unknown Input Observer (UIO) is implemented with a driving term that is a function of the tracking error. This approach permits achieving total robustness, even against exogenous disturbances coming from the ESO input. In more detail, in the classical ADRC, there is a cascade between the controller and the ESO, and the controller does not influence the ESO. In the proposed approach, there is an interconnection between the observer and the controller due to the driving term, so the observer can be considered embedded in the controller. In this way, all uncertainties associated with inverter nonlinearities, delays, and parameter variation of the input gain are automatically eliminated. To derive the proposed robust control law, the first step is to obtain the flux model and speed in canonical form. Since the model that we obtain is observable and reachable, to obtain steady-state null errors, a state feedback control law based on the assignment of the eigenvalues can be derived; however, this technique does not allow us to obtain steady-state null errors. So, the best way to achieve perfect tracking of a constant reference is to add a third variable to the model. So, unlike ADRC, where a classical ESO sourced by the input is used, a high-gain UIO is considered, with a driving term that is a function of the tracking error. A test setup has been suitably built to validate the proposed control technique. The machine under test is a 2.2kW IM SEIMEC model HF 100LA 4 B5 with an incremental encoder. The employed test setup consists of a three-phase 2.2 kW IM, a frequency converter that consists of a three-phase diode rectifier and a 7.5 kV A, three-phase VSI, and a dSPACE card (DS1103) with a PowerPC 604e at 400MHz and a floating-point DSP TMS320F240. The proposed innovative version of the ADRC has been experimentally tested on the test set-up described before. Two kinds of tests have been performed. The first test is a transient response at no load, while the second test is a load rejection test at a constant speed.

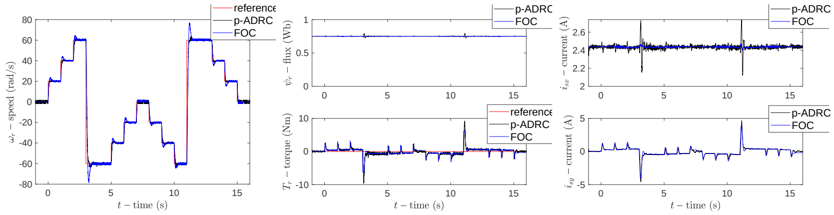

(a) reference and measured speed (b) flux and torque (c) currents

Fig. 1: Transient response at no load and constant flux - Experimental results.

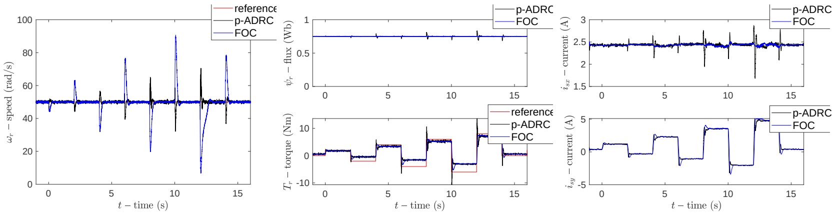

(a) reference and measured speed (b) flux and torque (c) currents

Fig. 2: Load rejection test at $50 rad/s$ and constant flux - Experimental results.

All the above figures show that both ADRC and FOC work properly, permitting the speed and rotor flux to track their references. From Fig.s 1 we can observe that i_{sx} is controlled to a constant value, permitting the rotor flux to be controlled to the constant rated value of 0.8 Wb. While i_{sy} shows a step-like waveform, with peaks occurring at each speed reference variation. The rotor flux and electromagnetic torque waveform exhibit the same shape of the corresponding i_{sx}, i_{sy}. As for the load rejection test, figures 2 show that both the proposed ADRC and the FOC exhibit good load rejection capabilities, with the electromagnetic torque quickly tracking the load one, thus permitting a fast recovery of the measured speed to its reference.

Deep Reinforcement Learning Platooning Control of Non-Cooperative Autonomous Vehicles in a Mixed Traffic Environment

Simone GENTILE[1,2,*],Danilo MENEGATTI[1], Andrea WRONA[1],
Antonio DI PAOLA[1,2] and Alessandro GIUSEPPI[1]

***Abstract*— Ensuring secure spacing between vehicles is vital for road safety, efficient traffic flow, and system stability in autonomous driving. While traditional cooperative platooning approach, relying on centralized coordination exploiting wireless network, faces practical implementation challenges due to communication constraints and diverse driving behaviors, this work introduces a scalable non-cooperative multi-agent platooning strategy based on Deep Reinforcement Learning, leveraging on decentralized decision-making principles.**

I. MOTIVATIONS AND INTRODUCTION

A wide number of studies have tackled control issues of multi–agent autonomous vehicles. Standard approaches involve linear consensus control [1], distributed robust control [2], sliding–mode control [3], and model predictive control [4]. This work contributes by implementing a non-cooperative control framework for autonomous vehicle platooning relying on inter-vehicle sensing only. The agents' aim is to adjust their velocities dynamically to ensure safe following distances and adapt to surrounding vehicle behavior, without the possibility of exchanging information over a wireless network.

II. MATHEMATICAL MODEL

The system scenario consists of a set of N AVs following a human–driven vehicle (HDV), which is considered to be the leader of the platoon. Each vehicle cannot exchange information with the other ones, but it can rely on a distance sensor mounted on the front bumper, which allows to measure how far the next vehicle is.

Dynamical models of a single AV are usually split into longitudinal dynamics, bounce and pitch dynamics and lateral, yaw and roll dynamics. [5]. This work focuses on the longitudinal dynamics, which is parallel to the ground and oriented along the direction of motion. Said dynamics is inherently nonlinear, and in literature it is usually linearized for tractable issues. In this work we use a fully nonlinear second–order model to describe the longitudinal dynamics of the AV, resulting from considering all the forces acting on the vehicles modeled as a point-mass.

Consider a single AV. Let $x = [x_1 \ x_2]^T = [p \ v]^T \in \mathbb{R}^2$ be the state of the dynamical system, corresponding to its position and velocity. The resulting dynamics is described via the following equations:

$$\begin{cases} \dot{x}_1 & = x_2 \\ \dot{x}_2 & = \dfrac{1}{m}\Big(F_{\text{T}} - F_{\text{AV}} - F_{\text{G}} - F_{\text{DRAG}}\Big) \end{cases}, \tag{1}$$

where F_{T} is the longitudinal thrust, $F_{\text{AV}} = \frac{\mu_v}{R_w} mg \cos\alpha$ the rolling friction, $F_{\text{G}} = mg \sin\alpha$ the gravity acting on a slope, and $F_{\text{DRAG}} = \frac{1}{2}\rho_{air} C_d A_v (v_w + x_2)^2$ is the aerodynamic drag. In particular, g is the gravitational acceleration, α is the slope of the surface, ρ_{air} the air density, v_w the speed of the wind, μ_v the rolling friction coefficient, R_w the wheel radius, m the mass, C_d the drag coefficient and A_v the cross-sectional area of the vehicle.

Assuming that the control input is the acceleration $u = \dfrac{F_{\text{T}}}{m} \in \mathbb{R}$, (1) can be written as $\dot{x} = f(x) + Bu$, in terms of the vector fields

$$f(x) = \begin{bmatrix} x_2 \\ -\dfrac{\mu_v}{R_w} g\cos(\alpha) - g\sin(\alpha) - \\ + \dfrac{1}{2m}\rho_{air} C_d A_v (v_w + x_2)^2 \end{bmatrix}, \quad B = \begin{bmatrix} 0 \\ 1 \end{bmatrix}. \tag{2}$$

The longitudinal dynamics of the HDV leader is modeled as a double integrator, with its input u^l corresponding to its acceleration as a noisy sinusoidal wave, mimicking the typical human behavior in traffic-waves conditions and defined as $u^l = (A + \hat{A}) \sin\big((\omega + \hat{\omega})t\big)$, with A, ω its amplitude and pulse, and $\hat{A} \in \mathcal{N}(\mu_{\hat{A}}, \sigma_{\hat{A}})$, $\hat{\omega} \in \mathcal{N}(\mu_{\hat{\omega}}, \sigma_{\hat{\omega}})$ the corresponding noises. The employment of the additive noises to both its amplitude and pulse try to model human interventions, such as sudden braking or full throttle events.

The non–coperative AVs' platoon is controlled with the introduction of a Fully Decentralized Multi–Agent DDPG (FD-MADDPG) algorithm, exploiting the Decentralized Training Decentralized Execution paradigm (DTDE). At any given time instant t, the state space of the i-th AV is given by

$$\mathcal{S}^i = \langle v^i(t), d^i_{i-1}(t) \rangle, \tag{3}$$

where $v^i(t) \in [v_{\min}, v_{\max}]$ represents its sensed velocity which is lower and upper bounded, and $d^i_{i-1}(t) \in [d_{\min}, d_{\max}]$ is the measurement of its distance from the vehicle in front.

The action space of each agent corresponds to the vehicle acceleration input, which is a saturated one:

$$\mathcal{A}^i = \langle u^i(t) \rangle, \qquad u^i(t) \in [u_{\min}, u_{\max}], \tag{4}$$

---

[1] Dept. of Computer, Control and Management Engineering “Antonio Ruberti”, Sapienza University of Rome, Via Ariosto 25, 00185 Rome - Italy.

[2] Dept. of Electrical and Information Engineering, Polytechnic of Bari, Via Re David 200, 70125 Bari - Italy.

[*] Corresponding author. Email: gentile@diag.uniroma1.it

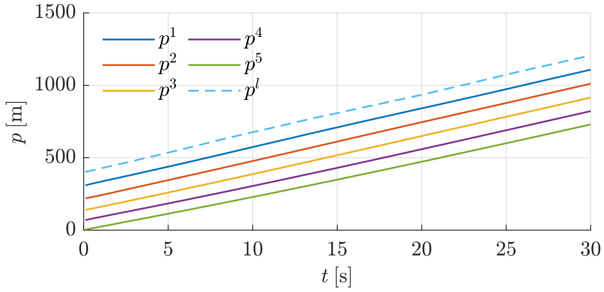

Fig. 1. Platoon's position evolution over time during evaluation phase.

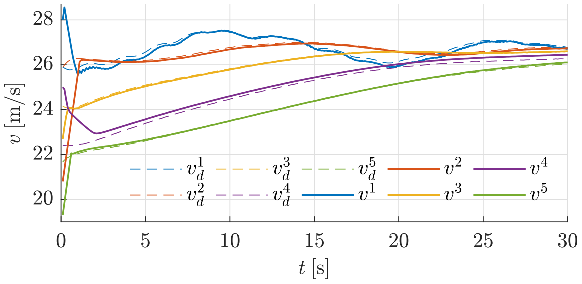

Fig. 2. Platoon's velocity evolution over time.

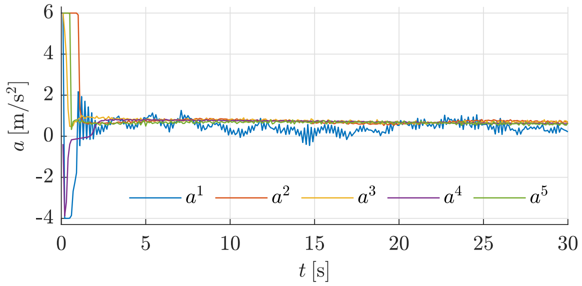

Fig. 3. Platoon's acceleration evolution over time.

where $u_{\min}$ corresponds to the maximum deceleration, and $u_{\max}$ to the maximum acceleration.

Given the platooning problem, our proposed approach is to control the velocity $v^i(t)$ of the i-th agent towards a desired value $v_d^i(t)$, which is computed as a function of its distance from the vehicle in front $d_{i-1}^i(t)$, so that the latter becomes a safe distance. In other words, in accordance to traffic regulations, we adjust $v^i(t)$ to make sure that $d_{i-1}^i(t)$ is an adequate stopping distance.

By approximating the i-th agent with a point-mass, $v_d^i(t)$ results from solving the following second–order equation:

$$d_{i-1}^i(t) = \frac{v_d^i(t)^2}{|u_{\min}|} + v_d^i(t)\, t_r, \tag{5}$$

where t_r is the AV reaction time, that may be set as a function of the sensor's bandwidth, data processing time, and control actuation bandwidth. The immediate reward $r^i(t)$ is shaped as follows:

$$r^i(t) = \begin{cases} -100, & \text{if} \quad d_{i-1}^i(t) < d_{\min} \\ -\big(v^i(t) - v_d^i(t)\big)^2, & \text{if} \quad d_{\min} < d_{i-1}^i(t) < d_{\max} \\ -\big(v^i(t) - v_{\max}\big)^2, & \text{otherwise.} \end{cases} \tag{6}$$

III. Simulations and Results

In order to validate the robustness of our proposed approach, we consider a platoon of five AVs following a HDV.

Starting from its initial state $x_0^i = [p_0^i \;\; v_0^i]^T$ at $t = 0$ [s], the i-th agent has to adjust its speed $v^i(t)$ according to its measured distance $d_{i-1}^i(t)$ from the vehicle in front. Having multiple AVs, at each time step t, they apply simultaneously the acceleration actions on the environment, observe the corresponding rewards and next states, and subsequently are trained in parallel. The episode ends if an agent gets too close to the vehicle in front, namely $d_{i-1}^i(t) < d_{\min}$, or if the time limit T is reached.

Considering that its initial distance from the vehicle in front and velocity is smaller than the ones of the others, as shown in Fig. 1, detailing the evolution of platoon's position over time during the evaluation phase.

As time goes by, each agent successfully keeps a safe distance from the vehicle in front by adjusting its own velocity, proving to have successfully learned the dynamics of the agent in front, as well as its own (see Fig. 1). In particular, given the velocity of the leader, the agents are able to follow their desired speed profile, as shown in Fig. 2 and, in the meantime, steering all the velocities towards a common value.

Fig. 3 depicts agents' control effort: note how all but the first AV, after an initial adjustment, keep a soft acceleration, whereas the AV following the leader shows several acceleration peaks, since it has to mimic the leader's velocity profile in traffic-waves conditions.

IV. Conclusions

This research activity is focused on a non-cooperative multi-agent platooning strategy to ensure safe distance keeping between vehicles. Simulations have proven the validity of the data-driven deep reinforcement learning methodology in steering vehicles' velocities towards the desired values.

References

[1] E. Shaw and J. K. Hedrick, "String stability analysis for heterogeneous vehicle strings," in *2007 American control conference*, pp. 3118–3125, IEEE, 2007.

[2] F. Gao, S. E. Li, Y. Zheng, and D. Kum, "Robust control of heterogeneous vehicular platoon with uncertain dynamics and communication delay," *IET Intelligent Transport Systems*, vol. 10, no. 7, pp. 503–513, 2016.

[3] D. Swaroop and J. K. Hedrick, "String stability of interconnected systems," *IEEE transactions on automatic control*, vol. 41, no. 3, pp. 349–357, 1996.

[4] S. Di Cairano, H. E. Tseng, D. Bernardini, and A. Bemporad, "Vehicle yaw stability control by coordinated active front steering and differential braking in the tire sideslip angles domain," *IEEE Transactions on Control Systems Technology*, vol. 21, no. 4, pp. 1236–1248, 2012.

[5] T. Ersal, I. Kolmanovsky, N. Masoud, N. Ozay, J. Scruggs, R. Vasudevan, and G. Orosz, "Connected and automated road vehicles: state of the art and future challenges," *Vehicle system dynamics*, vol. 58, no. 5, pp. 672–704, 2020.

Vision-Based Autonomous Navigation in Agricultural Rows

Denis Tognolo, Francesco Visentin, Riccardo Muradore

University of Verona, Strada Le Grazie 15, Ca' Vignal 2, 37134 Verona

`d.tognolo@phd.poliba.it`, `francesco.visentin@univr.it`,
`riccardo.muradore@univr.it`

Abstract: Agriculture faces new challenges in meeting the demands of a rapidly expanding global population, the constant reduction of the labor force, and significant climate changes. The integration of robotics into agricultural practices presents a promising solution to these critical issues, potentially enhancing efficiency, productivity, and sustainability in the sector.

Our research focuses on autonomous navigation in rows of orchards based on RGB-D data, a process that can be exploited in several more complex tasks such as plant monitoring, weed removal, pesticide application, precision planting, and automated harvesting [1] [2]. This task is particularly challenging in perception and control due to the environment's variability and irregularity. For this reason, we proposed a local planner that exploits RGB-D data, achieving a strategy that, up to a minimal prior path planning, is adaptable to several row-based cultivation structures. Additionally, compared to global planners, this method is more robust against unexpected or dynamic obstacles.

The core algorithm employs a hybrid automaton that alternates between two primary states: in-row navigation and out-row navigation. An additional state, exit-row, ensures the rover has completely exited the row. The state transitions are based on a perception routine delineating accessible and obstructed regions in the rover's path.

Based on the work by Aghi et al. [3], in-row navigation aims to dynamically correct a rectilinear trajectory by applying exponential control based on the norm of the horizontal deviation between the camera center and the in-row endpoint. This is determined as the center of mass of the most significant area beyond a pre-defined depth value acquired by the RGB-D camera. Exit-row navigation, instead, aims to perform a rectilinear trajectory for enough time to ensure the rover has completely exited the row. This trajectory is eventually corrected if an obstacle is detected in the central area. Finally, out-row navigation is based on a circular trajectory, which is dynamically adjusted according to the presence of obstacles in the central or turning-side areas. In particular, the desired linear velocity is reduced when one is detected proportionally with respect to its distance.

After extensive testing in different simulated environments, we have successfully demonstrated the effectiveness of our system in actual orchard rows. The results in both settings were promising, showcasing the potential of our approach.

As a future research, we aim to conduct further experiments in more diverse scenarios to validate the versatility and robustness of our method. In particular, we aim to introduce a dynamic adaptation of the sensing parameters, such as the distance thresholds, in order to make the system even more flexible. Moreover, we plan to also introduce an AI-based object classifier to avoid the detection of false obstacles such as high grass in the path.

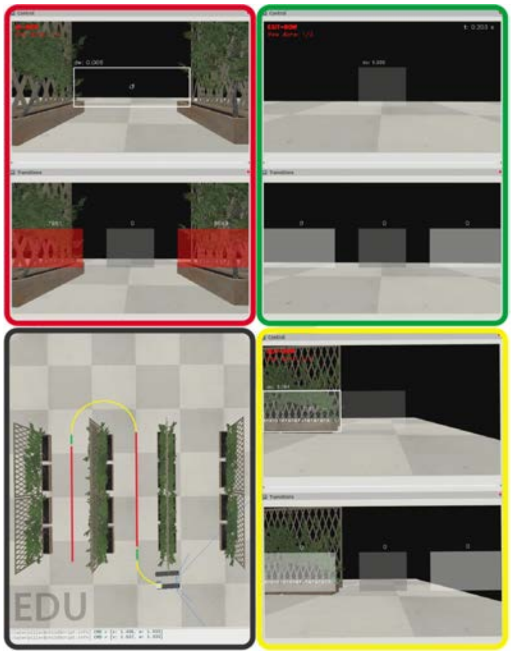

Fig. 1: Snapshots of the simulation illustrating task progression. Top left (red outline): in-row screen view. Top right (green outline): exit-row screen view. Bottom left (black outline): simulated environment view. Bottom right (yellow outline): out-row screen view.

References

1. L. F. P. Oliveira, A. P. Moreira, and M. F. Silva, “Advances in Agriculture Robotics: A State-of-the-Art Review and Challenges Ahead.” *Robotics*, vol. 10, no. 2, 2021.
2. F. Visentin, S. Cremasco, M. Sozzi, L. Signorini, M. Signorini, F. Marinello, and R. Muradore. “A mixed-autonomous robotic platform for intra-row and inter-row weed removal for precision agriculture.” *Computers and Electronics in Agriculture*, vol. 214, 2023.
3. D. Aghi, V. Mazzia, and M. Chiaberge, “Local motion planner for autonomous navigation in vineyards with a RGB-D camera-based algorithm and deep learning synergy.” *Machines*, vol. 8, no. 2, Art. no. 27, 2020.

A control system framework for counterfactuals: an optimization-based approach

Pierluigi Francesco De Paola [*][†][‡], Jared Miller[§], Alessandro Borri[‡],
Alessia Paglialonga[†], Fabrizio Dabbene[†]

Introduction

In the context of artificial intelligence classification problems, counterfactuals represent the minimum change that should occur in an instance to observe a diverse outcome from the classifier [1]. Counterfactuals have been widely applied to classification problems where classes are typically associated with risks, for instance with risk of developing a given disease or not, thus classes representing safe and unsafe sets [2]. From a theoretical perspective, counterfactuals suggest what should have been different in an instance (defined as *factual*, i.e. the input variable of the AI algorithm) to change with *minimum effort* the outcome of the AI algorithm. Indeed, although providing more insights with respect to the explainability of the decision of the algorithm, the *AI-driven* counterfactuals neglect the underlying dynamics of the considered system, consequently providing merely conceptual decisions, representing "virtual" conditions for the instances undergoing the change of class.

In this work we propose a control system theoretical formulation for counterfactuals, with the aim of assessing a physics-informed approach suitable to account for the underlying mechanisms driving the change of class. The control framework is derived by means of an optimal control problem, aimed at computing the minimum control law steering a given initial condition in an unsafe set (the *factual*) to the safe set. The terminal state defines the *counterfactual*. This problem is then cast in an infinite-dimensional problem in the space of the measures and subsequently solved by means of the moment-sum of squares (moment-SOS) hierarchy through a sequence of convex relations in the space of the moments, with the aim of deriving a general methodology suitable to be exploited nonlinear systems [3]. This work is preliminary to the integration of control and AI method to derive physics-informed personalized minimum recommendations for disease prevention.

Methodology

Consider a general optimal control problem in the form:

$$\min_{u(\cdot)} \quad J(x(t),u(t)) = H(x(T)) + \int_0^T h(x(t),u(t))\,dt \tag{1a}$$

$$\text{s.t.} \quad \dot{x}(t) = f(x(t),u(t)), \tag{1b}$$

$$x(0) \in X_0,\ x(t) \in X, \tag{1c}$$

$$x(T) \in X_T, \tag{1d}$$

$$u(t) \in U, \quad t \in [0,T], \tag{1e}$$

where $x(t) \in \mathbb{R}^n$ represents the state of the system at time t, $u(t) \in \mathbb{R}^m$ represents the control input, and $f : \mathbb{R}^n \times \mathbb{R}^m \to \mathbb{R}^n$ is the vector field describing the system dynamics, T is the terminal time, $H(x(T))$ is the terminal cost, a function of the final state $x(T)$, $h(x(t),u(t))$ is the running cost, a function of the state $x(t)$, the control $u(t)$. The goal is to find a control $u(t)$, over the interval $[0,T]$, that minimizes the cost functional $J(x(t),u(t))$, subject to the initial condition $x(0) \in X_0$. The problem can be translated in the space of measures as follows (primal linear program):

---

[*] Polytechnic University of Bari, Bari, Italy

[†] CNR-IEIIT, Turin, Milan, Italy

[‡] CNR-IASI, Rome, Italy

[§] Department of Information Technology and Electrical Engineering, ETH, Zurich, Switzerland

This work was supported in part by the European Union through the project PRAESIIDIUM "Physics Informed Machine Learning-Based Prediction and Reversion of Impaired Fasting Glucose Management"(call HORIZON-HLTH-2022-STAYHLTH-02) under Grant 101095672. Views and opinions expressed are however those of the authors only and do not necessarily reflect those of the European Union. The European Union can not be held responsible for them.

$$\begin{aligned} p^* = \min_{\mu,\mu_T} \quad & \langle h, \mu\rangle + \langle H, \mu_T\rangle && \text{(2a)}\\ \text{s.t.} \quad & \mathcal{L}^*\mu = \mu_0 - \mu_T && \text{(2b)}\\ & \operatorname{spt}(\mu) \subset ([0,T] \times X \times U), && \text{(2c)}\\ & \operatorname{spt}(\mu_T) \subset (X_T), && \text{(2d)} \end{aligned}$$

where the minimization occurs with respect to the occupation measure μ, that encodes the information of the controlled trajectories, and the terminal measure μ_T, for a given known initial measure $\mu_0 = \delta_{t_0=0} \otimes \delta_{x_0}$. The primal problem has a dual formulation in the cone of continuous functions [3], whose solution $v(0, x(0)) = \gamma$ is a subsolution of the Hamilton-Jacobi-Bellman PDE, which approximates the value function along trajectories. To solve the optimization problem, it is approximated through a sequence of finite-dimensional LMI problems in the space of moments, up to a given relaxation order d. The cost function to be minimized is the *effort* of the vector field as by definition of counterfactuals [1], here considered as function the L^2-norm of the control input u and defined as $\|u(t)\|_{L^2,[0,T]} = \left(\int_0^T |u(t)|^2\, dt\right)$. Counterfactuals are defined extracting the states associated with the moments of the terminal measure μ_T or simulating the system in closed-loop with the control law derived from the solution of the Hamilton-Jacobi-Bellman equation.

Illustrative example

We apply the proposed methodology to a general glucose-insulin regulation model, the well acknowledged model by Bergman et al. [4], described by the following system of differential equations:

$$\begin{aligned} \dot{x}_1 &= -p_1 x_1 - x_2 x_1 + p_1 G_b && \text{(3a)}\\ \dot{x}_2 &= -p_2 x_2 + p_3 x_3 && \text{(3b)}\\ \dot{x}_3 &= -n x_3 + p_4 u && \text{(3c)} \end{aligned}$$

where x_1, x_2, x_3 represent respectively the blood glucose concentration, the remote insulin and the serum insulin concentrations and the input u represents exogenous insulin administration. The safe set is defined as $80 \leq x_1 \leq 126$ mg/dl (cyan dashed line in Figure 1), as known from the clinical literature [5]. Fig.1 shows the results obtained by applying the proposed method. Counterfactuals are generated by solving the optimization problem in the space of the measures and represent the states reached at the terminal time T as the factuals (initial conditions, red dots, randomized over 100 points.) are steered by the dynamics of the system into the safe set with *minimum effort*.

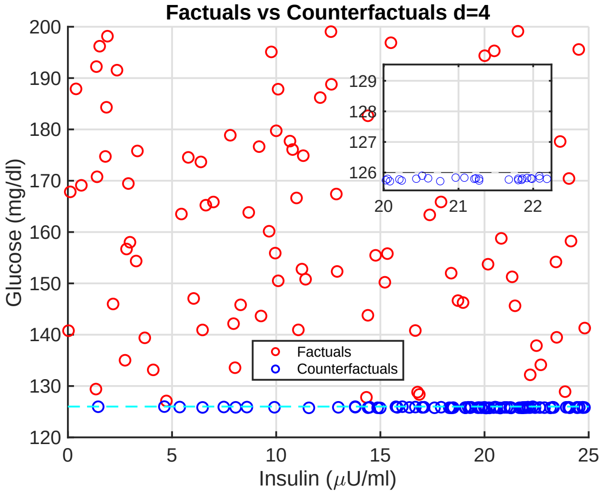

Figure 1: Factuals (red dots) and the associated counterfactuals (blue dots) as obtained by the proposed method

References

[1] R. Guidotti, "Counterfactual explanations and how to find them: literature review and benchmarking," *Data Mining and Knowledge Discovery*, pp. 1–55, 2022.

[2] M. Lenatti, A. Carlevaro, A. Guergachi, K. Keshavjee, M. Mongelli, and A. Paglialonga, "A novel method to derive personalized minimum viable recommendations for type 2 diabetes prevention based on counterfactual explanations," *Plos one*, vol. 17, no. 11, p. e0272825, 2022.

[3] J. B. Lasserre, D. Henrion, C. Prieur, and E. Trélat, "Nonlinear optimal control via occupation measures and lmi-relaxations," *SIAM journal on control and optimization*, vol. 47, no. 4, pp. 1643–1666, 2008.

[4] R. N. Bergman, Y. Z. Ider, C. R. Bowden, and C. Cobelli, "Quantitative estimation of insulin sensitivity.," *American Journal of Physiology-Endocrinology And Metabolism*, vol. 236, no. 6, p. E667, 1979.

[5] M. Whelan and L. Bell, "The english national health service diabetes prevention programme (nhs dpp): A scoping review of existing evidence," *Diabetic Medicine*, vol. 39, no. 7, p. e14855, 2022.

Recovering the governing equations of nonlinear dynamical systems by sparse identification from experimental data

Amarnath Venkatachalam(1), Lucia Valentina Gambuzza(1), Carlo Famoso(1) , Ludovico Minati(3), Giovanni Russo(2), Mattia Frasca(1)
(1) Department of Electrical, Electronic and Computer Engineering, University of Catania, Catania, Italy
(2) Department of Mathematics and Computer Science, University of Catania, Catania, Italy
(3) University of Electronic Science and Technology of China, Chengdu, China.

Abstract

In this work, we present an experimental study aimed at identifying the governing equations of a nonlinear circuit from experimental data. Our procedure involves acquiring state variables, constructing a library of potential nonlinear terms, and leveraging sparse regression techniques to iteratively refine this library. The goal is to derive a minimal set of terms that accurately describe the system dynamics. As an experimental case study, we focus on Chua's circuit, a well-known nonlinear electronic circuit characterized by its ability to exhibit chaotic behaviour through a combination of linear passive elements and a nonlinear active component. The circuit is described by the following equations:

$$\begin{aligned}\dot{x} &= \frac{1}{\tau}\alpha\big(y - h(x)\big)\\ \dot{y} &= \frac{1}{\tau}(x - y + z)\\ \dot{z} &= -\frac{1}{\tau}\beta y\end{aligned}\qquad \text{--------------------->}\ (1)$$

where x, y, and z are the state variables, and h(x) is the piece-wise linear function defined as:

$$h(x) = m0.x + 0.5(m1 - m0)\ (|x + 1| - |x - 1|)$$

The parameter τ is a time scaling factor. This system is known to produce the chaotic double scroll Chua attractor. The circuit schematic is illustrated in Fig. 1, and the equations are well-established as per [1], making it an ideal benchmark for validating our approach to reconstruct a dynamical system from experimental data. The procedure employs the sparse identification method introduced in [2], aiming to provide experimental validation. Our identification process involves acquiring the state variables, as shown in Fig. 2(a), and their derivatives. These derivatives can either be directly derived from the circuit or computed numerically. To model the circuit's behaviour, we construct a library $\theta(x)$ of potential nonlinear terms. This library includes a range of candidate terms, encompassing both linear and nonlinear functions of the circuit's state variables. By leveraging sparse regression techniques, we iteratively refine this library to identify the minimal set of terms necessary to describe the system dynamics. This process includes the identification of unknown factors ξ_i, which are the sparse coefficient vectors corresponding to each individual column. These individual sparse coefficient vectors ξ_i are then used to construct the sparse matrix Ξ. The iterative refinement process ensures that our model remains parsimonious while capturing the essential features of the system's behaviour. The presence of null elements in the sparse matrix allows us to eliminate spurious functions from our library $\theta(x)$.

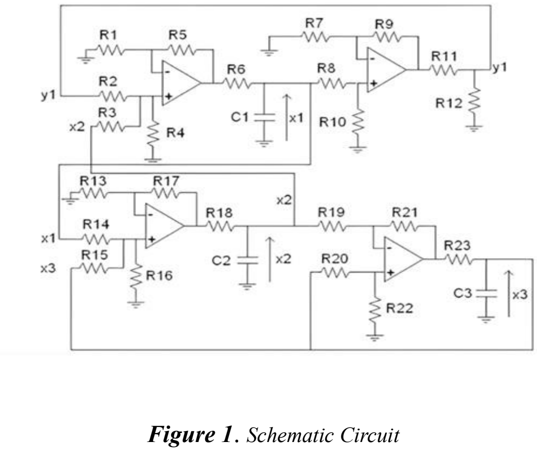

Figure 1*. Schematic Circuit*

Consequently, we derive the governing equations of the system. After deriving the governing equations, we use them to reconstruct the system's behaviour, resulting in the reconstructed variables shown in Fig. 2(b). The reconstructed trajectory, defined using these variables depicted in Fig. 2(d), is then compared with the attractor from experimental data as shown in Fig. 2(c) to validate our study. This comparison demonstrates the success of our study. By iteratively adjusting the model parameters to minimize the coefficient error shown in Fig. 2(e) and error between the actual and reconstructed data as shown in Fig. 2(f), we ensure that our model captures the underlying dynamics of Chua's circuit.

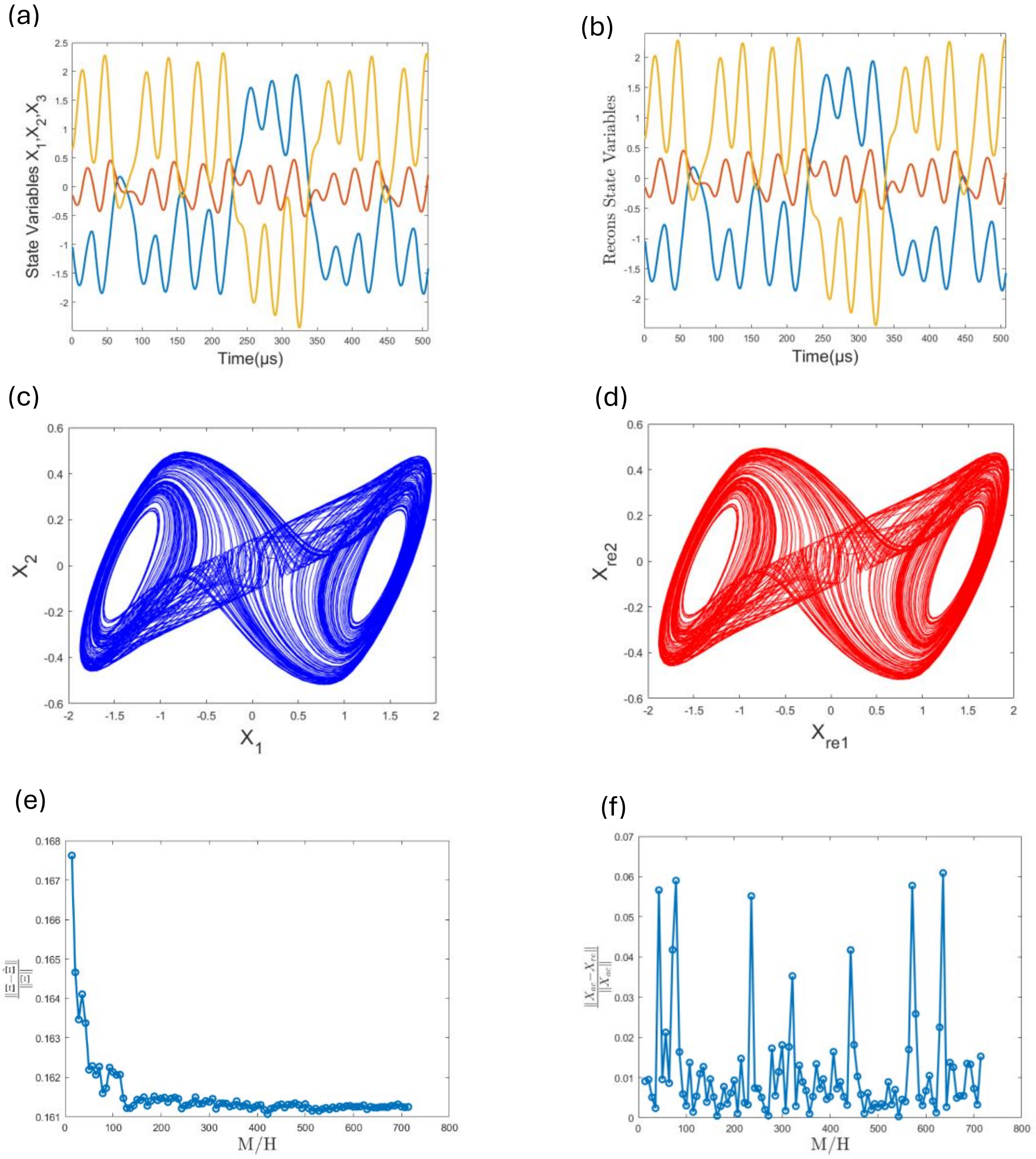

***Figure 2. (a)** State variables from the electronic circuit, **(b)** Reconstructed state variables, **(c)** Attractor from the electronic circuit, **(d)** Reconstructed attractor **(e)** Model Coefficient Error (Ec), **(f)** Performance Prediction Error (Ep),*

The equations obtained through sparse regression, detailing how the state variables x, y, and z evolve over time with specific parameters identified from experimental data. The saturation function (denoted as satur in this equation) as: satur = (|x + 1| − |x − 1|), Notably, the comparison between the equations derived from sparse regression (2) and the original equations (1) of the Chua's circuit reveals an exact match. This validation underscores the effectiveness of our approach in capturing the system's dynamics.

$$\begin{aligned} \dot{x} &= 2\mathrm{e}^4 satur - 3\mathrm{e}^4 x + 4.96\mathrm{e}^4 y \\ \dot{y} &= 2\mathrm{e}^4 x - 1.6\mathrm{e}^4 y + 2\mathrm{e}^4 z \qquad \text{---------------------->}\ (2) \\ \dot{z} &= -6\mathrm{e}^4 y \end{aligned}$$

[1] L. Fortuna, M. Frasca, M. G. Xibilia, Chua's Circuit Implementations: Yesterday, Today and Tomorrow. Singapore; Hackensack, NJ: World Scientific, 2009, pp. xi, 210.

[2] S. L. Brunton, J. L. Proctor, J. N. Kutz. (2016). Discovering governing equations from data by sparse identification of nonlinear dynamical systems. Proceedings of the National Academy of Sciences, 113(15),3932-3937.

Artificial Racing Coach: teaching humans how to maximize a racing vehicle's performance and drive at its limits

Sebastiano Taddei*†, Mattia Piccinini*, Edoardo Pagot‡, and Francesco Biral*
* Department of Industrial Engineering, University of Trento, 38123 Trento, Italy.
† Department of Electrical and Information Engineering, Politecnico di Bari, 70125 Bari, Italy.
‡ RE:LAB S.r.l., 42122 Reggio Emilia, Italy.

I. INTRODUCTION

The Artificial Racing Coach (ARC) is an interactive driving instructor that teaches humans to drive at the vehicle handling limits and sharpen their skill to achieve the best lap time. At the core, there is our Artificial Race Driver (ARD) [1], a hybrid AI-optimal control based real-time motion planning and control framework that autonomously learns the vehicle manoeuvrability envelope[1] and how to control it at the limits. Augmenting ARD with shared-control of the vehicle, an iterative teaching scheme, and auditory/visual/haptic feedbacks, we will be able to teach human drivers how to improve their performance around a racetrack starting from what the system has learnt from their driving style and skills.

This extended abstract is a brief summary of our ongoing research on the Artificial Race Driver and the Artificial Racing Coach. First, we will quickly introduce the main idea behind ARD, along with the latest advancements. Then, we will focus on how we intend to augment ARD to create ARC.

II. ARTIFICIAL RACE DRIVER

Figure 1 illustrates the Artificial Race Driver framework for minimum-time trajectory planning and control, highlighting the following key contributions.

1) A high-level motion planner that utilizes online economic nonlinear model predictive control (E-NMPC) to determine the time-optimal vehicle trajectory, incorporating a kineto-dynamical vehicle model and a long planning horizon of 400 meters.
2) A low-level feedforward neural steering controller (PhS-NN), designed with an internal structure inspired by vehicle dynamic laws, and integrated with a feedback steering controller.
3) A low-level longitudinal speed-tracking controller, developed based on an identified longitudinal dynamic model.
4) A four-round automatic learning scheme that combines open- and closed-loop manoeuvers to learn the planning and control models.

Previously in [1], we have shown that ARD is able to learn the vehicle dynamics of a black-box vehicle model and exploit this knowledge to plan and execute online minimum lap times. Recently, in two upcoming works, we devised a new formulation of the vehicle's manoeuvrability envelope [2], using a generalized polytopic formulation, and we showed how impactful the correct modelling of the vehicle's envelope is for the system's performance [3]. Thanks to this new formulation, we were able to reach lap-times just a few tenths of a second slower than the theoretical minimum achievable by the black-box vehicle model we are driving[2]. Let us briefly discuss the new envelope formulation.

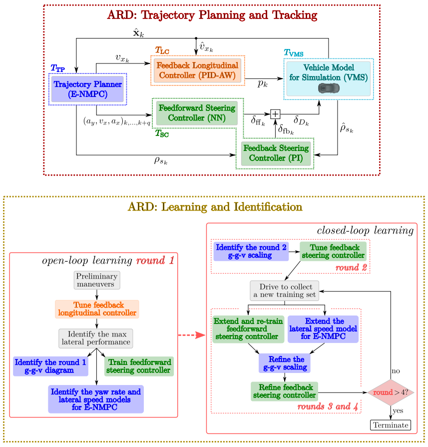

Fig. 1: Overall architecture of the Artificial Race Driver (ARD).

A. Generalized polytopic formulation

Figure 2 shows a vehicle's manoeuvrability envelope modelled using our new generalized polytopic formulation. Our formulation leverages convex polytopes and non-linear constraints to efficiently and accurately model the true envelope with just a few data points. The main idea can be summarized in three steps.

1) First, we model the vehicle's manoeuvrability envelope as a convex polytope. This results in an overestimation of the vehicle's capabilities in the non-convex regions, which usually coincide with the pure longitudinal acceleration limits.
2) Then, we correct the overestimation by adding non-linear constraints for the maximum and minimum longitudinal acceleration. This allows us to correctly model the non-convex regions on the envelope and avoid overestimating the vehicle's performance.
3) Lastly, we add two linear constraints to model the true vehicle's combined braking capabilities. Although, in theory, the vehicle can reach those regions, those are highly unstable and must be avoided to set minimum lap times.

This formulation is not only accurate, but also computationally efficient. Given that it is mostly based on linear constraints, it is lightweight and can be used for online motion planning, as we showed in [3].

Thanks to this new formulation, ARD can now plan more aggressive trajectories that are closer to the vehicle's limits, achieving faster lap times. Moreover, due to the generalized nature of the formulation, ARD can easily model any manoeuvrability envelope, allowing the system to adapt to the driver's skill level and driving style, crucial for the development of ARC, which is discussed next.

III. ARTIFICIAL RACING COACH

The Artificial Racing Coach is an extension of ARD that aims to teach human drivers how to drive at the vehicle handling limits and achieve the best lap time. ARC consists of three main components:

1) **Shared-control**: the human driver and the system share the control of the vehicle, with the system acting as a coach that helps the driver improve their performance.

---

[1] By manoeuvrability envelope we mean the ggv diagram of the vehicle, a 3D diagram of longitudinal acceleration, lateral acceleration, and longitudinal velocity.

[2] The theoretical minimum time was computed by solving an offline optimal control problem over the entire circuit using the full knowledge of the vehicle model.

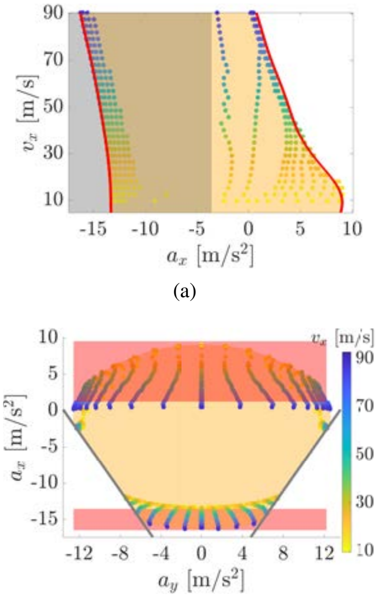

(a)

(b)

Fig. 2: New manoeuvrability envelope formulation based on convex polytopes and non-linear constraints. In orange the resulting envlope, in red the non-linear constraints for the maximum and minimum longitudinal acceleration, in grey the linear combined braking constraints. **(a)** Lateral view. **(b)** Top view.

2) **Iterative teaching scheme**: the system learns from the driver's initial performance and adapts its teaching strategy to help the driver gradually improve their performance.
3) **Interface**: the system provides real-time feedback to the driver (*e.g.,* auditory, visual, and haptic) to help them understand what they are doing wrong, why that is wrong, and how to correct it.

Several examples of shared-control systems for autonomous driving exists in literature, such as [4][5]. These works tend to consider the shared-control aspect and the interaction with the driver, focusing on safety and comfort in urban scenarios. However, to the best of our knowledge, none of them consider racing scenarios nor the teaching aspect of the system. The only work we are aware of that aims to teach drivers how to drive at the limits is [6], but it does not consider shared-control. To this end, we are developing ARC, a system that combines shared-control, an iterative teaching scheme, and an interface to teach human drivers how to drive at the limits and achieve the best lap time. Hereafter, a brief description of how we are developing each component.

A. *Shared-control*

The shared-control strategy allows ARD to correct the driver's mistakes without taking control away from them completely. ARD computes the time-optimal trajectory in real-time and converts it into vehicle controls (*i.e.,* steering, throttle, and brake inputs). The time-optimal trajectory is parametrized to mimic actual driver style and skills, and also professional racing driver style. This is necessary to smoothly guide the human driver from his to pro driving style. We are designing the shared-control strategy (both longitudinal and lateral) to be adaptive, meaning that it adjusts the level of assistance provided by ARD based on the driver's performance. For example, if the driver is deviating from the optimal racing line, ARD may apply some torque at the steering wheel to guide them back on track. If the driver is braking too late, ARD may at first provide some visual/auditory/haptic feedback, and if the driver does not react, ARD could take control of the brakes.

B. *Iterative teaching scheme*

The teaching scheme consists of a series of exercises that the driver can complete to learn different aspects of racing.

1) First, we let the driver drive on their own and derive their driving behaviour (*i.e.,* the manoeuvrability envelope).
2) Then, ARD starts from this behaviour and computes only trajectories that are similar to the ones the driver would take.
3) As the driver improves, ARD will compute more aggressive trajectories that the driver can learn from.

The idea is to use our new polytopic formulation to model the driver's envelope, enlarging it as the driver improves. This allows ARD to plan trajectories that are slightly outside the driver's capabilities, thus pushing the driver to improve. As the manoeuvres become more complex, the suggestions that come from the interface play a crucial role in the driver's learning process.

C. *Interface*

The interface is a crucial part of ARC. The driver needs to be able to interact with ARD in a way that is intuitive and easy to understand. The interface provides real-time feedback on the driver's performance and allows them to adjust their driving style accordingly. We intend to use a combination of visual and auditory cues to communicate with the driver, as well as haptic feedback to provide a more immersive experience. For example, the visual cues may come in the form of a racing line, projected using augmented reality, that the driver can follow. The auditory cues will be used to provide feedback on the driver's performance, such as when they are braking too late or not steering enough, and will come in the form of a scripted human interaction. The phrasing and timing of the suggestions will be carefully designed in collaboration with a speech expert to ensure that they are effective, easy to understand, and not distracting. Finally, the haptic feedback will be used to provide feedback on the vehicle controls, such as when the driver is applying too much throttle or not steering enough. We may use vibrations at the pedals and torque at the steering wheel to communicate this information to the driver.

REFERENCES

[1] M. Piccinini, S. Taddei, M. Larcher, M. Piazza, and F. Biral, "A physics-driven artificial agent for online time-optimal vehicle motion planning and control," *IEEE Access*, vol. 11, pp. 46 344–46 372, 2023.

[2] M. Piccinini, S. Taddei, E. Pagot, E. Bertolazzi, and F. Biral, "How Optimal is the Minimum-Time Manoeuvre of an Artificial Race Driver?" *Under Review at Vehicle System Dynamics*, 2024.

[3] M. Piccinini, S. Taddei, M. Piazza, and F. Biral, "Impacts of G-G-V Constraints Formulations on Online Minimum-Time Vehicle Trajectory Planning," in *17th IFAC Symposium on Control in Transportation Systems, CTS 2024*, 2024.

[4] S. J. Anderson, S. B. Karumanchi, K. Iagnemma, and J. M. Walker, "The intelligent copilot: A constraint-based approach to shared-adaptive control of ground vehicles," *IEEE Intelligent Transportation Systems Magazine*, vol. 5, no. 2, pp. 45–54, 2013, conference Name: IEEE Intelligent Transportation Systems Magazine. [Online]. Available: https://ieeexplore.ieee.org/abstract/document/6507273

[5] A. Benloucif, A.-T. Nguyen, C. Sentouh, and J.-C. Popieul, "Cooperative Trajectory Planning for Haptic Shared Control Between Driver and Automation in Highway Driving," *IEEE Transactions on Industrial Electronics*, vol. 66, no. 12, pp. 9846–9857, Dec. 2019, conference Name: IEEE Transactions on Industrial Electronics. [Online]. Available: https://ieeexplore.ieee.org/abstract/document/8624569

[6] R. Kaufman, J. Costa, and E. Kimani, "Effects of Multimodal Explanations for Autonomous Driving on Driving Performance, Cognitive Load, Expertise, Confidence, and Trust," Apr. 2024, arXiv:2401.04206 [cs]. [Online]. Available: http://arxiv.org/abs/2401.04206

Multi-agent Systems Methodologies and Frameworks for Edge-AI in Smart Environments

Daniel-Costel Bouleanu[1][2][3], Giancarlo Fortino[2], Costin Bădică[3]

[1] DEI, Politecnico di Bari, Bari, Italy
[2] DIMES, Università della Calabria, Rende, Italy
[3] CIT, University of Craiova, Craiova, Romania

1 Abstract

The Internet of Things (IoT) is transforming our world by integrating technology into every aspect of our lives, addressing social issues, and creating a smarter, more responsive environment [2]. IoT impacts various sectors, including industries, homes, agriculture, cities, healthcare, and energy efficiency. However, challenges such as the heterogeneity of IoT devices, lack of universal standards, convergence of digital and physical realms, and privacy issues complicate the systems [1]. With the number of interconnected devices projected to exceed 29 billion by 2030 [3], autonomous configuration and management become essential. Agents are a significant element, as they facilitate autonomous, socially reactive, and proactive computational activities, allowing IoT systems to adapt dynamically to environmental changes and user needs [4]. This capability is a perfect fit for addressing the challenges of IoT.

Our initial step is to develop a robust theoretical model that underpins the creation of an efficient Agent-Based Automatic Management Infrastructure. This mathematical model will serve as the cornerstone for ongoing research, facilitating the validation, design, and refinement of our system. It will also support a broad range of experiments, integrations, and targeted research initiatives. We will approach the problem as an optimization framework, enabling us to define both local and global objective functions. These functions will establish the performance metrics that need to be optimized, whether by individual agents or by the system as a whole. By allowing flexibility in the choice of objectives—be it minimizing energy consumption, maximizing efficiency, or optimizing resource allocation—our system can dynamically adapt to varying conditions and priorities. Agents, the fundamental components of our system, each manage specific state variables x_i, which are crucial to the system's operation. Through their interactions, agents contribute to achieving the overall system goals, while also optimizing their local objectives. This dual focus on local and global optimization not only enhances the system's adaptability but also provides us with a versatile toolset to fine-tune performance according to situational demands.

Additionally, we have begun developing a testbed to test and compare various algorithms, complementing our mathematical model and integrating both theoretical and practical methods. The initial testbed is an indoor localization

system utilizing IoT devices, categorized into two main types: *anchors* and *tags*. Anchors are stationary radio beacons positioned at fixed locations, serving as reference points for determining positions. Tags are devices attached to objects or carried by people that need to be located. The system uses trilateration algorithms to calculate the precise location of the tags, enabling accurate real-time tracking. The application operates in two modes, **Mode A**: Tags collect data on their distance to anchors and battery level, transmitting this to the server via MQTT. The server processes this data to calculate precise coordinates using a trilateration algorithm and **Mode B**: Tags calculate their coordinates based on distances to anchors and send these directly to the server.

By leveraging an Agent control layer to utilize the two modes, we have created an architecture that enhances the integration of microservices with MAS. Intelligent agents dynamically manage these microservices, improving resource allocation and operational efficiency based on real-time data. These agents enable the system to switch between computational modes and activate or deactivate services as needed, ensuring high performance with minimal resource waste. Consequently, the agents enhance the flexibility and responsiveness of the system and underscore the robustness of the microservices architecture.

Our work is an ongoing process, continuously evolving with new findings, improved methodologies, and advancements in the field. By combining the theoretical model with the physical testbed, we aim to create a comprehensive research foundation. This integrated environment will allow us to develop, model, and experiment freely, enabling us to achieve the best possible results.

References

1. Fortino, G., Galzarano, S., Gravina, R., Guerrieri, A., et al.: Agent-based development of wireless sensor network applications. In: WOA. pp. 123–132 (2011)
2. Savaglio, C., Ganzha, M., Paprzycki, M., Bădică, C., Ivanović, M., Fortino, G.: Agent-based internet of things: State-of-the-art and research challenges. Future Generation Computer Systems **102**, 1038–1053 (2020)
3. Vailshery, L.S.: Number of iot connected devices worldwide 2019-2023, with forecasts to 2030. Statista. Accessed: Nov **10** (2023)
4. Zambonelli, F., et al.: Towards a discipline of iot-oriented software engineering. In: WOA. pp. 1–7 (2016)

Drone as a Service in Logistics: a Review of Optimization and Control Techniques

Mojtaba Porghoveh, Raffaele Carli, *Senior Member, IEEE*, and Mariagrazia Dotoli, *Fellow, IEEE*

***Index Terms*— Logistics, Warehousing, Drone-as-a-service, Optimization, Control.**

I. INTRODUCTION

Logistics is a term which has its initial roots in the military context. However, it has now become a prevalent concept in the business domain, especially among manufacturing companies and warehouses. Warehousing operations takes up to 30 % of the total costs of the logistics and it is considered by many to be the heart of the logistics [1]. Few of the warehouse operations can be listed as: receiving the shipments, sorting items, labeling them and making datasheets, inventory management including cycle counting and monitoring and stock tracking, and maintaining a balancing the supply and demands of the objects.

Drones can assist warehousing and by providing automated inventory operations and surveillance processes. They also can be used as inspectors for safety and security of the warehouses or even performing operations at unreachable locations in warehouses. The cost of employing and maintaining the drone management system may be a hinder for the industry for employing drones to their business. However, drones as a Service (DaaS) strategy, offers various types of services performed by drones, including logistic operations, to other businesses allowing the customers to avoid establishing the drone management system themselves and reduce their costs. The adoption of drones in logistics and particularly warehousing, has assisted the industry in three different categories of inventory management, inspection and surveillance and infra-structure. Among the aforementioned, there is more evidence for the inventory management using DaaS [2]–[4]. In this work, we aim to provide a brief review of the literature of drones and their applications in indoor logistics from the control and optimization prospective. Our work provides a unified resource for those who seek a unified reference for the both optimization and control problems and techniques and the challenges which exist within the context of logistic drones. This study primarily aims to examine the optimization and control strategies for drones within enclosed spaces (indoor logistics), an area that has not been extensively explored in the literature. To the authors best knowledge, there has not been a thorough examination of optimization and control techniques used for drones in indoor logistics in a unified study. Therefore, this wok is to fill the perceived gap within the literature. More precisely, we intend to:

- classify the existing approaches published in recent years according to their design philosophies
- summarise the advantages and disadvantages of different guidance and control approaches;
- analyse the current challenges of using different methods for spaceflight and aerospace applications;

II. METHODOLOGY

The implementation of drones in logistics and warehousing is a current issue and fairly new, thus, the time span of this study is decided to be on the last 10 years from 2014 to 2024. Four databases of IEEE Xplore, Scopus, Web of Science, and ScienceDirect are looked into. Initially, 183 papers were collected by searching “drones in logistics.” After narrowing the focus to indoor logistics, 91 papers were removed. and, 32 additional papers were included. The final keywords used this research are selected by categorizing and reviewing the entries primarily found by searching the literature using the mentioned keyword are the combination of the words: ‘logistics’, "warehouse", ’inventory management’, with ’drone’. In the next step, we categorized the papers according to the following characteristics: Activity or the task of the drone as a service, control and optimization challenge of the task and the methodology to tackle this issue, and the architecture of the approach. Once the categorization is done, additional papers were added to the research entries. The proposed methodology has 9 steps. is showed in Fig. 1.

III. CONTROL AND OPTIMIZATION METHODS OF DRONES IN INDOOR LOGISTICS

Drones are an asset for internal logistics, however, they face multiple challenges that can limit their capabilities. In the following common problems and the solutions found in the literature to date, are listed. The main problems and the challenges of using drones in warehouses and internal logistics are listed in Table I.

For effective drone control in indoor logistics, localization is crucial. Handling underactuated quadrotor systems poses another challenge. We categorize controllers into artificial

The work of M. Porghoveh was supported by the National Recovery and Resilience Plan (NRRP) - “Patti territoriali” within the Italian National Ph.D. Program in Autonomous Systems (DAuSy). The work of R. Carli and M. Dotoli was supported in part by the National Recovery and Resilience Plan (NRRP), Mission 4 Component 2 Investment 1.3 - Call for tender No. 341 of March 15 2022 of Italian Ministry of University and Research (funded by the European Union – NextGenerationEU) under the project “MICS (Circular and Sustainable Made-in-Italy)” (project code: PE00000004).

M. Porghoveh, R. Carli, and M. Dotoli are with the Department of Electrical and Information Engineering of the Polytechnic of Bari, Italy (e-mail: m.porghoveh@phd.poliba.it, {raffaele.carli, mariagrazia.dotoli}@poliba.it).

TABLE I

MAIN OPTIMIZATION AND CONTROL CHALLENGES FOR INDOOR DRONES IN LOGISTICS

optimization problems	**control challenges**
mission scheduling	obstacle avoidance
routing planning	localization
jerk-minimizing	autonomous mission
battery usage minimization	collision avoidance

intelligence-based, linear, and nonlinear types. Amongst the linear controllers, evidently the famous PID controller is the most used controller for a variety of drone applications of in warehouses [5]. Other control methods, for instance, linear quadratic control, model predictive control, dynamic matrix control, are also used and they are implemented in the references [6], [7]. The most important advantage of model predictive control is that the constraints of the problem can be easily modelled, on the other hand, it costs heavy calculations. Sliding mode contoller, backstepping controller [8] and H-infinity controller [9] methods are among the nonlinear controllers used for indoor drone flight control. The optimization challenges such as rout planning, or realized as vehicle routing problems is dealt with heuristic and mathematical optimization techniques such as linear programming, or derivative based optimization techniques. Modelling the constraints such as flight time, payload, placing the charging hub(s) and the assigning the mission to the drone agents are the optimization problems that are dealt with the optimization techniques in [10], [11]

IV. CONCLUSION

In this paper, the most challenges of the implementation of drones in indoor logistics and warehousing are identified and categorized with the control and optimization perspective. The aim is to provide a brief reference that unifies this co-existing issue within the literature.

REFERENCES

[1] E. Companik, M. J. Gravier, and M. T. Farris II, "Feasibility of warehouse drone adoption and implementation," *Journal of Transportation Management*, vol. 28, no. 2, p. 5, 2018.

[3] L. Wawrla, O. Maghazei, and T. Netland, "Applications of drones in warehouse operations," *Whitepaper. ETH Zurich, D-MTEC*, p. 212, 2019.

[4] M. Beul, D. Droeschel, M. Nieuwenhuisen, J. Quenzel, S. Houben, and S. Behnke, "Fast autonomous flight in warehouses for inventory applications," *IEEE Robotics and Automation Letters*, vol. 3, no. 4, pp. 3121–3128, 2018.

[5] P. Burggräf, A. R. Pérez Martínez, H. Roth, and J. Wagner, "Quadrotors in factory applications: Design and implementation of the quadrotor's p-pid cascade control system: Modeling and implementation," *SN Applied Sciences*, vol. 1, no. 7, p. 722, 2019.

[6] G. Garimella, M. Sheckells, S. Kim, G. Baraban, and M. Kobilarov, "Improving the reliability of pick-and-place with aerial vehicles through fault-tolerant software and a custom magnetic end-effector," *IEEE Robotics and Automation Letters*, vol. 6, no. 4, pp. 7501–7508, 2021.

[7] N. Faedo, S. Olaya, and J. V. Ringwood, "Optimal control, mpc and mpc-like algorithms for wave energy systems: An overview," *IFAC Journal of Systems and Control*, vol. 1, pp. 37–56, 2017.

[2] B. Rahmadya, R. Sun, S. Takeda, K. Kagoshima, and M. Umehira, "A framework to determine secure distances for either drones or robots based inventory management systems," *IEEE Access*, vol. 8, pp. 170 153–170 161, 2020.

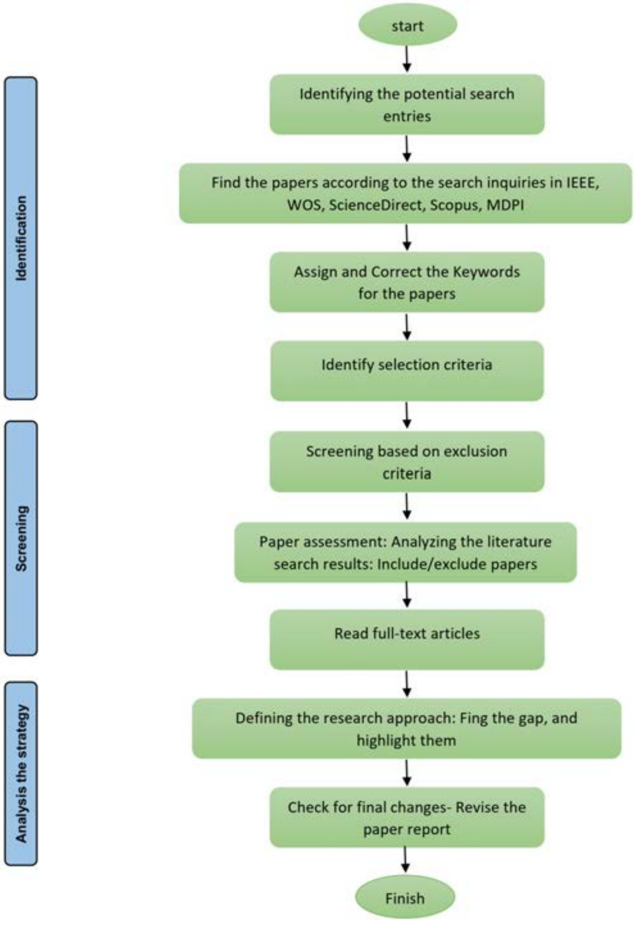

Fig. 1. Flowchart of the research approach

[8] F. Chen, R. Jiang, K. Zhang, B. Jiang, and G. Tao, "Robust backstepping sliding-mode control and observer-based fault estimation for a quadrotor uav," *IEEE Transactions on Industrial Electronics*, vol. 63, no. 8, pp. 5044–5056, 2016.

[9] A. Noormohammadi-Asl, O. Esrafilian, M. A. Arzati, and H. D. Taghirad, "System identification and h∞-based control of quadrotor attitude," *Mechanical Systems and Signal Processing*, vol. 135, p. 106358, 2020.

[10] J. A. Besada, A. M. Bernardos, L. Bergesio, D. Vaquero, I. Campaña, and J. R. Casar, "Drones-as-a-service: A management architecture to provide mission planning, resource brokerage and operation support for fleets of drones," in *2019 IEEE International Conference on Pervasive Computing and Communications Workshops (PerCom Workshops)*. IEEE, 2019, pp. 931–936.

[11] F. Gao, L. Wang, K. Wang, W. Wu, B. Zhou, L. Han, and S. Shen, "Optimal trajectory generation for quadrotor teach-and-repeat," *IEEE Robotics and Automation Letters*, vol. 4, no. 2, pp. 1493–1500, 2019.

Chattering-free Sliding Mode Control for Position and Attitude Tracking of a Quadrotor with a Cable-Suspended Load

Sara Gomiero and Karl von Ellenrieder

Free University of Bozen-Bolzano and Polytechnic of Bari
`sara.gomiero@student.unibz.it, s.gomiero@phd.poliba.it,`
`karl.vonellenrieder@unibz.it`

There are diverse applications in industry, agriculture and logistics which can benefit from the use of quadrotor Uncrewed Aerial Vehicles (UAVs) with cable-suspended payloads. Their control is a challenging topic, given the complex, nonlinear, and underactuated dynamics of the UAV and the oscillations of the cargo. To address this problem, one of the most promising robust controllers is the sliding mode controller (SMC). However, a drawback of first order SMC is the chattering phenomenon, caused by the discontinuity of the signum function included in the control signal [1]. This work proposes four chattering-free first order sliding mode controllers for position and attitude tracking of a quadrotor with a cable-suspended payload. Our approach, which is inspired by [2], permits computation of the sliding surface coefficients using a simple linearization of the dynamic model and Hurwitz Stability, and reduces the undesired oscillations via approximation with a saturation function.

The Lagrangian formulation [3] is used to develop a mathematical model of the cargo drone in matrix form, i.e. $M(q)\ddot{q}+C(q,\dot{q})\dot{q}+G(q) = BU$. The system is divided int [illegible] subsystem (UAS), an [illegible]

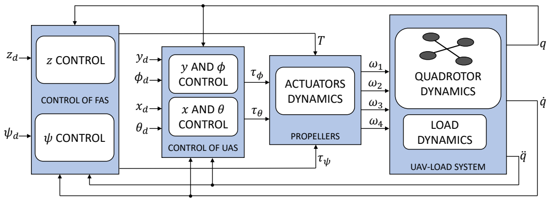

Fig. 1: Control scheme

The first step is to select a first order sliding surface associated with the desired behaviour of the system. Here, each sliding surface s is defined as a linear combination of the corresponding tracking error and its derivative. The second step is to drive the sliding surface to 0. Consequently, the sliding mode control consists of two terms: the equivalent control, which controls the system when the sliding surface is reached and it is found by requiring $\dot{s} = 0$; the switching control, which makes s converge to zero, by imposing the sliding condition

$$\dot{s} = -a\,\text{sign}\,(s) - bs.$$

For the UAS, the coefficients of the sliding manifolds are obtained via Hurwitz stability analysis from the linearized system.

Fig. 2 shows the results for $x_d = 2$ m, $y_d = 2$ m, $z_d = 2$ m, $\phi_d = 0$ rad, $\theta_d = 0$ rad, and $\psi_d = \pi/10$ rad. The simulations demonstrate the effectiveness of the proposed controllers for both tracking and chattering elimination. Even if minimization of the swing angles has not been addressed directly, the designed SMCs are robust to the oscillations of the cargo. The study represents a first step towards the development of robust controllers for trajectory tracking and stabilization of quadrotors with suspended payloads.

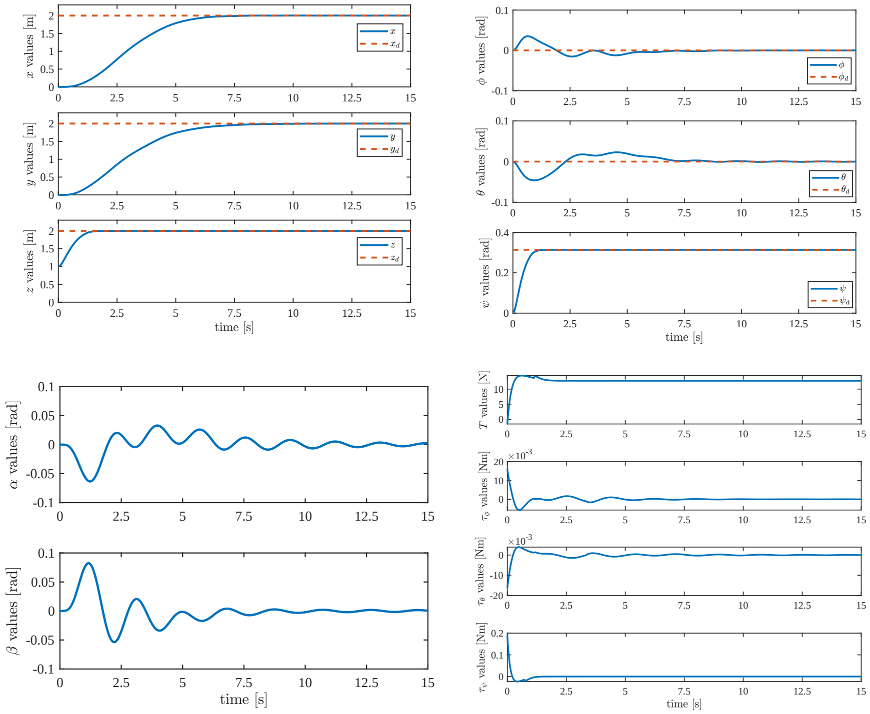

Fig. 2: Tracking and elimination of cargo oscillations and chattering

References

1. K. Kim, J. Park, and Y. Choi, “Chattering Free Sliding Mode Control,” in 2006 SICE-ICASE International Joint Conference, (Busan Exhibition & Convention Center-BEXCO, Busan, Korea), pp. 732–735, IEEE, 2006.
2. E.-H. Zheng, J.-J. Xiong, and J.-L. Luo, “Second order sliding mode control for a quadrotor UAV,” ISA Transactions, vol. 53, pp. 1350–1356, July 2014.
3. Z. Zhang, D. Zhang, D. Kong, and Y. Wang, “Real-Time Local Obstacle Avoidance and Trajectory Tracking Control of Quadrotor UAVs With Suspended Payload in Complex Environments,” IEEE Access, vol. 11, pp. 144017–144029, 2023.

Safety-driven mixed model and learning-based motion planning and control of autonomous systems

Mohammad Jeddi[1,2], Paolo Falcone[1]

(1) Autolab Group, Engineering Department “Enzo Ferrari”, University of Modena and Reggio Emilia, Italy

(2) Polytechnic University of Bari, Italy

Abstract

Autonomous systems, particularly vehicles and robots, are at the forefront of modern technological advancements. These systems must operate efficiently in crowded and structured environments, facing significant challenges in ensuring safety and adaptability. This research aims to contribute to the field of motion planning and control for autonomous systems, with a specific focus on autonomous driving at intersections, by combining the strengths of model-based and learning-based methodologies. The primary objective is to develop algorithms that are both safe and adaptive, addressing current limitations and pushing the boundaries of state-of-the-art technologies [1-3].

The initial phase of the project focuses on model-based methodologies, which rely on mathematical models, optimization tools, and algorithms. These approaches provide performance guarantees and ensure feasibility, though they often require significant computational resources. The research aims to optimize these methodologies, reducing their computational demands and enhancing their applicability in safety-critical scenarios, such as navigating intersections. In parallel, the project explores learning-based methods, which learn from data and experiments without relying on explicit models. These methods have shown promise in non-safety-critical applications due to their efficiency and adaptability. However, their lack of interpretability presents challenges in ensuring performance guarantees. The research develops techniques to improve the interpretability and reliability of learning-based approaches, making them suitable for safety-critical applications like intersection management.

The core innovation of this research lies in the integration of model-based and learning-based approaches. By harnessing the strengths of both methodologies, the project aims to achieve the following:

- Efficiency: Leveraging the computational advantages of learning-based methods.
- Adaptability: Ensuring that the systems can handle diverse and complex scenarios, particularly at intersections.
- Performance Guarantees: Providing safety and reliability through model-based methods.

Simulation

In this section, we define the problem as follows: Our system is impacted by two different stochastic disturbances occurring at different times. Our initial objective is to design two robust Model Predictive Controllers (MPC), specifically Tube MPCs, tailored to each disturbance. Subsequently, we aim to develop an outer controller using learning methods to switch between the inner controllers in response to the respective disturbances. The system we simulated is illustrated in the following block diagram. The proposed method will be compared with previous work.

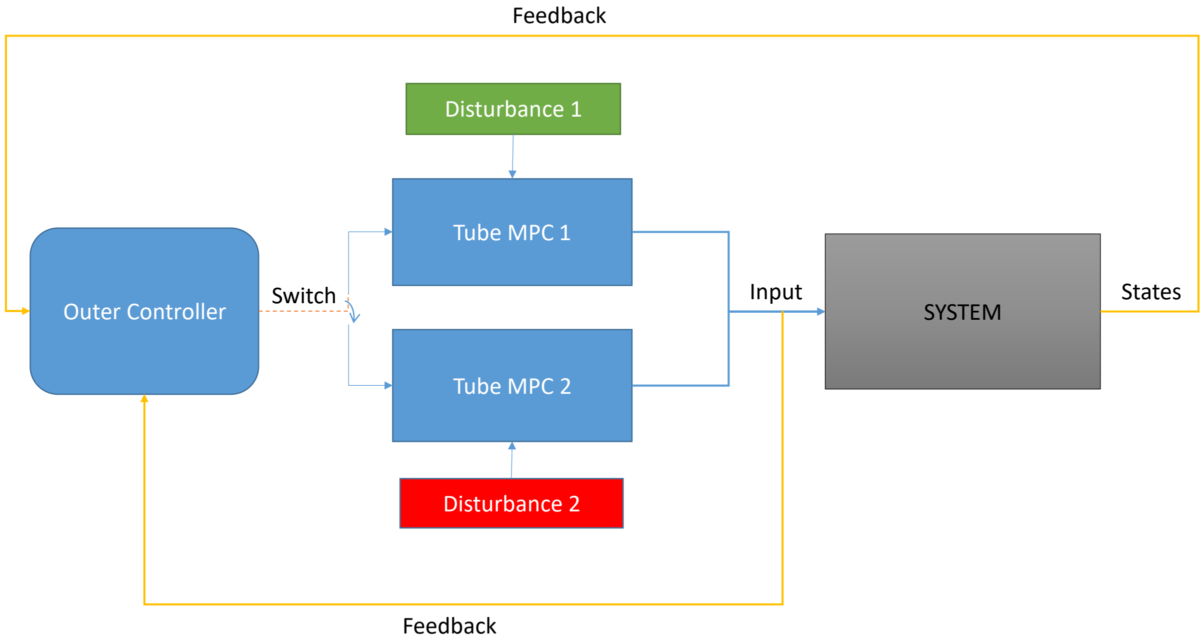

References

[1] I. Batkovic, U. Rosolia, M. Zanon, and P. Falcone, “A robust scenario mpc approach for uncertain multi-modal obstacles,” IEEE Control Systems Letters, vol. 5, no. 3, pp. 947–952, 2020.
[2] I. Batkovic, M. Zanon, M. Ali, and P. Falcone, “Real-time constrained trajectory planning and vehicle control for proactive autonomous driving with road users,” in Proc. Eur. Control Conf. (ECC), 2019.

[3]. Hult, Robert, Mario Zanon, Sebastien Gros, and Paolo Falcone. "Optimal coordination of automated vehicles at intersections: Theory and experiments." IEEE Transactions on Control Systems Technology 27, no. 6 (2018): 2510-2525.

Project co-funded by the European Union – Next Generation Eu - under the National Recovery and Resilience Plan (NRRP), Mission 4 Component 1 Investment 4.1 - *Decree No* 118 of Italian Ministry of University and Research - Concession Decree No. 2333 of the Italian Ministry of University and Research, Project code D93C23000450005, within the Italian National Program PhD Programme in Autonomous Systems (DAuSy).

Human-robot co-transport of flexible materials using deformation constraints

Alessandro Di Biase, Renat Kermenov, Sauro Longhi, Andrea Bonci

Polytechnic University of Marche, Ancona, via Brecce Bianche 10
Polytechnic of Bari, Bari, Via Re David 200
`a.dibiase8@phd.poliba.it`, `r.kermenov@pm.univpm.it`, `sauro.longhi@univpm.it`, `a.bonci@univpm.it`

The co-transport (collaborative-transport) of deformable materials such as fabrics, composite materials, cables, or wires poses significant challenges for industrial robotics due to the material's tendency to slide, stretch, and deform. Common approaches rely on force sensors [1], or with depth images and neural networks (NN) [2], to estimate and restore the material's ideal state. Methods face issues with force control effects and the industrial reliability, respectively.

We propose a new method based on the estimation of the deformability constraints of flexible materials. These constraints allow to obtain geometric parameters that enable the trajectory planning for a collaborative manipulator, ensuring deformation constraints are maintained throughout the transport process.

By estimating the shape of the fabric using a mathematical model under appropriate assumptions, we can simplify its complex dynamic modeling [3]. The fabric is represented as a set of stitches arranged in a pattern, with adjacent points linked by a mass-spring-damper relationship. The width, length, and density of points per surface are necessary parameters to simulate the fabric. The spring and damper parameters can be tuned to best fit the material used.

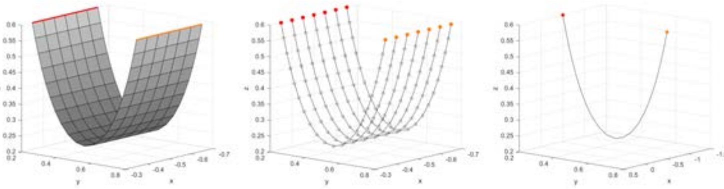

Fig. 1: From the fabric (left) to the catenary rapresentation (right)

This model can be further simplified using the catenary equation [4]. The fabric is considered as a parallel set of wire, linked perpendicularly to the handled edges, that are parallel to each other. All the wires are described by the catenary equation with the same coefficients.

An algorithm based on the catenary equation computes the desired distance between the handled points to achieve the desired deformation. A degree of freedom allows the human operator to choose the height difference between the robot's end-effector and the human's handling point. The robot must maintain the same angles found with trigonometry formulas based on the extremum points of the edge handled by the human operator.

This approach identifies the point the robot's end-effector has to reach. Two additional algorithms plan and execute corrective actions to maintain the desired fabric configuration, reaching continuously the desired points. The faster the robot's reaction time is, the more fluid and efficient the collaboration. The proposed method optimizes trajectory planning with near-time-optimal control, ensuring safety in accordance with ISO/TS 15066 guidelines.

The system is tested in a simulation scenario in which the human moves along a planned trajectory. The robot has an initial delay of $2s$, then begins its working loop: acquiring and computing the image for 0.1 seconds, then planning and executing the trajectory. The distance between the robot's end-effector and the human handling point, and its RMS value, are analyzed.

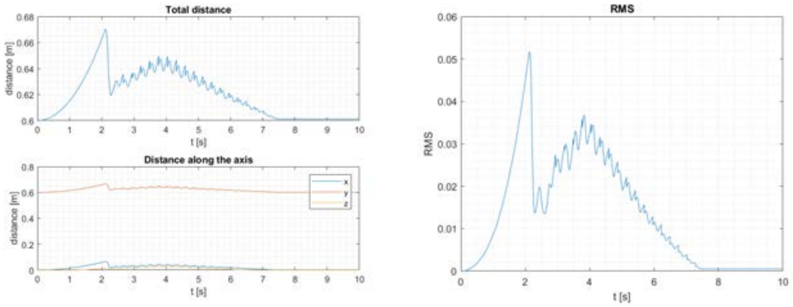

(a) Distance (b) RMS

Fig. 2: RMS

At around $2s$, the robot's end-effector is at the maximum distance from the human handling point, resulting in a peak RMS value. This moment marks the last instance of the robot's waiting condition, after which the robot reduces the error. While individual coordinate errors are minor, their cumulative effect is significant, highlighting how delays and physical limitations impact robot motion. Finally, the method is feasible solution that is easy to tune, quick to train, and sufficiently reliable for industrial applications.

References

1. E. Miguel, D. Bradley, B. Thomaszewski, B. Bickel, W. Matusik, M. Otaduy, and S. Marschner, "Data-driven estimation of cloth simulation models," *Computer Graphics Forum*, vol. 31, no. 2pt1, pp. 499–508, 2012. [Online]. Available: https://diglib.eg.org/handle/10.1111/cgf.2012.31.issue-2pt1
2. D. De Schepper, G. Schouterden, K. Kellens, and E. Demeester, "Human-robot mobile co-manipulation of flexible objects by fusing wrench and skeleton tracking data," *International Journal of Computer Integrated Manufacturing*, 2023.
3. B. Ben Boubaker, B. Haussy, and J. Ganghoffer, "Discrete models of woven structures. macroscopic approach," *Composites Part B: Engineering*, vol. 38, no. 4, pp. 498–505, 2007. [Online]. Available: https://www.sciencedirect.com/science/article/pii/S1359836806000540
4. J. Weil, "The synthesis of cloth objects," *Proceedings of the 13th annual conference on Computer graphics and interactive techniques*, 1986. [Online]. Available: https://api.semanticscholar.org/CorpusID:3259265

Socially-Aware Opinion-Based Navigation with Oval Limit Cycles for Human-Robot Interaction

Giulia d'Addato, Luigi Palopoli and Daniele Fontanelli

University of Trento and Polytechnic of Bari
`giulia.daddato@unitn.it, g.daddato1@phd.poliba.it,`
`luigi.palopoli@unitn.it, daniele.fontanelli@unitn.it`

The landscape of social robot navigation has grown considerably, with many approaches aimed at ensuring safe and efficient cooperation between robots and humans. Rapid decision-making and emulation of human-like navigation protocols, which involve non-verbal cues, are essential for fostering natural and smooth interactions. Existing reactive strategies, including social force models (SFMs), do not provide robust deadlock-free guarantees and may struggle in complex scenarios. The approach we propose addresses critical limitations of existing methods by integrating the robustness of potential fields [1] with the adaptability of nonlinear opinion dynamics [2]. This combination ensures reliable and efficient navigation in human-shared environments, guaranteeing collision avoidance and enhancing the robot's social acceptability in dynamic and unpredictable settings.

In this work, we leverage potential fields with an attractive field guiding the robot towards its goal. To enhance obstacle avoidance, we introduce a vortex field that pushes the robot towards an oval limit cycle around humans (Figure 1). This particular shape is a generalisation of the circular limit cycle model which allows to reduce trajectory curvature, minimise jerk, and respect human's personal space [3]. However, traditional potential fields may have some limitations such as jerky trajectories and oscillatory behaviour, and lack of control over the direction of rotation around obstacles.

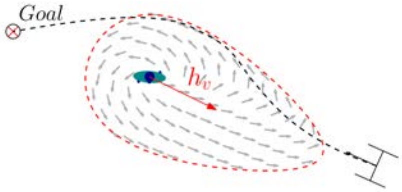

Fig. 1: Oval limit cycle and vortex repulsive field around the human [3]

To overcome these issues, we integrate opinion dynamics with potential fields to influence obstacle circumnavigation, ensuring smooth and predictable navigation. The opinion-driven robot navigation model [2] is useful in potentially conflicting situations like the human-corridor-passing problem. It allows the robot to regulate its angular velocity while continuously updating each agent's opinion in response to its own state, the opinions of others, and external stimuli. The

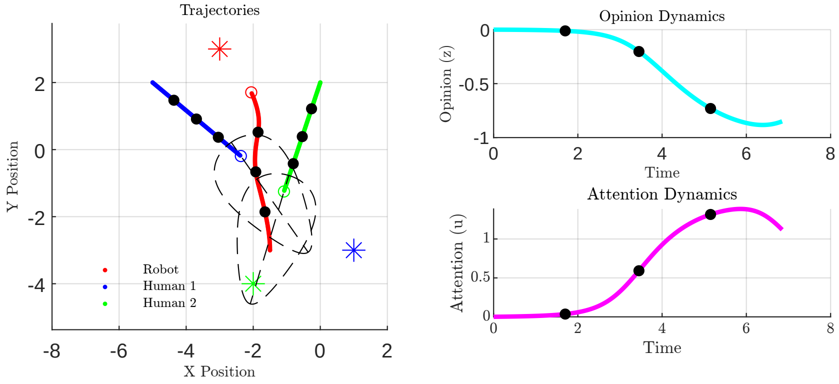

Fig. 2: On the left, the trajectories of the agents as they move towards their goals (stars); on the right, robot's opinion and attention over time. Temporal markers (black dots) are shown along the spatial trajectories, opinion and attention.

robot's opinion about its passing direction evolves dynamically, focusing on the human mover most rapidly approaching. A critical distance parameter adjusts the robot's attention as it approaches a human, prompting timely reactions. By integrating opinion dynamics with potential fields, we define the direction of rotation of the potential vortex, enabling anticipatory and smooth avoidance manoeuvres. In this way, the robot's dynamically evolving opinion influences the potential fields, ensuring fast and decisive movements, preventing deadlocks, and balancing reliability with efficiency.

Simulations and experiments confirm the effectiveness of the proposed method. Figure 2 illustrates a mobile robot navigating around two pedestrians using our approach. The robot successfully reaches its goal while gracefully avoiding the human along its way. The attention graph shows how the robot's attention rises with the proximity of a human. In terms of opinion, when a human is on the robot's left, it turns right, navigating counterclockwise, and vice versa for a human on its right. In conclusion, this study offers a promising solution for socially-aware robot navigation, enabling robots to dynamically adjust to human presence, thereby promoting harmonious human-robot coexistence.

References

1. O. Khatib, "Real-time obstacle avoidance for manipulators and mobile robots," Proceedings. 1985 IEEE International Conference on Robotics and Automation, St. Louis, MO, USA, 1985.
2. C. Cathcart, M. Santos, S. Park and N. E. Leonard, "Proactive Opinion-Driven Robot Navigation Around Human Movers," 2023 IEEE/RSJ International Conference on Intelligent Robots and Systems (IROS), Detroit, MI, USA, 2023.
3. M. Boldrer, M. Andreetto, S. Divan, L. Palopoli and D. Fontanelli, "Socially-Aware Reactive Obstacle Avoidance Strategy Based on Limit Cycle," in IEEE Robotics and Automation Letters, vol. 5, no. 2, pp. 3251-3258, April 2020.

Mesoscopic digital control for Practical String Stability of vehicular platoons

Pietro Bonsanto [1,2], Mattia Mattioni [3], Alessio Iovine [4], Elena De Santis [2] and Maria Domenica Di Benedetto [2]

Abstract— **In this paper, we propose a new piecewise constant mesoscopic feedback for practical string-stability of a platoon under sampled and quantized measurements. The design is based on a mesoscopic approach and is carried out over the sampled-data model associated to each vehicle.**

I. MOTIVATION AND INTRODUCTION

Traffic congestion, car accidents, bad driving, and pollution challenge researchers to develop intelligent vehicle control systems. A key issue is 'stop and go waves,' where disturbances in one vehicle amplify through following vehicles. In this view, String Stability (SS) [1] is crucial, ensuring a series of vehicles maintain a target distance and prevent perturbations from amplifying. Studies show that using macroscopic information, which aggregates data from the entire platoon, can ensure SS [2]. Moreover, communication devices between vehicles are vital, as seen with quantization preventing stability [3]. This paper examines an homogeneous platoon with quantized transmitted measurements. We propose a sampled-data mesoscopic controller using quantized information to investigate and preserve SS.

II. MODELING AND PROBLEM FORMULATION

A. Microscopic modeling

Let $\mathcal{I}_0^N$ be the set of N vehicles composing a platoon. Each vehicle is described by its longitudinal position, $r_i \in \mathbb{R}^+$, and its longitudinal speed $v \in \mathbb{R}^+$, such that we adopt as state vector $x_i = \begin{bmatrix} r_i & v_i \end{bmatrix}^\top$, $\forall\, i \in \mathcal{I}_0^N$. We will consider as state variable the error in position and velocity of two following vehicles $\chi_i := x_i - x_{i-1}$. Under the assumption of piecewise constant control, the sampled-data equivalent model [4] is given by

$$\chi_i(t_{k+1}) = A_{\mathtt{d}}\chi_i(t_k) + B_{\mathtt{d}}(u_i(t_k) - u_{i-1}(t_k)) \tag{1}$$

with $A_{\mathtt{d}} = e^{AT} = \begin{bmatrix} 1 & T \\ 0 & 1 \end{bmatrix}$, $B_{\mathtt{d}} = \int_0^T e^{As}\mathrm{d}sB = \begin{bmatrix} \frac{T^2}{2} \\ T \end{bmatrix}$ For all $t_k = kT$ being the sampling time, T sampling period. Assuming that $\Delta\bar{p} > 0$ is the desired inter-vehicular distance at steady state, the equilibrium point for the i^{th} system corresponds to the case where all the vehicles have the same speed and are at the same distance, i.e. $\chi_{e,i} = \bar{\chi} = [-\Delta\bar{p}\ 0]^\top$. In this context, we define the lumped state and the lumped equilibrium for $u_{i-1} = 0$ respectively as

$$\chi = \begin{bmatrix} \chi_0^\top \ \chi_1^\top & \cdots & \chi_N^\top \end{bmatrix}^\top, \chi_e = \begin{bmatrix} \bar{\chi}^\top & \bar{\chi}^\top & \dots & \bar{\chi}^\top \end{bmatrix}^\top \tag{2}$$

B. Macroscopic modeling

To model the function entailing the information along the platoon, we assume each vehicle receives partial aggregate information on the platoon. For $i \in \mathcal{I}_0^N$ we define this *macroscopic* information function as $\psi_{i-1}(\chi_i(t_k)) : \mathbb{R}^2 \times \underbrace{\cdots}_{\text{i times}} \times \mathbb{R}^2 \mapsto \mathbb{R}^2$, with the property that

$$|\psi_{i-1}(\chi_0(t_k), \cdots, \chi_{i-1}(t_k))| \leq c \max_{i \in \mathcal{I}_0^N} |\chi_{i-1}(t_k)|. \tag{3}$$

In the following, we assume this function to be received by the vehicles at the sampling instants only, i.e. t_k.

C. Problem Statement

Under the assumptions, the goal is to derive a piecewise constant controller that asymptotically tracks the desired distance given by the constant spacing policy $\Delta p_i^r(t_k) = -\Delta\bar{p}$, of the form

$$\begin{aligned} u_i(t_k) =& q(u_{i-1}(t_k)) + K_{\mathtt{d}} q(\chi_i(t_k)) \\ &+ F_{\mathtt{d}} q(\psi_{i-1}(q(\chi_0(t_k)), \dots, q(\chi_{i-1}(t_k)))) \end{aligned} \tag{4}$$

where $t_k = kT$ and $K_{\mathtt{d}}, F_{\mathtt{d}}$ are matrices to be specified later on and $q(\cdot)$ is the quantizer, such that $|y| \leq M \Rightarrow |q(y) - y| \leq \mu$. We want this controller to ensure practical String Stability (pSS) in the sense of the definition below.

Definition 2.1 (Practical String Stability): For all $i \in \mathcal{I}_0^N$, system (1) is said to be *practically string stable (pSS)* if there exists $\vartheta_\mu \geq 0$ such that the following conditions hold:

(i) for all $\varepsilon > 0$ there exists $\alpha_\varepsilon > 0$ such that for all $N \in \mathbb{N}$, $t_k \in \Delta$

$$\max_{i \in \mathcal{I}_0^N} |\chi_i(0) - \chi_{e,i}| < \alpha_\varepsilon \Rightarrow \max_{i \in \mathcal{I}_0^N} |\chi_i(t_k) - \chi_{e,i}| < \varepsilon + \vartheta_\mu; \tag{5}$$

(ii) the trajectories asymptotically approach the set $\mathcal{B}_{\vartheta_\mu}(\chi_e) = \left\{\chi \in \mathbb{R}^2 : |\chi - \chi_e| \leq \vartheta_\mu\right\}$, i.e.

$$\lim_{t_k \to \infty} |\chi_i(t_k)|_{\mathcal{B}_{\vartheta_\mu}(\chi_e)} = 0. \tag{6}$$

The problem is then formalized as follows.

pSS Digital Control Problem: Consider a platoon of vehicles described by (1) under the assumptions (piecewise

---

[1] *Università degli Studi dell'Aquila*, Via Vetoio - Coppito, 67100 L'Aquila `pietro.bonsanto@student.univaq.it`

[2] *Polytechnic of Bari, Dept. of Electrical and Information Engineering*, Via Re David 200 70125 Bari-Italy `p.bonsanto@phd.poliba.it`.

[3] *Dipartimento di Ingegneria Informatica, Automatica e Gestionale A. Ruberti* (Università degli Studi di Roma *La Sapienza*); Via Ariosto 25, 00185 Rome, Italy.

[4] *Laboratoire des Signaux et Systèmes* (L2S), CNRS, CentraleSupélec, Université Paris-Saclay; 3 Rue Joliot Curie, 91190 Gif-sur-Yvette, France

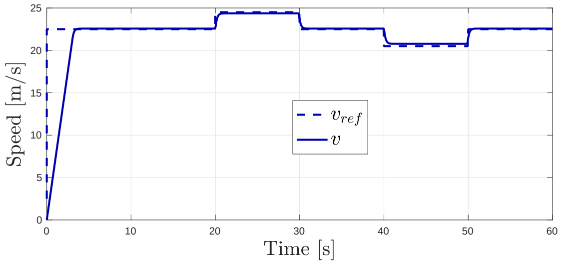

Fig. 1: Speed of the leader.

constant control and quantized measurements). Design a feedback law as in (4) making the equilibrium χ_e of the closed-loop platoon pSS with respect to μ in the sense of Definition 2.1.

III. MAIN RESULT

At this point, the main result can be stated.

Theorem 3.1: The *pSS Digital Control Problem* is solved by the control (4), $\psi_i(t_k)$ and the matrices $F_{\mathtt{d}}, K_{\mathtt{d}}$ verifying the conditions below:

1) the matrix $A_{\mathtt{d}} - B_{\mathtt{d}} K_{\mathtt{d}}$ is Schur;
2) there exists $c \in \mathbb{R}^+$ such that the macroscopic function verifies (3) for all $i \in \mathcal{I}_0^N$
3) the parameter $\gamma = (1-\alpha)^{-1} c\beta r g$ verifies $\gamma \in (0,1)$ for $\alpha = \max_{\lambda \in \sigma(A_{\mathtt{d}} - B_{\mathtt{d}} K_{\mathtt{d}})} |\lambda|, \beta = \frac{|A_{\mathtt{d}} - B_{\mathtt{d}} K_{\mathtt{d}}|}{\alpha}$, $g = |B_{\mathtt{d}}|, r = |F_{\mathtt{d}}|$.

Then, by setting $\kappa = |K_{\mathtt{d}}|$, the closed-loop platoon is pSS with $\vartheta_\mu = (1 - (\alpha + grc\beta)^{-1} \beta g \mu \left(\kappa + r(c+1) + 1\right)$.

IV. NUMERICAL RESULTS

We consider $N = 10$ vehicles. The constant reference distance is set $\Delta\bar{p} = 20$ m and the initial desired speed of the leader is 20 m/s, while the acceleration is bounded by $-7 \le u_i \le 7$ m/s^2. The color scale represents the vehicles from the head pair (0,1) (dark blue) to the tail one $(N-1, N)$ (light blue). The leader tracks a piecewise constant reference speed profile v_{ref}, as seen in Fig. 1. Nevertheless, we can see by Figs. 2a,2b that the perturbation decreases along the platoon, as expected, validating the theoretical result.

V. CONCLUSIONS

We propose a new sampled-data quantized mesoscopic controller to ensure practical string stability to a vehicle platoon, affected by sampling and quantization effects. The design is constructive, allowing control law parameters to be freely tuned for desired performance. Quantization broadens the approach's applicability.

REFERENCES

[1] D. Swaroop and J. K. Hedrick, "String stability of interconnected systems," *IEEE transactions on automatic control*, vol. 41, no. 3, pp. 349–357, 1996.

[2] M. Mirabilio, A. Iovine, E. De Santis, M. D. Di Benedetto, and G. Pola, "String stability of a vehicular platoon with the use of macroscopic information," *IEEE Transactions on Intelligent Transportation Systems*, vol. 22, no. 9, pp. 5861–5873, 2021.

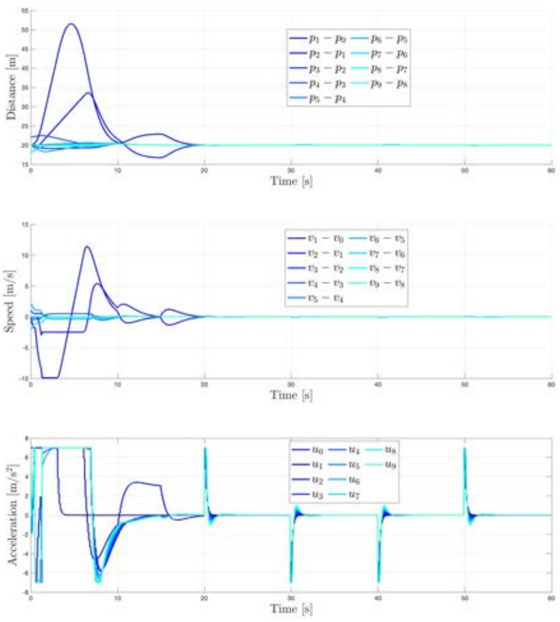

(a) The distance, velocity difference and acceleration of each vehicle

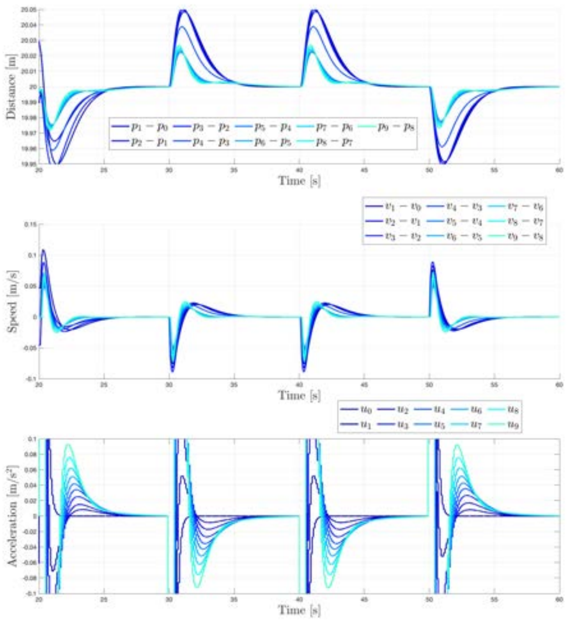

(b) Zoom of Fig. 2a.

[3] M. Di Ferdinando, P. Pepe, and E. Fridman, "Practical stability preservation under sampling, actuation disturbance and measurement noise, for globally lipschitz time-delay systems," in *Accounting for Constraints in Delay Systems*. Springer, 2022, pp. 109–124.

[4] S. Monaco and D. Normand-Cyrot, "Advanced tools for nonlinear sampled-data systems' analysis and control," *European journal of control*, vol. 13, no. 2-3, pp. 221–241, 2007.

ARIES: An Intelligent System for Landslide and Wildfire Risk Management

Giuseppi A., Di Paola A., Santopaolo A., Saif Saad S., Fiorini F. and Pietrabissa A.

University of Rome ”La Sapienza”, DIAG, Via Ariosto, 25
dipaola@diag.uniroma1.it, a.dipaola4@phd.poliba.it

***Abstract*—With the rise in frequency of environmental diseases like wildfires and landslides, protection and risk management have become critical challenges for assuring both the safety of human populations and the sustainability of ecosystems. In this direction, a suite of functionalities and solutions have been developed to support emergency operators in all phases of emergency management, from risk estimation to enviromental monitoring, early detection and response. The present paper provides an overview of the main algorithms that consistute the building blocks of the enviromental monitoring system developed within the ARIES project, founded by ESA, through a combination of dynamical systems, digital twins and convolutional neural networks, also reporting on its early validation activities.**

***Index Terms*—Convolutional Neural Networks, Digital Twins, Cellular Automata, Voronoi Tessellation, UAVs**

I. THE ARIES PROJECT: FUNCTIONAL ARCHITECTURE

This work presents the results and algorithms developed in the scope of the ARIES project, to address the challenges of efficient fire management through a satellite-enabled monitoring framework and the employment of UAVs. In particular, the main functionalities include:

- the development of a deep learning-based solution for joint estimation of both wildfire and landslide risk through an ad-hoc multi-channel convolutional neural network (CNN) architecture. Starting from remotely sensed satellite data, the proposed algorithm aims to make accurate long-term predictions, producing a pixel-wise risk assessment of the region of interest;
- the design of a fire spreading simulator that acts as a digital twin for the monitored area. By combining satellite data and real-time sensor measurements, the designed digital system behaves as a short-term risk predictor. The output is used to produce an optimal scheduling logic to achieve the best monitoring strategy for a fleet of patrolling drones;
- a CNN-based solution for real-time automated fire detection directly from ground or drone-mounted cameras.

The building blocks of the ARIES architecture, from the algorithms proposed to the emergency management process, are illustrated in Fig. 1.

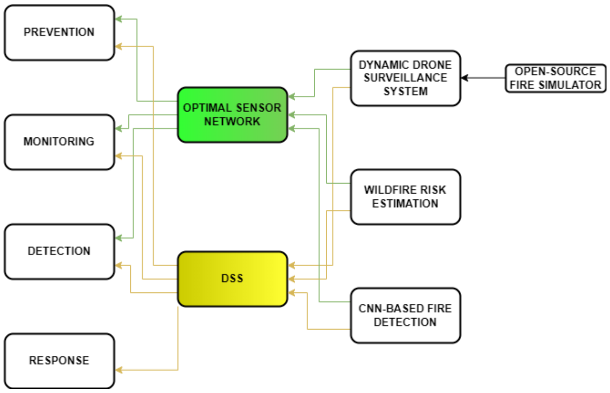

Fig. 1. The ARIES architecture. The DSS and the optimal sensor network are fed with the three main functionalities described in this work, developed to support the emergency management process (left).

A. CNN-based Long-term Risk Prediction

The first solution involves the design of a multi-channel CNN [1] aimed at producing a wildfire and landslide susceptibility analysis starting only from remotely sensed (offline) data. The neural network processes images related to the Normalized Difference Vegetation Index (NDVI), Digital Elevation Model (DEM), lithology, land cover, and other satellite sources [2] that are strongly related to the emergence of environmental hazards. The proposed architecture is illustrated in Fig. 2 and utilizes a combination of convolutional and deconvolutional layers, typical of autoencoders, to produce detailed risk maps for both fires and landslides. The network has been trained with a multi-objective loss function, given by the combination of a customized Weighted Mean Squared Error (MSE) evaluated over the fire masks and a Weighted Binary Cross Entropy (WBCE) over the landslides susceptibility examples.

B. Short-term Risk Management employing UAVs

The proposed short-term risk predictor emulates the fire spreading over the region by integrating offline satellite data with real-time sensor measurements. By the employment of the so-called Cellular Automata (CA) systems, the region has been divided in cells and a Digital Twin for the monitored area has been developed. The discrete system evolves according to the concepts of cell states, cell neighborhoods and transition functions. At each time step, the risk distribution is processed by the Voronoi Tessellation algorithm that identifies the waypoints after having performed an optimal partitioning of the area based on a distance measure, the field-of-view of drones' cameras, enhancing the monitoring efficiency [3]. An example

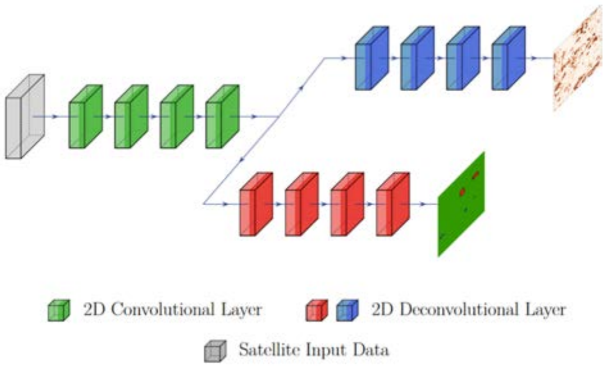

Fig. 2. CNN architecture employed for one-shot predictions for both landslides and wildfires in form of a risk map.

of the resulting Voronoi Tessellation starting from NDVI is shown in Fig. 3. A Dispatch Controller is employed, then, to select the target waypoint with the highest priority depending on the on-going situation. The architecture of the monitoring system described in this section is illustrated in Fig. 4.

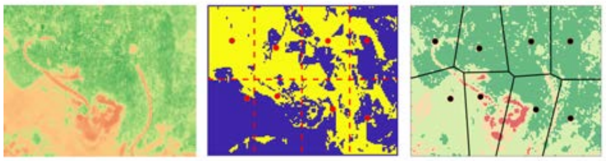

Fig. 3. From left to right: the NDVI computed over the test area, the heatmap generated from the fire probability distribution over cells and the resulting Voronoi partition of the region.

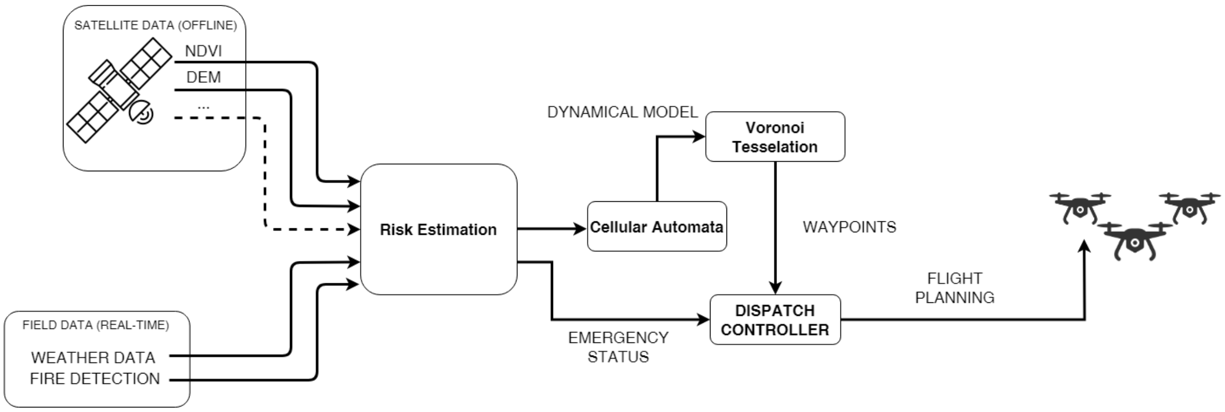

Fig. 4. Architecture of the drone-based surveillance system.

C. Real-time Fire Detection with CNNs

For real-time fire detection, a CNN-based solution using the U-Net proposed in [4] has been developed. This model processes images from ground and drone-mounted cameras to identify fire events promptly. Trained on an augmented dataset generated by merging and shuffling samples from the BoWFire Dataset and the Corsican Fire Database, the network has been validated achieving high accuracy on the test set.

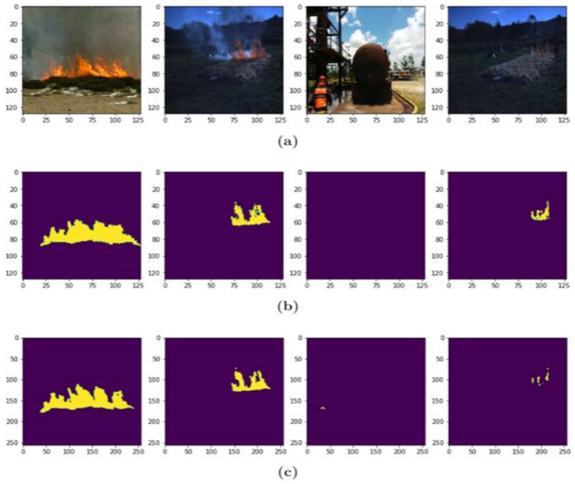

Fig. 5. Validation results of the CNN-based detector. From top to bottom: the input image, the ground truth and the U-Net prediction.

D. Case studies and results

The CNN-based long-term predictor has shown high performances, especially regarding the Recall score. The short-term risk management system was validated considering the ”Pineta di Roio” area (Italy), successfully simulating fire spreading events and optimizing drone patrols. The promising generalisation capabilities of the U-Net are highlighted from the results obtained on the test set (Fig. 5), crucial aspect to deploy the model in real-time applications.

REFERENCES

[1] Wang, Li and Li, Ruifeng and Shi, Hezi and Sun, Jingwen and Zhao, Lijun and Seah, Hock and Quah, Chee and Tandianus, Budianto, “Multi-Channel Convolutional Neural Network Based 3D Object Detection for Indoor Robot Environmental Perception,” Sensors, MDPI AG, Feb 2019.

[2] Louis Giglio and Luigi Boschetti, et al., “The Collection 6 MODIS burned area mapping algorithm and product,” Remote Sensing of Environment, Elsevier BV, vol. 13, pp. 72-85, Nov. 2018.

[3] Du, Qiang and Faber, Vance and Gunzburger, Max, “Centroidal Voronoi tessellations: Applications and algorithms,” SIAM review, vol. 44, pp. 637-676, 1999.

[4] Ronneberger, O. and Fischer, P. and Brox, T., “U-Net: Convolutional Networks for Biomedical Image Segmentation”, pp. 234-241.

Enhancing Extended Kalman Filters Performance through Covariance Estimation

Giorgio Manca, Mario Sassano, Sergio Galeani

University of Rome Tor Vergata
`g.manca5@phd.poliba.it`
{`mario.sassano`, `sergio.galeani`}`@uniroma2.it`

Keywords: Extended Kalman Filter, Covariance Estimation, Numerical Gradient Descent, Monte Carlo Optimization, Riemannian Optimization

Introduction

The Extended Kalman Filter (EKF) is a widely used algorithm for state estimation in nonlinear dynamic systems. Its performance critically depends on selecting accurate process and measurement noise covariance matrices, $\mathbf{Q}$ and $\mathbf{R}$. This work proposes an adaptive method for optimizing these matrices via numerical gradient descent and Monte Carlo optimization techniques.

Consider a discrete-time nonlinear time-invariant system:

$$\begin{cases} \mathbf{x}_{k+1} = \mathbf{f}(\mathbf{x}_k, \mathbf{u}_k) + \mathbf{w}_k \\ \mathbf{z}_k = \mathbf{h}(\mathbf{x}_k, \mathbf{u}_k) + \mathbf{v}_k \end{cases} \tag{1}$$

where $\mathbf{x}$ is the state, $\mathbf{z}$ is the output measurement, $\mathbf{u}$ is the input, $\mathbf{f}$ and $\mathbf{h}$ are the state transition and measurement functions, and $\mathbf{w}$ and $\mathbf{v}$ are the process and measurement Gaussian noise with covariance matrices $\mathbf{Q}$ and $\mathbf{R}$, respectively.

The standard EKF equations are [1]:

$$\begin{cases} \hat{\mathbf{x}}_{k|k-1} = \mathbf{f}(\hat{\mathbf{x}}_{k-1|k-1}, \mathbf{u}_{k-1}) \\ \mathbf{P}_{k|k-1} = \mathbf{F}_{k-1}\mathbf{P}_{k-1|k-1}\mathbf{F}_{k-1}^\top + \mathbf{Q}_{k-1} \\ \mathbf{K}_k = \mathbf{P}_{k|k-1}\mathbf{H}_k^\top (\mathbf{H}_k\mathbf{P}_{k|k-1}\mathbf{H}_k^\top + \mathbf{R}_k)^{-1} \\ \hat{\mathbf{x}}_{k|k} = \hat{\mathbf{x}}_{k|k-1} + \mathbf{K}_k(\mathbf{z}_k - \mathbf{h}(\hat{\mathbf{x}}_{k|k-1}, \mathbf{u}_k)) \\ \mathbf{P}_{k|k} = (\mathbf{I} - \mathbf{K}_k\mathbf{H}_k)\mathbf{P}_{k|k-1} \end{cases} \tag{2}$$

where $\hat{\mathbf{x}}$ is the estimate, $\mathbf{P}$ is the estimate covariance matrix, $\mathbf{K}$ is the Kalman gain, and $\mathbf{F}$ and $\mathbf{H}$ are the Jacobian matrices of $\mathbf{f}$ and $\mathbf{h}$ w.r.t. the state $\hat{\mathbf{x}}$.

Methodology

The proposed methodology involves defining a cost function based on the perceived error, which is the discrepancy between the EKF output $\mathbf{h}(\hat{\mathbf{x}}_{k|k-1}, \mathbf{u}_k)$ and the actual measurement $\mathbf{z}_k$:

$$J(\mathbf{Q}, \mathbf{R}) = \sum_{k=0}^{N-1} \left(\mathbf{z}_k - \mathbf{h}(\mathbf{x}_{k|k})\right)^\top \mathbf{W}^{-1} \left(\mathbf{z}_k - \mathbf{h}(\mathbf{x}_{k|k})\right) + \det(\mathbf{W}) \tag{3}$$

where N is the number of samples, and $\mathbf{W}$ is a weighting matrix that can be constructed starting from $\mathbf{Q}$ and $\mathbf{R}$ matrices as shown in [2].

To minimize the cost function (3), several simulations are performed in the neighborhood of the estimated state. The numerical gradient is computed by averaging the output measurements, and it is used to update estimates of $\mathbf{Q}$ and $\mathbf{R}$. Monte Carlo techniques are employed to find the optimal structure and values of these matrices. The optimization process follows these steps:

0. **Initialization**: Choose a initial guesses $\mathbf{Q}_0$ and $\mathbf{R}_0$.
1. **Simulation**: Run a batch of simulation using $\mathbf{Q}_i$ and $\mathbf{R}_i$ with different initial state estimate in a neighborhood $\hat{\mathbf{x}}_\mathbf{0}$.
2. **Evaluation**: Compute the cost function $J(\mathbf{Q}_i, \mathbf{R}_i)$ and its numerical gradient $\mathbf{G}_{Q_i}$ and $\mathbf{G}_{R_i}$ w.r.t. $\mathbf{Q}_i$ and $\mathbf{R}_i$, respectively.
3. **Update**: Use computed $\mathbf{G}_{Q_i}$ and $\mathbf{G}_{R_i}$ to adjust the covariance matrices as $\mathbf{Q}_{i+1}$= $\mathbf{\Gamma}(\mathbf{Q_i}, \mathbf{G_{Q_i}}, \sigma_i)$ and $\mathbf{R}_{i+1}$= $\mathbf{\Gamma}(\mathbf{R_i}, \mathbf{G_{R_i}}, \sigma_i)$, where $\mathbf{\Gamma}$ is defined as [3]:
$$\mathbf{\Gamma}(\mathbf{M}, \mathbf{G}, \sigma) := \mathbf{M}^{\frac{1}{2}} \exp(\sigma \mathbf{M}^{-\frac{1}{2}} \mathbf{G} \mathbf{M}^{-\frac{1}{2}}) \mathbf{M}^{\frac{1}{2}} \in \mathbb{S}^+, \; \forall \sigma \in [0,1] \tag{4}$$
with $\mathbb{S}^+ := \{\mathbf{X} \in \mathbb{R}^{n\times n}, n > 0 : \mathbf{X} = \mathbf{X}^\top \succ 0\}$.

It must be noted that with (4), $\mathbf{Q}$ and $\mathbf{R}$ move on the manifold $\mathbb{S}^+$, solving the problem of keeping them positive-definite. The parameter σ is analogous to the gradient descent step and must be chosen carefully.

Conclusion

Hereby, we propose a systematical approach to tune the covariance matrices $\mathbf{Q}$ and $\mathbf{R}$ for the improvement of EKF's performance, as opposed to classical methods that often rely on heuristical or experimental approaches. Numerical gradients and Monte Carlo optimization techniques are employed to achieve this goal. We also address the problem of maintaining $\mathbf{Q}$ and $\mathbf{R}$ positive-definite, in which preliminary efforts using direct gradient descent revealed difficulties.

Further investigation into optimization methods on Riemannian manifolds and other state-of-the-art approaches will advance the robustness and applicability of this technique in various real-world scenarios.

References

1. B. Siciliano, L. Sciavicco, L. Villani, G. Oriolo, *"Robotics: Modelling, Planning and Control"*, Springer London, 2010, doi: 10.1007/978-1-84628-642-1
2. V. A. Bavdekar, A. P. Deshpande, S. C. Patwardhan. *"Identification of process and measurement noise covariance for state and parameter estimation using extended Kalman filter"*, Journal of Process Control, vol. 21, pp. 585-601, Apr. 2011, doi: 10.1016/j.jprocont.2011.01.001
3. P.-A. Absil, R. Mahony, R. Sepulchre, *"Optimization Algorithms on Matrix Manifolds"*, Princeton University Press, 2008, doi: 10.1515/9781400830244

Safe Reinforcement Learning-Based Voltage Control in Nonlinear Power Systems

Sajjad Miralizadeh Jalalat, Antonio Russo, Alberto Cavallo

***Abstract*—High penetration of renewable energy sources (RES) adds further uncertainty to the power systems, which are complex and nonlinear as well. Reinforcement learning (RL) approaches, due to their good performance with stochastic nonlinear systems, recently attracted interests in the control of power system, including voltage regulation. However, ensuring the safety of these controllers is challenging because of potential instabilities. This work proposes a decentralized safe RL framework for voltage control using inverter-based DERs, guaranteeing exponential stability with specific Lipschitz constraints. Optimizing these bounds expands the search space for neural network controllers. The framework trains the neural network of each busbar using local measurements, eliminating the need for communication links. The method is tested on IEEE 15 and 33 busbar networks.**

I. Introduction

Modern power systems are increasingly complex due to the rise of distributed energy resources (DERs) like rooftop solar, electric vehicles, and battery storage, causing rapid voltage fluctuations beyond the capabilities of traditional controls. While power electronic inverters offer fast and flexible control, developing decentralized controllers that work solely on local measurements without real-time communication remains a significant challenge.

Several studies have explored using reinforcement learning (RL) for voltage control in power systems with algorithms such as deep Q-learning and actor-critic methods to manage devices like tap-changing transformers and inverter-based resources. However, these approaches often overlook stability requirements, typically assessed through simulations. This work proposes a decentralized safe RL framework ensuring exponential stability by employing engineered neural network controllers that comply with Lipschitz constraints.

The main contribution of this project is summarized in the following:

- Previous studies have mainly focused on radial networks, often neglecting the complexities and impact of meshed networks on controller performance.
- Linear and nonlinear models will be evaluated to identify an optimal operating domain for system stability.
- The impact of decentralized voltage regulation on active power flow between adjacent busbars will be assessed to ensure compliance with power system constraints.

A. Problem Formulation

Fig. 1 depicts the IEEE standard 15 busbar network, and because this network is a radial network, the linDistflow approach is formulated to model the dynamics of the busses voltages. The network model is as follows:

$$v = Rp + Xq + \mathbb{1} \tag{1}$$

where $\mathbb{1}$ is the one's vector. Matrices R, X, are positive definite and they describe the network, while p and q are vectors defining the active and reactive power of the bus bars [1], [2]. This study focuses on finding the optimal control q through inverter-based resources to minimize a given cost function. Denote $q_i = u_i(v_i)$ as the control law for each bus $i = 1, ..., N$, which is a mapping from voltage to reactive power. Let $v_{i,t}$ be the local voltage at the bus i at t_{th} iteration step, and denote $u_t = (u_1(v_{1,t}), ..., u_N(v_{N,t}))$. The q and v update iteratively as:

$$\begin{aligned} q_{t+1} &= q_t - u_t \\ v_{t+1} &= Rp + X(q_t - u_t) + \mathbb{1} \end{aligned} \tag{2}$$

The objective is to select the control u_t to minimize the cost function $C(u)$, subject to the iterative update rule

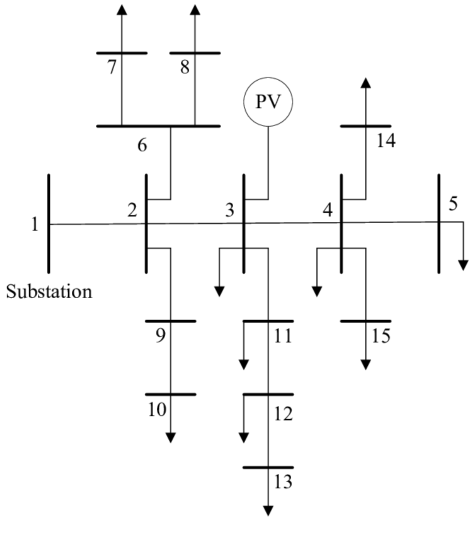

Fig. 1. IEEE standard 15 busbar network

S. Miralizadeh Jalalat, A. Russo and A. Cavallo are with Dipartimento di Ingegneria, Università degli Studi della Campania "Luigi Vanvitelli", 81031 Aversa, Italy (e-mail: {*sajjad.miralizadehjalalat, antonio.russo1, alberto.cavallo*}@unicampania.it).

Project co-funded by the European Union – Next Generation Eu - under the National Recovery and Resilience Plan (NRRP), Mission 4 Component 1 Investment 4.1 - Decree No. 118 (2nd March 2023) of Italian Ministry of University and Research - Concession Decree No. 2333 (22nd December 2023) of the Italian Ministry of University and Research, Project code D93C23000470005, within the Italian National Program PhD Programme in Autonomous Systems (DAuSy).

and saturation limit on u_t. The optimization problem is formulated as:

$$\begin{aligned} \min_{\mathbf{u}} & \, C(u) \\ s.t. \quad & q_{t+1} = q_t - u_t \\ & v_{t+1} = Rp + X(q_t - u_t) + \mathbb{1} \\ & \underline{u_t} \leq u_t \leq \overline{u_t} \\ & u_t \; is \; stabilizing \end{aligned} \tag{3}$$

where $\underline{u_t}$ and $\overline{u_t}$ are the lower and upper bounds for the control action at bus i, respectively. The origin of the system can be shifted by $v_t - \mathbb{1}$ denoted by $\hat{v}_t$.

For stabilizing the controller, reference [3] proves that as long as each controller u_i satisfies a Lipschitz constraint, the system is guaranteed to be locally exponentially stable. This theorem is mentioned below.

Theorem I.1. *Suppose a vector $\mathbf{k} = (k_1, ..., k_N)$ satisfies $0 < diag(\mathbf{k}) < 2X^{-1}$. Then if the derivative of the controller satisfies $u_i(0) = 0$ and $0 < \frac{du_i(\hat{v}_i)}{d\hat{v}_i} < k_i$ for all $i = 1, ..., N$, the equilibrium point $\hat{v} = 0$ of the dynamic system is locally exponentially stable.*

Now, with consideration that all feasible stabilizing u are in a convex set described by $\mathcal{S} = \{\nabla_{\hat{v}} u | 0 < \nabla_{\hat{v}} < 2X^{-1}\}$, each $\frac{du_i(\hat{v}_i)}{d\hat{v}_i}$ needs to be bounded by a separate k_i for bus $i = 1, ..., N$. Therefore, by optimally choosing the k, a larger search space for the neural network can be defined [3]. $\nabla_{\hat{v}}$ is defined as follows:

$$\nabla_{\hat{v}} = \begin{bmatrix} \frac{du_1(\hat{v}_1)}{d\hat{v}_1} & & \\ & \ddots & \\ & & \frac{du_N(\hat{v}_N)}{d\hat{v}_N} \end{bmatrix} \tag{4}$$

A neural network can be structured to fulfill the requirements for safe voltage control by having the optimal k values and satisfying conditions of Theorem 1. This neural network is designed based on the following Corollary.

Corollary I.1. *The condition for a locally stabilizing controller in Theorem I.1 is equivalent to:*

1) *$u_{\theta_i}(\hat{v}_{\theta_i})$ has the same sign as $\hat{v}_{\theta_i}$*
2) *$u_{\theta_i}(\hat{v}_{\theta_i})$ is monotonically increasing.*
3) *$\frac{du_i(\hat{v}_i)}{d\hat{v}_i} < k_i$.*

To fulfill these conditions, the activation function can be divided into positive and negative parts as follows:

$$\begin{aligned} & u_{\theta_i}(\hat{v}_{\theta_i}) = s_i ReLU(\mathbb{1}\hat{v}_i + b_i) + z_i ReLU(-\mathbb{1}\hat{v}_i + d_i) \\ & where \quad 0 < \sum_{j=1}^{l} s_i^j < k_i, \qquad \forall l = 1, 2, ..., m \\ & \qquad -k_i < \sum_{j=1}^{l} z_i^j < 0, \qquad \forall l = 1, 2, ..., m \\ & \qquad b_i^l = 0, b_i^l \leq b_i^{(l-1)} \qquad \forall l = 2, 3, ..., m \\ & \qquad d_i^l = 0, d_i^l \leq d_i^{(l-1)} \qquad \forall l = 2, 3, ..., m \end{aligned} \tag{5}$$

where s and z are weight vectors, and b and d are bias vectors of buses. m is the number of neurons and $\mathbb{1} \in \mathbb{R}^m$

B. Decentrilized Safe reinforcement learning

The Reinforce policy gradient method is a model-free RL algorithm that optimizes each state's policy by directly estimating the gradients of the expected reward with respect to the policy parameters, instead of using Bellman equations to calculate state and state-action value functions.The proposed method uses this method to sample initial states, simulate system dynamics, and collect state-action trajectories with corresponding rewards. These rewards, based on deviations from the desired state and control effort (6), are used to compute the loss as the negative mean of the product of log probabilities and normalized rewards. Gradients of this loss update the neural network controllers to enhance performance over time. Repeating this process across multiple episodes with decaying exploration noise leads to a control policy that minimizes voltage deviations and control effort. The gradient for updating weights of the neural network controller at bus i is obtained by [4].

$$r = -|\hat{v}_{i,t}| - \alpha |u_{i,t}| \tag{6}$$

$$\nabla J(\theta) = \mathbb{E}[\sum_{t=1}^{T} \nabla_\theta log \pi_\theta(u_{i,t}|\hat{v}_{i,t}) \sum_{t=1}^{T} C_i(u_{i,t})], \tag{7}$$

where α is a penalty factor for the control effort, θ is the parameter vector, π_θ is the taken policy at each state and $C_i(u(i,t))$ is the cumulative rewards of the taken actions.

II. Conclusions

This work addresses the complex challenges of voltage control in modern power systems through a decentralized safe RL framework. By ensuring stability through engineered neural network controllers, this approach offers a robust solution for managing the variability and uncertainty of DERs. The findings will contribute to the development of more resilient and efficient power systems.

The expected outcomes of our research include an enhanced understanding of meshed networks, filling the gaps left by previous studies that focused on radial networks and often overlooked the complexities of meshed networks and their impact on controller performance. By evaluating both linear and nonlinear models, we aim to identify optimal operating domains that ensure system stability under varying conditions. Additionally, we will assess the impact of decentralized voltage regulation on active power flow between adjacent busbars to ensure compliance with all power system constraints, thereby promoting more efficient and stable power network operations.

References

[1] W. Cui, J. Li, and B. Zhang, "Decentralized safe reinforcement learning for inverter-based voltage control," *Electric Power Systems Research*, vol. 211, p. 108609, 2022.

[2] H. Zhu and H. J. Liu, "Fast local voltage control under limited reactive power: Optimality and stability analysis," *IEEE Transactions on Power Systems*, vol. 31, no. 5, pp. 3794–3803, 2015.

[3] W. Cui, J. Li, and B. Zhang, "Decentralized safe reinforcement learning for inverter-based voltage control," *Electric Power Systems Research*, vol. 211, p. 108609, 2022.

[4] R. S. Sutton and A. G. Barto, *Reinforcement learning: An introduction.* MIT press, 2018.

Adaptive Deep Learning Controller for Nonlinear Systems with Contraction Theory

Marco Perin, Angelo Cenedese, Francesco Bullo

EXTENDED ABSTRACT

INTRODUCTION

Contracting dynamical systems exhibit remarkable convergence and robustness properties. In recent years, these properties have made contraction theory a valuable tool for developing robust controllers and advanced convergence analysis techniques. In this work, we leverage contraction theory alongside neural networks to develop a non-linear feedback controller capable of performing trajectory-tracking tasks effectively.

Existing works: This work builds upon several recent papers, notably [1] and [2], while also incorporating insights from [3]. In [1], the authors present a method for synchronizing a network of identical agents to a leader, which is an autonomous system. Conversely, [2] addresses the task of trajectory tracking, where the leader is not an autonomous system but is instead controlled by a feedforward input. Both papers utilize deep neural networks to solve these problems through a two-step approach, which is also employed in this work. Additionally, [3] extends the framework of Control Contraction Metrics (CCMs) with adaptive control arguments, a methodology echoed in [4].

Contribution: Compared to state-of-the-art methods, the controller here proposed incorporates an adaptation layer to address parametric uncertainties in the system of interest. Our controller draws inspiration from recent works using Lyapunov-like arguments [1, 2] and standard adaptive control techniques [3], integrating in the former controller design an adaptive control term.

Although still a work-in-progress, this approach has already shown promising results in simulation, even in the presence of added noise.

RESULTS

A. Description and methodology

1) System: Regarding the type of systems considered, this framework can work for very general cases, being able to control non-linear control affine (with state-dependent g) systems, possibly time-varying, where a pair (x, u) is tasked to track a desired reference trajectory (x_r, u_r). In detail, the mathematical model in (1) is used

$$\dot{x} = f(x) \ + g(x)u \qquad - \Delta^T(x)\vartheta \tag{1a}$$

$$\dot{x}_r = f(x_r) + g(x_r)u_r(t) - \Delta^T(x_r)\vartheta \tag{1b}$$

where the last term in the equations accounts for the uncertainties, and ϑ is the system parameter set.

Indeed, the main assumption, made in this preliminary work is that the uncertainties need to satisfy the matching condition, meaning that the uncertain term can be written as $\Delta^T(x)\vartheta = g(x)\phi(x)\vartheta$, that means that the uncertainties lies in the image of the input matrix $g(x)$.

Starting from an original Feedback Controller [2]

$$u_F = u_r(t) + (\kappa(x_r(t)) - \kappa(x(t))) \tag{2}$$

an Adaptive Deep Learning Controller is introduced, whose structure is given as in (3)

$$u_A = u_r(t) + (\kappa(x_r(t)) - \kappa(x(t))) + \phi^T(x)\hat{\vartheta}(t) \tag{3a}$$

$$\dot{\hat{\vartheta}} = \Gamma[\phi(x)g(x)P(x,t)(x - x_r) + \sigma\vartheta] \tag{3b}$$

where $\kappa(\cdot)$ is the learned controller, $P(\cdot)$ is the learned metric, $\phi^T(x)$ is the uncertainty matrix, $\hat{\vartheta}$ is the parameter estimate, Γ and σ are respectively a matrix and a scalar gain,

2) Controller design: The controller design includes a learning process and is divided in two phases. The first one consists of finding a matrix $P = P^T \succ 0$ that satisfies the contraction condition in (4a) and (4b), where the second step consists in learning a suitable feedback control law $\kappa(\cdot)$ satisfying (4c).

$$L_f P(\cdot) - \rho P(\cdot) g(\cdot) g^T(\cdot) P(\cdot) \preceq -\lambda P(\cdot) \tag{4a}$$

$$L_g P(x,t) = 0 \tag{4b}$$

$$\frac{\delta \kappa}{\delta x}(x,t) = P(x,t) g(x) \tag{4c}$$

B. Numerical validation

System description: The system employed for these simulations is the well-known Lorentz attractor model, used in the literature because it is nonlinear and chaotic, and provides a good benchmark for controllers. Its model is the one in (5), with parameters $(\sigma, \rho, \beta) = (10, 28, 8/3)$ making the system chaotic:

$$\begin{bmatrix} \dot{x}_1 \\ \dot{x}_2 \\ \dot{x}_3 \end{bmatrix} = \begin{bmatrix} \sigma(x_2 - x_1) \\ x_1(\rho - x_3) - x_2 \\ x_1 x_2 - \beta x_3 \end{bmatrix} + \begin{bmatrix} 1 \\ 2 + s(x_1) \end{bmatrix} \left[u - \phi^T(x)\vartheta \right] \tag{5}$$

This work is partially supported by the EU Next-Generation (PNRR) within the Italian National Ph.D. Program in Autonomous Systems (DAuSy). M. Perin and A. Cenedese are with the University of Padova, Italy. F. Bullo is with the University of California, Santa Barbara, United States

Contacts: `marco.perin.6@studenti.unipd.it`

$s(\cdot)$ standing for the *sine* operator, and scalar input u taking the form of u_F or u_A (respectively, (2) and (3)). Simulations are run in two cases, presenting how the controller works under $\phi(x)$ having multiple dimension.

1) One-parameter ϑ: For this simulation, $\phi(x) = [-x_1]$, and it is possible to see how the controller with adaptation (u_A) outperforms the one without (u_F) after a short time in Figure 1. Indeed, the tracking error is gradually reduced with the proposed approach, while it can be appreciated that it does not decrease (and is not negligible) otherwise.

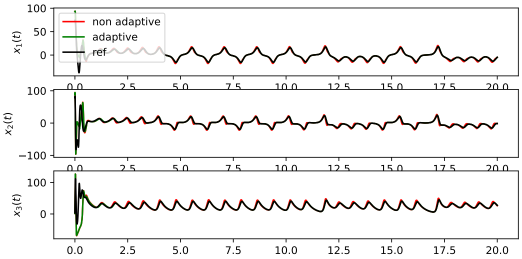

(a) State

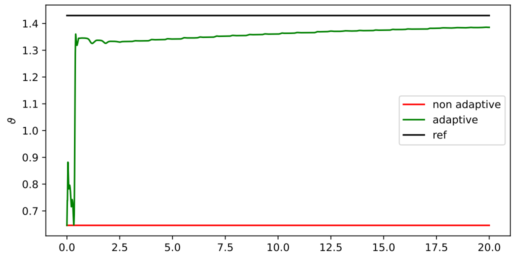

(b) Parameter

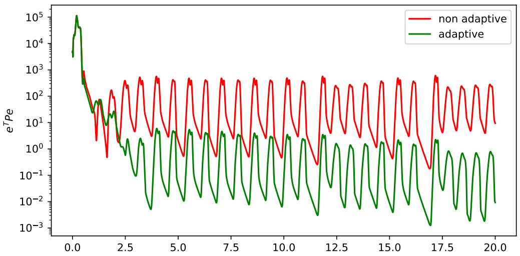

(c) Error

Fig. 1: Time simulation with one parameter

2) Two-parameters ϑ: With two parameters, namely having $\phi(x) = \begin{bmatrix} -x_1 \\ x_2 - x_1 \end{bmatrix}$, the controller is working as well, still leading to correctly decreasing the tracking error, as it can be seen in Figure 2. Note that the parameters do not converge to the true ones, but this is an expected behaviour, as the controller is not designed to estimate them, but just to reduce the tracking error.

CONCLUSION

Our preliminary results indicate that the adaptive control law proposed is effective and holds promise as an enhancement to the existing solution. Ongoing studies aim to broaden the applicability to a wider range of uncertain parameters and improve convergence. Should these efforts prove successful, the next steps would involve implementing the controller in a realistic simulation scenario, followed by experimental tests on a real device.

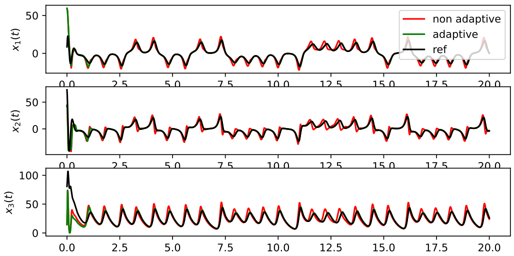

(a) State

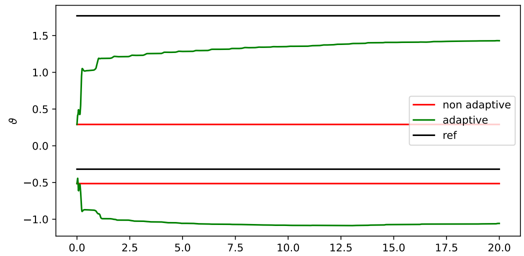

(b) Parameter

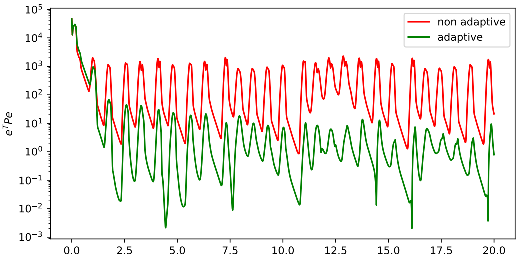

(c) Error

Fig. 2: Time simulation with two parameters

REFERENCES

[1] Mattia Giaccagli et al. "Synchronization in Networks of Nonlinear Systems: Contraction Analysis via Riemannian Metrics and Deep-Learning for Feedback Estimation." May 2023. URL: `https://hal.science/hal-03801100`.

[2] Samuele Zoboli, Steeven Janny, and Mattia Giaccagli. "Deep learning-based output tracking via regulation and contraction theory." In: *IFAC-PapersOnLine*. 22nd IFAC World Congress 56.2 (Jan. 1, 2023), pp. 8111–8116. ISSN: 2405-8963. DOI: `10.1016/j.ifacol.2023.10.966`.

[3] Hiroyasu Tsukamoto, Soon-Jo Chung, and Jean-Jacques Slotine. "Learning-based Adaptive Control using Contraction Theory." In: 2021 60th IEEE Conference on Decision and Control (CDC). ISSN: 2576-2370. Dec. 2021, pp. 2533–2538. DOI: `10.1109/CDC45484.2021.9683435`.

[4] Brett T. Lopez and Jean-Jacques E. Slotine. "Adaptive Nonlinear Control With Contraction Metrics." In: *IEEE Control Systems Letters* 5.1 (2021), pp. 205–210. DOI: `10.1109/LCSYS.2020.3000190`.

A novel multiobjective optimal LQ control strategy for energy harvesting in vehicle suspension systems

Paul Christian Tesso Woafo, Gianfranco Gagliardi, Alessandro Casavola
Dipartimento DIMES
Universitá della Calabria, Dimes Department
Rende, Italia
tessowoafo.paulchristian@unical.it

***Abstract*—A novel optimal LQR state-feedback control law is proposed for energy harvesting maximization in regenerative suspension systems where an actively governed electromechanical actuator is used in place of the viscous damper. A special LQR cost function is considered that directly maximizes the electrical power generated by the electromechanical actuator. Other conflicting control objectives, such as ride comfort and road handling, may be considered along with the energy harvesting objective in the proposed control setup, allowing one to directly trade-off among them depending on the application. Specifically, as an example, a condition for trading-off between energy harvesting and ride comfort is added to the optimization problem via forcing a bound on the so called Ride Index. The proposed control law is finally contrasted with other two control strategies usually considered in the literature for energy harvesting applications and is compared in simulative studies via MATLAB and Simulink on a full-car model.**

I. INTRODUCTION

A technology that attempts to convert the kinetic and potential energy of the suspensions into electrical energy via an electromechanical generator instead of dispersing it is called a regenerative suspension system, see [1] for a recent survey. If an electric or hybrid car featured one of these, the energy it collected could be put toward charging the battery, extending the range of the car.

This work presents a novel solution solving a non-standard optimal LQR control design problem with a cost function that maximizes directly the electrical power generated by the MMLA actuator of a full-car suspension system, rather than being the standard integral of the sum of state and input norms. Additionally, a bound on the Ride Index was taken into consideration as a secondary objective to be optimized together with the energy harvesting requirement in order to demonstrate how the LQR synthesis problem can handle multiobjective optimization problems using the ε-constraints approach [2]. The proposed optimal LQR controller is contrasted with the H_2 optimal MIPC controller proposed in [3] and with the viscous regenerative damper (RD) control strategy that behaves mimicking a standard passive viscous damper. The simulations confirm the advantages of the proposed solution over the previous ones.

The paper is organized as follows. Section II presents the full car model and regenerative suspension configuration. In Section III the Linear Quadratic Regulator is reformulated by using a new objective function that maximizes the power. Finally, numerical results are presented in Section IV and some conclusions end the paper.

II. THE FULL CAR MODEL AND REGENERATIVE SUSPENSION CONFIGURATION

We consider the following model [3]:

$$\left\{\begin{array}{rcl} I_r\ddot{\varphi}_s & = & -k_f t_f(z_{s_1}-z_{u_1})+k_f t_f(z_{s_2}-z_{u_2})-k_r t_r(z_{s_3}-z_{u_3}) \\ & & +k_r t_r(z_{s_4}-z_{u_4})+t_f f_1-t_f f_2+t_r f_3-t_r f_4 \\ I_p\ddot{\theta}_s & = & -k_f a(z_{s_1}-z_{u_1})-k_f a(z_{s_2}-z_{u_2})+k_r b(z_{s_3}-z_{u_3}) \\ & & +k_r b(z_{s_4}-z_{u_4})+af_1+af_2-bf_3-bf_4 \\ m_s\ddot{z}_s & = & -k_f(z_{s_1}-z_{u_1})-k_f(z_{s_2}-z_{u_2})-k_r(z_{s_3}-z_{u_3}) \\ & & -k_r(z_{s_4}-z_{u_4})+f_1+f_2+f_3+f_4 \end{array}\right. \tag{1}$$

where:

- I_p and I_r correspond to the pitch and roll motions;
- $f_i(t)$, $i=1,\dots,4$ are the force actuators;

III. LINEAR QUADRATIC FORMULATION

A. State-space realization

Let the regenerative suspension system be model by the following state-space representation

$$\begin{array}{rcl} \dot{x}(t) & = & Ax(t)+Bu(t)+Ew(t) \\ z(t) & = & C_z x(t)+D_{zu}u(t)+F_{zw}w(t) \end{array} \tag{2}$$

where system matrices can be found in the extended work.

In (2), $x(t)$ denotes the system state, $u(t)$ the input, $z(t)$ the objective vector and $w(t)$ the zero-mean, unitary variance white noise that models the road profile z_r. In particular, we have the following system vectors

$$x=\begin{bmatrix} z_r \\ z_s \\ \dot{z}_s \\ z_u \\ \dot{z}_u \end{bmatrix}, \quad u=i, \;\; z=\ddot{z}_s \tag{3}$$

In order to quantify the riding comfort adequately, the above state-space representation is extended by introducing dynamic weighting filters to better shape in frequency the vector z according to the ISO-2631 standard. Denoting by (A_k,B_k,C_k,D_k) the state-space representation of the filter $W_k(s)$

$$\begin{array}{rcl} \dot{x}_k & = & A_k x_k+B_k z \\ \tilde{z} & = & C_k x_k+D_k z \end{array}$$

with state x_k, it is possible to introduce the following augmented state

$$x_g=\begin{bmatrix} x^T & x_k^T \end{bmatrix}^T \tag{4}$$

All augmented matrices can be found in the extended work.

Average Electrical Power			
	$RI = 0.25$	$RI = 0.47$	$RI = 0.70$
RD	35.18*4[W]	35.18*4[W]	35.18*4[W]
H_2 MIPC	40.52*4[W]	43.03*4[W]	48.84*4[W]
LQR	56.1*4[W]	56.47*4[W]	56.55*4[W]

TABLE I
AVERAGE ELECTRICAL POWER WITH $RI = 0.25$, $RI = 0.47$ AND $RI = 0.70$

B. The constrained LQR approach via LMIs

The electrical power is negative (the actuator behaves as a generator) so we want to minimize it to obtain more power. The following cost index can be considered

$$J = \varepsilon(v_{emf}^T i + R_a i^2) = \varepsilon(2 v_{emf}^T N_a i + i^T R_a i) \tag{5}$$

where v_{emf} is the back EMF voltage and $\varepsilon(.)$ is the expected value under stationary conditions. By identification, $N_a = 0.5$ and R_a is the armature's resistance.

$$\begin{aligned} v_{emf} &= K_v(\dot{z_s} - \dot{z_u}) && (6) \\ i &= -K_{LQ} x && (7) \\ \dot{z_s} - \dot{z_u} &= G^T x, \text{with } G^T = [0010-10000] && (8) \end{aligned}$$

After all developments, we have the following LMI.

$$\left\{ \begin{array}{c} [P_{LQC}, Y_{LQC}] = argmin_{P,Y,X}(\mathrm{tr}(-2K_v G N_a Y) + R_a * \mathrm{tr}(X)) \\ s.t \\ P > 0; \\ A_g P - B_{gu} Y + P A_g^T - Y^T B_{gu}^T < 0; \\ \begin{bmatrix} X & Y \\ Y^T & P \end{bmatrix} > 0 \\ \begin{bmatrix} A_g P - B_{gu} Y + (A_g P - B_{gu} Y)^T & B_{gw} & (C_{gz} P - D_{gzu} Y)^T \\ B_{gw}^T & -\alpha * I & D_{gzw}^T \\ C_{gz} P - D_{gzu} Y & D_{gzw} & -\alpha * I \end{bmatrix} < 0 \end{array} \right. \tag{9}$$

If a solution exists, the optimal controller is given by

$$K_{LQC} = Y_{LQC} P_{LQC}^{-1} \tag{10}$$

IV. SIMULATIONS

The control approaches will be compared on the same full car model, actuator and driving scenario. The vehicle chosen is a standard class **C** car. All simulations parameters can be found in the extended paper.

Figure 1 depicts the acceleration $\ddot{z}_s(t)$, actuation current $u(t)$, harvested electrical power $P_e(t)$ and harvested electrical energy $E_e(t)$ of the three control laws. The LQR without condition on the Ride Index gives us a power and energy of **57.89W** and **8684J** respectively. The Viscous Regenerative damper gives us a power and energy of **35.18W** and **5277J** respectively.

We note that the unconstrained LQR achieves the greatest energy harvesting among the three control laws. It is followed by the MIPC H_2 in terms of energy harvesting. However, the comfort provided by the LQR is the worst.

Let us improve the results by adding an adequate constraint on the Ride Index with the constrained LQR control strategy. For reason of brievety, we can't present the plots for all wheels and for the different RI but the average powers and energies are in Table I and II.

V. CONCLUSIONS

This paper has proposed a comparative study between three control laws: regenerative damper, MIPC H_2 and LQR. The results obtained show that the LQR control with this particular cost achieves greater energy harvesting than the MIPC H_2 and the regenerative damper. The condition on the Ride index constrains the acceleration provided by the control law at an acceptable result. Future work will deal with the application of this approach to other systems such as Marine Wave Energy Converters which need less control objectives than cars.

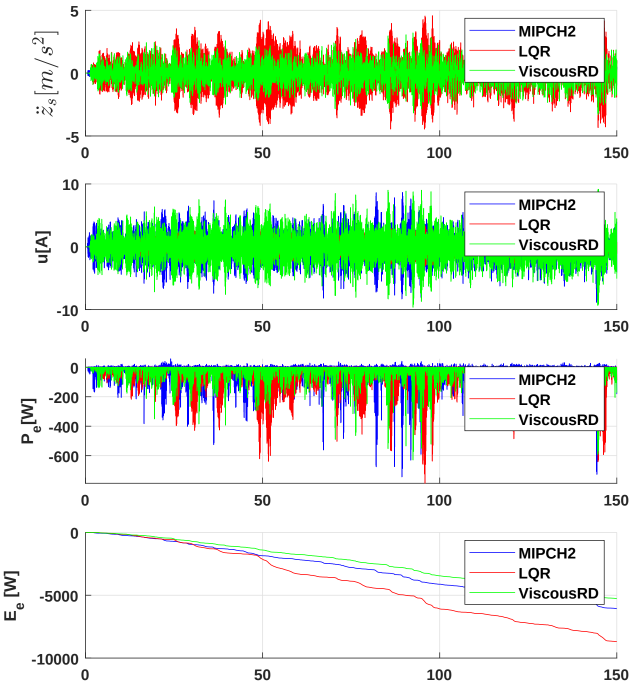

Fig. 1. Without condition on RI - Acceleration $\ddot{z}_s(t)$, actuation current $u(t)$, harvested electrical power $P_e(t)$ and harvested electrical energy $E_e(t)$ for a single wheel

Average Electrical Energy			
	$RI = 0.25$	$RI = 0.47$	$RI = 0.70$
RD	5277*4[J]	5277*4[J]	5277*4[J]
H_2 MIPC	6072*4 [J]	6455*4[J]	7326*4[J]
LQR	8415*4[J]	8470*4[J]	8482*4[J]

TABLE II
AVERAGE ELECTRICAL ENERGY WITH $RI = 0.25$, $RI = 0.47$ AND $RI = 0.70$

REFERENCES

[1] H. E. Tseng and D. Hrovat, "State of the art survey: active and semi-active suspension control", *Vehicle System Dynamics*, Vol. 53, N. 7, pp. 1034-1062, 2015.

[2] S. Lattanzio and J. Scruggs, "Maximum power generation of a wave energy converter in a stochastic environment," Proceedings of the IEEE International Conference on Control Applications, pp. 1125 –1130, 2011. doi: 10.1109/CCA.2011.6044428.

[3] A.Casavola, F. Tedesco and P.Vaglica, "H_2 and H_∞ Optimal Control Strategies for Energy Harvesting by Regenerative Shock Absorbers in Cars," *Vibration*, vol.3, no.2, pp.99-115, 2020.

Improved stability of electrolyte-gated carbon nanotube field-effect transistor-based sensors

Anna Tagliaferri[1,2], Bajramshahe Shkodra[1], Martina Aurora Costa Angeli[1], Mattia Petrelli[1],
Antonio Altana[1,3], Pietro Ibba[1], Paolo Lugli[1,3], and Luisa Petti[1]

[1]Sensing Technologies Laboratory (STL), Faculty of Engineering, Free University of Bozen-Bolzano, 39100 Bolzano, Italy
[2]Faculty of Agricultural, Environmental and Food Sciences, Free University of Bozen-Bolzano, 39100 Bolzano, Italy
[3]Competence Center for Mountain Innovation Ecosystems, Free University of Bozen-Bolzano, 39100 Bozen, Italy

***Abstract*—Electrolyte-gated carbon nanotube field-effect transistors (EG-CNTFETs) offer great promise for biosensing, but face instability challenges. This work demonstrates that incorporating a lipophilic membrane on the semiconducting channel reduces stabilization time to 34 minutes, compared to an hour for state-of-the-art devices. The membrane also causes the on-off ratio to increase over time, from 9.76 ± 4.16 to 24.55 ± 20.99 in one hour, while devices without the membrane show a decrease. Moreover, the sensor performance remains robust for up to 12 hours and 5 repeated uses. As proof-of-concept, the devices were functionalized with an ion-selective membrane for ammonium ion, achieving a linear detection range from 0.01 mM to 100 mM. These improvements not only advance EG-CNTFET-based biosensors for food, biomedical, and environmental applications, but also open up possibilities for their integration into robotic autonomous systems, e.g., for remote monitoring in dangerous environments, reducing risks to human operators.**

***Index Terms*—Technology, Manufacturing, Sensors**

I. INTRODUCTION

Electrolyte-gated field-effect transistors (EG-FETs) replace the traditional dielectric material with an electrolyte, forming electric double layers (EDLs) at the electrolyte-semiconductor and gate-electrolyte interfaces upon voltage application [1]. Due to the low thickness of the EDLs, the induced capacitance is much higher than that of traditional dielectrics, allowing to maintain the voltage low and still induce significant current amplification [2]. The presence of the electrolyte and the low voltage measurements make the EG-FET the perfect candidate to work with biological samples, e.g., for health, food, and environmental monitoring. Carbon nanotubes (CNTs), with their high carrier mobility and flexibility, are increasingly used in EG-FETs, paving the way for advanced EG-CNTFET-based biosensors [2]. As biosensors, EG-CNTFETs hold great potential for integration in autonomous robots, for example for environmental monitoring, where their high sensitivity enables the detection of trace pollutants and toxins. Additionally, their low voltage operation is suitable for remote battery-powered systems, e.g., autonomous robots deployed in hard-to-reach and potentially dangerous environments, such as those used in disaster response [3]. Moreover, thanks to their flexibility, EG-CNTFETs could be integrated into soft robots to sense environmental changes and trigger chemical actuators, causing the robot to move or change shape in response [4]. This contribution tackles the issues of stability in EG-CNTFET biosensors, as we present an efficient and cost-effective method to prevent CNT degradation by encapsulating the single-walled carbon nanotube (SWCNT) channel with a lipophilic membrane. This approach enhances resilience to environmental and electrical stress and reduces stabilization time to 34 minutes, which is half the time of current state-of-the-art devices [5]. As a proof-of-concept, we show that our encapsulated EG-CNTFETs can detect ammonium ions (NH_4^+) in concentrations ranging from 0.01 to 100 mM by adding an ion-selective membrane to the gate electrode.

II. MATERIALS AND METHODS

The planar EG-CNTFET (Figure 1a) was fabricated using the protocol from [6]. A SWCNT ink in sodium carboxymethyl cellulose (CMC) surfactant was then spray-deposited on the interdigitated electrodes (IDEs) area, following the optimized protocol developed by [7]. A lipophilic membrane ("Membrane A" from [8]) was dropcasted in two layers (first $8\,\mu L$, then $7\,\mu L$) to ensure coverage of the $8.9\,mm^2$ IDE area. An ammonium-selective membrane containing nonactin ionophore, prepared in accordance with the recipe in [9], was used to functionalize the gate; $10\,\mu L$ of the membrane were deposited on the electrode and dried for 12 hours at $4\,°C$. A conditioning step in $1\,mM$ ammonium in 0.1x PBS in ambient conditions followed. Morphological characterization of the fabricated devices included atomic force microscopy, scanning electron microscopy, and profilometry to assess SWCNT distribution and membrane thickness. Electrical characterization and stability assessment involved measuring the resistance between source and drain (R_{DS}) and repeatedly collecting 40 transfer and output characteristics using a semiconductor device parameter analyzer. Evaluation of sensor performance was conducted by dropcasting NH_4^+ in the chamber every 10 minutes to test 5 different concentrations: $0.01\,mM$, $0.1\,mM$, $1\,mM$, $10\,mM$ and $100\,mM$ in 0.1x phosphate buffer saline (PBS). The NH_4^+ measurements were carried out recording the current in output (I_{DS}) in response to a fixed bias, namely gate voltage $V_{GS}{=}-0.8\,V$ and drain voltage $V_{DS}{=}-0.1\,V$.

III. RESULTS

With this study we demonstrated the stability of EG-CNTFETs with an added lipophilic membrane. Initial char-

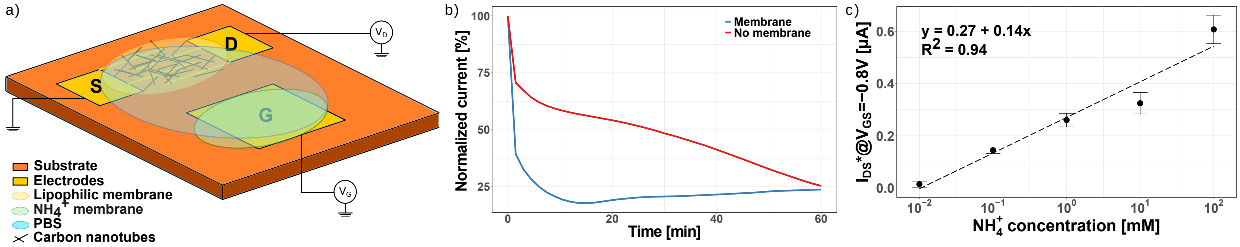

Figure 1: a) Scheme of EG-CNTFET biosensor. b) Comparison of normalized $\mathrm{I_{ON}}$ trends for two devices: the one without the membrane (red) exhibits a steady decrease, while the one with membrane encapsulation (blue) initially decreases before increasing again. c) Calibration curve of the biosensor for $\mathrm{NH_4^+}$ detection. The sensor exhibits good linearity over the range of concentrations tested.

acterization revealed a dense, uniformly dispersed random network of SWCNTs and an optimal membrane thickness of $45\,\mu\mathrm{m}$. Figure 1b depicts how the normalized ON current ($\mathrm{I_{ON}}$), i.e., the $\mathrm{I_{DS}}$ detected at $\mathrm{V_{GS}}{=}-0.8\,\mathrm{V}$ normalized over the ON current of the first recorded transfer; the curves obtained show how the current in the bare devices declines in a steep linear way ($n = 3$), while encapsulated ones stabilize within 33.8 ± 12.9 minutes ($n = 6$). Albeit showing a lower current amplitude, encapsulated devices remained stable for up to 12 hours and could be reused 5 times. The on/off ratio was also calculated to evaluate variations in performance over time: bare devices showed a decrease from 88.7 ± 29.9 to 61.1 ± 23.9. Encapsulated devices, however, exhibited improving stability, with the on-off ratio increasing from 9.76 ± 4.16 to 24.55 ± 20.99 in one hour. As a proof-of-concept, an ion-selective membrane with nonactin was used to detect ammonium, showing a linear range from 0.01 to $100\,\mathrm{mM}$ with a 94.71% coefficient of determination.

IV. CONCLUSION

This work highlights how SWCNTs instability was tackled by encapsulating the channel in a lipophilic membrane; this lead to stabilization in 34 minutes and increased resilience, allowing measurements up to 12 hours and 5 separate times. The functionality as biosensor was demonstrated by the adding an ion-selective membrane on the gate, leading to the detection of $\mathrm{NH_4^+}$ in the concentration range typically present in sweat. Our easy and inexpensive approach to achieving highly stable EG-CNTFETs represents a powerful strategy for implementing such devices in many biosensing applications that are not limited to ion-selective membranes. Additionally, our system is well-suited for integration into robotic platforms, thanks to the reusability feature, which is not possible with standard bare devices. This facilitates the full automation of sample collection and analysis, reducing variability in measurements and leading to more reliable results.

REFERENCES

[1] Fabrizio Torricelli, Demetra Z Adrahtas, Zhenan Bao, Magnus Berggren, Fabio Biscarini, Annalisa Bonfiglio, Carlo A Bortolotti, C Daniel Frisbie, Eleonora Macchia, George G Malliaras, et al. Electrolyte-gated transistors for enhanced performance bioelectronics. *Nature Reviews Methods Primers*, 2021.

[2] Bajramshahe Shkodra, Mattia Petrelli, Martina Aurora Costa Angeli, Denis Garoli, Nako Nakatsuka, Paolo Lugli, and Luisa Petti. Electrolyte-gated carbon nanotube field-effect transistor-based biosensors: Principles and applications. *Applied Physics Reviews*, 2021.

[3] Robin R. Murphy, Satoshi Tadokoro, and Alexander Kleiner. *Disaster Robotics*, pages 1577–1604. Springer International Publishing, Cham, 2016.

[4] Liangjie Wang, Zhengran Yi, Yan Zhao, Yunqi Liu, and Shuai Wang. Stretchable conductors for stretchable field-effect transistors and functional circuits. *Chem. Soc. Rev.*, 52:795–835, 2023.

[5] Alireza Molazemhosseini, Fabrizio Antonio Viola, Felix J. Berger, Nicolas F. Zorn, Jana Zaumseil, and Mario Caironi. A Rapidly Stabilizing Water-Gated Field-Effect Transistor Based on Printed Single-Walled Carbon Nanotubes for Biosensing Applications. *ACS Applied Electronic Materials*, 2021.

[6] Anna Tagliaferri, Bajramshahe Shkodra, Mattia Petrelli, Pietro Ibba, Luisa Petti, Paolo Lugli, and Martina Aurora Costa Angeli. Improved stability of carbon nanotube electrolyte-gated field-effect transistors through lipophilic membrane encapsulation. In *2023 IEEE BioSensors Conference (BioSensors)*. IEEE, 2023.

[7] Bajramshahe Shkodra, Mattia Petrelli, Martina Aurora Costa Angeli, AKM Sarwar Inam, Paolo Lugli, and Luisa Petti. Optimization of the spray-deposited carbon nanotube semiconducting channel for electrolyte-gated field-effect transistor-based biosensing applications. *IEEE Sensors Journal*, 2022.

[8] Saumya Joshi, Vijay Deep Bhatt, Ewa Jaworska, Markus Becherer, Krzysztof Maksymiuk, Agata Michalska, and Paolo Lugli. Using lipophilic membrane for enhanced-performance aqueous gated carbon nanotube field effect transistors. *physica status solidi (a)*, 2018.

[9] Tomas Guinovart, Amay J Bandodkar, Joshua R Windmiller, Francisco J Andrade, and Joseph Wang. A potentiometric tattoo sensor for monitoring ammonium in sweat. *Analyst*, 2013.

Optimization and Monitoring of Pharmaceutical Processes through Statistical Data Analysis

Daniele Antonucci [1], Davide Bonanni[2], Luca Consolini [1] and Gianluigi Ferrari[1]

[1] Department of Engineering and Architecture, University of Parma, Via delle Scienze, 181/a, 43124 Parma PR, Italia
[2] GlaxoSmithKline Manufacturing SpA, Strada Provinciale Asolana, 90, 43056 S.Polo, Torrile PR, Italia
`d.antonucci1@phd.poliba.it`, `davide.x.bonanni@gsk.com`,
`luca.consolini@unipr.it`, `gianluigi.ferrari@unipr.it`

Batch manufacturing process remains the primary method for industrial production. The goals in a batch process are: (I) Reliability, by minimizing operational risks; and (II) Efficiency, providing high production standards while reducing the production cost. However, it is essential to consider and closely monitor the significant drawbacks associated with a batch manufacturing process: (I) Complex and dynamic systems that are highly susceptible to disruptions or deviations in each phase; (II) Quality control issues within a batch can lead to entire batches being rejected; and (III) Inconsistent product quality between batches can lead to inconsistent product quality if the manufacturing process is not optimized. The proposed method involves the following steps:

- Data analysis and preprocessing: Golden batches have been analyzed and Principal Component Analysis (PCA) has been used. PCA is a widely-used method that transforms the original dataset into a set of uncorrelated variables known as Principal Components (PCs) [1]. By applying PCA to a 2D matrix—where each batch, consisting of $\mathbf{J}$ time points and $\mathbf{K}$ features, is stacked vertically—patterns within the data can be identified and trajectories can be traced.
- Training phase: A non-linear approach, specifically employing an LSTM model, has been employed for time-series prediction. LSTM models are adept at detecting abnormal behavior in non-linear systems by analyzing NOC batches and calculating metrics to identify deviations [2]. Moreover, LSTMs may handle scenarios with multi-step inputs or outputs as well. By training individual LSTM models on each batch within the dataset, a collection of models is created, each capturing unique patterns specific to its batch. During training, these models periodically average their learned parameters to form a global model. This final model incorporates the key characteristics from all individual models, leading to more accurate predictions compared to training a single model on the entire dataset [3].

Experimental results shows that by employing a strategic training of several models for each training batch, it may enhance the evaluation of historical batches using pre-built models and the online monitoring of batches through single data point prediction. Additionally, an optimization approach could be beneficial for finding the optimal hyper-parameters for the given dataset.

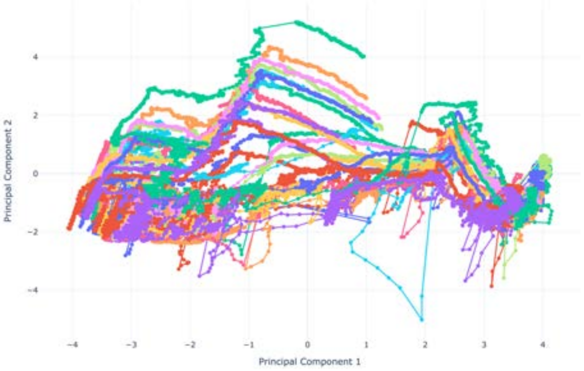

Fig. 1: Projection of batch processes to Principal Components. Each colored line represents a batch. PCA correctly identify similar pattern on each batch.

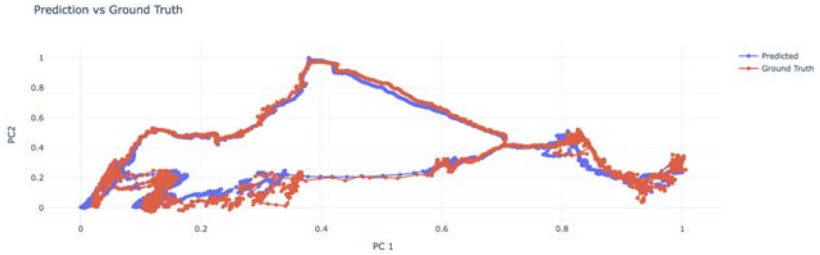

Fig. 2: Prediction vs Ground Truth of a test batch with 5 input steps and 1 output step.

References

1. Greenacre, Michael and Groenen, Patrick J. F. and Hastie, Trevor and D'Enza, Alfonso Iodice and Markos, Angelos and Tuzhilina, Elena, "Principal component analysis," Nature Reviews Methods Primers, num. 1, Dec. 2022.
2. Hiu, Junqiang and Pan, Chunlu and Lei, Fan and Hu, Dongbin and Zuo, Hongfu, "Fault prediction of bearings based on LSTM and statistical process analysis," Reliability Engineering & System Safety, vol. 214, p. 107646, Oct. 2021.
3. Huang, Zitong and Chen, Ze and Dong, Bowen and Liang, Chaoqi and Zhou, Erjin and Zuo, Wangmeng, "IMWA: Iterative Model Weight Averaging Benefits Class-Imbalanced Learning Tasks," Computer Vision and Pattern Recognition (cs.CV), Apr. 2024.

Session 4A: Optimization

An Adaptive Heuristic Approach to Wood Sawing Optimization

Seyed Mohsen Hosseini and Angelika Peer
Faculty of Engineering, Free University of Bozen-Bolzano, 39100, Bolzano, Italy

Abstract— **Automating and optimizing wood processing have been of significant importance to improve efficiency in sawmills. This study presents a quality-driven constructive heuristic approach for solving the live sawing optimization problem. This deals with cutting rectangular boards from cylindrical logs with circular cross sections. The heuristic is adaptive regarding the existence of defects inside the logs that can be detectable after each cut. Thus, the cutting pattern is updated after each cut with new scanned information about internal defects in the log. The problem is a two-dimensional strip bin-packing problem with the objective of orthogonal packing of a given set of rectangular items into a set of strips inside a circle to maximize the sawing yield. We apply a combination of sorting, placement, and searching policies, along with an online strategy to build a feasible cutting that enables guillotine cuts and quality consideration for wood sawing. Our approach outperforms the current state of the art in improving sawing efficiency.**

I. INTRODUCTION

The integration of automation and optimization in wood processing has recently gained more attention for improving efficiency. Advances in mathematical modeling, optimization algorithms, and control techniques have enabled modern sawmills to reduce costs and increase yields. Sawing optimization, which determines the optimal pattern for cutting logs to maximize yield and minimize losses, is fundamental to wood processing [1].

The need to optimize wood sawing has driven innovations in defect detection and yield improvement. For example, [2] used linear programming to maximize yields for different product sizes. Due to geometric constraints, mixed-integer linear and nonlinear programming were later used for more accurate models [3]. However, high computational complexity limits their scalability, leading to heuristic approaches. The bottom-left (BL) and bottom-left-fill (BLF) heuristics are popular for bin-packing problems, offering practical solutions despite limitations in handling circular containers and large-scale problems [4].

Scanners are essential for log sawing optimization to detect geometry and defects. While costly scanners detect internal defects, smaller sawmills favor low-cost laser scanners, such as the one in Fig. 1. However, these affordable scanners only detect surface defects after each cut by scanning the open face.

Although previous research studies have made progress toward the optimization of wood sawing, the integration of online defect detection concerning quality sawing algorithms which use affordable laser scanners has not been researched so far. This research fills in this gap by presenting an adaptive heuristic quality-driven algorithm which is based on a variant of the BLF algorithm, while updating the cutting pattern in a dynamic way with online detection of inside defects. By combining sorting, placement, and searching policies and an online defect detection strategy, this approach establishes an important robust solution for wood sawing operations.

II. THE PROPOSED ONLINE ADAPTIVE HEURISTIC FOR WOOD SAWING

Our approach combines the principles of a variant of the BLF heuristic with online defect detection. The cutting patterns are dynamically updated based on the defect data available at the time so as to maximize the number and value of the rectangles packed within the circle cross-section of the log. We modify the original BLF heuristic for strip cutting capability due to the constraints of sawing machines which only allows them for guillotine cuts. (see Fig. 2 for a visual representation).

A. Priority Lists

We use three priority lists of products: P1, P2, and P3, with P1 being of the highest priority due to urgent customer orders that need to be delivered. The first to be fitted are rectangles in P1. If a rectangle in P1 cannot be fit, then an inspection is made in P2. Products in P1 and P2 must be free of any defects. This is followed by P3. Rectangles from P3 are allowed to be with some defective areas.

B. A Variant of the BLF Algorithm

The BLF algorithm proposed in this study fills each rectangle into the lowest and leftmost available position of each strips. The BLF algorithm can also fill the gaps by immediately searching for feasible rectangles to fill gaps as soon as any gap is created, thereby improving the efficiency of packing without memorizing many points.

C. Regions and Scenarios

The sawing pattern generation is divided into three regions: *Region 1*, which is a central strip where the largest rectangles

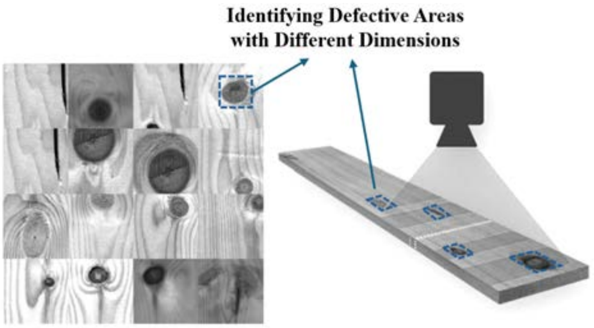

Fig. 1: Defect detection on wood surfaces using laser scanners.

are placed; *Region 2*, which is filled with the remaining rectangles, and *Region 3*, where the processing is again similar to Region 2 but after a 180° rotation of the log. Each region follows specific placement scenarios: *Scenario 1* places rectangles if the height difference between successive rectangles is equal or less than a small threshold, while *Scenario 2* searches for smaller rectangles to fill where significant gaps exist, and *Scenario 3* leaves gaps as waste if no suitable rectangles are found.

D. Adaptive Online Update Strategy

The adaptive heuristic strategy starts with no consideration of defects at the generation of the initial cutting pattern using the first scan information of the outer hull of the log, providing log dimensions. After the first cut (open face), the log surface is scanned again to detect any defects on the surface. If it finds defects, the whole area around each defect is considered as a *defective area* in the search space. This area is defined as a *rectangle* that encompasses the defect with a small defined margin to ensure the entire defect is within the marked area (the red area in Fig. 2). This area can be filled only by the products from the least-priority list P3, where defects are allowed in the products. The heuristic is then re-run considering these defective areas to create a new cutting pattern with the updated condition. If the defective area persists in the later cuts as well, the algorithm continues with the existing pattern. In the case of new defects detected, new defective areas are defined and the heuristic re-runs to come up with a new pattern again. This iterative process will now ensure every cut takes into account defects to optimize quality and yield for sawn timber.

III. SIMULATION AND DISCUSSION

To evaluate our proposed online adaptive heuristic, we conducted simulations on various test problems using inputs such as rectangle dimensions, priority lists (P1, P2, P3) with product values, and the log's cross-sectional size. The simulations were implemented in Python on a personal computer with an Intel Core i5-8365U @ 1.6 GHz CPU, 16 GB RAM, running Windows 10 (64-bit), with parameters from [1]. Table I reports the results for different problem sizes, i.e., *Small* with r = 10 and N = 8, *Medium* with r = 30 and N = 15, and *Large* with r = 50 and N = 35, where r is the radius of the circle and N is the number of rectangles. The final *yield* (ratio of selected rectangle area to circle area), *price* of products in the presence of log defects, and total *running time* of the program are presented. We compared the traditional BL method, our offline heuristic method, and our adaptive online heuristic method.

The results show that our adaptive online heuristic yields almost similar results to the offline heuristic but with higher final product values due to dynamic adaptation with defect detection, ensuring better quality outputs. Also, the running time remains reasonable, making it suitable for real industrial environments.

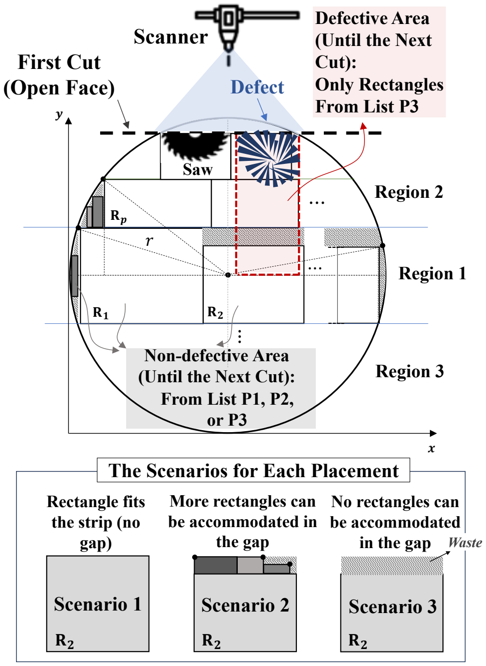

Fig. 2: The strategy for placement and defect updating.

TABLE I: The comparison of results.

Method	Problem Size	Yield (%)	Price (€)	Running Time (s)
Traditional BL	Small	52	32	0.22
	Medium	78	110	0.54
	Large	84	310	0.69
Offline Heuristic	Small	59	40	0.34
	Medium	84	124	0.55
	Large	91	331	0.70
Adaptive Online Heuristic	Small	57	48	0.61
	Medium	84	135	0.79
	Large	90	344	0.98

IV. CONCLUSIONS

This study introduced an adaptive heuristic approach for wood sawing optimization. The method combines online defect detection with an improved variant of the bottom-left-fill (BLF) heuristic. The method dynamically updates cutting patterns to increase yield, product quality and value. The simulation results showed that our heuristic not only maintains high yield efficiency but also enhances the final product value in reasonable computation times, proving its effectiveness and practical applicability in the presence of wood defects.

REFERENCES

[1] S. M. Hosseini and A. Peer, "Improving wood yield recovery in live sawing using strip-bottom-left-fill bin-packing heuristic," in *2023 IEEE ETFA*, pp. 1–8, 2023.

[2] S. Koch *et al.*, "Integer linear programming for a cutting problem in the wood-processing industry: a case study," *Int. Trans. Oper. Res.*, vol. 16, pp. 715–726, 2009.

[3] I. Hinostroza *et al.*, "Board cutting from logs: Optimal and heuristic approaches for the problem of packing rectangles in a circle," *Int. J. Prod. Econ.*, vol. 145, no. 2, 2013.

[4] E. K. Burke *et al.*, "A new bottom-left-fill heuristic algorithm for the two-dimensional irregular packing problem," *Oper. Res.*, vol. 54, pp. 587–601, 2006.

Distributed stochastic optimization with uncertain coupling constraint

Alessandro Del Duca [1], Fredy Ruiz[1]

[1]Dipartimento di Elettronica, Informazione e Bioingegneria, Politecnico di Milano, Milan, Italy
{alessandro.delduca, fredy.ruiz}@polimi.it

Societal-scale challenges like climate change mitigation and adaptation, pandemic control and healthcare, and the transition towards Smart Infrastructure Systems in sectors like energy and transportation are dominant drivers for societal transformation in the upcoming decades. The systems involved in those challenges share three crucial features which must be accounted for when facing them:

- **Large scale:** The systems in question are intrinsically large-scale and remarkably complex due to the humongous number of decision variables.
- **Multi-agent:** The systems comprise diverse" agents", decision-making entities with partial information about the global system who can only act on individual decisions. Agents communicate through a communication network to drift the system towards an operating point that maximises the participant's benefit.
- **Uncertainty handling:** These systems are partially known and uncertain by nature. The agents must make decisions in a complex, possibly time-varying, environment with partial information on the effect of their decisions on the global system.

The renewed interest in distributed and multi-agent optimisation observed in these years should be no surprise. This framework is suitable for addressing all the features that were previously cited.

Our work focuses on developing computationally efficient dual-based distributed optimization algorithms capable of handling uncertain global coupling constraints, which naturally arise in many distributed systems, including resource sharing.

We consider the following distributed optimization program:

$$\begin{aligned} \mathcal{P} : & min_{\{x_i\}_{i=1}^m} \sum_{i=1}^{m} f_i(x_i) \\ & s.t. \\ & x_i \in X_i \ \forall i = 1..m \\ & \mathbf{P}\{\delta \in \Delta : \sum_{i=1}^{m} g_i(x_i, \delta) > 0\} < \epsilon \end{aligned} \tag{1}$$

Where each agent $i = 1, 2 \ \ldots \ m$ can act on a private set of control variables x_i, and minimize its cost function f_i, while satisfying both local constraints $x_i \in X_i$ and a global uncertain coupling constraint:

$$\mathbf{P}\{\delta \in \Delta : \sum_{i=1}^{m} g_i(x_i^*, \delta) > 0\} < \epsilon \tag{2}$$

An uncertain coupling constraint is a powerful tool for modelling constraints which unpredictably act on the multi-agent system. The coupling constraint generally cannot be satisfied deterministically without diminishing the system's performance; by controlling the risk level ϵ, it is possible to tune the risk-performance tradeoff. We use the scenario approach to handle uncertainty and solve chance-constrained optimization problems. This approach allows us to find a solution that satisfies the constraints with a predefined confidence level β, provided that the number of scenarios is chosen to satisfy 3:

$$\bar{\epsilon} = 1 - \sqrt[N-\rho]{\frac{\beta}{\binom{N}{d}}} \tag{3}$$

where the number ρ is the best-known bound of the Helly's dimension of the problem.

To decrease the number of required scenarios, the affine geometry of the chance-constraint (2) is exploited to reduce the upper-bound for its Helly dimension [1] [2]. We proved that under some special structures of (2) the number ρ doesn't depend on the number of agents m.

Leveraging on the problem's separable structure and a Helly's bound which doesn't depend on m, we develop a scalable distributed dual-decomposition scheme [3], where each agent solves a local problem and communicates information to its neighbours over a communication graph to iteratively steer all the agents' private solutions to the global one without disclosing agents' private information.

The methodology is applied to the distributed optimization of aggregated micro-grids, a relevant example of a large-scale multi-agent system with uncertain coupling constraints.

In microgrids, single Distributed Energy Resources (DER) fail to influence the power grid alone; studying methods to aggregate small-capacity generators and storage systems to provide market capabilities to such resources is crucial. Groups of DERs and loads form microgrids that can be aggregated into a single virtual power plant (VPP), a grid-connected entity capable of participating in the energy market, as shown in figure 1.

The VPP must optimize the economics of each microgrid while satisfying power balance constraints over the entire aggregation. The power balance is uncertain due to the stochastic nature of the microgrid's assets. Examples of uncertainty sources in the power balance are solar production and load consumption, while structural uncertainty elements are found in the modelling of batteries and generators. Also, communication uncertainties such as delays and asset unavailability are present in the system.

A preliminary result is tested with four microgrids over a time-varying communication network. We choose a risk factor $\epsilon = 0.2$ and a confidence $\beta = 1e - 6$, resulting in $N = 258$ required scenarios. After optimising for x_i, we test it on $M = 1300$ unseen scenarios and compute the violation probability $V(x^*) = 8.92\%$, which is lower than the risk factor chosen $\epsilon = 20\%$

We are collaborating with Hitachi Energy to develop a VPP benchmark comprised of three virtual machines communicating over the cloud via HTTPS protocol to test the impact of real-time communication in distributed uncertain algorithms for microgrid applications.

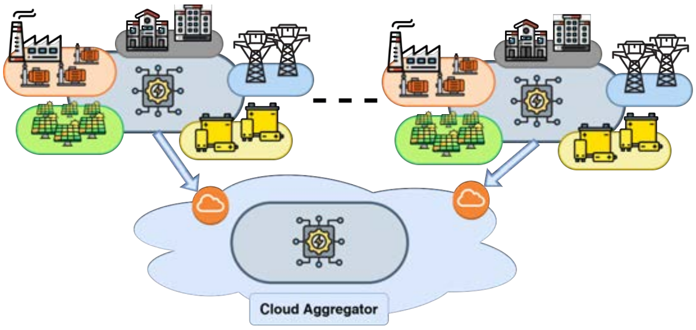

Fig. 1: On-Cloud microgrid aggregation.

References

[1] G. Schildbach, L. Fagiano, and M. Morari, "Randomized solutions to convex programs with multiple chance constraints," *SIAM Journal on Optimization*, vol. 23, no. 4, pp. 2479–2501, 2013.

[2] X. Zhang, S. Grammatico, G. Schildbach, P. Goulart, and J. Lygeros, "On the sample size of random convex programs with structured dependence on the uncertainty," *Automatica*, vol. 60, pp. 182–188, 2015.

[3] A. Falsone, K. Margellos, M. Prandini, and S. Garatti, "A scenario-based approach to multi-agent optimization with distributed information∗∗research was partially supported by epsrc uk, grant ep/p03277x/1." *IFAC-PapersOnLine*, vol. 53, no. 2, pp. 20–25, 2020, 21st IFAC World Congress.

InDi: An Indirect/Direct method for Optimal Control Problems

Enrico Bertolazzi, Francesco Biral
Dipartimento di Ingegneria Industriale
University of Trento

***Abstract*—Literature shows that direct methods are the most popular approach for solving optimal control problems due to their robustness and effective constraint handling. Conversely, indirect methods, though more challenging to implement, offer greater accuracy by deriving necessary optimality conditions via Pontryagin's Maximum Principle and solving two-point boundary value problems. These methods provide deeper insights into the problem structure, crucial for theoretical analysis and efficient algorithms development. This study demonstrates that it is possible to construct numerical approximations that leverage both direct and indirect methods, inheriting the advantages and properties of each.**

***Index Terms*—Optimal Control, Direct Methods, Indirect Methods, Numerical Optimization**

Optimal control problems are extensively found in various fields of engineering and have been applied successfully in an increasing number of cases [7]–[10], [12], [13]. These problems involve optimizing a performance criterion, often complicated by high dimensionality and nonlinearity. Literature shows that *direct methods* are the most popular approaches, discretizing the problem into a constrained minimization task solvable with numerical optimization techniques. Their popularity stems from robustness, effective constraint handling, and powerful computational tools. Conversely, *indirect methods* provide more accurate solutions by deriving optimality conditions using Pontryagin's Maximum Principle and solving two-point boundary value problems. Although more challenging, indirect methods offer deeper insights into problem structure and optimal solutions, aiding theoretical analysis and efficient algorithm development.

- Direct methods transcribe continuous optimal control problems into a finite-dimensional nonlinear optimization problem (NLP). This allows the use of powerful numerical optimization techniques, solved by standard algorithms like IPOPTand DIDO, or custom-tailored NLP solvers.

  Direct methods are versatile and robust, with Runge-Kutta and Pseudo-Spectral methods being particularly efficient and accurate. Runge-Kutta uses fixed-step integration, while Pseudo-Spectral methods employ high-order polynomials for spectral collocation to discretize control and state trajectories.

  Various software packages support these methods, each with unique features and capabilities. Popular options include: GPOPS-II, ICLOCS2, ACADOS, CasADi, falcon.m, DIDO, Forces Pro, Pyomo, Gekko.
- Indirect methods, based on the calculus of variations and Pontryagin's Principle of Maximum, offer a unique approach to optimal control by providing necessary optimality conditions through Boundary Value Problems (BVPs) that minimize the Hamiltonian. These methods derive differential equations and boundary conditions to yield the optimal control and state trajectories.

  Although theoretically strong, indirect methods face criticism due to the complex symbolic manipulations required [2]. Recent advancements in Computer Algebra Systems (CAS) and automatic differentiation libraries have alleviated these challenges, automating much of the symbolic computation.

  A persistent challenge in indirect methods is handling switching points, where optimal control strategies change abruptly. Strategies like penalty formulations and interior point approaches effectively address this issue, facilitating solutions for complex engineering problems with switching dynamics [4], [5].

  Despite advancements, practical software implementations of indirect methods are limited. Notable exceptions include Beluga, which solves optimal control problems using advanced numerical techniques, and PINS [4], which provides robust solutions for problems with complex dynamics and constraints.

This work introduces a novel numerical method tailored for solving optimal control problems, which can be interpreted as stemming from either a direct or an indirect approach.

The quest to connect the solutions obtained from the discretization of direct methods with those from indirect methods is not new. The principle of covector mapping (CMP) [11] has demonstrated that a mapping can make the solution of direct methods equivalent to that of indirect methods when using pseudospectral collocation techniques.

Similarly to CMP, this study introduces a mapping approach for the finite difference scheme that links the discretized equations of indirect methods with those of direct transcription applied to implicit dynamics. Revisiting the discretization of the indirect method as one derived from direct transcription, allows for the hybridization of solution techniques and algorithms from both families of methods, leveraging their respective strengths.

This innovative formulation shows great promise for indirect methods, facilitating the adoption of regularization techniques typically associated with direct approaches. This is achieved

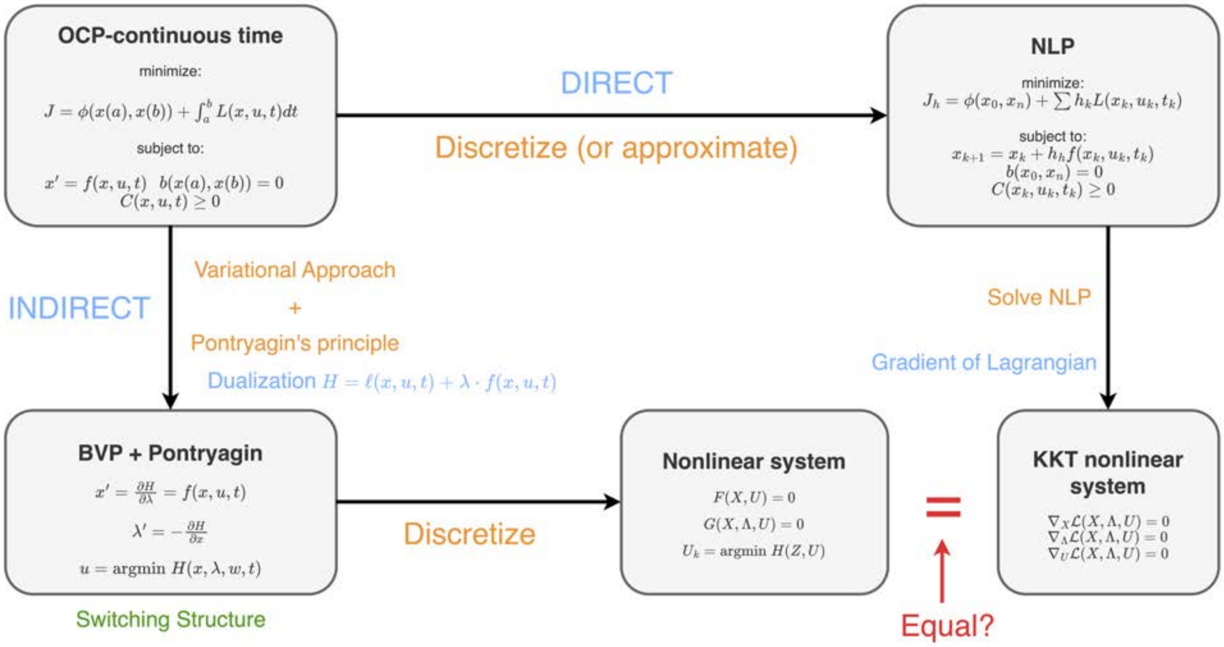

Fig. 1. Diagram direct/indirect methods. Usually not commutative.

while retaining the explicit solution of the control as a function of the states and co-states within a bi-level optimization framework, significantly enhancing numerical performance.

The flexible formulation introduced here enables the incorporation of numerical techniques derived from direct methods, such as proximal methods, aiming to develop a robust solver that maintains the efficient structure of Newton's damped method used in solving indirect methods.

Moreover, the proposed mapping extends its applicability to encompass implicit dynamics, thereby providing a comprehensive solution strategy for a broader range of optimal control problems and applications.

A comparison of indirect only and direct only approach for some selected optimal control problem is presented in reference [5] while [3] present an application with the new proposed approach.

REFERENCES

[1] J.A.E. Andersson, J. Gillis, G. Horn, J.B. Rawlings, M. Diehl: CasADi – A software framework for nonlinear optimization and optimal control. Mathematical Programming Computation **11**(1), 1–36 (2019).

[2] J.T. Betts: Practical Methods for Optimal Control and Estimation Using Nonlinear Programming, Second Edition. Society for Industrial and Applied Mathematics, second edn. (2010).

[3] E. Bertolazzi, F. Biral: A Direct/Indirect Approach to Optimal Control Problems, LNCS NUMTA 2023 Conference Proceeding, in press.

[4] F. Biral, E. Bertolazzi, P. Bosetti: Notes on numerical methods for solving optimal control problems. IEEJ Journal of Industry Applications **5**(2), 154–166 (2016)

[5] N. Dal Bianco, E. Bertolazzi, F. Biral, M. Massaro: Comparison of direct and indirect methods for minimum lap time optimal control problems. Vehicle System Dynamics **57**(5), 665–696 (2019).

[6] A. Huber, M. Gerdts, E. Bertolazzi: Structure exploitation in an interior-point method for fully discretized, state constrained optimal control problems. Vietnam Journal of Mathematics **46**(4), 1089–1113 (2018).

[7] D.J. Limebeer, A.V. Rao: Faster, higher, and greener: Vehicular optimal control. IEEE Control Systems Magazine **35**(2), 36–56 (2015).

[8] B. Michaud, F. Bailly, E. Charbonneau, A. Ceglia, L. Sanchez, M. Begon: Bioptim, a python framework for musculoskeletal optimal control in biomechanics. IEEE Transactions on Systems, Man, and Cybernetics: Systems **53**(1), 321–332 (2023).

[9] D. Morante, M. Sanjurjo Rivo, M. Soler: A survey on low-thrust trajectory optimization approaches. Aerospace **8**(3) (2021).

[10] M. Piccinini, M. Larcher, E. Pagot, D. Piscini, L. Pasquato, F. Biral: A predictive neural hierarchical framework for on-line time-optimal motion planning and control of black-box vehicle models. Vehicle System Dynamics **61**(1), 83–110 (2023).

[11] I.M. Ross: A historical introduction to the convector mapping principle (2005), The NPS Institutional Archive, `https://core.ac.uk/reader/36722476`

[12] E. Trélat: Optimal control and applications to aerospace: Some results and challenges. Journal of Optimization Theory and Applications **154**(3), 713–758 (2012).

[13] A. Zignoli, F. Biral: Prediction of pacing and cornering strategies during cycling individual time trials with optimal control. Sports Engineering **23**(1) (2020).

A control theory approach to convex optimization with inequality constraints

V. Cerone, S. M. Fosson, S. Pirrera, D. Regruto

Abstract— **We propose a novel continuous-time algorithm for inequality-constrained strongly convex optimization inspired by proportional-integral control. Compared to the popular primal-dual gradient dynamics, our approach simplifies the proof of exponential convergence. Moreover, through several examples, we show that the proposed algorithm may converge faster than primal-dual gradient dynamics.**

I. INTRODUCTION

Primal-dual gradient dynamics (PDGD) is a well-established continuous-time algorithm that solves constrained optimization problems. Introduced in [1], it consists of a primal-descent, dual-ascent gradient method achieving the saddle point of the Lagrangian of the problem.

We have recently witnessed a renewed interest in PDGD thanks to its effectiveness in several engineering applications and control problems. In recent literature, several works have addressed the study of the stability and convergence of PDGD. This algorithm is globally exponentially convergent for smooth, strongly convex problems, see, e.g., [2].

This paper proposes a novel continuous-time algorithm for smooth, strongly convex problems with inequality constraints. By starting from the definition of a suitable augmented Lagrangian, the key idea is to control the dynamics of the primal variable through the Lagrange multipliers of the problem by implementing a feedback control method inspired by proportional-integral (PI) control. The contribution of the paper is twofold. On the one hand, we prove the exponential convergence of the proposed method for strongly convex functions. On the other hand, we show its practical effectiveness through numerical simulations.

This work partially extends the framework proposed in [3], where we develop a feedback control approach for equality-constrained problems, specializing in PI control and feedback linearization. In this paper, we retrieve the key ideas of the PI control algorithm proposed in [3], and we develop a novel PI approach for the case of inequality constraints. In particular, this extension requires a novel convergence analysis starting from a peculiar augmented Lagrangian.

II. PROBLEM FORMULATION

Let $f : \mathbb{R}^n \to \mathbb{R}$ be a smooth, strongly convex function. We consider the constrained optimization problem

$$\min_{x\in\mathbb{R}^n} f(x) \quad \text{s.t.} \quad h(x) = Cx - d \leq 0 \tag{1}$$

where $C \in \mathbb{R}^{m,n}$, $d \in \mathbb{R}^m$ and "$\leq$" denotes the componentwise inequality. We consider the following augmented Lagrangian, used, e.g., in [4], [2], to deal with the inequality constraints:

$$\mathcal{L}(x, \lambda) = f(x) + g(x, \lambda) \tag{2}$$

where we define $g : \mathbb{R}^{n+m} \to \mathbb{R}$ as

$$\begin{aligned} g(x,\lambda) &= \sum_{j=1}^{m} g_j(x, \lambda_j) \quad \text{with} \\ g_j(x,\lambda_j) &= \\ &= \begin{cases} \lambda_j h_j(x) + \dfrac{\rho}{2} h_j^2(x) & \text{if } h_j(x) \geq -\dfrac{\lambda_j}{\rho}; \\ -\dfrac{1}{2\rho}\lambda_j^2 & \text{otherwise} \end{cases} \end{aligned} \tag{3}$$

where $\rho > 0$ is a design hyperparameter.

As noticed in [2], the saddle point of (2)-(3) corresponds to the saddle point of the standard Lagrangian; see, e.g., [4, Chapter 3] for details. As shown in [2, Eq. (9)], PDGD for problem (2)-(3) corresponds to the dynamic system

$$\begin{aligned} \dot{x} &= -\nabla_x \mathcal{L}(x, \lambda) = -\nabla f(x) - \nabla_x g(x, \lambda) \\ \dot{\lambda} &= \eta \nabla_\lambda g(x, \lambda), \qquad \eta > 0. \end{aligned} \tag{4}$$

In [2], the authors show that PDGD has a unique equilibrium point that satisfies the first-order KKT conditions for (1). Furthermore, PDGD is globally exponentially convergent. The computed convergence rate τ_{ineq} depends on several constants; therefore, it is hard to assess it explicitly.

As to strongly convex problems with $h(x) = 0$, in [3], we show that PDGD corresponds to an integral control system that regulates $h(x)$ to zero, based on standard Lagrangian for equality constraints problem. In this system, the Lagrange multipliers λ play the role of the control input. In [3], we design a PI control, which usually has a faster convergence rate than PDGD.

III. PROPOSED METHOD: CONTROLLED MULTIPLIERS

This section proposes a novel PI control approach to solve (1). A natural extension of the PI approach proposed in [3] would be

$$\begin{aligned} \dot{x} &= -\nabla_x \mathcal{L}(x, \lambda) = -\nabla f(x) - \nabla_x g(x, \lambda) \\ \dot{\lambda} &= K_i \nabla_\lambda g(x, \lambda) + K_p \frac{d}{dt} \nabla_\lambda g(x, \lambda) \end{aligned} \tag{5}$$

The authors are with the Dipartimento di Automatica e Informatica, Politecnico di Torino, Corso Duca degli Abruzzi 24, 10129 Torino, Italy.

Proving that (5) is exponentially convergent is challenging. For this motivation, we modify (5) as follows:

$$\begin{aligned}\dot{x} &= -\nabla_x \mathcal{L}(x,\lambda) = -\nabla f(x) - \nabla_x g(x,\lambda) \\ \dot{\lambda} &= K_i \nabla_\lambda g(x,\lambda) + K_p J_h(x)\dot{x}.\end{aligned} \tag{6}$$

We replace $\frac{d}{dt}\nabla_\lambda g(x,\lambda)$ by $J_h(x)\dot{x}$. The difference between the proposed approach and PDGD in (4) and (6) is in the presence of the additional term $K_p J_h(x)\dot{x}$ in the dynamics of λ.

IV. CONVERGENCE ANALYSIS

In this section, we analyse the convergence of the dynamic system (6). We define

$$z(t) := (x(t)^\top, \lambda(t)^\top)^\top \tag{7}$$

and

$$z^\star := (x^{\star\top}, \lambda^{\star\top})^\top \tag{8}$$

is the equilibrium point of (6), which corresponds to a saddle point of $\mathcal{L}(x,\lambda)$. The following result holds.

***Proposition** 1:* The equilibrium point of (6) satisfies the KKT conditions for problem (1).

Proof: (Sketch). The result follows from the definition of equilibrium point and some algebraic manipulations. ■

***Theorem** 1 (Global exponential convergence):* Let us assume that C is full rank and there exist $0 < \underline{c} \leq \overline{c}$ such that $\underline{c}I \preceq CC^\top \preceq \overline{c}I$. Let $\rho < \overline{c}^{-1}$. Then, there exist real positive constants α_1 and α_2 such that

$$\|x(t) - x^\star\|_2 \leq \alpha_1 e^{-\frac{1}{2}\mu t}, \quad \|\lambda(t) - \lambda^\star\|_2 \leq \alpha_2 e^{-\frac{1}{2}\mu t} \tag{9}$$

where

$$\mu \leq \min\left\{\frac{1}{2}K_p\underline{c}, \frac{2K_i\underline{g} - K_p\overline{g}^2}{K_i}\right\} \tag{10}$$

where $0 < \underline{g} \leq \overline{g}$ depends on $f(x)$ and $h(x)$ in (1).

Proof: (Sketch). We check that $V\big(z(t)\big) = \big(z(t) - z^\star\big)^\top P\big(z(t) - z^\star\big)$ where $P := \begin{pmatrix} \sigma I_n & 0 \\ 0 & I_m \end{pmatrix} \in \mathbb{R}^{m+n,m+n}$, $\sigma > 0$ is a Lyapunov function satisfying $\dot{V}(z(t)) \leq -\mu V(z(t))$ for the considered dynamics. ■

***Remark** 1:* A theoretical comparison of the convergence rates μ and τ_{ineq} in [2] is challenging due to the fact τ_{ineq} depends on many constants that are not easy to assess. Conversely, we can estimate μ straightforwardly.

***Remark** 2:* The proof of Theorem 1 is simpler than the proof in [2] because of the diagonal form of the selected Lyapunov function.

A. Convergence rate: illustrative example to compare PI and PDGD

We propose a simple illustrative example to compare the convergence rates of (4) and (6). Consider the scalar quadratic optimization problem $min_{x\in\mathbb{R}}\frac{1}{2}wx^2$ subject to $x \leq 0$, where $w > 0$.

The closed-loop dynamics of both PDGD and PI control correspond to a switched LTI system with two modes. By evaluating the state space matrices in each mode, we conclude that, in the second mode, PI and PDGD enjoy the same rate of convergence. Concerning the first mode, we notice that for PDGD it is not possible to increase the convergence rate beyond $w + \rho$. Conversely, for PI, the eigenvalues are complex conjugate by choosing K_i sufficiently large, and the convergence rate is $K_p + w + \rho$.

V. NUMERICAL EXAMPLES

A. Example 1: Quadratic programming

In this simulation, we consider a strongly convex quadratic programming (QP) with randomly generated vectors and matrices. We set dimensions $n = 50$ and $m = 45$, and parameters $K_i = \eta = 1$ and $K_p = -0.7$.

We perform 100 random runs with different realizations, and we observe that PI requires fewer iterations than PDGD in all the runs. In Table V-A, we report some statistics comparing the convergence speed of PI and that of PDGD.

	mean	standard deviation	worst case
N PDGD	8128.3	491.9	9361
N PI	6903.2	312.1	7613
T PDGD	1.23×10^{-1}	8.04×10^{-3}	1.53×10^{-1}
T PI	1.02×10^{-1}	4.74×10^{-3}	1.15×10^{-1}

B. Example 2: Linear system identification

We apply our approach to a problem of system identification. We consider the problem of identifying a stable LTI system $H(z)$ using N uncertain input-output measurements $\{u_k, \tilde{y}_k\}$, where $\tilde{y}_k = y_k + \eta_k$, y_k is the noise-free output and η_k is noise.

We select model structure $\tilde{H}(z,\theta) = \sum_{i=1}^{P}\theta_i B_i(z)$, with $B_i(z)$ stable first-order filters. We look for the value of the parameter θ that minimizes the ℓ_∞-norm of the simulation error

$$\theta^* = \arg\min_{\theta\in\mathbb{R}^P} \|y_k(\theta) - \tilde{y}_k\|_\infty. \tag{11}$$

This problem is easily recast to a linear programming problem. We integrate (6) and (4) setting $K_i = \nu = 1$ and $K_p = -0.5$. Both algorithms provide FIT $= 98.5\%$, but the PI algorithm is about two times faster than PDGD.

VI. CONCLUSIONS

We propose a novel continuous-time algorithm to solve strongly convex optimization problems with inequality constraints. By elaborating on the feedback PI control approach proposed in [3], we develop a variant of primal-dual gradient dynamics in which an additional term adjusts the dynamics and enhances the convergence speed. We prove that the proposed method is globally exponentially convergent. The effectiveness of the proposed algorithm is shown through numerical simulations.

REFERENCES

[1] T. Kose, “Solutions of saddle value problems by differential equations,” *Econometrica*, vol. 24, no. 1, pp. 59–70, 1956.

[2] G. Qu and N. Li, “On the exponential stability of primal-dual gradient dynamics,” *IEEE Control Syst. Lett.*, vol. 3, no. 1, pp. 43–48, 2019.

[3] V. Cerone *et al.*, “A new framework for constrained optimization via feedback control of lagrange multipliers,” *submitted to IEEE Trans. Autom. Control*, 2024.

[4] D. P. Bertsekas, *Constrained Optimization and Lagrange Multiplier Methods.* Academic Press, New York, NY, USA., 1982.

Feedback Control of the Exploitation-Exploration Trade-off in Set Membership Global Optimization

Mattia Alborghetti, Giulio Montecchio, Lorenzo Sabug Jr., Lorenzo Fagiano, Fredy Ruiz

***Abstract*— Trading off exploration and exploitation is a crucial task in global (or black-box) optimization, to balance the search for better local optimizers with the refinement of already-found ones. Often, such a trade-off is not easily controlled by the user, as it depends non-trivially on the tuning parameters of the selected algorithm. A new concept is proposed here, where the share of exploitation moves over the total number of iterations is regulated by a feedback control law, to achieve a user-defined set-point. This concept is applied to the recently proposed Set Membership Global Optimization (SMGO) technique, resulting in a modified algorithm. Together with computational improvements the resulting approach is extensively tested and compared with other methods. The statistical tests indicate that the new algorithm has better iteration-based optimization performance than the original one, at the same time shortening the computational times by around one order of magnitude. This extended abstract is based on a recently presented conference paper [1].**

***Keywords*— global optimization, set membership, algorithm design.**

I. INTRODUCTION

In many scientific, engineering, and social applications, constrained optimization problems are non-convex and often lack closed-form objective and constraint expressions, relying instead on simulations or experiments. These are known as black-box, derivative-free, or global optimization problems. To address these, four major approaches exist: direct search, population-based, surrogate model-based, and Lipschitz-based methods [2]. Among these, Bayesian optimization (BO), using Gaussian process (GP) models and acquisition functions, is particularly popular. However, BO's exploitation/exploration trade-off is often tuned by trial and error, and its computational burden is high.

This work introduces a feedback loop to dynamically adapt the exploitation/exploration balance in a novel method, called Set Membership Global Optimization (SMGO), improving its performance and providing a more intuitive way for the user to distribute the sampling budget.

II. PROBLEM DESCRIPTION

Consider the minimization of a real-valued cost function $f : \mathcal{X} \to \mathbb{R}$, subject to S constraints $g_s : \mathcal{X} \to \mathbb{R}, s = 1, \dots, S$, where $\mathcal{X} \subset \mathbb{R}^D$, is a compact, convex set in a D-dimensional real space, referred as the search set:

$$\begin{array}{ll} \min\limits_{\boldsymbol{x} \in \mathcal{X}} & f(\boldsymbol{x}) \\ \text{s.t.} & g_s(\boldsymbol{x}) \geq 0, s = 1, \dots, S. \end{array}$$

The only required assumption is the Lipschitz continuity and boundedness of f and g_s over $\mathcal{X}$, defining generally unknown Lipschitz constants for the cost function and constraints. Under this assumption, we know a finite global minimum exists and we want to find it by applying the so-called Set-Membership Global Optimization (SMGO). At the heart of the approach is a SM-based non-parametric model on the data set, to estimate Lipschitz constants and upper and lower bounds on the hidden cost function and constraints. These bounds are then used either in an exploitation routine, to select a point with the largest expected improvement, or in an exploration one, to designate a point with large estimated uncertainty. The algorithm carries out an expected-improvement test to evaluate if it is estimated to improve on the current best value by a large enough quantity given by the parameter α. If such a test is passed, the exploitation candidate point is sampled, otherwise, the algorithm explores. A detailed description of the method can be found in [3].

III. METHOD: FEEDBACK CONTROL OF THE EXPLOITATION/EXPLORATION TRADE-OFF

The trade-off between exploitation and exploration is a crucial factor for the practical convergence rate of a global optimizer. In SMGO, a non-negative parameter α controls this trade-off. However, directly tuning α has various drawbacks. The application of a fixed threshold limits the accuracy of the optimum that the algorithm can possibly achieve. Moreover, the relationship between α and the amount of exploitation steps performed is highly dependent on the specific problem, so the tuning of α may need each time a tedious trial and error procedure.

To address this problem, we propose an adaptive approach, where the value of α is set by a feedback loop with a discrete-time proportional-integral (PI) controller (see Fig. 1).

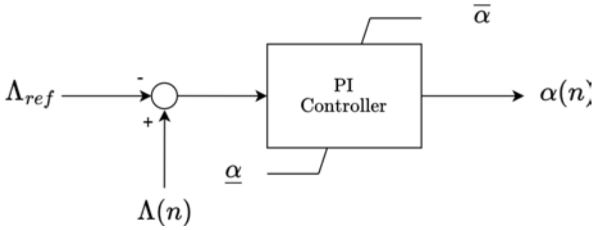

Fig. 1: Scheme of the exploitation/exploration trade-off controller.

The user's preference is now encoded by a new parameter, Λ_{ref}, which is a reference for the exploitation ratio

$$\Lambda(n) = \frac{N_\theta(n)}{n}. \qquad (1)$$

i.e. the share of implemented exploitation moves $N_\theta(n)$ (with successful expected improvement test) over the total number n of performed iterations. Defining the tracking error $e(n) = \Lambda(n) - \Lambda_{\text{ref}}$, we compute $\alpha(n)$ according to a standard PI

M. Alborghetti, L. Sabug, L. Fagiano and F. Ruiz are with the Department of Electronics, Information and Bioengineering, Politecnico di Milano, Piazza Leonardo da Vinci 32, 20133 Milano, Italy. Email: {name.surname}@polimi.it

G. Montecchio is with Robert Bosch GmbH, Robert-Bosch-Campus, 71272 Renningen, Germany. Email: giulio.montecchio@de.bosch.com.

This research has been supported by Fondazione Cariplo under grant n. 2022-2005, project "NextWind - Advanced control solutions for large scale Airborne Wind Energy Systems" and by the Italian Ministry of University and Research under grants "DeepAirborne - Advanced Modeling, Control and Design Optimization Methods for Deep Offshore Airborne Wind Energy" (NextGenerationEU fund, project P2022927H7) and the Extended Partnership "NEST - Network 4 Energy Sustainable Transition".

		Mean Optimum			Optimum Std			Computational time (s)		
Problem	*D*	*E-SMGO*	*BO*	*G-MS*	*E-SMGO*	*BO*	*G-MS*	*E-SMGO*	*BO*	*G-MS*
T1	**2**	6.019e-01	6.005e-01	5.998e-01	3.2e-03	6.3e-04	4.7e-09	5.0	1210.3	0.14
T2	**2**	2.537e-01	2.542e-01	2.532e-01	4.2e-04	5.9e-04	1.4e-08	3.8	722.0	0.15
T3	**2**	-1.998e+00	-2.000e+00	-1.995e+00*	4.1e-03	5.5e-06	1.3e-02*	4.0	491.2	0.17
STYB	**2**	-7.830e+01	-7.833e+01	-7.366e+01*	5.3e-02	2.6e-03	7.8e+00*	5.0	666.6	0.14
STYB	**10**	-2.806e+02	-3.378e+02	-3.384e+02**	3.9e+01	1.1e+01	2.3e+01**	6.2	526.3	0.06
G04	**2**	-3.054e+04	-3.052e+04	-3.067e+04	8.8e+01	4.0e+01	2.3e-06	12.7	4713.5	0.12
G05MOD	**4**	5.259e+03	5.218e+03	5.126e+03	9.5e+01	2.5e+01	9.9e-10	10.4	3548.6	0.08
G08	**2**	-8.733e-02	-9.581e-02	-6.333e-02*	9.4e-03	1.8e-05	3.6e-02*	4.9	1066.5	0.11
G09	**7**	1.841e+03	7.541e+02	Inf**	1.2e+03	2.6e+01	NaN**	9.9	4531.8	0.09
G12	**3**	-9.584e-01	-1.000e+00	-9.603e-01	2.6e-02	8.4e-05	3.7e-02	4.6	1272.0	0.11
G23MOD	**9**	-3.900e+03	-3.383e+03	-3.900e+03	0.0e+00	8.5e+01	0.0e+00	7.0	3309.1	0.06
G24	**2**	-5.475e+00	-5.426e+00	-5.508e+00	3.9e-02	1.2e-01	2.0e-14	5.4	1671.8	0.18

TABLE I: Results of 50 independent runs on benchmark functions with a budget of $N = 500$ function evaluations for *E-SMGO*, Bayesian optimization (*BO*) and gradient-based multistart (*G-MS*).
*: exhibits convergence to a local (not global) optimum in some of the fifty runs by graphical interpretation.
**: prematurely finished optimization due to the exceeding of maximum function evaluations in some of the fifty trials.

controller with an anti-windup structure to handle saturation and ensure compliance with model hypotheses.

Note that the positive feedback in Figure 1 is justified by the fact that larger values of $\alpha(n)$ lead to more difficult improvement tests, encouraging lower values of $\Lambda(n)$ (1).

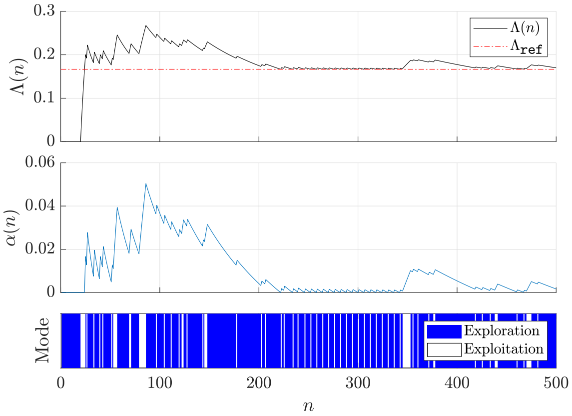

Fig. 2: Example of close loop control of the exploitation ratio during the optimization of a benchmark function using a PI controller.

A typical behavior of the ratio $\Lambda(n)$ and factor $\alpha(n)$ along iterations is presented in Fig. 2. A theoretical analysis of the effect of the PI gains on the algorithm behavior is difficult to carry out and would certainly require additional assumptions on the cost function, which would be hardly verifiable and quite limiting. On the other hand, we found that tuning of these gains is not as critical as the original tuning of the parameter α. We always used the same values in all our tests without noticing any performance degradation.

IV. Benchmark results

We tested the introduced algorithmic improvements on a set of 12 non-convex benchmark optimization problems from [4], with different search-space dimensions, function properties, and feasible region volume as a fraction of the search set volume. Simulations have shown that our enhanced version (*E-SMGO*) is much more computationally efficient, requiring nearly one order of magnitude lower computational time than the original *SMGO*, delivering similar or better quality and accuracy of the optimal solution. Moreover, applying the feedback controller reduces significantly the discrepancy between the desired exploitation-exploration ratio and the actual one. More detailed results are presented in [1].

We solved the benchmark problems also with two other well-established optimizers: *gradient-based multistart* (*G-MS*) and *Bayesian optimization* (*BO*), using the same function evaluation budget N, to ensure that the comparison is not influenced by the computational time of individual cost functions (Table I). As a general conclusion, based on these results, *BO* provides slightly more precise optimal solution values compared to *E-SMGO*, but requires significantly higher execution time. On the other hand, *G-MS* outperforms the other methods in terms of computational efficiency and it exhibits the smallest standard deviation among alternatives, except for the cases when they remain trapped in a local minimum (* Table I). Moreover, it requires many function evaluations for gradient computation, especially in high-dimensional cases where a single gradient descent can exhaust the entire budget (** Table I). This can degrade the optimal result, particularly with a limited function budget, as is common in complex, costly real-world problems [5]. It's also significant to underline that *G-MS* cannot provide a feasible solution for **G09** in 20 out of 50 tests.

V. Conclusion

This work presented a novel approach to regulate the trade-off between exploitation and exploration in global optimization algorithms, based on feedback control and deployed in the Set Membership Global Optimization (SMGO) technique. These changes have been tested on twelve benchmark functions, showing that the enhanced SMGO strategy generally improves over the original version in terms of iteration-based optimization performance, while requiring much lower computational effort. Moreover, a state-of-the-art comparison demonstrates good optimization-based performance, positioning it between randomized local solvers and time-consuming global methods.

References

[1] S. L. J. F. L. R. F. Alborghetti Mattia, Montecchio Giulio, “Controlling the exploitation/exploration trade-off in global optimization: a set membership approach,” in *American Control Conference*, 2024.

[2] M. A. Gelbart, J. Snoek, and R. P. Adams, “Bayesian Optimization with Unknown Constraints,” mar 2014, pp. 1–14.

[3] L. J. Sabug, “On data-driven optimization in the design and control of autonomous systems,” Ph.D. dissertation, Politecnico di Milano, 2023.

[4] L. Sabug, F. Ruiz, and L. Fagiano, “SMGO-Δ: Balancing caution and reward in global optimization with black-box constraints,” *Information Sciences*, vol. 605, pp. 15–42, 2022. [Online]. Available: https://www.sciencedirect.com/science/article/pii/S0020025522004376

[5] G. Montecchio and M. Alborghetti, “Global optimization of pulse patterns for an electrical drive via set membership methods,” Master's thesis, Politecnico di Milano, 2023.

Robust Variable-Horizon MPC with Adaptive Terminal Constraints

R. Quartullo, G. Bianchini, A. Garulli, A. Giannitrapani
Dipartimento di Ingegneria dell'Informazione e Scienze Matematiche, Università di Siena

Model Predictive Control (MPC) techniques conventionally address optimal control problems by minimizing a cost function dependent on state and input variables over a fixed-length prediction horizon. Recent advancements have expanded this framework to incorporate the prediction horizon length as a variable within the optimization problem. This is particularly crucial in applications requiring task completion within minimal time or specific deadlines, such as spacecraft rendezvous and docking with moving targets, and robotic motion planning. These scenarios benefit from integrating the prediction horizon length into the MPC cost function.

Time-optimal MPC represents one approach, where the goal is to minimize the prediction horizon length. A notable strategy involves a bi-level optimization scheme, where the inner problem remains a fixed-horizon optimal control problem, and the outer problem seeks to minimize horizon length while maintaining inner problem feasibility. Alternative approaches include optimizing the sampling time as part of the control variables or employing exponentially increasing stage costs to achieve time-optimality and closed-loop stability. The Lyapunov stability of minimum-time MPC has also been a focal point of study. Shrinking-time MPC offers another strategy by design, systematically reducing the horizon length at each time step. This technique has been applied in scenarios like helicopter landing and energy-efficient train operation, which uniquely considers bounded input disturbances to retain recursive feasibility. The Variable-Horizon MPC (VH-MPC) framework generalizes these concepts by treating the prediction horizon length as a cost function variable. This approach was first explored for linear systems with bounded process disturbances in [1], achieving recursive feasibility and finite-time convergence using a tube-based MPC method. However, this method's performance can be conservative due to its reliance on worst-case disturbance sequences.

In this paper, we introduce a robust VH-MPC scheme designed to intercept moving targets with known trajectories in the presence of bounded process disturbances. The key innovation is an adaptive mechanism for the terminal set in the tube-MPC optimization problem. In particular, the optimization problem is stated on the nominal state and input sequence considering tightened constraint, allowing for constraint satisfaction against all possible disturbances, as typical in tube-MPC formulation [2]. In the perspective of intercepting a reference trajectory, an equality terminal constraint with a point on the reference would be the ideal choice. However, due to disturbances, this approach cannot guarantee recursive feasibility or finite-time convergence to a bounded set. For this reason, we propose a control algorithm, in which the main idea is to keep solving the problem with the equality terminal constraint as long as the problem is feasible and the optimal cost decreases by at least a positive quantity with respect to the previous step. Whenever this does not occur, the terminal constraint is expanded into a set, whose design is crucial for ensuring recursive feasibility and finite-time convergence. The rationale behind this approach is that, on the one hand, the use of a terminal equality constraint favors a minimum-distance approach to the docking point. On the other hand, the use of the terminal set is instrumental for recursive feasibility, which allows for convergence of the optimal cost. In this work, the desired properties of the algorithm are theoretically demonstrated, as well as the size of the set in which the state trajectories of the closed-loop system are guaranteed to terminate. It turns out that, the latter set, resulting from the described adaptive mechanism, is much smaller than the one guaranteed by the control scheme proposed in [1], in which the sequence of terminal constraints is fixed.

The validity of the proposed control scheme (hereafter denoted as ATCS) has been also demonstrated through numerical simulations on two case studies: a double integrator is considered to illustrate the main features of the proposed VH-MPC strategy with adaptive terminal constraint sequence; the second case study considers a realistic scenario, in which a controlled satellite is required to intercept an uncontrolled tumbling object (such as a defunct satellite or space debris). For the first example, a Monte Carlo simulation across different initial conditions has been conducted. Figure 1 displays the final states for our control laws compared to the one proposed in [1] (hereafter denoted as FTCS). It can be observed that ATCS drives the states to a relatively small neighborhood of the origin, achieving a mean terminal distance of 0.38. Conversely, the FTCS drives the state trajectories much farther away from the origin, with an average final state norm of 6.74. For the rendezvous scenario, we obtained similar results, allowing for a much closer proximity to the target. In fact, Figure 2 shows the trajectories of the servicer satellite obtained by two laws in comparison. Moreover, since the procedure would require solutions of mixed-integer programs (being the horizon an optimization variable), the heuristic proposed in [3] is adopted in order to deeply reduce the computational burden.

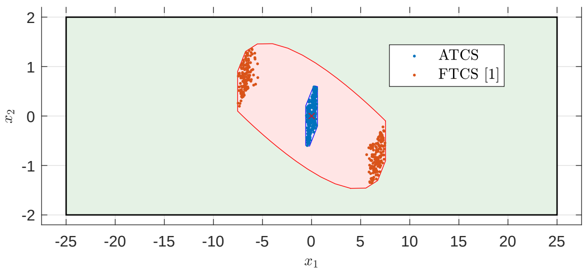

Figure 1: Double Integrator. Final states obtained by applying ATCS (blue dots) and FTCS (red dots). The blue and the red sets are the sets in which the two compare laws are guaranteed to terminate.

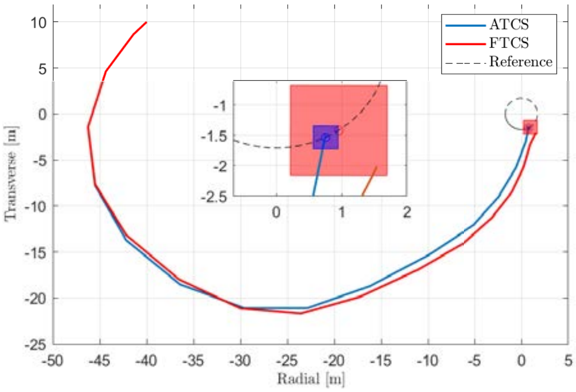

Figure 2: Rendezvous scenario. Trajectories resulting from ATCS and FTCS. The reference trajectory of the capture point is depicted in black.

References

[1] A. Richards and J. P. How, “Robust variable horizon model predictive control for vehicle maneuvering,” *International Journal of Robust and Nonlinear Control*, vol. 16, no. 7, pp. 333–351, 2006.

[2] J. B. Rawlings, D. Q. Mayne, and M. Diehl, *Model predictive control: theory, computation, and design*, vol. 2. Nob Hill Publishing Madison, WI, 2017.

[3] M. Leomanni, R. Quartullo, G. Bianchini, A. Garulli, and A. Giannitrapani, “Variable-horizon guidance for autonomous rendezvous and docking to a tumbling target,” *Journal of Guidance, Control, and Dynamics*, vol. 45, no. 5, pp. 846–858, 2022.

Pseudo-Transient Continuation for Enhanced Quadratic Programming and Optimal Control

Lorenzo Calogero, Michele Pagone, and Alessandro Rizzo

I. INTRODUCTION

Quadratic programming (QP) solvers that join effectiveness with a simple implementation are becoming essential in the field of optimal control, specifically when dealing with real-time applications with strict timing constraints and limited computational resources. To address this need, we present a novel high-performance QP solution method based on pseudo-transient continuation (PTC). PTC is a numerical technique that transforms multivariate nonlinear equations into autonomous systems that converge to the solution sought. In our approach, we recast the general QP Karush-Kuhn-Tucker (KKT) conditions into a system of equations and employ PTC to solve the latter to attain the optimal solution. Importantly, we provide theoretical guarantees demonstrating the global convergence of our PTC-based solver to the optimal solution of any given QP. To showcase the effectiveness of PTC, we employ it within the domain of Model Predictive Control (MPC). Specifically, numerical simulations are carried out on the MPC control of a quadrotor – a demanding dynamical system – highlighting excellent results in accurately executing the control task and ensuring lower computational times compared to conventional QP solvers.

II. PSEUDO-TRANSIENT CONTINUATION FOR QUADRATIC PROGRAMMING

Consider a multivariate nonlinear equation in the form

$$F(x) = 0, \quad F : \mathbb{R}^n \to \mathbb{R}^n, \tag{1}$$

having a set of solutions $S = \{x \in \mathbb{R}^n : F(x) = 0\}$. Pseudo-transient continuation (PTC) [1] seeks a functional $f(F(x)) : \mathbb{R}^n \to \mathbb{R}^n$ such that the autonomous system

$$\dot{x} = f(F(x)) \tag{2}$$

has a set of equilibrium points $S^* \subseteq S$ and converges (at least locally) to one of such equilibria, i.e.,

$$f(F(x(t))) \to 0, \ \ x(t) \to x^* \in S^* \ \text{ for } \ t \to +\infty. \tag{3}$$

In this work, we leverage PTC to efficiently solve general convex quadratic programs (QPs) in the following form:

$$\min_y \frac{1}{2} y^\top H y + c^\top y \quad \text{s.t.} \quad Cy = p, \quad Dy \leq q, \tag{4}$$

where $y \in \mathbb{R}^n$ is the vector of decision variables; $H \in \mathbb{R}^{n \times n}$, $H = H^\top \succ 0$; $C \in \mathbb{R}^{N_E \times n}$ and $p \in \mathbb{R}^{N_E}$ represent the N_E equality constraints, C has full row rank; $D \in \mathbb{R}^{N_I \times n}$ and $q \in \mathbb{R}^{N_I}$ represent the N_I inequality constraints. Since the cost and the inequality constraints of (4) are convex functions, it admits a unique global minimum y^*. PTC allows to solve (4) for its global optimum with high computational performance. In this perspective, two fundamental steps have to be performed:

1. by manipulating the Karush-Kuhn-Tucker (KKT) conditions associated with (4), recast them as a system of equations like (1), having as unique solution the global optimum of (4);
2. derive sufficient conditions characterizing F such that, for given functionals f, the global asymptotic convergence of (2) to its unique equilibrium is guaranteed.

These two steps are assessed in Sections II-A and II-B, respectively.

A. Conversion of QP KKT Conditions into a System of Equations

Let us consider the Lagrangian of (4), i.e.,

$$\mathcal{L}(y, \mu, \lambda) = \frac{1}{2} y^\top H y + c^\top y - \mu^\top (Cy - p) - \lambda^\top (Dy - q), \tag{5}$$

where $\mu \in \mathbb{R}^{N_E}$ and $\lambda \in \mathbb{R}^{N_I}$ are the Lagrange multipliers. If a triple (y^*, μ^*, λ^*) satisfies the KKT conditions, i.e.,

$$\nabla_y \mathcal{L}(y, \mu, \lambda) = Hy + c - C^\top \mu - D^\top \lambda = 0, \quad Cy = p, \tag{6a}$$

$$Dy \leq q, \quad \lambda \leq 0, \quad \lambda^\top (Dy - q) = 0, \tag{6b}$$

then y^* is also the global minimum of (4). According to [2], conditions (6b) can be equivalently rewritten as

$$(D)_{i,\cdot}\, y = q_i \ \text{ if } \ \lambda_i \leq 0, \quad (D)_{i,\cdot}\, y < q_i \ \text{ if } \ \lambda_i = 0, \tag{7}$$

where $(D)_{i,\cdot}$ denotes the i-th row of D. (7) is also equivalent to the following system of piecewise affine equations [2]:

$$Dy = \phi_{[-\infty,q]}(Dy - \alpha\lambda), \tag{8}$$

where $\alpha \in \mathbb{R}_{>0}$ and $\phi_{[a,b]}(z)$ denotes the asymmetric saturation of the vector $z \in \mathbb{R}^{N_I}$ by $[a, b]$, whose expression is

$$\phi_{[a,b]}(z) \equiv \left[\phi_{[a_i,b_i]}(z_i)\right]_{i=1}^{N_I}, \ \phi_{[a_i,b_i]}(z_i) = \begin{cases} a_i & \text{if } \ z_i < a_i, \\ z_i & \text{if } \ a_i \leq z_i \leq b_i, \\ b_i & \text{if } \ z_i > b_i. \end{cases} \tag{9}$$

Hereafter, for notation clarity, we denote $\phi_{[-\infty,q]}$ as ϕ.

The KKT conditions (6) can be then rewritten as a system of equations as follows:

$$Hy + c - C^\top \mu - D^\top \lambda = 0, \quad Cy - p = 0, \tag{10a}$$

$$Dy - \phi(Dy - \alpha\lambda) = 0. \tag{10b}$$

The system of equations (10) can be simplified as

$$y = G' D^\top \lambda + h', \tag{11a}$$

$$\mu = (CH^{-1}C^\top)^{-1}(p - CH^{-1}(D^\top \lambda - c)), \tag{11b}$$

$$G\lambda + h - \phi((G - \alpha I)\lambda + h) = 0, \tag{11c}$$

where

$$\begin{aligned} G' &= H^{-1} - H^{-1}C^\top (CH^{-1}C^\top)^{-1} CH^{-1}, \\ h' &= H^{-1}(C^\top (CH^{-1}C^\top)^{-1}(CH^{-1}c + p) - c), \\ G &= DG'D^\top, \quad h = Dh'. \end{aligned} \tag{12}$$

Only (11c) has to be solved for λ, since y and μ are function of λ only. Also, since (11) admits a unique solution (y^*, μ^*, λ^*), then λ^* is the unique solution of (11c).

B. Global Convergence of PTC for QPs Solution

To prove that any QP problem (4), when rewritten as a system of equations (11), can be effectively solved through PTC and exhibits

---

The authors are with the Politecnico di Torino, Department of Electronics and Telecommunications, 10129 Turin, Italy (e-mail: {`lorenzo.calogero`, `michele.pagone`, `alessandro.rizzo`}`@polito.it`). *(Corresponding author: Alessandro Rizzo.)*

The work of L. Calogero was supported by the NGEU-PNRR Project (MUR - D.M. 352/2022). The work of M. Pagone and A. Rizzo was supported by the MOST (Sustainable Mobility National Research Center) and funded by the European Union NextGenerationEU Project (PNRR - Mission 4, Component 2, Investment 1.4 - D.D. 1033 17/06/2022) under Grant CN00000023.

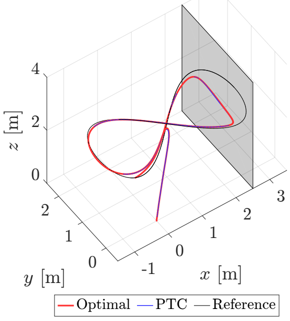

Figure 1. MPC quadrotor control: comparison of PTC closed-loop trajectory with the globally optimal one.

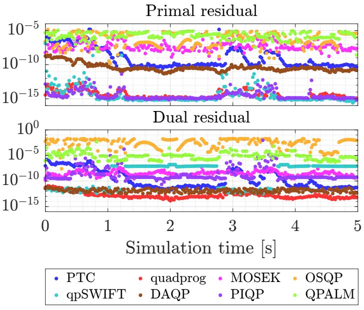

Figure 2. Primal and dual residuals on the MPC solution obtained by each solver.

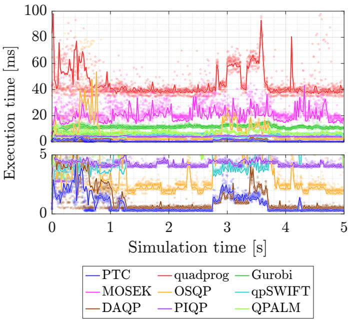

Figure 3. Execution time of each MPC control step, with detail of the range $[0, 5]$ ms.

Solver	Exec. time		Iterations	
	Max	Mean	Max	Mean
PTC	4.19	0.85	20	3
quadprog	98.04	45.02	90	7
Gurobi	14.23	10.96	24	16
MOSEK	43.20	20.17	49	24
OSQP	53.64	6.17	2875	329
qpSWIFT	6.33	4.73	18	14
DAQP	8.74	1.43	23	3
PIQP	4.98	4.28	13	11
QPALM	13.29	6.82	49	28

Table 1. Execution time (in ms) and iterations (single MPC control step).

global convergence to its optimum, we introduce Theorem 1, reporting a sufficient condition for the PTC autonomous system (2) to be globally asymptotically stable in the sense of Lyapunov.

Theorem 1. *Assume that: i) the multivariate nonlinear equation* (1), *i.e.,* $F(x) = 0$, *has a unique solution* x^**; ii) there exists a symmetric and positive definite matrix* $M \in \mathbb{R}^{n \times n}$ *such that*

$$(x - x^*)^\top M F(x) > 0, \quad \forall x \neq x^*. \tag{13}$$

Then, the system

$$\dot{x} = -\beta F(x), \quad \beta \in \mathbb{R}_{>0} \tag{14}$$

has a unique equilibrium point in x^* *and such equilibrium is globally asymptotically stable (GAS).*

Proof. We refer the reader to the full paper [3]. ☐

We then show, in Proposition 1, that the KKT system of equations (11) satisfies Theorem 1 and, thus, can be solved via PTC.

Proposition 1. *Let us consider* (11c) *and denote it as* $F(\lambda) = 0$. *Then, the system*

$$\dot{\lambda} = -\beta F(\lambda), \quad \beta \in \mathbb{R}_{>0} \tag{15}$$

has a unique equilibrium point λ^**, coinciding with the solution of* (11c)*, and such equilibrium is GAS.*

Proof. We refer the reader to the full paper [3]. ☐

III. APPLICATION OF PTC TO MODEL PREDICTIVE CONTROL

To assess the performance of PTC, we consider the following Model Predictive Control (MPC) problem:

$$\begin{aligned} \min_{\hat{u}_{\cdot|k}, \hat{x}_{\cdot|k}} \quad & J_k(\hat{u}_{\cdot|k}, \hat{x}_{\cdot|k}) \\ \text{s.t.} \quad & i = 0, 1, \dots, N_p - 1, \\ & \hat{x}_{0|k} = x_k, \quad \hat{x}_{i+1|k} = A_k \hat{x}_{i|k} + B_k \hat{u}_{i|k} + b_k, && \text{(16a)} \\ & \underline{u} \leq \hat{u}_{i|k} \leq \overline{u}, \quad \underline{x} \leq \hat{x}_{i|k} \leq \overline{x}, && \text{(16b)} \end{aligned}$$

$$\begin{aligned} J_k(\hat{u}_{\cdot|k}, \hat{x}_{\cdot|k}) = & \sum_{i=0}^{N_p-1} \left(\|\hat{x}_{i|k} - x_{r,k+i}\|_Q^2 + \|\hat{u}_{i|k}\|_R^2 \right) + \\ & \sum_{i=1}^{N_p-1} \left(\|\hat{u}_{i|k} - \hat{u}_{i-1|k}\|_{R_\Delta}^2 \right) + \|\hat{x}_{N_p|k} - x_{r,k+N_p}\|_P^2, && \text{(16c)} \end{aligned}$$

where $\hat{u}_{i|k} \in \mathbb{R}^{n_u}$, $\hat{x}_{i|k} \in \mathbb{R}^{n_x}$ are the inputs and states predicted i steps ahead at time k, respectively; x_r is the state reference trajectory; (16c) is the MPC cost function ($\|x\|_M^2 \equiv \frac{1}{2} x^\top M x$); (16a) are the prediction model constraints; (16b) are inputs and states constraints. The MPC optimal control problem (16) can be rewritten to match the QP formulation (4); thus, it can be fast solved for its global optimum by PTC with global convergence guarantees, in view of the results presented in Section II.

As nonlinear plant to control, we select the Euler-Lagrange quadrotor model in [4]. The control task is to track a lemniscate reference trajectory, partially crossing an infeasible region of space (see Figure 1). To deploy the linear MPC (16) to control the nonlinear continuous-time plant, we adopt the sequential quadratic programming (SQP) approach with real-time iteration (RTI) to discretize and linearize the plant.

IV. SIMULATIONS AND RESULTS

PTC is compared with the following conventional QP solvers: the active-set solvers quadprog and DAQP; the interior-point solvers Gurobi, MOSEK, qpSWIFT, and PIQP; the operator splitting solver OSQP; the augmented Lagrangian solver QPALM.

Simulations are performed with MATLAB® 2023b on a 13th Gen Intel® Core™ i7 CPU at 1.7 GHz. The full source code is available online[1]. The PTC autonomous system (15) is numerically integrated using the explicit Runge-Kutta 2(3) method.

Figure 1 reports the quadrotor closed-loop trajectory, obtained by solving the MPC problem (16) with PTC. This trajectory is rather coincident with the globally optimal one (estimated with Gurobi by setting very low optimality tolerances).

To further assess the goodness of the obtained MPC solutions, Figure 2 reports the primal and dual residuals at each time instant and for every solver. We see that PTC consistently achieves low residuals that stay below the thresholds defined by the optimality criteria. On the contrary, some of the other solvers fail to deliver an acceptable dual residual.

Finally, Figure 3 compares, for each solver, the execution time of each MPC control step, reporting both the actual time values (solid lines) and Monte Carlo envelopes (scatter plots), obtained by randomly selecting 50 initial states x_0 from the feasible set $[\underline{x}, \overline{x}]$. Results are summarized in Table 1, including the number of iterations required by each solver. We observe that PTC outperforms all other solvers in terms of both maximum and average computational time.

REFERENCES

[1] T. Han and Y. Han, "Solving large scale nonlinear equations by a new ODE numerical integration method," *Applied Mathematics*, vol. 1, no. 3, pp. 222–229, 2010.

[2] W. Li and J. Swetits, "A new algorithm for solving strictly convex quadratic programs," *SIAM Journal on Optimization*, vol. 7, no. 3, pp. 595–619, 1997.

[3] L. Calogero, M. Pagone, and A. Rizzo, "Enhanced Quadratic Programming via Pseudo-Transient Continuation: An Application to Model Predictive Control," *IEEE Control Systems Letters*, vol. 8, pp. 1661–1666, 2024.

[4] L. Calogero, M. Mammarella, and F. Dabbene, "Learning Model Predictive Control for Quadrotors Minimum-Time Flight in Autonomous Racing Scenarios," *IFAC-PapersOnLine*, vol. 56, no. 2, pp. 1063–1068, 2023.

---

[1] `gitlab.com/PoliToComplexSystemLab/qp_ptc`.

Session 4B: Control of energy systems

Forecasting Wind Power: A Comparative Study of Parametric and Non-parametric Approaches Using Real-World Data

Department of Electrical, Computer and Biomedical Engineering
University of Pavia

Marco Capelletti, Giuseppe De Nicolao

Abstract

Integrating renewable energy sources into the power grid introduces significant uncertainty, making probabilistic wind power forecasting crucial. This study compares two methods: parametric Beta regression with natural spline preconditioning and non-parametric Quantile Regression Forests (QRFs). Using SCADA data from the Penmanshiel wind farm and wind forecasts from the Copernicus project, models were evaluated for a 6-hour ahead forecasting horizon. Beta regression effectively captured complex power distribution patterns influenced by varying wind speeds, while QRFs, despite providing valid probabilistic forecasts, exhibited higher variance and required meticulous hyperparameter tuning. The findings highlight the challenges and prospects of flexible modeling for probabilistic wind power forecasts.

Problem statement

Probabilistic wind power forecasting has two primary objectives: enabling wind farm owners to optimize revenue and bidding strategies in the day-ahead electricity market, and helping Transmission System Operators (TSOs) manage grid imbalances and activate storage or backup power resources proactively.

Accurate wind power prediction relies on power curve models, which describe the performance of wind turbines and wind farms. Two main forecasting approaches exist: indirect and direct. The indirect approach uses a power curve model derived from actual data and fed with weather forecasts from meteorological providers. The direct approach links weather forecasts to power output, typically via machine learning techniques. The whole problem becomes even more challenging when, instead of point predictions, one aims at probabilistic predictions, providing the statistical distribution of future wind power.

While the identification of probabilistic models of measurement-based power curves for indirect forecasting is addressed in [CRDN24], it is still open if such parametric models can capture the complexities that can be learnt by machine learning methods used in the direct forecasting framework. In this work, we focus on probabilistic prediction within the direct framework, exploiting SCADA data from the Penmanshiel wind farm and wind forecasts from the Copernicus project. The objective is to develop a parametric approach and compare its performances to that of QRFs, a machine learning nonparametric method.

In order to study the statistical distribution of the power given the wind speed forecast, power curve data were divided into bins of 2 $\mathrm{m\,s^{-1}}$ along the wind speed forecast axis, ranging from 0 to 18 $\mathrm{m\,s^{-1}}$. The resulting distributions in Fig. 1 display significant variations with wind speed: the conditional distribution of wind power appears right-skewed at low speeds, "U"-shaped at intermediate speeds, and left-skewed at high speeds. This heterogeneity highlights the complexity, non-Gaussian nature, heteroscedasticity, and asymmetry of the power distribution, emphasizing the inadequacy of Gaussian models for these data.

Given this complexity, one could argue the inadequacy of parametric approaches and the need for highly flexible non parametric models. We will somehow question this prejudice by showing that all the features of the wind power distribution can be captured by a parametric model belonging to the category of Generalized Linear Models.

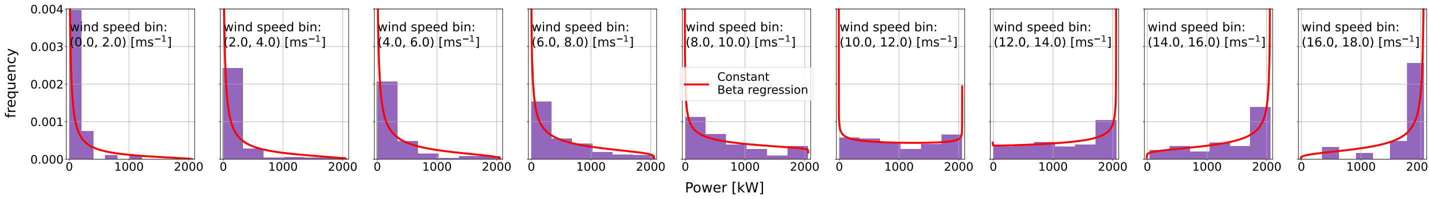

Figure 1: Distribution of measured wind power within specific wind speed forecast ranges for a 6-hour ahead forecast horizon. Notably, the distribution, right skewed for low wind speed, becomes U-shaped and eventually left skewed for high wind speed.

Method

This study compares two direct approaches for wind power forecasting: parametric Beta regression and non-parametric Quantile Regression Forests (QRFs).

Beta regression, a type of Generalized Linear Model (GLM), extends ordinary linear regression by using a link function $g(\cdot)$ to handle response variables with non-Normal error distributions. While logistic and double exponential links are common in wind power applications, they may not adequately capture the diverse shapes of wind power curves.

In contrast, following [CRDN24], a hybrid two-step approach is proposed:

Step 1: Preconditioner Estimation. Estimate a preconditioner $s(X)$, where X is typically the wind speed covariate. For example, using a natural spline $s(X;\alpha)$, fit parameters α via nonlinear least squares. This provides a flexible initial approximation of the power curve, accommodating its complex, nonlinear shape.

Step 2: Integration into a Beta GLM. Incorporate the preconditioner $s(X)$ into a Beta GLM by modifying the link function $g(\cdot)$ such that:

$$\mu = g^{-1}(\eta) = \frac{1}{1+\exp(-\eta - s(X))}.$$

Here, η is a linear combination of covariates with coefficients β_j, estimated during this step. This allows the model to refine the initial approximation while retaining the robust probabilistic framework provided by the Beta distribution.

On the other hand, Quantile Regression Forests (QRFs), an extension of random forests, can be used to model the wind power distribution as a function of wind speed forecasts[MR06]. QRFs operate by constructing an ensemble of trees and estimating the conditional distribution of the response variable based on weighted observed response variables.

The distinguishing feature of QRFs lies in their ability to estimate conditional quantiles, offering a non-parametric and accurate approach to infer the relationship between predictor variables and the full conditional distribution of the response variable. This makes QRFs suitable for applications where capturing the entire distributional range of outcomes is crucial, such as in wind power forecasting under varying environmental conditions.

In order to

The proposed method was validated using real measurement SCADA data and forecast data. For the measurement data, SCADA data from the first Senvion MM82 turbine at Penmanshiel wind farm in the UK was utilized [Plu23]. Forecast data were sourced from the Copernicus European project, specifically the UK Met Office 10m u and v wind components, spanning 8 forecast horizons (6, 12, 18, 24, 30, 36, 42, and 48 hours ahead). These forecasts were retrieved starting from midnight at the exact coordinates of the wind turbine (55°54'17.9"N, 2°17'30.7"W), with a horizontal resolution of 1° x 1°.

The analysis period covered from August 1, 2017, to July 1, 2021. The dataset was split into training and test sets sequentially: training data from August 1, 2017, to December 31, 2019, and test data from January 1, 2020, to July 1, 2021.

To ensure data quality, a conservative cleaning approach was employed, filtering out outliers by excluding periods of downtime and curtailment. This was achieved by verifying that the SCADA variable 'Lost Production to Downtime and Curtailment Total (kWh)' was equal to zero.

Initially, our analysis focused on the first forecasting horizon, which is 6 hours ahead, starting from midnight.

The findings demonstrate that the Beta regression model effectively captures the diverse shapes of the power distribution, accommodating the complexities introduced by varying wind speeds, see Fig. 2a). Conversely, QRF also provided valid probabilistic forecasts, but it exhibited higher variance, see Fig. 2b). This might be due to the need for meticulous hyperparameter tuning. Despite these differences, both approaches yielded meaningful and comparable probabilistic forecasts, with Beta Regression benefiting from greater interpretability.

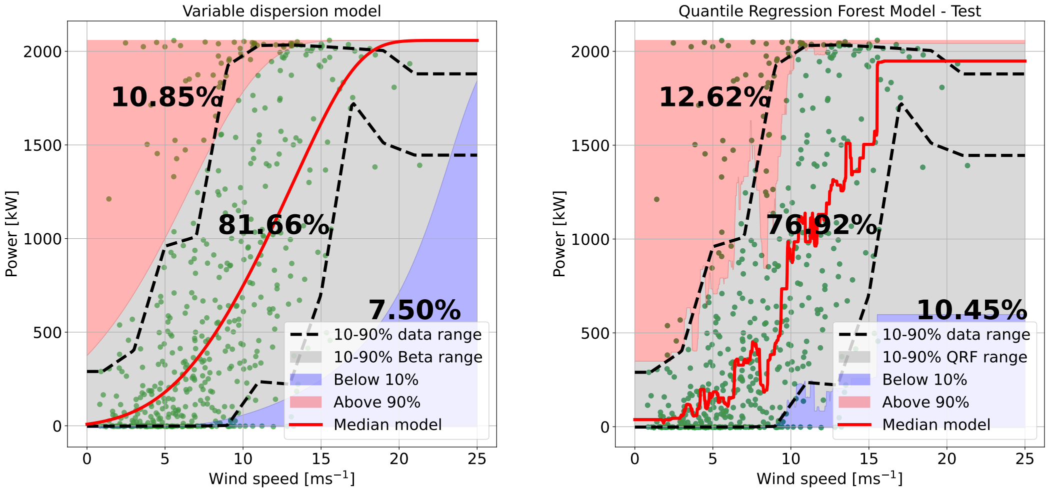

(a) Variable dispersion Beta model

(b) Quantile regression forest model

Figure 2: Evaluation of Beta regression models with variable dispersion (left) and Quantile Regression Forest (QRF) models (right) for test data over a 6-hour ahead forecast horizon. Both graphs display the median (red line) and prediction intervals at the 10th percentile (purple-shaded area) and the 90th percentile (light red-shaded area). The grey area indicates where 80% of the data points should fall according to the model. The bold black numbers show the percentages of test data within these zones, demonstrating that the models produce a reasonably adequate description of the wind power distribution for sequential test data. Despite careful hyperparameter tuning via cross-validation using the Python Optuna toolbox, some overfitting is evident in the QRF model.

Conclusions

Beta regression with natural spline preconditioning demonstrated fully capable to capture the diverse and non-Gaussian characteristics of wind power distributions. Also Quantile Regression Forests (QRFs) yielded valid probabilistic forecasts, but exhibited higher variance, necessitating meticulous hyperparameter tuning. In conclusion, both methods proved effective for wind power forecasting, with Beta regression somehow superior in terms of interpretability and consistency.

References

[CRDN24] Marco Capelletti, Davide M Raimondo, and Giuseppe De Nicolao. Wind power curve modelling: A probabilistic beta regression approach. *Renewable Energy*, page 119970, 2024.

[MR06] Nicolai Meinshausen and Greg Ridgeway. Quantile regression forests. *Journal of machine learning research*, 7(6), 2006.

[Plu23] Charlie Plumley. Penmanshiel wind farm data, August 2023.

Humans-in-the-Building: Getting Rid of Thermostats in Comfort-Based Energy Management Control Systems[$\star$]

[$\star$] This work has been published in *IEEE Control Syst. Lett.*, vol. 8, pp. 1493-1498, 2024,
DOI: 10.1109/LCSYS.2024.3412650.

Jiali Wang, Yang Tang, and Luca Schenato

I. Introduction. The Energy Management Control Systems present in today's Building Automation Systems (BASs) typically utilize thermostats, potentially integrated with humidity, CO_2, and occupancy sensors, to regulate internal temperature within a predefined range to optimize energy consumption. However, direct feedback from occupants regarding their personal comfort is rarely considered. Thermal comfort is internationally defined as a psychological state of satisfaction with the surrounding temperature. Some researchers view it as an environmental attribute linked to physical climate and the control of heating, ventilation, and air conditioning (HVAC) control, while others see it as a subjective sensation, with no perfect conditions to satisfy everyone. Even under ideal temperatures, less than 70% of people may feel comfortable. Thus, thermal comfort is influenced by indoor and outdoor temperatures, occupant expectations, and individual tolerance levels.

Understanding the diverse thermal comfort perceptions of occupants amidst fluctuating room temperatures is crucial for comprehending their physiological responses and assessing how individual differences influence the determination of optimal room temperature. The overall comfort/discomfort of occupants is directly determined by their perceptions of negative and positive thermal sensations. Discomfort, akin to a "complaint," arises when occupants experience deviations from their ideal room temperature levels. Categorizing individuals' temperature responses as personal (dis)comfort signals facilitates the derivation of individually customized optimal indoor temperatures, enhancing overall comfort.

Integrating residents' comfort perceptions into the energy management process is crucial for enhancing energy management systems (EMS) and promoting residents' well-being. This involves ensuring occupant comfort while reducing energy consumption, a balance that poses a significant challenge. Therefore, this work proposes a new thermal control paradigm, referred to as "humans-in-the-buildings", where individuals can directly signal their discomfort to the energy management system which thus adjusts the HVAC control inputs accordingly.

Currently, research on BASs primarily focuses on how to reduce the energy consumption of buildings, without fully taking into account the thermal comfort of each occupant in real-time. Although some works have considered user thermal comfort optimization, they are either open-loop control approaches or rely on predictive models, without taking into account the actual user feedback. In contrast, our approach centers on individual comfort, recognizing occupant diversity, and aims to minimize energy consumption significantly while incorporating real-time occupant feedback.

The contribution is twofold. First, compared with [1] where occupants' comfort is estimated based on physiological signals obtained by devices like smart wristbands and therefore the occupants have a passive role, in this work we establish a thermal comfort model where occupants actively generate discomfort signals according to individual preferences which are then used by the EMS to achieve optimal indoor temperature. The second contribution is that, based on real-time occupants' comfort signals, we propose a novel method to determine the optimal indoor temperature range, aiming at minimizing discomfort for the various occupants while reducing building energy consumption as much as possible. This is an innovative approach as it does not require to know the exact comfort profile of the occupants which is difficult to capture and might even change over time.

II. User Comfort Modeling and Signaling. We model a building as M adjacent rooms, each with N occupants and one HVAC system. Each occupant i, holds a temperature sensation signal remote controller η_i which is equipped with three buttons representing cold ($\eta(t) = +1$), normal ($\eta(t) = 0$), and hot ($\eta(t) = -1$) signals, respectively. Each occupant can be periodically asked by the EMS to select their current sensation or can directly enter it as needed. We assume that the (dis)comfort level of each occupant can be modeled by a function, referred as signed discomfort function $\widetilde{f}_i(T_r) : \mathbb{R} \to (-1, 1)$. The signed discomfort function is continuous and strictly monotonically decreasing with $\widetilde{f}_i(-\infty) = -\widetilde{f}_i(+\infty) = 1$. The temperature T_i^* such that $\widetilde{f}_i(T_i^*) = 0$, is defined as the ideal comfort temperature of the occupant i. The absolute discomfort function $f_i(T_r)$

J. Wang is with the Key Laboratory of Smart Manufacturing in Energy Chemical Process, Ministry of Education, East China University of Science and Technology, Shanghai 200237, China, and also with the Department of Information Engineering, University of Padova, 35131 Padova, Italy (e-mail: jialiwang@mail.ecust.edu.cn).

Y. Tang is with the Key Laboratory of Smart Manufacturing in Energy Chemical Process, Ministry of Education, East China University of Science and Technology, Shanghai 200237, China (e-mail: yangtang@ecust.edu.cn).

L. Schenato is with the Department of Information Engineering, University of Padova, 35131 Padova, Italy (email: schenato@dei.unipd.it).

is defined as $f_i(T_r) := |\widetilde{f}_i(T_r)|$. We define the thermal comfort tolerance of each occupant as Δ_i. As a result, the signaling of each occupant is:

$$\eta_i(T_r, \Delta_i) = \begin{cases} +1, & T_r < T_i^* - \Delta_i, \\ 0, & T_i^* - \Delta_i \le T_r \le T_i^* + \Delta_i, \\ -1, & T_r > T_i^* + \Delta_i. \end{cases}$$

To achieve optimal indoor temperature, it's crucial to determine the total number of occupants in discomfort at any room temperature: $g(T_r, \{\Delta_i\}) = \sum_i^N |\eta_i(T_r, \Delta_i)| \in \mathbb{N}$, where $\{\Delta_i\}$ represents all occupants' thermal comfort tolerances. Ideally, the EMS should adjust the temperature to minimize the number of uncomfortable occupants: $\Upsilon^* := \arg\min_{T_r} g(T_r, \{\Delta_i\})$. However, $g(T_r, \{\Delta_i\})$ might not be quasi-convex, Υ^* might not be compact, and guaranteeing comfort for all occupants may be impossible. Thus, the EMS needs to learn each user's comfort profile to estimate Υ^*, which is challenging and raises privacy concerns. To address this, we consider the sum of all occupants' discomfort signals: $h(T_r, \{\Delta_i\}) := \sum_{i=1}^N \eta_i(T_r, \Delta_i) \in \mathbb{Z}$.

The total discomfort signal sum h is a monotonically decreasing stepwise function where $h(-\infty, \{\Delta_i\}) = -h(+\infty, \{\Delta_i\}) = N$. The set of optimal temperature with respect to the function $h(\cdot)$ is $\Upsilon := [T_{\min}, T_{\max}] = \{T_r : h(T_r, \{\Delta_i\}) = 0\}$, where $T_{\min}$ and $T_{\max}$ represent the minimum and maximum optimal indoor temperatures, respectively. It can be noticed that in some scenarios in which the $\{\Delta_i\}$ are larger, the two sets Υ and Υ^* coincide and it is possible to satisfy all occupants, i.e. $g(\Upsilon^*, \{\Delta_i\}) = 0$. Then, $\Upsilon = \Upsilon^*$ and $g(\Upsilon^*, \{\Delta_i\}) = 0$ if and only if $\max_i\{T_i^* - \Delta_i\} < \min_j\{T_j^* + \Delta_j\}$. Moreover, if the previous condition is satisfied, we have $T_{\min} = \max_i\{T_i^* - \Delta_i\}$ and $T_{\max} = \min_j\{T_j^* + \Delta_j\}$.

III. Comfort-Based Control Design. To minimize energy consumption while maintaining optimal thermal comfort levels, we need to address the following optimization problem:

$$\begin{aligned} T_r^* = \arg\min_{T_r} P(T_{\text{ext}}, T_r) &= \arg\min_{T_r} \mu(|T_{\text{ext}} - T_r|), \\ \text{s.t.} \quad h(T_r, \{\Delta_i\}) &= 0, \end{aligned}$$

where P represents the power consumption of the EMS, and $\mu(x)$ is monotonically increasing and $\mu(0) = 0$. Then, the optimal indoor temperature T_r^* is given by

$$T_r^* = \Psi(T_{\text{ext}}, \{\Delta_i\}) = \begin{cases} T_{\min}, & T_{\text{ext}} < T_{\min}, \\ T_{\text{ext}}, & T_{\min} < T_{\text{ext}} < T_{\max}, \\ T_{\max}, & T_{\text{ext}} > T_{\max}. \end{cases}$$

To implement the indoor temperature control policy, the EMS would typically need $T_{\min}$, $T_{\max}$, and measurements of room temperature T_r and external temperature T_{ext}, along with the occupants' discomfort profiles. However, the EMS can bypass this by using the real-time cumulative discomfort signal $y(t) := h(T_r(t), \{\Delta_i\})$ as an error signal. The EMS heats the room if $y(t) > 0$ and cools it if $y(t) < 0$, aiming for $T_r(t) \to \Upsilon$. When $y(t) = 0$, $T_r(t)$ is within Υ, and no control is needed as thermodynamics will align room and external temperatures naturally, $T_r(t) - T_{\text{ext}}(t) \to 0$. Thus, the optimal energy policy can be achieved using real-time feedback without needing temperature sensors.

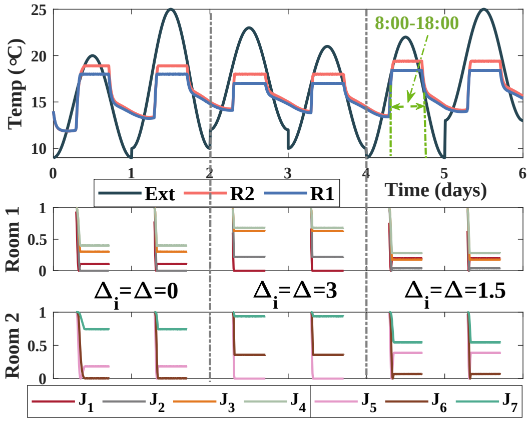

Fig. 1. Indoor Temperature and User Discomfort Over Six Days with HVAC Control.

If the EMS is able to implement the previous indoor temperature control policy, then it is possible to consider the absolute value $\widehat{f}_i$ of the closed-loop discomfort experienced by user i as $\widehat{f}_i(T_{\text{ext}}, \{\Delta_i\}) := f_i(T_r^*) = f_i(\Psi(T_{\text{ext}}, \{\Delta_i\}))$. It is reasonable to consider the worst case among all possible external temperatures via the following "cost":

$$\begin{aligned} J_i(\{\Delta_i\}) &:= \max_{T_{\text{ext}}} \widehat{f}_i(T_{\text{ext}}, \{\Delta_i\}) = \max_{T_{\text{ext}}} f_i(\Psi(T_{\text{ext}}, \{\Delta_i\})) \\ &= \max\{f_i(T_{\min}), f_i(T_{\max})\}. \end{aligned}$$

This performance index is important since it allows to evaluate the impact of the set of thermal comfort tolerances $\{\Delta_i\}$ selected by the users. Ideally, $\{\Delta_i\}$ should be selected to keep J_i as small as possible for all users.

IV. Simulations. Finally, the effectiveness of the proposed comfort-based control is substantiated through simulations conducted on multiple adjacent rooms established building dynamics modeling. We simulated the indoor temperatures of two adjacent rooms in a building over six working days, with occupants present from 8:00-18:00. The HVAC system operated only during this time if occupants signaled discomfort; otherwise, indoor temperatures varied with outdoor fluctuations, as shown in Fig. 1. The outdoor temperature ranged between 9° and 25°, with daily minima and maxima randomly generated. For the 4 users in Room 1 and 3 users in Room 2, we categorized the days into three comfort tolerance levels: $\Delta = 0, 3, 1.5$. It was observed that at $\Delta = 1.5$, overall discomfort was minimized, while at $\Delta = 0$ or $\Delta = 3$, discomfort differences among users were larger. Rapid discomfort changes occurred due to low morning temperatures, and room temperatures varied in response to occupant discomfort signals.

References

[1] S. Jung, J. Jeoung, and T. Hong, "Occupant-centered real-time control of indoor temperature using deep learning algorithms," *Build. Environ.*, vol. 208, p. 108633, 2022.

Optimal scheduling and real-time control of a microgrid with an electrolyzer and a fuel cell systems using a reference governor approach

Yassine Ennassiri [a], Giulio Ferro [a] Loredana Magistri [b], Michela Robba [a]

a) Department of Informatics, Bioengineering, Robotics and Systems Engineering, University of Genoa, Genoa 16145, Italy

b) Thermochemical Power Group (TPG), DIME, University of Genoa, Via Montallegro 1, 16145 Genoa, Italy

This work proposes a novel approach for the optimal scheduling and control of a microgrid with an electrolyzer and fuel cell systems, both of proton exchange membrane (PEM) technology [1]. It is based on a hierarchical procedure constituted of two levels of optimization: a higher level based on an economic optimization for the optimal scheduling of different components of the microgrid and a lower level for the real-time control of the hydrogen systems: PEM electrolyzer (PEMEZ) and PEM fuel cell (PEMFC) [2]. The flexible operation imposed by the higher level leads to a violation of the limits designed by the manufacturer of the hydrogen components, specifically when switching from one power level to another. The current proportional-integral (PI) controllers integrated into those systems cannot handle this issue, which provokes a premature ageing phenomenon of the materials and leads to poor performance. In the present paper, at the lower level, a reference governor (RG) real-time control approach has been added to the PI controller to ensure the respect of the operating limits and guarantee better performances (Figure 1). The focus has been given to the stack's temperature ($T^{FC}_{st,t}$ / $T^{EZ}_{st,t}$) in both the electrolyzer and fuel cell systems as the control objective because of its direct influence on the material's durability and, by extension, on efficiency [3][4]. The bi-level optimization and control architecture has been applied and validated through simulations using data from a real-world case study, specifically the Savona Campus Smart Polygeneration Microgrid [5] (Figure 2). The results showed a significant reduction in the overshoots of the stack's temperature compared to the PI controller.

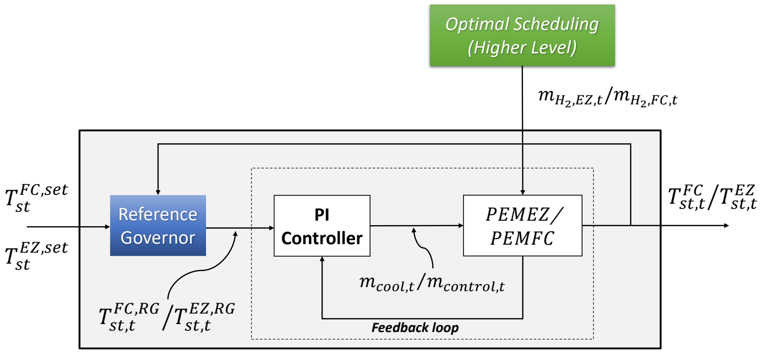

Figure 1 The RG scheme

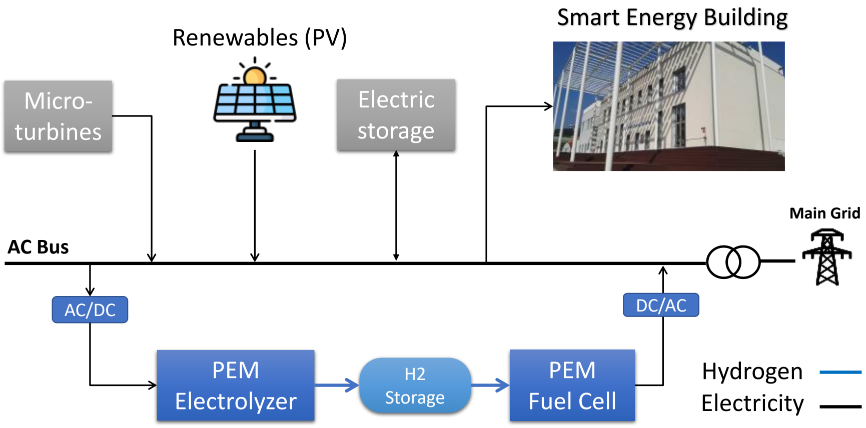

Figure 2 The Microgrid case study

In summary, the main contribution of this work can be summarized as follows:

- Introducing a bi-level optimization architecture that optimizes microgrid component scheduling while ensuring system stability in the face of economic variability, addressing a critical challenge in microgrid management.
- Developing a temperature control technique, seamlessly integrated with the widely used Proportional-Integral (PI) controller using the Reference Governor (RG) approach. This technique enhances temperature control within hydrogen systems, maintaining them within manufacturer-specified limits, and can be easily implemented alongside existing PI controllers for practical applications.
- Demonstrating the effectiveness of this methodology through a practical case study within the Savona Campus microgrid's. This application highlights the real-world value of our contributions by improving transient temperature control, a crucial aspect often challenging conventional PI controllers.

REFERENCES

[1] R. Zahedi, M. Moeini-Aghtaie, Operational strategy optimization of a hybrid green power system based on fuzzy logic controller with considering for optimal sizing and analysis of different priorities for energy storage, Sustainable Energy, Grids and Networks. 32 (2022) 100809.
[2] Y. Han, G. Zhang, Q. Li, Z. You, W. Chen, H. Liu, Hierarchical energy management for PV/hydrogen/battery island DC microgrid, International Journal of Hydrogen Energy. 44 (2019) 5507–5516.
[3] Y. Pu, Q. Li, W. Chen, H. Liu, Hierarchical energy management control for islanding DC microgrid with electric-hydrogen hybrid storage system, International Journal of Hydrogen Energy. 44 (2019) 5153–5161.
[4] Y. Zhang, W. Wei, Decentralized coordination control of PV generators, storage battery, hydrogen production unit and fuel cell in islanded DC microgrid, International Journal of Hydrogen Energy. 45 (2020) 8243–8256.
[5] M. Caliano, F. Delfino, M. Di Somma, G. Ferro, G. Graditi, L. Parodi, M. Robba, M. Rossi, An Energy Management System for microgrids including costs, exergy, and stress indexes, Sustainable Energy, Grids and Networks. 32 (2022) 100915.

On the Kite-Platform Interactions in Offshore Airborne Wind Energy Systems: Frequency Analysis and Control Approach

Sofia Trombini, Lorenzo Fagiano

I. INTRODUCTION

Airborne Wind Energy (AWE) systems are innovative devices that harness high-altitude winds to generate electricity [1]. These systems consist of tethered aircraft or kites that can fly at altitudes exceeding 300 meters, benefiting from more intense and constant winds. Due to their lightweight and simple structure, they are strong candidates to play a crucial role in the transition to sustainable energy, complementing established renewable technologies.

Over the past 20 years, AWE research has focused on inland implementations to ensure robustness and reliability throughout all operational phases. However, future deployment targets include deep offshore applications, offering benefits like lighter floating platforms compared to wind turbines, stronger winds at lower altitudes, and ample space for AWE farms. Currently, the literature on offshore AWE is limited to articles [2] and [3], along with the experience of the previous company Makany Power [4], the only one that attempted to test AWE systems offshore. The research presented here aims to expand our knowledge of the offshore application. This involves not only developing a model for the components but also studying the interaction between the kite and the platform, identifying potential challenges, and proposing suitable control solutions.

II. SYSTEM MODEL

The system comprises two main components: the AWE system and the platform. The AWE system under consideration is a pumping-flexible system consisting of a 360 m^2 soft kite and a single tether. On the other hand, the platform is a 10-meter-deep spar-buoy (i.e., a cylinder) connected to the seabed via four symmetric catenary mooring lines. We employ a specific mathematical model for each component, resulting in the definition of the equations of motion of the entire system. A point-mass model is chosen for the AWE system [5], where the kite's position is described using three variables: the angle of elevation θ, the angle of orientation ϕ and the distance between the kite and the origin of the fixed reference frame r. Newton's equations of motion for the three variables are then represented as $\ddot{\theta}(t) = \frac{F_\theta(t)}{m(t)\,r(t)}$, $\ddot{\phi}(t) = \frac{F_\phi(t)}{m(t)\,r(t)\,\sin(\theta(t))}$, $\ddot{r}(t) = \frac{F_r(t)}{m(t)}$, where F_θ, F_ϕ and F_r encompass all the forces acting on the kite, including the aerodynamic force, the apparent force, the gravitational force, and the tether traction force. The tether traction force specifically acts as a simple elastic force, as the tether is treated as a spring. In terms of the flight control approach, we have chosen the strategy outlined in [6]. The algorithm involves selecting two user-defined target points, P_+ and P_-, in the (θ,ϕ) plane. These points are used to calculate a reference course for the kite at each time step $k \in \mathbb{Z}$ of the digital control loop. At any given time, only one target point is active, and the kite should be directed towards that point. With the kite's position and the active target point, a lower controller determines the steering input necessary for the kite to follow the correct trajectory.

The platform model follows the assumptions of linear potential flow theory: the platform and its mooring are modelled as a mass-spring-damper system with the addition of specific hydrodynamic forces and moments. This results in the following equation of motion $M\ddot{v}(t) = F^h(t) + F^r(t) + F^{exc}(t) + F^m(t) + F^t(t)$ where $v(t) = [x_P(t)\ y_P(t)\ z_P(t)\ \omega_{x_P}(t)\ \omega_{y_P}(t)\ \omega_{z_P}(t)]^T$ are the displacements (i.e., surge, sway and heave) and rotations with respect to the platform centre of gravity, $M \in \mathbb{R}^{6\times6}$ is the mass-inertia matrix, vector $F^h \in \mathbb{R}^6$ contains the hydrostatic restoring force and moment, F^r the radiation force and moment, F^{exc} the wave excitation force and moment, F^m the mooring force and moment and F^t the tether traction force and moment applied on the platform. NEMOH software [7] and a system identification procedure are used to determine the hydrodynamic parameters. Finally combining the two dynamic models, we can represent the entire system as $\dot{x(t)} = f(x(t), F^{exc}(t), \vec{W}(t))$ where $x(t) = [\theta(t)\ \phi(t)\ r(t)\ \dot{\theta}(t)\ \dot{\phi}(t)\ \dot{r}(t)\ x_P(t)\ y_P(t)\ z_P(t)\ \omega_{x_P}(t)\ \omega_{y_P}(t)\ \omega_{z_P}(t)\ \dot{x_P}(t)\ \dot{y_P}(t)\ \dot{z_P}(t)\ \dot{\omega_{x_P}}(t)\ \dot{\omega_{y_P}}(t)\ \dot{\omega_{z_P}}(t)]^T$ and $F^{exc}(t), \vec{W}(t)$ are the exogenous inputs due to the wave and the wind.

III. ANALYSIS

As the two subsystems of offshore AWE are connected by the tether, the traction force is the main point of contact between the components and is the focus of our analysis. Initially, we examined how the wave impacts the cable force and the kite motion, emphasizing the distinctions between onshore and offshore systems with different types of waves. We specifically tested two wave intensities modeled with

This work has been funded by the European Union–Next Generation EU in the context of the project PNRR M4C2, Investimento 1.3 DD. 341 del 15 marzo 2022 – NEST – Network 4 Energy Sustainable Transition – Spoke 2 - PE00000021 - D43C22003090001, by the Italian Ministry of University and Research under grants "P2022927H7 - DeepAirborne – Advanced Modeling, Control and Design Optimization Methods for Deep Offshore Airborne Wind Energy", and by Fondazione Cariplo, Italy under grant n. 2022-2005, project "NextWind - Advanced control solutions for large scale Airborne Wind Energy Systems".

Sofia Trombini and Lorenzo Fagiano are with the Dipartimento di Elettronica, Informazione e Bioingegneria (DEIB), Politecnico di Milano. E-mail addresses: sofia.trombini@polimi.it; lorenzo.fagiano@polimi.it.

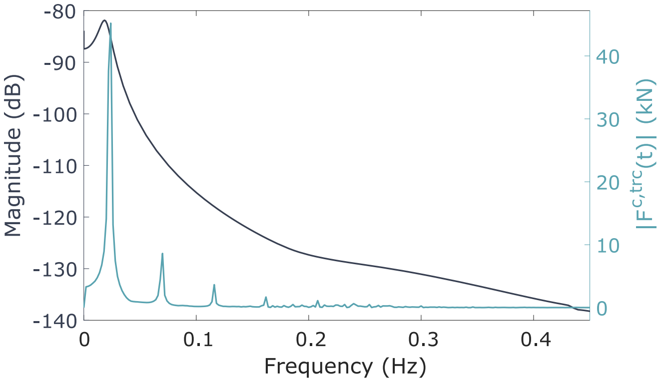

Fig. 1: Bode diagram of the frequency response of y_P w.r.t the traction force y-component, and spectrum of the latter for wave A and tether length L = 900 m.

the JONSWAP spectrum: the first wave (wave A) had a significant height of 0.5 m and a peak wave period of 3.7 s, while the second wave (wave B) was more intense with a height of 2 m and a period of 7.5 s. The simulations revealed that as the wave strength increases, so do the oscillations of the tether force and the flight trajectory. However, the system controllability and operability are still ensured for the presented values.

In our analysis, we next looked at the platform resonances to see if the main spectral components of tether force in different directions closely match the platform resonance peaks. We found that they may fall within the same range. Specifically, when we examine Figure 1, we can see that in the y direction, the resonance peak is at $0.0185 Hz$, which corresponds to the principal component of the tether force. This causes increased motion of the platform and potential damage to the structure. Further investigation revealed that, with the chosen control approach, the overlap depends on the length of the tether, as the flight frequency (and consequently the traction force frequency) decreases with increasing length.

IV. Control approach

Given the considerations of the previous section, we propose a control approach to avoid excitation of the platform resonances. The idea is to modify the flight control approach by adjusting the length of the flown figure-eight trajectories by suitably modifying the target points locations, P_- and P_+, to indirectly regulate the frequency of the tether force oscillations. To initiate this, we determine a desired path frequency f^*_{traj} away from the platform resonance peaks. Using this value and the average kite speed $\bar{v_k}$, we calculate the trajectory length as $L^*_{traj} = \bar{v_k}/f^*_{traj}$. Simultaneously, we can estimate the trajectory length geometrically as $L_{traj} = 2(\Delta\theta + \Delta\phi)L$. By further elaborating on the concept of $\Delta\theta$ and $\Delta\phi$ with other computations on the kite eight-path, we can link the definition of L_{traj} with the target points. Finally, by combining the equations for L^*_{traj} and L_{traj}, we can determine the desired target points at each step. In simulation, we tested this simple algorithm and found the control approach to be effective. Figure 2 demonstrates how the platform sway motion is over 50% smaller compared to the platform motion with the original control approach.

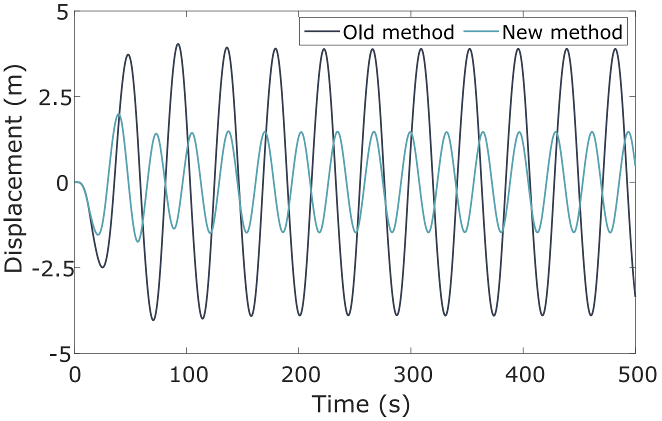

Fig. 2: Platform sway motion in wave A scenario, using L = 1100 m.

V. Conclusions

The analysis and simulations show that the intensity of the waves and the resulting platform motion affect flight paths, but the AWE system can still operate. However, there is a possibility of significant platform movements, undesired wing motion, increased loads and damage to floating components due to potential overlap between tether frequencies and spar resonances. In order to prevent this event from happening, we demonstrated how a simple change in the control algorithm can effectively keep us away from resonances and reduce the motion of the floating spar. Future research will focus on the interaction between the kite and platform in all operational phases of the AWE system, as well as new control approaches to optimize the system's performance. Eventually, we will work on designing a custom platform for offshore AWE.

References

[1] L. Fagiano, M. Quack, F. Bauer, L. Carnel, and E. Oland, "Autonomous airborne wind energy systems: accomplishments and challenges," *Annual Review of Control, Robotics, and Autonomous Systems*, vol. 5, pp. 603–631, 2022.

[2] A. Cherubini, R. Vertechy, and M. Fontana, "Simplified model of offshore airborne wind energy converters," *Renewable Energy*, vol. 88, pp. 465–473, 2016.

[3] A. Cherubini, G. Moretti, and M. Fontana, *Dynamic Modeling of Floating Offshore Airborne Wind Energy Converters*, 04 2018, pp. 137–163.

[4] M. Power, "Harnessing wind energy with kites to create renewable electricity." [Online]. Available: https://x.company/projects/makani/

[5] M. Canale, L. Fagiano, and M. Milanese, "High altitude wind energy generation using controlled power kites," *IEEE Transactions on Control Systems Technology*, vol. 18, no. 2, pp. 279–293, 2010.

[6] L. Fagiano, A. U. Zgraggen, M. Morari, and M. Khammash, "Automatic crosswind flight of tethered wings for airborne wind energy: Modeling, control design, and experimental results," *IEEE Transactions on Control Systems Technology*, vol. 22, no. 4, pp. 1433–1447, 2014.

[7] A. Babarit and G. Delhommeau, "Theoretical and numerical aspects of the open source BEM solver NEMOH," in *11th European Wave and Tidal Energy Conference (EWTEC2015)*, Nantes, France, Sep. 2015.

A Game-Theoretical Control Framework for Transactive Energy Trading in Energy Communities

Nicola Mignoni, Juan Martinez-Piazuelo, Raffaele Carli,
Carlos Ocampo-Martinez, Nicanor Quijano, and Mariagrazia Dotoli

I. INTRODUCTION

As the advent of distributed energy resource technologies has increased the independence of grid actors from central power providers, the problem of efficiently controlling the overall operational apparatus has not yet thoroughly been solved [1]. The problem of distributed Generalized Nash Equilibrium (GNE) computation in multi-agent systems has recently received significant attention from game theoretical perspectives [2]. This abstract summarizes [3], which extends [4], where the community members have private cost functions coupled with each other through the monetary price at which each member sells its energy. As the main technical contribution, we provide sufficient conditions on the private cost and energy pricing functions to ensure the strong monotonicity of the overall pseudo-gradient mapping, which is in turn a sufficient condition to guarantee the convergence of the considered ADMM-type algorithm.

II. PROBLEM STATEMENT

Consider an energy community with $N \in \mathbb{Z}_{\geq 2}$ agents indexed by the set $\mathcal{A} = \{1, 2, \ldots, N\}$. The interaction and communication among agents is characterized by the connected and undirected graph $\mathcal{G} = (\mathcal{A}, \mathcal{E})$ with no self-loops. We denote $\mathcal{A}_i = \{j \in \mathcal{A} \colon (i,j) \in \mathcal{E}\}$ as the set of neighbors of agent i, and we let $N_i = |\mathcal{A}_i|$. Every agent $i \in \mathcal{A}$ is allowed to trade energy with its neighbors over $T \in \mathbb{Z}_{\geq 1}$ with t_k being a generic time slot and $k \in \mathcal{T} = \{1, 2, \ldots, T\}$. For all $(i,j,t) \in \mathcal{A} \times \mathcal{A}_i \times \mathcal{T}$, let $\hat{x}_{ijt} \in \mathbb{R}_{\geq 0}$ denote the energy that agent i buys from agent j at time t, let $\check{x}_{ijt} \in \mathbb{R}_{\geq 0}$ denote the energy that agent i sells to agent j at time t, and let $p_{ijt} \in \mathbb{R}_{\geq 0}$ denote the monetary price at which agent i sells its energy to agent j at time t. For a feasible energy trade, we need that $\hat{x}_{ijt} = \check{x}_{jit}$ and $\check{x}_{ijt} = \hat{x}_{jit}$. Let z be a placeholder notation for either $\hat{x}$, $\check{x}$, or p, and define the vectorization given by $\mathbf{z}_{ij} = \operatorname{col}(z_{ijt})_{t \in \mathcal{T}}$, $\mathbf{z}_i = \operatorname{col}(\mathbf{z}_{ij})_{j \in \mathcal{A}_i}$, $\mathbf{z} = \operatorname{col}(\mathbf{z}_i)_{i \in \mathcal{A}}$, and $\mathbf{z}_{-i} = \operatorname{col}(\mathbf{z}_{ji})_{j \in \mathcal{A}_i}$, where $n_i = TN_i$ and $n = \sum_{i \in \mathcal{A}} n_i$. Every agent $i \in \mathcal{A}$ is thus responsible for computing its own decision $(\hat{\mathbf{x}}_i, \check{\mathbf{x}}_i, \mathbf{p}_i)$ subject to the constraints given by $(\hat{\mathbf{x}}_i, \check{\mathbf{x}}_i) \in \mathcal{X}_i$, defining the local constraint set of agent i, $\hat{\mathbf{x}}_i = \check{\mathbf{x}}_{-i}$, and $\check{\mathbf{x}}_i = \hat{\mathbf{x}}_{-i}$, $\mathbf{p}_i \in \mathbb{R}^{n_i}_{\geq 0}$, imposing an agreement between neighbouring agents regarding their energy trades. Therefore, the decision of agent i is feasible only if $(\hat{\mathbf{x}}_i, \check{\mathbf{x}}_i, \mathbf{p}_i) \in \Omega_i(\hat{\mathbf{x}}_{-i}, \check{\mathbf{x}}_{-i}) \times \mathbb{R}^{n_i}_{\geq 0}$, with $\Omega_i(\hat{\mathbf{x}}_{-i}, \check{\mathbf{x}}_{-i}) = \{(\hat{\mathbf{x}}_i, \check{\mathbf{x}}_i) \in \mathcal{X}_i \colon \hat{\mathbf{x}}_i = \check{\mathbf{x}}_{-i}, \check{\mathbf{x}}_i = \hat{\mathbf{x}}_{-i}\}$. Consequently, the set of feasible collective decisions for the entire energy community is given by $\Omega \times \mathbb{R}^n_{\geq 0}$, where $\Omega = \left\{(\hat{\mathbf{x}}, \check{\mathbf{x}}) \in \prod_{i \in \mathcal{A}} \mathcal{X}_i \colon \hat{\mathbf{x}} = \mathbf{B}\check{\mathbf{x}}\right\}$. Here, $\mathbf{B} = \operatorname{col}(\mathbf{B}_i)_{i \in \mathcal{A}} \in \mathbb{B}^{n \times n}$, and $\mathbf{B}_i \in \mathbb{B}^{n_i \times n}$ is the (unique) matrix that satisfies $\mathbf{z}_{-i} = \mathbf{B}_i \mathbf{z}$, for any placeholder $z \in \{\hat{x}, \check{x}, p\}$ and all $i \in \mathcal{A}$. Based on the considered framework, every agent $i \in \mathcal{A}$ computes its own decision $(\hat{\mathbf{x}}_i, \check{\mathbf{x}}_i, \mathbf{p}_i)$ to simultaneously solve the optimization problems (OPs) given by

$$\min_{\hat{\mathbf{x}}_i, \check{\mathbf{x}}_i} f_i(\hat{\mathbf{x}}_i, \check{\mathbf{x}}_i, \mathbf{p}_i, \mathbf{p}_{-i}) \ \text{ s.t. } (\hat{\mathbf{x}}_i, \check{\mathbf{x}}_i) \in \Omega_i(\hat{\mathbf{x}}_{-i}, \check{\mathbf{x}}_{-i}) \tag{1a}$$

$$\min_{\mathbf{p}_i} \frac{\rho_i}{2} \left\| \mathbf{p}_i - \mathbf{g}_i(\hat{\mathbf{x}}_{-i}) \right\|^2 \ \text{ s.t. } \mathbf{p}_i \in \mathbb{R}^{n_i}. \tag{1b}$$

Here, $f_i \colon \mathbb{R}^{4n_i}_{\geq 0} \to \mathbb{R}$ is the local cost function of agent i, $\rho_i \in \mathbb{R}_{>0}$ is a weighting parameter, and $\mathbf{g}_i \colon \mathbb{R}^{n_i}_{\geq 0} \to \mathbb{R}^{n_i}_{\geq 0}$ is the (non-negative) local pricing function of agent i. Hence, solving the OP in (1a) yields the energy transactions that agent i should execute to minimize its operational costs $f_i(\cdot,\cdot,\cdot,\cdot)$, whilst solving the OP in (1b) yields the energy-selling prices of agent i. The GNEP for the energy community is to compute a collective decision $(\hat{\mathbf{x}}^*, \check{\mathbf{x}}^*, \mathbf{p}^*) \in \Omega \times \mathbb{R}^n_{\geq 0}$ such that $f_i\left(\hat{\mathbf{x}}^*_i, \check{\mathbf{x}}^*_i, \mathbf{p}^*_i, \mathbf{p}^*_{-i}\right) \leq f_i\left(\hat{\mathbf{x}}_i, \check{\mathbf{x}}_i, \mathbf{p}^*_i, \mathbf{p}^*_{-i}\right)$ and $\left\| \mathbf{p}^*_i - \mathbf{g}_i\left(\hat{\mathbf{x}}^*_{-i}\right) \right\|^2 \leq \left\| \mathbf{p}_i - \mathbf{g}_i\left(\hat{\mathbf{x}}^*_{-i}\right) \right\|^2$, for all $(\hat{\mathbf{x}}_i, \check{\mathbf{x}}_i) \in \Omega_i\left(\hat{\mathbf{x}}^*_{-i}, \check{\mathbf{x}}^*_{-i}\right)$, all $\mathbf{p}_i \in \mathbb{R}^{n_i}_{\geq 0}$, and all $i \in \mathcal{A}$. Such a collective decision $(\hat{\mathbf{x}}^*, \check{\mathbf{x}}^*, \mathbf{p}^*)$ is termed as a GNE for the energy community. In this work, we focus on the so-called variational GNE (vGNE) [5].

For all $i \in \mathcal{A}$, the functions $f_i(\cdot,\cdot,\cdot,\cdot)$ and $\mathbf{g}_i(\cdot)$ are continuously differentiable, $f_i(\cdot,\cdot,\mathbf{p}_i,\mathbf{p}_{-i})$ is (jointly) convex for every fixed $(\mathbf{p}_i, \mathbf{p}_{-i})$, and $\nabla_{\hat{\mathbf{x}}_i} f_i(\hat{\mathbf{x}}_i, \check{\mathbf{x}}_i, \cdot, \cdot)$ and $\nabla_{\check{\mathbf{x}}_i} f_i(\hat{\mathbf{x}}_i, \check{\mathbf{x}}_i, \cdot, \cdot)$ are $\hat{L}_i$-Lipschitz continuous and $\check{L}_i$-Lipschitz continuous for every fixed $(\hat{\mathbf{x}}_i, \check{\mathbf{x}}_i)$, respectively. Moreover, the pseudo-gradient $\mathbf{q}(\hat{\mathbf{x}}, \check{\mathbf{x}}, \mathbf{p}) = \begin{bmatrix} \operatorname{col}\left(\nabla_{\hat{\mathbf{x}}_i} f_i(\hat{\mathbf{x}}_i, \check{\mathbf{x}}_i, \mathbf{p}_i, \mathbf{p}_{-i})\right)_{i \in \mathcal{A}} \\ \operatorname{col}\left(\nabla_{\check{\mathbf{x}}_i} f_i(\hat{\mathbf{x}}_i, \check{\mathbf{x}}_i, \mathbf{p}_i, \mathbf{p}_{-i})\right)_{i \in \mathcal{A}} \\ \operatorname{col}\left(\rho_i\left(\mathbf{p}_i - \mathbf{g}_i(\hat{\mathbf{x}}_{-i})\right)\right)_{i \in \mathcal{A}} \end{bmatrix} \in \mathbb{R}^{3n}$ is μ-strongly monotone. Finally, Ω is a closed convex set with a non-empty relative interior. It follows that there exists a unique vGNE for the considered energy community [5, Theorem 2.3.3]. Besides, from [6, Theorem 3.9] it holds that every vGNE is also a GNE (yet the converse is not true in general). Consequently, computing a vGNE is sufficient to solve the considered GNEP. We provide sufficient conditions on the functions $f_i(\cdot,\cdot,\cdot,\cdot)$ and $\mathbf{g}_i(\cdot)$ to guarantee the μ-strong monotonicity of the pseudo-gradient $\mathbf{q}(\cdot,\cdot,\cdot)$.

Proposition 1: Suppose that every agent $i \in \mathcal{A}$ has functions $f_i(\hat{\mathbf{x}}_i, \check{\mathbf{x}}_i, \mathbf{p}_i, \mathbf{p}_{-i}) = \psi_i(\hat{\mathbf{x}}_i, \check{\mathbf{x}}_i) + \mathbf{p}^\top_{-i}\hat{\mathbf{x}}_i - \mathbf{p}^\top_i \check{\mathbf{x}}_i$ and $\mathbf{g}_i(\hat{\mathbf{x}}_{-i}) = \mathbf{Q}_i \hat{\mathbf{x}}_{-i} + \mathbf{r}_i$, where $\psi_i \colon \mathbb{R}^{2n_i}_{\geq 0} \to \mathbb{R}$ is twice continuously differentiable and θ_i-strongly convex in all its arguments, $\mathbf{Q}_i \in \mathbb{R}^{n_i \times n_i}_{\geq 0}$, and $\mathbf{r}_i \in \mathbb{R}^{n_i}_{\geq 0}$. Moreover, denote

$\underline{\theta} = \min_{i\in\mathcal{A}} \theta_i$ and $\overline{\lambda} = \max_{i\in\mathcal{A}} \lambda_{\max}\left(\mathbf{Q}_i^\top \mathbf{Q}_i\right)$, and let $\rho_i = \rho \in \mathbb{R}_{>0}$, for all $i \in \mathcal{A}$. If there exists a $\mu \in (0, \rho)$ such that $\underline{\theta} - \mu \geq \frac{\max\left\{2,\, \rho^2\overline{\lambda}\right\}}{\rho-\mu}$ then the pseudo-gradient $\mathbf{q}(\cdot,\cdot,\cdot)$ is μ-strongly monotone.

III. THE PROPOSED APPROACH

We reformulate the OPs in (1) in an equivalent yet more convenient form. Let $y_{ijt} \in \mathbb{R}$ be an auxiliary variable to be computed by agent i, and define $\mathbf{y}_{ij}$, $\mathbf{y}_i$, $\mathbf{y}$, and $\mathbf{y}_{-i}$. By introducing constraint $\check{x}_{ijt} = y_{ijt}$, shared constraints can be equivalently stated as the four constraints: $\hat{\mathbf{x}}_i = \mathbf{y}_{-i}$, $\check{\mathbf{x}}_{-i} = \mathbf{y}_{-i}$, $\check{\mathbf{x}}_i = \mathbf{y}_i$, and $\hat{\mathbf{x}}_{-i} = \mathbf{y}_i$. As such, the decision of each agent $i \in \mathcal{A}$ now regards the tuple $(\hat{\mathbf{x}}_i, \check{\mathbf{x}}_i, \mathbf{y}_i, \mathbf{p}_i) \in \tilde{\Omega}_i(\mathbf{y}_{-i}) \times \Phi_i(\check{\mathbf{x}}_i) \times \mathbb{R}^{n_i}_{\geq 0}$, with $\tilde{\Omega}_i(\mathbf{y}_{-i}) = \{(\hat{\mathbf{x}}_i, \check{\mathbf{x}}_i) \in \mathcal{X}_i \colon \hat{\mathbf{x}}_i = \mathbf{y}_{-i}\}$ and $\Phi_i(\check{\mathbf{x}}_i) = \{\mathbf{y}_i \in \mathbb{R}^{n_i} \colon \mathbf{y}_i = \check{\mathbf{x}}_i\}$. On the other hand, the feasible set regarding such augmented decisions for the entire energy community is given by $\Psi \times \mathbb{R}^n_{\geq 0}$, where $\Psi = \left\{(\hat{\mathbf{x}}, \check{\mathbf{x}}, \mathbf{y}) \in \prod_{i\in\mathcal{A}} \mathcal{X}_i \times \mathbb{R}^n \colon \hat{\mathbf{x}} = \mathbf{B}\mathbf{y}, \check{\mathbf{x}} = \mathbf{y}\right\}$. Ψ is a closed convex set with non-empty relative interior. For every $i \in \mathcal{A}$, the OPs in (1) can then be equivalently redefined as

$$\min_{\hat{\mathbf{x}}_i, \check{\mathbf{x}}_i} f_i\left(\hat{\mathbf{x}}_i, \check{\mathbf{x}}_i, \mathbf{p}_i, \mathbf{p}_{-i}\right) \text{ s.t. } (\hat{\mathbf{x}}_i, \check{\mathbf{x}}_i) \in \tilde{\Omega}_i\left(\mathbf{y}_{-i}\right) \tag{2a}$$

$$\min_{\mathbf{y}_i, \mathbf{p}_i} \frac{\rho_i}{2} \left\|\mathbf{p}_i - \mathbf{g}_i\left(\hat{\mathbf{x}}_{-i}\right)\right\|^2 \text{ s.t. } (\mathbf{y}_i, \mathbf{p}_i) \in \Phi_i\left(\check{\mathbf{x}}_i\right) \times \mathbb{R}^{n_i} \tag{2b}$$

Note that in contrast to the OP in (1a), for a given agent i, the OP in (2a) is decoupled from the decisions $\hat{\mathbf{x}}_{-i}$ and $\check{\mathbf{x}}_{-i}$ of other agents, i.e., the inter-agent coupling in (2a) is only due to variables $\mathbf{p}_{-i}$ and $\mathbf{y}_{-i}$. Therefore, simultaneously solving (2a) for all i and under a fixed pair $(\mathbf{y}', \mathbf{p}')$ is equivalent to solving the OP given by $\min_{\hat{\mathbf{x}}, \check{\mathbf{x}}} \sum_{i\in\mathcal{A}} f_i\left(\hat{\mathbf{x}}_i, \check{\mathbf{x}}_i, \mathbf{p}'_i, \mathbf{p}'_{-i}\right)$ subject to $(\hat{\mathbf{x}}, \check{\mathbf{x}}) \in \prod_{i\in\mathcal{A}} \tilde{\Omega}_i\left(\mathbf{y}'_{-i}\right)$, which is separable over $\mathcal{A}$. Similarly, the inter-agent coupling in (2b) is only obtained through variable $\hat{\mathbf{x}}_{-i}$. Thus, simultaneously solving (2b) for all i and under a fixed pair $(\hat{\mathbf{x}}', \check{\mathbf{x}}')$ is equivalent to solving the OP given by $\min_{\mathbf{y}, \mathbf{p}} \sum_{i\in\mathcal{A}} \frac{\rho_i}{2} \left\|\mathbf{p}_i - \mathbf{g}_i\left(\hat{\mathbf{x}}'_{-i}\right)\right\|^2$ s.t. $(\mathbf{y}, \mathbf{p}) \in \prod_{i\in\mathcal{A}} \Phi_i\left(\check{\mathbf{x}}'_i\right) \times \mathbb{R}^{n_i}$, which is separable over $\mathcal{A}$ as well. Based on these observations, we remark that Gauss-Seidel ADMM-type GNEP solving methods [7] can be applied to the OPs in (2) following a three-block iterative scheme rather than iterating over the total number of agents. Consequently, in this paper, we adapt [7, Algorithm 4.1] to our framework. For every agent $i \in \mathcal{A}$, let $\hat{\mathbf{u}}_i \in \mathbb{R}^{n_i}$ and $\check{\mathbf{u}}_i \in \mathbb{R}^{n_i}$ be the Lagrange multipliers associated to the coupling constraints $\hat{\mathbf{x}}_i = \mathbf{y}_{-i}$ and $\check{\mathbf{x}}_i = \mathbf{y}_i$, respectively. Besides, define $\hat{\mathbf{u}}, \check{\mathbf{u}} \in \mathbb{R}^n$. Let $k \in \mathbb{Z}_{\geq 0}$ denote the iteration index, and let $\hat{\mathbf{x}}^k$, $\check{\mathbf{x}}^k$, $\mathbf{y}^k$, $\mathbf{p}^k$, $\hat{\mathbf{u}}^k$, and $\check{\mathbf{u}}^k$, denote the values of the corresponding optimization variables at iteration k. Applying [7, Algorithm 4.1] yields the (sequential) updates given by

$$\left(\hat{\mathbf{x}}^{k+1}, \check{\mathbf{x}}^{k+1}\right) = \operatorname*{arg\,min}_{(\hat{\mathbf{x}}, \check{\mathbf{x}}) \in \mathcal{X}} \left\{ \sum_{i\in\mathcal{A}} f_i\left(\hat{\mathbf{x}}_i, \check{\mathbf{x}}_i, \mathbf{p}_i^k, \mathbf{p}_{-i}^k\right) + \begin{bmatrix} \hat{\mathbf{u}}^k \\ \check{\mathbf{u}}^k \end{bmatrix}^\top \begin{bmatrix} \hat{\mathbf{x}} \\ \check{\mathbf{x}} \end{bmatrix} + \frac{\gamma_1}{2} \left\| \begin{bmatrix} \hat{\mathbf{x}} - \hat{\mathbf{x}}^k \\ \check{\mathbf{x}} - \check{\mathbf{x}}^k \end{bmatrix} \right\|^2 + \frac{\beta}{2} \left\| \begin{bmatrix} \hat{\mathbf{x}} - \mathbf{B}\mathbf{y}^k \\ \check{\mathbf{x}} - \mathbf{y}^k \end{bmatrix} \right\|^2 \right\}$$

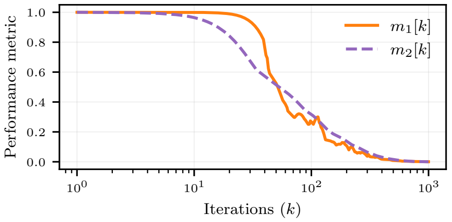

Fig. 1. Evolution of the selected performance metrics over 10^3 iterations. Without loss of generality, the initial condition is taken as $\hat{\mathbf{x}}_i^0, \check{\mathbf{x}}_i^0, \mathbf{y}_i^0, \mathbf{p}_i^0, \hat{\mathbf{u}}_i^0, \check{\mathbf{u}}_i^0 = \mathbf{0}_{n_i}$, for all $i \in \mathcal{A}$.

$$\left(\mathbf{y}^{k+1}, \mathbf{p}^{k+1}\right) = \operatorname*{arg\,min}_{(\mathbf{y}, \mathbf{p}) \in \mathbb{R}^{2n}} \left\{ \sum_{i\in\mathcal{A}} \frac{\rho_i}{2} \left\|\mathbf{p}_i - \mathbf{g}_i\left(\hat{\mathbf{x}}_{-i}^{k+1}\right)\right\|^2 - \begin{bmatrix} \hat{\mathbf{u}}^k \\ \check{\mathbf{u}}^k \end{bmatrix}^\top \begin{bmatrix} \mathbf{B}\mathbf{y} \\ \mathbf{y} \end{bmatrix} + \frac{\gamma_2}{2} \left\| \begin{bmatrix} \mathbf{y} - \mathbf{y}^k \\ \mathbf{p} - \mathbf{p}^k \end{bmatrix} \right\|^2 + \frac{\beta}{2} \left\| \begin{bmatrix} \hat{\mathbf{x}}^{k+1} - \mathbf{B}\mathbf{y} \\ \check{\mathbf{x}}^{k+1} - \mathbf{y} \end{bmatrix} \right\|^2 \right\}$$

$$\begin{bmatrix} \hat{\mathbf{u}}^{k+1} \\ \check{\mathbf{u}}^{k+1} \end{bmatrix} = \begin{bmatrix} \hat{\mathbf{u}}^k \\ \check{\mathbf{u}}^k \end{bmatrix} + \beta \begin{bmatrix} \hat{\mathbf{x}}^{k+1} - \mathbf{B}\mathbf{y}^{k+1} \\ \check{\mathbf{x}}^{k+1} - \mathbf{y}^{k+1} \end{bmatrix},$$

where $\mathcal{X} = \prod_{i\in\mathcal{A}} \mathcal{X}_i$, and $\gamma_1, \gamma_2, \beta \in \mathbb{R}_{>0}$ are constant parameters of the algorithm. If $\gamma_1, \gamma_2, \beta \in \mathbb{R}_{>0}$ and γ_2 satifies that $\gamma_2 > (1/\mu)\left(4\beta^2 + \sum_{i\in\mathcal{A}}\left(\hat{L}_i^2 + \check{L}_i^2\right)\right)$, then the iterations converge strongly to the unique vGNE of the GNEP.

IV. AN ILLUSTRATIVE NUMERICAL SIMULATION

We illustrate the proposed framework through a numerical simulation over a 24 hours period, i.e., $T = 24$, considering an energy community comprised of 2 ERs, 9 prosumers, and 3 ESSs, i.e., $N = 14$. We consider a random undirected topology plus a star graph with an ER as the central node. Agents' parameters are sampled from realistic energy productions and consumption dataset. We let $\gamma_1 = \beta = 0.5$, and we set $\gamma_2 = 112$. Figure 1 depicts the evolution of the performance metrics $m_1[k] = \left\|\hat{\mathbf{x}}^k - \mathbf{B}\check{\mathbf{x}}^k\right\|_\infty / \left\|\hat{\mathbf{x}}^1 - \mathbf{B}\check{\mathbf{x}}^1\right\|_\infty$, $m_2[k] = \|\mathbf{c}^k - \mathbf{c}^*\|_\infty / \|\mathbf{c}^1 - \mathbf{c}^*\|_\infty$, where $\mathbf{c} = \mathrm{col}(\hat{\mathbf{x}}, \check{\mathbf{x}}, \mathbf{p})$ and $\mathbf{c}^* = \mathrm{col}(\hat{\mathbf{x}}^*, \check{\mathbf{x}}^*, \mathbf{p}^*)$ is the unique GNE of the energy community.

REFERENCES

[1] V. Z. Gjorgievski, S. Cundeva, and G. E. Georghiou, "Social arrangements, technical designs and impacts of energy communities: A review," *Renewable Energy*, vol. 169, pp. 1138–1156, 2021.

[2] J. Martinez-Piazuelo, N. Quijano, and C. Ocampo-Martinez, "Decentralized charging coordination of electric vehicles under feeder capacity constraints," *IEEE Transactions on Control of Network Systems*, vol. 9, no. 4, pp. 1600–1610, 2021.

[3] N. Mignoni, J. Martinez-Piazuelo, R. Carli, C. Ocampo-Martinez, N. Quijano, and M. Dotoli, "A game-theoretical control framework for transactive energy trading in energy communities," in *2024 European Control Conference (ECC)*. IEEE, 2024.

[4] N. Mignoni, P. Scarabaggio, R. Carli, and M. Dotoli, "Control frameworks for transactive energy storage services in energy communities," *Control Engineering Practice*, vol. 130, p. 105364, 2023.

[5] F. Facchinei and J.-S. Pang, *Finite-dimensional variational inequalities and complementarity problems*. Springer, 2003, vol. 1.

[6] F. Facchinei and C. Kanzow, "Generalized Nash equilibrium problems," *Annals of Operations Research*, vol. 175, no. 1, pp. 177–211, 2010.

[7] E. Börgens and C. Kanzow, "ADMM-type methods for generalized Nash equilibrium problems in Hilbert spaces," *SIAM Journal on Optimization*, vol. 31, no. 1, pp. 377–403, 2021.

A User Based HVAC System Management Through Blockchain Technology and Model Predictive Control

Giuseppe Olivieri[1], Gaetano Volpe[1], Agostino Marcello Mangini[1], *Senior, IEEE*,
Maria Pia Fanti[1], *Fellow, IEEE*

***Index Terms*— HVAC management system, Blockchain, Model Predictive Control, Long short-term memory.**

I. EXTENDED ABSTRACT

A. Introduction

The quest for energy efficiency and consumption control is fundamental from an environmental perspective since fifty percent of building energy consumption is used in Heating, Ventilation, and Air-Conditioning (HVAC) systems [1]. Hence, effective HVAC control techniques for energy consumption minimization and thermal comfort guarantee have attracted the attention of researchers. In order to simultaneously maximize comfort and minimize energy consumption, it is essential to manage the building network (district) in a way that optimally balances real-time energy usage.

While existing regulations have initiated some changes, traditional penalty-based systems often fail to encourage full user compliance. Emerging researchers advocate for integrating blockchain technology, like proposing a novel system that dynamically rewards or penalizes users based on their real-time energy consumption. This approach promises enhanced security and privacy, addressing key concerns in energy management [2].

Thus, our work introduces an innovative HVAC management system connected with the District Energy Management System (DEMS), building on our prior research on energy-efficient systems and control methodologies [3], [4]. It classifies users into Consumption Classes using a K-means clustering algorithm, determining rewards or penalties based on their energy consumption behavior, implemented through a blockchain platform to ensure transparency and security. The novelty lies in the integration of Model Predictive Control (MPC) combined with a Long Short-Term Memory (LSTM) network [5], which users can follow to achieve more virtuous energy consumption classes. The proposed system architecture, depicted in Figure 1, leverages blockchain technology to securely handle dynamic energy consumption data and optimize HVAC settings while maintaining user comfort.

B. HVAC Control System

Our system architecture contemplate an HVAC control system at the DEMS level to enhance user management of HVAC consumption. The system architecture, illustrated in Figure 1, outlines its primary components.

The DEMS acquires the electricity invoice from the energy supplier at the conclusion of the billing cycle, along with data concerning weather conditions, calendar days, and legal constraints. This data is notarized via transactions on a blockchain platform to ensure integrity and transparency. Concurrently, IoT devices transmit the states of the HVAC systems, such as thermostat setpoints and operational intervals, which are dynamically monitored and stored on the blockchain.

The blockchain is utilized to classify users into different Consumption Classes at the end of each billing period, rewarding efficient energy use and penalizing inefficient consumption. Classifications are performed using a K-means clustering algorithm; rewards and penalties are determined accordingly. The blockchain further automates the payment process based on the user's classification, ensuring transparency and reducing administrative overhead.

To guide users in improving their consumption class, a MPC strategy is employed. The MPC calculates the optimal thermostat setpoints for the HVAC system and determines the intervals during which the system should be activated or deactivated. Combined with a LSTM network that predicts indoor temperatures and energy consumption, the proposed system facilitates real-time HVAC management, ensuring user comfort while minimizing energy usage.

This integrated approach enables a fine-grained control mechanism that dynamically adjusts to both user behavior and external factors, thereby aligning with broader energy optimization goals.

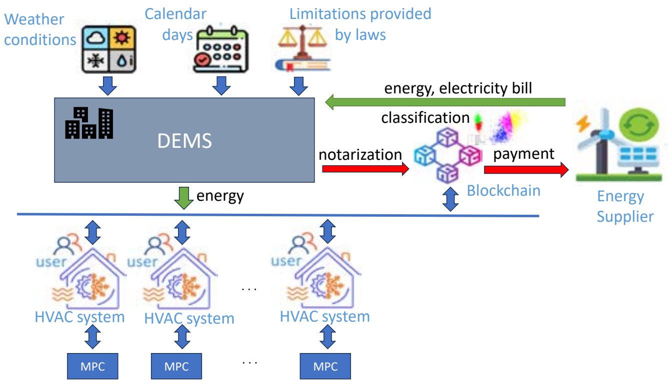

Fig. 1: System Architecture

Moreover, by integrating Smart Contracts, the blockchain automates user classification into Consumption Classes and processes payments based on energy consumption behavior, as outlined in our more complete study [4]. This decentralized approach mitigates the risk of data tampering and enhances the reliability of the overall system.

C. District User Clustering and Class Follower Problem

The proposed HVAC control system not only monitors but also strategically categorizes users within the district into specific Consumption Classes. The K-means clustering algorithm that performs the categorization classifies users relying on feature metrics such as average indoor temperature, relative outdoor temperature, thermostat settings, and HVAC operational times. As illustrated in Figure 2, the algorithm partitions users into clusters, each corresponding to a distinct Consumption Class, ranging from the most efficient to the least.

Each class carries specific rewards and penalties to encourage energy-efficient behaviors. Users in more virtuous classes benefit from lower energy costs, while those in less virtuous classes

---

[1] Department of Electrical and Information Engineering, Polytechnic University of Bari, 70126 (BA) Bari, Italy. g.olivieri@phd.poliba.it; (gaetano.volpe, agostinomarcello.mangini, mariapia.fanti)@poliba.it.

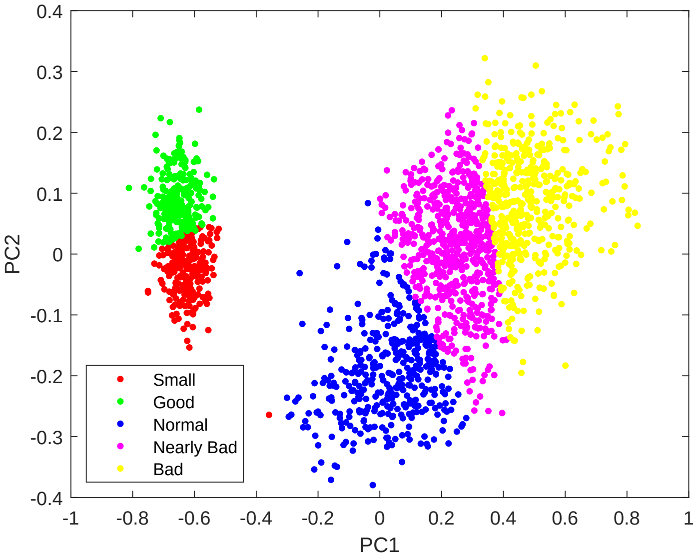

Fig. 2: K-means clustering

face higher penalties. These classifications are dynamically updated and securely recorded on the blockchain platform, which is a pseudonym, ensuring transparency and accuracy.

To help users improve their energy consumption profile, we introduce the Class Follower Problem (CFP). This problem is addressed using a MPC strategy, which determines the optimal thermostat settings and HVAC operational intervals. By adhering to the MPC guidelines, users can modify their consumption patterns to achieve the class standards of more energy-efficient groups.

By training the LSTM network on historical and environmental data, the system achieves a higher degree of accuracy, as it predicts indoor temperatures and energy consumption, thus enabling the MPC to make data-driven adjustments that optimize both energy usage and comfort levels.

Leveraging these advanced technologies within the blockchain environment provides a secure and efficient method for HVAC management across the district. Our architecture ensures a cohesive flow from data collection and user classification to real-time control, thereby optimizing energy consumption while ensuring user comfort and satisfaction.

Overall, the district-level application of the proposed HVAC control system aligns with broader energy efficiency goals, adapting dynamically to user behaviors and external factors. The synergy of blockchain, K-means clustering, MPC, and LSTM networks offers a comprehensive solution for modern smart cities and energy management systems, fostering sustainable practices and efficient energy consumption.

D. Control System Design and Simulation

At the core of the system, LSTM networks are utilized to predict the thermodynamic behavior of buildings. These networks are trained using historical data related to indoor and outdoor temperatures, thermostat setpoints, and HVAC operational states. The LSTM models accurately forecast future indoor temperatures and energy consumption, enabling more informed control decisions.

The control system's effectiveness is validated through simulations using EnergyPlus, a building energy simulation software. In these simulations, the algorithm's capacity to manage energy consumption and maintain thermal comfort in various scenarios is tested. The use of LSTM networks enhances the system's responsiveness to changing conditions, while the MPC ensures that the HVAC operations remain within optimal bounds.

This integrated approach allows users to transition to more virtuous energy consumption classes by following the guidelines of the control system. The system provides a clear pathway for users to achieve energy savings and improve their classification by modifying their HVAC usage behaviors based on the recommendations provided.

The control system exemplifies the potential of combining predictive analytics with real-time optimization techniques to achieve significant improvements in energy management within smart districts. Our work shows the feasibility and benefits of advanced machine learning and control strategies for sustainable HVAC management.

E. Case Study & Conclusions

The case study presented in our work validates the proposed control system integrated with DEMS in a district in Bari, Italy. The area comprises 2000 users and their respective HVAC systems, all connected to a centralized management system. Data on each user's energy consumption, including thermostat setpoints and operational intervals, were collected over a billing period and processed using the proposed K-means clustering algorithm.

The users were categorized into five distinct Consumption Classes based on their energy consumption behaviors: *Small*, *Good*, *Normal*, *Nearly Bad*, and *Bad*. These classifications were then used to assign rewards or penalties. Initially, a user classified in the *Nearly Bad* class aimed to improve their classification to the *Good* and *Normal* classes in separate scenarios.

The implemented MPC strategy, supported by the LSTM-based predictive model, optimized the user's HVAC settings to help achieve the desired class improvement. The control mechanism demonstrated effective tracking of the target classes, adjusting thermostat setpoints and HVAC operational times dynamically. This resulted in significant energy consumption reductions while maintaining indoor temperature comfort within acceptable ranges.

The class tracking error showed convergence to minimal residual errors, suggesting a robust adaptation to user behavioral changes. Energy consumption data revealed that users following the system's recommendations could transition to more virtuous energy classes, consequently lowering their energy costs.

In conclusion, this work successfully integrates blockchain technology, MPC, and LSTM networks to enhance HVAC system management at the district level. The combined approach provides a transparent, secure, and dynamic method for optimizing energy consumption, aligning with broader sustainability goals. The case study in Bari illustrates the practical applicability and benefits of the proposed system, achieving both energy efficiency and user comfort.

Future work involves scaling to larger districts, integrating renewable energy, and conducting seasonal tests.

REFERENCES

[1] X. Deng, Y. Zhang, Y. Zhang, and H. Qi, "Toward smart multizone hvac control by combining context-aware system and deep reinforcement learning," *IEEE Internet of Things Journal*, vol. 9, pp. 21010–21024, Nov 2022.

[2] O. Van Cutsem, D. Ho Dac, P. Boudou, and M. Kayal, "Cooperative energy management of a community of smart-buildings: A blockchain approach," *International Journal of Electrical Power & Energy Systems*, vol. 117, p. 105643, 2020.

[3] G. Olivieri, G. Volpe, A. M. Mangini, and M. Pia Fanti, "A district energy management approach based on internet of things and blockchain," in *2022 IEEE Intl Conf on Dependable, Autonomic and Secure Computing, Intl Conf on Pervasive Intelligence and Computing, Intl Conf on Cloud and Big Data Computing, Intl Conf on Cyber Science and Technology Congress (DASC/PiCom/CBDCom/CyberSciTech)*, pp. 1–6, Sep. 2022.

[4] G. Olivieri, G. Volpe, A. M. Mangini, and M. P. Fanti, "A user based hvac system management through blockchain technology and model predictive control," *IEEE Transactions on Automation Science and Engineering*, pp. 1–14, 2024.

[5] J. Bi, X. Zhang, H. Yuan, J. Zhang, and M. Zhou, "A hybrid prediction method for realistic network traffic with temporal convolutional network and lstm," *IEEE Transactions on Automation Science and Engineering*, vol. 19, pp. 1869–1879, July 2022.

EXTENDED ABSTRACT
Modeling and Predictive Control of District Heating Systems via Physics-Informed Recurrent Neural Networks

Laura Boca de Giuli, Alessio La Bella and Riccardo Scattolini

***Abstract*—This work proposes a novel methodology to identify the model of a district heating system (DHS) exploiting physics-informed neural networks. The approach consists in leveraging multiple recurrent neural networks (RNNs) and in embedding the physical topology of the DHS within their interconnections. Compared to standard RNNs, this modeling technique enables faster training and higher accuracy. The developed approach paves the way for the design of a nonlinear model predictive control (NMPC) strategy, allowing to minimize production costs, enhance system efficiency and ensure compliance with operational constraints across the entire DHS.**

I. INTRODUCTION

DHSs are recognized as crucial for achieving energy transition objectives due to their high efficiency. Traditionally, these systems are operated using rule-based control strategies, which do not fully exploit their efficiency potential, highlighting the need for advanced optimization-based control strategies. To develop advanced schemes such as NMPC, an accurate model of the system is needed. Purely physics-based models require a large number of parameters [1], often leading to intractable complex models. Conversely, purely data-based models typically lack physical insights, which may result in unreliable models. Given that DHSs are characterized by a large amount of operational data and a known network topology, a novel physics-informed machine learning (PI-ML) [2] methodology is here proposed. This consists in interconnecting different RNNs according to the DHS topology and in jointly learning them from data though a unique training procedure. This physics-informed RNN (PI-RNN) method shows enhanced modeling performance with reduced complexity compared to standard RNN models. Moreover, the proposed modeling approach can be effectively employed to design an NMPC regulator, minimizing production costs and increasing system efficiency while respecting the desired operational constraints across the whole DHS network. The presented approach is tested on a known DHS benchmark [1], yielding promising results from both modeling and control perspectives.

II. SYSTEM DESCRIPTION

A DHS typically comprises the following components: *i)* the supply network, where high-temperature water flows from the heating station to the thermal loads, *ii)* the return network, where cold-temperature water flows from the thermal loads back to the heating station, *iii)* the heating station, which absorbs water from the return network and injects it at a higher temperature into the supply network, and *iv)* the thermal loads, which absorb water from the supply network and inject it back into the return network. Given that the topology of a DHS is generally well-known, it can be represented as a structured graph $\mathcal{G} = (\mathcal{N}, \mathcal{E})$, where $\mathcal{N}$ denotes the set of nodes and $\mathcal{E} \subseteq \mathcal{N} \times \mathcal{N}$ represents the set of edges, with $n = |\mathcal{N}|$. Moreover, $\mathcal{N}_c$ is defined as the set containing all nodes with thermal loads. Each node represents an element of the DHS, such as a thermal load, the heating station, or a junction among multiple pipes, and includes connections to both the supply and return networks. The edges represent the physical interactions among the system nodes. For each ith node, the set of inlet neighbors, i.e., the ones having a physical influence on it, is denoted by $\mathcal{I}_i = \{j \in \mathcal{N} \mid \exists\,(j,i) \in \mathcal{E}\}$. The case study analysed in this work is the AROMA DHS [1], whose graphical representation is shown in Fig. 1(a). The controllable input is the heating station supply temperature, T_0^s, while the thermal load demands $\{P_i^c\}_{\forall i \in \mathcal{N}_c}$ represent the disturbances. Overall, the system input is $u = [T_0^s, \{P_i^c\}'_{\forall i \in \mathcal{N}_c}]'$. The selected outputs are instead $y = [T_0^r, q_0, P_0, \{T_i^s, T_i^c, q_i^c\}'_{\forall i \in \mathcal{N}_c}]'$. Specifically, T_0^r, q_0 and P_0 are the heating station return temperature, water flow, and power, respectively. T_i^s, T_i^c and q_i^c are the supply temperature, output temperature, and water flow of each thermal load, respectively. The detailed physical modeling of the considered DHS benchmark is available in [1].

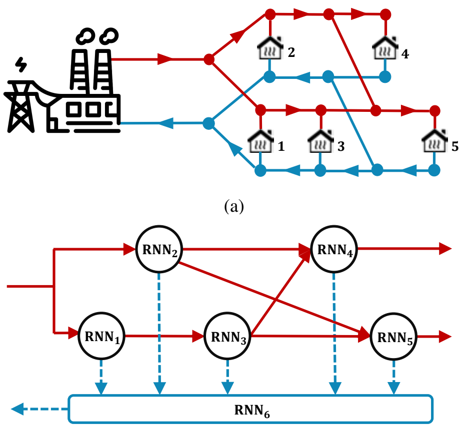

(a)

(b)

Fig. 1: (a) Schematic representation of the AROMA DHS [1]; (b) PI-RNN architecture for the AROMA DHS.

III. PHYSICS-INFORMED RECURRENT NEURAL NETWORK

To develop a data-based model of a DHS, RNNs are used, being particularly suitable to approximate nonlinear dynamical systems due to their universal approximation capabilities. However, purely data-based identification approaches may lack physical insights, leading to unreliable models. A novel PI-ML algorithm is here proposed. Unlike many PI-ML approaches that incorporate known mathematical relationships into the loss

Laura Boca de Giuli, Alessio La Bella and Riccardo Scattolini are with Dipartimento di Elettronica, Informazione e Bioingegneria, Politecnico di Milano, Piazza Leonardo da Vinci 32, 20133 Milan, Italy ({`laura.bocadegiuli`, `alessio.labella`, `riccardo.scattolini`}`@polimi.it`).

function for training the RNN [2], the proposed method leverages the physical information regarding the DHS topology. This physics-informed RNN (PI-RNN) methodology involves interconnecting different RNNs according to the physical structure of the system, so that the overall PI-RNN architecture resembles the DHS topology, as depicted in Fig. 1(b). In other words, each node of the system (e.g., each thermal load) is paired with a corresponding submodel $\mathcal{M}_i$, reading as

$$\mathcal{M}_i : \begin{cases} x_i(k+1) = & f_i(x_i(k), v_i(k); \Theta_i) \\ y_i(k) = & g_i(x_i(k), v_i(k); \Theta_i) \end{cases}, \tag{1}$$

where f_i and g_i are generic functions, $x_i \in \mathbb{R}^{n_{x_i}}$, $v_i \in \mathbb{R}^{n_{v_i}}$ and $y_i \in \mathbb{R}^{n_{y_i}}$ are the ith submodel state, input, and output variables, respectively, and Θ_i is the vector of parameters that must be tuned during the identification procedure. Each $\mathcal{M}_i$ is designed to have as input $v_i = [u_i, \{y^{[j]}\}'_{\forall j \in \mathcal{I}_i}]'$, which includes its local inputs u_i and the output variables of its inlet neighbor submodels $\{y^{[j]}\}_{\forall j \in \mathcal{I}_i}$, so as to embed the physical influence among the DHS nodes. Thus, the submodels $\mathcal{M}_i$ are interconnected according to the DHS topology defined by $\mathcal{G} = (\mathcal{N}, \mathcal{E})$. Introducing $x = \{x_i\}_{i=1}^n \in \mathbb{R}^{n_x}$, $u = \{u_i\}_{i=1}^n \in \mathbb{R}^{n_u}$, $y = \{y_i\}_{i=1}^n \in \mathbb{R}^{n_y}$, $\Theta = \{\Theta_i\}_{i=1}^n$, the overall PI-RNN model reads as

$$\mathcal{M} : \begin{cases} x(k+1) = f(x(k), u(k); \Theta) \\ y(k) = g(x(k), u(k); \Theta) \end{cases}. \tag{2}$$

Finally, the developed physics-informed model $\mathcal{M}$ of the DHS is learned from data through a unique training procedure. More details on the proposed methodology are available in [3].

IV. NONLINEAR MODEL PREDICTIVE CONTROL

To optimally operate the DHS, an NMPC strategy is formulated, exploiting the PI-RNN model. Considering a sampling period τ_s and a prediction horizon of N steps, the following problem is solved at each time instant $t = k_s\tau_s$, with $k_s \in \mathbb{N}$:

$$\min_{T_0^s(\cdot)} \sum_{k=k_s}^{k_s+N-1} (c_{el}(k)P_0(k)/\eta) \tag{3a}$$

subject, $\forall\, k \in \{k_s, \dots, k_s+N-1\}$, to (2) and

$$x(k_s) = \hat{x}_0, \tag{3b}$$

$$\underline{y} \le y(k) \le \overline{y}. \tag{3c}$$

The cost function (3a) minimizes the production cost of the heating station, taking into account the time-varying price c_{el} and the heating station's thermal efficiency η. The system state x must be initialized at each NMPC iteration with $\hat{x}_0$, estimated by a properly designed observer, as evident from (3b). Finally, (3c) is included to comply with temperature and power limits.

V. CASE STUDY

The proposed modeling and control approaches are tested in simulation on the AROMA DHS [1]. To accurately identify the system dynamics, a dataset of input-output samples is collected. A PI-RNN is compared to a standard RNN, specifically employing the Gated Recurrent Unit (GRU) network. Both models are trained with a 15690-sample dataset over 1500 epochs. Fig. 2(a) shows the comparison between the FIT trend of a 54-state standard GRU and a PI-GRU one, witnessing that the PI-GRU achieves better fitting performance (FIT = 83.6% against 54.5%) and faster training (91 minutes against 145). As also evident from the predicted trends of some output variables, the PI-GRU (Fig. 2(c)) outperforms the standard GRU (Fig. 2(b)). Finally, Table I shows that an NMPC using a PI-GRU model is superior in terms of production costs (C_p), thermal losses (P_{loss}) and computational time (t_{avg}) reduction compared to an NMPC using a standard GRU and to a rule-based strategy with fixed supply temperature.

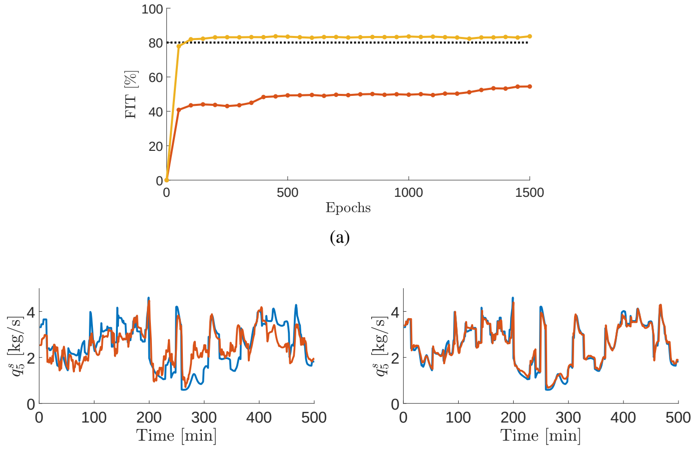

(a)

(b)

(c)

Fig. 2: (a) FIT trend of a standard GRU (orange) and of a PI-GRU (yellow); (b) q_5^c identified by the standard GRU (orange) with respect to the measured value (blue); (c) q_5^c identified by the PI-GRU (orange) with respect to the measured value (blue).

TABLE I: Comparison among the adopted control strategies.

	C_p	t_{avg}	P_{loss}
NMPC (PI-GRU)	881.4 €	17 s	10.4 kW
NMPC (standard GRU)	907.2 €	40 s	16.0 kW
Rule-based strategy	936.8 €	-	32.0 kW

VI. CONCLUSIONS

A novel PI-ML methodology is proposed for DHSs. It is shown that interconnecting multiple RNNs by resembling the DHS topology leads to significant improvements in terms of faster training procedures and higher identification accuracy compared to traditional RNNs. The developed PI-RNN model is leveraged for the design of an NMPC, able to minimize production costs, increase system efficiency and adhere to operational constraints across the entire DHS. Future work includes extending this approach to generic networked systems (e.g., electrical networks, chemical plants) and developing a training procedure to enforce stability properties in the learned models.

REFERENCES

[1] R. Krug, V. Mehrmann, and M. Schmidt, "Nonlinear optimization of district heating networks," *Optimization and Engineering*, vol. 22, no. 2, pp. 783–819, 2021.

[2] A. Karpatne, R. Kannan, and V. Kumar, *Knowledge guided machine learning: Accelerating discovery using scientific knowledge and data.* CRC Press, 2022.

[3] L. Boca de Giuli, A. La Bella, and R. Scattolini, "Physics-informed neural network modeling and predictive control of district heating systems," *IEEE Trans. on Control Systems Technology*, vol. 32, no. 4, pp. 1182–1195, 2024.

A dual bisection approach to economic dispatch of generators with prohibited operating zones

Lucrezia Manieri, Alessandro Falsone, Maria Prandini

I. INTRODUCTION

Unit Commitment (UC) and Economic Dispatch (ED) are crucial for power systems operation. UC [1] determines which generating unit will be possibly activated to satisfy a forecasted electricity demand along some reference time horizon, while ED [2] allocates the demand in each time slot by defining the actual amount of power that each committed generator has to produce in that time slot. The Economic Dispatch Problem (EDP) can be solved after the UC problem or jointly, in an integrated manner.

In this work, we address EDPs that aim at minimizing the cost of supplying the required energy demand via generators with prohibited operating regions. Following [3], we adopt a formulation comprising continuous and binary decision variables, quadratic cost, non-convex local constraints, and a scalar quadratic coupling constraint accounting for power losses. Due to the presence of binary variables, the problem has a combinatorial complexity that makes its resolution challenging and calls for suitable resolution schemes. Here, we propose a duality-based approach integrating the bisection iterative scheme in [4] to tackle computational complexity, while guaranteeing finite time feasibility of the primal iterates and a cost that is not increasing throughout iterations.

II. PROBLEM FORMULATION

We consider an EDP with m generator units, each producing a power $P_i \geq 0$, which is zero if the generator i does not participate in the energy provision at the considered time slot and is positive otherwise.

The cost J_i for unit i to produce an amount of power P_i is given by the quadratic cost function

$$J_i(P_i) = \omega_{i0} + \omega_{i1}P_i + \omega_{i2}P_i^2, \tag{1}$$

where ω_{i0}, ω_{i1} and ω_{i2} are positive scalar coefficients specific for generator i, for $i = 1, \ldots, m$.

Generators can have *prohibited zones* within their domain of operation due to physical limitations of individual power plant components (e.g. avoiding amplification of the vibrations in a shaft bearing). Thus, each power P_i will satisfy (only) one of the following conditions

$$P_i = 0, \tag{2a}$$

$$\underline{P}_{i,j} \leq P_i \leq \bar{P}_{i,j} \qquad \text{for some } j \in \{1, \ldots, N_i\}, \tag{2b}$$

where $[\underline{P}_{i,j}, \bar{P}_{i,j}]$, $j = 1, \ldots, N_i$ are operating regions such that $\underline{P}_{i,1} = P_i^{\min} > 0$, $\bar{P}_{i,N_i} = P_i^{\max} > P_i^{\min}$, $\underline{P}_{i,j} < \bar{P}_{i,j}$, and $\bar{P}_{i,j-1} < \underline{P}_{i,j}$. Condition (2) can be translated into a set of linear inequalities by adding N_i auxiliary binary decision variables, one per each interval $j = 1, \ldots, N_i$, that are set to 1 if P_i belongs to the j-th allowed power interval, and 0 otherwise. The operation may also be subject to ramp limits, which typically require

$$-\underline{\Delta}_i \leq P_i - P_{i,0} \leq \bar{\Delta}_i, \tag{3}$$

where $P_{i,0}$ denotes the power provided by generator i in the previous time slot, whilst $\bar{\Delta}_i > 0$ and $\underline{\Delta}_i > 0$ denote the maximum power increase or decrease, respectively, that generator i can allow. Finally, in order to meet a certain power demand $P_d \geq 0$, all generators should satisfy the following (scalar) constraint

$$\sum_{i=1}^{m} P_i - P_\ell(\vec{P}) \geq P_d, \tag{4}$$

that accounts also for power losses $P_\ell(\vec{P})$, with $\vec{P} = [P_1 \cdots P_m]^\top$, which can be computed using Kron's loss formula [5, Section 7.7] as

$$P_\ell(\vec{P}) = \sum_{i=1}^{m}\sum_{j=1}^{m} b_{ij}P_iP_j + \sum_{i=1}^{m} b_{i0}P_i + b_{00}, \tag{5}$$

with b_{ij}, b_{i0}, b_{00}, $i, j = 1, \ldots, m$, being suitable coefficients.

The resulting optimization problem is thus given by

$$\min_{P_1,\ldots,P_m} \quad \sum_{i=1}^{m} J_i(P_i) \tag{6a}$$

$$\text{subject to:} \quad \sum_{i=1}^{m} P_i - P_\ell(\vec{P}) \geq P_d \tag{6b}$$

$$P_i \in \mathcal{P}_i \quad i = 1, \ldots, m, \tag{6c}$$

where $\mathcal{P}_i$ is the set of feasible power outputs for generator i defined by (2)-(3), and $J_i(P_i)$, $P_\ell(\vec{P})$ defined in (1) and (5) respectively. Problem (6) has a quadratic cost (6a), a quadratic *global* constraint (6b) involving the decision variables of all generators, and m *local* constraints (6c), each involving the power of a single generator. Since the local set $\mathcal{P}_i$ is the intersection between an interval and a union of disjoint intervals arising from commission/decommission and prohibited zones, (6) is a non-convex problem, which is difficult to solve. In this work, we leverage the scalar nature of the *global* constraint (6b) to reduce the computational complexity and compute a solution of (6).

III. PROPOSED APPROACH

It is easy to show that (6) fits the framework addressed in [4] and, hence, it can be solved via the dual bisection

---

The authors are with the Dipartimento di Elettronica Informazione e Bioingegneria, Politecnico di Milano, Via Ponzio 34/5, 20133 Milano, Italy. Email: `name.surname@polimi.it`.

Algorithm 1 Bisect EDP

```
1: $\underline{\lambda} \leftarrow 0$ , $\bar{\lambda} \leftarrow \lambda_{\text{start}}$ in (9)
2: $\vec{P} \leftarrow \arg\min_{\{P_i \in \mathcal{P}_i\}_{i=1}^m} \mathcal{L}(\vec{P}, \bar{\lambda})$
3: if $\sum_{i=1}^m P_i - P_\ell(\vec{P}) = P_d$ then
4:     return $\vec{P}$
5: end if
6: $\vec{P}_{\text{best}} \leftarrow \vec{P}$
7: repeat
8:     $\hat{\lambda} \leftarrow \frac{1}{2}(\bar{\lambda} + \underline{\lambda})$
9:     $\vec{P} \leftarrow \arg\min_{\{P_i \in \mathcal{P}_i\}_{i=1}^m} \mathcal{L}(\vec{P}, \hat{\lambda})$
10:    if $\sum_{i=1}^m P_i - P_\ell(\vec{P}) = P_d$ then
11:        return $\vec{P}$
12:    else if $\sum_{i=1}^m P_i - P_\ell(\vec{P}) > P_d$ then
13:        $\vec{P}^{\text{best}} \leftarrow \vec{P}$
14:        $\bar{\lambda} \leftarrow \hat{\lambda}$
15:    else if $\sum_{i=1}^m P_i - P_\ell(\vec{P}) < P_d$ then
16:        $\underline{\lambda} \leftarrow \hat{\lambda}$
17:    end if
18: until some stopping criterion is met
19: return $\vec{P}_{\text{best}}$
```

Unit	GA [7]	PSO [3]	Bi-B&B [8]	Algorithm 1
P_1	474.81	447.50	447.40	447.08
P_2	178.64	173.32	173.24	173.19
P_3	262.21	263.47	263.38	263.93
P_4	134.28	139.06	138.98	139.06
P_5	151.90	165.48	165.39	165.58
P_6	74.18	87.13	87.05	86.63
$\Delta_J(\cdot)$	$\mathbf{1.0 \cdot 10^{-3}}$	$\mathbf{4.2 \cdot 10^{-4}}$	$\mathbf{-2.6 \cdot 10^{-5}}^*$	$\mathbf{1.5 \cdot 10^{-9}}$
$E(\cdot)$	$3.7 \cdot 10^{-4}$	$3.8 \cdot 10^{-4}$	$-2.4 \cdot 10^{-5*}$	$1.5 \cdot 10^{-9}$

TABLE I

COMPARISON OF THE SOLUTION OBTAINED VIA ALGORITHM 1 WITH THOSE OBTAINED BY STATE-OF-THE-ART COMPETITORS ON AN IEEE BENCHMARK PROPOSED IN [3]. THE SOLUTION MARKED WITH $*$ VIOLATES THE AGGREGATE DEMAND CONSTRAINT.

(DualBi) algorithm proposed in [4]. The approach leverages Lagrangian duality to lift constraint (6b) to the cost function and turn problem (6) from a quadratically constrained non-convex program into a program that is still non-convex but with a quadratic cost function only. This is done by introducing a (single) Lagrange multiplier $\lambda \geq 0$, which allows to define the Lagrangian function

$$\mathcal{L}(\vec{P}, \lambda) = \sum_{i=1}^{m} J_i(P_i) + \lambda\Big(P_d + P_\ell(\vec{P}) - \sum_{i=1}^{m} P_i\Big), \tag{7}$$

and pose the dual problem

$$\max_{\lambda \geq 0} \varphi(\lambda) = \max_{\lambda \geq 0} \min_{\{P_i \in \mathcal{P}_i\}_{i=1}^m} \mathcal{L}(\vec{P}, \lambda). \tag{8}$$

which is convex, despite (6) is non-convex, and scalar.

The dual problem (8) can be, thus, solved via the bisection method introduced in [4], that takes advantage of the scalar nature of the dualized constraint to compute a feasible primal solution in finite time.

The procedure is reported in Algorithm 1. The bisection starts with an interval $[\underline{\lambda}, \bar{\lambda}] = [0, \lambda_{\text{start}}]$ (cf. Step 1), where

$$\lambda_{\text{start}} = \frac{\sum_{i=1}^m \Big(J_i(\tilde{P}_i^{\max}) - \min_{P_i \in \mathcal{P}_i} J_i(P_i)\Big)}{\sum_{i=1}^m \tilde{P}_i^{\max} - P_\ell(\tilde{\vec{P}}^{\max}) - P_d} \tag{9}$$

is selected according to [4, Theorem 2] to ensure that the optimal dual solution $\lambda^\star$ of (8) is contained in the interval $[0, \lambda_{\text{start}}]$. A first *feasible* power allocation $\vec{P}$ is computed by minimizing the Lagrangian in (7) with $\lambda = \bar{\lambda} = \lambda_{\text{start}}$ (cf. Step 2). If such allocation matches the demand P_d exactly (cf. Step 3), then it is also *optimal* and is readily returned in Step 4; otherwise, it is saved as the current best allocation $\vec{P}_{\text{best}}$ in Step 6 and the algorithm proceeds to the bisection loop (cf. Steps 7-18).

At each bisection iteration, a new allocation $\vec{P}$ is obtained by minimizing the Lagrangian in (7) for $\lambda = \hat{\lambda}$ (cf. Step 9), with $\hat{\lambda}$ midpoint of the interval $[\underline{\lambda}, \bar{\lambda}]$ (cf. Steps 8). If such allocation meets the demand P_d exactly (cf. Step 10) it is readily returned in Step 11. Otherwise, the extreme points $\underline{\lambda}, \bar{\lambda}$ are updated based on whether constraint (6b) has been over-penalized (c.f. Steps 12-14) or under-penalized (c.f. Step 15-16). The loop continues until some stopping criterion is met (e.g. when the length of the interval $[\underline{\lambda}, \bar{\lambda}]$ falls below a certain threshold). Whenever the loop stops, the algorithm returns the best allocation found $\vec{P}_{\text{best}}$ (cf. Step 19).

The procedure is guaranteed to either converge to an optimal primal solution in a finite number of iterations or generate a sequence of feasible primal solutions with non-increasing cost (see [6, Theorem 1] for more details).

IV. NUMERICAL SIMULATION

Numerical simulations on IEEE benchmark EDPs described in [3, Section V.A] show that the approach outperforms state-of-the-art competitors, including stochastic (possibly hybrid) heuristic methods [3], [7] and exact resolution schemes based on implicit enumeration [8]. Table I shows the results obtained for a benchmark with $m = 6$ generators. State-of-the-art strategies provide solutions that either yield a higher production cost or do not meet the aggregate power demand.

Tests on randomly generated instances with increasing size show that the proposed approach is scalable and able to compute near-optimal solutions consistently. We refer the reader to [6] for more details.

REFERENCES

[1] R. Kerr, J. Scheidt, A. Fontanna, and J. Wiley, "Unit commitment," *IEEE Transactions on Power Apparatus and Systems*, no. 5, 1966.

[2] B. Chowdhury and S. Rahman, "A review of recent advances in economic dispatch," *IEEE Transactions on Power Systems*, vol. 5, no. 4, pp. 1248–1259, 1990.

[3] Z. L. Gaing, "Particle swarm optimization to solving the economic dispatch considering the generator constraints," *IEEE Transactions on Power Systems*, vol. 18, no. 3, pp. 1187–1195, 2003.

[4] L. Manieri, A. Falsone, and M. Prandini, "Dualbi: A dual bisection algorithm for non-convex problems with a scalar complicating constraint," *arXiv preprint arXiv:2402.03013*, 2024.

[5] H. Saadat, *Power Systems Analysis*, 3rd ed. McGraw-hill, 2010.

[6] L. Manieri, A. Falsone, and M. Prandini, "A dual bisection approach to economic dispatch of generators with prohibited operating zones," *IEEE Control Systems Letters*, 2024.

[7] P.-H. Chen and H.-C. Chang, "Large-scale economic dispatch by genetic algorithm," *IEEE transactions on power systems*, vol. 10, no. 4, pp. 1919–1926, 1995.

[8] T. Ding, R. Bo, F. Li, and H. Sun, "A bi-level branch and bound method for economic dispatch with disjoint prohibited zones considering network losses," *IEEE Transactions on Power Systems*, vol. 30, no. 6, pp. 2841–2855, 2014.

Session 5A: Machine learning and control

Symbolic regression for industrial applications: an NN-based approach

Marco Calapristi, Luca Patanè, Francesca Sapuppo, Riccardo Caponetto, Maria Gabriella Xibilia
Department of Engineering, *University of Messina*, Messina, Italy

I. INTRODUCTION

Symbolic regression (SR) is a machine learning technique that aims to discover the underlying relationship between input and output values by examining the space of all mathematical formulas and selecting the equations that best fit the data. The search space is defined by combinations of input features, admissible mathematical operators and the continuous set of numerical constants. The ultimate goal of SR is to produce interpretable solutions that can be trusted and to enable information sharing between experts, as the model can benefit from heuristic knowledge from humans in the loop. Moreover, it can provide new insights about the system under study. SR is usually implemented using Genetic Programming (GP), a computational technique originally proposed by Koza [1]. This method iteratively generates solutions to minimize a given cost function, evolving random equations over generations. SR-based models can be used to develop interpretable soft sensors (SS), which serve to estimate process variables from the available input data. Such models find many applications in the process industry when the quantities of interest are hard to measure, require expensive equipment, or are subject to physical constraints that would delay the measurement process [2]. It is important to underline that SS design process, to extract the dynamics of the modelled process, often relies on both current and past values of inputs and previous system outputs, significantly increasing the problem's dimensionality. Conventional GP frameworks, such as PySR [3] used in this work, struggle to find an optimal solution for problems with many features, as each input regressor exponentially expands the search space. One possible solution is to use dimensionality reduction algorithms such as principal component analysis (PCA). However, this would inevitably worsen the interpretability of the model, which is the main focus of SR. An alternative approach, here proposed, consists of using a neural network to reduce a complex problem with high dimensionality into smaller problems with sparse inputs that can be fitted separately. The proposed approach is therefore able to extend SR to high-dimensional datasets by using precisely engineered neural networks. This concept was originally introduced in [4] and extended to soft sensors for dynamical systems in the present study, where the NN is used to capture the system dynamics of each input and formulate an encoding of these dynamics using SR to express the output in terms of the generated encodings.

II. SULFUR RECOVERY UNIT DESCRIPTION

Two SSs were designed using the proposed methodology to model a sulfur recovery unit (SRU) located in a refinery plant in Sicily, Italy. The two models aim to estimate the concentration of hydrogen sulfide (H_2S) and sulfur dioxide (SO_2) in the tail stream of the industrial plant. This industrial process has already been used as a benchmark for different methods in other works [5]–[7]. The process has five inputs which are the *MEA* and *SWS* gas flows, the corresponding air flows *AIR_MEA* and *AIR_SWS*, and a further airflow input *AIR_MEA_2*. An online analyzer measures the concentration of both gases to regulate the ratio of air to feed to maximize sulfur extraction. In addition, a closed-loop control system regulates an additional air flow (*AIR_MEA_2*) based on the tail gas composition, which improves the control mechanism. However, acid gases damage the chemical sensors over time, which requires frequent maintenance. While maintenance does not interrupt the operation of the system, it disables the additional airflow mechanism, which degrades the overall performance. An SS could replace the physical sensor during maintenance phases and also provide redundant estimates for fault detection.

III. RESULT SUMMARY

The Sulfur line 4 was chosen for this work [2]. The available data consists of 17,264 samples obtained with a sampling time of one minute. These were divided into training (70%), validation (15%) and test sets (15%), taking into account temporal dependencies within the process when moving the data and normalizing each set using z-score normalization. A block diagram of the NN used is shown in Figure 1. To simplify the structure, a small number of neurons was used in the fully connected encoding hidden layers. The predictions of the encoding layers on the training dataset were recorded and used as target values for the PySR framework, resulting in five different models, one for each encoded input. The operators considered in the fitting process are $+, -, *, /, sin, exp, sqrt, tan, sinh, tanh$ and real constants, setting the maximum length to 30. Each operator was assigned a weight of 1, and some combinations of operators were prevented that would be either redundant or uninterpretable, such as $sin(tanh(x))$ or $sin(sin(x))$. Both the H_2S and the SO_2 input encodings are given in Eq. 1 and 2, respectively.

The research has been developed under the Italian PRIN MUR Project "Green SENSing systems based on Bacterial Cellulose (SENSBC)" PRIN_2022HSYJEF_002, CUP: J53D23003460006.

$$
\begin{aligned}
e_{1,H_2S} &= (0.01u_1 + 0.1)(2.5u_1 + 1.8u_1z^{-5} - 5.3u_1z^{-9}) - 0.04\\
e_{2,H_2S} &= 0.1u_2 + 0.1u_2z^{-9} + 0.1\sin(u_2z^{-3} - 0.4(0.6 - u_2z^{-1})^2)\\
e_{3,H_2S} &= 0.36\sin(u_3z^{-7} - u_3z^{-5} + u_3z^{-9} + \tan(u_3 - 1.2u_3z^{-5}))\\
&\quad - 0.14\\
e_{4,H_2S} &= -0.36\tanh\left(\frac{0.11}{u_4}\right)\tanh\left(\left(\frac{0.1}{u_4z^{-7}} - u_4 - u_4z^{-1}\right)^2 - u_4\right)\\
&\quad (u_4z^-3 + 1.16)\\
e_{5,H_2S} &= -\tanh\left(u_5z^{-3} - u_5 + \sin(0.5u_5z^{-7} + 0.5u_5z^{-9} - u_5) + 1.2\right)\\
&\quad + 0.11
\end{aligned}
\tag{1}
$$

$$
\begin{aligned}
e_{1,SO_2} &= 0.27u_1z^{-9} - 0.27u_1z^{-1} - 0.02\sin(2.15in_1z^{-9} - 0.66)\\
&\quad + \tanh\left(u_1 + u_1z^{-5} - 2u_1z^{-9} + 0.13\right)\\
e_{2,SO_2} &= 0.21\tanh\left(0.47 - \sin(u_2z^{-5} + \frac{u_2z^{-9}(u_2z^{-3} - u_2z^{-7}}{u_2z^{-3}}\right)\\
e_{3,SO_2} &= \tanh(\sinh(u_3 - u_3z^{-9} + (u_3z^{-1} - u_3z^{-7})^2\\
&\quad - \exp(-u_3 + 1.7u_3z^{-3}))\\
e_{4,SO_2} &= 0.08\sin((u_4z^{-9})^2) + 0.2\sin\left(1.5u_4z^{-7} - \frac{0.2}{u_4}\right)\\
&\quad - \tanh(u_4 - u_4z^{-3} - u_4z^{-5} + u_4z^{-9})\\
e_{5,SO_2} &= \tanh(0.67u_5 - 0.38u_5z^{-5} - 0.29u_5z^{-9} + 0.45) + 0.17u_5z^{-5}\\
&\quad - 0.17u_5z^{-3}
\end{aligned}
\tag{2}
$$

This shows that the two networks produce slightly different equations which could also be an indication that the input dynamics affect the two concentrations differently. The equations are expressed in terms of the same input u_i, where $i \in [1, 5]$, at different time shifts. For a more compact notation, the temporal shifts are indicated using the unary delay operator z^{-1}, which means that $u_i(t)z^{-k} = u_i(t-k)$, where $k \in [0, 1, 3, 5, 7, 9]$ to reflect the considered time shifts as adopted in [2]. Each equation was selected from a *hall of fame* list ordered by complexity (number of terms). To give preference to simpler equations for better interpretability, the equation that maximizes the index J was selected :

$$
J = \frac{-\Delta\log(MSE)}{\Delta c} \tag{3}
$$

where MSE is the mean squared error, c is the candidate solution complexity, which may be expressed as $\boldsymbol{O} \cdot \boldsymbol{w}$, where $\boldsymbol{O}$ is the set of involved operators and $\boldsymbol{w}$ is the associated cost. The output relationships were discovered using the same set of functions and hyperparameters, with the only modification being the maximum length, set to 50 to allow further exploration of the mathematical search space. The equations for H_2S and SO_2 concentration are presented in Eq. 4, where the terms e_i in the equations, each refer to the relative encoded product of the NN for the five input signals.

$$
\begin{aligned}
[H_2S] &= 0.51\left(\exp\left(\frac{0.4e_3}{1-e_5} - 0.8e_1 + 0.4e_5 + \tan(e_5)\right)\right)^2\\
[SO_2] &= 0.04sinh(e_1 + 0.46) + 0.04tanh^2(e_3) + 0.3 - 0.46(e_5)
\end{aligned}
\tag{4}
$$

To properly compare the NN-aided SR and the plain SR approach, two models were also fit with the same previously introduced hyperparameters.

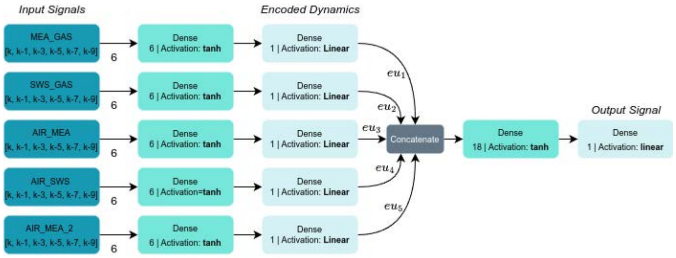

Fig. 1. Block diagram for the utilized NN architecture.

	R^2	$RMSE$
NN	$\mathbf{(0.89, 0.91)}$	$\mathbf{(0.014, 0.0002)}$
SR	$(0.77, 0.86)$	$(0.02, 0.017)$
NN-SR	$(0.89, 0.90)$	$(0.014, 0.014)$

TABLE I
LOSS METRICS FOR THE THREE CONSIDERED APPROACHES ON THE TEST DATASET. THE PERFORMANCES FOR BOTH MODELS ESTIMATING THE H_2S AND THE SO_2 ARE GIVEN IN PARENTHESES.

As shown in Table I and Figure 2, both the NN and NN-supported SR methods show superior performance. It can be seen, especially in the presence of peaks, which are of greater importance for controlling the process the temporal evolution of the $S0_2$ reported in Figure 2 (b) shows a better approximation of the NN-SR in the peak estimation compared to the plain SR. Moreover, the NN and NN-SR predictions show similarities due to the partially shared dynamic encodings. To summarise, the proposed approach makes it possible to develop interpretable soft sensors with comparable performance to other state-of-the-art black-box approaches.

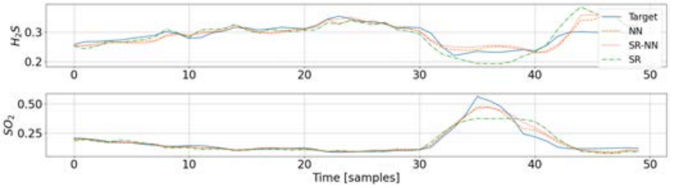

Fig. 2. Predictions of NN, SR, and NN-aided SR on a portion of the test dataset.

REFERENCES

[1] J. R. Koza, *Genetic Programming: On the Programming of Computers by Means of Natural Selection*. Cambridge, USA: MIT Press, 1992.

[2] L. Fortuna, S. Graziani, A. Rizzo, M. G. Xibilia *et al.*, *Soft sensors for monitoring and control of industrial processes*. Springer, 2007, vol. 22.

[3] M. Cranmer, "Interpretable machine learning for science with pysr and symbolicregression.jl," 2023.

[4] M. Cranmer, A. Sanchez-Gonzalez, P. Battaglia, R. Xu, K. Cranmer, D. Spergel, and S. Ho, "Discovering symbolic models from deep learning with inductive biases," 2020.

[5] Y.-C. Bo, P. Wang, X. Zhang, and B. Liu, "Modeling data-driven sensor with a novel deep echo state network," *Chemometrics and Intelligent Laboratory Systems*, vol. 206, p. 104062, 2020.

[6] B. Bidar, F. Shahraki, J. Sadeghi, and M. M. Khalilipour, "Soft sensor modeling based on multi-state-dependent parameter models and application for quality monitoring in industrial sulfur recovery process," *IEEE Sensors Journal*, vol. 18, no. 11, pp. 4583–4591, 2018.

[7] L. Patanè and M. G. Xibilia, "Echo-state networks for soft sensor design in an sru process," *Information Sciences*, vol. 566, pp. 195–214, 2021.

On the Existence of Equilibria in Learning-Based Games

Paolo Scarabaggio, Nicola Mignoni, Raffaele Carli, and Mariagrazia Dotoli

I. INTRODUCTION

Convexity (or concavity) is the cornerstone of equilibrium theory. From the first works by Von Neumann, mathematical elegance and theoretical tractability have steered multi-agent decision-making models in the safe harbor of convexity. Under this assumption, computing equilibria is, in fact, equivalent to convex programming [1].

The search for convexity at all costs has recently gone against the advent of machine learning (ML) with its inherent and pervasive non-convexity [2]. Indeed, ML's attitude of embracing non-convexity has led to groundbreaking advances in significant challenges, such as speech and image recognition, text generation, and many more [3]. Among ML's approaches, deep neural networks (DNNs) have proven to be successful in many prediction tasks, particularly in predicting decisions [4]. Thus, they are the perfect candidates for approximating the behavior of agents in a strategic interaction framework such as a game.

This paper explores and integrates the robustness of game theoretic frameworks in managing conflicts among agents with the capacity of ML approaches, such as DNNs, to capture complex agent behaviors.

II. PRELIMINARIES ON GAME THEORY

Let us consider the standard mathematical setting of non-cooperative games [5]. Thus, let us consider a set of N agents $\mathcal{N}$, indexed by $i \in \mathcal{N} := \{1, ..., N\} \subseteq \mathbb{N}$ each with decision variables $\mathbf{x}_i \in \mathbb{R}^{n_i}$, for some $n_i \in \mathbb{N}$. Moreover, let $n := \sum_{i \in \mathcal{N}} n_i$. We define vector $\mathbf{x}_{-i} := \mathrm{col}(\mathbf{x}_1, \ldots, \mathbf{x}_{i-1}, \mathbf{x}_{i+1}, \ldots, \mathbf{x}_N) \in \mathbb{R}^{n-i}$, where $n_{-i} := n - n_i$, which collects the strategies of all agents but i, as well as vector $\mathbf{x} := \mathrm{col}(\mathbf{x}_1, \ldots, \mathbf{x}_i, \ldots, \mathbf{x}_N) \in \mathbb{R}^n$, collecting the strategy of all agents. Each agent $i \in \mathcal{N}$ tries to minimize a (possibly non-convex) cost function $f_i(\mathbf{x}_i, \mathbf{x}_{-i}) : \mathbb{R}^n \times \mathbb{R}^{n-n_i} \to \mathbb{R}$ by choosing a strategy in a (possibly non-convex) feasible set $\mathbf{x}_i \in \Omega_i \subseteq \mathbb{R}^n$. One can thus define the so-called Nash equilibrium problem (NEP) as the following N interdependent optimization problem:

$$\forall i \in \mathcal{N}: \quad \underset{\mathbf{x}_i \in \Omega_i}{\text{minimize}} \ f_i(\mathbf{x}_i, \mathbf{x}_{-i}). \tag{1}$$

A standard requirement, often introduced in related works, is that for each $i \in \mathcal{N}$ and for every $\mathbf{x}_{-i}$, the function $f_i(\cdot, \mathbf{x}_{-i})$ is convex and continuously differentiable. This requirement is necessary for setting up many fixed-point formulations used to demonstrate the existence and convergence of Nash equilibria [6].

III. LEARNING-BASED NASH GAMES

The applicability of multi-agent models as in (1), is limited by (i) the possibility of finding suitable functions that realistically model agents' preferences and (ii) constraining their formulation to be convex. Despite the challenging task of defining a function that realistically approximates agents' preferences, several applications allow for measuring agents' behavior in the sense of evaluating their response to a given environment whose state depends on given parameters and other agents' decisions.

Thus, let $\mathcal{E} := \mathcal{S} \times \Omega$ abstract an environment whose state is (uniquely) determined by a certain scenario $\mathbf{s} \in \mathcal{S} \subset \mathbb{R}^m$, and the collective actions taken by the agents $\mathbf{x} \in \Omega$. From the perspective of agent $i \in \mathcal{N}$, however, only set $\mathcal{E}_i := \mathcal{S}_i \times \Omega_{-i}$ is accessible, represents the information agent $i \in \mathcal{N}$ acquires regarding scenario $\mathbf{s} \in \mathcal{S}$. Moreover, let $\Omega_{-i} := \Omega_1 \cap \cdots \cap \Omega_{i-1} \cap \Omega_{i+1} \cap \cdots \cap \Omega_N$ constitute the set of all strategies but the one of player $i \in \mathcal{N}$. Formally, we can introduce an observer which maps $(\mathbf{s}, \mathbf{x}) \mapsto \mathrm{col}(g_i(\mathbf{s}), h_i(\mathbf{x}_{-i}))$ for some $h_i : \Omega_{-i} \to \mathbb{R}^{p_i}$. The latter represents the information quota that agent i receives regarding other agents strategies. Therefore, each agent has a possibly limited view of the environment, albeit a full knowledge of some function of the other's decisions. In full-information games, one has $h(\mathbf{x}_{-i}) = \mathbf{x}_{-i}$.

Such a formulation allows us to define the training set and target vector against which each agent $i \in \mathcal{N}$ can develop its response strategy. Equipped with a dataset $\mathcal{T}_i$, we can define a feed-forward DNN composed of layers $l \in \mathcal{L} := \{1, ..., |\mathcal{L}|\} \subseteq \mathbb{N}$. The output of each layer $\mathbf{x}_l \in \mathbb{R}^{|\mathcal{P}_l|}$ can be computed as:

$$\mathbf{x}_l = \Phi_l\left(\mathbf{W}_l \mathbf{x}_{l-1} + \mathbf{b}_l\right), \quad \forall l \in \mathcal{L} \tag{2}$$

where $\mathbf{W}_l \in \mathbb{R}^{|\mathcal{P}_l| \times |\mathcal{P}_{l-1}|}$ is the weight matrix, $\mathbf{b}_l \in \mathbb{R}^{|\mathcal{P}_l|}$ the bias vector and $\Phi_l(\cdot) : \mathbb{R}^{|\mathcal{P}_l|} \to \mathbb{R}^{|\mathcal{P}_l|}$ the activation function of the layer. By setting $\mathbf{x}_0 \in \mathbb{R}^{|\mathcal{P}_0|}$ as the input and $\mathbf{x}_{|\mathcal{L}|} \in \mathbb{R}^{|\mathcal{P}_{|\mathcal{L}|}|}$ as the output of the DNN, we can define the overall input-output relationship of the network in the following form:

$$\mathbf{x}_{|\mathcal{L}|} = \Phi\left(\mathbf{x}_0\right) \tag{3}$$

where $\Phi(\cdot) = \Phi_{|\mathcal{L}|} \circ \Phi_{|\mathcal{L}|-1} \circ \cdots \circ \Phi_1(\cdot)$.

Thus we can approximate the behavior of agent $i \in \mathcal{N}$ as:

$$\forall i \in \mathcal{N}: \quad \mathbf{x}_i = \mathrm{proj}_{\Omega_i}\left\{\Phi_i\left(\begin{bmatrix} g_i(\mathbf{s}) \\ h_i(\mathbf{x}_{-i}) \end{bmatrix}\right)\right\}. \tag{4}$$

where $\mathbf{x}_i$ is the response of agent $i \in \mathcal{N}$ yielded by the feed-forward DNN when the actions of other agents are $\mathbf{x}_{-i} \in \mathbb{R}^{n-n_i}$ under scenario $\mathbf{s} \in \mathcal{S}$.

Remark 1. *Once trained,* (4) *becomes an alternative approach to evaluating* $\mathbf{x}_i = \mathrm{argmin}_{\mathbf{x}_i \in \Omega_i} f_i(\mathbf{x}_i, \mathbf{x}_{-i})$*, as in* (1).

P. Scarabaggio, N. Mignoni, R. Carli, and M. Dotoli are with the Department of Electrical and Information Engineering of the Polytechnic of Bari, Italy. (e-mail: {`paolo.scarabaggio, nicola.mignoni, raffaele.carli, mariagrazia.dotoli`}@poliba.it).

IV. EXISTENCE AND UNIQUENESS OF EQUILIBRIA

Having redefined agents' behavior, the standard setting for Nash equilibria does not hold here. Thus, let us search for different equilibrium conditions and introduce a notion of *Learning-Based Nash Equilibrium* (LBNE).

Definition 1 (Learning-Based Nash Equilibrium)**.** *A LBNE is a strategy profile* $\mathbf{x}^* \in \Omega$ *such that, for any* $\mathbf{s} \in \mathcal{S}$*:*

$$\forall i \in \mathcal{N}: \quad \mathbf{x}_i^* = \operatorname{proj}_{\Omega_i}\left\{\Phi_i\left(\begin{bmatrix} g_i(\mathbf{s}) \\ h_i(\mathbf{x}_{-i}^*)\end{bmatrix}\right)\right\}. \tag{5}$$

Next, we argue that an LBNE equilibrium exists under the following assumptions.

Assumption 1. *For each* $i \in \mathcal{N}$ *the feed-forward DNN* $\Phi_i(\cdot)$*, approximating the agent response, is Lipschitz continuous with constant* γ_i*, while* $h_i : \Omega_{-i} \to \mathbb{R}^{p_i}$ *is 1-Lipschitz continuous.*

Proposition 1 (Existence)**.** *Every game satisfying Assumption 1, has at least one LBNE.*

Proposition 2 (Uniqueness)**.** *Every game satisfying Assumption 1 with* $\left(\sum_{i\in\mathcal{N}} \gamma_i^2\right)^{1/2} < 1$ *has only one LBNE.*

Requiring the feed-forward DNN $\Phi_i(\cdot)$ to be Lipschitz continuous with constant γ_i is equivalent to requiring that for each layer $l_i \in \mathcal{L}_i$, given $\mathbf{y}_l, \mathbf{z}_l \in \mathbb{R}^{|\mathcal{P}_l|}$, there exists $\gamma_l \in \mathbb{R}_{\geq 0}$ such that $\|\left(\mathbf{W}_l \mathbf{y}_{l-1} + \mathbf{b}_l\right) - \left(\mathbf{W}_l \mathbf{z}_{l-1} + \mathbf{b}_l\right)\| \leq \gamma_l \|\mathbf{y}_{l-1} - \mathbf{z}_{l-1}\|$, and that given $\mathbf{y}_l, \mathbf{z}_l \in \mathbb{R}^{|\mathcal{P}_l|}$ it holds $\|\Phi_l\left(\mathbf{y}_{l-1}\right) - \Phi_l\left(\mathbf{z}_{l-1}\right)\| \leq \|\mathbf{y}_{l-1} - \mathbf{z}_{l-1}\|$.

V. ILLUSTRATIVE EXAMPLE

As an illustrative example, let us consider an energy community model comprising smart energy users. Each agent $i \in \mathcal{N}$ behaves selfishly, choosing its energy consumption strategy $\mathbf{x}_i$ from a convex and compact feasible set Ω_i, i.e., $\mathbf{x}_i \in \Omega_i$. The energy cost in the community follows a dynamic pricing scheme, where the cost incurred by agent $i \in \mathcal{N}$ depends on the strategies of other agents $\mathbf{x}_{-i}$ [7]. Specifically, we assume that the energy cost for each consumer is an aggregation of other agents' strategies and thus can be computed as:

$$h_i(\mathbf{x}_{-i}) := \sum_{j\in\mathcal{N}\setminus\{i\}} P_{i,j}\mathbf{x}_j \tag{6}$$

where $P_{i,j}$ indicates the strength of the influence of agent $j \in \mathcal{N}$ on agent $i \in \mathcal{N}$, with 0 denoting no influence.

To train the DNNs approximating agents' behavior, we utilize data from the *Low Carbon London* project [8]. The dataset includes energy consumption in kWh per half hour, unique household identifiers, dates, and times for approximately 1,100 customers subjected to dynamic energy prices. For the training process, we select 100 customers from the dataset. We train a different DNN for each customer using timestamp information and the corresponding energy price as input features. The target value for each DNN is the respective customer's energy consumption. Thus, each DNN aims to approximate a customer's behavior in deciding how much energy to use in a specific time slot based on the energy price.

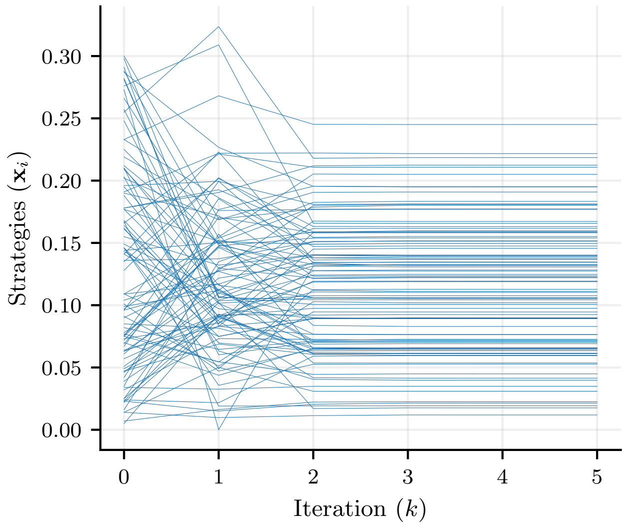

Figure 1. Strategy convergence of agents using Algorithm 1.

We employ DNNs composed of 5 linear layers with 64 neurons each and fullsort activation functions.

In Fig. 1, we show the convergence of strategies to an LBNE using the *Picard-Banach Distributed Scheme*.

VI. CONCLUSION

This paper challenges the conventional reliance on convexity in game theory, recognizing the limitations it imposes when agents' utility functions cannot be adequately represented preserving this assumption. Unlike conventional approaches that model agents' behaviors with convex cost functions, we propose using deep neural networks (DNNs) to compute the agents' response actions. Introducing a technical assumption on parameters of the DNN, we establish the existence and uniqueness of equilibria.

As a future work, it would be interesting to extend the proposed framework to games with coupling constraints.

REFERENCES

[1] B. Brooks and P. J. Reny, "A canonical game–nearly 75 years in the making–showing the equivalence of matrix games and linear programming," *Available at SSRN 3851583*, 2021.

[2] C. Jin, P. Netrapalli, R. Ge, S. M. Kakade, and M. I. Jordan, "On nonconvex optimization for machine learning: Gradients, stochasticity, and saddle points," *Journal of the ACM (JACM)*, vol. 68, no. 2, pp. 1–29, 2021.

[3] A. Maier, C. Syben, T. Lasser, and C. Riess, "A gentle introduction to deep learning in medical image processing," *Zeitschrift für Medizinische Physik*, vol. 29, no. 2, pp. 86–101, 2019.

[4] A. Rosenfeld and S. Kraus, "Predicting human decision-making," in *Predicting Human Decision-Making: From Prediction to Action*. Springer, 2018, pp. 21–59.

[5] C. De Persis and S. Grammatico, "Distributed averaging integral nash equilibrium seeking on networks," *Automatica*, vol. 110, p. 108548, 2019.

[6] J. F. Nash Jr, "Equilibrium points in n-person games," *Proceedings of the national academy of sciences*, vol. 36, no. 1, pp. 48–49, 1950.

[7] D. Paccagnan, B. Gentile, F. Parise, M. Kamgarpour, and J. Lygeros, "Distributed computation of generalized nash equilibria in quadratic aggregative games with affine coupling constraints," in *2016 IEEE 55th conference on decision and control (CDC)*. IEEE, 2016, pp. 6123–6128.

[8] "Low Carbon London - UKPN Innovation," Oct. 2023, [Online; accessed 21. Mar. 2024]. [Online]. Available: https://innovation.ukpowernetworks.co.uk/projects/low-carbon-london

Sample Efficient Certification of Discrete-Time Barrier Functions

Sampath Kumar Mulagaleti, Andrea Del Prete

***Abstract*— We present a sample-efficient approach to certify barrier functions of discrete-time dynamical systems. Our approach divides the 0-sublevel set of the candidate barrier function in multiple segments, and derives sampling resolution bounds in each segment to verify the barrier function with a user-specified decay rate.**

I. INTRODUCTION

We develop a procedure to verify barrier functions for discrete-time dynamical systems of the form $x^+ = f(x)$ with measurable state $x \in \mathbb{R}^n$. A function $h : \mathbb{R}^n \to \mathbb{R}$ is a barrier function if there exists some scalar function $\alpha : \mathbb{R} \to \mathbb{R}$ verifying $|\alpha(y)| \in (0, |y|)$ if $y \neq 0$ and $\alpha(0) = 0$, along with with a set $D \subset \mathbb{R}^n$ satisfying

$$h(f(x)) - h(x) \leq -\alpha(h(x)), \qquad \forall\ x \in D. \tag{1}$$

Then, $S(b) := \{x : h(x) \leq b\}$ is an invariant set for any $b \geq 0$ verifying $S(b) \subseteq D$. The region $S(0)$ is attractive, and $x_0 \in S(0)$ implies $x_t \in S(0)$ for all $t \geq 0$. If the system is subject to constraints $x \in X$, then h is a *safe* barrier function if $S(0) \subseteq X \cap D$.

We present our discussion for the linear function $\alpha(y) := \alpha y$ defined with some decay rate $\alpha \in (0, 1)$. Barrier functions can be synthesized by solving variants of the robust feasibility problem

$$\text{Find } h : \begin{cases} S(0) \subseteq X, \\ S(0) \subseteq \{x : h(f(x)) \leq (1-\alpha)h(x)\}. \end{cases}$$

Unfortunately, except in specific settings such as polynomial parameterizations, e.g., [2], solving the synthesis problem exactly is intractable. This necessitates the adoption of sampling-based approaches for solving the synthesis problem, followed by a verification step to develop safety certificates, e.g., [6], [7]. Broadly, verification approaches can be divided into three categories: Generalizing from finite samples using Lipschitz constants, e.g., [5]; analyzing reachability of the candidate functions, e.g., [8]; and counter-example synthesis, e.g., [4]. We focus on the first approach, i.e., based on verifying the inclusions of the synthesis problem through sampling, and generalizing the results using Lipschitz constants. We assume that the inclusion $S(0) \subseteq X$ is verified, and target the verification of the inclusion

$$h(x) \leq (1-\alpha)h(x), \qquad \forall\ x \in S(0). \tag{2}$$

The proposed work hinges on the following rationale:
1) Typically, we encounter closed-loop systems of the form $x^+ = \bar{f}(x, \nu(x))$, where $\nu(\cdot)$ is a feedback controller that results from an optimization problem, e.g., a Model Predictive Controller (MPC), such that computing the control input at a given state requires solving an optimization problem. Hence, our approach focuses on sample efficiency while verifying (2).
2) A candidate function h is a barrier function if it satisfies (1) for any $\alpha \in (0, 1)$. Hence, we exploit a relaxation of this constant in a spirit similar to [1].

II. APPROACH

Suppose we are given a candidate barrier function $h(x)$ and $\alpha \in (0, 1)$. Defining $\gamma_0 := \min_{x \in S(0)} h(x)$, consider a sequence of scalars $\{\gamma_0, \cdots, \gamma_q\}$ verifying $\gamma_{i-1} < \gamma_i \leq 0$ with $\gamma_q = 0$. Using these scalars, define the sets $C_i := \{x : h(x) \in (\gamma_{i-1}, \gamma_i]\}$, and suppose we sample $\{x^i_j \in C_i, j \in \{1, \cdots, N_i\}\}$ for all i. Verify

$$h(f(x^i_j)) - (1-\alpha)h(x^i_j) \leq -\delta,\ \forall\ j \in \{1, \cdots, N_i\} \tag{3}$$

for each $i \in \{1, \cdots, q\}$ for some $\delta \geq 0$.
Problem: Derive conditions on $\{\gamma_0, \cdots, \gamma_q\}$ and samples $\{x^i_j \in C_i, j \in \{1, \cdots, N_i\}\}$ under which verification of (3) implies h is a barrier function.
We tackle this problem using the fact that h is a barrier function if there exists some $\bar{\alpha} \in (0, 1)$ such that

$$r(x) := h(f(x)) - h(x) \leq -\bar{\alpha}h(x), \qquad \forall\ x \in C_i, i \in \{1, \cdots, q\}. \tag{4}$$

Observe that the scalar $\bar{\alpha}$ is not necessarily equal to the decay constant α used while synthesizing the function $h(x)$. As we will see, $\bar{\alpha} > \alpha$, since it accounts for robustness of verification through sampling.

Proposition 1: Consider any arbitrary sequence $\{\gamma_0, \cdots, \gamma_q\}$, and suppose that the samples verifying (3) satisfy the epsilon-net condition

$$\forall\ x \in C_i,\ \exists\ j \in \{1, \cdots, N_i\}\ :\ \|x - x^i_j\| \leq \epsilon_i \tag{5}$$

for all $i \in \{1, \cdots, q\}$. Then, $h(x)$ is a barrier function verifying (4) with $\bar{\alpha} := \alpha/(1-\mu)$ for any $\mu \in (0, 1-\alpha)$ if the sampling resolution parameter ϵ_i verifies

$$\epsilon_i \leq \frac{\delta}{L_r + \alpha L_h} - \frac{1}{L_r + \alpha L_h}\left(\frac{\alpha\mu}{1-\mu}\right)\gamma_i \tag{6}$$

The authors are with University of Trento, Italy.

for all $i \in \{1, \cdots, q\}$, where L_h and L_r are Lipschitz constants of the function $h(x)$ and $r(x)$ respectively. ■

Proposition 1 presents a way to verify if $h(x)$ is a valid barrier function, where μ is the *verification accuracy* parameter. While relaxations of this form have been used previously to verify stability from data, to the best of our knowledge, this is the first application to use them for verifying invariance. By choosing μ close to zero, we have $\bar{\alpha}$ close to 1: this choice can be interpreted as being interested in verifying invariance of the set $S(0)$. On the other hand, by choosing μ close to $1-\alpha$, we have $\bar{\alpha}$ close to α, such that we would be verifying contraction property of the barrier function. A procedure that exploits Proposition 1 is outlined in Algorithm 1.

Algorithm 1 Barrier function verifier

```
Require: $f(x)$, $h(x)$, $\alpha \in (0,1)$, $\mu \in (0, 1-\alpha)$, $\delta \geq 0$
  1. Estimate Lipschitz constants $L_h$ and $L_f$ of $f$ and $f$, set $L_r = L_h L_f + L - h$
  2. Select $\{\gamma_0, \cdots, \gamma_q\}$
  3. Compute $\{\epsilon_1, \cdots, \epsilon_q\}$ verifying (6)
  4. Sample $\{x_j^i \in C_i, j \in \{1, \cdots, N_i\}\}$ verifying (5)
  if (3) is verified for each $i \in \{1, \cdots, q\}$ then
      Return Verification success
  else
      Return Verification fail
  end if
```

For an efficient implementation of Algorithm 1, the research questions being explored are:

1) Estimating L_h and L_f: Currently, a sampling-based approach is adopted. Other approaches can potentially be explored to estimate these constants, e.g., [3].

2) Selecting q and γ such that the number of samples is minimized: While a linear interpolation between γ_0 and q is a viable option, current investigation focuses on exploiting geometry of the underlying set.

3) Sampling from sets C_i: Constructing ϵ-nets verifying (5) is currently done using rejection sampling. While this involves the computationally inexpensive evaluation of $h(x)$, the proportion of number of samples rejected can be very high. Procedures to identify *better* sets to perform rejection sampling can be developed to improve efficiency. Probabilistic approaches that give lower-bounds on the number of samples to synthesize ϵ-nets can be used to provide confidence-based guarantees.

III. PRELIMINARY NUMERICAL RESULTS

For simplicity of presentation, we consider the linear system $x^+ = \begin{bmatrix} 1 & 0.2 \\ -0.2 & 0.8 \end{bmatrix} x + \begin{bmatrix} 0 \\ 0.2 \end{bmatrix} u$ equipped with the nonlinear feedback controller $u = \nu(x)$, where

$$\nu(x) := \arg\min_u \ell(u; x)) \text{ s.t. } h(x^+) \leq (1-\alpha)h(x) - \delta$$

where $\ell(u;x) := \|u - Kx\|_2^2$, $h(x)$ is a single-layered neural network with 8 hidden softmax units. The matrix $K \in \mathbb{R}^{1\times 2}$ is the LQR feedback gain corresponding to identity matrices Q and R. We select $\alpha = 0.2$ and $\delta = 0.01$. Note that $\nu(x)$ is the solution of a nonlinear optimization problem, and our goal is to verify if $h(x)$ is a barrier function. To this end, we simulate Algorithm 1 with $\mu = 0.4$, such that $\bar{\alpha} = 0.33$. Using a data-driven procedure, we identify the Lipschitz constants $L_f = 1.668$ and $L_h = 2.254$. Computing $\gamma_0 = -2.729$, we then estimate the number of samples $N_{\text{tot}} = \sum_{i=1}^{q} N_i$ required to satisfy (5) for a certified verification:

q	1	2	3	4	5
$N_{\text{tot}}(\times 10^6)$	3.75	2.12	1.48	1.14	0.93
q	6	7	8	9	10
$N_{\text{tot}}(\times 10^6)$	0.79	0.69	0.61	0.56	0.51

Note that $q = 1$ corresponds to a single set, i.e., $C_1 = S(0)$. As expected, we observe a reduction in the number of samples required for verification as q increases. A study of whether there exists some $\hat{q}$ after which N_{tot} increases is a subject of future study.

REFERENCES

[1] Nicholas Boffi, Stephen Tu, Nikolai Matni, Jean-Jacques Slotine, and Vikas Sindhwani. Learning stability certificates from data. In Jens Kober, Fabio Ramos, and Claire Tomlin, editors, Proceedings of the 2020 Conference on Robot Learning, volume 155 of Proceedings of Machine Learning Research, pages 1341–1350. PMLR, 16–18 Nov 2021.

[2] Andrew Clark. Verification and synthesis of control barrier functions. In 2021 60th IEEE Conference on Decision and Control (CDC), pages 6105–6112, 2021.

[3] Mahyar Fazlyab, Alexander Robey, Hamed Hassani, Manfred Morari, and George J. Pappas. Efficient and accurate estimation of lipschitz constants for deep neural networks, 2023.

[4] Andrea Peruffo, Daniele Ahmed, and Alessandro Abate. Automated and Formal Synthesis of Neural Barrier Certificates for Dynamical Models. arXiv e-prints, page arXiv:2007.03251, July 2020.

[5] Spencer M. Richards, Felix Berkenkamp, and Andreas Krause. The lyapunov neural network: Adaptive stability certification for safe learning of dynamical systems. In Aude Billard, Anca Dragan, Jan Peters, and Jun Morimoto, editors, Proceedings of The 2nd Conference on Robot Learning, volume 87 of Proceedings of Machine Learning Research, pages 466–476. PMLR, 29–31 Oct 2018.

[6] Jacob Steinhardt and Russ Tedrake. Finite-time regional verification of stochastic non-linear systems. The International Journal of Robotics Research, 31(7):901–923, May 2012.

[7] Hongchao Zhang, Junlin Wu, Yevgeniy Vorobeychik, and Andrew Clark. Exact verification of relu neural control barrier functions. In A. Oh, T. Naumann, A. Globerson, K. Saenko, M. Hardt, and S. Levine, editors, Advances in Neural Information Processing Systems, volume 36, pages 5685–5705. Curran Associates, Inc., 2023.

[8] Huan Zhang, Tsui-Wei Weng, Pin-Yu Chen, Cho-Jui Hsieh, and Luca Daniel. Efficient neural network robustness certification with general activation functions. In S. Bengio, H. Wallach, H. Larochelle, K. Grauman, N. Cesa-Bianchi, and R. Garnett, editors, Advances in Neural Information Processing Systems, volume 31. Curran Associates, Inc., 2018.

Stability of Nonexpansive Monotone Systems and Application to Recurrent Neural Networks

Diego Deplano, *Member, IEEE*, Mauro Franceschelli, *Senior Member, IEEE*, Alessandro Giua, *Fellow, IEEE*

***Abstract*— This abstract presents a novel result for continuous-time smooth monotone systems: if the system is nonexpansive w.r.t. a diagonally weighted infinity norm and if there is at least one equilibrium point, then all trajectories converge to one of them. Differently from the current literature trend, the system is not required to be contractive but merely nonexpansive, thus allowing for multiple equilibrium points. Sufficient conditions on the vector field are provided to verify nonexpansiveness, which are then applied in the context of Recurrent Neural Networks (RNNs), thus identifying a class monotone RNNs whose trajectories are convergent even though their dynamics is not contractive.**

I. INTRODUCTION

Contraction theory is becoming a popular framework, providing powerful tools for establishing stability properties of nonlinear dynamical systems. In general, a (time-invariant) dynamical system is said to be contractive if every two trajectories converge to one another, thus resulting in systems with a unique equilibrium. On the other hand, convergence of trajectories toward equilibrium points is still possible when the system is not contractive but only nonexpansive, that is every two trajectories do not diverge from one another. It is clear that the class of nonexpansive systems is broader than contractive systems, naturally allowing for multiple equilibrium points. While classical approaches mostly focus on contraction with respect to the Euclidean ℓ_2-norm, recent works have shown that the stability of monotone systems can be studied for contractive systems [1] and nonexpansive systems [2] with respect to non-Euclidean norms. Monotone systems are such that any pair of ordered initial conditions give rise to ordered trajectories [3]. We have recently shown that smooth monotone dynamical systems satisfy a stricter notion of monotonicity called *type-K monotonicity* [2]. The main contribution of this abstract is to show how type-K monotonicity can be leveraged to prove that [4]:

- Trajectories of smooth monotone systems that are nonexpansive w.r.t. a diagonally weighted sup-norm converge toward equilibrium points, if any exist (Proposition 1);
- Smooth monotone systems are nonexpansive if and only if they are subhomogeneous (Theorem 1);

We also apply our novel results to the convergence analysis of Recurrent Neural Networks (RNNs), with a focus on Hopfield and firing-rate dynamics [2]. In particular, we prove that:

- Monotonicity and subhomogeneity of these neural networks ensure convergence of their state trajectories even if their dynamics are not contractive (Theorem 2).

II. MAIN RESULTS

We consider continuous-time autonomous *dynamical systems* $\dot{\boldsymbol{x}}(t) = f(\boldsymbol{x}(t))$, with $\boldsymbol{x}(t) \in \mathcal{X}$ denoting the *state* of the system at time $t \in \mathbb{R}$ and $\mathcal{X} \subseteq \mathbb{R}^n$ denotes the *state space*.

Assumption 1: *The vector field $f : \mathcal{X} \to \mathbb{R}^n$ is continuously differentiable and the state space $\mathcal{X} \subseteq \mathbb{R}^n$ is convex.*

Under Assumption 1, the Jacobian of the vector field f is denoted by $Df(x)$. A dynamical system can be described in terms of its flow $\varphi(t, \boldsymbol{x}_0)$ denoting the state at time t as

$$\boldsymbol{x}(t) = \varphi(t, \boldsymbol{x}_0), \quad \forall t \geq 0, \quad \text{with} \quad \boldsymbol{x}(0) = \boldsymbol{x}_0.$$

Definition 1 (Nonexpansiveness and contractivity): *Let $\|\cdot\|$ be a norm in $\mathbb{R}^n$. A system on $\mathcal{X} \subseteq \mathbb{R}^n$ is nonexpansive if for all $\boldsymbol{x}_0, \boldsymbol{y}_0 \in \mathcal{X}$ it holds*

$$\|\varphi(t, \boldsymbol{x}_0) - \varphi(t, \boldsymbol{y}_0)\| \leq \|\boldsymbol{x}_0 - \boldsymbol{y}_0\|, \qquad t \geq 0.$$

If the inequality holds strictly, the system is contractive.

Definition 2 (Monotonicity): *A system on $\mathcal{X} \subseteq \mathbb{R}^n$ is "monotone" if for all $\boldsymbol{x}_0, \boldsymbol{y}_0 \in \mathcal{X}$ it holds:*

$$\boldsymbol{x}_0 \leq \boldsymbol{y}_0 \Rightarrow \varphi(t, \boldsymbol{x}_0) \leq \varphi(t, \boldsymbol{y}_0), \quad \forall t \geq 0.$$

Definition 3 (Type-K Monotonicity): *A system on $\mathcal{X} \subseteq \mathbb{R}^n$ is "type-K monotone" if it is monotone and if for all $\boldsymbol{x}_0, \boldsymbol{y}_0 \in \mathcal{X}$ and for all $i = 1, \ldots, n$ it holds:*

$$\boldsymbol{x}_0 \leq \boldsymbol{y}_0 \, \wedge \, x_{0,i} < y_{0,i} \Rightarrow \varphi_i(t, \boldsymbol{x}_0) < \varphi_i(t, \boldsymbol{y}_0), \quad \forall t \geq 0.$$

We have recently shown in [2] that for continuous-time smooth dynamical systems, monotonicity and type-K monotonicity are equivalent properties, and they can be verified by the sign structure of the Jacobian of the vector field.

Lemma 1: *For a system $\dot{\boldsymbol{x}}(t) = f(\boldsymbol{x}(t))$ under Assumption 1, the following statements are equivalent:*

(a) The system is monotone;
(b) The system is type-K monotone;
(c) The Jacobian $Df(\boldsymbol{x})$ is Metzler for all $\boldsymbol{x} \in \mathcal{X}$.

A nice feature of type-K monotonicity is that it allows to prove convergence toward equilibrium points for systems that admit at least one equilibrium point [4] and are nonexpansive w.r.t. a weighted sup-norm

$$\|\boldsymbol{x}\|_{\infty,[\boldsymbol{\eta}]^{-1}} = \max_{i=1,\cdots,n} \eta_i^{-1} |x_i|.$$

Work supported by project e.INS- Ecosystem of Innovation for Next Generation Sardinia (cod. ECS 00000038) funded by the Italian Ministry for Research and Education (MUR) under the National Recovery and Resilience Plan (NRRP) - MISSION 4 COMPONENT 2, "From research to business" INVESTMENT 1.5, "Creation and strengthening of Ecosystems of innovation" and construction of "Territorial R& D Leaders".

Diego Deplano, Mauro Franceschelli, and Alessandro Giua are with the DIEE, University of Cagliari, 09123, Italy. Emails: {`diego.deplano`, `mauro.franceschelli,giua`}`@unica.it`.

Proposition 1: *Consider a system $\dot{\boldsymbol{x}}(t) = f(\boldsymbol{x}(t))$ under Assumption 1 satisfying the following:*

- *the system is monotone nonexpansive w.r.t. $\|\cdot\|_{\infty,[\boldsymbol{\eta}]^{-1}}$;*
- *the set of equilibrium points $\mathcal{F}(f) \neq \emptyset$ is not empty.*

Then all equilibrium points are stable and each trajectory converges asymptotically to one of them.

The proof of this result is hinged on the one-to-one relation between systems that are nonexpansive w.r.t. $\|\cdot\|_{\infty,[\boldsymbol{\eta}]^{-1}}$ and those that are nonexpansive w.r.t. $\|\cdot\|_{\infty}$, which by [5, Lemma 2.7.2] are "$\boldsymbol{\eta}$-subhomogeneous" with $\boldsymbol{\eta} = \mathbf{1}$.

Definition 4 (Subhomogeneity): *A dynamical system on $\mathcal{X} \in \mathbb{R}^n$ is "$\boldsymbol{\eta}$-subhomogeneous", where $\boldsymbol{\eta} \in \mathbb{R}^n_+$ is a positive vector, if for all initial conditions $\boldsymbol{x}_0 \in \mathcal{X}$ it holds:*

$$\varphi(t, \boldsymbol{x}_0 + \alpha\boldsymbol{\eta}) \leq \varphi(t, \boldsymbol{x}_0) + \alpha\boldsymbol{\eta}, \qquad forall \alpha \geq 0,\ \forall t \geq 0.$$

Since under Assumption 1 monotonicity and type-K monotonity are equivalent by Lemma 1, then type-K monotonicity and $\mathbf{1}$-subhomogeneity ensure stability of equilibrium points [2, Lemma 4] and convergence of all trajectories to equilibrium points [2, Theorem 1]. As this proof sketch may suggest, subhomogeneity is necessary and sufficient for nonexpansiveness [4].

Theorem 1: *Consider a monotone system $\dot{\boldsymbol{x}}(t) = f(\boldsymbol{x}(t))$ under Assumption 1. Then, it is $\boldsymbol{\eta}$-subhomogeneous if and only if it is nonexpansive w.r.t. $\|\cdot\|_{\infty,[\boldsymbol{\eta}]^{-1}}$.*

We also provide two equivalent necessary and sufficient conditions for $\boldsymbol{\eta}$-subhomogeneity for monotone systems [4].

Lemma 2: *For a monotone system $\dot{\boldsymbol{x}}(t) = f(\boldsymbol{x}(t))$ under Assumption 1, the following statements are equivalent:*

(a) the system is $\boldsymbol{\eta}$-subhomogeneous;
(b) the vector field satisfies $f(\boldsymbol{x}+\alpha\boldsymbol{\eta}) \leq f(\boldsymbol{x})$, $\forall \boldsymbol{x} \in \mathcal{X}, \alpha \geq 0$;
(c) the Jacobian satisfies $Df(\boldsymbol{x})\boldsymbol{\eta} \leq \mathbf{0}$, $\forall \boldsymbol{x} \in \mathcal{X}$.

III. Stability of Nonexpansive Monotone RNNs

We consider two models of RNNs [6], the Hopfield and the firing-rate models, with dynamics

$$\dot{\boldsymbol{x}}(t) = f_{\mathrm{H}}(\boldsymbol{x}(t)) := -C\boldsymbol{x}(t) + A\Phi(\boldsymbol{x}(t)) + \boldsymbol{b}, \qquad (1)$$

$$\dot{\boldsymbol{x}}(t) = f_{\mathrm{FR}}(\boldsymbol{x}(t)) := -C\boldsymbol{x}(t) + \Phi(A\boldsymbol{x}(t) + \boldsymbol{b}), \qquad (2)$$

where $C \in \mathbb{R}^{n\times n}$ is a positive diagonal matrix, $A \in \mathbb{R}^{n\times n}$, $\boldsymbol{b} \in \mathbb{R}^n$ is a constant input, and $\Phi : \mathbb{R}^n \mapsto \mathbb{R}^n$ is an activation function satisfying Assumption 2.

Assumption 2: *Activation functions are diagonal, i.e., $\Phi(\boldsymbol{x}) = [\phi_1(x_1), \cdots, \phi_n(x_n)]^\top$ where each $\phi_i : \mathbb{R} \mapsto \mathbb{R}$ is continuously differentiable and globally Lipschitz, i.e., there exists finite $d_1 \leq d_2$ such that for all $i = 1, \ldots, n$ it holds*

$$\frac{d}{dx}\phi_i(x) \in [d_1, d_2], \qquad \forall x \in \mathbb{R},$$

and the Lipschitz constant is given by $\overline{d} = \max\{|d_1|, |d_2|\}$

We have the following result [4].

Theorem 2: *Consider Hopfield and firing-rate neural networks as in eqs.* (1)-(2) *with activation function satisfying Assumption 2. Let $A_\star = \min\{d_1 A, d_2 A\}$ and $A^\star = \max\{d_1 A, d_2 A\}$ satisfy the following conditions:*

a) $A_\star$ is Metzler (monotonicity);
b) $\exists \boldsymbol{\eta} \in \mathbb{R}^n_+ :\ (A^\star - C)\boldsymbol{\eta} \leq \mathbf{0}$ ($\boldsymbol{\eta}$-subhomogeneity).

Then, all their trajectories converge to some equilibrium point, if any exists.

As an example, consider a Hopfield or a firing-rate RNN with dynamics ruled by

$$C = I, \quad A = \begin{bmatrix} 0 & 0.5 \\ 2 & 0 \end{bmatrix}, \quad \phi(x) = \tanh(x),$$

where Assumption 2 is satisfied with $d_1 = 0$ and $d_2 = 1$. The system satisfies all conditions of Theorem 2:

- Assumption 1 is satisfied because the activation function is the continuously differentiable hyperbolic tangent;
- The system is monotone since the Jacobian $Df(\boldsymbol{x}_0) \geq -C$ is Metzler for any $\boldsymbol{x}_0 \in \mathbb{R}^n$ according to Lemma 1, because C is diagonal.
- The system is $\boldsymbol{v}_1$-subhomogeneous according to Lemma 2, because the Jacobian satisfies $Df(\boldsymbol{x}_0)\boldsymbol{v}_1 \leq (A - C)\boldsymbol{\eta} = A\boldsymbol{v}_1 - C\boldsymbol{v}_1 = \boldsymbol{v}_1 - \boldsymbol{v}_1 = \mathbf{0}$

This means that all trajectories converge to some equilibrium point, even though the system is not contractive (cfr. [6]) but merely nonexpansive w.r.t. to the $\|\cdot\|_{\infty,[\boldsymbol{\eta}]^{-1}}$ for $\boldsymbol{\eta} = \boldsymbol{v}_1$ where $\boldsymbol{v}_1 = [1,\ 2]^\top$ is the eigenvector of A associated with the eigenvalue $\lambda_1 = 1$, according to Theorem 1.

Remark 1: *Other examples of nonexpansive RNNs that are nonexpansive but not contracting can be found for any nonnegative matrix $A \geq 0$ and choosing:*

1) *$C = \lambda_{\text{MAX}} I$, where λ_{MAX} is the largest eigenvalue of A. In this case, the system is nonexpansive w.r.t. $\|\cdot\|_{\infty,\boldsymbol{v}^{-1}}$ where $\boldsymbol{v}$ is the eigenvector associated with λ_{MAX};*
2) *$C = diag(A\mathbf{1})$. In this case, the system is nonexpansive w.r.t. $\|\cdot\|_{\infty}$;*
3) *$C = diag((A\boldsymbol{\eta}))[\boldsymbol{\eta}]^{-1}$ for any $\boldsymbol{\eta} \geq 0$. In this case, the system is nonexpansive w.r.t. $\|\cdot\|_{\infty,\boldsymbol{\eta}^{-1}}$.*

References

[1] S. Jafarpour, A. Davydov, and F. Bullo, "Non-euclidean contraction theory for monotone and positive systems," *IEEE Transactions on Automatic Control*, 2022.

[2] D. Deplano, M. Franceschelli, and A. Giua, "Novel stability conditions for nonlinear monotone systems and consensus in multi-agent networks," *IEEE Transactions on Automatic Control*, pp. 1–14, 2023.

[3] D. Angeli and E. D. Sontag, "Monotone control systems," *IEEE Transactions on Automatic Control*, vol. 48, no. 10, pp. 1684–1698, 2003.

[4] D. Deplano, M. Franceschelli, and A. Giua, "Stability of nonexpansive monotone systems and application to recurrent neural networks," *IEEE Control Systems Letters*, 2024.

[5] B. Lemmens and R. Nussbaum, *Nonlinear Perron-Frobenius Theory*. Cambridge University Press, 2012.

[6] A. Davydov, A. V. Proskurnikov, and F. Bullo, "Non-euclidean contractivity of recurrent neural networks," in *IEEE American Control Conference (ACC)*, 2022, pp. 1527–1534.

Stability and constraint satisfaction in Recurrent Neural Network based Model Predictive Control

Irene Schimperna[1] and Lalo Magni[1]

Abstract— **This abstract summarises our research on Recurrent Neural Network (RNN) based Model Predictive Control (MPC). First the advantages of the use of RNN models in MPC are detailed. Then it is reported how the key issues of stability, constraint satisfaction and offset-free tracking have been solved in the MPC design, based on different classes of RNN.**

I. INTRODUCTION

Model Predictive Control (MPC) relies on accurate models to predict the dynamics of the system under control. In some situations obtaining a physical model of a nonlinear plant can be difficult and expensive, because the system under control is complex or because there is a lack of knowledge about the internal laws that govern the system. For this reason, the use of nonlinear, black-box models in MPC gained increasing popularity in recent years, thanks to the availability of large amount of data and to the increase in the available computing power. In particular, the class of Recurrent Neural Network (RNN) models is very effective in learning nonlinear plant dynamics, and only requires input-output data for the training [1]. In order to guarantee that the effect of the state initialization vanishes, and that a small input variation does not lead to a large state variation, it is useful to consider RNN models that satisfy an Incremental Input-to-State Stability (δISS) property.

Some key issues in the design of RNN based MPC are the stability of the closed loop and the robustness to uncertainties. The effect of uncertainties is particularly critical when state or output constraints are considered. In this case, it is necessary to rely on robust MPC techniques to guarantee robust feasibility and constraint satisfaction despite the uncertainties [2]. Moreover, it is possible to apply schemes for offset-free nonlinear MPC [3] to achieve null tracking error at steady state in presence of model-plant mismatch and persistent disturbances.

The aim of this abstract is to summarise how all of these aspects of MPC design have been considered for different classes of RNN in our papers [4], [5], [6], [7], [8].

II. RECURRENT NEURAL NETWORKS FOR MPC

RNN are particularly suitable to model nonlinear systems because their mathematical structure is the same of a discrete-time dynamical system, including one or more state equations and an output transformation. These equations depend on matrices of weights that are tuned using a learning procedure. Many different classes of RNN have been proposed in the literature, that differ for the structure of the state and output equations. The choice of the most appropriate architecture depends on the application.

In MPC design a typical choice is to consider δISS RNN models. In fact δISS RNN comes with the knowledge of an open loop incremental Lyapunov function for the model, that can be exploited in MPC design. Moreover, the use of RNN as models for MPC requires the introduction of a state observer in the control loop. In fact the state of RNN models has no physical meaning, but it encodes the memory of the past inputs of the plant. Hence, when the model is used to provide the predictions for the MPC, it is important to initialize the state in a meaningful way, that is consistent with the past history of the plant. Since δISS can be thought as an open-loop observability property, the use of δISS RNN facilitates the design of the observer.

In our research we have considered Long Short-Term Memory (LSTM) and Gated Recurrent Unit (GRU) networks, that are the classes of RNN with the best prediction accuracy in many tasks, and the recently proposed Recurrent Equilibrium Networks (REN) [9]. For the first two classes of networks, the δISS condition can be satisfied including an additional penalizing term the training loss. Instead, in REN models, another promising approach is used to guarantee δISS, that consist in parametrizing the network in a way that guarantees the δISS property while performing the training in an unconstrained way, without the need of adding regularization terms in the training loss.

III. MPC DESIGN

RNN based MPC consists in a finite horizon optimal control problem, where the evolution of the states of the system is predicted with the RNN model and is initialized with the observer state estimation. The considered stage cost is quadratic and penalizes the deviation of the RNN states and inputs with respect to their references, and constraints may be present in the optimization depending on the considered control problem. Then, the system input is obtained as the first element of the optimal input sequence, according to the receding horizon principle.

In the design of stabilizing MPC with RNN models the following aspects have been considered.

1) Stability: Stability is one of the key issues when designing an MPC, and is typically guaranteed with methods based on long enough prediction horizons or on the design of the terminal ingredients [2]. For RNN based MPC, we have chosen to use an approach based on terminal ingredients

---

[1] Irene Schimperna and lalo Magni are with Department of Civil and Architecture Engineering, University of Pavia, via Ferrata 3, Pavia, 27100, Italy. (e-mails: irene.schimperna01@universitadipavia.it, lalo.magni@unipv.it).

because it allows to maintain the prediction horizon short and computational load lower, but in the literature there are also successful approaches based on long enough prediction horizons [10]. Moreover, if the system under control is open loop incrementally stable and a δISS-Lyapunov function is known, it is possible to exploit this information for the design of the stabilizing terminal ingredients for the MPC. In particular, the terminal cost can be chosen as the δISS-Lyapunov function, possibly rescaled if needed. Then, a terminal set is required only in presence of state/output constraints, and can be obtained as a suitable sublevel set of the Lyapunov function. If only input constraints are present, the globality of the δISS property allows to avoid the introduction of a terminal set, so that the optimization is feasibile independently on the system initial state.

In the case of REN models, the knowledge of a δISS-Lyapunov function comes directly from the proof of stability [7]. Instead, in the case of LSTM [5] and GRU [6], the δISS-Lyapunov functions are obtained with some elaboration of the stability conditions, that are not directly based on Lyapunov functions arguments [11], [12].

2) Output constraints: The presence of output constraints calls for the use of robust MPC to guarantee recursive feasibility and constraint satisfaction in presence of all the uncertainties. In RNN based MPC the sources of uncertainty are the modelling errors, the possible external disturbances and the estimation error of the observer. When a probabilistic description of the disturbance is not available, a common method is to use deterministic worst case bounds of the uncertainties to derive a tightening for the original constraints. In order to explicitly take into account the observer estimation error, the constraint tightening approach proposed in [13] can be employed. This method is based on incremental Lyapunov functions of the model and and of the observer estimation error, that in RNN based MPC are already available because are used to enforce stability, and has a simple formulation. This approach has been successfully applied with GRU models in [6] and with LSTM models in [5], where also the issue of offset-free tracking has been considered.

3) Incremental input constraints: Incremental input constraints are constraints on the variation of the input variable between subsequent time steps, i.e. on $\Delta u_k \triangleq u_k - u_{k-1}$, where u denotes the system input and k the discrete time variable. Very often the input variation is only penalized in the cost, but in many applications the satisfaction of incremental input constraints can be very important to guarantee the safety of the system. The most natural way to manage this kind of constraints is to consider Δu as the optimization variable of the MPC, and to introduce a discrete time integrator to obtain the control variable u. However, the system enlarged with the integrator is no more δISS. A possible solution to achieve stability in this case is to introduce a terminal equality constraint only on the non-δISS part of the system, i.e. on the state of the discrete time integrator, and to consider a terminal weight based on a δISS-Lyapunov function of the original model state.

We have considered the issue of incremental input constraints in the case of generic RNN models in [8].

4) Offset-free tracking: When the model used by the MPC and the dynamics of the real plant do not coincide, a common issue is that in presence of constant references the closed loop system shows a non null asymptotic tracking error. One of the most common solutions to this problem is the use of offset-free MPC, where the model is augmented with a properly designed constant disturbance, to be estimated by the observer together with the states of the model. Then, at each time step the input and state references for the MPC are updated on the base of the current values of the output reference and of the disturbance estimation. This method in combination with LSTM models have shown its effectiveness in presence of input constraints in [4] and of input and output constraints in [5].

REFERENCES

[1] F. Bonassi, M. Farina, J. Xie, and R. Scattolini, "On recurrent neural networks for learning-based control: Recent results and ideas for future developments," *Journal of Process Control*, vol. 114, pp. 92–104, 2022.

[2] J. B. Rawlings, D. Q. Mayne, and M. M. Diehl, *Model Predictive Control: Theory, Computation, and Design*. Santa Barbara, California: Nob Hill Publishing, 2019.

[3] M. Morari and U. Maeder, "Nonlinear offset-free model predictive control," *Automatica*, vol. 48, no. 9, pp. 2059–2067, 2012.

[4] I. Schimperna, C. Toffanin, and L. Magni, "On offset-free model predictive control with long short-term memory networks," in *12th IFAC Symposium on Nonlinear Control Systems*, 2023, pp. 156–161.

[5] I. Schimperna and L. Magni, "Robust offset-free constrained model predictive control with long short-term memory networks," *IEEE Transactions on Automatic Control*, 2024.

[6] ——, "Robust constrained nonlinear model predictive control with gated recurrent unit model," *Automatica*, vol. 161, p. 111472, 2024.

[7] ——, "Recurrent equilibrium network models for nonlinear model predictive control," in *8th IFAC Conference on Nonlinear Model Predictive Control*, 2024.

[8] I. Schimperna, G. Galuppini, and L. Magni, "Recurrent neural network based mpc for systems with input and incremental input constraints," *IEEE Control Systems Letters*, 2024.

[9] M. Revay, R. Wang, and I. R. Manchester, "Recurrent equilibrium networks: Flexible dynamic models with guaranteed stability and robustness," *IEEE Transactions on Automatic Control*, 2023.

[10] F. Bonassi, A. La Bella, M. Farina, and R. Scattolini, "Nonlinear MPC design for incrementally ISS systems with application to GRU networks," *Automatica*, vol. 159, p. 111381, 2024.

[11] E. Terzi, F. Bonassi, M. Farina, and R. Scattolini, "Learning model predictive control with long short-term memory networks," *International Journal of Robust and Nonlinear Control*, vol. 31, no. 18, pp. 8877–8896, 2021.

[12] F. Bonassi, M. Farina, and R. Scattolini, "On the stability properties of gated recurrent units neural networks," *Systems & Control Letters*, vol. 157, p. 105049, 2021.

[13] J. Köhler, F. Allgöwer, and M. A. Müller, "A simple framework for nonlinear robust output-feedback MPC," in *2019 18th European Control Conference (ECC)*. IEEE, 2019, pp. 793–798.

Session 5B: Vehicles

Control for Vehicle Interactions in Highway Setting

Elisa Gaetan[1,2], Laura Giarré[1] and Paolo Falcone[1,3]

I. INTRODUCTION

Nowadays, deterministic and stochastic multi-agent systems find applications in different fields. Within a network of agents, their states can be influenced by many factors, like the surrounding peers, some external actions, or the environment itself, due to the present interactions. Focusing on traffic context, the interactions among vehicles, including their degree of cooperation, can either enhance or penalize the performance of individual vehicles as well as traffic flow, while also impacting safety positively or negatively. Therefore, being able to predict drivers' behavior or their degree of cooperation, could result in enhancements, particularly in addressing challenges such as path planning or traffic control. In this work, we design a Markovian behavioral model for a human driver. Once it has been established, we incorporate it into a broader control framework, specifically targeting the control of lane-change maneuvers.

II. ILLUSTRATIVE EXAMPLE

As illustrative example, we propose to consider a two-lane highway scenario with two vehicles (Fig. 1). In this setup, the yellow vehicle A_C is a control vehicle that acts as an actuator and has to influence velocity and/or lane position of the blue vehicle A_M. The idea is to utilize A_C as a form of a safety car, an agent capable of influencing the movements of A_M. Realistically, A_C cannot foresee the moves of A_M in advance, but it can predict the most likely decisions of A_M, according to a decision-making model based on everyday experience (i.e., past observations), and act to modify them according to a desired behavior. The actual controller is locally implemented on A_C.

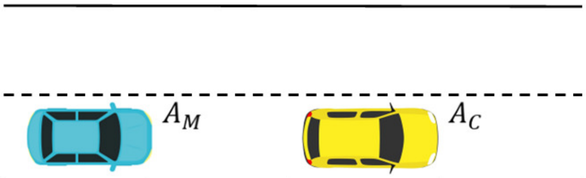

Fig. 1: Two-lane highway scenario.

III. VEHICLE'S MOTION MODEL

Inspired by [1], and under the assumption that the coordinate y is the lane number ($y = 1$ for the rightmost lane, $y = N_{lanes}$ for the leftmost one), the motion model for the vehicle along the highway is

$$x_{k+1} = x_k + v_k \Delta k, \tag{1a}$$
$$y_{k+1} = y_k + \psi_k, \tag{1b}$$
$$v_{k+1} = v_k + a_k \Delta k. \tag{1c}$$

Thus, $\boldsymbol{x}_k = [x_k, y_k, v_k]$ is the state of the vehicle, and $\boldsymbol{u}_k = [a_k, \psi_k]$ is the acceleration and lane-change input.

IV. DECISION-MAKING MODEL OF THE MARKOVIAN VEHICLE

We model the decision-making process of the driver as a Markov Chain, whose states belong to the set $\mathcal{S} = \mathcal{A} \times \mathcal{L}$, where $\mathcal{A}$ and $\mathcal{L}$ are the discrete sets of acceleration and lane-change commands respectively, which correspond to the input $\boldsymbol{u}_k$ of the kinematic model (1).
As the decision-making process is a Discrete-Time Markov Chain, it evolves the equation $\Pi_{k+1} = Q_k^T \Pi_k$, where Π_k is the state probability vector and Q_k the transition matrix, composed by the conditional probabilities $\Pr(a_{k+1}, \psi_{k+1} | a_k, \psi_k)$.

V. CONTROL ARCHITECTURE

As stated previously, the control vehicle A_C does not know the decisions of A_M in advance. However, A_C could predict A_M's decisions by exploiting the Markovian behavioral model and derive the best control action. Fig. 2 shows the control logics, where the blocks *Kinematic motion model of control vehicle* and *Kinematic motion model of Markovian vehicle* implement the model (1) for both A_C and A_M respectively. The block *Markovian behavioral and decision-making model* describes the decision-making process of A_M, which outputs the input $\boldsymbol{u}^M$ to the model (1). Finally, the *Scenario-tree MPC* derives the best control action $\boldsymbol{u}^C$ for A_C, based on the current position of A_M and the control objectives.

A. Scenario-tree model predictive control algorithm

The controller design in our approach is inspired by the principles underlying Stochastic Model Predictive Control [2], [3], [4]. However, in our scenario, we assume that the decisions of A_M are determined by the evolution of a Markov Chain, yielding a probability vector Π. A decision block then selects an input $\boldsymbol{u}^M$ corresponding to the Markovian state in $\mathcal{S}$ with the highest probability. Hence, we can

---

[1] E. Gaetan, L. Giarré and P. Falcone are with the Engineering Department 'Enzo Ferrari', University of Modena and Reggio Emilia, Modena, Italy. {`elisa.gaetan, laura.giarre, paolo.falcone`}`@unimore.it`

[2] E. Gaetan is also with the Italian National PH.D. DAUSY, Politecnico di Bari, Bari, Italy. `e.gaetan@phd.poliba.it`

[3] P. Falcone is also with the Department of Electrical Engineering, Chalmers University of Technology, Gothenburg, Sweden. `paolo.falcone@chalmers.se`

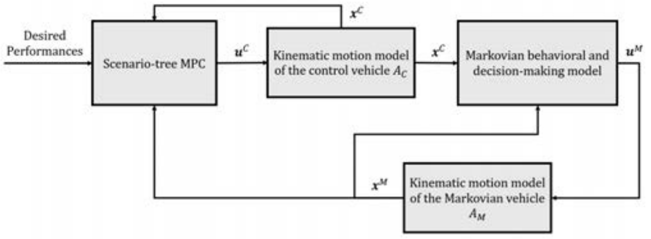

Fig. 2: Control logics.

adopt a scenario tree approach to account for the evolution of the probability vector along the control horizon as in [5]. Algorithm 1 shows the pseudo-code of our scenario-tree optimizer. The employed cost function is $J(\boldsymbol{x}^{ref}, \hat{\boldsymbol{x}}^M) = (\hat{\boldsymbol{x}}^M - \boldsymbol{x}^{ref})^T Q_{err} (\hat{\boldsymbol{x}}^M - \boldsymbol{x}^{ref})$, where Q_{err} is a diagonal matrix, and the elements on the principal diagonal are the weights for errors in x position, lane, and velocity respectively.

Algorithm 1 Scenario-tree optimizer

```
$T \leftarrow$ Simulation length
$N_c \leftarrow$ Prediction horizon
$\boldsymbol{x}^{ref} \leftarrow$ Reference
for $k = 1, \dots, T$ do
    for iterations $i = 1, \dots, N_c$ do
        $\mathcal{U}_i^C \leftarrow$ Compute all the feasible $\boldsymbol{u}^C$ for $A_C$
        for $\boldsymbol{u}_j^C \in \mathcal{U}_i^C$ do
            $\boldsymbol{x}_j^C \leftarrow$ State of $A_C$, applying $\boldsymbol{u}_j^C$ in (1)
            Derive the corresponding $Q_j$ and $\Pi_j$.
            $\hat{\boldsymbol{u}}_j^M \leftarrow \mathrm{argmax}_{s \in \mathcal{S}} \Pi_j$
            $\hat{\boldsymbol{x}}_j^M \leftarrow$ State of $A_M$, applying $\hat{\boldsymbol{u}}_j^M$ in (1)
            $\mathrm{cost}_j^i \leftarrow \mathrm{cost}_j^{i-1} + J(\boldsymbol{x}^{ref}, \hat{\boldsymbol{x}}_j^M)$
        end for
    end for
    Find the control input sequence that leads to the minimum cost and apply the first control action $\boldsymbol{u}^C$.
end for
```

VI. RESULTS

Here, we present (some of) the results obtained from numerical simulations when our control scheme is used in the traffic scenario in Fig. 1. Our objective is to control the lane position of A_M and guide it to achieve the maximum allowed velocity, which we set as $v_{max} = 130\,\mathrm{km/h} \approx 36\,\mathrm{m/s}$. As desired performance, we set $y^{ref} = 1$ until $k = 32\,\mathrm{s}$, and subsequently $y^{ref} = 2$, with $v^{ref} = v^{max}$.

To appreciate the effects of the proposed controller on the decision-making process of A_M, snapshots from a simulation are reported in Fig. 3, where the positions of A_C and A_M at the time instants $k = \{32, 33, 34\}\mathrm{s}$, are shown along with the corresponding Markovian probability vectors. The state probabilities are visualized using a color map, ranging from blue to yellow for smaller to higher probabilities. In the color map, the x-axis represents the values in the set of accelerations $\mathcal{A}$ in increasing order (with $a_4 = 0\,\mathrm{m/s^2}$), while the y-axis represents different values of lane-moves ($\psi_1 = -1, \psi_2 = 0, \psi_3 = +1$).

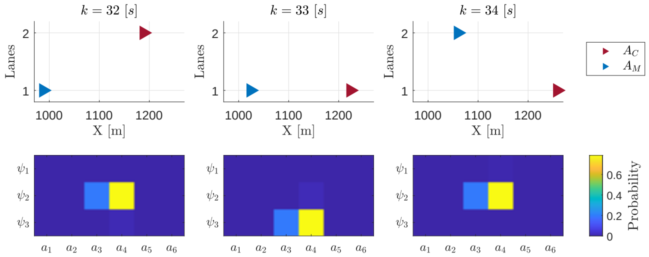

Fig. 3: Snapshots from a single simulation.

The snapshot at $k = 32\,\mathrm{s}$ illustrates the scenario when the lane reference has been changed from lane 1 to lane 2. At this time, A_M is still driving in the first lane, and its probability vector indicates that, without any change in the scenario, it would continue on the same lane with the same velocity. This is evident as the higher probability is associated with the state $(a = 0\,\mathrm{m/s^2}, \psi = 0)$. Hence, to encourage A_M to change lanes, A_C moves to the first lane, as shown in the snapshot at $k = 33\,\mathrm{s}$. Consequently, this modifies the transition matrix Q of A_M, and thus the probability vector. Indeed, now the most likely decision for the next instant is $s = (a = 0\,\mathrm{m/s^2}, \psi = +1)$. Finally, in $k = 34\,\mathrm{s}$, A_M is indeed in the second lane, while A_C maintains itself in the first lane. Moreover, by observing the associated color map, we note that this scenario is not going to change, as the next most likely decision is again $(a = 0\,\mathrm{m/s^2}, \psi = 0)$.

VII. CONCLUSION AND FUTURE WORK

In this work, we have investigated the interactions between vehicles in the specific environment of highways and formulated a mathematical framework for describing how drivers' decisions can change according to the moves of the surrounding vehicles, exploiting this formulation in a control architecture. Future works will focus on extending the framework to a scenario with multiple vehicles and/or more than two lanes. Moreover, validating our model through traffic simulators and real datasets is undergoing.

REFERENCES

[1] S. Karimi and A. Vahidi, "Receding Horizon Motion Planning for Automated Lane Change and Merge Using Monte Carlo Tree Search and Level-K Game Theory," in *2020 American Control Conference (ACC)*, 2020, pp. 1223–1228.

[2] M. Maiworm, T. Bäthge, and R. Findeisen, "Scenario-based Model Predictive Control: Recursive Feasibility and Stability," *IFAC-PapersOnLine*, vol. 48, no. 8, pp. 50–56, 2015.

[3] D. Bernardini and A. Bemporad, "Scenario-based model predictive control of stochastic constrained linear systems," in *Proceedings of the 48h IEEE Conference on Decision and Control (CDC) held jointly with 2009 28th Chinese Control Conference*. Shanghai: IEEE, Dec. 2009, pp. 6333–6338.

[4] D. De La Penad, A. Bemporad, and T. Alamo, "Stochastic Programming Applied to Model Predictive Control," in *Proceedings of the 44th IEEE Conference on Decision and Control*. Seville, Spain: IEEE, 2005, pp. 1361–1366.

[5] A.-T. Tran, A. Muraleedharan, H. Okuda, and T. Suzuki, "Scenario-based stochastic MPC for vehicle speed control considering the interaction with pedestrians," *IFAC-PapersOnLine*, vol. 53, no. 2, pp. 15 325–15 331, 2020.

Stop-and-Go Traffic Wave Attenuation: A Shared Control Approach

Erica Salvato[1], Lorenzo Elia[1], Gianfranco Fenu[1], and Thomas Parisini[1,2,3]

***Abstract*— We present a novel approach to address the challenge of stop-and-go wave mitigation in congested vehicular traffic scenarios. The proposed solution involves equipping human-driven vehicles with a controller that can effectively assist the driver by merging human input with the underlying automation input through arbitration. Specifically, our approach integrates a convex combination of human and automation inputs within the controller through a continuous and derivable sharing function. This integration allows for the fusion of human decision-making capabilities with automation's perception of the environment. We provide extensive microscopic simulation results to demonstrate the effectiveness of the proposed approach. In addition, some theoretical guarantees are established for both the stability of individual vehicles and the string stability.**

In vehicular traffic management, stop-and-go waves pose significant safety and efficiency challenges, especially with human drivers involved [1]. While autonomous vehicles can adhere to predefined guarantees, human-driven vehicles lack such predictability, leading to instability conditions influenced by individual driver choices. This unpredictability underscores the need for innovative approaches to mitigate the negative impact of stop-and-go waves. One promising solution involves integrating human-driven vehicles with advanced driver assistance systems (ADAS) [2], allowing automation to offer continuous support to drivers at the control level and adaptive authority throughout the driving experience. Current vehicles equipped with ADAS utilize various warning signals and control activities, such as park assist, lane departure warning systems, and longitudinal and lateral control interchange [3].

In this paper, inspired by findings from [4], we propose equipping human-driven vehicles with an ADAS featuring a newly designed shared control strategy to deal with the traffic waves problem. This strategy combines feedback control with human driver input through arbitration, facilitating seamless integration of both elements. Unlike previous approaches employing a hysteresis switch-sharing function, we introduce a novel sharing function characterized by a raised-cosine (RC) profile [5], which is bounded and smooth. By integrating human decision-making with automation's environmental awareness, we aim to enhance platoon stability, thereby reducing fluctuations in vehicle movements.

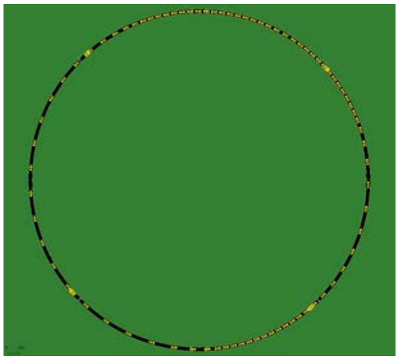

Fig. 1: Considered framework in SUMO.

We consider a single-lane platoon of M, $M > 1$, homogeneous vehicles of length l_i, navigating on a circular road of length L. Each vehicle indexed as i follows the vehicle indexed as $i-1$ $\forall i \in \{1, \dots, M\}$, forming the platoon with vehicle 1 leading and vehicle M trailing. The result is a car-following (CF) model. We denote by $x_i^{(k)}$, $v_i^{(k)}$, and $a_i^{(k)}$ the position, the velocity and the acceleration of the i-th vehicle at the k-th time instant, respectively. Given an initial position $x_i^{(0)}$ and an initial speed $v_i^{(0)}$, the i-th vehicle dynamics, subject to a sequence of accelerations $a_i^{(0)}$, $a_i^{(1)}$, ... at fixed time interval T_s, is completely defined as follows:

$$\begin{aligned} x_i^{(k+1)} &= x_i^{(k)} + T_s v_i^{(k)} \\ v_i^{(k+1)} &= v_i^{(k)} + T_s a_i^{(k)}. \end{aligned} \tag{1}$$

Each vehicle is assumed forward motion only, no backward or turning manoeuvres are allowed. The maximum forward speed for each i-th vehicle is denoted by v_i^{M} and is assumed to be known and constant $\forall i \in \{1, \dots, M\}$. In addition, its minimum acceleration, denoted by $a_i^{\mathrm{m}} < 0$, and its maximum acceleration, denoted by $a_i^{\mathrm{M}} > 0$, are both given and constant $\forall i \in \{1, \dots, M\}$. We assume to work in a scenario with human-driven vehicles only, and we describe the influence of the $i-1$-vehicle on the i-th vehicle according to the Intelligent Driver Model (IDM) presented in [6]:

$$a_{h_i}^{(k)} = a_i^{\mathrm{M}} \left[1 - \left(\frac{v_i^{(k)}}{\bar{v}_i} \right)^{\delta} - \left(\frac{\bar{s}_i + \bar{t}_{i,h} v_i^{(k)} - \frac{v_i^{(k)} \Delta v_i^{(k)}}{2\sqrt{a_i^{\mathrm{M}} |a_i^{\mathrm{m}}|}}}{s_i^{(k)}} \right)^2 \right], \tag{2}$$

where $\bar{v}_i$ is the desired speed in free-flow traffic conditions, $\bar{t}_{i,h}$ is the minimum steady-state time gap, $\bar{s}_i$ is the clearance from the $i-1$-th vehicle in stand-still situations, and δ is a parameter usually set to 4. We denote by $e_h = (s_{e_h}, 0, v_{e_h})$ the equilibrium state, i.e., the state for which (2) equals 0. We assume a congested traffic scenario, i.e., $0 < v_{e_h} << \bar{v}_i$.

According to [7], we choose to model the feedback

[1] Department of Engineering and Architecture, University of Trieste, Italy.
[2] Department of Electrical and Electronic Engineering, Imperial College London, London SW7 2AZ, UK.
[3] KIOS Research and Innovation Center of Excellence, University of Cyprus, CY-1678 Nicosia, Cyprus
e-mail: lorenzo.elia@studenti.units.it, erica.salvato@dia.units.it, fenu@units.it, t.parisini@gmail.com

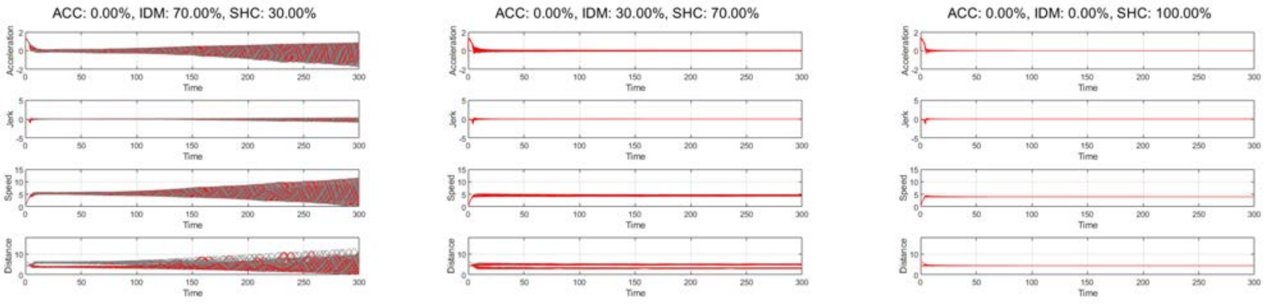

(a) (b) (c)

Fig. 2: Simulation with three different penetration percentages of vehicles equipped with shared control in a scenario with $\beta = 0.25$. The IDM behaviour in gray, while in red the behaviour of vehicles equipped with our sharing control strategy

controller as a second-order transfer function described by:

$$a_{f_i} = k_p\left(s_i^{(k)} + l_i - \bar{t}_{i,f} v_i^{(k)}\right) + k_d\left(\Delta v_i^{(k)}\right) \tag{3}$$

where $k_p \in \mathbb{R}$ and $k_d \in \mathbb{R}$ are two control gains, while $\bar{t}_{i,f}$ is the desired steady-state time gap.

Inspired by the findings of [4] we define the shared-control input of the i-th vehicle a_{s_i} as a combination of the feedback control input a_{f_i} and the human driver input a_{h_i}:

$$a_{s_i}^{(k)} = \left(1 - \sigma_i\left(t_i^{(k)}\right)\right) a_{f_i}^{(k)} + \sigma_i\left(t_i^{(k)}\right) a_{h_i}^{(k)}, \tag{4}$$

where $\sigma_i : \mathbb{R}^+ \to [0,\, 1] \subset \mathbb{R}$, referred to as the *sharing function*, is used to quantify the proportion in which control authority is distributed between the driver and the feedback controller.

Differently from [4], where a hysteresis sharing function has been proposed, here we introduce a σ_i defined as follows:

$$\sigma_i\left(t_i^{(k)}\right) = \begin{cases} 0 & \text{if } t_i^{(k)} < t_{i_{f2h}}\left(1 - \beta_i\right) \\ 1 & \text{if } t_i^{(k)} > t_{i_{f2h}}\left(1 + \beta_i\right) \\ \frac{1-\cos(\alpha)}{2} & \text{otherwise} \end{cases} \tag{5}$$

where $t_{i_{f2h}}$ defines the time gap corresponding to a 50% driver and feedback controller authority, β_i determines the slope of σ_i, and $\alpha = \dfrac{\pi\left(t_i^{(k)} - t_{i_{f2h}}\right)}{2\beta_i t_{i_{f2h}}} + \dfrac{\pi}{2}$.

Given the above-described scenario, our control objective is to find a feedback control input a_{f_i} and a sharing function σ_i that, properly combined with the human driver input a_{h_i} (2), effectively mitigate the stop-and-go wave, i.e. the overall stability is guaranteed.

We perform simulations using the proposed framework implemented on the Simulator of Urban MObility (SUMO) [8] as depicted in Figure 1. For our simulation scenario, we considered a single-lane circular road with a circumference of $L = 898.24\,\mathrm{m}$ accommodating $M = 80$ vehicles, each having a length of $l = 5\,\mathrm{m}$. Each simulation starts with vehicles evenly distributed along the ring, with an initial speed of $0\,\mathrm{m\,s^{-1}}$.

We first perform a simulation with only human-driven vehicles. The results, as depicted in Figure 3, indicate an unstable scenario, according to the string instability condition highlighted in [9]. Figure 2 reports simulation results with increasing penetration percentage of vehicles equipped with shared control, relative to the total number of vehicles in the simulation, when β value allows to meet the conditions related to both local and string stability (that for space reasons we do not report).

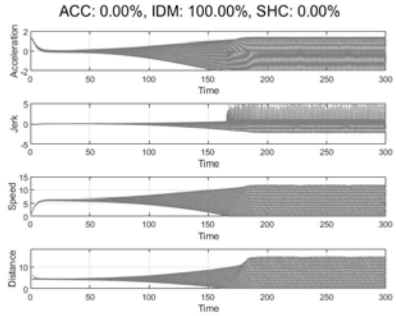

Fig. 3: Simulation with only IDM

REFERENCES

[1] G. Orosz, R. E. Wilson, R. Szalai, and G. Stépán, “Exciting traffic jams: Nonlinear phenomena behind traffic jam formation on highways,” *Physical review E*, vol. 80, no. 4, p. 046205, 2009.

[2] M. Marcano, S. Díaz, J. Pérez, and E. Irigoyen, “A review of shared control for automated vehicles: Theory and applications,” *IEEE Transactions on Human-Machine Systems*, vol. 50, no. 6, pp. 475–491, 2020.

[3] J. Nidamanuri, C. Nibhanupudi, R. Assfalg, and H. Venkataraman, “A progressive review: Emerging technologies for adas driven solutions,” *IEEE Transactions on Intelligent Vehicles*, vol. 7, no. 2, pp. 326–341, 2021.

[4] J. Jiang, A. Astolfi, and T. Parisini, “Robust traffic wave damping via shared control,” *Transportation Research Part C: Emerging Technologies*, vol. 128, p. 103110, 2021.

[5] J. G. Proakis and M. Salehi, *Digital communications*. McGraw-hill, 2008.

[6] M. Treiber, A. Hennecke, and D. Helbing, “Congested traffic states in empirical observations and microscopic simulations,” *Physical review E*, vol. 62, no. 2, p. 1805, 2000.

[7] V. Milanés and S. E. Shladover, “Modeling cooperative and autonomous adaptive cruise control dynamic responses using experimental data,” *Transportation Research Part C: Emerging Technologies*, vol. 48, pp. 285–300, 2014.

[8] M. Behrisch, L. Bieker, J. Erdmann, and D. Krajzewicz, “SUMO – Simulation of Urban MObility,” 2011.

[9] Z. Zhou, L. Li, X. Qu, and B. Ran, “A self-adaptive idm car-following strategy considering asymptotic stability and damping characteristics,” *Physica A: Statistical Mechanics and its Applications*, vol. 637, p. 129539, 2024.

Identification of Cyclists' Route Choice Criteria

S. Ardizzoni[1], M.Laurini[1], R. Praxedes[1], L.Consolini[1], M.Locatelli[1]

[1]Dipartimento di Ingegneria e Architettura, Università degli Studi di Parma
Parco Area delle Scienze, 181/A, Parma, Italy

Abstract

The transition to more sustainable and green forms of transportation is increasingly becoming a priority in developed countries. In particular, bicycles, electric bicycles, and electric scooters are a convenient mode of transportation for short range and urban travels. Understanding how users (or simply cyclists, in what follows) choose their routes depending on various road characteristics is fundamental if one aims at increasing the number of cyclists (and, hence, decreasing the number of motor vehicles users) or improving the existing cycling infrastructure, helping decision makers take more informed actions when assigning budget for infrastructural interventions (see, e.g., [5]).

A quantitative method for assessing the quality of roads from a cyclist's point of view is given by the concept of Bicycle Level of Service (BLOS), which has first been introduced in the late '80s – early '90s in [2, 3]. Its aim is to measure quantitatively several qualitative aspects of road segments with respect to cyclists' perception. As we know from several studies (see, for instance, [1, 6]), cyclists may not use distance as the only objective function when choosing which route to follow. For instance, the presence of bike facilities may heavily influence the route choice (see, e.g., [4]), resulting in longer paths in which the amount of road sections with bike facilities seems to be maximized. However, this is just one example of how the features of a road portion may influence the cyclists' choice. In its original formulation, despite its innovative aspect, the BLOS was affected by some shortcomings like the lack of statistical calibration and a subjective methodology in assigning road features values. One of the most critical aspects in BLOS is that of determining the weighting factors multiplying the quantities associated to the various considered aspects of a road section. Obtaining a "good" set of coefficients can require data collection, surveying users, normalization and homogenization of different measurement scales, and it also requires validation and continuous calibration of the obtained formula.

The main contribution of this work is an optimization approach to detect the BLOS for various user groups, leveraging knowledge of the true paths followed by them, accessible, for example, through data collected by bike-sharing services. This BLOS identification can be particularly useful when addressing the problem of bike network optimization, in which one wishes to maximize the benefit of infrastructural interventions given a limited budget.

In our work we assume that r basic objective functions (i.e., road features) are given and that users consider a combination of such functions in order to determine the path to be followed. This is equivalent to defining a BLOS formula in which only r factors are involved. The road network is represented by a graph and each basic objective function is defined assigning costs to all arcs of this graph. We consider a BLOS formula which is a convex combination of the considered features, hence the coefficients of the BLOS formulas, also called weights in what follows, are all assumed to be in $[0, 1]$ and their sum is equal to one. We assume that each user has their own r-dimensional weight vector, and follows a shortest path (SP) over the graph representing the road network, where the costs

of the arcs are a convex combination of the r basic costs, with coefficients of the convex combination corresponding to the entries of the weight vector. We also assume that users may have different behaviors and, thus, select their paths according to different weight vectors. Therefore, our goal is that of identifying both the set of weighting factors that users perceive, and the probability with which users would consider such weights. In other words, we assume that there is not a unique BLOS formula that suits all users but we aim at identifying different BLOS formulas for different users segments.

In our work, we formalize the general problem and we first consider a simplified version where the set of possible weights is assumed to be known in advance. For this problem, we propose a bilevel optimization formulation, and derive a polynomial-time algorithm for its solution. Next, we present the optimization problem with unknown set of weights, and we discuss some properties of the function to be minimized. Moreover, we discuss how the data needed for the problem definition can be collected, also pointing out possible difficulties and limitations of the proposed approach. Identification can be based on two different types of data:

1. on observations of traffic flow on (a subset of) network edges;
2. on the routes traveled by a certain sample of users.

Based on the type of data available, we define a different objective function for the optimization problem. For both the cases, we propose a solution algorithm for that problem. Finally, we present some experiments on the bicycle network of the city of Parma, based on the data provided by Dott. This company operates approximately 300 free-floating e-bikes in the city of Parma and provided us with 2000 trips taken by their users. Using the optimization method presented in this work, we investigated and attempted to classify the primary route choice criteria, defined as a linear combination of the three road features: distance, road security and practicability. Road security for bicycles refers to the measures and conditions that ensure the safety and protection of cyclists while using roadways. It involves several key aspects such as protection from vehicular traffic, speed limit for cars, presence of signage, markings and bike box. The practicability of a road refers to how suitable and functional it is for use by cyclists under various conditions. This encompasses several factors, such as the width of the road, the pavement material and maintenance, the presence of bottlenecks and protrusion.

References

[1] R. Buehler and J. Dill. Bikeway networks: A review of effects on cycling. *Transport Reviews*, 36(1):9–27, 2016. Cycling as Transport.

[2] W. Davis. Bicycle safety evaluation. Technical report, Auburn University: Chattanooga, TN, USA, 1987.

[3] B. Epperson. Evaluating suitability of roadways for bicycle use: Toward a cycling level-of-service standard. *Transportation Research Record*, 1438:9–16, 1994.

[4] C. Howard and E. K. Burns. Cycling to work in phoenix: Route choice, travel behavior, and commuter characteristics. *Transportation Research Record*, 1773(1):39–46, 2001.

[5] H. Liu, W. Y. Szeto, and J. Long. Bike network design problem with a path-size logit-based equilibrium constraint: Formulation, global optimization, and matheuristic. *Transportation Research Part E*, 127:284–307, 2019.

[6] J. Pucher and R. Buehler. Making cycling irresistible: Lessons from the Netherlands, Denmark and Germany. *Transport Reviews*, 28(4):495–528, June 2008.

A Deep Reinforcement Learning Approach for Route Planning of Autonomous Vehicles*

Francesco Paparella, Giuseppe Olivieri, Gaetano Volpe,
Agostino Marcello Mangini, *Senior Member, IEEE*, Maria Pia Fanti, *Fellow, IEEE*

Abstract— **Urban autonomous driving has the potential to enhance both safety and efficiency of transportation in environments also in complex traffic conditions. However, new services and approaches are necessary to manage Autonomous Vehicles in the real traffic. This paper introduces a novel approach to optimize routing in the urban settings by Deep Reinforcement Learning (DRL) techniques. A modular DRL architecture is proposed to obtain a route able to minimize the length of the paths, minimize the number of turns during the travel and select the dedicated lanes.**

I. INTRODUCTION

With the evolution of the urban autonomous driving, the choice of personalized and optimal routes is emerging as a crucial element in the context of roadway planning. The customization of routes is based on the dynamic adaptation of pathways in response to urban context variables, such as traffic and user preferences. Optimizing routes and travel times is a way to reduce congestion, decrease gas emissions and contribute to global efforts to mitigate climate change.

In the recent years, the research and innovation areas focus on Cooperative, Connected and Automated Mobility topics and services for managing and controlling autonomous driving systems.

For instance, some novel contributions enlighten that the most modern technologies based on Information and communications technologies, such as Connected and Cooperative Services, Artificial Intelligence and Big Data allow to connect users, vehicles and infrastructures in an intelligent, efficient, safe and sustainable manner [1], [2].

Indeed, DRL is a promising solution especially in the domains of driving policy, predictive perception, path and motion planning, and low level controller design. Open issues include: validating the performance of RL based systems, the simulation-reality gap, sample efficiency, designing good reward functions and incorporating safety into decision making RL systems for autonomous agents.

This paper aims to address these gaps and considers the basic problem of designing suitable routes in the cities for Autonomous Vehicles (AVs) by focusing on multi objectives such as the length of the routes, the requirements of minimizing the turns during the travel and the selection of dedicated lanes. The problem is solved by applying a novel modular DRL model based on the training of agents associated with the AVs.

Since considering all the possible routes of the cities for completing the training is a very time consuming and complex task, we address such issue by proposing a modular DRL architecture based on the division of the city in a set of zones. A set of agents is trained and each agent is associated to routes starting from a zone and ending to a different one. The AV will select the route that exhibits the best multi-objective strategy enlightened by the best value of the reward. The modular approach allows us to train the agents in parallel and in limited urban areas.

The proposed modular DRL based strategy is applied to the city center of Bari, a town of Southern Italy and the agents are trained in a simulation environment. Some results show the advantages of the proposed methodology.

This paper has been accepted for presentation and publication at the 2024 IEEE International Conference on Systems, Man, and Cybernetics conference, Kuching, Malaysia. October 6-10th 2024.

II. PROBLEM FORMULATION

Let us consider an AV that has to travel in the city: the problem is to find the optimal path p starting from a generic point of the city to a final point with the aim of minimizing the length of the route, minimizing the number of right and left turns and using the lanes dedicated to the AVs.

The road network is modeled as a graph $G(J, E)$ where the set of nodes $J = \{j | j = 1, ..., n\}$ is the set of junctions or intersections and the set of edges $E = \{e_1, e_2, ...e_m\}$ denotes the set of the city streets. In particular, it holds that an edge $e_i = (j, r) \in E$ if there exists a street starting from $j \in J$ and ending to $r \in J$. Moreover, we consider a set of edges $E_p \subset E$ that are priority edges, i.e., they correspond to streets dedicated to the AVs. We consider the problem of determining the route that connects a pair of edges $c = (e_s, e_f)$ where e_s is the starting edge and e_f is the ending edge. A possible route connecting the pair $c = (e_s, e_f)$ is a path p represented by a sequence of edges $p = (e_s, ...e_j, .., e_f)$. The problem to be solved for a given pair $c = (e_s, e_f)$, is determining the optimum path exhibiting the minimum path length, the minimum number of right/left turns crossed and the maximum number of priority traveled routes.

III. THE MODULAR DRL ARCHITECTURE APPROACH

In the proposed system an RL agent is associated with the AV that chooses the best action to obtain the minimum

---

F. Paparella, G. Olivieri, G. Volpe, A. M. Mangini and M. P. Fanti are with the Department of Electrical and Information Engineering,Polytechnic University of Bari, 70125 Bari, Italy (f.paparella7@phd.poliba.it; g.olivieri@phd.poliba.it; gaetano.volpe@poliba.it; agostinomarcello.mangini@poliba.it; mariapia.fanti@poliba.it).

distance, with the minimum number of right/left turns and the maximum number of priority edges.

A. State Space and Action Space

The state of the agent at time $s(t) \in S$ at time t is the following:

$$s(t) = [x(t), \phi_v(t), e_{(}t)]$$

where $x(t) = (Lat(t), Lon(t))$ denotes the latitude $Lat(t)$ and the longitude $Lon(t)$ of the position of the AV at time t respectively, $\phi_v(t)$ represents the heading angle of the AV and $e(t) \in E$ is the edge occupied by the AV at time t.

When an AV arrives to a node $j \in J$ at time t, it can change the edge and can decide among three possible actions: $A = \{Gostraight, Turnright, Turnleft\}$.

B. Multi-objective Reward function

We define a Multi-objective Reward function made by a reward for shortest path, by left and right turns and finally a reward to use a priority path for the AV.

1) Shortest path: To describe a reward that show how the agent moves towards the destination edge, we define the distance $d(t)$ between the current edge at time t, and the destination edge e_f. In case of the current distance $d(t)$ is less than the distance $d(t-1)$ at time $t-1$, then it means that the AV moves towards destination, instead if $d(t)$ is higher that the distance $d(t-1)$, then the agent moves far. The reward function is defined as follows:

$$r_{shortest}(t) = \begin{cases} 1 & \text{if } d(t) \leq d(t-1) \\ -0.5 & \text{otherwise.} \end{cases} \tag{1}$$

2) Avoiding left/right turns: If the modulus of the difference between the angle at time t $\phi(t)$ and the angle $\phi(t+1)$ at time $t+1$ is greater than a fixed angle ϕ_{fixed}

$$r_{TlTr}(t) = \begin{cases} -1 & \text{if } |\phi(t) - \phi(t-1)| \geq \phi_{fixed} \\ 0 & \text{otherwise.} \end{cases} \tag{2}$$

3) Priority lanes: For considering the priority lanes, it is enough to define a positive reward if at the step t, the current edge $e(t) \in E_p$:

$$r_{priority}(t) = \begin{cases} 1 & \text{if } e(t) \in E_p \\ 0 & \text{otherwise.} \end{cases} \tag{3}$$

4) Multi-objective reward: A multi-objective reward function r_{tot} at each time t is formulated as follows:

$$r_{tot}(t) = \alpha r_{shortest} + \beta r_{TlTr}(t) + \gamma r_{priority}(t) \tag{4}$$

where α, β and γ are the weights assigned to each reward component.

C. The Modular DRL Architecture

In this paper, we propose a modular architecture approach in which the set E is partitioned in N subsets such that $E = E_1 \cup E_2 \cup ... E_N$ and $E_i \cap E_j = \emptyset \quad \forall i, j = 1, 2, \ldots, N$ and $i \neq j$. Then, we train N agents in a parallel fashion, each with a randomly selected pair $c_i = (e_s, e_f)$, where $e_s \in E_i$ and $e_f \in E_j \quad \forall i, j = 1, \ldots, N$.

The advantage of the proposed modular strategy is that the main problem is split in N smaller sub-problems that cover all different zones of the map and can be trained in parallel.

IV. SIMULATION ENVIRONMENT AND TRAINING SETUP

We consider a map of the city centre of Bari extracted from *OpenStreetMap*. The modular DRL training is implemented in *Python* language using the *RLLib* libraries with *SUMO* simulator and *TraCi* interface. The results of the training for both modular and exhaustive strategies are depicted in Fig. 1.

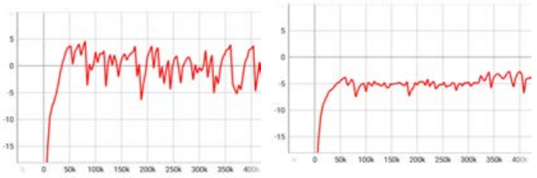

(a) Agent 1 (b) Agent 2

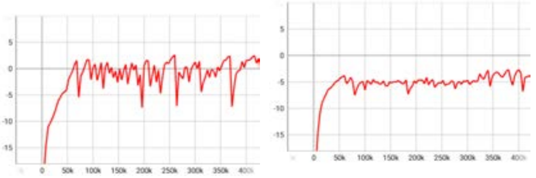

(c) Agent 3 (d) Exhaustive

Fig. 1: DRL episode mean reward with modular strategy.

Since the mean reward obtained by the four agents is greater than the one obtained by the exhaustive approach, it is evident that the modular DRL strategy is better in terms of performance.

V. CONCLUSION

The approach used in this paper highlights the effectiveness of the modular Deep Reinforcement Learning (DRL) approach in urban routing optimization. By integrating modular DRL algorithms, we are able to dynamically adapt to changing urban traffic conditions and user preferences.

The future research will integrate the proposed modular DRL approach with other technologies such as vehicle-to-everything (V2X) communication in order to enable more efficient and safer coordination of urban traffic.

REFERENCES

[1] L. Liang, H. Ye, and G. Y. Li, “Toward intelligent vehicular networks: A machine learning framework,” *IEEE Internet of Things Journal*, vol. 6, pp. 124–135, Feb 2019.

[2] A. Pompigna and R. Mauro, “Smart roads: A state of the art of highways innovations in the smart age,” *Engineering Science and Technology, an International Journal*, vol. 25, p. 100986, 2022.

Route Optimization in Precision Agriculture Settings: a Multi-Steiner TSP Formulation

Antonio Furchì[1], Martina Lippi[1], Renzo Fabrizio Carpio[1], Andrea Gasparri[1]

***Abstract*— In this abstract, we propose a route planning strategy for heterogeneous mobile robots in Precision Agriculture (PA) settings. Given a set of agricultural tasks to be performed at specific locations, we formulate a multi-Steiner Traveling Salesman Problem (TSP) to define the optimal assignment of these tasks to the robots as well as the respective optimal paths to be followed. Costs for travelling from one location to another, for maneuvering and for executing the task as well as limited energy capacity of the robots are considered. In addition, we propose a sub-optimal formulation to mitigate the computational complexity. The approach is validated in a simulated orchard with three heterogeneous aerial vehicles performing inspection tasks.**

I. INTRODUCTION

Continuous plant-by-plant monitoring and targeted interventions are key features of the Precision Agriculture (PA) paradigm, that potentially enable increased crop productivity while reducing waste. Deploying multiple, and possibly heterogeneous, mobile robots in the field, which autonomously navigate among plants and carry out agricultural tasks, provides an effective solution to realizing the PA paradigm, as depicted in Figure 1. However, realistically, in large-scale PA settings, agricultural tasks may be required in locations that are sparse with respect to the size of the field and low in number compared to the total number of plants. Hence, a fundamental question to be addressed is to define which robot should treat which plants and choose the respective path according to appropriate optimality metrics. In this regard, the following existing formulations address similar problems. The simple Traveling Salesman Problem (TSP) [1] requires a *single* robot to visit *all* the possible locations, the Steiner TSP [2] requires a *single* robot to visit a subset of locations, the multi TSP [3] requires multiple robots to visit *all* possible locations, while the vehicle routing [4] requires multiple robots with limited capacity to visit *all* the locations.

Contribution: Differently from the papers in the literature, we propose a *multi-Steiner TSP* extending the Steiner TSP to *i) multiple* heterogeneous mobile robots and *ii)* allowing to visit only a subset of all possible locations within the field, as typical for PA settings. In doing so, we also take into account energy capacity constraints and turning costs for which we introduce a novel field modeling. Note that maneuvering or turning operations are typically costly in terms of both time and energy, requiring, for example, high torques to the motors to be executed. Finally, we provide a sub-optimal formulation mitigating the computational burden.

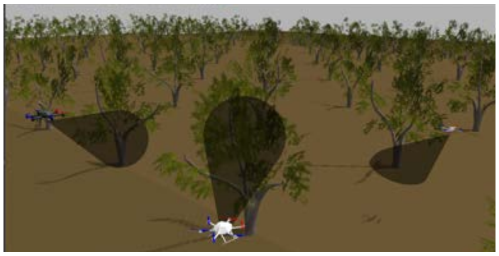

Fig. 1: Example of operating scenario.

II. SYSTEM MODELING

Field modeling: We model the orchard field as a directed graph $\mathcal{G} = (\mathcal{V}, \mathcal{E})$, referred to as *field* graph, where each node v_i in $\mathcal{V}$ is associated with a location, with position $p_i \in \mathbb{R}^3$, where an agricultural task can be carried out and each edge $(v_i, v_j) \in \mathcal{E}$ is associated with a possible passage from location v_i to v_j. A depot location, associated with the vertex $v_0 \in \mathcal{V}$, is present in the field and all the robots have to depart from and return to it. Moreover, the subset $\mathcal{V}_s \subseteq \mathcal{V} \setminus \{v_0\}$ of vertices denotes the locations to serve, i.e., where agricultural tasks must be carried out. Note that large-scale orchards are generally characterized by a high number of nodes, i.e., $|\mathcal{V}| \gg 1$, where only a few of them must be processed with agricultural tasks, i.e., it generally holds $|\mathcal{V}_s| \ll |\mathcal{V}|$. Additionally, we introduce the set $\mathcal{E}_c$ of all the pairs of consecutive edges, i.e., collecting pairs (e_p, e_q), such that there exist $e_p = (v_t, v_v)$ and $e_q = (v_v, v_h)$, with $\{v_t, v_v, v_h\} \in \mathcal{V}$. Given a pair of consecutive edges, we denote as $\varphi_{p,q}$ the angle between the respective vectors $u_p = p_t - p_v$ and $u_q = p_h - p_v$.

Given the field graph, we build an additional graph $\bar{\mathcal{G}} = (\bar{\mathcal{V}}, \bar{\mathcal{E}})$, called *orientation* graph which models the relations between couples of edges in $\mathcal{E}$. These relations are needed to handle turning costs with generic field topologies. In detail, each vertex $\bar{v}_k \in \bar{\mathcal{V}}$ is associated with an edge e_k of the field graph, i.e, $\bar{v}_k = e_k = (v_t, v_i)$ $\forall e_k \in \mathcal{E}$, and each edge $\bar{e}_k \in \bar{\mathcal{E}}$ is associated with consecutive edges of the field graph, i.e., $\bar{e}_k = (\bar{v}_p, \bar{v}_q)$ exists if $(e_p, e_q) \in \mathcal{E}_c$. An edge $\bar{e}_k = (\bar{v}_p, \bar{v}_q)$ is labeled with a tuple $(\bar{l}_k, \varphi_{p,q})$, where $\bar{l}_k = l_p + l_q$ is the overall length of the edges e_p and e_q and $\varphi_{p,q}$ is the angle between the edges. Moreover, we introduce the set $\bar{\xi}_i^+$ collecting the edges in $\bar{\mathcal{E}}$ which eventually flow into node $v_i \in \mathcal{V}$ of the field graph, and $\bar{\xi}_i^-$ collecting the edges in $\bar{\mathcal{E}}$ which originate from node $v_i \in \mathcal{V}$.

Robots modeling: A set $\mathcal{R} = \{r_1, ..., r_m\}$ of m robots is available to perform agricultural tasks. Each robot r_j has a limited energy capacity denoted by K_j and is characterized by the following temporal costs: *i)* $c_j^e \in \mathbb{R}$, representing

---

[1] Roma Tre University, Italy
Corresponding author: M. Lippi, *martina.lippi@uniroma3.it*

the unit temporal cost for traversing an edge, *ii)* $c_j^t \in \mathbb{R}$, representing the unit temporal cost for turning, and *iii)* $c_{i,j}^s \in \mathbb{R}, \forall v_i \in \mathcal{V}_s$, representing the temporal service cost for performing an agricultural task on node v_i. Similarly, we introduce the respective unit energy costs ε_j^e, ε_j^t, ε_j^s for each robot r_j, representing the consumed energy in the time unit.

III. MULTI-STEINER TSP

Problem Statement: We introduce the following binary decision variables: $x_{k,j} \in \{0,1\}, \forall \bar{e}_k \in \bar{\mathcal{E}}, r_j \in \mathcal{R}$, encoding the route assigned to robot r_j, which is 1 if robot r_j has to traverse the edge $\bar{e}_k$ of the orientation graph, 0 otherwise, and $s_{i,j} \in \{0,1\}$, $\forall v_i \in \mathcal{V}_s, r_j \in \mathcal{R}$, encoding the nodes to serve by robot r_j along the assigned route, which is 1 if robot r_j serves the vertex v_i belonging to $\mathcal{V}_s$, i.e., perform an agricultural task on node $v_i \in \mathcal{V}_s$, 0 otherwise. Note that the condition $x_{k,j} = 1$, with $\bar{e}_k = (\bar{v}_p, \bar{v}_q)$ implies that robot r_j has to traverse both edges $e_p \in \mathcal{E}$ and $e_q \in \mathcal{E}$ of the field graph. We aim to optimally determine for each robot r_j *i)* which agricultural tasks it has to perform, i.e., $s_{i,j}$, $\forall v_i \in \mathcal{V}_s$, and *ii)* its route, i.e., $x_{k,j}$, $\forall \bar{e}_k \in \bar{\mathcal{E}}$, while complying with energy capacity constraints. The optimality is intended to minimize both the maximum and the cumulative temporal cost by all the robots, comprising costs to traverse the edges, turn and perform agricultural tasks.

Problem Formulation: Let us introduce the following aggregate temporal costs for each robot r_j:

$$C_j^e(x_j) = \sum_{\bar{e}_k \in \bar{\mathcal{E}}} c_j^e \cdot \bar{l}_k \cdot x_{k,j}, \quad C_j^s(s_j) = \sum_{v_i \in \mathcal{V}_s} c_{i,j}^s \cdot s_{i,j},$$
$$C_j^t(x_j) = \sum_{\bar{e}_k = (\bar{v}_p, \bar{v}_q) \in \bar{\mathcal{E}}} c_j^t \cdot \varphi_{p,q} \cdot x_{k,j}$$

where C_j^e and C_j^t are the overall temporal costs of robot r_j to traverse the edges and to turn, respectively, and C_j^s is the overall service time for agricultural tasks performed by r_j. Note that the turning costs are easily computed thanks to the orientation graph model. We define the overall temporal cost of robot j as $C_j(x_j, s_j) = \alpha\, C_j^e(x_j) + \beta\, C_j^t(x_j) + \gamma\, C_j^s(s_j)$ with $\alpha, \beta, \gamma \in \mathbb{R}^+$ positive weights, and denote the maximum cost among the robots by $C_{\max} = \max_{r_j \in \mathcal{R}} C_j(x_j, s_j)$. We can now formally state our novel multi-Steiner TSP formulation as follows:

$$\min_{x_{ij},\, s_{ij}} \quad C_{\max} + \textstyle\sum_{r_j \in \mathcal{R}} C_j(x_j, s_j) \tag{1a}$$

s.t.

$$\textstyle\sum_{r_j \in \mathcal{R}} s_{i,j} = 1, \qquad \forall v_i \in \mathcal{V}_s \tag{1b}$$

$$\textstyle\sum_{\bar{e}_p \in \xi_i^+} x_{p,j} \geq s_{i,j}, \qquad \forall v_i \in \mathcal{V}_s, \forall r_j \in \mathcal{R} \tag{1c}$$

$$\textstyle\sum_{\bar{e}_q \in \xi_0^-} x_{q,j} \geq s_{i,j}, \qquad \forall v_i \in \mathcal{V}_s, \forall r_j \in \mathcal{R} \tag{1d}$$

$$\textstyle\sum_{\bar{e}_p \in \xi_i^+} x_{p,j} = \sum_{\bar{e}_q \in \xi_i^-} x_{q,j}, \qquad \forall v_i \in \mathcal{V}, \forall r_j \in \mathcal{R} \tag{1e}$$

$$\sum_{\bar{e}_p \in \xi_i^-} f_{p,j} - \sum_{\bar{e}_q \in \xi_i^+} f_{q,j} = s_{i,j}, \qquad \forall v_i \in \mathcal{V}_s, \forall r_j \in \mathcal{R} \tag{1f}$$

$$\sum_{\bar{e}_p \in \xi_i^-} f_{p,j} = \sum_{\bar{e}_q \in \xi_i^+} f_{q,j}, \qquad \begin{array}{l}\forall v_i \in \mathcal{V} \setminus \{\mathcal{V}_s\}, v_i \neq v_0, \\ \forall r_j \in \mathcal{R}\end{array} \tag{1g}$$

$$\begin{array}{l}\varepsilon_j^e C_j^e(x_j) + \varepsilon_j^t C_j^t(x_j) \\ \quad + \varepsilon_j^s C_j^s(s_j) \leq K_j,\end{array} \qquad \forall r_j \in \mathcal{R} \tag{1h}$$

$$s_{i,j} \in \{0,1\}, \qquad \forall v_i \in \mathcal{V}_s, \forall r_j \in \mathcal{R} \tag{1i}$$

$$x_{k,j} \in \{0,1\}, \qquad \forall \bar{e}_k \in \bar{\mathcal{E}}, \forall r_j \in \mathcal{R} \tag{1j}$$

$$0 \leq f_{k,j} \leq |\mathcal{V}_s| \cdot x_{k,j}, \qquad \forall \bar{e}_k \in \bar{\mathcal{E}}, \forall r_j \in \mathcal{R}. \tag{1k}$$

The objective, according to (1a), is to determine the decision variables while minimizing the maximum temporal cost $C_{\max}$ and the cumulative weighted temporal cost of the robotic platforms, i.e., $\sum_{r_j \in \mathcal{R}} C_j(x_j, s_j)$. In this way, we aim to minimize the total time to perform all the agricultural tasks, while avoiding unnecessary motions by all the robots.

Regarding the constraints, Eq. (1b) requires that each node $v_i \in \mathcal{V}_s$ is served by exactly one robot; Eq. (1c) states that, in order for a robot to serve a node $v_i \in \mathcal{V}_s$, the node must be entered by the robot; Eq. (1d) implies that, if a robot r_j has to serve at least one node, then it has to exit the depot v_0; Eq. (1e) states that each time a robot r_j enters a node v_i, the same robot must also exit it; Eqs. (1f)-(1g) refer to the single commodity flow formulation [5] which allows avoiding the generation of disjoint loops in the robots' routes; Eq. (1h) bounds the overall energy consumption of a robot r_j to its capacity K_j; finally, Eqs. (1i)-(1j) impose the binary nature of the decision variables $x_{k,j}, s_{i,j}$ $\forall i, j, k$, while Eq. (1k) regulates the commodity flow variables $f_{k,j}$.

Sub-optimal formulation: Since the formulated multi-Steiner TSP is NP-hard, we propose a sub-optimal formulation which reduces the problem dimensionality thus mitigating its computational load. The basic idea is to decompose the original formulation into multiple polynomial problems which require overall substantially less computational time to be solved, and then, to define a final optimization problem involving a reduced number of variables. More specifically, we build a *service* graph in polynomial time, which embeds the information of the minimum cost paths between service nodes for each robot, and then use the latter graph to compute the decision variables. The sub-optimality of this strategy arises from the fact that the optimization of the turning costs at the service nodes is relaxed. However, this is reasonable in the case the number of agricultural tasks to perform is significantly lower than the number of possible field locations, i.e., $|\mathcal{V}_s| \ll |\mathcal{V}|$, as typical for PA settings. The detailed description of the sub-optimal formulation along with the formal characterization of the optimality gap and extensive simulation campaigns can be found in [6].

REFERENCES

[1] K. Srivastava et al., "An approach for route optimization in applications of precision agriculture using UAVs," *Drones*, vol. 4, 2020.

[2] L. Fotio Tiotsop et al., "An integer linear programming model for efficient scheduling of UGV tasks in precision agriculture under human supervision," *Comput. & Operations Res.*, vol. 114, 2020.

[3] M. Burger et al., "Complete field coverage as a multi-vehicle routing problem," *IFAC Proceedings Volumes*, vol. 46, 2013.

[4] D. Rojas Viloria et al., "Unmanned aerial vehicles/drones in vehicle routing problems: a literature review," *Int. Trans. Oper. Res.*, 2021.

[5] A. N. Letchford et al., "Compact formulations of the steiner traveling salesman problem and related problems," *Europ. J. Operat. Res.*, 2013.

[6] A. Furchì et al., "Route optimization in precision agriculture settings: a multi-steiner tsp formulation," *IEEE Trans. Autom. Sci. Eng.*, 2023.

A Distributed Online Heuristic for a Large-scale Workforce Task Assignment and Multi-Vehicle Routing Problem

Diego Deplano, *Member, IEEE*, Carla Seatzu, *Senior, IEEE*, Mauro Franceschelli, *Senior, IEEE*

***Abstract*— This abstract presents an heuristic online optimization algorithm, based on gossiping, to solve a workforce routing, task assignment, and scheduling problem with privacy by design, drawing inspiration from multi-vehicle routing problems. A real case study is considered, which involves a large number of technicians tasked with refurbishing and repairing a large number of photo booth machines spread across a wide geographic area, spanning a country. The heuristic can be used both offline and online to accommodate delays and unforeseen impediments encountered by technicians. The objective is to maximize enterprise profit by effectively managing the workforce. The proposed method inherently safeguards the privacy of real-time geolocation data for the entire workforce, ensuring it remains undisclosed and inaccessible to the company's ICT infrastructure. Numerical simulation – on real data supplied by DEDEM S.p.A. – demonstrate the performance of the proposed heuristic in terms of expected net profit for the company.**

I. INTRODUCTION

In this work, we examine a real case study provided by the company DEDEM S.p.A – an international company with a long history in the passport photo sector, starting in 1962 with the installation of the first photo booth machine in Rome, Italy – which requires managing a large workforce of technicians responsible for refurbishing and repairing numerous photo booths across the entire Italian territory. The core of the problem involves a dynamic multi-depot (MD) multi-trip (MT) vehicle routing problem (VRP) with time windows (TW) [1]. However, the various extensions and modifications necessary to practically address their workforce management issues make the scenario particularly challenging from a computational perspective. Considering its current workforce of approximately 1 thousand technicians, each tasked with $10 \div 20$ daily assignments distributed geographically, there are up to 20 thousand daily tasks to be addressed. Consequently, this necessitates the development of ad-hoc heuristics. In particular, in our complex scenario, we consider multiple technicians departing from different depots and encountering tasks at each visited position, each with a specified duration and an hourly profit upon completion. Thus, the round trips to be found must maximize the net profit, factoring in both travel expenses and the revenue generated from task completion. Tasks are naturally prioritized based on their proximity to the technician's depot and their potential profitability. To address the company's requirements, we additionally incorporate the following features, further intensifying the complexity of the problem: (i) not all tasks are mandatory; instead, tasks should only be undertaken if they contribute to the net profit; (ii) tasks require specific skills for execution, which should be possessed by the assigned technician; (iii) tasks must be executed within specific time windows and also within the working hours of the technician that performs it, accounting for the time needed to return to their depot; (iv) the problem horizon is pushed beyond a single day, which entails that multiple routes along with their scheduling must be devised for each technician, spanning across multiple days. The above-described problem is threefold: 1) an assignment problem, because tasks must be assigned to the technicians; 2) a routing problem, because the optimal route to visit the tasks must be provided; 3) a scheduling problem, because the time of the day in which tasks are executed changes the profit.

II. A GOSSIP-BASED HEURISTIC ALGORITHM

Let S the set of technicians' depots, by P the set of tasks, and by D_ℓ the set of intra-day depots, one for each extra day $\ell = 1, \dots, d-1$. Let The potential routes that the technicians may travel are modeled by a directed graph $G = (V, E)$, where the set of nodes V consists of the union between the sets S, P, and ℓ and each edge $(i, j) \in E$ correspond to a viable path between locations $i, j \in V$. The MILP formulation make use of the following set of variables: Boolean variables $X_{i,j} \in \{0, 1\}$ denoting the motion of any technician through $(i, j) \in E$; Continuous variables $F_{i,j,k} \in [0, 1]$ denoting the motion of any technician from position $k \in V$ through $(i, j) \in E$; Continuous variables $U_{i,j} \geq 0$ denoting the time at which the motion of any technician through $(i, j) \in E$ occurs.

The cost function to be minimized consists of three terms:

$$f(X, F, U) = \textsc{fuel}(X) + \textsc{tech}(F) - \textsc{tasks}(X, U). \quad (1)$$

Firstly, the cost associated with the fuel consumed by the technicians during the scheduled trip:

$$\textsc{fuel}(X) = \textstyle\sum_{(i,j)\in E} f_{ij} d_{ij} X_{i,j},$$

where $f_{ij} \geq 0$ (*eur/km*) denotes the fuel cost for the path $(i, j) \in E$, which takes into account the average speed on that path; $d_{ij} \geq 0$ (*km*) denotes the distance between locations i, j. Secondly, the cost associated with the technicians' activities:

$$\textsc{tech}(F) = \textstyle\sum_{i\in S} q_i \sum_{j\in P} F_{i,j,i} + \sum_{\ell\in 1}^{d-1} \sum_{i\in D_\ell} q_i \sum_{j\in P} F_{i,j,i},$$

where $q_i > 0$ (*eur*) represents a fixed daily cost of technician $i \in S$. Thirdly, the profit associated with the tasks' execution:

$$\textsc{tasks}(X,U) = \textstyle\sum_{j\in P} g_j \sum_{i\in V} [(24\cdot d - t_{ij} - \delta_i) X_{i,j} - U_{i,j}],$$

where $g_j > 0$ (*eur/hour*) denotes the hourly profit of task the j-th task; t_{ij} (*hour*) denotes the travel time of path $(i, j) \in E$; $\delta_i > 0$ (*hour*) denotes the time needed to execute the i-th task.

Remark 1: *We omit the presentation of the set of constraint for space limitation, which can be found in [2].*

We now describe the proposed a heuristic sub-optimal approach based on *gossiping* – a distributed computing technique used to disseminate information efficiently across a network of nodes – to minimize eq. (1) when the complete problem becomes too large to be solved optimally. The strategy is that of picking at random one pair of technicians and computing a local optimal solution by considering the tasks already assigned to them, if any, together with some unassigned tasks. Once the optimal solution is found, another pair of technicians is considered, until it is not possible anymore to improve any of the schedule for each pair. This approach is quite efficient for mainly two reasons: 1) each local optimization problem is much easier to solve if compared to the global problem; 2) local optimizations involving different technicians can be run simultaneously in parallel. We limit the above described gossip technique over a subset of all these pairs by exploiting their geographical distribution. We do so by means of the so-called "*Delaunay graph*" [3].

Definition 1: *Considering the set of points S scattered over a geometric space, the Delaunay graph $G_D = (S, E_D)$ is the graph whose set of edges in E_D forms a triangulation such that no point in S is inside the circumcircle of any triangle formed by the edges of E.*

The Delaunay graph provides a nice connectivity structure among the input points because for any given node, its incident edges are connected to the nodes that are closer to it than any other node in the set. More importantly, the maximum number of edges in a Delaunay graph is equal to $3n - 6$ for $n \geq 3$, i.e., it increases linearly with the number of nodes, which scales much better than a complete graph with a number of edges equal to $n(n-1)/2$, which increases quadratically. The Delaunay graph is constructed online based solely on the technicians' current tasks, thereby circumventing intrusive geolocation and ensuring technician privacy. The proposed approach can be used both offline, to compute an initial solution to the problem, and online, to continue improving the initial solution while taking into account the following realistic occurrences: delays due to traffic jams or unexpected complications during the execution of the tasks or sudden unavailability of some technicians: in this case, the algorithm is able to re-arrange the schedules of the technicians in order to minimize the loss; availability of new technicians or new tasks: in this case, the algorithm is able to compute new solutions in real time in order to increase the profit. We have implemented the proposed heuristic in Python programming language, utilizing Gurobi 11.0 (with Academic Licence) as the optimization solver.

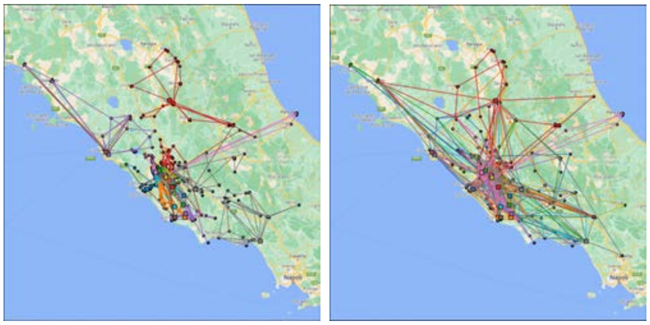

Fig. 1: (Left) Real routes retrieved from DEDEM S.p.A.'s data. Some tasks are not executed due to time window constraints. (Right) Routes obtained by the proposed heuristic. Improved routing and assignments allow more tasks to be executed.

III. NUMERICAL SIMULATIONS

We now discuss a numerical simulation of the proposed heuristic using real data provided by DEDEM S.p.A.. We have collected anonymized data of 16 technicians' tours in a working week of 5 days for a total of 932 tasks to be executed across 5 Italian regions (Lazio, Campania, Toscana, Umbria, Abruzzo). The actual routes taken by the technicians are illustrated in Fig. 1, encompassing 814 tasks (approximately 88% of the total available) completed over a span of 5 workdays. The expected profit, computed as per eq. (1), amounts to € $281.695, 14$. A closer inspection of Fig. 1 reveals that the company currently assigns tasks to technicians based on their geographic proximity.

1) Heuristic offline solution: We simulate the execution the heuristic solution during the weekend to compute a solution for the next working week. The algorithm ran for a total of about 36 hours, from Saturday at 1 AM to Sunday at 1 PM. The routes of the heuristic solution are illustrated in Fig. 1, encompassing 832 tasks (approximately 90% of the total available) completed over a span of 5 workdays. The expected profit, computed as per eq. (1), amounts to € $326.318, 66$. When compared with the real routes, the solution found by the proposed heuristic allows to perform 18 more tasks ($> 2\%$) with an extra profit of € $44.623, 52$ ($> 15\%$).

2) Heuristic online solution: We now consider the scenario in which an unexpected event does not allow the normal execution of the tasks in the schedule: a technician, to which were assigned 19 tasks, is unavailable on the first day, which would cause a profit loss of € $11.094, 52$ if no action is taken. We simulate the real-time execution of the proposed heuristic during the first day of the workweek. Within the first two hours of the day, 17 out of 19 tasks were assigned to other technicians, after which it continued to optimize the routes for the remainder of the day without assigning any additional tasks, but still changing them if convenient. At the end of the day, the profit loss is € $1.055, 41$, less than 10% of the maximum possible loss.

ACKNOWLEDGMENTS

We gratefully acknowledge and thank DEDEM s.p.a. and Federico Lama for the data and support.

REFERENCES

[1] L. Zhen, C. Ma, K. Wang, L. Xiao, and W. Zhang, "Multi-depot multi-trip vehicle routing problem with time windows and release dates," *Transportation Research Part E: Logistics and Transportation Review*, vol. 135, p. 101 866, 2020.

[2] D. Deplano, C. Seatzu, and M. Franceschelli, "A distributed online heuristic for a large-scale workforce task assignment and multi-vehicle routing problem," *IEEE Conference on Automation Science and Engineering*, 2024.

[3] D. P. Dobkin, S. J. Friedman, and K. J. Supowit, "Delaunay graphs are almost as good as complete graphs," *Discrete & Computational Geometry*, vol. 5, pp. 399–407, 1990.

Session 5C: Path planning

Neural Motion Primitives
for Online Time-Optimal Vehicle Trajectory Planning

Mattia Piccinini*, Simon Gottschalk†, Matthias Gerdts†, and Francesco Biral*
* Department of Industrial Engineering, University of Trento, 38123 Trento, Italy.
† Institute for Applied Mathematics and Scientific Computing, Universität der Bundeswehr München, D-85577 Neubiberg, Germany.

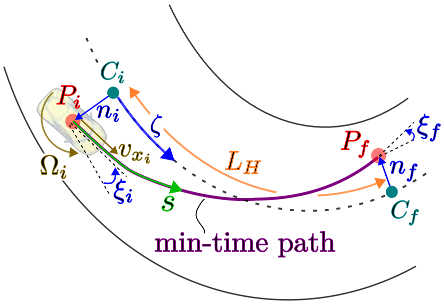

Fig. 1: PathPoly-NN approximates the minimum-time vehicle path joining the waypoints P_i and P_f.

I. Introduction

Autonomous vehicle racing is becoming increasingly popular in research as a platform to advance autonomous driving technologies. Recently, graph-based trajectory planners have been developed for autonomous racing with obstacle avoidance [1]. These planners use a graph of *motion primitives*, which are trajectories connecting pairs of waypoints. The existing methods to compute motion primitives are optimization-based, geometric curve-based, and learning-based, each with its drawbacks: optimization methods are computationally heavy, geometric curves neglect the vehicle dynamics, and neural networks need large training sets to generalize well.

This paper presents novel neural network (NN)-based motion primitives for autonomous racing, aimed at learning and generalizing the minimum-time vehicle trajectories. A detailed description of our motion primitives can be found in our recent work [2]. Here, we provide a brief overview.

II. Methods

Our novel motion primitives have two key components:

1) *PathPoly-NN*: A new NN to compute the minimum-time path.
2) *FW-BW Method* [3]: A semi-analytical solution to compute the minimum-time vehicle speed profile, considering the longitudinal dynamics and a speed-dependent g-g diagram constraint.

A. PathPoly-NN

PathPoly-NN is a neural network designed to learn the vehicle paths obtained from a minimum-time economic nonlinear model predictive controller (E-NMPC). As shown in Fig. 1, PathPoly-NN generates the path connecting the waypoints P_i and P_f, with a center-line distance L_H varying from 4 to 45 meters. Longer horizons can be achieved by concatenating multiple motion primitives. The path is described using the curvilinear coordinates $\{\zeta, n, \xi\}$: ζ is the curvilinear abscissa along the center-line, n is the lateral position, and ξ is the relative yaw angle.

1) Inputs: As shown in Fig. 1, the inputs of PathPoly-NN are:

- The initial lateral coordinate n_i (in point P_i), relative yaw angle ξ_i, forward speed v_{x_i}, yaw rate Ω_i, and the first and second derivatives $\{n_i', n_i''\}$ with respect to ζ.
- The final lateral coordinate n_f (in point P_f), relative yaw angle ξ_f, and the derivatives $\{n_f', n_f''\}$ with respect to ζ.
- The road curvature κ_i in the initial center-line point C_i, and the curvature variation $\Delta\kappa$ over the horizon.

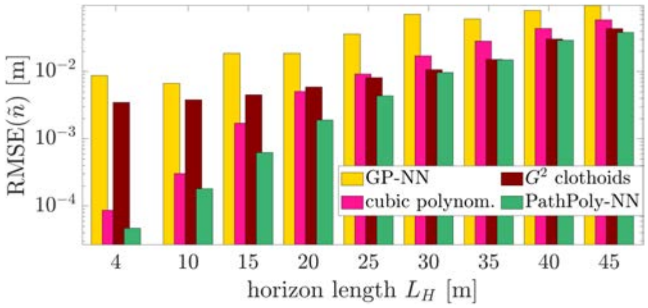

Fig. 2: Comparing the RMS of the lateral coordinate prediction error ($\tilde{n}$) on the test dataset, using PathPoly-NN and the benchmarks. Our PathPoly-NN outperforms the benchmarks for all the considered values of L_H.

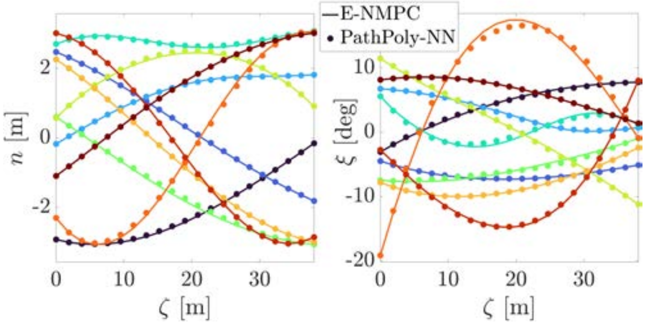

Fig. 3: Comparing the lateral coordinates n and relative yaw angles ξ computed by PathPoly-NN and E-NMPC, for different scenarios.

Let us collect the inputs in the following vectors $\boldsymbol{p}$ and $\tilde{\boldsymbol{p}}$:

$$\begin{aligned} \boldsymbol{p} &= \begin{bmatrix} n_i & \xi_i & v_{x_i} & \Omega_i & n_f & \xi_f & \kappa_i & \Delta\kappa \end{bmatrix}^T \\ \tilde{\boldsymbol{p}} &= \begin{bmatrix} n_i' & n_i'' & n_f' & n_f'' \end{bmatrix}^T \end{aligned} \tag{1}$$

2) Outputs: PathPoly-NN computes the lateral coordinate $n(\zeta)$ of the vehicle path by combining two neural polynomial functions:

$$\begin{aligned} n(\zeta) = {} & \overbrace{\left[\left(\sum_{q=1}^{D} f_{1_q}(\boldsymbol{p}, \tilde{\boldsymbol{p}}) \cdot \zeta^q \right) + n_i \right]}^{\text{first neural polynomial}} \phi\left(\frac{L_H}{2} - \zeta \right) + \\ & + \underbrace{\left[\left(\sum_{q=1}^{D} f_{2_q}(\boldsymbol{p}, \tilde{\boldsymbol{p}}) \cdot (\zeta - L_H)^q \right) + n_f \right]}_{\text{second neural polynomial}} \phi\left(\zeta - \frac{L_H}{2} \right) \end{aligned} \tag{2}$$

Here, D is the polynomial degree, and $\phi(\cdot)$ is an activation function that combines the two polynomials. The functions $\{f_{1_q}(\cdot), f_{2_q}(\cdot)\}$ combine feedforward NNs with analytical components, ensuring the boundary conditions $\{n_i, \xi_i, n_f, \xi_f, n_i', n_i'', n_f', n_f''\}$ are exactly met (see [2] for details). PathPoly-NN also computes the path's curvilinear abscissa $s(\zeta)$, curvature profile $\kappa_p(\zeta)$, and relative yaw angle $\xi(\zeta)$, using relations among the curvilinear coordinates.

3) Training & Testing: PathPoly-NN is trained with supervised learning, to approximate the solutions of minimum-time E-NMPC on 5 circuits, with different prediction horizons L_H. The test set contains the E-NMPC solutions on a new track. The E-NMPC problem uses a kineto-dynamical vehicle model and g-g acceleration constraints, as described in [2]. The total number of training examples is 18000, which is significantly smaller than the 2.7 million examples

Horizon length L_H	**CPU time**							
	E-NMPC (benchmark)		**cubic polynomials + FW-BW** (benchmark)		**G^2 clothoids + FW-BW** (benchmark)		**PathPoly-NN + FW-BW**	
	Mean	Max	Mean	Max	Mean	Max	Mean	Max
20 m	4534.6 µs	22509.0 µs	361.1 µs	460.8 µs	303.7 µs	550.6 µs	**46.2** µs	70.1 µs
35 m	5407.2 µs	31229.4 µs	754.7 µs	956.4 µs	592.0 µs	823.3 µs	**48.5** µs	82.8 µs
45 m	7016.0 µs	42163.3 µs	1190.3 µs	1423.0 µs	752.8 µs	968.5 µs	**53.4** µs	103.1 µs

TABLE I: Comparing the CPU times to compute a motion primitive, using the proposed method (last two columns) and the benchmarks.

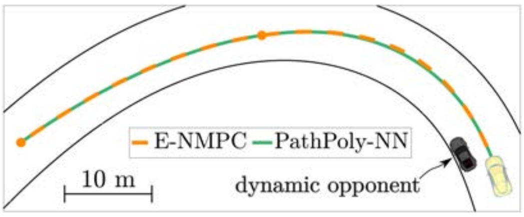

	CPU time	**Maneuver time**
E-NMPC	195205.4 µs	3.632 s
PathPoly-NN + FW-BW	**98.1** µs	**3.647** s

Fig. 4: Example of dynamic obstacle avoidance. Our motion primitives closely approximate the E-NMPC maneuver, with a noticeable decrease in CPU times.

(6000 circuits) used to train the NN of [4]. Indeed, the specialized architecture of PathPoly-NN yields a better generalization with small training sets.

III. RESULTS

We evaluate our motion primitives using the following criteria:

- Accuracy of the vehicle path (lateral coordinate n, relative yaw angle ξ) and speed profile, w.r.t. minimum-time E-NMPC.
- Computational efficiency.

Our motion primitives are compared with the following methods:

1) Minimum-time E-NMPC.
2) A *general-purpose* neural network (GP-NN), similar to [4].
3) Cubic polynomials, used by [5].
4) G^2 clothoid curves, used by [1].

Our motion primitives and all the benchmarks are implemented in `C++` code, and are executed on a 2.6 GHz 6-Core Intel i7 processor. Fig. 2 plots the accuracy (RMS of the lateral deviation $\tilde{n}$) of PathPoly-NN and the benchmarks on the test dataset, for different horizon lengths L_H. Fig. 3 shows that PathPoly-NN accurately approximates the lateral coordinate n and the relative yaw angle ξ of the E-NMPC vehicle path, on unseen test scenarios. Table I reports the corresponding computational times. In comparison with the general purpose neural network (GP-NN), our PathPoly-NN achieves better generalization and accuracy (around one order of magnitude in RMSE), with a much smaller number of parameters (284 vs 11476). Compared with cubic polynomials and G^2 clothoids, our primitives are more accurate and faster in computation by 1-2 orders of magnitude. Our motion primitives yield similar vehicle trajectories and maneuver times as minimum-time E-NMPC, with computational times two orders of magnitude lower. Indeed, in the example scenarios of Fig. 5, the PathPoly-NN's maneuver is the closest to the E-NMPC one. The corresponding speed profile is also close to the E-NMPC one, yet with local differences due to the different path curvatures. Conversely, cubic polynomials and G^2 clothoids yield suboptimal or infeasible trajectories. Fig. 6 plots the concatenation of two motion primitives: in the transition between two primitives, our PathPoly-NN provides a continuous curvature profile, which is the closest to the E-NMPC solution.

Future work will integrate the new motion primitives into the graph-based planner of [1] for dynamic collision avoidance, in challenging scenarios. An example of dynamic obstacle avoidance is shown in Fig. 4, where our primitives closely approximate the E-NMPC maneuver, with a noticeable decrease in computational time.

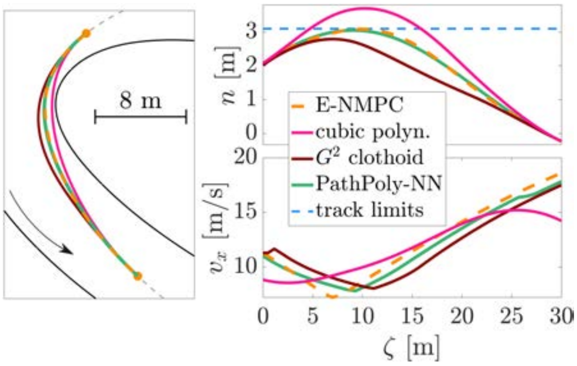

	Feasibility	**Maneuver time**
E-NMPC	✓	**2.123** s
Cubic polynom. + FW-BW	✗ (out of road)	2.114 s
G^2 clothoid + FW-BW	✓	2.276 s
PathPoly-NN + FW-BW	✓	**2.150** s

Fig. 5: Comparing the vehicle paths, lateral coordinates n, and vehicle speed v_x generated by our PathPoly-NN and the benchmarks (cubic polynomials and G^2 clothoids), on a corner of the Pista Azzurra circuit.

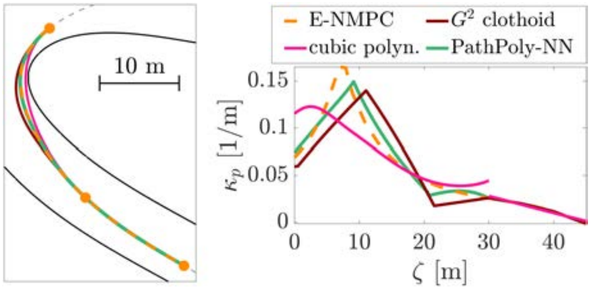

Fig. 6: Concatenation of two motion primitives: our PathPoly-NN provides a continuous path curvature κ_p, which is the closest to the E-NMPC solution.

REFERENCES

[1] M. Piazza, M. Piccinini, S. Taddei, and F. Biral, "Mptree: A sampling-based vehicle motion planner for real-time obstacle avoidance," *IFAC-PapersOnLine*, vol. 58, no. 10, pp. 146–153, 2024, 17th IFAC Symposium on Control of Transportation Systems CTS 2024.

[2] M. Piccinini, S. Gottschalk, M. Gerdts, and F. Biral, "Computationally efficient minimum-time motion primitives for vehicle trajectory planning," *IEEE Open Journal of Intelligent Transportation Systems*, 2024, under review.

[3] M. Frego, E. Bertolazzi, F. Biral, D. Fontanelli, and L. Palopoli, "Semi-analytical minimum time solutions with velocity constraints for trajectory following of vehicles," *Automatica*, vol. 86, pp. 18–28, 2017.

[4] S. Garlick and A. Bradley, "Real-time optimal trajectory planning for autonomous vehicles and lap time simulation using machine learning," *Vehicle System Dynamics*, vol. 60, no. 12, pp. 4269–4289, 2022.

[5] T. Stahl, A. Wischnewski, J. Betz, and M. Lienkamp, "Multilayer graph-based trajectory planning for race vehicles in dynamic scenarios," in *2019 IEEE Intelligent Transportation Systems Conference (ITSC)*, 2019, pp. 3149–3154.

Following Zero-curvature Paths Using the Non-orthogonal Bishop Parametrization

Filip Dyba* and Marco Frego

***Abstract*—The Serret–Frenet frame is widely used as an orthonormal basis of $\mathbb{SO}(3)$, but it cannot be applied to curves with zero-curvature arcs due to the frame indefiniteness. We discuss an alternative based on the Bishop frame and show the advantage both in simulation and with a robotic arm.**

***Index Terms*—Bishop Parametrization, Fixed-base Manipulator, Path Following**

I. INTRODUCTION

The Path Following (PF) task is one of the main robotic problems, requiring to enforce a robot to approach the desired path and move along it [1]. Such a control problem definition is favourable, especially for autonomous robots, due to the lack of time dependency. A path is described purely geometrically and can be easily obtained with motion planning algorithms.

There are different ways to solve the PF problem. One of the most suitable approaches is based on curvilinear parametrizations [2], [3]. They allow defining a local frame which evolves along a curve according to its geometry. However, the Serret–Frenet parametrization, which is frequently applied to the PF task, e.g. [4], [5], has serious disadvantages. If the curvature is equal to zero, a singularity emerges in the frame definition. Indeed, the Serret–Frenet frame is undefined in zero-curvature points and prone to discontinuous changes in the evolution along the curve [6]. Therefore, a description using the Bishop parametrization [7] has been developed to control a robot performing the PF task [8], [9]. In this work, we focus on a fixed-base manipulator.

II. ROBOT DESCRIPTION W.R.T. THE BISHOP FRAME

The Bishop frame [7] consists of three vectors spanning an orthonormal basis in $\mathbb{R}^3$, $\{\boldsymbol{T}, \boldsymbol{N}_1, \boldsymbol{N}_2\}$, where $\boldsymbol{T}$ is the vector tangent to a curve, while $\boldsymbol{N}_1$ and $\boldsymbol{N}_2$ are normal vectors, chosen arbitrarily in the initial state to span relatively parallel vector fields. Once selected, the Bishop frame preserves its uniqueness and minimizes rotations along a curve.

Let us define the *curvilinear distance*, s, which is the distance on the path from its beginning, and a matrix comprising the basis vectors, $\boldsymbol{S} = \begin{bmatrix}\boldsymbol{T} & \boldsymbol{N}_1 & \boldsymbol{N}_2\end{bmatrix} \in \mathbb{SO}(3)$. Then, the frame evolution along the curve is given by the equation

$$\frac{\mathrm{d}\boldsymbol{S}(s)}{\mathrm{d}s} = \boldsymbol{S}(s)\begin{bmatrix} 0 & -k_1(s) & -k_2(s) \\ k_1(s) & 0 & 0 \\ k_2(s) & 0 & 0 \end{bmatrix} = \boldsymbol{S}(s)\boldsymbol{W}(s), \quad (1)$$

where $k_1(s)$ and $k_2(s)$ are geometric invariants of a curve depending on its curvature and torsion [7]. Having defined the frame evolution along a path, the robot description with respect to the path is now developed. Assuming that the manipulator guidance point, located in its end-effector, is non-orthogonally projected onto the path, the following model of the robot kinematics with respect to the path is obtained [5]

$$\dot{\boldsymbol{d}} = \boldsymbol{S}^T\boldsymbol{J}\dot{\boldsymbol{q}} - \begin{pmatrix}\dot{s} & 0 & 0\end{pmatrix}^T - \dot{s}\boldsymbol{W}\boldsymbol{d} = \boldsymbol{G}\dot{\boldsymbol{q}} + \boldsymbol{F}, \quad (2)$$

where $\boldsymbol{d}$ is the end-effector position with respect to the Bishop frame, $\boldsymbol{J}$ is the Jacobian projecting joint velocities into the end-effector velocities in the Cartesian space, and $\boldsymbol{q}$ is the vector of joint positions in the configuration space.

III. CONTROL LAW

The robot description with respect to the path has the form of a non-integrable constraint of the first order. If it is satisfied, the manipulator follows the given path correctly. Due to the similarity to non-holonomic constraints, the control law is designed based on the backstepping algorithm. Firstly, a kinematic controller is proposed to satisfy the constraint (2)

$$\dot{\boldsymbol{q}}_{\text{ref}} = \boldsymbol{G}^{\#}(\dot{\boldsymbol{d}}_d - \boldsymbol{K}_k\boldsymbol{e}_{\boldsymbol{d}} - \boldsymbol{F}), \quad (3)$$

where $\boldsymbol{d}_d$ is the desired position with respect to the Bishop frame, $\boldsymbol{e}_{\boldsymbol{d}} = \boldsymbol{d} - \boldsymbol{d}_d$ is the path following error, $\boldsymbol{K}_k$ is the positive-definite gain matrix, and $\boldsymbol{G}^{\#}$ denotes the Moore–Penrose pseudoinverse of $\boldsymbol{G}$. However, the generated velocity profiles, $\dot{\boldsymbol{q}}_{\text{ref}}$, cannot be commanded directly, due to the robot dynamics. Hence, a universal dynamic controller, the λ - tracking algorithm [10], is used to perform the reference velocity profiles

$$\boldsymbol{u} = -K(t)\boldsymbol{E}(t), \quad (4)$$

where $\boldsymbol{E}(t) = \boldsymbol{K}_d\dot{\boldsymbol{e}}_{\boldsymbol{q}} + \boldsymbol{K}_p\boldsymbol{e}_{\boldsymbol{q}}$ and $\dot{\boldsymbol{e}}_{\boldsymbol{q}} = \dot{\boldsymbol{q}} - \dot{\boldsymbol{q}}_{\text{ref}}$ is the velocity profile following error, $\boldsymbol{K}_d$, $\boldsymbol{K}_p$ are positive-definite matrices, and $K(t)$ is the coefficient tuned by the adaptation law

$$\dot{K}(t) = \begin{cases} (\|\boldsymbol{E}(t)\| - \lambda) \cdot \|\boldsymbol{E}(t)\|, & \|\boldsymbol{E}(t)\| > \lambda, \\ 0, & \|\boldsymbol{E}(t)\| \le \lambda, \end{cases} \quad (5)$$

where $\lambda > 0$ is the arbitrarily selected radius of the dead zone.

IV. STUDY RESULTS

The proposed control law was used to follow a straight line, which is the most evident example of a zero-curvature path. The experimental validation was conducted using a redundant KINOVA® *Gen3 Ultra lightweight robot* and the dedicated KINOVA® Kortex™ software (C++). The simulation

---

$\star$ Correspondence to F. Dyba (filip.dyba@pwr.edu.pl), who is with the Department of Cybernetics and Robotics, Wroclaw University of Science and Technology, Wroclaw, Poland.

M. Frego (mfrego@unibz.it) is with the Faculty of Engineering of the Free University of Bozen-Bolzano, Bolzano-Bozen, Italy.

study was performed for an equivalent direct-drive model of the manipulator in `Matlab/Simulink` environment. The achieved results are presented in the following figures. In Fig. 1, the performed path, the Bishop frame evolution, and the path following errors are shown for both simulation and experimental studies; in Fig. 2, the velocity profile following errors are compared.

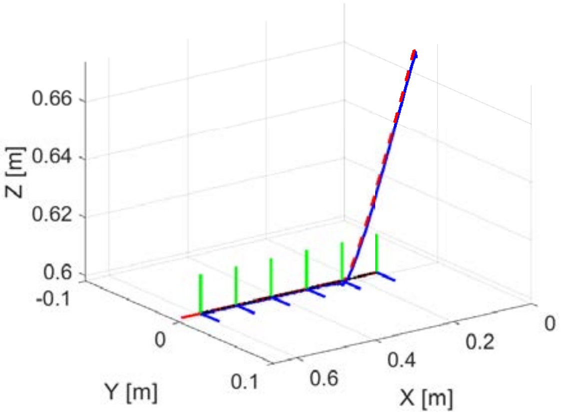

(a) Performed path and Bishop frame evolution

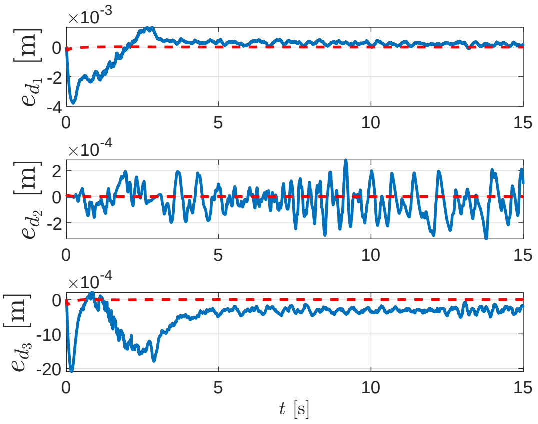

(b) Path following errors

Fig. 1: Path following (blue solid: Experiment, red dashed: Simulation)

V. CONCLUSIONS

The obtained results are consistent and confirm the usefulness of the proposed control law. The desired path is followed correctly and the errors tend to zero. However, in the experimental results more noise may be observed. It results from the sensor accuracy and disturbances which were not considered in the simulation study. Nonetheless, the errors are negligibly small and do not impact the successful manipulator performance. It is concluded that the proposed algorithm based on the non-orthogonal Bishop parametrization is an efficient method to follow paths with zero-curvature points.

ACKNOWLEDGMENT

The work was supported by the project Minigrants for doctoral students of the Wroclaw University of Science and Technology.

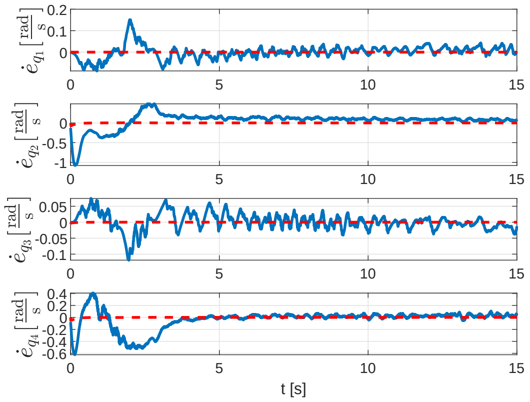

(a) Large joints

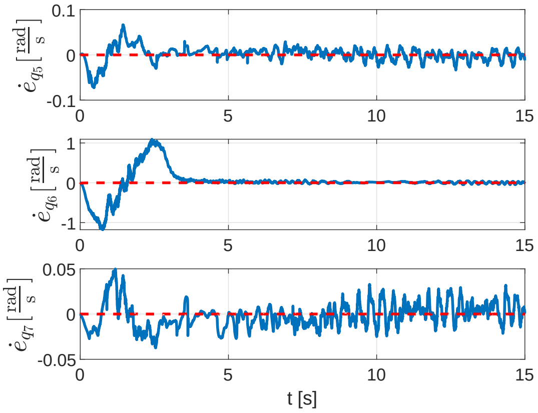

(b) Small joints

Fig. 2: Velocity profile following errors (blue solid: Experiment, red dashed: Simulation)

REFERENCES

[1] N. Hung *et al.*, "A review of path following control strategies for autonomous robotic vehicles: Theory, simulations, and experiments," *J. of Field Robotics*, vol. 40, no. 3, pp. 747–779, 2023.

[2] J. Oprea, *Differential Geometry and Its Applications*. Cleveland State University: Prentice Hall, Washington, 2007.

[3] M. Frego, "Closed form parametrisation of 3d clothoids by arclength with both linear varying curvature and torsion," *Applied Mathematics and Computation*, vol. 421, p. 126907, 2022.

[4] I. Lugo-Cárdenas, S. Salazar, and R. Lozano, "Lyapunov Based 3D Path Following Kinematic Controller for a Fixed Wing UAV," *IFAC-PapersOnLine*, vol. 50, no. 1, pp. 15 946–15 951, 2017.

[5] A. Mazur and F. Dyba, "The Non-orthogonal Serret–Frenet Parametrization Applied to the Path Following Problem of a Manipulator with Partially Known Dynamics," *Archives of Control Sciences*, vol. 33, no. 2, pp. 339–370, 2023.

[6] D. Carroll, E. Köse, and I. Sterling, "Improving Frenet's Frame Using Bishop's Frame," *J. of Mathematics Research*, vol. 5, pp. 97–106, 2013.

[7] R. L. Bishop, "There is more than one way to frame a curve," *The American Mathematical Monthly*, vol. 82, no. 3, pp. 246–251, 1975.

[8] I. Kaminer *et al.*, "Path following for small unmanned aerial vehicles using $\mathcal{L}_1$ adaptive augmentation of commercial autopilots," *Journal of Guidance, Control, and Dynamics*, vol. 33, no. 2, pp. 550–564, 2010.

[9] F. Dyba and A. Mazur, "Comparison of curvilinear parametrization methods and avoidance of orthogonal singularities in the path following task," *Journal of Automation, Mobile Robotics and Intelligent Systems*, vol. 17, no. 3, pp. 46–64, 2024.

[10] A. Mazur and C. Schmid, "Adaptive λ-tracking for rigid manipulators," in *Romansy 13. Theory and practice of robots and manipulators*, A. Morecki, G. Bianchi, and C. Rzymkowski, Eds. Vienna: Springer Vienna, 2000, pp. 103–112.

Autonomous Lunar Rendezvous Trajectory Planning and Control Using Nonlinear MPC and Pontryagin's Principle

Giordana Bucchioni, Michele Pagone, Carlo Novara

I. INTRODUCTION

We propose a Nonlinear Model Predictive Control (NMPC) technique, based on the Pontryagin Minimum Principle [1], for a minimum-propellant autonomous spacecraft (SC) rendezvous maneuver in a non-Keplerian Lunar orbits. The relative motion between the chaser and the target is described by the nonlinear dynamics of the circular restricted three body-problem, written in a moving reference frame called Local-Vertical-Local-Horizontal (LVLH), posing unique challenges due to the complex and unstable dynamics of near-rectilinear halo orbits [2]. Key aspects of the proposed NMPC include trajectory optimization, maneuver planning, and real-time control, highlighting its ability to satisfy complex mission requirements, while ensuring safe and efficient spacecraft operations, in the presence of input and nonlinear/non-convex state constraints. The proposed formulation allows us to design minimum-propellant controller, by minimizing the $\mathcal{L}_1$ of the controlled input within the cost function, enabling an optimal control signal resulting to be bang-bang in time [3]. As proof of the actuality of the topic, the case study based on the Artemis III mission – where the docking of the Orion spacecraft (herein called chaser) to the Gateway station (herein called target) is planned – is illustrated in order to demonstrate the efficiency of the proposed approach to perform the very last part of the rendezvous operations, showcasing its potential for enhancing target tracking accuracy, while reducing propellant consumption and ensuring the reliability of the manoeuvre.

II. SPACECRAFT DYNAMICS AND RVD SCENARIO

The rendezvous manoeuvre is performed following a series of way-points – called hold-points – and, in the results are also contemplated the presence of a spherical obstacle that shall be avoided and a conic line-of-sight constraints for the final phase of the maneuver (see Figure 1). The choice of a spherical shape (and/or ellipsoidal) is motivated by the fact that the safety zones of a space object usually have this kind of shape.

The relative position of the chaser ρ with respect to the target, in the LVLH reference frame, is described by the following nonlinear affine-in-the-input system of differential equations [4]:

$$\begin{aligned}\ddot{\rho} = &-2\big[\mathbf{\Omega}_{IL}\big]\dot{\rho} - \big[\dot{\mathbf{\Omega}}_{IL}\big]\rho - \big[\mathbf{\Omega}_{IL}\big]^2\rho + \\ &+ \mu\left(\frac{\mathbf{r}_{ot}-\mathbf{r}_{om}}{||\mathbf{r}_{ot}-\mathbf{r}_{om}||^3} - \frac{\rho+\mathbf{r}_{ot}-\mathbf{r}_{om}}{||\rho+\mathbf{r}_{ot}-\mathbf{r}_{om}||^3}\right) + \\ &+ (1-\mu)\left(\frac{\mathbf{r}_{ot}-\mathbf{r}_{oe}}{||\mathbf{r}_{ot}-\mathbf{r}_{oe}||^3} - \frac{\rho+\mathbf{r}_{ot}-\mathbf{r}_{oe}}{||\rho+\mathbf{r}_{ot}-\mathbf{r}_{oe}||^3}\right) + u,\end{aligned} \tag{1}$$

where $\mathbf{\Omega}_{IL}$ is the angular velocity of the LVLH frame with respect to an inertial frame, μ and $(1-\mu)$ are the nornalized positions of Earth and Moon in the synodic frame, and $\mathbf{r}_{om}, \mathbf{r}_{om}, \mathbf{r}_{oe}$ are the distance of the Moon, SC, and Earth with respect to the Earth-Moon system center of mass, respectively. The operator $\big[\mathbf{\Omega}_{IL}\big]$ consists of the skew-symmetric matrix for the vector cross-product.

III. PONTRYGIN-BASED MPC APPROACH

The chaser-target relative dynamics can be viewed as an affine-in-the-input nonlinear system

$$\dot{x}(t) = f(x(t)) + u(t) \tag{2}$$

where $x(t) \in \mathcal{X} \subseteq \mathbb{R}^{n_x}$ is the state vector at time $t \in \mathbb{R}$, $u(t) \in \mathcal{U} \subseteq \mathbb{R}^{n_u}$ is the input vector (where $\mathcal{U} \ni 0$ is a convex, closed, and compact set). The measurements of the state vector are sampled with period $T_S > 0$. At each sampling time $t = t_k$, a prediction of the system state $\hat{x}(t)$ over the time interval $[t_k, t_k+T_p]$ is performed, where $T_p \geq T_S$ is the prediction horizon.

The nonlinear MPC optimal control problem is formulated as follows.

$$\begin{aligned}&u^* = \arg\min_u J\big(x(t), u(t)\big) \\ &\text{subject to:} \\ &\dot{\hat{x}}(\tau) = f(\hat{x}(\tau)) + \hat{u}(\tau), \quad \hat{x}(t_k) = x(t_k), \\ &\hat{x}(\tau) \in \mathcal{X} \subset \mathbb{R}^{n_x}, \ \hat{u}(\tau) \in \mathcal{U} \subset \mathbb{R}^{n_u}, \quad \forall \tau \in [t_k, t_k+T_p].\end{aligned} \tag{3}$$

Hence, associating to each solution $\hat{x}$ of (3) the tracking error $\tilde{x}(\tau) = \hat{x}(\tau) - x_r$, we employ the following performance index

$$J = \int_{t_k}^{t_k+T_p} \big(\|\tilde{x}(\tau)\|^2_{\mathbf{Q}} + \|\mathbf{R}\hat{u}(\tau)\|_2\big)\ \mathrm{d}\tau \ + \|\tilde{x}(t_k+T_p)\|^2_{\mathbf{P}}. \tag{4}$$

According to [5], the Hamiltonian of the system, for the RvD scenario is

$$H_{RvD} = \tilde{x}^T\mathbf{Q}\tilde{x} + \|\mathbf{R}u\|_2 + \lambda_r^T\dot{\rho} + \lambda_v^T\ddot{\rho}. \tag{5}$$

where λ_r and λ_v are the covectors associated to the chaser relative position ρ and the relative velocity $\dot{\rho}$, respectively. Whereby, accounting (1), one has

$$\begin{aligned}H_{RvD} = \tilde{x}^T\mathbf{Q}\tilde{x} + \|\mathbf{R}u\|_2 + \lambda_r^T\dot{\rho} + \lambda_v^T\Big[&-2\big[\mathbf{\Omega}_{IL}\big]\dot{\rho} + \\ &-\big[\dot{\mathbf{\Omega}}_{IL}\big]\rho - \big[\mathbf{\Omega}_{IL}\big]^2\rho + \mu\ell(\rho) + (1-\mu)\kappa(\rho) + u\Big]\end{aligned} \tag{6}$$

where $\ell(\rho)$ and $\kappa(\rho)$ are auxiliary functions depending on the chaser/target positions with respect to the Earth and the Moon.

We define the magnitude of the thrust acceleration as $\Gamma \doteq \|u\|_2$ and the thrust acceleration unit vector as $\bar{u}$. Considering that $\mathbf{R}$ is a diagonal definite positive matrix, whose entries are all equal (common setting in the aerospace MPC design), we consider $\|\mathbf{R}u\|_2 = \|\mathbf{R}\|_2\|u\|_2$. We introduce the notion of primer vector, the unit vectors referred to the velocity co-state represent the engines optimal firing direction and defined as $p \doteq -\lambda_v$. Hence the optimal acceleration direction is, $\bar{u}^* = p/P$, being

G. Bucchioni is with the Department of Information Engineering, Università di Pisa. M. Pagone and C. Novara are with the Department of Electronics and Telecommunications, Politecnico di Torino. Corresponding author: `giordana.bucchioni@unipi.it`.

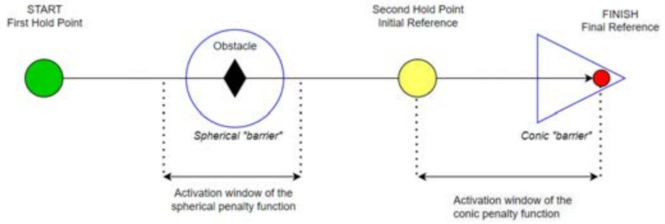

Fig. 1. Scheme of the main mission benchmarks.

$P = \|p\|_2 = -\lambda_v^T \bar{u}^*$ the primer vector magnitude. By the previous notion, the Hamiltonian turns into

$$H_{RvD} = -(P - \|\mathbf{R}\|_2)\Gamma + \lambda_r^T \dot{\rho} + \lambda_v^T \Big[-2\big[\boldsymbol{\Omega}_{IL}\big]\dot{\rho} + -\big[\dot{\boldsymbol{\Omega}}_{IL}\big]\rho - \big[\boldsymbol{\Omega}_{IL}\big]^2 \rho + \mu\ell(\rho) + (1-\mu)\kappa(\rho) \Big]. \tag{7}$$

Hence, the Hamiltonian must be minimized over the choice of the thrust magnitude Γ, which appears linearly in (7). Thus, the optimal control problem solution would lead to an input signal with an infinite magnitude. If the admissible input set is bounded, the minimization of the Hamiltonian depends only on the algebraic sign of the Γ coefficient, which, in aerospace literature is defined as switching function $\Upsilon = P - \|\mathbf{R}\|_2$. The sign of Υ defines the policy for the engines power on/off and the thrust is allowed to assume only the maximum or zero value. The optimal direction of the thrust is driven by $p = -\lambda_v$. Therefore, the optimal control policy is:

$$u^* = \begin{cases} \Gamma_{max} \dfrac{p}{\|\lambda_v\|_2} & \text{if} \quad \Upsilon > 0, \\ 0 & \text{if} \quad \Upsilon \leq 0, \end{cases} \tag{8}$$

where, according to the Pontryagin principle, the evolution of the costate is described by

$$\dot{\lambda} = -\nabla_x H_{RvD}. \tag{9}$$

Finally, the state constraints are implemented within the optimal control problem by employing the penalty function approach, in the PMP framework, described in [1].

IV. Simulation Results

The results show how the proposed control technique is capable of successfully performing the rendezvous approach with satisfying accuracy on the relative state at the docking point and fuel-saving performances. The first phase of the maneuver, going from the initial conditions, to the intermediate hold point located in $[-100, -5, -5]^\top$ km, is shown in Figure 2, while the final target approach in Figures 3-4. Beside the accuracy in tracking the hold point and target locations, it is worth to appreciate the capability of the spacecraft in autonomously coping state constraints, whereas they can be both nonlinear and non convex.

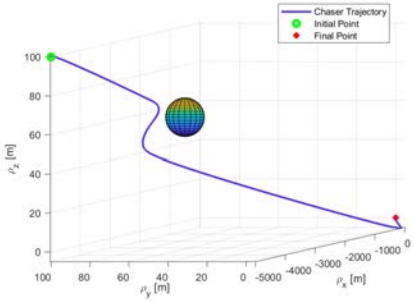

Fig. 2. Chaser approaching trajectory and obstacle avoidance.

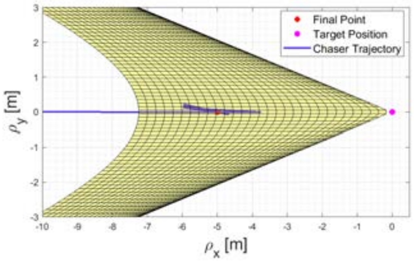

Fig. 3. Chaser proximity maneuver and line-of-sight constraint satisfaction: top view

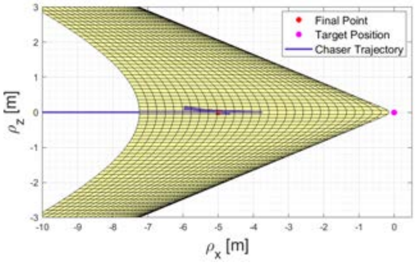

Fig. 4. Chaser proximity maneuver and line-of-sight constraint satisfaction: side view

References

[1] M. Pagone, M. Boggio, C. Novara, A. Proskurnikov, and G. C. Calafiore, "Continuous-time nonlinear model predictive control based on Pontryagin minimum principle and penalty functions," *International Journal of Control, in press*, 2024.

[2] W. S. Koon, M. W. Lo, J. E. Marsden, and S. D. Ross, "Dynamical systems, the three-body problem and space mission design," in *Equadiff 99: (In 2 Volumes)*. World Scientific, 2000, pp. 1167–1181.

[3] M. Pagone, M. Boggio, C. Novara, and S. Vidano, "A Pontryagin-based NMPC approach for autonomous rendez-vous proximity operations," in *Proceedings of the 2021 IEEE Aerospace Conference (50100)*, 2021, pp. 1–9.

[4] G. Franzini and M. Innocenti, "Relative motion dynamics in the restricted three-body problem," *Journal of Spacecraft and Rockets*, vol. 56, no. 5, pp. 1322–1337, 2019.

[5] G. Bucchioni, F. Alfino, M. Pagone, and C. Novara, "A minimum-propellant Pontryagin-based nonlinear MPC for spacecraft rendezvous in lunar orbit," in *Proceedings of the 2023 IEEE 62st Conference on Decision and Control (CDC)*, 2023.

A non smooth numerical optimization approach to the 3-Point Dubins Problem (3PDP)

Mattia Piazza*, Enrico Bertolazzi* and Marco Frego§
* Department of Industrial Engineering, University of Trento; Via Sommarive 9, 38123 Trento, Italy.
§ Faculty of Engineering, Free University of Bozen-Bolzano; Piazza Università 1, 39100 Bolzano-Bozen, Italy.

I. INTRODUCTION

In mobile robotics and autonomous vehicles, *motion* or *path-planning* involves computing an optimal trajectory between an initial and final configuration. Feasible paths must satisfy constraints such as the upper bound for path curvature, related to the vehicle's minimum turning radius ($\kappa_{\max} = 1/\rho_{\min}$), and constant speed. The *Markov-Dubins path* (MDP)[1] computes the minimum length path ($\min \int_0^L 1\,\mathrm{d}\ell$) between two points ($\mathbf{P_i} = (x_i, y_i)$ and $\mathbf{P_f} = (x_f, y_f)$) with given initial and final orientations (ϑ_i and ϑ_f) and a maximum curvature constraint ($\kappa_{\max} > 0$)[2]. The *Multipoint Markov-Dubins Problem* (MPMDP) generalizes this to a sequence of points using interpolation with Dubins paths [3], fixing only the initial and final orientations.

A special case of MPMDP is the *Three Points Dubins Problem* (3PDP), which has applications in high-level planners for the Dubins Travelling Salesman Problem (DTSP) [4]. This path passes through three points, $\mathbf{P_i}$, $\mathbf{P_m}$, and $\mathbf{P_f}$, with given initial and final orientations, ϑ_i and ϑ_f, and a free middle point $\mathbf{P_m}$. The problem is one-dimensional, with the only unknown being the angle at the middle point, ϑ_m. Once ϑ_m is determined, the solution becomes trivial. The solution is discontinuous and non-smooth, often requiring brute force, Dynamic Programming, or NLP/MINLP methods [5]. Some works approximate the solution assuming only CSC paths and discarding CCC [6]. Others use inversive geometry [6] and solve nonlinear systems with bisection, improving computational time by 14 times. Chen *et al.*[7] propose a polynomial-based method computing up to 180 pairs of Dubins paths. Parlangeli *et al.*[5] present a geometry-based method using an ellipse, achieving a 150-fold speed-up compared to DBM.

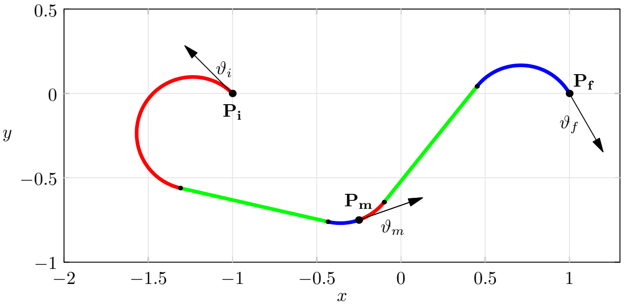

Fig. 1: Example and scheme of an instance of the 3PDP. This path is an example of type LSLSR.

II. DERIVATION OF THE DUBINS PATH WITH TRIGONOMETRY

The original problem can be simplified by translating, rotating, and scaling the configuration so that $x_i = y_i = 0$ and $x_f = d$, $y_f = 0$, with a unitary maximum curvature $\kappa_{\max} = 1$. The transformation involves translating by $-(x_i, y_i)$, rotating around $(0,0)$ by an angle $-\phi$ where $\phi = \operatorname{atan2}(y_f - y_i, x_f - x_i)$, and scaling by $\kappa_{\max}^{-1} = \rho_{\min}$. Thus, $d = \left((x_f - x_i)^2 + (y_f - y_i)^2\right)^{1/2} / \kappa_{\max}$, $\alpha = \vartheta_i + \phi$ and $\beta = \vartheta_f + \phi$ become the initial and final angles. The solution is a sequence of three curves (lines or arcs), expressed as, for $j \in 0, 1, 2$,

$$\begin{cases} x(\ell) = x_j + s(\sin(\vartheta_j + s\ell) - \sin\theta_j) + (1 - s^2)\ell\cos\theta_j, \\ y(\ell) = y_j + s(\cos\theta_j - \cos(\vartheta_j + s\ell)) + (1 - s^2)\ell\sin\theta_j, \\ \theta(t) = \vartheta_j + s\ell, \end{cases}$$

Where ℓ is the curvilinear abscissa, $x(\ell)$ and $y(\ell)$ are the coordinates, and $\theta(\ell)$ is the orientation [8]. Define $x_0 = y_0 = 0$ and $\vartheta_0 = \alpha$ as the initial point. When $s = 0$, the function represents a line segment; when $s = 1$, the curve is a left-turning arc of a unit circle; and when $s = -1$, the arc turns right. The Dubins problem involves three segments (CSC or CCC) with known initial and final coordinates and headings in the transformed system. We can separate solutions into two families based on the presence or absence of the middle singular arc (a line segment): CSC and CCC.

A. Case CSC

This case occurs when $s_2 = 0$ and, depending on the signs of s_1 and s_3, results in the curves LSL, RSR, LSR, and RSL. It can be divided into two subcases: CSC^+, where the two circular arcs turn in the same direction (LSL and RSR), and CSC^-, where the arcs turn in opposite directions (LSR and RSL). Each subcase has two different solutions. We use the following notation for compactness:

$$\begin{aligned} \mathcal{S}^- &= \sin\alpha - \sin\beta, \quad \mathcal{C}^- = \cos\alpha - \cos\beta, \\ \mathcal{S}^+ &= \sin\alpha + \sin\beta, \quad \mathcal{C}^+ = \cos\alpha + \cos\beta, \\ \mathcal{P}_{\alpha,\beta} &= \{\sin\alpha, \cos\alpha, \sin\beta, \cos\beta\}. \end{aligned}$$

1) The subcase CSC^+: LSL and RSR:

This solution type falls into the case $\mathrm{CSC}^+$where $s_2 = 0$ and $s_1 = s_3 = s$. Hence, we can rewrite the problem in terms of the parameters $\mathcal{P}_{\alpha,\beta}$ and solve for ϑ_S and the lengths ℓ_1 and ℓ_3 as follows:

$$\begin{aligned} \vartheta_S^{\mathrm{CSC}^+} &= \operatorname{atan2}\left(-\mathcal{C}^-,\, d + s\,\mathcal{S}^-\right) \mod \pi, \\ \ell_1^{\mathrm{CSC}^+} &= s(\vartheta_S^{\mathrm{CSC}^+} - \alpha) \mod 2\pi, \\ \ell_2^{\mathrm{CSC}^+} &= (d + s\,\mathcal{S}^-)\cos\vartheta_S^{\mathrm{CSC}^+} - s\,\mathcal{C}^-\sin\vartheta_S^{\mathrm{CSC}^+}, \\ \ell_3^{\mathrm{CSC}^+} &= s(\beta - \vartheta_S^{\mathrm{CSC}^+}) \mod 2\pi. \end{aligned}$$

The derivatives of the lengths with respect to α and β are:

$$\begin{aligned} \partial_\alpha(\ell^{\mathrm{CSC}^+}) &= s(\cos(\vartheta_S^{\mathrm{CSC}^+} - \alpha) - 1), \\ \partial_\beta(\ell^{\mathrm{CSC}^+}) &= s(1 - \cos(\beta - \vartheta_S^{\mathrm{CSC}^+})). \end{aligned}$$

2) The subcase CSC^-: LSR and RSL:

This solution type falls into the case CSC^-, where $s_2 = 0$ and $s_1 = s$ and $s_3 = -s$, obtaining a polynomial equation:

$$\vartheta_S = \pi + 2\arctan(X),\ \cos\vartheta_S = \frac{X^2 - 1}{X^2 + 1},\ \sin\vartheta_S = \frac{-2X}{X^2 + 1}.$$

Therefore, we can obtain a quadratic equation in X as follows

$$0 = (2 - \mathcal{C}^+)\,X^2 + 2(s\,d + \mathcal{S}^+)\,X + (2 + \mathcal{C}^+).$$

Furthermore, we can substitute ϑ_S and solve for the lengths.

$$\begin{aligned} \vartheta_S^{\mathrm{CSC}^-} &= \operatorname{atan2}(-2X, X^2 - 1), \\ \ell_1^{\mathrm{CSC}^-} &= s(\vartheta_S^{\mathrm{CSC}^-} - \alpha) \mod (2\pi), \\ \ell_2^{\mathrm{CSC}^-} &= (d + s\,\mathcal{S}^+)\cos\vartheta_S^{\mathrm{CSC}^-} - s\,\mathcal{C}^+\sin\vartheta_S^{\mathrm{CSC}^-}, \\ \ell_3^{\mathrm{CSC}^-} &= s(\vartheta_S^{\mathrm{CSC}^-} - \beta) \mod (2\pi). \end{aligned}$$

And the derivatives of the lengths with respect to α and β are:

$$\begin{aligned} \partial_\alpha(\ell^{\mathrm{CSC}^-}) &= s(\cos(\vartheta_S^{\mathrm{CSC}^-} - \alpha) - 1), \\ \partial_\beta(\ell^{\mathrm{CSC}^-}) &= s(1 - \cos(\beta - \vartheta_S^{\mathrm{CSC}^-})). \end{aligned}$$

The upper bound of the derivative is 2 (Lipschitz constant).

TABLE I: Benchmark test with mean μ and standard deviation σ of iterations and computational times.

Method	Iter		Time (ms)		N. DC
	μ(N)	σ(N)	μ(T)	σ(T)	
PS	85.53	10.65	0.174	0.0359	171.1
PS + 748	46.27	10.74	0.122	0.0309	92.5
PT	73.69	7.96	0.149	0.0256	147.4
PT + 748	54.98	8.74	0.115	0.0253	109.9
DBM	360	0.0	54.845	3.2101	720
iDPP [3]	128	0.0	19.455	0.7400	256

B. Case CCC

The case CCC, happening when $s_2 \neq 0$ $(s_1 = s_3 = -s_2 = s)$:

$$t^{\mathrm{CCC}} = \frac{3+\cos(\alpha-\beta) - s\,d\,\mathcal{S}^-}{4} - \frac{d^2}{8}, \text{ if } t^{\mathrm{CCC}} \in [-1,1]$$
$$\ell_2 = \arccos(t^{\mathrm{CCC}}) \quad \text{and} \quad \ell_2 = 2\pi - \arccos(t^{\mathrm{CCC}});$$

solve the linear systems where $\tilde{\alpha} = \alpha - s\ell_2$ and $\tilde{\beta} = \beta + s\ell_2$:

$$\begin{bmatrix} \sin\alpha - \sin\tilde{\alpha} & s(\cos\alpha - \cos\tilde{\alpha}) \\ \cos\alpha - \cos\tilde{\alpha} & s(\sin\tilde{\alpha} - \sin\alpha) \end{bmatrix} \begin{bmatrix} \cos\ell_1 \\ \sin\ell_1 \end{bmatrix} = \frac{1}{2} \begin{bmatrix} s\,d + \mathcal{S}^- \\ \mathcal{C}^- \end{bmatrix},$$

$$\begin{bmatrix} \sin\tilde{\beta} - \sin\beta & s(\cos\beta - \cos\tilde{\beta}) \\ \cos\tilde{\beta} - \cos\beta & s(\sin\tilde{\beta} - \sin\beta) \end{bmatrix} \begin{bmatrix} \cos\ell_3 \\ \sin\ell_3 \end{bmatrix} = \frac{1}{2} \begin{bmatrix} s\,d + \mathcal{S}^- \\ \mathcal{C}^- \end{bmatrix}.$$

Compute ℓ_1 and ℓ_3 and discard the solutions that do not satisfy $\alpha + s(\ell_1^{\mathrm{CCC}} - \ell_2^{\mathrm{CCC}} + \ell_3^{\mathrm{CCC}}) = \beta \mod 2\pi$.
The derivatives of the lengths with respect to α and β are:

$$\partial_\alpha(\ell^{\mathrm{CCC}}) = \pm\frac{\sin(\alpha-\beta) + s\,d\cos\alpha}{2\sqrt{1-(t^{\mathrm{CCC}})^2}} - s,$$
$$\partial_\beta(\ell^{\mathrm{CCC}}) = s \mp \frac{\sin(\alpha-\beta) + s\,d\cos\beta}{2\sqrt{1-(t^{\mathrm{CCC}})^2}}.$$

The sign depends on the second solution for ℓ_2 is used.

III. THREE POINTS DUBINS PROBLEM (3PDP)

Three Points Dubins Problem solution is a concatenation of 2 Dubins paths, yielding the total length sum of the two elementary Dubins paths lengths [9]. Given the angle of the middle point being the only unknown variable, ℓ_{total} is a function of ϑ_m

$$\ell_{\text{total}}(\vartheta_m) = \ell_{\text{dub1}}(\vartheta_m) + \ell_{\text{dub2}}(\vartheta_m),$$
$$\ell'_{\text{total}}(\vartheta_m) = \ell'_{\text{dub1}}(\vartheta_m) + \ell'_{\text{dub2}}(\vartheta_m).$$

With the results of the previous section, the derivatives are:

$$\ell'_{\text{dub1}}(\vartheta_m) = \partial_\beta \ell_{\text{dub1}} \partial_{\vartheta_m} \beta_1,$$
$$\ell'_{\text{dub2}}(\vartheta_m) = \partial_\alpha \ell_{\text{dub2}} \partial_{\vartheta_m} \alpha_2.$$

Recalling that for a single segment $\vartheta_i = \alpha - \phi$ and $x_f = d$, $y_f = 0$, $\vartheta_f = \beta - \phi$ and $\phi = \operatorname{atan2}(y_f - y_i, x_f - x_i)$, we get $\partial_{\vartheta_m}\beta_1 = 1$ and $\partial_{\vartheta_m}\alpha_2 = 1$.
However, both angles $\phi_1 = \operatorname{atan2}(y_m - y_i, x_m - x_i)$ and $\phi_2 = \operatorname{atan2}(y_f - y_m, x_f - x_m)$ do not depend on ϑ_m and can be considered as constants,

$$\ell'_{\text{total}}(\vartheta_m) = \partial_{\beta_1}\ell_{\text{dub1}}(\vartheta_i, \beta_1 - \phi_1) + \partial_{\alpha_2}\ell_{\text{dub2}}(\alpha_2 - \phi_2, \vartheta_f).$$

The lengths are piecewise continuous functions of ϑ_m. Therefore, we need to use a numerical method to find the optimal angle ϑ_m that minimizes the total length of the path (figure 2).

IV. NUMERICAL TESTS AND RESULTS

We tested our algorithm, which uses pattern search and root finding, on 10 000 random 3PDP against the brute force method (DBM) and the iterative Dubins path planner (iDPP). Table I and Table II show that our algorithm outperforms the benchmarks in iterations and computational time. Using root finding further reduces iterations and time while achieving machine-precision optimal solutions.

TABLE II: Comparison between the number of iterations and time with respect to brute force DBM.

Algorithm	Iteration number ratio	Time ratio
Pattern search	4.27013	325.655
Pattern search + 748	6.57409	471.777
Pattern trichotomy	4.93803	374.726
Pattern trichotomy + 748	6.67441	493.497
iDPP [3]	2.8125	2.82009
IM [6]	n/a	5
PBM [7]	n/a	25-45
GBM [5]	n/a	150

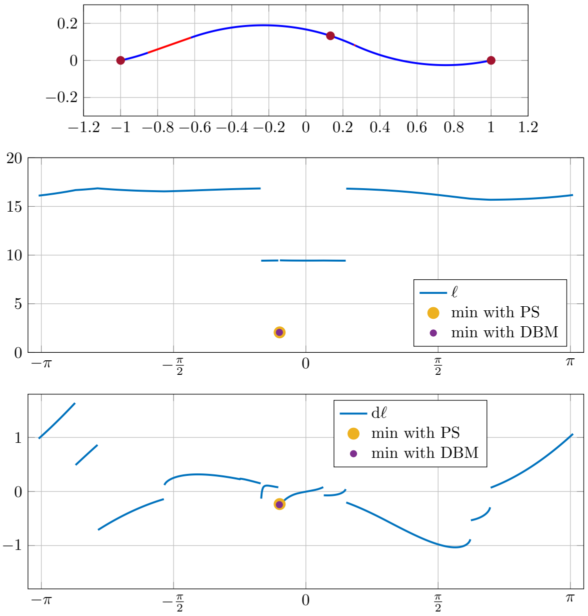

Fig. 2: Example of the total length of a three-point Dubins path

REFERENCES

[1] A. A. Markov, “Some examples of the solution of a special kind of problem on greatest and least quantities,” *Soobshch. Karkovsk. Mat. Obshch*, vol. 1, pp. 250–276, 1887.
[2] C. Y. Kaya, “Markov–Dubins path via optimal control theory,” *Computational Optimization and Applications*, vol. 68, no. 3, pp. 719–747, Dec 2017.
[3] M. Frego, P. Bevilacqua, E. Saccon, L. Palopoli, and D. Fontanelli, “An Iterative Dynamic Programming approach to the Multipoint Markov-Dubins Problem,” *IEEE Robotics and Automation Letters*, vol. 5, no. 2, pp. 2483–2490, 2020.
[4] L. Li, D. Shi, S. Jin, S. Yang, C. Zhou, Y. Lian, and H. Liu, “Exact and Heuristic Multi-Robot Dubins Coverage Path Planning for Known Environments,” *Sensors*, vol. 23, no. 5, 2023.
[5] G. Parlangeli, D. De Palma, and R. Attanasi, “A novel approach for 3PDP and real-time via point path planning of Dubins’ vehicles in marine applications,” *Control Eng. Pract.*, vol. 144, p. 105814, 2024.
[6] A. Sadeghi and S. L. Smith, “On efficient computation of shortest dubins paths through three consecutive points,” in *2016 IEEE 55th Conference on Decision and Control (CDC)*, 2016, pp. 6010–6015.
[7] Z. Chen and T. Shima, “Shortest Dubins paths through three points,” *Automatica*, vol. 105, pp. 368 – 375, 2019.
[8] E. Bertolazzi and M. Frego, “A note on robust biarc computation,” *CAD and Applications*, vol. 16, no. 5, pp. 822–835, 2019.
[9] M. Piazza, E. Bertolazzi, and M. Frego, “A Non-Smooth Numerical Optimization Approach to the Three-Point Dubins Problem (3PDP),” *Algorithms*, vol. 17, no. 8, 2024.

Tracking of Clothoids via Internal Model Principle

Nicola Mimmo[1], Marco Frego[2], Angelika Peer[2]

Abstract— **Clothoids are curves characterised by linear curvature. Their use is transversal in many applications ranging from motorway junctions to computer graphics passing through computer numerically controlled machines. Tracking these curves has an impact on efficiency in many fields. We present some preliminary results on a control system for the tracking of clothoids that relies on the so-called Internal Model Principle.**

I. INTRODUCTION

In control theory, trajectory tracking is an important field of research because it enables many other applications, which are based on precision, efficiency, resilience to disturbances, and adaption to unforeseen events that move the current state of a system far from its prescribed nominal position.

A paradigm for solving the trajectory tracking problem requires the knowledge of the current tracking error and the model that generates the reference trajectory [1]. Then, given the current tracking error, the asymptotic tracking of trajectories is related to the ability of the control system to embed the model that generates the reference signal. The techniques that exploit this fundamental approach go under the umbrella of the Internal Model Principle (IMP) [2]. The corresponding component of the controller that generates the control needed to keep the tracking error zero, uniformly on time, is called the Internal Model Generator (IMG).

Clothoids are used to design paths and trajectories starting with their intrinsic parametrisation. Examples in this family that can be represented with clothoids are lines, biarcs, Dubins, Reeds-Shepp and helices. An advantage of these primitives is that they naturally possess arclength parametrisation, and also, their curvature has a special (read simple) expression of the arclength, e.g., it is linear for clothoids. This latter property is of paramount importance because it is strictly connected with the lateral accelerations that a body endures during the motion. This reflects in the comfort of passengers, in the mechanical stress suffered by the parts of a vehicle, and it has a deep connection with what our brain perceives as visually appealing and is a fundamental concept in aesthetic shape design. They also represent the natural trajectories a car-like generates when moving at a constant speed [3].

We propose the design and adoption of an Internal Model Generator and the related control system when the exogenous model is a smooth sequence of planar clothoid curves travelled with constant speed. While the existence of the IMG is ensured in [4], finding it for a generic nonlinear system represents a challenging task. In this respect, its application to a clothoidal model is new and proposed here for the first time.

II. PROBLEM FORMULATION

This section describes the elements that constitute the studied system, formulates the problem, and offers a solution.

a) Plant: The plant herein considered is a 2D double integrator system, whose position, velocity, and controlled acceleration are $p, v, u \in \mathbb{R}^2$. It represents, for instance, the model of a vehicle, whose dynamics is

$$\begin{aligned} \dot{p} &= v, \quad p(t_0) = p_0, \\ \dot{v} &= u, \quad v(t_0) = v_0, \end{aligned} \tag{1}$$

where $p_0, v_0 \in \mathbb{R}^2$ denote the position and velocity at time $t = t_0 \in \mathbb{R}$. Thanks to the form of the above equations, the plant is modelled as a chain of integrators.

b) Reference: The reference trajectory is given by the exogenous system $w := \texttt{col}(r, \theta, \kappa, \sigma) \in \mathbb{R}^5$ and represents a clothoid spline, where $r \in \mathbb{R}^2$ is the reference position, $\theta \in \mathbb{R}$ denotes the reference course angle, $\kappa \in \mathbb{R}$ is the reference curvature, and $\sigma \in \mathbb{R}$ denotes the reference sharpness, which is piece-wise constant, since it is the derivative of the curvature, which, in turn, for a clothoid, is a linear function. The model that generates the spline is

$$\dot{w} = s(w), \quad w(t_0) = w_0, \tag{2}$$

where $w_0 \in \mathbb{R}^5$ denotes the initial conditions and $s(w) := \texttt{col}(\cos\theta, \sin\theta, \kappa, \sigma, 0)$. From w, the reference position is extracted using the selection matrix $H := [I_{2\times 2} \; 0_{2\times 3}]$ as $r = Hw$. In what follows, the property of the clothoid spline sharpness σ to have a *time interval* is used. In other words, the sharpness of the clothoid splines, which is piece-wise constant, has jumps that are at least $\Delta T > 0$ separated.

c) Tracking error: Having defined the plant and the reference, it is possible to formulate and characterise the (position) tracking error $e := p - r$ and its derivative $\dot{e}$, that are collected in the vector $\xi \in \mathbb{R}^4$,

$$\xi := \texttt{col}(\xi_1, \xi_2) = \texttt{col}(e, \dot{e}). \tag{3}$$

Let ξ be the vector of the errors and their first derivative as in (3), define $q(w)$ as

$$q(w) := H\ddot{w} = H\frac{\partial s(w)}{\partial w} s(w), \tag{4}$$

---

[1] The author is with the Department of Electrical, Electronic, and Information Engineering "Guglielmo Marconi", University of Bologna, Bologna, Italy. Email: nicola.mimmo2@unibo.it

[2] The authors are with the Faculty of Engineering of the Free University of Bozen-Bolzano, Bolzano, Italy. Email: {marco.frego, angelika.peer}@unibz.it

then,

$$\begin{aligned} \dot{\xi}_1 &= \xi_2, & \xi_1(t_0) &= \xi_{1,0}, \\ \dot{\xi}_2 &= u - q(w), & \xi_2(t_0) &= \xi_{2,0}. \end{aligned} \tag{5}$$

The acceleration error is thus $u - q(w)$, hence $q(w)$ represents the unknown reference acceleration that the control u should be able to replicate, in order to keep the error $e(t) = 0$ for any $t \geq t_0$.

d) Assumptions and hypotheses: Before stating the tracking problem, some assumptions are required:

1) Constant speed. The reference trajectory is travelled at a constant (unitary) speed.
2) Regularity of reference. The initial condition w_0, the reference curvature $\kappa(t)$ and sharpness $\sigma(t)$ are bounded. In other words, there exist $\kappa_{\max} > 0$ and $\sigma_{\max} > 0$ bounding $\|\kappa(t)\|_\infty \leq \kappa_{\max}$ and $\|\sigma(t)\|_\infty \leq \sigma_{\max}$. Moreover, σ has a time interval $\Delta T > 0$.
3) Measurable error. The tracking error e, the derivative $\dot{e}$, and the speed v are measurable. The sensor suite provides the following output:

$$y := \texttt{col}(y_1, y_2, y_3) = \texttt{col}(\xi, v),$$

with $y_1, y_2, y_3 \in \mathbb{R}^2$.

The first assumption does not represent a limitation of the presented approach but rather a simplification of this preliminary study. Indeed, given a model of the generator of the speed profile, it is possible to extend the proposed IMG to include it. The second assumption is reasonable for a feasible trajectory that takes into account the minimum turning radius (or maximum curvature) of a non-holonomic vehicle. A similar argument holds for the regularity of the derivative of the curvature σ. The third assumption, in line with assumptions in [4], is added to characterise the used hypotheses regarding the measurability of the tracking errors.

Problem 1. *Consider the error vector* (3)*, its dynamics* (5) *and the Assumptions. Let $\epsilon > 0$ be a prescribed performance index in terms of clothoid tracking accuracy. Then, design a control u such that the trajectories of* (5) *are bounded and $\|\xi_1(t)\| \leq \epsilon$ for all $t \geq t^\star$, for any initial conditions $(p(t_0), v(t_0)) \in \mathcal{S}_0$, with $\mathcal{S}_0$ being a non-empty set of initial conditions of* (1)*, for some $t^\star \geq t_0$, and for any sharpness σ satisfying the Assumptions with sufficiently long time interval ΔT and small $\sigma_{\max}$.*

III. PROPOSED SOLUTION

The first claim is that $n = 3$ is large enough to implement an IMG that solves Problem 1. Then, introduce $\eta := \texttt{col}(\eta_1, \eta_2, \eta_3) \in \mathbb{R}^3$, and consider

$$\begin{aligned} \alpha_1(\eta, \hat{\gamma}(y)) &:= \left[S\gamma(\eta)\right]^\top \hat{\gamma}(y), \\ \gamma(\eta) &:= \texttt{col}(\cos\eta_1, \sin\eta_1), \\ \hat{\gamma}(y) &:= \frac{y_3 - y_2}{\|y_3 - y_2\|}, \end{aligned} \tag{6}$$

with

$$S := \begin{bmatrix} 0 & -1 \\ 1 & 0 \end{bmatrix}.$$

The quantity $\gamma(\eta)$ represents the vehicle's velocity that the control system wants to impose, whereas $\hat{\gamma}(y)$ is the estimate of the reference vehicle's velocity, such that $\left[S\gamma(\eta)\right]^\top \hat{\gamma}(y)$ can be thought as the velocity error. The second claim is that the following control system solves Problem 1:

$$\dot{\eta} = A\,\eta + G\,\alpha_1(\eta, \hat{\gamma}(y)), \qquad \eta(t_0) = \eta_0, \tag{7a}$$

$$u = \frac{\partial\gamma(\eta)}{\partial\eta}\dot{\eta} + \alpha_2(\eta, y), \tag{7b}$$

with A a shift matrix of dimension 3, $\eta_0 \in \mathbb{R}^3$, $\alpha_2(\eta, y) := -c^2 y_1 - c(y_2 + y_3) + c\gamma(\eta)$, and with $c > 0$ and $G \in \mathbb{R}^3$ being design parameters. We can now state the main theoretical result of our study.

Theorem 1. *Consider the dynamics of the tracking error* (5)*, the Assumptions and let $\epsilon > 0$ be a desired performance index. Then, there exist $c^\star, t^\star, \Delta T^\star, \sigma^\star > 0$ and $G \in \mathbb{R}^3$ such that for any $c \geq c^\star$, any piece-wise constant σ with time interval $\Delta T \geq \Delta T^\star$ and such that $\sigma_{\max} < \sigma^\star$, the control law u, output of system* (7)*, solves Problem 1.*

IV. CONCLUSIONS AND FUTURE RESEARCH DIRECTIONS

We presented preliminary results on an internal model-based control system for the asymptotic tracking of clothoids. An internal model generator is proposed under classic assumptions about the boundedness of the reference position, curvature, and sharpness, and the measurability of tracking errors. It is worth noting that the approaches currently available in the literature do not provide a solution to the problem under consideration. Future works will focus on removing limitations such as the need for a sharpness that remains constant for sufficiently long periods. Moreover, also the stability proofs will be formalised.

ACKNOWLEDGMENTS

This work has been supported by the Grant "Design Of Cooperative Energy-aware Aerial plaTforms for remote and contact-aware operations" (DOCEAT) funded by the Italian MUR, n. 2020RTWES4, CUP n. E63C22000410001.

REFERENCES

[1] A. Isidori and C. I. Byrnes, "Output regulation of nonlinear systems," *IEEE Trans. on Automatic Control*, vol. 35, no. 2, pp. 131–140, 1990.

[2] B. Francis and W. Wonham, "The Internal Model Principle of control theory," *Automatica*, vol. 12, no. 5, pp. 457–465, 1976.

[3] M. Frego, E. Bertolazzi, F. Biral, D. Fontanelli, and L. Palopoli, "Semi-analytical minimum time solutions with velocity constraints for trajectory following of vehicles," *Automatica*, vol. 86, pp. 18–28, 2017.

[4] L. Marconi, L. Praly, and A. Isidori, "Output stabilization via nonlinear Luenberger observers," *SIAM Journal on Control and Optimization*, vol. 45, no. 6, pp. 2277–2298, 2007.

Time-optimal speed planning under jerk constraints

Stefano Ardizzoni, Luca Consolini, Mattia Laurini, and Marco Locatelli*

Consider the problem of computing a minimum-time motion of a car-like vehicle from a start configuration to a target one, while avoiding collisions (obstacle avoidance), and satisfying kinematic, dynamic, and mechanical constraints (for instance, on velocities, accelerations and maximal steering angle). It is common to solve this problem in two steps. First, we use a geometric path planner to find a suitable path. Then, we perform minimum-time speed planning on the planned path (see, for instance, [1, 3, 4]). Clearly, this approach is sub-optimal with respect to a single-step procedure, in which we plan the geometric path and the speed law at the same time. However, this choice considerably simplifies the problem. In this paper, we assume that the path that joins the initial and final configurations is assigned, and we aim at finding the time-optimal speed law that satisfies some kinematic and dynamic constraints. The problem can be reformulated as an optimization problem, and it is quite relevant from a practical point of view. In particular, in automated warehouses, the speed laws of Automated Guided Vehicles (AGVs) are typically planned under acceleration and jerk constraints. We compute a time-optimal control law, taking into account constraints on maximum speed, tangential and lateral acceleration, and jerk. We propose a convex relaxation of the original nonconvex problem, where nonconvexity is due to the jerk constraints (see [2]). We reformulate the relaxed problem as a second order cone programming (SOCP) problem. This allows solving the problem very efficiently with modern solvers. We consider the following problem, which is the discretized version of the previously described speed planning problem.

$$\min_{w \in \mathbb{R}^n} \sum_{i=2}^{n-1} \frac{h}{\sqrt{w_i}}$$

where w is the squared speed, h is the time step and w is subject to the following constraints

$$\begin{aligned}
& w_1 = w_n = 0 && && (1)\\
& 0 \leq w_i \leq w_i^{\max} && i = 2, \dots, n-1, && (2)\\
& w_{i+1} - w_i \leq hA, && i = 1, \dots, n-1, && (3)\\
& w_i - w_{i+1} \leq hA, && i = 1, \dots, n-1, && (4)\\
& (w_{i-1} - 2w_i + w_{i+1})\sqrt{w_i} \leq h^2 J, && i = 2, \dots, n-1, && (5)\\
& -(w_{i-1} - 2w_i + w_{i+1})\sqrt{w_i} \leq h^2 J, && i = 2, \dots, n-1, && (6)
\end{aligned}$$

where: constraints (1) are the initial and final interpolation conditions; $w_{\max}$ and A, are bounds for speed and acceleration, imposed through constraints (2), and (3), (4), respectively, and constraints (5) and (6) impose a bound on the time derivative of the acceleration (also called "jerk"). By adding variables t_i, $i = 2, \dots, n-1$, and setting, for each $i = 2, \dots, n-1$:

$$t_i = \frac{h}{\sqrt{w_i}}, \quad \Delta w_i = \frac{w_{i-1} - 2w_i + w_{i+1}}{hJ}, \tag{7}$$

we can relax the problem into a convex one by replacing the equality constraints with inequalities

---

[*] All authors are with the Dipartimento di Ingegneria e Architettura, Università degli Studi di Parma, Parco Area delle Scienze, 181/A, 43124 Parma, Italy. E-mails: {`stefano.ardizzoni`, `luca.consolini`, `mattia.laurini`, `marco.locatelli`}`@unipr.it`.

$t_i \geq \frac{h}{\sqrt{w_i}}$. We end up with the following convex problem

$$\begin{array}{lll} \min\limits_{w,t} & \sum\limits_{i=2}^{n-1} t_i & \\ & w_1 = w_n = 0 & \\ & 0 \leq w_i \leq w_i^{\max} & i = 1, \dots, n. \\ & t_i \geq \Delta w_i & i = 2, \dots, n-1 \\ & t_i \geq -\Delta w_i & i = 2, \dots, n-1 \\ & t_i \geq \frac{h}{\sqrt{w_i}} & i = 2, \dots, n-1 \\ & w_{i+1} - w_i \leq Ah & i = 2, \dots, n-1 \\ & w_i - w_{i+1} \leq Ah & i = 2, \dots, n-1 \end{array} \tag{8}$$

In spite of many attempts to give a formal proof that the relaxed problem is exact, up to now we have not been able to derive this fact, although we conjecture that this is the case. However, we prove that any feasible solution w of the original problem, induces a feasible solution (w, t) with $t_i = \frac{h}{\sqrt{w_i}}$ of the relaxation (8). As a consequence, if the optimal solution $(w^\star, t^\star)$ of the convex relaxation (8) is such that $w^\star$ is feasible for the original one, then $w^\star$ is also optimal for it, and the convex relaxation has the same optimal value of the original problem. This motivates the following algorithm for solving our problem. First, we solve convex relaxation (8) as a second-order cone program (SOCP). Then, to complete the algorithm, in case $w^\star$ is not feasible, we use $(w^\star, t^\star)$ as the starting condition for a generic nonconvex solver. Note that we cannot remove the last step since we do not have a formal proof of the exactness of the problem. Moreover, it is necessary if we consider a generalization of our problem, in which constraint parameters A, J vary with step i. Indeed, the conjecture turns out to be false as soon as we extend the class of problems, in particular, by allowing different bounds for the jerk along the trajectory. It has also been shown that the convex relaxation can be rewritten as a SOCP problem. This has a relevant practical impact, since solvers for SOCP problems are quite efficient and allow solving large instances within tenths of a second.

As a possible topic for future research, we are interested in evaluating the performance of the proposed approach to robotic manipulators. These problems can be reformulated in a way similar to the problems addressed in this paper. We do not expect to be able to extend our conjecture to such problems, but we do expect that, even in cases where the convex relaxation is not exact, the final solution returned by the proposed solution algorithm has a small percentage gap with respect to the optimal one.

References

[1] C. G. L. Bianco. Optimal velocity planning for autonomous vehicles under kinematic constraints. *IFAC Proceedings Volumes*, 39(15):126–131, 2006.

[2] L. Consolini, M. Locatelli, and A. Minari. A sequential algorithm for jerk limited speed planning. *IEEE Transactions on Automation Science and Engineering*, 19(4):3192–3209, 2022.

[3] M. Frego, E. Bertolazzi, F. Biral, D. Fontanelli, and L. Palopoli. Semi-analytical minimum time solutions for a vehicle following clothoid-based trajectory subject to velocity constraints. In *2016 European Control Conference (ECC)*, pages 2221–2227, June 2016.

[4] J. Hauser and A. Saccon. Motorcycle modeling for high-performance maneuvering. *IEEE Control Systems Magazine*, 26(5):89–105, 2006.

Session 6A: Modelling and estimation

A Lasso approach to secure state estimation for cyber-physical systems

V. Cerone S. M. Fosson D. Regruto F. Ripa

Abstract— **The development of algorithms for secure state estimation in vulnerable cyber-physical systems has been gaining attention in the last years. A consolidated assumption is that an adversary can tamper a relatively small number of sensors. In this paper, we propose a Lasso-based approach and we analyse its effectiveness. We theoretically derive conditions that guarantee successful attack/state recovery and we develop a sparse state observer. We compare the proposed methods to the state-of-the-art algorithm via numerical simulations.**

I. INTRODUCTION

A cyber-physical system (CPS) is a collection of computing devices that interact with the physical world, through sensors and actuators, and with one another, through communication networks. Applications of the CPS paradigm include industrial control processes, smart power grids, wireless sensor networks, electric ground vehicles and cooperative driving technologies. A relevant research line considers the problem of secure state estimation (SSE) for CPSs in the presence of sensor attacks, that inject false data to manipulate the measurements. We expect that an adversary conceives an unpredictable intrusion, that is, we have no information on its dynamics. The unique realistic assumption on sensor attacks is sparsity: only a relatively small number of sensors is accessible, due to, e.g., large dimensionality and physical deployment of CPSs.

The identification of the attack support, i.e., the subset of tampered sensors, is a combinatorial problem that does not scale well for large dimensional systems. By leveraging the sparsity assumption, one can exploit ℓ_1-based sparsity-promoting decoders to recast the problem into constrained convex optimization; see, e.g., [1], [2]. Since these approaches are still computationally intense, [3] introduces a faster event-triggered projected gradient (ETPG) approach, whose structure is prone to recursive SSE. The provided sufficient conditions for the convergence of ETPG are quite restrictive. The work [4] addresses this issue by a satisfiability modulo theory approach, called Imhotep-SMT, which is suitable for small/medium dimensional problems.

In this work, we propose a Lasso approach, see [5], to SSE of CPSs under sparse sensor attacks and we analyse its effectiveness. Moreover, we design a sparsity-promoting Luenberger-like observer by starting from the iterative soft thresholding algorithm for Lasso and we propose some numerical results.

II. PROBLEM STATEMENT

As in [1], [3], we consider CPSs that can be modeled as

$$\begin{aligned} x(k+1) &= Ax(k) \\ y(k) &= Cx(k) + a(k) \end{aligned} \tag{1}$$

where $x(k) \in \mathbb{R}^n$ is the state, $y(k) \in \mathbb{R}^p$ is the measurement vector, $a(k) \in \mathbb{R}^p$ is the attack vector. We assume that each sensor i takes a measurement $y_i(k) \in \mathbb{R}$. If $a_i(k) \neq 0$, sensor i is under attack. The SSE problem is as follows.

Problem 1: For some $\tau \leq n$ and $k \geq \tau - 1$ given A, C and $y = (y(k-\tau+1)^\top, \dots, y(k)^\top)^\top \in \mathbb{R}^{p\tau}$, estimate $x(k-\tau+1)$ in the presence of sparse sensor attacks.

Let us denote $\widetilde{a} = (a(k-\tau+1)^\top, \dots, a(k)^\top)^\top \in \mathbb{R}^{p\tau}$ and $\widetilde{x} = x(k-\tau+1) \in \mathbb{R}^n$, while $I \in \{0,1\}^{p\tau, p\tau}$ is the identity matrix. We have $y = \begin{pmatrix} \mathcal{O} & I \end{pmatrix} \begin{pmatrix} \widetilde{x}^\top & \widetilde{a}^\top \end{pmatrix}^\top$ where $\mathcal{O} = \begin{pmatrix} C^\top & (CA)^\top & \cdots & (CA^{\tau-1})^\top \end{pmatrix}^\top \in \mathbb{R}^{p\tau, n}$. If $\tau = n$, $\mathcal{O}$ is the observability matrix of the attack-free system; we assume $\operatorname{rank}(\mathcal{O}) = n$.

III. LASSO APPROACH

By taking into account the sparsity of $\widetilde{a}$, we propose the following Lasso formulation for Problem 1:

$$(x^\star, a^\star) = \underset{x \in \mathbb{R}^n, a \in \mathbb{R}^{p\tau}}{\operatorname{argmin}} \frac{1}{2} \|y - \mathcal{O}x - a\|_2^2 + \lambda \|a\|_1 \tag{2}$$

where $\lambda > 0$. An interesting feature of classic Lasso is that there is a tight condition, denoted as "irrepresentable", that guarantees the recovery of the correct support; see, e.g., [6]. In this work, we perform an irrepresentable condition analysis for (2), by taking into account the structure of the "sensing matrix" $\begin{pmatrix} \mathcal{O} & I \end{pmatrix}$ and the ℓ_1 regularization applied only to variables a.

In the following, $\mathcal{S}$ is the support of $\widetilde{a}$ and $\bar{\mathcal{S}}$ is its complementary set. $\mathcal{O}_{\mathcal{S}} \in \mathbb{R}^{h,n}$ and $\mathcal{O}_{\bar{\mathcal{S}}} \in \mathbb{R}^{p\tau - h, n}$ are the submatrices of $\mathcal{O}$ with *rows* in $\mathcal{S}$ and in $\bar{\mathcal{S}}$, respectively. Finally, we denote by $\|\cdot\|_\infty$ the ℓ_∞ matrix norm.The following result holds.

Theorem 1: Let us assume that $\begin{pmatrix} \mathcal{O} & I_{\mathcal{S}} \end{pmatrix} \in \mathbb{R}^{p\tau, n+h}$ is full rank. Lasso is successful, i.e., by solving it we identify the attack support, if $\left\| \mathcal{O}_{\bar{\mathcal{S}}}^{\dagger\top} \mathcal{O}_{\mathcal{S}}^\top \right\|_\infty < 1$ where $\mathcal{O}_{\bar{\mathcal{S}}}^{\dagger\top}$ is the right pseudo-inverse of $\mathcal{O}_{\bar{\mathcal{S}}}^\top$.

A qualitative interpretation of this result is that the rows of $\mathcal{O}_{\mathcal{S}}$ must be "sufficiently orthogonal" to the columns of $\mathcal{O}_{\bar{\mathcal{S}}}^\dagger$. We refer the reader to [7] for the proof of the theorem and extedend considerations.

IV. SPARSE SOFT OBSERVER FOR ONLINE SSE

In this section, we move towards recursive, online SSE. We consider Problem 1 in a dynamic perspective: we aim at

---

* The authors are with the Dipartimento di Automatica e Informatica, Politecnico di Torino, corso Duca degli Abruzzi 24, 10129 Torino, Italy; e-mail: sophie.fosson@polito.it. This work is part of the project NODES which has received funding from the MUR – M4C2 1.5 of PNRR with grant agreement no. ECS00000036.

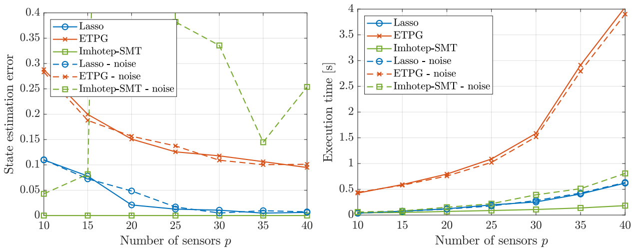

Fig. 1. Lasso vs ETPG vs Imhotep-SMT, $n = 20$, $s = p/5$ sensors under attack. The measurements are either noise-free and with noise bound 10^{-4}. The results are averaged over 50 runs.

estimating the current state, or a delayed version, using the last $p\tau$ measurements. If $\tau = 1$, this an online (not delayed) SSE. This calls for fast recursive online algorithms.

In [3], the authors address this problem by developing a recursive version of ETPG, named ETPL. As an alternative, we develop an online version of the iterative soft thresholding algorithm (ISTA, [8]), that we name sparse soft observer, summarized in Alg. 1. We use the following notation: $\mathbf{a}(k) = (a(k-\tau+1)^\top, \dots, a(k)^\top)^\top$, $\mathbf{y}(k) = (y(k-\tau+1)^\top, \dots, y(k)^\top)^\top$.

Algorithm 1 Sparse soft observer

```
for all $k = \tau - 1, \tau, \dots$ do
    Measurements and estimated measurements update
        $\mathbf{y}(k) = \mathcal{O}x(k-\tau+1) + \mathbf{a}(k)$
        $\hat{\mathbf{y}}(k) = \mathcal{O}\hat{x}(k) + \hat{\mathbf{a}}(k)$        (3)
    ISTA step: gradient step + soft thresholding
        $\begin{pmatrix}\hat{x}^+ \\ \hat{\mathbf{a}}^+\end{pmatrix} = \begin{pmatrix}\hat{x}(k) \\ \hat{\mathbf{a}}(k)\end{pmatrix} - \nu\,(\mathcal{O} \quad I)^\top\,[\hat{\mathbf{y}}(k) - \mathbf{y}(k)]$        (4)
        $\hat{\mathbf{a}}(k+1) = \mathrm{S}_{\nu\lambda}\left[\hat{\mathbf{a}}^+\right]$        (5)
    State update
        $\hat{x}(k+1) = A\hat{x}^+$        (6)
end for
```

V. NUMERICAL RESULTS

A. Lasso approach

We test the proposed Lasso approach on random, synthetic CPSs and we compare it to ETPG by [3] and Imhotep-SMT by [4]. We assume that the attack support is time-invariant with cardinality s. The attacks have magnitude in $[4, 5]$, which is sufficiently large to sabotage the state estimation, but not enough large to produce clear, plainly detectable outliers in the measurements. We assess the accuracy in terms of state estimation error $\|\hat{x} - \widetilde{x}\|_2 / \|\widetilde{x}\|_2$.

In Fig. 1, we see that Lasso outperforms ETPG both in accuracy and run time. Since we consider small/medium dimensions, Imhotep-SMT is the best approach to achieve the exact solution in fast time, in the noise-free case; nevertheless, it is not robust to noise. In contrast, Lasso and ETPG are robust to small noise.

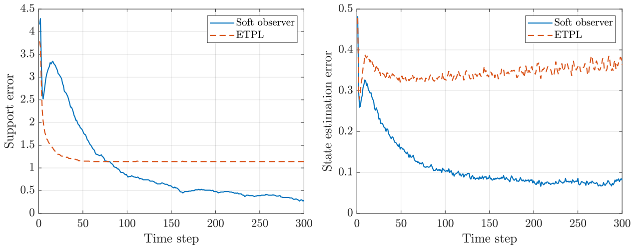

Fig. 2. Sparse soft observer vs ETPL; $n = 10$, $p = 15$, $s = 3$, $\tau = 1$. The results are averaged over 100 runs.

B. Sparse soft observer

We test the proposed sparse soft observer for recursive and online SSE and we compare it to ETPL [3]. We consider th state estimation error $\|\hat{x} - \widetilde{x}\|_2 / \|\widetilde{x}\|_2$ and support error, defined as In Fig. 2 the corresponding state estimation error and support error $\sum_j |\mathbf{1}(\hat{\mathbf{a}}_j \neq 0) - \mathbf{1}(\widetilde{a}_j \neq 0)|$, where $\mathbf{1}(v) = 1$ if v is true and 0 otherwise. The sparse soft observer is more accurate and ETPL does not always converge to the right support. The execution times are $7 \cdot 10^{-5}$ seconds for ETPL and $4 \cdot 10^{-6}$ seconds for the sparse soft observer.

VI. CONCLUSIONS

We propose a Lasso approach for secure state estimation in cyber-physical systems under sparse sensor attacks. We analyse the properties of Lasso to identify the attack and, as a consequence, to recover the state. Furthermore, by starting from the iterative soft thresholding algorithm for Lasso, we develop a sparse soft observer to perform online estimation. Through numerical results, we show that the proposed Lasso approach is valuable with respect to state-of-the-art methods, although it exploits less information, e.g., on the sparsity pattern.

REFERENCES

[1] H. Fawzi, P. Tabuada, and S. Diggavi, “Secure estimation and control for cyber-physical systems under adversarial attacks,” *IEEE Trans. Autom. Control*, vol. 59, no. 6, pp. 1454–1467, 2014.

[2] M. Pajic, I. Lee, and G. J. Pappas, “Attack-resilient state estimation for noisy dynamical systems,” *IEEE Trans. Control Netw. Syst.*, vol. 4, no. 1, pp. 82–92, 2017.

[3] Y. Shoukry and P. Tabuada, “Event-triggered state observers for sparse sensor noise/attacks,” *IEEE Trans. Autom. Control*, vol. 61, no. 8, pp. 2079–2091, 2016.

[4] Y. Shoukry, P. Nuzzo, A. Puggelli, A. L. Sangiovanni-Vincentelli, S. A. Seshia, and P. Tabuada, “Secure state estimation for cyber-physical systems under sensor attacks: A satisfiability modulo theory approach,” *IEEE Trans. Autom. Control*, vol. 62, no. 10, pp. 4917–4932, 2017.

[5] R. Tibshirani, “Regression shrinkage and selection via the Lasso,” *J. Roy. Stat. Soc. Series B*, vol. 58, pp. 267–288, 1996.

[6] J. J. Fuchs, “On sparse representations in arbitrary redundant bases,” *IEEE Trans. Inf. Theory*, vol. 50, no. 6, pp. 1341–1344, 2004.

[7] V. Cerone, S. M. Fosson, D. Regruto, and F. Ripa, “Lasso-based state estimation for cyber-physical systems under sensor attacks,” in *Proc. SysID*, 2024.

[8] I. Daubechies, M. Defrise, and C. De Mol, “An iterative thresholding algorithm for linear inverse problems with a sparsity constraint,” *Comm. Pure Appl. Math.*, vol. 57, no. 11, pp. 1413–1457, 2004.

Negativizability: a Useful Property for Distributed State Estimation and Control in Cyber-Physical Systems

Camilla Fioravanti[1], Stefano Panzieri[2], and Gabriele Oliva[1]

***Abstract*— This submission aims to present an interesting property of linear and time-invariant systems, namely *negativizability*: a pair (A, C) is negativizable if a gain matrix K exists such that $A - KC$ is negative definite. Leveraging this property, we propose a novel fully distributed estimation and control scheme that allows each agent to locally perform the computation of its estimation and control gain matrices. Notably, unlike other methodologies in the literature, our approach considers an *interdependent* setting that is natively integrable with the interconnected structure of cyber-physical systems. To conclude, we extended the proposed methodology to address the distributed estimation problem in the case of nonlinear systems.**

***Index Terms*— Cyber-Physical Systems, Distributed State Estimation, Multi-Agent Systems, Nonlinear Systems.**

I. INTRODUCTION

In recent years, distributed state estimation has emerged as a focal point of research and application in multi-agent and Cyber-Physical Systems (CPSs) [1], where the main goal is to estimate the state of the system by building local observers that rely on partial measurements and neighbors' estimations [2], [3]. In this context, definite matrices often play a fundamental role as they are, for instance, pivotal for Lyapunov stability analysis of linear systems. Large attention has been also paid to the problem of designing adequate gains [4], [5] that guarantee that closed-loop dynamical matrices become Hurwitz (at continuous time) or Schur (at discrete time). However, to the best of our knowledge, the problem of designing gains ensuring that closed-loop dynamical matrices become negative definite has not been considered. Moreover, recent approaches in the literature all consider the analysis of the full dynamical system as a *monolithic* entity, partially measured by a set of distributed sensors that collectively aim to obtain the state estimation of the entire system. This framework, in addition to requiring the agents to have global knowledge of information concerning the system, e.g., the entire dynamics, is often inefficient and implausible in a distributed context like a CPS.

In this submission, we aim to fill this gap by exploiting the *negativizability* property, that we characterize in [6] providing a necessary and sufficient condition for the related problem to be solvable, and investigating the relation between negativizability, observability, and detectability. Moreover, by resorting to a generalization of the Gershgorin Circle Criterion to the case of block-partitioned non-symmetric matrices [7], we show how negativizability can be the basis for a distributed state estimation and control schemes. Most notably, such schemes allow the agents to find gains by only relying on information that is locally available at each agent. Interestingly, the proposed scheme can be applied to directed graphs and allows the modification of the gains by a single agent in the case there is a local change in the dynamics. Moreover, as we show in [8], the proposed methodology applies to the case of nonlinear systems.

II. THE NEGATIVIZABILITY PROPERTY

In [6] we introduce a formal definition of negativizability.

Definition 1 (Negativizable pair): A pair (A, C) with $A \in \mathbb{R}^{n\times n}$ and $C \in \mathbb{R}^{q\times n}$ is *negativizable* if there is a $K \in \mathbb{R}^{n\times q}$ such that $A - KC$ is negative definite.

The definition is followed by the related problem.

***Problem** 1 (Negativizability Problem):* Let $A \in \mathbb{R}^{n\times n}$ and $C \in \mathbb{R}^{q\times n}$ be given. Find $K \in \mathbb{R}^{n\times q}$ such that $A - KC$ is negative definite.

In this section, we aim to investigate when a pair (A, C) is negativizable and, when a solution exists, to provide a viable mechanism to solve the corresponding problem. Notice that, since $A - KC$ is not symmetric in general; therefore, the matrix K we are looking for must be such that

$$KC + C^T K^T - (A + A^T) \succ 0.$$

In order to characterize a condition for the negativizability problem to be solvable, it is convenient to equivalently reformulate the problem as follows.

***Proposition** 1:* Let $A \in \mathbb{R}^{n\times n}$ and $C \in \mathbb{R}^{q\times n}$ be given, and let us define

$$\boldsymbol{\xi} = \begin{bmatrix} K_{11} & \dots & K_{1q} & \dots & K_{n1} & \dots & K_{nq} \end{bmatrix}^T.$$

The negativizability problem for the pair (A, C) is equivalent to finding $\boldsymbol{\xi} \in \mathbb{R}^{nq}$ such that $\sum_{i=1}^{nq} \xi_i F_i - F_0 \succ 0$, with

$$\begin{aligned} F_0 &= A + A^T \\ F_{(u-1)q+v} &= \boldsymbol{e}_u \mathtt{row}_v(C) + \mathtt{row}_v^T(C)\boldsymbol{e}_u^T \end{aligned} \tag{1}$$

for all $u \in \{1, \dots, n\}$ and all $v \in \{1, \dots, q\}$; notice that $\boldsymbol{e}_u$ is the u-th vector in the canonical basis of $\mathbb{R}^n$ and $\mathtt{row}_v(C)$ is the v-th row of C.

The main advantage of the above equivalent formulation of the negativizability problem is that it amounts to a *Definite Programming* (DP) feasibility problem; a necessary and sufficient feasibility condition exists for this class of problems, namely, the semidefinite version of the Farkas Lemma.

---

[1] Department of Engineering, University Campus Bio-Medico of Rome, Via Alvaro del Portillo, 21 - 00128 Roma, Italy. E-mails: {c.fioravanti, g.oliva}@unicampus.it.

[2] Department of Civil, Computer Science and Aeronautical Technologies Engineering, University Roma Tre, Via della Vasca Navale 79, 00146, Rome, Italy. E-mail: stefano.panzieri@uniroma3.it

Corollary 1: The negativizability problem is feasible if and only if no $Y \in \mathbb{R}^{n\times n}$ exists such that:

$$i) Y \neq 0; \qquad ii) Y = Y^T; \qquad iii) Y \succeq 0;$$
$$iv) C(Y + \mathtt{diag}(Y)) = 0_{q\times n}; \quad v) \mathtt{trace}((A + A^T)Y) \geq 0.$$

Notice that, under the assumption that (A, C) is negativizable, a viable way to numerically address the negativizability problem, up to a tolerance factor $0 < \epsilon \ll 1$, is to resort to a *Semidefinite Programming* (SDP) formulation, i.e., to solve the following optimization problem.

$$\min_{\boldsymbol{\xi}\in\mathbb{R}^{nq}} \quad \boldsymbol{c}^T\boldsymbol{\xi} \qquad \text{s.t.} \quad \sum_{i=1}^{nq} \xi_i F_i - F_0 - \epsilon I_n \succeq 0, \tag{2}$$

where $F_0, \dots, F_{nq}$ are defined in Eq. (1). Since we are interested in a feasible solution, we can assume $\boldsymbol{c} = \boldsymbol{0}_{nq}$.

The next remark highlights that the problem at hand can be easily cast in a form that is useful for control.

Remark 1: Given matrices $A \in \mathbb{R}^{n\times n}$ and $B \in \mathbb{R}^{n\times q}$, by definition a matrix K exists such that $A - BK \prec 0$ if and only if the pair (A^T, B^T) is negativizable.

III. DISTRIBUTED ESTIMATION FOR CPSS

Let us consider a cyber-physical system composed of N interdependent subsystems, which interact both at the physical and cyber level according to a graph topology $G = \{V, E\}$, in general directed, which is assumed to be the same for both layers. In particular, let us assume that the physical layer of the i-th subsystem is represented by the following dynamics

$$\begin{cases}\dot{\boldsymbol{x}}_i(t) = A_{ii}\boldsymbol{x}_i(t) + \sum_{j\in\mathcal{N}_i^{\mathtt{in}}} A_{ij}\boldsymbol{x}_j(t) + B_i\boldsymbol{u}_i(t),\\ \boldsymbol{y}_i(t) = C_i\boldsymbol{x}_i(t),\end{cases}$$

where $A_{ii} \in \mathbb{R}^{n_i\times n_i}$, $A_{ij} \in \mathbb{R}^{n_i\times n_j}$, $B_i \in \mathbb{R}^{n_i\times p_i}$ and $C_i \in \mathbb{R}^{q_i\times n_i}$. In this view, within the physical layer, an edge (v_j, v_i) exists whenever the i-th subsystem is influenced by the j-th one. Regarding the cyber layer, we assume that each subsystem j acts as an *agent* and can transmit information to an agent i if there is an edge (v_j, v_i) in the graph. Moreover, we assume each agent knows only local information about the system, i.e., A_{ii}, B_i, C_i, as well as A_{ij} for all its in-neighbors $j \in \mathcal{N}_i^{\mathtt{in}}$.

Let us now consider a scenario where each agent aims at estimating its own state vector via a distributed Luenberger-type observer, i.e.,

$$\dot{\boldsymbol{z}}_i(t) = A_{ii}\boldsymbol{z}_i(t) + \sum_{j\in\mathcal{N}_i^{\mathtt{in}}} A_{ij}\boldsymbol{z}_j(t) + B_i\boldsymbol{u}_i(t) + K_i(\boldsymbol{y}_i(t) - C_i\boldsymbol{z}_i(t)),$$

where $K_i \in \mathbb{R}^{n_i\times q_i}$. We define the estimation error for the i-th agent as $\boldsymbol{e}_i(t) = \boldsymbol{x}_i(t) - \boldsymbol{z}_i(t) \in \mathbb{R}^{n_i}$ and consider the following assumption.

Assumption 1: For each subsystem $i \in \{1, \dots, N\}$ the pair

$$\left(A_{ii} + \sum_{j\neq i} \|A_{ij}\| I_{n_i} + \beta I_{n_i},\, C_i\right) \tag{3}$$

is negativizable for some $\beta > 0$.

We now show that the state estimation problem amounts to solving N local negativizability problems.

Theorem 1: Let Assumption 1 hold and let $\widehat{K}_i \in \mathbb{R}^{n_i\times q_i}$ be a matrix that solves the negativizability problem for the i-th pair in Eq. (3). Then, choosing $K_i = \widehat{K}_i$ for all agents $i \in 1, \dots, N$, the estimation error reaches zero asymptotically. Notice that G is in general directed and, interestingly, this simple scheme works also in this case, as it requires each agent i to receive the estimated state $\boldsymbol{z}_j(t)$ from all its in-neighbors. A few remarks are now in order.

Remark 2: Given the local nature of the negativizability problems required for the above state estimation application, we observe that the agents are either able to solve their own problem or to decide that the problem admits no solution.

1) Extension to Nonlinear Systems:

In [8], we show that the proposed protocol can be applied to the case of nonlinear state estimation, with the following dynamics

$$\begin{cases}\dot{\boldsymbol{x}}_i(t) = A_{ii}\boldsymbol{x}_i(t) + \sum_{j\in\mathcal{N}_i^{\mathtt{in}}} A_{ij}\boldsymbol{x}_j(t) + \boldsymbol{f}_i(\overline{\boldsymbol{x}}_i(t), t),\\ \boldsymbol{y}_i(t) = C_i\boldsymbol{x}_i(t),\end{cases}$$

where $\overline{\boldsymbol{x}}_i(t)$ is the stack of the vectors $\boldsymbol{x}_j(t) \in \mathbb{R}^{n_j}$ corresponding to all agents $j \in \mathcal{N}_i^{\mathtt{in}} \cup \{i\}$, and we suppose $\boldsymbol{f}_i(\overline{\boldsymbol{x}}_i(t), t)$ is Lipschitz in its first argument in all $\mathbb{R}^n$ and is known to the $i-$th agent. Moreover, we propose a novel fully distributed algorithm to estimate an upper bound on the Lipschitz constant, needed to perform the estimation, which is based on knowledge of the local constants $\overline{\ell}_i$ that are experienced at each subsystem.

Theorem 2: Suppose for all $t \geq 0$, the overall nonlinear function $\boldsymbol{f}(\boldsymbol{x}, t)$ is Lipschitz (in its first argument) in $(-\gamma, \gamma)^n$, i.e., in the open hypercube in $\mathbb{R}^n$ with side 2γ, centered in the origin. Finally, for all $t \geq 0$ and all $\boldsymbol{x} \in (-\gamma, \gamma)^n$, the Lipschitz constant $\overline{\ell}$ of the overall nonlinear function $\boldsymbol{f}(\boldsymbol{x}(t), t)$ is upper-bounded by

$$\overline{\ell} \leq \sqrt{\left(\max_{i=1,\dots,N}\{|\mathcal{N}_i^{\mathtt{out}}|\} + 1\right)\max_{i=1,\dots,N}\{\overline{\ell}_i^2\}}.$$

REFERENCES

[1] S. Park and N. C. Martins, "Design of distributed lti observers for state omniscience," *IEEE Transactions on Automatic Control*, vol. 62, no. 2, pp. 561–576, 2016.

[2] A. Mitra and S. Sundaram, "Distributed observers for lti systems," *IEEE Transactions on Automatic Control*, vol. 63, no. 11, pp. 3689–3704, 2018.

[3] L. Wang, J. Liu, A. S. Morse, and B. D. Anderson, "A distributed observer for a discrete-time linear system," in *2019 IEEE 58th Conference on Decision and Control (CDC).* IEEE, 2019, pp. 367–372.

[4] A. J. Savas, S. Park, H. V. Poor, and N. E. Leonard, "On separation of distributed estimation and control for lti systems," in *2022 IEEE 61st Conference on Decision and Control (CDC).* IEEE, 2022, pp. 963–968.

[5] C. Fioravanti, E. Makridis, G. Oliva, M. Vrakopoulou, and T. Charalambous, "Distributed estimation and control for lti systems under finite-time agreement," *IEEE Transactions on Automatic Control*, 2024.

[6] C. Fioravanti, S. Panzieri, and G. Oliva, "Negativizability: A useful property for distributed state estimation and control in cyber–physical systems," *Automatica*, vol. 157, p. 111240, 2023.

[7] C. Tretter, *Spectral theory of block operator matrices and applications.* World Scientific, 2008.

[8] C. Fioravanti, S. Panzieri, and G. Oliva, "A distributed nonlinear estimation scheme for cyber-physical systems," *IEEE Control Systems Letters*, submitted.

Data-driven delay estimation in reaction-diffusion systems

Rami Katz[1], Giulia Giordano[1] and Dmitry Batenkov[2]

***Abstract*— For a reaction-diffusion equation with unknown right-hand side and non-local measurements subject to unknown constant measurement delay, we consider the nonlinear inverse problem of estimating the associated leading eigenvalues and measurement delay from a finite number of noisy measurements. We propose a reconstruction criterion and, for small enough noise intensity, prove existence and uniqueness of the desired approximation and derive closed-form expressions for the first-order condition numbers, as well as bounds for their asymptotic behavior in a regime when the number of measurements tends to infinity and the inter-sampling interval length is fixed. We present numerical simulations indicating that the exponential fitting algorithm ESPRIT is first-order optimal, namely, its first-order condition numbers have the same asymptotic behavior as the analytic ones in this regime.**

I. INTRODUCTION AND PROBLEM STATEMENT

Reaction-diffusion equations (RDEs) are widely used to model phenomena in physics and engineering. Almost all existing control and observation techniques for RDEs assume explicit knowledge of the spatial operator of the system or of the eigenvalue/eigenfunction pairs corresponding to its modes; however, their identification is a challenging problem, and realistic, constructive and implementable data-driven identification techniques for RDEs are still missing. Here, we consider the 1D RDE with unknown right-hand side

$$z_t(x,t) = (p(x)z_x(x,t))_x + q(x)z(x,t), \tag{1}$$

where $x \in (0,1)$, $z(x,t) \in \mathbb{R}$, $z(0,t) = z(1,t) = 0$, and the *unknown* smooth functions $p,q : [0,1] \to \mathbb{R}$ in (1) satisfy the bounds $0 < \underline{p} \le p(x) \le \overline{p} < \infty$ and $\underline{q} \le q(x) \le \overline{q}$, with *unknown* constants. The spatial operator in (1) has an infinite monotone sequence of simple eigenvalues $\{\lambda_n\}_{n=1}^{\infty}$ satisfying $\lim_{n\to\infty}\lambda_n = \infty$ [1]. The eigenvectors $\{\psi_n\}_{n=1}^{\infty}$ form a complete orthonormal system in $L^2(0,1)$. We subsequently denote $[n] = \{i \in \mathbb{N}\ ;\ 1 \le i \le n\}$.

We consider non-local measurements

$$y(t) = \int_0^1 c(x)z(x,t-D)dx \in \mathbb{R}, \quad t \ge 0, \tag{2}$$

where the *unknown* constant measurement delay has a *known* bounds, $0 < D < D_{\max}$, while the kernel $c \in L^2(0,1)$ has coefficients $\{c_n\}_{n=1}^{\infty}$ satisfying the following assumption.

Assumption 1: There exist $N_1, N_2 \in \mathbb{N}$ such that

(a) $c_n = 0$ for all $n > N_1 + N_2$,

(b) c_n are *known and nonzero* for $n \in [N_1]$,

(c) $c_k = \varepsilon\tilde{c}_k$ $\forall k \in [N_1+N_2]\setminus[N_1]$, where for some $M_c > 0$ $|\tilde{c}_k| \le M_c|c_n|$, $\forall n \in [N_1]$ and $\forall k \in [N_1+N_2]\setminus[N_1]$. ◇

Hence, $c \in L^2(0,1)$ is a bandlimited measurement kernel, supported on $\{\psi_n\}_{n=1}^{N_1+N_2}$, with known and nonzero projection coefficients on $\{\psi_n\}_{n=1}^{N_1}$. Also, the projection coefficients on $\{\psi_n\}_{n=N_1+1}^{N_2}$ are small in comparison to those on $\{\psi_n\}_{n=1}^{N_1}$: the measurement kernel c includes a main lobe on the frequency domain $\{\lambda_n\}_{n=1}^{N_1}$ and a *structured noise* with small intensity $\varepsilon > 0$ on the frequency domain $\{\lambda_n\}_{n=N_1+1}^{N_2}$, which emanates from measuring 'undesirable' system modes.

We set $z(\cdot,t) = z(\cdot,0)$, $t < 0$. Employing modal decomposition [2], we present the solution to system (1) as

$$z(x,t) = \sum_{n=1}^{\infty} z_n(t)\psi_n(x), \quad z_n(t) = \langle z(\cdot,t),\psi_n\rangle, \quad n \in \mathbb{N}. \tag{3}$$

Assumption 2: For $z(\cdot,0) \in L^2(0,1)$, $z_n(0) \neq 0$ is *known* for $n \in [N_1]$. Furthermore, $|z_k(0)|/|z_n(0)| \le M_z$ for some $M_z > 0$, all $n \in [N_1]$ and all $k \in [N_1+N_2]\setminus[N_1]$. ◇

Differentiating under the integral sign in (3) and integrating by parts, we have $\dot{z}_n(t) = -\lambda_n z_n(t) \Longrightarrow z_n(t) = e^{-\lambda_n t}z_n(0)$, $\forall n \in \mathbb{N}$. Substituting the latter into (2), for $t \ge D_{\max}$ we obtain

$$y(t) = \sum_{n=1}^{\infty} c_n z_n(0)e^{\lambda_n D}e^{-\lambda_n t}, \quad c_n = \langle c,\psi_n\rangle, \quad n \in \mathbb{N}. \tag{4}$$

Our goal is to estimate the delay D and a finite number of dominant modes λ_n, based on noisy "snapshots" of the system output taken at *finitely many* uniformly distributed time steps with arbitrary inter-sampling period length.

Assumption 3: The system measurements are taken *only* at times $\{t_k := k\Delta + D_{\max}\}_{k=0}^{2N_1-1}$, with step-size $\Delta > 0$. ◇

Subject to Assumptions 1-3, the measurements (4) at the available times $\{t_k\}_{k=0}^{2N_1-1}$ can be presented as

$$y(t_k) = \sum_{n=1}^{N_1} y_n e^{-\lambda_n k\Delta} + \varepsilon \sum_{n=N_1+1}^{N_1+N_2} y_n e^{-\lambda_n k\Delta}, \tag{5}$$

for $k = 0,\ldots,2N_1-1$, where

$$y_n := \begin{cases} c_n z_n(0)e^{\lambda_n(D-D_{\max})}, & n \in [N_1] \\ \tilde{c}_n z_n(0)e^{\lambda_n(D-D_{\max})}, & n \in [N_1+N_2]\setminus[N_1] \end{cases} \tag{6}$$

satisfy $|y_k|/|y_n| \le M_c M_z =: M_y$, $\forall n \in [N_1], k \in [N_1+N_2]\setminus[N_1]$, since $D < D_{\max} \Rightarrow e^{(\lambda_k-\lambda_n)(D-D_{\max})} < 1$ for such indices.

Objective: Given the measurements (5) and $N_0 \in [N_1]$, estimate the eigenvalues $\{\lambda_n\}_{n=1}^{N_0}$ and the constant delay D.

The *equivalent problem* of recovering $\{y_n,\lambda_n\}_{n=1}^{N_1}$ from the measurements (5) is known as *exponential fitting* [3], [4]. For $\varepsilon = 0$, we can recover $\{y_n,\lambda_n\}_{n=1}^{N_1}$ *exactly*. If $\varepsilon > 0$, the structured measurement noise introduces estimation errors. Here we study the analytic estimation errors due to noise, to first order in ε, and show that the ESPRIT algorithm is first-order optimal in achieving the identification objective, thereby gaining insight into the system (1).

The considered problem is highly challenging because (i) only *finitely many* measurements are available for the reconstruction procedure, for any triplet (Δ, N_1, N_2); (ii) although

---

[1] Department of Industrial Engineering, University of Trento.

[2] Department of Applied Mathematics, Tel Aviv University, Israel.

(1) is a linear system, the task of recovering $\{D, \lambda_n\}_{n=1}^{N_0}$ from the measurements (5) is a *nonlinear inverse problem*, as the measurements depend *nonlinearly* on these parameters.

Our main results are the following. We define a reconstruction criterion, and prove existence and uniqueness of the associated approximation, if the intensity ε of the structured noise is not too large. We introduce first-order condition numbers describing how the ε-noise is amplified in the reconstruction errors, and show their asymptotic behavior in a specific parameter regime. In the considered regime, we show that the approximation numerically computed via the ESPRIT algorithm [5] is first-order optimal: its first-order condition numbers exhibit the same asymptotic behaviour as the analytic ones. A complete version of this work, including all the proofs and preliminary results, can be found in [6].

II. MAIN RESULTS

Given (5), we introduce the map

$$\mathscr{F}\left(\left\{\hat{y}_n, \hat{\lambda}_n\right\}_{n=1}^{N_1}; \varepsilon\right) = \operatorname{col}\left\{\sum_{n=1}^{N_1} \hat{y}_n e^{-\hat{\lambda}_n k\Delta} - y(t_k)\right\}_{k=0}^{2N_1-1}. \tag{7}$$

For the approximation candidate $\hat{P} := \left\{\hat{y}_n, \hat{\lambda}_n\right\}_{n=1}^{N_1}$, function $\mathscr{F}(\hat{P};\varepsilon)$ returns the discrepancy between measurements $\{y(t_k)\}_{k=0}^{2N_1-1}$ and "virtual measurements" $\left\{\sum_{n=1}^{N_1} \hat{y}_n e^{-\hat{\lambda}_n k\Delta}\right\}_{k=0}^{2N_1-1}$. We look for estimates $\hat{P}$ that maintain the equality $\mathscr{F}(\hat{P};\varepsilon) = 0$ even with $\varepsilon > 0$. Given $\hat{P}$, $\hat{D}^{(n)} = \log\left(\hat{y}_n (c_n z_n(0) e^{-\hat{\lambda}_n D_{\max}})^{-1}\right)/\hat{\lambda}_n$ can then be used as an approximation of D, provided there is n for which $\hat{y}_n (c_n z_n(0) e^{-\hat{\lambda}_n D_{\max}})^{-1}$ is positive.

To keep the presentation simpler, we assume $N_2 = 1$, but our results remain identical for an arbitrary fixed $N_2 \in \mathbb{N}$. Setting $\phi_n := e^{-\lambda_n \Delta}$, $\hat{\phi}_n = e^{-\hat{\lambda}_n \Delta}$, $n \in [N_1 + 1]$, the measurements in (5) can then be rewritten as

$$y(t_k) = \sum_{n=1}^{N_1} y_n \phi_n^k \; + \; \varepsilon \; y_{N_1+1} \; \phi_{N_1+1}^k, k \in \{0\} \cup [2N_1 - 1]. \tag{8}$$

Theorem 1: $\exists \varepsilon_* > 0$ and unique C^1 functions $\hat{P}(\varepsilon) := \left\{\hat{y}_n(\varepsilon), \hat{\lambda}_n(\varepsilon)\right\}$ s.t $\hat{P}(0) = \{y_n, \lambda_n\}_{n=1}^{N_1}$ and $\forall |\varepsilon| < \varepsilon_*$, $\mathscr{F}(\hat{P};\varepsilon) = 0 \iff \hat{P} = \hat{P}(\varepsilon)$. $\hat{P}(\varepsilon)$ satisfies, as $\varepsilon \to 0$,

$$\begin{gathered}\hat{\xi}_n(\varepsilon) - \xi_n = \mathscr{K}_\xi(n; N_1, \Delta)\varepsilon + o_{n,N_1,\Delta}(\varepsilon), \; \xi \in \{\lambda, y\}, \\ \begin{bmatrix} \mathscr{K}_y(n; N_1, \Delta) \\ \mathscr{K}_\lambda(n; N_1, \Delta) \end{bmatrix} = y_{N_1+1} \begin{bmatrix} H_{\Phi,n}(\phi_{N_1+1}) \\ -\frac{1}{\Delta y_n \phi_n} \tilde{H}_{\Phi,n}(\phi_{N_1+1}) \end{bmatrix}, \; n \in [N_1], \end{gathered} \tag{9}$$

where $H_{\Phi,n}(z) = \left[1 - 2(z - \phi_n) L'_{\Phi,n}(\phi_n)\right] L^2_{\Phi,n}(z)$ and $\widetilde{H}_{\Phi,n}(z) = (z - \phi_n) L^2_{\Phi,n}(z)$, with $L_{\Phi,n}(z) = \prod_{j \neq n} \frac{z - \phi_j}{\phi_n - \phi_j}$, $n \in [S]$, are the Hermite interpolation basis polynomials associated with $\Phi = \{\phi_n\}_{n=1}^{N_1}$.

The terms $\mathscr{K}_y(n; N_1, \Delta)$ and $\mathscr{K}_\lambda(n; N_1, \Delta)$, $n \in [N_1]$ are the *first order (in ε) condition numbers* of the problem. Henceforth, we will suppress their dependence on N_1, Δ for brevity.

Theorem 1 implies that an ε-perturbation in the measurements is amplified in the reconstruction errors $\varepsilon^{-1} e_\xi(n) := \varepsilon^{-1}(\hat{\xi}_n(\varepsilon) - \xi_n)$, $\xi \in \{\lambda, y\}$ (see (9)) by the condition numbers $\mathscr{K}_y(n)$ and $\mathscr{K}_\lambda(n)$, when seeking for $\hat{P}$.

We consider the **asymptotic analysis** of $\mathscr{K}_y(n)$ and $\mathscr{K}_\lambda(n)$, of which we wish to determine the dependence on N_1 and Δ. We focus on the

$$\underline{\text{Regime:}} \; \Delta \text{ fixed and } N_1 \to \infty \tag{10}$$

corresponding to growing support of the kernel $c \in L^2(0,1)$ in the frequency domain, subject to Assumption 1.

Theorem 2: Recall the first-order condition numbers $\mathscr{K}_\lambda(n)$ and $\mathscr{K}_y(n)$ in (9). Let $n \in \mathbb{N}$. Given $\Delta > 0$, there exist some $\gamma_y(n,\Delta) > 0$ and $\gamma_\lambda(n,\Delta) > 0$ such that, as $N_1 \to \infty$,

$$\begin{aligned}|\mathscr{K}_y(n)| &\leq \gamma_y(n,\Delta) \cdot |z_{N_1+1}(0)\tilde{c}_{N_1+1}| e^{-\frac{2}{3}\Delta \upsilon N_1^3 \left(1 + O(N_1^{-1})\right)}, \\ |\mathscr{K}_\lambda(n)| &\leq \gamma_\lambda(n,\Delta) \cdot e^{-\frac{2}{3}\Delta \upsilon N_1^3 \left(1 + O(N_1^{-2})\right)}. \qquad \diamond\end{aligned}$$

III. NUMERICAL EXAMPLE: PDE DELAY ESTIMATION

We consider (1) with constant $p \equiv q \equiv 0.1$, eigenvalues $\lambda_n = n^2\pi^2 - q$ and eigenfunctions $\psi_n(x) = \sqrt{2}\sin(n\pi x)$. The initial condition satisfies $z_n(0) = (-1)^{n+1}/(\sqrt{2}n^3)$. Numerical simulations show that the first-order condition numbers of the ESPRIT algorithm [5] exhibit the same asymptotic behaviour as $\mathscr{K}_\lambda(n)$ and $\mathscr{K}_y(n)$ in the regime (10). We consider (2) with delay $D = 1/12$ and sampling step size $\Delta = 1/25$; $D_{\max} = 1/10$, for each $1 \leq N_1 \leq 10$. The kernel c is chosen according to Assumption 1 with random $c_n \in [1,2]$ and $\varepsilon = 0.01$. The measurement (2) is computed and sampled at the points $t_k = D_{\max} + k\Delta$, for $0 \leq k \leq 2N_1 - 1$, giving the measurements $\operatorname{col}\{y(t_k)\}_{k=0}^{2N_1-1}$ defined by (5). We apply the ESPRIT algorithm to $\operatorname{col}\{y(t_k)\}_{k=0}^{2N_1-1}$ and recover $\{\hat{\lambda}_n^{ESP}\}_{n=1}^{N_1}$ directly. Then, since $c_n, z_n(0), D_{\max}$ are known, we can recover the approximation to D from the coefficients $\hat{y}_n^{ESP}$ as $D \approx \hat{D}_{ESP}^{(1)} := \log\left(\hat{y}_1^{ESP}\left(c_1 z_1(0) e^{-\hat{\lambda}_1^{ESP} D_{\max}}\right)^{-1}\right)/\hat{\lambda}_1^{ESP}$. The errors $|\hat{\lambda}_1^{ESP} - \lambda_1|$ and $|\hat{D}_{ESP}^{(1)} - D|$ are shown in Fig. 1.

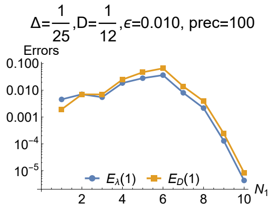

Fig. 1: Errors in λ_1 and the estimated delay.

REFERENCES

[1] Y. Orlov, "On general properties of eigenvalues and eigenfunctions of a Sturm-Liouville operator: comments on "ISS with respect to boundary disturbances for 1-D parabolic PDEs"," *IEEE Transactions on Automatic Control*, vol. 62, no. 11, pp. 5970–5973, 2017.

[2] R. Katz and E. Fridman, "Finite-dimensional boundary control of the linear Kuramoto-Sivashinsky equation under point measurement with guaranteed L^2-gain," *IEEE Transactions on Automatic Control*, vol. 67, no. 10, pp. 5570–5577, 2022.

[3] V. Pereyra and G. Scherer, *Exponential Data Fitting and Its Applications*. Bentham Science Publishers, 2010.

[4] D. Batenkov, G. Goldman, and Y. Yomdin, "Super-resolution of near-colliding point sources," *Information and Inference: A Journal of the IMA*, vol. 10, no. 2, pp. 515–572, 2021.

[5] R. Roy and T. Kailath, "ESPRIT-estimation of signal parameters via rotational invariance techniques," *IEEE Transactions on Acoustics, Speech, and Signal Processing*, vol. 37, no. 7, pp. 984–995, 1989.

[6] R. Katz, G. Giordano, and D. Batenkov, "Data-driven delay estimation in reaction-diffusion systems via exponential fitting - full version," 2024. [Online]. Available: http://giuliagiordano.dii.unitn.it/docs/Katz2024.pdf

Nonlinear Data-Driven Moment Matching using RKHS

MATTEO SCANDELLA
University of Bergamo

ALESSIO MORESCHINI
Imperial College London

THOMAS PARISINI
University of Trieste
Imperial College London

1 Introduction

Due to the continuously increasing data volumes from simulation, control, and experimental measurements the study of large-scale systems became a prominent research area in systems and control theory [1]. Hence, to reduce the computational complexity of numerical simulations and facilitate the design of controllers, interpolatory model reduction methods aim to construct a reduced-order model that interpolates the transfer function of the large-scale model at selected interpolation points. Moment matching techniques, which fall under the category of interpolatory methods, are numerically reliable as they can be simply implemented by means of Krylov projectors to achieve interpolation without the need to explicitly evaluate the transfer function. This technique involves matching the moments of an underlying system with an interpolant, potentially of lower order.

The notion of moment matching has been redefined in the time domain for linear and nonlinear systems [2]. In the time-domain analysis, assuming that a steady-state response exists, the concept of moment involves studying the output response of the underlying system driven by a signal generator defined by the desired interpolation points. However, with the increasing availability of high-dimensional data and advancements in computational power, data-driven model reduction has gained significant attention in recent years. In the moment matching framework, the problem of estimating the moment of an unknown system from input-output data was earlier considered in [3] employing the ordinary least squares approach. Yet, ordinary least-squares arguments undergo ill-conditioned optimization problems. Specifically, when the number of variables exceeds the number of observations the problem eventually leads to an infinite number of solutions. Further, the presence of noisy data in datasets may also impact the estimation of a meaningful moment of the unknown system.

Here, we are presenting our recent results [4] where we considered the problem of estimating the moment of a nonlinear Multi-Input Multi-Output (MIMO) system with feedthrough. Specifically, given noisy data obtained by measuring the output of a certain system we construct a data-driven moment matching method which employs Tikhonov regularization in the Reproducing Kernel Hilbert Spaces (RKHSs), see [5]. We estimate the moment function from a Hilbert space according to a data adherence criterion expressed using a regularized optimization problem composed of two terms: the empirical cost risk and a regularization term. Hence, taking advantage of the regularized term the optimization problem introduces further constraints which render the solution always uniquely determined.

2 Moment Matching

Consider a MIMO continuous-time nonlinear dynamical system of order $n_\mathrm{x} \in \mathbb{N}$ with $n_\mathrm{u} \in \mathbb{N}$ inputs and $n_\mathrm{y} \in \mathbb{N}$ outputs described by equations of the form

$$\dot{x}(t) = f(x(t), u(t)), \qquad x(0) = x_0, \tag{1a}$$

$$y(t) = h(x(t), u(t)), \tag{1b}$$

with $x(t) \in \mathbb{R}^{n_\mathrm{x}}$, $u(t) \in \mathbb{R}^{n_\mathrm{u}}$, $y(t) \in \mathbb{R}^{n_\mathrm{y}}$, $x_0 \in \mathbb{R}^{n_\mathrm{x}}$ and smooth mappings $f : \mathbb{R}^{n_\mathrm{x}} \times \mathbb{R}^{n_\mathrm{u}} \to \mathbb{R}^{n_\mathrm{x}}$ and $h : \mathbb{R}^{n_\mathrm{x}} \times \mathbb{R}^{n_\mathrm{u}} \to \mathbb{R}^{n_\mathrm{y}}$ such that $f(0,0) = 0$ and $h(0,0) = 0$. Furthermore, we assume that (1) is locally observable, locally accessible and locally exponentially stable around the origin.

To define the notion of moment for system (1) we consider a *signal generator* described by equations of the form

$$\dot{\omega}(t) = s(\omega(t)), \qquad \omega(0) = \omega_0, \tag{2a}$$

$$u(t) = \ell(\omega(t)), \tag{2b}$$

in which $\omega(t) \in \Omega$ and $u(t) \in \mathbb{R}^{n_\mathrm{u}}$, with $\Omega \subset \mathbb{R}^{n_\omega}$ a sufficiently small open, connected, invariant neighborhood containing the origin, whereas the smooth mappings $s : \Omega \to \mathbb{R}^{n_\omega}$ and $\ell : \Omega \to \mathbb{R}^{n_\mathrm{u}}$ are such that $s(0) = 0$ and $\ell(0) = 0$, respectively. Moreover, we assume that (2) is locally observable and neutrally stable. Before introducing the notion of moment for nonlinear systems, we make the following assumption.

Assumption 1. *There exists a mapping $\pi : \Omega \to \mathbb{R}^{n_\mathrm{x}}$ with $\pi(0) = 0$, locally defined in Ω, which is the unique solution of the partial differential equation*

$$\frac{\partial \pi}{\partial \omega}(\omega)\, s(\omega) = f\big(\pi(\omega), \ell(\omega)\big). \tag{3}$$

Definition 1 (Moment)**.** *Consider system (1) and the signal generator (2). The moment of system (1) at (s, ℓ) is defined as $h(\pi(\cdot), \ell(\cdot))$ where π is the unique solution of the partial differential equation (3).*

The notion of time-domain moment for nonlinear systems has been defined in [2] in terms of the steady-state response of the cascade interconnection of system (1) with the signal generator (2) as represented in Fig. 1.

Theorem 1 (See [2]). *Consider system (1) and the signal generator (2). Suppose Assumption 1 hold. Then the moment of system (1) at (s, ℓ) is in a one-to-one relation with the steady-state response of the output y of the interconnected system.*

Definition 2 (Moment Matching [2]). *A system described by equations*

$$\dot{\xi}(t) = \bar{f}(\xi(t), u(t)), \qquad \xi(0) = \xi_0, \tag{4a}$$

$$\bar{y}(t) = \bar{h}(\xi(t), u(t)), \tag{4b}$$

with $\xi(t) \in \mathbb{R}^{n_\xi}$ and $\bar{y}(t) \in \mathbb{R}^{n_y}$ is called model of (1) at (s, ℓ) if (4) has the same moment at (s, ℓ) as (1).

3 Data-Driven Moment Matching

We focus on the case in which the state-space model of (1) is unknown and only noisy measurements of the form $z(t) := y(t) + e(t) \in \mathbb{R}^{n_y}$ are measurable for all $t \in \mathbb{R}$, where $y(t)$ is the output of the interconnected model and $e(t) \in \mathbb{R}^{n_y}$ is an additive white noise as shown in Fig. 1. In particular, we define the dataset

$$\mathcal{D} = \left\{ \left(\bar{t}_i, \bar{\omega}_i, \bar{u}_i, \bar{z}_i \right) \right\}_{i=1}^{N} \subseteq \mathbb{R} \times \Omega \times \mathbb{R}^{n_u} \times \mathbb{R}^{n_y} \tag{5}$$

where $N \in \mathbb{N}$ is the amount of data collected, for all $i \in \{1, \ldots, N\}$, $\bar{t}_i$ is the i-th sampling time, $\bar{\omega}_i = \omega(\bar{t}_i)$, $\bar{u}_i = u(\bar{t}_i)$, and $\bar{z}_i = z(\bar{z}_i)$. For simplicity, we define $\bar{q}_i := (\bar{\omega}_i, \bar{u}_i) \in \mathcal{Q} := \Omega \times \mathbb{R}^{n_u}$.

From the properties of the interconnected system and the definition of moment, we have

$$z(t) = h(\pi(\omega(t)), \ell(\omega(t))) + \tau(t) + e(t)$$

where, for all $t \in \mathbb{R}$, the function $\tau : \mathbb{R} \to \mathbb{R}^{n_y}$ describes the output transient response that decay exponentially. Hence, we define the estimator of the moment $\hat{\mu}$ as the solution of the optimization problem

$$\hat{\mu} := \underset{\mu \in \mathcal{H}}{\operatorname{argmin}} \sum_{i=1}^{N} \left| \bar{z}_i - \mu(\bar{q}_i) \right|^2 + \rho \left| \mu \right|_{\mathcal{H}}^2, \tag{6}$$

where $\mathcal{H}$ is a RKHS containing functions that map $\mathcal{Q}$ to $\mathbb{R}^{n_y}$, $|\cdot|_{\mathcal{H}}$ is the norm on $\mathcal{H}$, and $\rho > 0$ is a parameter to be tuned. The optimization problem (6) accepts a unique solution that can be computed analytically using the Representer theorem [5]. In particular, we have

$$\forall q \in \mathcal{Q}, \qquad \hat{\mu}(q) = \sum_{i=1}^{N} (k_{\bar{q}_i} c_i)(q) = \sum_{i=1}^{N} k(\bar{q}_i, q) c_i,$$

where $k : \mathcal{Q} \times \mathcal{Q} \to \mathbb{R}^{n_y \times n_y}$ is the kernel associated with $\mathcal{H}$.

The following proposition provides a way to select a viable kernel.

Proposition 1. *Given Assumption 1, the RKHS $\mathcal{H}$ contains only valid moment functions only if $k(0, 0) = \mathbf{0}_{n_y \times n_y}$.*

Finally, we also show that the effect of the transient on the estimator decay exponentially with time as perceivable from the local exponential stability of the model.

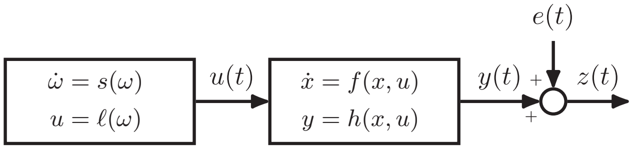

Figure 1: Block diagram of the interconnected system.

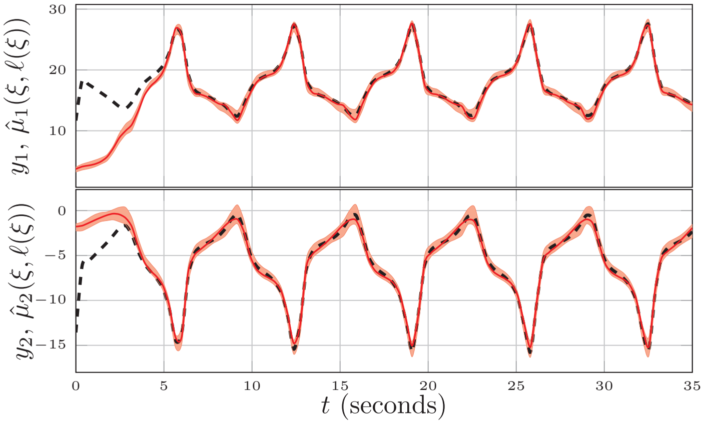

Figure 2: Time history of the ideal moment (dashed line, black), estimated moment of the estimation with the median performance of the Monte Carlo experiment (solid line, red) and the range of all the Monte Carlo experiments (light red area).

4 Numerical Example

In this section, we validate the proposed methodology by estimating the moment of an unknown DC-to-DC Ćuk converter [6] from some noisy measured data. We let the signal generator be a Van der Pol oscillator [7]. The results of a Monte Carlo simulation are summarized in Fig. 2.

References

[1] A. C. Antoulas. *Approximation of Large-scale Dynamical Systems.* Adv. Des. Control. Society for Industrial and Applied Mathematics, 2005.

[2] A. Astolfi. “Model Reduction by Moment Matching for Linear and Nonlinear Systems”. In: *IEEE Trans. Autom. Control* 55.10 (2010), pp. 2321–2336.

[3] G. Scarciotti et al. “Data-driven model reduction by moment matching for linear and nonlinear systems”. In: *Automatica* 79 (2017), pp. 340–351.

[4] A. Moreschini et al. “Nonlinear Data-Driven Moment Matching in Reproducing Kernel Hilbert spaces”. In: *Proc. 22nd Eur. Control Conf.* 2024.

[5] C. A. Micchelli et al. “On Learning Vector-Valued Functions”. In: *Neural Comput.* 17.1 (2005), pp. 177–204.

[6] H. Rodriguez et al. “Adaptive partial state feedback control of the DC-to-DC Cuk converter”. In: *Proc. Am. Control Conf.* Vol. 7. 2005, pp. 5121–5126.

[7] B. van der Pol. “LXXXVIII. On “relaxation-oscillations””. In: *Lond. Edinb. Dublin Philos. Mag. J. Sci.* 2.11 (1926), pp. 978–992.

Two novel Frameworks for Cyber-Physical Anomaly Detection in Industrial Control Systems

Simone Guarino[*,1], Ernesto del Prete[3], Luca Faramondi[1], Francesco Flammini[2], Roberto Setola[1]

[1]Engineering Department, Campus Biomedico University, Rome, Italy
[2]Department of Technological Innovations and Safety of Plants, Products and Anthropic Settlements, INAIL, Italy
[3]IDSIA USI-SUPSI, Department of Innovative Technologies, University of Applied Sciences and Arts of Southern Switzerland, Lugano, CH

*[*s.guarino@unicampus.it](mailto:s.guarino@unicampus.it)*

In recent years, Industrial Cyber-Physical Systems (ICPS) within Industrial Control Systems (ICS) have faced increasing cyber-attacks due to greater connectivity, adoption of open-source protocols, and use of off-the-shelf products. These attacks can cause cyber anomalies like unauthorized IP addresses and data flow disruptions, potentially leading to physical asset breakdowns and compromising the ICS infrastructure. In this regard, it is crucial to ascertain whether these physical failures stem from cyber anomalies or from malfunctions in the physical components due to factors like aging, insufficient maintenance, or intentional physical sabotage [1,2]. Cyber-Physical Anomaly Detection (CPAD) algorithms address the joint monitoring of cyber and physical data that result in the detection of cyber, physical, and cyber-physical anomalies over the ICS. Such algorithms fall into three categories: signature-based, detecting known attacks via a database; behavior-based, identifying anomalies by learning normal behavior using data-driven approaches like machine learning; and specification-based, detecting anomalies by modelling ICS through probabilistic or mathematical methods. Recently, scientific literature has been investigating more and more the possibility of merging both behavior-based and specification-based algorithms to reduce false positives, commonly produced by behavior-based methods, and to lower the computational load associated with mathematical and probabilistic modelling, the primary drawback of specification-based approaches. Nevertheless, there is still little attention on deploying such "hybrid" algorithms to both the cyber and physical domains of the ICS, as the scientific literature mainly focuses on the monitoring of cyber anomalies [3]. Moreover, considering the distributed nature of ICPSs which are mainly deployed in critical infrastructures, like water treatment, and smart grids, there is a need to provide distributed multi-source and multi-modal CPAD algorithms that can detect anomalies in the different assets of the same infrastructure. Such algorithms may leverage data, feature, and decision fusion techniques that can merge the predictions of multiple, possibly redundant, detectors with the aim of making an agreed decision about an ongoing cyber, physical, or cyber-physical threat. Nevertheless, decision fusion techniques suffer from the possible presence of faulty detectors which could negatively weigh the final decision [4]. This motivates the dynamic self-adaptation of decision fusion to run-time uncertainty in order to prevent performance degradation and increase fault tolerance. Such self-adaptation is enabled by decision fusion's explainability, which can be defined as the ability of decision fusion to provide insight into how many, which, and to what extent possibly faulty detectors contribute to the final decision.

Considering the limitations in current scientific literature, this work proposes two novel frameworks, namely "*A hybrid behavior-and Bayesian network-based framework for cyber–physical anomaly detection*" and "*A two-level fusion framework for cyber-physical anomaly detection*".

The first contribution proposes a novel hybrid “multi-formalism” CPAD framework for combining the outcomes of unsupervised behavior-based anomaly detectors applied to cyber and physical data through the adoption of a static Bayesian network. In more detail, the framework consists of two behavior-based anomaly detection modules that monitor separately and simultaneously the behavior of cyber and physical data acquired from the ICPS in order to detect and localize cyber, physical, and cyber-physical anomalies over the plant. By filtering and combining the outputs of the behavior-based anomaly detection modules through a Bayesian network-based modelling, the framework is able to: (I) provide the detection probability of cyber, physical, and cyber-physical anomalies; (II) improve the trustworthiness of the detected anomalies by taking into account the anomaly detectors’ confidence about their decisions; and (III) localize the detected anomalies, taking into account possible cascading effects over the cyber-physical process.

The second contribution proposes a novel flexible framework for multi-source and multi-modal CPAD which enables the combination of multiple and redundant CPAD detectors by means of a Time-Varying Dynamic Bayesian Network (TV-DBN) implemented as an explainable decision fusion technique. The framework involves two phases, namely the setup and inference phases. The former involves splitting the referenced ICPS into distributed subsystems and implementing the first detector-level fusion by training CPAD detectors on historical cyber-physical data, whereas the latter involves collecting evidence in terms of crisp labels from the multiple ICPS distributed subsystems and processing such evidence through the second ensemble-level fusion. Explainable ensemble-level fusion is implemented by a decision fusion technique that involves proportional voting inside a self-adaptive TV-DBN. This approach penalizes faulty detectors, excluding them from the decision fusion process if their reputation falls below an acceptable threshold. The framework and explainable decision fusion technique allow for: I) weighing evidence from CPAD detectors by taking into account the confidence about their decision; II) evaluating CPAD detectors’ behavior, i.e. their reputation, over time, based on their past decisions; and III) dynamically including or excluding CPAD detectors when performing ensemble-level fusion.

Acknowledgement

This work was supported by the Italian National Project INAIL BRIC 2023 ID 44 “Industrial Cyber Shield (ICS)” under CUP C83C22001460001.

References

[1] Faramondi, L., Flammini, F., Guarino, S., & Setola, R. (2021). A hardware-in-the-loop water distribution testbed dataset for cyber-physical security testing. IEEE Access, 9, 122385-122396.

[2] Faramondi, L., Flammini, F., Guarino, S., & Setola, R. (2023, July). Evaluating machine learning approaches for cyber and physical anomalies in scada systems. In 2023 IEEE International Conference on Cyber Security and Resilience (CSR) (pp. 412-417). IEEE.

[3] Faramondi, L., Flammini, F., Guarino, S., & Setola, R. (2023). A hybrid behavior-and Bayesian network-based framework for cyber–physical anomaly detection. Computers and Electrical Engineering, 112, 108988.

[4] Guarino, S., Vitale, F., Flammini, F., Faramondi, L., Mazzocca, N., & Setola, R. (2023). A two-level fusion framework for cyber-physical anomaly detection. IEEE Transactions on Industrial Cyber-Physical Systems, 2, 1-13.

Session 6B: Control theory

Distributed Control of a System of Systems via Consensus Alternating Direction Method of Multipliers: a Quadruple Tank Application

Matteo Aicardi[1], Alessandro Bozzi[1], Simone Graffione[1], Roberto Sacile[1], Enrico Zero[1]

I. INTRODUCTION

The problem of controlling a System of Systems (SoS) has been tackled with both distributed and centralized approaches. The distributed strategy is usually adopted when different agents may have a partial observation of the whole system and can control a subset of the subsystems by sharing information among them. The goal of this work is to provide a general control algorithm that can be used to control in a distributed manner an unconstrained multi agent System of Systems, while also testing it in a real environment where disturbances may happen. In particular, the coordination problem was formalized and solved by using a combination of the Model Predictive Control (MPC) paradigm, Linear Quadratic Tracking (LQT) techniques, and Consensus Alternating Direction Method of Multipliers (C-ADMM).

II. SYSTEM ARCHITECTURE AND ALGORITHM

A. System Model

Let S represent a non-linear differentiable system with dynamics defined by the function $f(x,u)$ and let S_d be its linearized around the equilibrium pair (x_e,u_e) and discretized with sampling time T_s version:

$$S_d : x(k+1) = Ax(k) + Bu(k) \tag{1}$$

where $x(k) \in \mathbb{R}^N$ and $u(k) \in \mathbb{R}^U$ represent the deviation of the state and the control variables from the equilibrium point and $A \in \mathbb{R}^{N\times N}$ and $B \in \mathbb{R}^{N\times U}$ describe the system dynamics. The objective is defined as making the system track, for an arbitrary long period of time T_{obj}, a set of state references while trying to keep the control variables as close as possible to the equilibrium values. In order to do it, a receding horizon approach is chosen and the centralized cost function that will be recursively minimized is:

$$\begin{aligned} J(x,u) = \sum_{k=0}^{T-1} & [(x(k)-x^*(k))'Q(x(k)-x^*(k)) + \\ & + u(k)'Ru(k)] + (x(T)-x^*(T))'Q_T(x(T)-x^*(T)) \end{aligned} \tag{2}$$

with $T \ll T_{obj}$ being the control problem horizon while, to keep computations simple, Q, Q_T and R are the diagonal positive definite weight matrices. Now, let the $j-th$ agent, where $j = 1,\dots,M$, have access to information from only a specific portion of the system. A subsystem S_j can be defined to represent the part of S_d of which the dynamics are known to agent j and that is also directly measurable by it. However, agent j may not be able to directly manipulate all the inputs that affect the subsystem's state. It is supposed that, between the M subsystems S_j, all the state variables and inputs of the system S_d appear at least once.

$$S_j : \begin{cases} x_j(k+1) = A_j x_j(k) + B_j u_j(k) \\ y_j(k) = C_j x_j(k) \end{cases} \tag{3}$$

where $x_j \in \mathbb{R}^{N_j}$ represents the subset of the N_j state variables that compose the dynamics known by agent j, $u_j \in \mathbb{R}^{U_j}$ is the subset of all the control variables in u that affects x_j, and C_j is the matrix used to retrieve measurements of agents involved in the subset. Unless some sensor failure happens, it is always assumed $C_j = I_{N_j}$. Subsequently, a cost function is defined for each agent as:

$$\begin{aligned} J_j(x_j,u_j) = \sum_{k=0}^{T-1} & \big[(x_j(k)-x_j^*(k))'Q_j(x_j(k)-x_j^*(k)) + \\ & + u_j(k)'R_j u_j(k)\big] + \\ & + (x_j(T)-x_j^*(T))'Q_j(T)(x_j(T)-x_j^*(T)) \end{aligned} \tag{4}$$

$$J(x,u) = \sum_{j=1}^{M} J_j(x_j,u_j) \tag{5}$$

with suitable positive definite diagonal weight matrices Q_j, $Q_j(T)$ and R_j.

B. Control Algorithm

The C-ADMM can then be employed to solve the coordination problem that arises due to multiple agents "sharing" a control input (while only a single agent can actually manipulate it). By duplicating the control variables inside u_j and extending the vector to contain all the inputs in u for each agent j, while also exploiting the use of the MPC paradigm (more details can be found in [1]), the optimization problem that needs to be solved can be written as:

$$\min_{v_1,v_2,\dots,v_M} \quad \sum_{j=1}^{M} J_j(x_j,v_j) \tag{6a}$$

$$\begin{aligned} \text{s.t.} \quad & x_j(k+1) = A_j x_j(k) + B_j v_j(k) \\ & \forall j \in [1,\dots,M] \quad k = 0,\dots,T-1 \end{aligned} \tag{6b}$$

$$\begin{aligned} & v_j(k) = z(k) \\ & \forall j \in [1,\dots,M-1], k=0 \end{aligned} \tag{6c}$$

where v_j is the aforementioned extended control vector, z is the standard consensus vector used in C-ADMM, matrices B_j and R_j are updated to be consistent with the new input vectors, and (6c) are the consensus constraints required

---

[1] All the authors are with the Department of Informatics, Bioengineering, Robotics and Systems Engineering (DIBRIS), University of Genoa, Genoa, 16145 Italy

to hold just for the first time instant ($k = 0$) due to the simplification introduced thanks to the use of MPC. Then, as usually done, the Augmented Scaled form Lagrangian of the problem, dropping the time argument, can be defined as:

$$L_\rho = \sum_{j=1}^{M} \left[J_j(x_j, v_j) + \frac{\rho}{2} \left\| v_j - z + \frac{\lambda_j}{\rho} \right\|^2 - \frac{1}{2\rho} \|\lambda_j\|^2 \right] \tag{7}$$

Where $\rho > 0$ is the penalty parameter for all the vectors of constraints, and λ_j is the Lagrangian multipliers vector of the $j-th$ vector of constraints. When minimizing the Lagrangian formulation with respect to a single control vector, after a few computations, the minimization problem can be traced back to a standard LQT optimization problem. This, by denoting with s the generic iteration step, leads to the final formulation of the control algorithm:

$$\begin{aligned}
v_1^{*(s)} &= \tilde{R}_1^{-1} \frac{\rho}{2} \left(z^{(s)} - \frac{\lambda_1^{(s)}}{\rho} \right) \\
&\;. \\
v_M^{*(s)} &= \tilde{R}_M^{-1} \frac{\rho}{2} \left(z^{(s)} - \frac{\lambda_M^{(s)}}{\rho} \right) \\
&\;. \\
v_1^{(s+1)} &= \underset{v_1}{\operatorname{argmin}}\, L_\rho(v_1, .., v_M^{(s)}, v_1^{*(s)}, .., v_M^{*(s)}, \lambda_1^{(s)}, .., \lambda_M^{(s)}) \\
&\;. \\
v_M^{(s+1)} &= \underset{v_M}{\operatorname{argmin}}\, L_\rho(v_1^{(s)}, .., v_M, v_1^{*(s)}, .., v_M^{*(s)}, \lambda_1^{(s)}, .., \lambda_M^{(s)}) \\
z^{(s+1)} &= \frac{1}{M} \sum_{j=1}^{M} \left[v_j^{(s+1)} + \left(\frac{1}{\rho} \right) \lambda_j^{(s)} \right] \\
\lambda_1^{(s+1)} &= \lambda_1^{(s)} + \rho \left(v_1^{(s+1)} - z^{(s+1)} \right) \\
&\;. \\
\lambda_M^{(s+1)} &= \lambda_M^{(s)} + \rho \left(v_M^{(s+1)} - z^{(s+1)} \right)
\end{aligned} \tag{8}$$

The formulation of the control reference v_j^* is found to make the *argmin* step of the algorithm solvable with dynamical programming. Additionally, since the MPC simplification are still employed, the control references will be 0 for all the time instants successive to the first. Finally, the update steps of z and all the λ_j refer to the control vector at $k = 0$.

III. CASE STUDY AND RESULTS

All of the experiments performed in this work were done on a system as that of Figure 1. In particular, the system was linearized around an equilibrium point and discretized with a sampling time of $T_s = 0.2 sec$.

In the first case a simulated environment is used and the focus is put onto tanks 1 and 3, with their state references being:

$$\begin{aligned}
h_1^* &= 0 \quad h_2^* = 0.3 + 0.5\cos(0.1t) \\
h_3^* &= 0 \quad h_4^* = 0.3 + 0.5\cos(0.1t)
\end{aligned} \tag{9}$$

An external "step-like" disturbance of 2.5 cm of water is added in the tanks at time instants $t_1 = 60$ s and $t_3 = 105$. The result can be seen in Fig. 2.

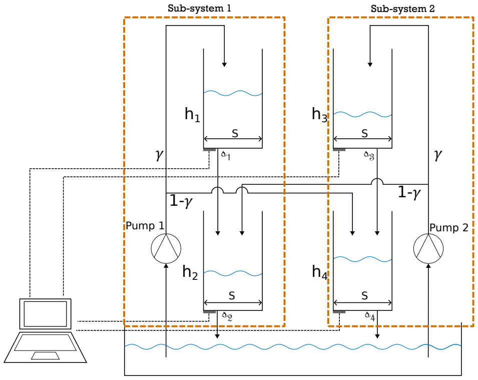

Fig. 1. Quadruple Tank Plant system configuration.

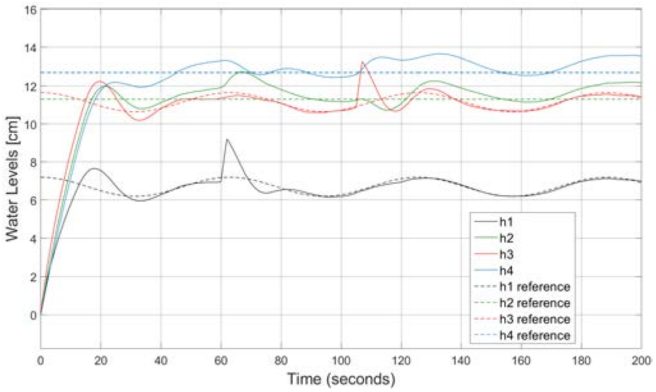

Fig. 2. Water tank levels with respect to the references in the numerical simulation with external noise.

In the second experiment instead, the real system created by Quanser was tested with the state references now flipped and a similar noise was added at around $t = 105$. The outcome can be seen in Fig. 3 and also shows how using a Kalman Filter helped diminishing the impact of a faulty sensor, as it can be seen by looking at the actual level of tank 4.

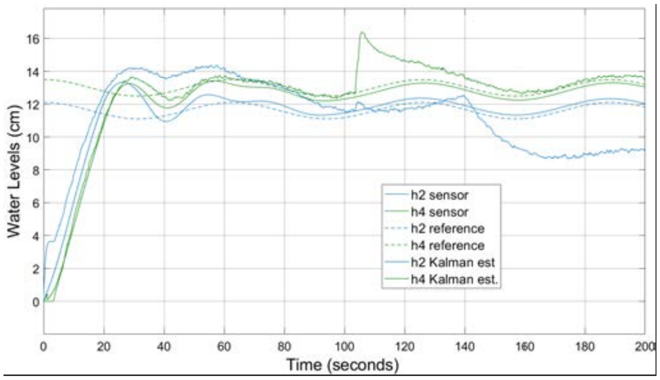

Fig. 3. Water tank levels with respect to the references with the second water sensor not working, with external noise, and using the Kalman filter.

REFERENCES

[1] M. Aicardi, A. Bozzi, S. Graffione, R. Sacile, and E. Zero, "Alternating direction method of multipliers in distributed control of a system of systems: Application to a quadruple tank plant," *Control Engineering Practice*, vol. 149, p. 105972, 2024.

Data-Driven Controller Tuning for MIMO Systems: A Set-Membership Approach

Andres Cordoba-Pacheco[1]**, Fredy Ruiz**[1]

[1]Dipartimento di Elettronica, Informazione e Bioingegneria, Politecnico di Milano, Milan, Italy
{andresfelipe.cordoba, fredy.ruiz}@polimi.it

In the field of control systems, Single-Input Single-Output (SISO) systems have historically received significant attention due to their straightforward mathematical modeling and analysis [2]. However, real-world applications often involve Multi-Input Multi-Output (MIMO) systems, which present greater challenges due to their multivariable nature where each input can affect multiple outputs [4], this research is focused on extending the Set-Membership Data-Driven (SMDD) approach, originally developed for SISO systems, to MIMO systems. The SMDD approach directly tunes controllers from input-output data without requiring plant model identification, thereby simplifying the tuning process while assuming data sets are affected by Unknown But Bounded (UBB) noise [5].

The SMDD framework involves a control system where the controller is parameterized as a linear combination of fixed basis functions. The parameters are found by minimizing the difference between the desired reference model and the actual closed-loop transfer function, see Fig. 1. This minimization provides the best controller parameters that stabilize the system while achieving the desired performance, given a set of noisy input-output data, $\mathcal{D} = \{u(k), y(k), k = 1, 2, \cdots, N\}$ collected from the plant, and provides a closed loop stability certificate. The Unknown But Bounded (UBB) noise/disturbances $v(k)$ are constrained by $||v(k)||_\infty \leq \epsilon$, where ϵ is the unknown bound on the maximum amplitude of the noise. Therefore, the tuning involves solving an estimation problem with UBB additive noise, efficiently managed through a Set Membership formulation.

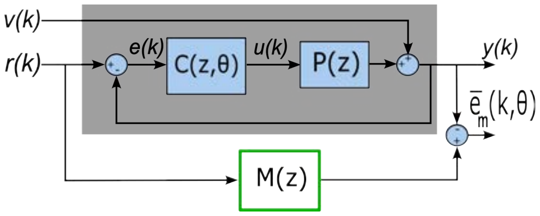

Fig. 1: Control System Tuning Structure.

When analyzing MIMO systems, where matrix commutativity does not hold, data-driven tuning approaches used in SISO systems cannot be directly applied to controller design. Taking into account the methodology presented in [3] to avoid the commutativity problem in matrices, graphically described in Fig. 2. This research outline an extension of the SMDD method to MIMO systems, leveraging the characteristics of the SMDD approach used in SISO applications.

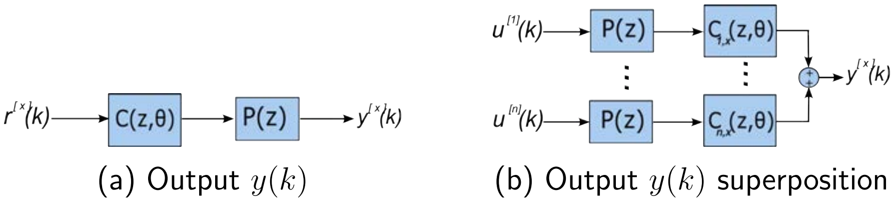

(a) Output $y(k)$ (b) Output $y(k)$ superposition

Fig. 2: Commutation Blocks

Even though the amount of data and the number of experiments increase, leveraging the commutativity between the matrices allows the matching error in Fig. 1 to be redrawn in a simplified way, as shown in Fig. 3. For this reason, the solution of the SMDD approach for MIMO systems can be found.

Aditionally, a detailed comparison with the Virtual Reference Feedback Tuning (VRFT) methodology as outlined in [1],is provided. Fig. 4 shows the step response for both inputs in a $2x2$ MIMO system.

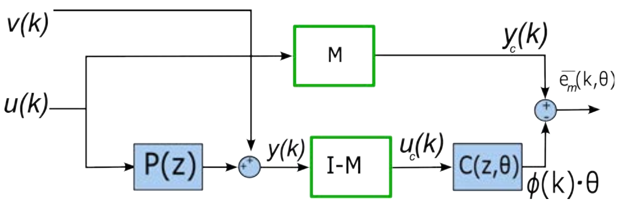

Fig. 3: Modified Matching Error

It also illustrates the cross-coupling effects between the inputs and outputs. Both controllers guarantee a stable response that effectively tracks the step reference signals; however, upon closer examination, both controllers exhibit some overshoots and are not perfectly decoupled. In this case, the SMDD approach demonstrates better performance than the VRFT method, as show in the figures.

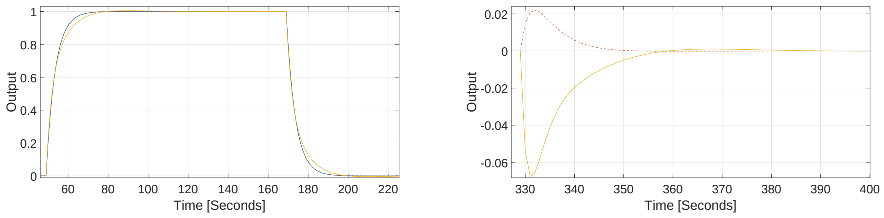

(a) Output $y_1(k)$ (b) cross-coupling $y_1(k)$

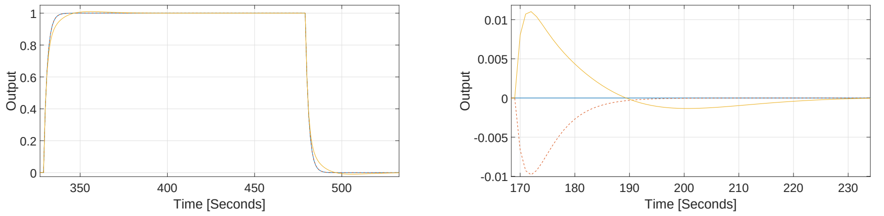

(c) Output $y_2(k)$ (d) cross-coupling $y_2(k)$

Fig. 4: Output $y(k)$: $Reference - Model$ Blue, $SMDD$ Red, $VRFT$ Yellow

Throughout this research, it is evidenced that the SMDD controllers demonstrated better performance in terms of stability and response tracking compared to the VRFT controllers. Both methods were tested under identical conditions, and the results showed that the SMDD approach resulted in more stable and well-decoupled responses. Key performance indicators such as rise time, overshoot, and settling time were used to evaluate the performance and responsiveness of the MIMO system. Aditionally Integral Square Error (ISE) and Integral Absolute Error (IAE) were calculated to evaluate the decoupling error, validating the effectiveness of the SMDD approach.

References

[1] Lucíola Campestrini, Diego Eckhard, Lydia Andrea Chía, and Emerson Boeira. Unbiased MIMO VRFT with application to process control. *Journal of Process Control*, 39:35–49, 2016.

[2] Neera Jain and Andrew G. Alleyne. Comparison of SISO and MIMO control techniques for a diagonally dominant vapor compression system. In *2009 American Control Conference*, pages 1580–1585, 2009.

[3] Masashi NAKAMOTO. A direct method to calculate control parameters by using input and output data. *Transactions of the Society of Instrument and Control Engineers*, 42(8):863–868, 2006.

[4] Ujjwal, H.P Singh, and Neelam Verma. Self-tuning of Multivariable Plant. In *2020 IEEE International Conference on Technology, Engineering, Management for Societal impact using Marketing, Entrepreneurship and Talent (TEMSMET)*, pages 1–6, 2020.

[5] Freddy Valderrama and Fredy Ruiz. Limited-complexity controller tuning: A set membership data-driven approach. *European Journal of Control*, 58:82–89, 2021.

Modeling sensor degradation for Water Quality Monitoring

Marino Pavone, Nicola Epicoco, Giordano Pola, Andrea Manno

Department of Engineering, Computer Science and Mathematics, Center of Excellence DEWS,

University of L'Aquila

Extended abstract

Sensors occupy a very sensitive role in modern society, despite the extraordinary boom of brand-new applications related with the progress in sensing technologies, and they can be considered as pillar in the Industry 4.0 framework. As a matter of fact, sensors are the cornerstone for the majority of security systems. Critical damages (in economic, environmental, and health terms) can be caused by the failure of a single sensor, making sensors' reliability an aspect of primary attention in all safety applications.

Abrupt sensors fault are frequent, but the most common situation shows sensors that slowly vary their sensing capabilities along time, generating the so-called Concept Drift (CD).

This issue is hard to diagnose and can silently supply corrupted information in many control (or system identification) problems, inducing nonuniform control action, excessive actuators efforts, or wrong statistical inference.

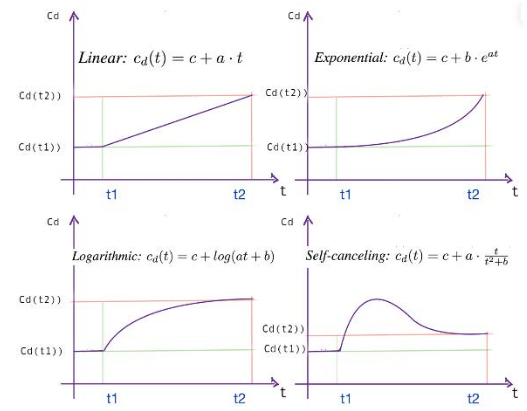

Figure 1: Degradation trends

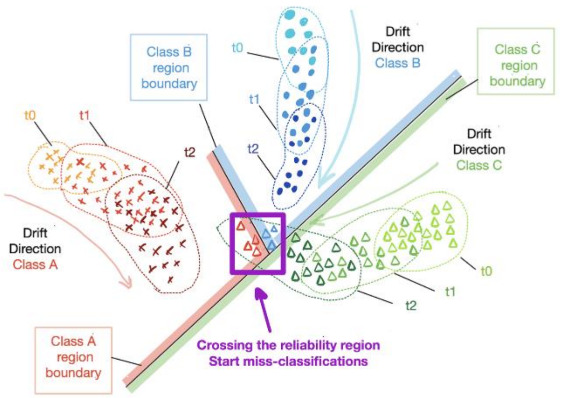

Figure 2: Degradation speed trends

The drift simulation is not trivial since we are dealing with completely unpredictable phenomenas that affect all the sensors employed nonuniformly, and the process can be triggered at any instant of the node life.

Preventive actions like sensor redundancy and continuous maintenance, are commonly employed in case of very severe sensor reliability requirements, such as in avionics, nuclear plants, dams, heavy mechanical industry, and many more applications. On the contrary, a lot of applications that do not have a so relevant security impact, can not motivate such economic effort.

Water Quality Monitoring (WQM) is of indisputable importance, due not only to the risks to human health and environment, but also in its potential to affect a large region in a relatively short time [1]. The advantage of collecting chemical sensor data for ensuring water pureness is an extremely powerful solution against abusive landfill, excessive pesticide usage, and industrial discharge. On the other side it requires an important displacement of resources since a typical WQM scenario is constituted by a wide area sensor network, for which constant maintenance and redundant sensors installation often remains an infeasible solution for both economical and practical reasons.

The development of the Machine Learning (ML) sector has significantly broadened the ways they can be used. In fact, chemical and electrochemical applications are hard to model analytically, primarily because model-based approaches require strong expertise and knowledge in chemistry, and they are only suitable for protected environments (e.g. pipelines) in which there is a limited incidence of external/hard-observable factors [4]. Machine leaning models are proved to be an effective way to deal with chemical classification problem [1]. The main limitation of those methodologies in WQM stay in the high susceptibility of chemical sensors to corrosion phenomena. Being continuously in contact with organic or corrosive substances and varying temperatures along the day, chemical sensors often tend to fail, making their reliability strongly decreasing over time.

It is possible to find several CD handling techniques in the literature [2], all of them require the possibility to collect new supervised data for the estimation of the drift effect according to their time variation. In this way the drift dynamics can be identified and corrected. So, sensor nodes placement must be as capillary as possible in order to precisely Geo localize water contamination. This aspect directly translates in additional costs in the infrastructure maintenance

This research discusses a possible approach for CD handling in WQM by using Machine Learning classifiers as "fake-supervisors" for labeling incoming new data. To this aim, the classifier must be reliable inside a certain neighborhood of the original training dataset centroids. Hence, by collecting data through a commercial WQM sensor, we simulate the aging process by means of an electrochemical corrosion model [5].

In order to properly simulate a likely similar degradation pattern, a degradation function has been implemented in python. Starting from any multi-sensor set of data, the function establishes a simulation time object and generate a syntetic degraded dataset according to the degradation pattern defined by the user. The possible degradation parameters are: degradation intensity values, degradation velocity trend (see Fig.1), degradation starting time and the sensor end of useful life time.

The results of the comparison shows that in terms of accuracy over time in Fig. 3, which shows a pairwise comparison of the considered techniques, it is notable that both K-nearest neighbors algorithm and classification Trees with raw data achieve almost perfect classification when no drift occurs. Even the models trained with PCA data (only the first 4 principal components were used for the training phase) show the same classification accuracy, highlighting the considerable redundancy of the proposed dataset. Neural Networks instead present a starting accuracy of almost 99% for the model with raw data and slightly suffers the loss of information on the 4-features PCA transformed data model, dropping to 97% of accuracy. Regardless of the used ML technique, relevant differences can be observed when the PCA is used in the presence of drift. PCA seems to mitigate more the effect of the drift in the accuracy dropping speed, especially for NN which has significantly recorded the slower accuracy drop trend.

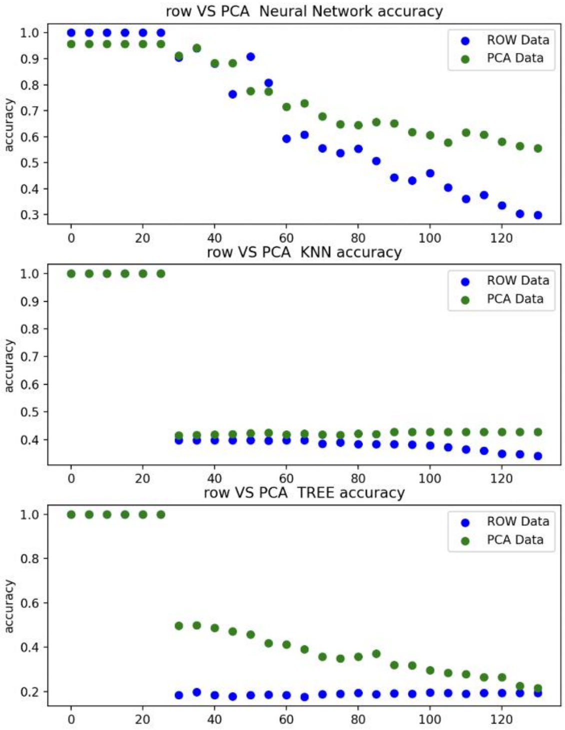

The experiment is repeated with different substances among the original 15 sub dataset and with different degradation patterns. All the experiments have shown the same classifiers behavior, confirming the significant superiority of the Neural Networks against all the simulated CD, and the noticeable effect of the PCA transformation in slowing the accuracy drop.

References

[1] M. Pavone, N. Epicoco, F. Magliocca, G. Pola, "A generalized approach for Feature Selection in Water Quality Monitoring," 31st Med. Conf. on Control and Automation, pp. 599-604, 2023.

[2] A. Jadhav and N. Jadhav, "Learning using Concept Drifts: An overview", 4th Int. Conf. on Computing Communication Control and Automation, 2018.

[3] J. Baranwal et al., "Electrochemical sensors and their applications: A review", Chemosensors, 10, 363, 2022.

[4] M. Singer, "29 - Top-of-the-line corrosion", In Trends in Oil and Gas Corrosion Research and Technologies, A.M. El-Sherik (Eds.), Woodhead Pub., pp. 689-706, 2017

[5] N. Perez, "Electrochemistry and corrosion science", Springer Cham (Ed.), 2004.

An opinion dynamics model for collective risk perception

Lorenzo Zino
Politecnico di Torino, Torino, Italy, `lorenzo.zino@polito.it`

Daniele Vilone
National Research Council, Roma, Italy, `daniele.vilone@istc.cnr.it`

Francesca Giardini and Ming Cao
University of Groningen, Groningen, Netherlands, {`f.giardini,m.cao`}`@rug.nl`

Background

The collective response to an emergency is a complex emergent phenomenon, whose study is of paramount importance in social science and risk management [1]. However, few analytically-tractable mathematical models have been proposed in the literature to study such an important phenomenon. On the one hand, social-psychological efforts typically focus on elucidating the individual-level risk interpretation process [2, 3], overlooking how this leads to collective emergent behaviors. On the other hand, classical mathematical models focus on an abstract representation of opinion dynamics [4], neglecting the specific characteristics of risk perception. To the best of our knowledge, few agent-based models have been proposed for this purpose [5], but they rely on complex mechanisms which hinder establishing rigorous analytical results, ultimately calling for the development of a novel analytically-tractable model for collective risk perception.

In particular, we fill in this gap by leveraging the mathematical theory of opinion dynamics [4, 6]. Specifically, we consider a scenario in which an institution broadcasts an estimate on the nature of the risk of a given emergency. However, it is known from the social psychology literature that individuals, besides receiving institutional information, they also exchange information with their peers and re-elaborate it on the basis of their own risk perception [2, 3]. Our model, proposed in [7], encapsulates these key features, ultimately yielding a realistic and analytically-tractable framework to study how social interactions and individual traits shape the collective risk perception.

Model

We consider n individuals connected through a time-invariant network that captures social influence. Each individual $i \in \mathcal{V}$ is characterized by an opinion $x_i(t) \in [0,1]$, which represents individual i's *risk perception* on the emergency at time $t \in \mathbb{N}$, and by three parameters: *risk sensitivity* $\rho_i \in \{+1, 0, -1\}$, which can be high, neutral, or low; *trust in institutions* $\tau_i \in [0,1]$; and *trust in peers* $\mu_i \in [0,1]$ (with $\tau_i + \mu_i \leq 1$), which capture how much i values information gathered from the two different sources. Individuals' opinion evolves over time according to a two-step mechanism, in accordance with observations from the social-psychology literature on risk interpretation [2, 3]: i) they gather information from the institution and from peers; ii) they process it according to their own risk sensitivity. For simplicity, we denote the intermediate step of the update process from $x_i(t)$ to $x_i(t+1)$ as $z_i(t)$.

Step I (information gathering). At each time step $t \in \mathbb{N}_+$, each individual receives information from the institutions about the nature of the risk. Specifically, the institution broadcasts a (constant) signal $\iota \in [0,1]$, which quantifies the *nature of the risk*, where $\iota = 0$ means no risk and $\iota = 1$ corresponds to maximal risk. At the same time, individuals also gather information from their peers [2]. Specifically, each individual i interacts with a peer j, selected uniformly at random among i's neighbors. Then, j decides to share their opinion $x_j(t)$ with i with probability equal to $f_j(x_j(t))$, where $f_j : [0,1] \to [0,1]$ is a function termed *sharing probability* that maps the opinion of individual j to their tendency to communicate it and captures the fact that people tend to transmit information that is in accordance with their risk perception [3]. Finally, individual i revises their opinion by averaging their current one with the information received from the different sources of information, with weights given by the trust in institutions τ_i and in peers μ_i, respectively, following a standard linear averaging process used in opinion dynamics models [4], i.e.,

$$z_i(t) = (1 - \mu_i - \tau_i)x_i(t) + \mu_i \sum_{j=1}^{n} A_{ij}(t)x_j(t) + \tau_i \iota, \quad (1)$$

where $A_{ij}(t) = 1$ if j shares their opinion with i at time t and 0 otherwise, and $A_{ii} = 1$ if i does not receive information from their peers at time t and 0 otherwise.

Step II (opinion processing). After revising their opinion using the information gathered from external sources (institutions and peers), individuals further process it based no their own risk sensitivity. Specifically, following [3], we assume that each individual i updates their opinion as

$$x_i(t+1) = \begin{cases} \frac{1}{2}(1 + z_i(t)) & \text{if } \rho_i = +1, \\ z_i(t) & \text{if } \rho_i = 0, \\ \frac{1}{2}z_i(t) & \text{if } \rho_i = -1. \end{cases} \quad (2)$$

Overall, the entire two-step opinion update mechanism can be cast in a compact form as a linear averaging dynamics on a time-varying network (see [7] for more details), which can be interpreted as a Friedkin–Johnsen opinion dynamics model [8]. However, the complexity of the network formation process (which is inherently time-varying and state-dependent) does not allow to directly apply the existing results, making the study of our model nontrivial.

Results

We observe that the opinion of each individual, $x_i(t)$, may not necessarily converge to a steady-state, but it can oscillate, due to the stochastic nature of the process, as reported in the left panel of Fig. 1. However, we can define the temporal average opinion of agent i as

$$y_i(t) := \frac{1}{t+1} \sum_{s=0}^{t} x_i(s), \tag{3}$$

for which we can prove the following convergence result, under some reasonable assumption on the network connectivity and the positiveness of the sharing probability, the nature of the risk, and trust in the institution.

Theorem 1 The temporal average opinion $y_i(t)$ converges almost surely to a steady state $\bar{y}_i$, for all $i \in \{1, \dots, n\}$.

The proof, which can be found in [7], rely on a two-step argument. First, we focus on the mean dynamics $m_i(t) = \mathbb{E}[x_i(t)]$, for which we write the recursive equation

$$m_i(t+1) = \big(1-\lambda_i\big) \sum_{j=1}^{n} W_{ij}(m(t)) m_j(t) + \lambda_i u_i, \tag{4}$$

where λ_i and u_i are constants (that depends on the model parameters), and $\mathbf{W}(x(t))$ is a state-dependent and weighted adjacency matrix, and we prove its convergence, leveraging tools from linear averaging models on time-varying networks [6]. Second, we prove that the process is ergodic [9], implying that if $m_i(t)$ converges to $\bar{m}_i$, then it also holds true that $\lim_{t\to\infty} y_i(t) = \bar{m}_i$.

The result in Theorem 1, not only guarantees convergence, but provides also a way to compute the steady-state value, by computing the equilibria of (4). However, in general, the computation of such a steady state is nontrivial since (4) consists of a system of n coupled nonlinear equations. However, for specific implementations of the model, we are able to establish a closed-form solution. Specifically, we focus on the scenario in which individuals interact on a complete networks and trust parameters are homogeneous across the population, but individuals have heterogeneous risk perception. In such a scenario, the network symmetry allows us to reduce the problem to 3 coupled equations [7, Theorem 2 and Proposition 5], from which we can conclude that the presence of even a minority of individuals with high risk sensitivity could lead to a systematic overestimation of the risk, potentially triggering mass panic reactions.

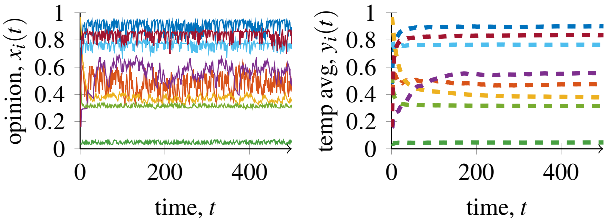

Figure 1: Temporal evolution of (left) opinions and (right) temporal average for a simulation of the model.

Conclusion

The formulation of an analytically-tractable model for risk perception that rely on the mathematical theory of opinion dynamics and its analysis pave the way for several avenues of future research, including i) the extension of our analytical results to unveil the impact of the network structure and heterogeneity across the population on the system's emergent behavior; ii) the expansion of our model, incorporating further real-world features (e.g., the presence of media which may bias the information broadcast by the institution and the presence of polarization in social networks); iii) the validation of the model in real-world scenarios, using experimental and survey data on risk perception.

References

[1] M. K. Lindell, "Disaster studies," *Curr. Sociol.*, vol. 61, no. 5-6, pp. 797–825, May 2013.

[2] C. W. Scherer and H. Cho, "A social network contagion theory of risk perception," *Risk Anal.*, vol. 23, no. 2, pp. 261–267, 2003.

[3] J. R. Eiser *et al.*, "Risk interpretation and action: A conceptual framework for responses to natural hazards," *Int. J. Disaster Risk Reduct.*, vol. 1, pp. 5–16, Oct. 2012.

[4] B. D. O. Anderson and M. Ye, "Recent advances in the modelling and analysis of opinion dynamics on influence networks," *Int. J. Autom. Comput.*, vol. 16, no. 2, pp. 129–149, 2019.

[5] F. Giardini and D. Vilone, "Opinion dynamics and collective risk perception: An agent-based model of institutional and media communication about disasters," *J. Artif. Soc. Soc. Simul.*, vol. 24, no. 1, p. 4, 2021.

[6] A. V. Proskurnikov and R. Tempo, "A tutorial on modeling and analysis of dynamic social networks. Part II," *Annu. Rev. Control*, vol. 45, pp. 166–190, 2018.

[7] L. Zino, F. Giardini, D. Vilone, and M. Cao, "On modeling collective risk perception via opinion dynamics," *Eur. J. Control*, p. 101036, 2024.

[8] N. E. Friedkin and E. C. Johnsen, "Social Influence and Opinions," *J. Math. Sociol.*, vol. 15, no. 3-4, pp. 193–206, 1990.

[9] C. Ravazzi, P. Frasca, R. Tempo, and H. Ishii, "Ergodic Randomized Algorithms and Dynamics Over Networks," *IEEE Trans. Control Netw. Syst.*, vol. 2, no. 1, pp. 78–87, 2015.

PK-PD model identification with a Branch and Bound algorithm

Giulia Di Credico[1], Luca Consolini[1], Mattia Laurini[1], Marco Locatelli[1],
Marco Milanesi[2], Michele Schiavo[2] and Antonio Visioli[2]

Keywords: PK-PD model, Wiener problem, non-linear identification, Branch and Bound method

I. INTRODUCTION

Automatic control algorithms can be employed as important assistant tools for a correct and safe procedure of anaesthesia. This is usually performed during surgical operations and/or during treatment in the intensive care unit by propofol and/or remifentanil administration. The goal is to achieve a desired Depth of Hypnosis status (DoH) which is monitored with the bispectral index (BIS), a dimensionless number between 0 and 100 based on the analysis of the electroencephalogram (EEG). The lower limit corresponds to a flat EEG signal, while the upper one indicates a fully awake patient. Purpose of the anaesthesiologist is to furnish and guarantee over time the correct dosage of drug to fast induce DoH in patient and to maintain the BIS level in the target range $[40,60]$, corresponding to an optimal balance between the risk of awareness and the heaviness of the hypnosis. From the mathematical point of view, the most common compartmental Pharmacokinetics-Pharmacodynamics models, as described in the linear ODE system (1), state the exchange of one drug (or more in realistic applications) among three fundamental compartments. Output of the PK-PD model is the effect-site concentration, which in turn algebraically determines the BIS level through the non-linear Hill function (2). In this work, we address the problem of identification of all the parameters apart from $E0$, which can be measured at the beginning of the induction phase, with a Branch and Bound research method, for which difficulties are compelled by the non-linear dependence of the model itself on the patient related constants we want to determine.

A. Patient based PK-PD model and Hill function

Concentration and the effect of the hypnotic agent are governed by a PK/PD model with three compartments:

$$\begin{cases} \dot{q}_1(t) = -(k_{10}+k_{12}+k_{13})q_1(t) + k_{21}q_2(t) + k_{31}q_3(t) + v(t) \\ \dot{q}_2(t) = k_{12}q_1(t) - k_{21}q_2(t) \\ \dot{q}_3(t) = k_{13}q_1(t) - k_{31}q_3(t) \\ \dot{C}_e(t) = k_{1e}(q_1(t)/V_1) - k_{e0}C_e(t) \end{cases} \tag{1}$$

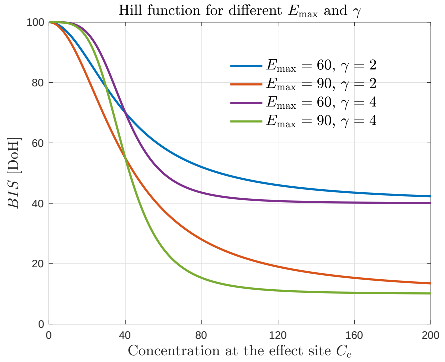

Fig. 1: Hill function plot for different identification parameters (assuming $E_0 = 100$ and $C_{e50} = 40$ fixed).

with q_1, q_2, q_3 being the drug masses, expressed in mg, respectively in the primary (blood and liver), in the fast (muscles and viscera) and in the slow compartment (fat and bones). The input v is the drug mass-flow, expressed in mg/s. Variable C_e is the effect-site concentration, expressed in mg/L. The transfer rates k_{ij}, for $i, j \in \{1,2,3\}$, and the drug elimination rates k_{10}, k_{e0}, are expressed in s^{-1}. The measured output is the BIS value, computed from C_e through the following Hill function:

$$BIS(t) = h(C_e(t)) = E_0 - E_{\max}\left(\frac{C_e(t)^{\gamma}}{C_{e50}^{\gamma} + C_e(t)^{\gamma}}\right), \tag{2}$$

where C_{e50} is the effect-site concentration that corresponds to half of the maximum effect. At each instant t, $BIS(t)$ belongs to range $[E_0 - E_{\max}, E_0]$. Constant E_0 represents the BIS level of a fully awake and alert patient, while $E_0 - E_{\max}$ is the maximum achievable effect with drug administration. The exponent $\gamma > 1$, controls the patient's sensitivity to the hypnotic agent governing the drop of the BIS level with respect to the C_e, as shown in Figure 1. The objective of this work is the identification of $E_{\max}$ and γ, parameters onto which the model depends non linearly. Identification procedure, as explained in the following sections, relies on the residual minimization of the corresponding ARX model, ideally depending on a recorded sampling of the BIS signal and drug dosage during surgery.

B. The corresponding Wiener model

System (1)-(2) can be understood as a Wiener problem, bolus function $\nu(t)$ and the effect site concentration $C_e(t)$ being respectively the input and the output of the system. Defining the sampling period $T > 0$, for each $k \in \mathbb{Z}$ we set $u(k) = \nu(kT)$ and the normalized samples of the effect site concentration $c(k) = C_e(kT)/C_{e50}$. It is indeed provable that, given the general ARX model

$$\begin{aligned} c(k) = &-\alpha_1 c(k-1) - \ldots - \alpha_N c(k-N) \\ &+\beta_1 u(k-1) + \ldots + \beta_M u(k-M), \end{aligned} \tag{3}$$

---

[1] Dipartimento di Ingegneria e Architettura, Università degli Studi di Parma, Italy.

[2] Dipartimento di Ingegneria Meccanica e Industriale, Università degli Studi di Brescia, Italy.

This work has been developed under the PRIN 2022 project "ACTIVA-Automatic Control of Total IntraVenous Anesthesia", CUP D53D23001180006 funded by European Union – Next Generation EU.

the solution of (1) satisfies (3) if $M = N = 4$. In addition, by defining the sampled BIS signal $y(k) = BIS(kT)$ we can write

$$c(k) = g^{-1}_{\gamma, E_{\max}}(y(k)) = \left(\frac{E_0 - y(k)}{E_{\max} - E_0 + y(k)} \right)^{1/\gamma} \tag{4}$$

allowing to express the normalized concentration as output of the inverse Hill function.

II. Identification problem

We assume to know input-output signals $u(k)$ and $y(k)$ for a finite enumeration of sampling instants $0, 1, \ldots, n$. Identification of the optimal point $p = (\gamma, E_{\max})$, which we assume affine to a enough large box $P_0 = [\gamma^-, \gamma^+] \times [E^-_{\max}, E^+_{\max}]$, with $E^-_{\max}$ set such that $E^-_{\max} - E_0 + \min_k y(k) > 0$ and $\gamma^- > 1$, is pursued as well as the estimation of the optimal ARX variable vector $x = (\alpha_1, \ldots, \alpha_M, \beta_1, \ldots, \beta_N) \in \mathbb{R}^{M+N}$ that minimize the residual (3), leading to the study of the optimization problem

$$\min_{p \in P_0, x \in \mathbb{R}^{M+N}} \sum_{k = \max\{M,N\}}^{n} \left(c(k) + \sum_{i=1}^{N} c(k-i)\alpha_i - \sum_{i=1}^{M} u(k-i)\beta_i \right)^2, \tag{5}$$

with $c(k)$ computable from the output samples through (4). Enhancing the matrix-vector structure of (5)

$$\min_{p \in P_0, x \in \mathbb{R}^{M+N}} \left\| A(p) \, [1, x]^\top \right\|^2 \tag{6}$$

where $A(p) \in R^{n \times (M+N+1)}$ is a $\mathscr{C}^2$ function, it is immediate to state that the dependence of the matrix on a set of parameters makes it non-convex and non-linear. However, problem (6) reduces to an exact linear regression whenever the resolution algorithm compels the exact collocation of p in the box P.

III. Branch and Bound

We define $\mathscr{P}$ and $f^* : \mathscr{P} \to \mathbb{R}$ respectively as the set of boxes included in P_0 and the function

$$f^*(P) = \min_{p \in P, x \in \mathbb{R}^\ell} \hat{f}(p, x) = \min_{p \in P, x \in \mathbb{R}^\ell} \left\| A(p) \, [1, x]^\top \right\|^2. \tag{7}$$

Further, we set $f(p) = \min_{x \in \mathbb{R}^\ell} \hat{f}(p, x)$ and we assume that it exists a function $L : \mathscr{P} \to \mathbb{R}$ such that

$$(\forall P \in \mathscr{P}) \; L(P) \leq f^*(P). \tag{8}$$

Any L satisfying (8) is indicated as a *lower bound* function of f^*. Further, let function $r : \mathscr{P} \to \mathbb{R}^q$ be such that $(\forall P \in \mathscr{P}) \; r(P) = p_m$, with p_m being the central point of the box (but choice of other points is permitted as well). If $\ell = M + N$, $q = 2$, Algorithm 1 [2] solves optimization problem (6), implementing, in particular, a binary tree with nodes associated to a restriction of Problem (8) to a box obtained from a recursive splitting of the initial box P_0. Note that the choice of the lower bound function L is critical for the performance of Algorithm 1 and therefore we address the reader to [1] for a detailed discussion on the efficient computation of L.

Id	γ_{ob}	$E_{\max,ob}$	N	M	$\lvert f^*(P_0) \rvert$	# LBs	$\lVert \hat{p} - p^* \rVert$
1	2.24	94.1	2	2	9.44*e*-8	49635	0.0073
			3	3	3.13*e*-10	96415	0.0024
2	4.29	86	2	2	1.46*e*-6	39571	0.0085
			3	3	1.04*e*-7	72179	0.0661
3	4.10	80.7	2	2	1.29*e*-6	33905	0.0089
			3	3	7.81*e*-8	65609	0.0616
4	2.18	102	2	2	1.43*e*-7	43383	0.0086
			3	3	2.62*e*-10	91699	0.0018
5	2.46	85.3	2	2	1.51*e*-7	52887	0.0039
			3	3	7.46*e*-10	94013	0.0006
6	2.42	147	2	2	1.05*e*-7	33885	0.0348
			3	3	1.20*e*-10	77747	0.0043

TABLE I: Numerical results.

IV. Numerical tests

We considered the patients database in [1] (Table 1), taking into account data related to the first 6 individuals, differentiated by age, height, weight and gender. In particular, $\hat{p} = (\gamma_{ob}, E_{\max,ob})$ furnishes the benchmark constants for the identification experiments. Procedure in Algorithm 1 explores identification starting with the box $B_0 = [1, 8] \times [40, 160]$. Induction interval of 300 second is sampled with a period of $T = 1$s. Indicating with $H[\cdot]$ the Heviside step function, the input

$$v(t) = 10 \cdot H[10 - t] + 3 \cdot (H[t - 10] - H[t - 25])$$

represents a bolus of anaesthetic drug administrated in the first 10 seconds, followed by a period of 15 seconds of lower infusion. We set $N = M$ in the ARX model (3), avoiding to consider the case of a full order level $N = M = 4$, since the input signal is too short to lead to a significant contribution from the slow compartment in the BIS evaluation. The sampled signal $y_{id}(k)$ is constructed solving (1) and using Hill function (2) with parameters related to patient number id. Table I presents the results of the numerical experiments: in particular the fifth column collects the total number of computed lower bounds, and the last one is the norm of the difference between the estimated value p^* of the parameters of the Hill function and their true values $\hat{p}$. Note that using half the nodes compared to the $N = 3$ case, a second order model results sufficient for an accurate identification.

References

[1] G. Di Credico et al., *A Branch and Bound method for the exact parameter identification of the PK/PD model for anesthetic drugs*, arXiv preprint arXiv:2403.16742

[2] D. Scholz, *Geometric Branch-and-bound Methods and Their Applications*, Springer-Verlag New York, 2012.

Algorithm 1 Main Branch and Bound algorithm

```
Input → solution tolerance $\varepsilon$, Output → optimal solution $p^*$
  1) Let $\zeta$ be a list of boxes and initialize $\zeta = \{P_0\}$.
  2) Set $UB = f(r(P_0))$, and $p^* = r(P_0)$.
  3) If $\zeta = \varnothing$, stop. Else set $\delta_{\min} = \min\{\delta(\eta) \mid \eta \in \zeta\}$.
  4) Select a box $\eta \in \zeta$, with $\delta(\eta) = \delta_{\min}$ and split it into
     two equal smaller sub-boxes $\eta_1$, $\eta_2$ along the dimension
     of maximum length.
  5) Delete $\eta$ from $\zeta$ and add $\eta_1$ and $\eta_2$ to $\zeta$.
  6) Update $UB = \min\{UB, f(r(\eta_1)), f(r(\eta_2))\}$. If $UB =$
     $f(r(\eta_j))$ with $j \in \{1,2\}$, set $p^* = r(\eta_j)$.
  7) Let $\zeta = \zeta \setminus \{\kappa \in \zeta \mid UB \leq (1+\varepsilon)L(\kappa)\}$.
  8) Return to Step 3.
```

Multidimensional Opinion Dynamics with General Confidence Sets*

Anton V. Proskurnikov
Politecnico di Torino, Italy
`anton.p.1982@ieee.org`

Iryna S. Zabarianska
Moscow Institute of Physics and Technology, Russia
`akshiira@yandex.ru`

Introduction

Models of opinion formation have attracted significant attention from the interdisciplinary research community, engaging scholars and scientists across fields such as sociology, engineering, and physics. Bounded confidence models [1], among the simplest nonlinear models of opinion formation, are notable for their complex and sophisticated dynamics. The classical Hegselmann-Krause model illustrates the evolution of scalar opinions influenced by "homophilous" social dynamics, where each actor adjusts their opinion based on similar opinions from their peers while disregarding dissimilar ones. Existing generalizations to the case of multidimensional opinions usually assess the similarity of opinions based on their proximity in Euclidean space or another norm. In contrast, we propose a generalized model in which two opinions are considered similar if their deviation lies within a specified confidence set. This set is not necessarily a ball in any metric and can be unbounded; the only requirement is that it exhibits certain symmetry properties.

Model Description

Consider a group of n individuals (social agents), whose opinions changes at discrete moments of time $t = 0, 1, \ldots$ The agent $i \in \{1, \ldots, n\}$ at time t has a multidimensional opinion represented by a vector $\xi^i(t) = (\xi^i_1(t), \ldots, \xi^i_d(t)) \in \mathbb{R}^d$. The interpretation of the opinion vector may vary. Such an opinion can, for instance, convey an individual's stance towards a particular object, a dimension that cannot be encapsulated by a single scalar quantity. Take, for example, an opinion regarding the optimal distribution of a resource (material, financial, etc.) among multiple recipients or an individual's viewpoints on d distinct topics. When individuals form their own opinions, each agent considers only opinions that are "similar" to their own, with similarity defined by a confidence set $\mathcal{O}(t) \subseteq \mathbb{R}^d$. This set may be time-dependent and unbounded. Specifically, at time t, agent i trusts the opinions of agents from the set

$$\mathcal{N}_i(t) \triangleq \{j : \xi^j(t) \in \xi^i(t) + \mathcal{O}(t)\}.$$

Formally, $\mathcal{N}_i$ depends not only on time but also on the entire family of opinions $(\xi^j(t))_{j=1}^n$; but we write $\mathcal{N}_i(t)$ for the sake of brevity. Assume that $\mathbf{0} \in \mathcal{O}(t)$, indicating that the agent trusts their own opinion, i.e., $i \in \mathcal{N}_i(t)$.

At each step, the opinion of agent i is formed by averaging the trusted "similar" opinions, resulting in the dynamics

$$\xi^i(t+1) = \frac{1}{|\mathcal{N}_i(t)|} \sum_{j \in \mathcal{N}_i(t)} \xi^j(t), \quad i = 1, 2, \ldots, n. \tag{1}$$

Main Results: The Model Behavior for Symmetric Confidence Sets

We analyze the asymptotic behaviors of system (1), specifically focusing on the convergence of opinions and their limits as $t \to \infty$. In the stationary case, where $\mathcal{O}$ does not depend on time, these values represent the system's equilibria. Our first result is as follows.

Theorem 1 *Let the confidence set be symmetric: $\mathcal{O}(t) = -\mathcal{O}(t)$ for all $t \geq 0$. Then the opinions described by system* (1) *converge to finite limits $\xi^i(\infty) \triangleq \lim_{t\to\infty} \xi^i(t)$, $i = 1, \ldots, n$.*

If, in addition, $\mathbf{0} \in \mathbb{R}^d$ is an interior point of the set $\bigcap_{t \geq t_0} \mathcal{O}(t)$ for some $t_0 \geq 0$, the opinions cease to change after a finite number of steps: $\xi^i(t) = \xi^i(t+1)$ for t being large.

Theorem 1 does not specify how the limit opinions of a social group are structured for a given initial condition. At the same time, under certain conditions it is possible to classify all limit opinions, as the following result shows.

---

[*] The work is supported by the project 2022K8EZBW "Higher-order interactions in social dynamics with application to monetary networks", funded by European Union – Next Generation EU within the PRIN 2022 program (D.D. 104 - 02/02/2022 Ministero dell'Universitá e della Ricerca). This manuscript reflects only the authors' views and opinions, and the Ministry cannot be considered responsible for them.

Theorem 2 *Let the confidence set $\mathcal{O}$, satisfying the conditions of the theorem 1, be time-invariant. The family of opinion vectors $(\xi_i^*)_{i=1}^n$ is the equilibrium of the system (1) if and only if any two opinions from this set are either coincident $\xi_i^* = \xi_j^*$ or "dissimilar" in the sense that $\xi_i^* - \xi_j^* \notin \mathcal{O}$. If $\mathbf{0}$ serves an interior point of $\mathcal{O}$, then any solution of the system (1) converges (in a finite time) to one of these equilibria.*

The key idea of the proofs [3] relies on convergence of type-symmetric consensus algorithms, as outlined in [1, Lemma 6] and [2, Lemma 1], retracing the analysis of the multidimensional Hegselmann-Krause model.

Beyond Symmetry and Homogeneity: Some Counterexamples

Heterogeneous agents: Periodic Orbits. We first note that the key implicit assumption in Theorems 1 and 2 – the homogeneity of agents – is crucial. Extending the model by replacing a common confidence set $\mathcal{O}$ with a family of sets $\mathcal{O}_i$ and adjusting $\mathcal{N}_i(t)$ accordingly: $\mathcal{N}_i(t) = \{j : \xi^j(t) - \xi^i(t) \in \mathcal{O}_i\}$, can result in periodic orbits. For example, consider the case where $n = 3$. Let $\mathcal{O}_1 = (-3, 3) \setminus \{-1, 1\}$ and $\mathcal{O}_2 = \mathcal{O}_3 = (-1, 1)$. Initially, agents have opinions $\xi^1(0) = 0$, $\xi^2(0) = -1$, and $\xi^3(0) = 2$. Agents 2 and 3 will keep their opinions constant, while agent 1's opinion alternates between 0 and 1 at even and odd time steps. To generalize this to $n > 3$, simply add $n - 3$ agents with $\mathcal{O}_i = (-1, 1)$ positioned far enough from agents 1, 2, and 3 so their dynamics remain unaffected. Thus, the opinion of a single "deviant" agent with alternative views may not converge, even if the other agents maintain constant opinions.

Asymmetric Confidence Set: Periodic Orbits. Without symmetry in the sets $\mathcal{O}(t)$, the system can also exhibit periodic solutions. Consider the confidence set $\mathcal{O} = \{(-8, 14) \setminus \mathbb{Z}\} \cup \{-8, -6, 0, 14\}$ Choose the initial opinions of six agents have the values indicated in Fig. 1a. Using induction on $t = 0, 1, \ldots$ it can be easily checked that agents $1, 2, 6$ are isolated (trusting only themselves), yet influence (Fig. 1b) the other agents who change their opinions in the cyclic order:

$$\xi^3(1) = \frac{\xi^3(0) + \xi^6}{2} = \xi^5(0), \quad \xi^5(1) = \frac{\xi^5(0) + \xi^2}{2} = \xi^4(0), \quad \xi^4(1) = \frac{\xi^4(0) + \xi^1}{2} = \xi^3(0).$$

(a) n = 6 opinions at $t = 0$

(b) The topology of the confidence graph

Figure 1: Periodic solution caused by asymmetric confidence: (a) the initial condition; (b) the graph of interactions

Asymmetric Confidence Set: Infinite-Time Convergence and Non-Equilibrium Limit Point. In the absence of symmetry, converging solutions generally do not terminate in finite time, and their limits need not be equilibria. An example is illustrated in Fig. 2, where the confidence set $\mathcal{O} \subset \mathbb{R}^2$ is a union of the open half-plane $\{\xi_1 > 0\}$ with the closed ball centered at the origin of radius $r > 0$. This confidence set is not symmetric, but contains $\mathbf{0}$ as an internal point. The initial opinions of three agents are indicated in Fig. 2b. If $\|\xi^2(0) - \xi^3(0)\|_2 \geq 2r$, then the opinions of agents 2 and 3 will never change, while the opinion of agent 1 converges over infinite time to the midpoint of the line segment connecting ξ^2 and ξ^3. However, choosing $r = \|\xi^2(0) - \xi^3(0)\|_2/2$, the limit opinions do not constitute an equilibrium.

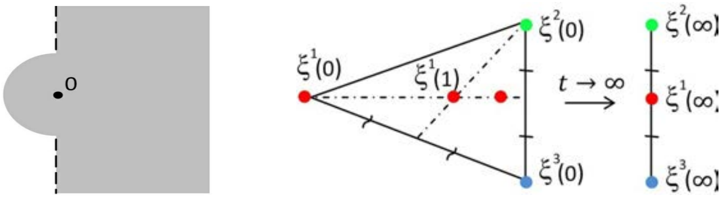

(a) Confidence set.

(b) Opinion dynamics.

Figure 2: No finite-time convergence without symmetry for $\|\xi^2(0) - \xi^3(0)\|_2 \geq 2r$: (a) confidence set $\{\xi_1 > 0\} \cup B_r(\mathbf{0})$ and (b) convergence of ξ^1 in infinite time to the midpoint of the line segment connecting ξ^2 and ξ^3

References

[1] Bernardo C., Altafini C., Proskurnikov A., Vasca F. Bounded confidence opinion dynamics: A survey // Automatica. 2024. Vol.159. P.111302.

[2] Proskurnikov A., Tempo R. A tutorial on modeling and analysis of dynamic social networks. Part II//Annual Reviews in Control. 2018. Vol. 145. P.166-190

[3] Zabarianska I., Proskurnikov A., Opinion Dynamics with Set-Based Confidence: Convergence Criteria and Periodic Solutions (under review)//online as ArXiv: 2408.01753.

Session 6C: Control of actuators

Control and Driving Technologies for Soft Robots based on Dielectric Elastomer Actuators

Paolo Roberto Massenio[1,2], Giovanni Soleti[2], Carmen Perri[1,2], Gianluca Rizzello[2], and David Naso[1]

***Abstract*— Dielectric Elastomer Actuators (DEAs) are highly attractive in the context of soft robotics due to their high flexibility, large deformations, and self-sensing capabilities. However, DEA-based soft robots face control challenges, such as nonlinearities and complex dynamics, complicating the design of model-based control strategies for position regulation and trajectory tracking. Additionally, the high voltage required to actuate DEAs often necessitates the use of bulky and expensive voltage amplifiers, which hinder portability and cost-effectiveness. This extended abstract briefly summarizes recent solutions proposed by the authors to address these challenges.**

I. CONTROL OF DEA-BASED SOFT ROBOTS

The soft robotic system considered in this work is shown in Fig. 1. It features a planar module with a T-shaped structure composed of two plates connected by a soft, flexible backbone, compressed by two pre-tensioned rolled DEAs. When a high voltage is applied to one DEA its stiffness decreases, causing the structure to bend toward the unactuated DEA. This module can also be used to construct modular soft tentacle arms. From a control standpoint, the system in Fig. 1(a) faces typical challenges of DEA-based systems, such as severe elastic nonlinearities, viscoelastic creep, and control input limitations. It also encounters common issues in soft robotics, including underactuation (2 DEAs for 3 DOF), kinematic nonlinearities, and a configuration-dependent actuation matrix. These factors present significant obstacles to developing a model-based control strategy for position regulation or trajectory tracking.

In [1], the first attempt at designing a closed-loop position controller using a model-based approach for the considered system was presented. Noteworthy, this work introduced for the first time a position control scheme for a multi-DOF DEA-based structure. The control problem was formulated within the optimal control framework, addressing nonlinearities stemming from viscoelasticity and actuator coupling using the Adaptive Dynamic Programming (ADP) approach. The objective was to significantly enhance dynamics in terms of settling time and reduced oscillations compared to open-loop responses. Additionally, input constraints were integrated by introducing a novel bounding function capable of accommodating also asymmetric input bounds.

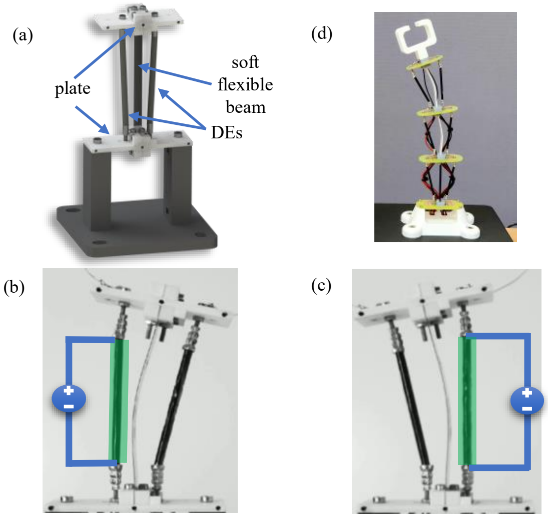

Fig. 1. Considered system and actuation principle: (a) single module; (b) left DEA actuated; (c) right DEA actuated; (d) full tentacle arm prototype.

By changing the geometric parameters of the system, bistability of the structure can be achieved. Bistability is a key concept utilized in the design of energy-efficient soft robotic structures, allowing them to maintain a deformed shape without additional energy consumption. Furthermore, it significantly enhances the system's range of motion, albeit at the cost of losing proportional regulation. To address this challenge, we implemented in [2] a feedback control scheme to maintain proportional regulation while preserving the large displacements enabled by the bistable design. In particular, we presented and experimentally validated a port-Hamiltonian model for the DEA-driven soft robot. Using this model, we developed an energy-based control law based on passivity theory to stabilize unstable open-loop configurations. We provided sufficient conditions for the existence of a class of stabilizing controllers and introduced a Linear Matrix Inequality (LMI) algorithm for practical controller design.

In [3], a significant advancement in the control design of the DE-based soft robot was presented, focusing on trajectory tracking. We introduced a nonlinear change of coordinates that transformed the system into the collocated form, simplifying controller design by decoupling the control inputs from the configuration-dependent actuation matrix. This coordinate transformation was well-defined within a subset of the robot's configuration space, derived using a geometric argument to analytically determine the feasible subset of configurations which ensured the invertibility of the transformation. Leveraging this change of coordinates, trajectory tracking was achieved through a partial feedback

[1] Department of Electrical and Information Engineering,
Polytechnic University of Bari, 70126 Bari, Italy
e-mail: {paoloroberto.massenio; carmen.perri; david.naso}@poliba.it
[2] Department of Systems Engineering,
Saarland University, Saarbrücken, Germany
e-mail: {giovanni.soleti; gianluca.rizzello}@imsl.uni-saarland.de

linearization scheme, and we investigated the stability of resulting zero dynamics under constant references.

Finally, in [4], we recently proposed a more general framework particularly suited for controlling soft robots with variable stiffness actuators that exhibit a non-negligible internal dynamics. The goal was to design a feedback law to achieve a target closed-loop mechanical impedance with desired elastic and damping values, while ensuring the actuator remains passive at the mechanical interaction port. This created a modular motion control framework where actuators can be controlled independently of the mechanical structure, ensuring overall stability. We plan to apply this framework to both DEA-based soft robots and other smart material-based structures, such as those using shape memory alloys.

Future work includes refining the model with external loads, experimentally validating the control strategies, and developing trajectory planning techniques for the soft robot shown in Fig. 1.

II. CUSTOM DRIVING CIRCUIT FOR DEAS

The high-voltage (HV) needed to actuate DEAs, typically between 1 and 3.5 kV, represents their most critical aspect. Off-the-shelf amplifiers are commonly used for HV control up to 20kV. However, these devices are bulky, heavy, and expensive, primarily intended for laboratory use.

In [5], we introduced a novel HV driving circuit for DEAs. The circuit consists of a cascade configuration including a resonant circuit, a three-coil transformer, a Greinacher doubler-rectifier element, and an active discharging stage. Figure 2 shows the circuit along with its block diagram. This design is compact, lightweight, cost-effective, and controllable via PWM input. It produced voltages ranging from 0 to 3 kV using a modulated low voltage input ranging from 0 to 6 V, achieving an unprecedented goal for a circuit with such small size and cost. To precisely control the HV delivered to the DEA and to compensate the inherent performance differences between the custom circuit and the laboratory equipment, model-based closed-loop control is essential. Therefore, a control-oriented dynamic model was also developed in [5], with the goal of describing the relationship between the low-voltage input signal and the HV output during both charging and discharging phases of the DEA. Balancing accuracy with computational efficiency was challenging due to nonlinear and switching components. Two models were developed for the charging and discharging phases and integrated into a single switching model. Experimental validation showed over 92% prediction accuracy for input signals up to 5 Hz and above 79% up to 100Hz. However, the soft robotic application described above requires actuation frequencies below tens of hertz.

A motion control scheme for the HV circuit was introduced and experimentally validated in [6]. The proposed scheme involves a cascade architecture that combines an outer position control loop for a conic DEA, utilizing a PID controller in series with a square root function, with an inner voltage loop that finely regulates the HV delivered to the DEA. The switching model is used to derive a small-signal model of the circuit. This small-signal model is then used to design a linear voltage control loop for the driving electronics using a frequency domain approach. After comparing the input-output behaviour of the HV circuit with and without the voltage regulation loop (i.e., the inner loop), the proposed controller was tested in combination with the outer position loop. Experimental validation showed that the performance achieved by the proposed approach was comparable to that of expensive and bulky laboratory amplifiers, while the lack of the inner voltage control loop has a significant impact on the overall positioning accuracy.

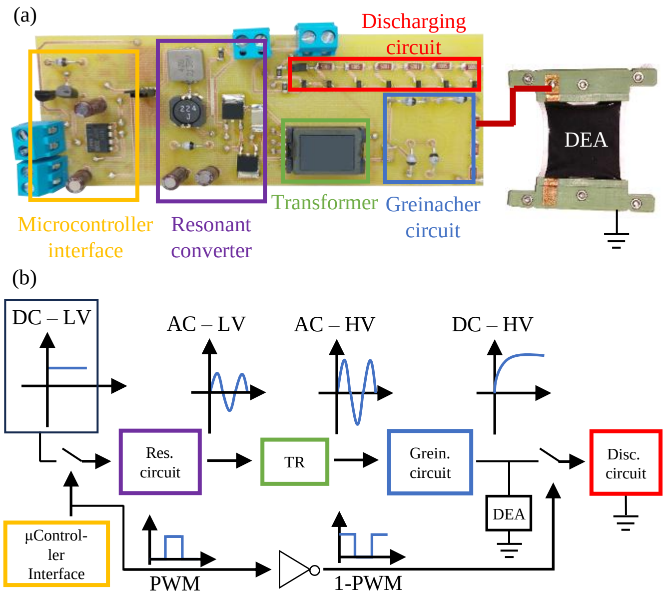

Fig. 2. HV driving circuit. (a) Circuit picture; (b) Circuit block diagram.

Future developments include designing a nonlinear controller to further reduce the performance gap between the HV circuit and commercial amplifiers.

REFERENCES

[1] P. R. Massenio, J. Prechtl, D. Naso, and G. Rizzello, "Nonlinear optimal control of a soft robotic structure actuated by dielectric elastomer artificial muscles," in *2022 IEEE/ASME International Conference on Advanced Intelligent Mechatronics (AIM)*. IEEE, July 2022.

[2] G. Soleti, J. Prechtl, P. R. Massenio, M. Baltes, and G. Rizzello, "Energy based control of a bi-stable and underactuated soft robotic system based on dielectric elastomer actuators*," *IFAC-PapersOnLine*, vol. 56, no. 2, p. 7796–7801, 2023.

[3] G. Soleti, P. R. Massenio, J. Kunze, and G. Rizzello, "Nonlinear coordinate transformation and trajectory tracking control of an underactuated soft robot driven by dielectric elastomers," in *2024 IEEE 7th International Conference on Soft Robotics (RoboSoft)*. IEEE, Apr. 2024.

[4] G. Rizzello and P. R. Massenio, "Passivity-based impedance control of a class of nonlinear actuators with internal dynamics," in *2024 IEEE 18th International Conference on Advanced Motion Control (AMC)*. IEEE, Feb. 2024.

[5] C. Perri, B. Holz, P. R. Massenio, D. Naso, and G. Rizzello, "Design, modeling, and experimental validation of a high voltage driving circuit for dielectric elastomer actuators," *IEEE Transactions on Industrial Electronics*, vol. 71, no. 5, p. 5083–5093, May 2024.

[6] C. Perri, P. R. Massenio, D. Naso, and G. Rizzello, "Closed loop positioning of a dielectric elastomer actuator driven by a feedback-controlled high voltage circuit," in *2024 IEEE 18th International Conference on Advanced Motion Control (AMC)*. IEEE, Feb. 2024.

Adaptive Reference Governor for DC-DC Converters based on Model Predictive Control

Gionata Cimini, Riccardo Felicetti, Francesco Ferracuti, Luca Cavanini, and Andrea Monteriù

I. INTRODUCTION

DC-DC power converters are pivotal components in modern electronics for voltage regulation, such as in DC microgrids, photovoltaic power generation, brushless DC motors, automotive, and consumer electronics. Although advanced control laws for DC-DC converters are mature and demonstrate excellent results, standard PID controllers tend to dominate the manufacturers' production for industrial applications. Replacing a low-level controller of a power converter is often infeasible or unsuitable, and even when it might be physically possible, industrial certifications for stability and robustness might prevent the change (see ISO 26262 for automotive).

When the converter cannot be replaced, Reference Governors (RGs) represent an appealing solution and are most often designed as an Model Predictive Control (MPC) problem. In the literature, the RG applications for DC-DC power converters assume the mathematical model is a time-invariant white-box model. This represents a limitation, because power converters behaviour depends on various factors, including converter topology, its components, the load characteristics, and the operating conditions. Moreover, the RG necessitates a closed-loop model, which includes the low-level controller, which is probably not disclosed by the manufacturer.

The objective of this work is to overcome these limitations by proposing an adaptive RG that combines a linear time-variant MPC based on a black-box model that is identified in real-time. What is here proposed and experimentally validated is a plug-and-play solution (see Fig. 1) to improve the transient behaviour of DC-DC converters that: *i).* fits a wide range of converters, *ii).* is self-tuning (i.e., no prior modeling effort), *iii).* is proven to run in real-time on cheap, conventional control boards, *iv).* does not require to alter the original controller.

This abstract constitutes a shortened version of a full paper currently under review for the IEEE Transactions on Control Systems Technology.

II. RECURSIVE LEAST SQUARES IDENTIFICATION RLS$_{\text{FO}}$

Consider the closed-loop DC-DC converter, denoted with the dashed box in Fig. 1. Assuming that such closed-loop system can be modeled using a SISO First Order (FO) linear time variant system, its model boils down to $y_k - a_k y_{k-1} = b_k u_{k-1}$, where $y_k, u_k \in \mathbb{R}$ are the output voltage and the reference at the time step k. Assuming unitary gain in steady-state, $b_k = 1 - a_k$ holds, and $a_k \in \mathbb{R}$ can be estimated with Recursive Least Squares (RLS) with a forgetting factor λ_k.

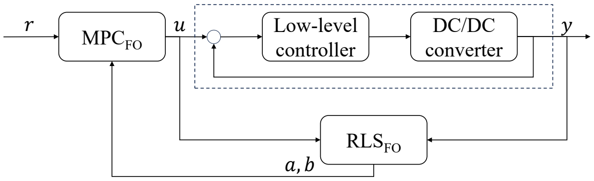

Fig. 1: Complete control scheme.

In usual operating conditions, the reference voltage r_k is piecewise constant, posing a challenge for system identification, as such simple signal are known to be non-persistently exciting [1]: if unmanaged, the outcome is parameter drift and/or covariance blowup [2]. Thus, we employ a conditional parameter update policy, stopping the update when the input is not sufficiently exciting [2] (namely, in steady-state). The total amount of FLoating-point OPerations (FLOPs) required by the identification routine, named RLS$_{\text{FO}}$, is 15, and the memory allocation needed to run is 12 floats, including input data.

III. REAL-TIME ADAPTIVE MPC$_{\text{FO}}$

At each time k, we pose the following optimization problem

$$\begin{aligned} \min_{u_i, x_{i+1}} \quad & \frac{1}{2}\sum_{i=0}^{p-1}\left(\|y_{i+1}-r_k\|^2_{w_y} + \|u_i - u_{i-1}\|^2_{w_\delta}\right) \\ \text{s.t.} \quad & x_{i+1} = a_k x_i + b_k u_i \\ & y_{i+1} = c_k x_{i+1} \end{aligned} \tag{1}$$

Defining the input increment $\delta_k = u_k - u_{k-1}$, and $z = [\delta_k \ x_{k+1} \ \dots \ \delta_{k+p-1} \ x_{k+p}]^\mathsf{T} \in \mathbb{R}^m$, with $m = 2p$, problem (1) can be rewritten as the equivalent parametric Quadratic Programming (QP) problem

$$\begin{aligned} z^* = \arg\min_{z \in \mathbb{R}^m} \quad & \frac{1}{2} z^\mathsf{T} H z + z^\mathsf{T} F \theta \\ \text{s.t.} \quad & Ez = e \end{aligned} \tag{2}$$

where $H \in \mathbb{R}^{m \times m}$ is diagonal and positive definite, $F \in \mathbb{R}^{m \times p}$, $\theta = \begin{bmatrix} r_k & \dots & r_k \end{bmatrix}^\mathsf{T} \in \mathbb{R}^p$, and $E \in \mathbb{R}^{p \times m}$, $e \in \mathbb{R}^p$ embed the dynamics of model. We present here the generic steps of a *direct* method to solve the QP problem (2).

Theorem 1: Let us define $D = \operatorname{diag}(\begin{bmatrix} \ell, \dots, \ell \end{bmatrix})$, with $\ell = \begin{bmatrix} w_\delta^{-1} & (c_k w_y)^{-1} \end{bmatrix}^\mathsf{T}$, $h = F\theta$ and $\bar{h} = DDh$. Let λ be the vector of Lagrange multipliers for QP problem (2), and

---

G. Cimini is with ODYS S.r.l., 20159 Milano, Italy (e-mail: gionata.cimini@odys.it).

R. Felicetti, F. Ferracuti, L. Cavanini, and A. Monteriù are with the Department of Information Engineering, Università Politecnica delle Marche, Via Brecce Bianche 12, Ancona, 60131, Italy (e-mail: r.felicetti@univpm.it; f.ferracuti@univpm.it; l.cavanini@univpm.it; a.monteriu@univpm.it).

L. Cavanini is also with Industrial Systems and Control Ltd, Culzean House, 36 Renfield Street, Glasgow G2 1LU, UK (e-mail: l.cavanini@isc-ltd.com).

$DE^{\mathsf{T}} = QR$, $Q = \begin{bmatrix} Q_1 & Q_2 \end{bmatrix}$, $R = \begin{bmatrix} \bar{R}^{\mathsf{T}} & 0_p^{\mathsf{T}} \end{bmatrix}^{\mathsf{T}}$, where Q is an orthogonal matrix, $Q^{\mathsf{T}}Q = I_m$, $Q_1 \in \mathbb{R}^{p\times p}$, $Q_2 \in \mathbb{R}^{p\times p}$, and $\bar{R} \in \mathbb{R}^{p\times p}$ is an upper triangular matrix. Then the optimal pair (z^*, λ^*) can be derived by solving the system of equations

$$\begin{aligned} \bar{R}^{\mathsf{T}}\bar{R}\lambda^* &= E\bar{h} + e \\ z^* &= DD(E^{\mathsf{T}}\lambda^* - h) \end{aligned} \tag{3}$$

Computing (z^*, λ^*) from system (3) can be seen as solving *directly* the Karush–Kuhn–Tucker (KKT) system with a *Schur complement method* based on QR-factorization and pivoting on H. The Schur method is rarely applied in practice, because it requires the nonsingularity of H, and it is generically hard to compute, unless H^{-1} is known, or the numbers of rows of E is small. However, the structure of the present QP problem makes H^{-1} easy to compute.

The throughput for computing z^* with (3) is dominated by the QR factorization of DE^{T}. Thus, we have developed a new factorization algorithm (QR$_{\text{FO}}$) tailored for computing $\bar{R}$ under the assumption of the sparsity pattern of E (not reported here for brevity). We based our method on Givens rotations, which are efficient at zeroing specific elements below the diagonal of a given matrix [3]. The total amount of FLOPs required by QR$_{\text{FO}}$ is $5p+10(p-1)+\max(0, 6(p-2))$. The total amount of FLOPs required by MPC$_{\text{FO}}$ for solving (3) is $p^2+27p+6$.

IV. EXPERIMENTAL RESULTS

The algorithm is tested on a C2000 Delfino Micro-Controller Unit (MCU) LAUNCHXL-F28379D (200 MHz clock frequency), paired with a Buck Converter BoosterPack BOOSTXL-BUCKCONV by Texas Instruments™. We set $w_y = 1$, $w_\delta = 0.5$, $\lambda_k = 0.975$, and $p = 6$ in the MPC$_{\text{FO}}$. We compare the performances of MPC$_{\text{FO}}$ with the low-level controller (without MPC$_{\text{FO}}$), that is a PI controller for voltage mode control whose default (pre-tuned) parameters are kept: $K_p = 0.1$, $K_i = 0.008$, 200 kHz sampling frequency, and $[0, 0.6]$ duty cycle saturation. The sampling frequency for RLS$_{\text{FO}}$ and MPC$_{\text{FO}}$ are set to 10 kHz.

In the transient reported in Fig. 2, the device is turned on: the required voltage is 2 V, while the load is 7Ω. The solid blue line is the output voltage y_k with MPC$_{\text{FO}}$, the yellow dashed line is the original reference r_k, and the orange dashed line is the reference modified by MPC$_{\text{FO}}$ u_k. For comparison, the output voltage without MPC$_{\text{FO}}$ is represented by a solid black line. Fig. 2 also reports the outcome of the RLS$_{\text{FO}}$. The shaded area highlights the activation of parameter identification. For $t < 0$ s, the initial conditions $a_k = 0$, $b_k = 1$ describe a model with no dynamics. The RLS$_{\text{FO}}$ returns its first estimation of a_k and b_k after 0.135 ms. The estimation is refined in the subsequent steps and, consequently, the reference is increased to speed up the transient. After 1.23 ms, the system is in steady-state and the identification is turned off because the persistent excitation condition is not met. Using the MPC$_{\text{FO}}$, the rise time is reduced by 58.8% and the IAE is reduced by 24.8%, while the overshoot increases from 4.0% to 6.0%. Fig. 2 also shows the currents using the MPC$_{\text{FO}}$, which result to be comparable in magnitude to the baseline controller.

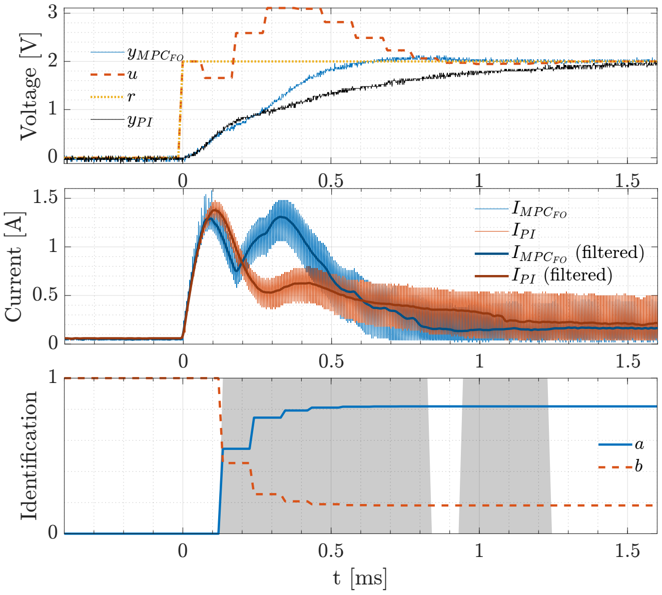

Fig. 2: Buck converter: switching on.

Computationally, QR$_{\text{FO}}$ massively outperforms popular linear algebra packages (LAPACK 3.10.0, EIGEN 3.4.0), and MPC$_{\text{FO}}$ is faster than a tailored condensing routine: the improvements are larger than an order of magnitude (detailed results are here omitted for brevity). To show the performance of MPC$_{\text{FO}}$, we compare it with an equivalent adaptive RG using the *adaptive MPC* functionality of the Model Predictive Control Toolbox™ from MATLAB®. The compared algorithms are deployed on the F28379D MCU using the *Embedded Coder*. Fig. 3 shows that MPC$_{\text{FO}}$ is faster by a factor starting from 3.6x (for prediction horizon $p = 4$) to 184x for $p = 40$. The difference is substantial also in memory occupancy. With $p = 6$, we have 0.32 kB for the MPC$_{\text{FO}}$, and 0.82 kB for the one produced by MATLAB® tools. The execution in the experimental setup configuration ($p = 6$) requires 219 FLOPs and a memory allocation of 33 floats, allowing the MPC$_{\text{FO}}$ to seamlessly run up to 20 kHz with $p = 6$ on the F28379D MCU.

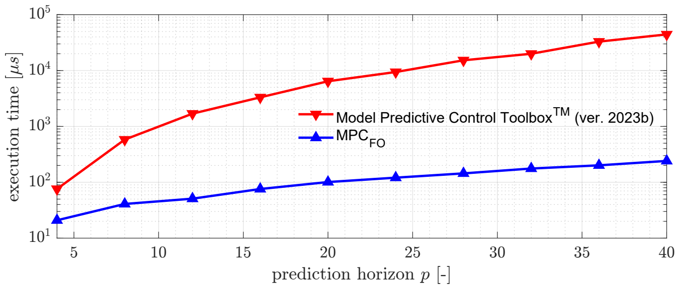

Fig. 3: Execution time comparison on the F28379D.

REFERENCES

[1] B. D. Anderson, "Exponential convergence and persistent excitation," in *1982 21st IEEE Conf. on Decision and Control*. IEEE, 1982, pp. 12–17.

[2] N. R. Sripada and D. G. Fisher, "Improved least squares identification for adaptive controllers," in *1987 American Control Conference*. IEEE, 1987, pp. 2027–2037.

[3] J. H. Wilkinson, *The algebraic eigenvalue problem*. Oxford University Press, Inc., 1988.

Model-Based Optimal Control of Modular Multilevel Converters Using Ideal Capacitor Voltages Reference

Davide Tebaldi and Roberto Zanasi

***Abstract*—This extended abstract addresses the modeling and control of modular multilevel converters.**

I. INTRODUCTION

Different multilevel converter topologies are available in the literature, including cascaded H-bridges multilevel converters [1], flying-capacitors multilevel converters [2], and Modular Multilevel Converters (MMCs) (MMCs) [3]. In this extended abstract, MMCs in half-bridge configuration are modeled and controlled using a new cascade topology. The advantages coming from the new important concept of having time-varying capacitor voltages [4], that are the harmonic content and tracking error reduction in the load current, are then shown and commented in detail.

II. MODELING

The inductive part of the MMC dynamic model is given by:

$$\underbrace{\begin{bmatrix} L+L_a & L_a \\ L_a & L+L_a \end{bmatrix}}_{\mathbf{L}_L} \dot{\mathbf{I}}_L = -\underbrace{\begin{bmatrix} R+R_a & R_a \\ R_a & R+R_a \end{bmatrix}}_{\mathbf{A}_L} \underbrace{\begin{bmatrix} I_1 \\ I_2 \end{bmatrix}}_{\mathbf{I}_L} + \underbrace{\begin{bmatrix} V_1 \\ V_2 \end{bmatrix}}_{\mathbf{V}_C} + \underbrace{\begin{bmatrix} -1 \\ -1 \end{bmatrix}}_{\mathbf{b}_L} V_a. \tag{1}$$

The capacitive part of the MMC dynamic model is given by:

$$\underbrace{\begin{bmatrix} \mathbf{C}_1 & \mathbf{0} \\ \mathbf{0} & \mathbf{C}_2 \end{bmatrix}}_{\mathbf{L}_c} \dot{\mathbf{v}}_c = -\underbrace{\begin{bmatrix} \mathbf{R}_{c_1}^{-1} & \mathbf{0} \\ \mathbf{0} & \mathbf{R}_{c_2}^{-1} \end{bmatrix}}_{\mathbf{R}_c^{-1}} \mathbf{v}_c + \underbrace{\begin{bmatrix} \mathbf{T}_1 & \mathbf{0} \\ \mathbf{0} & -\mathbf{T}_2 \end{bmatrix}}_{\mathbf{T}_{12}} \underbrace{\begin{bmatrix} I_1 \\ I_2 \end{bmatrix}}_{\mathbf{I}_L},$$

$$\underbrace{\begin{bmatrix} V_1 \\ V_2 \end{bmatrix}}_{\mathbf{V}_C} = -\mathbf{T}_{12}^{\mathrm{T}} \underbrace{\begin{bmatrix} \mathbf{v}_{c1} \\ \mathbf{v}_{c2} \end{bmatrix}}_{\mathbf{v}_c} - \underbrace{\begin{bmatrix} n\,R_{d,on} & 0 \\ 0 & n\,R_{d,on} \end{bmatrix}}_{\mathbf{R}_{d,on}} \underbrace{\begin{bmatrix} I_1 \\ I_2 \end{bmatrix}}_{\mathbf{I}_L} + \underbrace{\begin{bmatrix} 1 \\ -1 \end{bmatrix}}_{\mathbf{d}_c} V_{dc},$$

$$\mathbf{C}_1 = \mathrm{diag}(C_1, \cdots, C_n), \quad \mathbf{C}_2 = \mathrm{diag}(C_{n+1}, \cdots, C_{2n}),$$
$$\mathbf{R}_{c_1} = \mathrm{diag}(R_{c_1}, \cdots, R_{c_n}), \mathbf{R}_{c_2} = \mathrm{diag}(R_{c_{n+1}}, \cdots, R_{c_{2n}}),$$

$$\mathbf{v}_{c1} = \begin{bmatrix} V_{c_1} \\ \vdots \\ V_{c_n} \end{bmatrix}, \mathbf{v}_{c2} = \begin{bmatrix} V_{c_{n+1}} \\ \vdots \\ V_{c_{2n}} \end{bmatrix}, \mathbf{T}_1 = \begin{bmatrix} T_1 \\ \vdots \\ T_n \end{bmatrix}, \mathbf{T}_2 = \begin{bmatrix} T_{n+1} \\ \vdots \\ T_{2n} \end{bmatrix}. \tag{2}$$

The meaning of the parameters and variables in systems (1)-(2) can be found in [4]-Fig. 1.

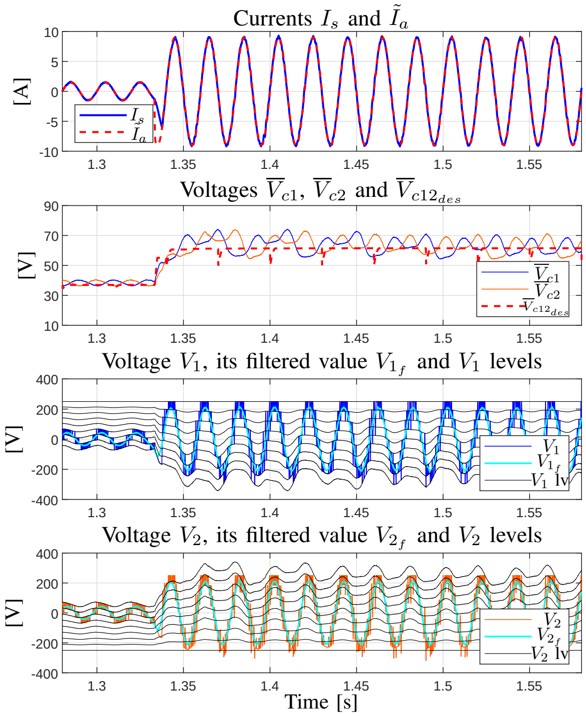

Fig. 1. Results of the first simulation: zoom-in. First subplot: actual and desired load currents I_s and $\tilde{I}_a$. Second subplot: actual and desired average capacitor voltages $\overline{V}_{c1}$, $\overline{V}_{c2}$ and $\overline{V}_{c12_{des}}$. Third subplot: switching voltage V_1, filtered voltage V_{1_f} and available levels for voltage V_1. Fourth subplot: switching voltage V_2, filtered voltage V_{2_f} and available levels for voltage V_2.

III. CONTROL AND SIMULATION

Two simulations have been performed on the complete MMC model (1)-(2) adopting the system and control parameters reported in [4]-Table 1. In the first simulation, the ideal reference $\overline{V}_{c12_{des}}$ computed in [4]-Sec. 3.2.3 is employed, whereas the second simulation is performed using a constant reference $\overline{V}_{c12_{des}}$ instead, and approximately equal to the minimum value which is strictly needed to follow the desired load current $\tilde{I}_a$ during the whole simulation, which is given by the case $I_{aM} = 9$ A representing the most demanding situation. The first simulation results are zoomed-in in Fig. 1. The MCC is controlled using the cascade architecture proposed in [4], which is reported in Fig. 2 of this abstract. The amplitude spectra of the load current in the first and second simulation are shown in Fig. 3. Fig. 1 shows that: 1) the load current I_s always tracks $\tilde{I}_a$, except for very short transients when

---

The authors are with the Department of Engineering ”Enzo Ferrari”, University of Modena and Reggio Emilia, Modena, Italy. `davide.tebaldi@unimore.it`, `roberto.zanasi@unimore.it`

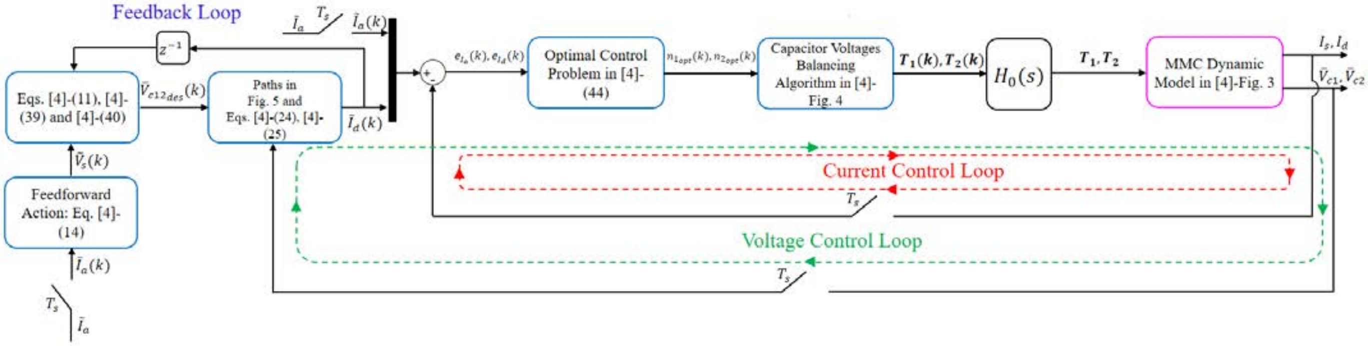

Fig. 2. Proposed cascade control architecture for modular multilevel converters. The light-blue blocks are the discrete-time control blocks, while the magenta block represents the controlled system.

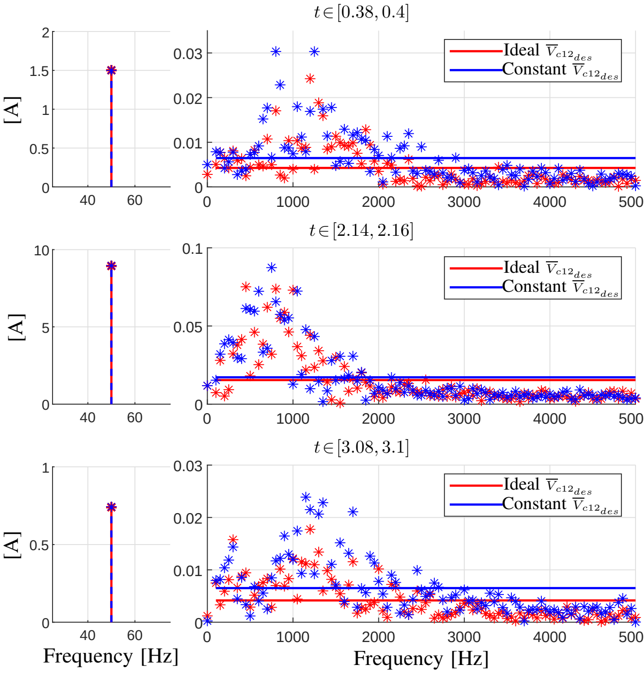

Fig. 3. Results of the first and second simulation. Right subplots: amplitude spectrum of the load current I_s at high higher frequencies. Left subplots: amplitude of the fundamental harmonic of the load current I_s.

the amplitude I_{aM} changes; 2) the average capacitor voltages voltages $\overline{V}_{c1}$ and $\overline{V}_{c2}$ in the converter arms always track the ideal reference $\overline{V}_{c12_{des}}$. Fig. 1 specifically shows that the available voltage levels (black characteristics in the figure) generating voltages V_1 and V_2 are much closer to each other whenever I_{aM} is lower. This brings two important advantages: 1) a lower harmonic content in the resulting load current I_s; 2) a better tracking of current I_s itself, leading to a cleaner sinusoid. This can be clearly seen from Fig. 3, where the left subplots show the amplitude of the load current fundamental harmonic, the asterisks on the right subplots of Fig. 3 show the amplitude of the load current higher-order harmonics (i.e. at frequency greater than 50 Hz in the considered case), while the continuous lines report the average amplitude over the higher-order harmonics. Fig. 3 shows that: 1) the average amplitude of the load current spectrum is approximately the same for both the first and the second simulations when $I_{aM} = 9$ A (second subplot), while 2) the average amplitude of the load current spectrum is significantly reduced in the first simulation using the ideal capacitor voltages reference when $I_{aM} = 1.5$ A and $I_{aM} = 0.75$ A (first and third subplots).

IV. CONCLUSION

In this extended abstract, we addressed the modeling and the model-based cascade control of MMCs. The new concept of ideally varying the average capacitor voltages reference in the converter arms is proposed. Such ideal voltage reference represents the minimum value which is strictly necessary to properly track the desired load current while, at the same time, minimizing the tracking error and the harmonic content in the generated load current itself. The simulation results show that the new proposed control architecture allows to achieve: a) balancing of the capacitor voltages; b) tracking of the ideal voltage reference for the average capacitor voltages in order to minimize the tracking error and the harmonic content in the load current; c) tracking of the desired load and circulating current profiles. At the same time, the tracking error and the harmonic content in the load current are minimized, thus enhancing all the intrinsic main advantages of multilevel converters.

REFERENCES

[1] J.-N. Chiasson, L.-M. Tolbert, K.-J. McKenzie, Z. Du, “Control of a multilevel converter using resultant theory”, *IEEE Trans. Control Syst. Technol.*, vol. 11, no. 3, pp. 345-354, May. 2003, DOI: 10.1109/TCST.2003.810382.

[2] R. Zanasi, D. Tebaldi, “Modeling control and robustness assessment of multilevel flying-capacitor converters”, *Energies*, 2021, 14(7), 1903, DOI: 10.3390/en14071903.

[3] P. Montero-Robina, A. Marquez, M. S. A. Dahidah, S. Vazquez, J. I. Leon, G. Konstantinou, L. G. Franquelo, “Feedforward modulation technique for more accurate operation of modular multilevel converters”, *IEEE Trans. Power Electron.*, vol. 37, no. 2, pp. 1700-1710, Feb. 2022, DOI: 10.1109/TPEL.2021.3104984.

[4] D. Tebaldi, R. Zanasi, “Model-based cascade control of single-phase Modular Multilevel Converters using ideal capacitor voltages reference”, *Control Engineering Practice*, vol. 151, 2024, DOI: 10.1016/j.conengprac.2024.106031

Modeling and control of an impacting electromagnetic actuator via hybrid Lyapunov techniques

Beatrice Zambotti, Yassine Ariba, Frederic Gouaisbaut, Luca Zaccarian

***Abstract*—We model and control an impacting electromagnetic actuator using hybrid Lyapunov techniques. The proposed model accounts for the main magnetic effects and the mechanical stops inherent in the system's design, which impose limitations on its range of motion. Additionally, the objective is to synthesize a control law with reduced complexity, enabling precise regulation of the position of the actuator's moving part. The proposed control strategies include an LQ-based method for ensuring local stability and an energy-based backstepping approach for enhanced performance. An extended version of this abstract can be found in [1], [2].**

I. INTRODUCTION AND MODELING

Electromagnetic actuators are electromechanical devices that leverage the principles of electromagnetism to convert electrical energy into mechanical energy. They are recognized as an efficient technology for high-performance actuation systems and find widespread application across the industry. However, electromagnetic actuators exhibit complex and nonlinear dynamics, which causes the control of these devices to be a non-trivial task. Moreover, magnetic elements are subject to various magnetic phenomena, such as magnetic saturation and flux fringing, that may interfere with the system's operation. Our actuator is designed to operate within a limited range of positions $[p_{\text{min}}, p_{\text{max}}]$, causing impacts with the mechanical constraints of the structure during operation.

Considering the state variable $x = [x_1 \quad x_2 \quad x_3]^T = [p \quad \dot{p} \quad i]^T$, with p the position of the moving part and i the current that flows through the coil, the actuator can be modeled as a hybrid dynamical system

$$\begin{aligned} \dot{x} &= \begin{bmatrix} x_2 \\ \frac{1}{m}(-F_{\text{mag}}(x_1, x_3) - \lambda x_2 - k(x_1 - p_{\text{rest}}) \\ \frac{1}{L(x_1)}(u - Rx_3 - x_2 x_3 \frac{dL(x_1)}{dx_1}) \end{bmatrix}, \quad x \in C \\ x^+ &= \begin{bmatrix} x_1 \\ -\kappa x_2 \\ x_3 \end{bmatrix}, \quad x \in D \end{aligned} \tag{1}$$

where λ is the damping coefficient, k is the stiffness coefficient, p_{rest} is the airgap value at the rest position of the spring, u is the control input voltage, R is the coil's electrical resistance, and $p \mapsto L(p)$ is the inductance. The flow and jump set are defined as $C := \{x : p_{\text{min}} \leq x_1 \leq p_{\text{max}}\}$ and $D := \{x : x_1 = p_{\text{min}}, x_2 \leq 0\} \cup \{x : x_1 = p_{\text{max}}, x_2 \geq 0\}$.

II. MAGNETIC FORCE AND INDUCTANCE IDENTIFICATION FOR CONTROL DESIGN AND VALIDATION

To complete the electromagnetic actuator's model, two methods to model the magnetic force and inductance are presented and are represented in Fig. 1.

A. Magnetic force and inductance model for validation

The magnetic force is parameterized as a polynomial function of current i and airgap p as

$$F_{\text{mag}}(p, i) = \begin{bmatrix} 1 \\ p \end{bmatrix}^{\{n_p\}T} M \begin{bmatrix} 1 \\ i \end{bmatrix}^{\{n_i\}} \tag{2}$$

where $\begin{bmatrix} 1 \\ x \end{bmatrix}^{\{d\}} = [1 \; x \; x^2 \; ... \; x^d]^T$. The matrix $M \in \mathbb{R}^{(n_p+1)\times(n_i+1)}$ can be identified based on the measurements $\{F_{\text{meas},k}\}_1^{n_{\text{meas}}}$ by solving the following constrained optimization problem, with constraints tailored to mimic the physical behavior of the magnetic force

$$\begin{aligned} &\text{minimize} \quad J = \sum_{k=1}^{n_{\text{meas}}} \frac{1}{F^2_{\text{meas},k}} (F_{\text{meas},k} - F_{\text{mag}}(p_k, i_k))^2 \\ &\text{subject to} \quad \begin{cases} F_{\text{mag}}(p, 0) = 0, & \forall e \in [0, p_{\text{max}}] \\ \frac{\partial F_{\text{mag}}(p,i)}{\partial i} > 0, & \forall e \in (0, p_{\text{max}}], i \in (0, i_{\text{max}}] \\ \frac{\partial F_{\text{mag}}(p,i)}{\partial p} < 0, & \forall e \in (0, p_{\text{max}}], i \in (0, i_{\text{max}}] \end{cases} \end{aligned} \tag{3}$$

The inductance $p \mapsto L(p)$, is modeled as in [3] as a series of reluctances and can be expressed as

$$L(p) = \frac{N^2}{\rho_x p + \rho_0} \tag{4}$$

where N is the number of coil windings, ρ_x is the overall airgap reluctance, and ρ_0 is the overall magnetic circuit reluctance.

B. Magnetic force and inductance model for control design

As visible in Fig. 1, the magnetic force assumes a linear behavior with respect to the current after reaching an airgap-dependent saturation limit. Consequently, we may identify a linear component $F_{\text{lin}} = si$, where the identified slope s assumes a common value for every different airgap. To focus on the saturation-like characteristics of the force, such a linear component $F_{\text{lin}}(i)$ can be subtracted from the overall measured force, resulting in $F_{\text{sat}}(p, i) = F_{\text{meas}}(p, i) - F_{\text{lin}}(i)$. Then we may fit the theoretical model of the magnetic force

$$F_{\text{mag,th}}(p, i) = -\frac{1}{2} i^2 \psi(p). \tag{5}$$

$\psi(p)$ represents the derivative of the inductance as a function of the airgap and needs to be identified. Exploiting the derivative of expression (4), a fitting for the function $\psi(p)$ in (5) was performed by optimizing the selection of q_1, q_2

Beatrice Zambotti is with the LAGEPP-CNRS, Université Claude Bernard Lyon 1, 43 boulevard du 11 novembre 1918, 69100, Villeurbanne, France (e-mail: beatrice.zambotti@etu.univ-lyon1.fr).

Yassine Ariba is with the LAAS-CNRS, University of Toulouse, INSA, 31400 Toulouse, France (email: yariba@laas.fr).

Frederic Gouaisbaut is with the LAAS-CNRS, University of Toulouse, UPS, 31400 Toulouse, France (email: fgouaisb@laas.fr).

Luca Zaccarian is with the LAAS-CNRS, University of Toulouse, 31400 Toulouse, France, and also with the Department of Industrial Engineering, University of Trento, 38122 Trento, Italy (e-mail: zaccarian@laas.fr).

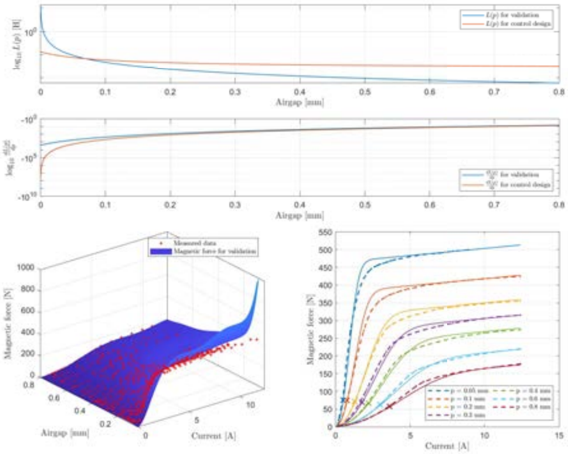

Fig. 1: Top: models for the inductance. Middle: models for the derivative of the inductance. Bottom left: comparison between measured data and magnetic force model for validation. Bottom right: comparison between measured data (dashed line) and magnetic force model for control design (solid line).

and q_3 in the expression $\psi(p) = -\frac{q_1}{(q_2 p + q_3)^2}$. By integrating $\psi(p)$ it is possible to derive the expression for the inductance

$$L(p) = \frac{q_1}{q_2(q_2 p + q_3)} + c. \tag{6}$$

By combining the discussed components, we obtain the complete magnetic force model

$$F_{\text{mag}}(p,i) = f_{\text{max}}(p) \tanh\left(-\frac{1}{2} i^2 \frac{\psi(p)}{f_{\text{max}}(p)}\right) + si, \tag{7}$$

where $f_{\text{max}}(p)$ characterizes the transition between the saturated and the unsaturated regions and is the following function of the airgap $f_{\text{max}}(p) = z_1 e^{z_2 p} + z_3 e^{z_4 p}$, for suitable parameters z_1, z_2, z_3, z_4.

III. CONTROL DESIGN

For each equilibrium $x^\star = [x_1^\star, x_3^\star, x_3^\star]$, we define here the error coordinates $e_1 = x_1 - x_1^\star$, $e_2 = x_2 - x_2^\star$, $e_3 = x_3 - x_3^\star$, $v = u - u^\star$ and and derive in this section control laws that ensure asymptotic stability of the origin of the hybrid system

$$\begin{aligned}
\dot{e} &= \begin{bmatrix} e_2 \\ \frac{1}{m}\left(\frac{1}{2}(e_3 + x_3^\star)^2 \psi(x_1) - s(e_3 + x_3^\star) \right. \\ \left. -\lambda e_2 - k(e_1 + x_1^\star - p_{\text{rest}})\right) \\ \frac{1}{L(x_1)}(v - Re_3 - e_2(e_3 + x_3^\star)\psi(x_1)) \end{bmatrix}, & e + x^\star \in C \\
e^+ &= \begin{bmatrix} e_1 \\ -\kappa e_2 \\ e_3 \end{bmatrix} = A_J e := \begin{bmatrix} 1 & 0 & 0 \\ 0 & -\kappa & 0 \\ 0 & 0 & 1 \end{bmatrix} e, & e + x^\star \in D
\end{aligned} \tag{8}$$

A. LQ linearization-based control design

A first solution to locally asymptotically stabilize the origin of the hybrid error dynamics (8) is given here by following the intuitive approach of ensuring a quadratic Lyapunov decrease along a linearization of the flow dynamics in (8) and across the jump dynamics in (8), which is already linear. The corresponding hybrid dynamics is

$$\dot{e} = Ae + Bv, \qquad e + x^\star \in C \tag{9a}$$

$$e^+ = A_J e, \qquad e + x^\star \in D \tag{9b}$$

where $A = \begin{bmatrix} 0 & 1 & 0 \\ \frac{1}{2m} x_3^{\star 2} \frac{\partial \psi(x_1^\star)}{\partial e_1} - \frac{k}{m} & -\frac{\lambda}{m} & \frac{1}{m} x_3^\star \psi(x_1^\star) - \frac{s}{m} \\ 0 & -\frac{x_3^\star \psi(x_1^\star)}{L(x_1^\star)} & -\frac{R}{L(x_1^\star)} \end{bmatrix}$ and $B = \begin{bmatrix} 0 \\ 0 \\ \frac{1}{L(x_1^\star)} \end{bmatrix}$. For the linearized dynamics (9), we design an LQ-based linear state feedback stabilizer as $v = Ke$, where the gain K is optimally selected by solving the following convex optimization, where $Q > 0$ and $R > 0$ are tuning parameters to be selected by the user,

$$\max_{\beta, W, X} \; \beta, \quad \text{subject to} \tag{10}$$

$$W := \begin{bmatrix} w_{11} & 0 & w_{13} \\ 0 & w_{22} & 0 \\ w_{13} & 0 & w_{33} \end{bmatrix} \geq \beta I > 0$$

$$\begin{bmatrix} \text{He}(AW + BX) & W^T & X^T \\ W & -Q^{-1} & 0 \\ X & 0 & -R^{-1} \end{bmatrix} < 0$$

and then choosing $K = XW^{-1}$. Due to the block diagonal structure of W in (10), the closed-loop dynamics ensures local decrease along flows of the Lyapunov function $V_\ell(e) = e^T W^{-1} e$, non-increase across jumps (impacts), and the following upper bound β^{-1} on the LQ performance index:

$$J = \int_0^\infty e(t)^T Q e(t) + v(t)^T R v(t) \mathrm{d}t \leq \beta^{-1} |e(0)|^2. \tag{11}$$

Theorem 1 *For any $Q = Q^T > 0 \in \mathbb{R}^{nxn}$ and $R = R^T > 0 \in \mathbb{R}^{mxm}$, assume that there exist matrices $W = W^T > 0 \in \mathbb{R}^{nxn}$, $X \in \mathbb{R}^{mxn}$, and a scalar β satisfying* (10). *Then, with the selection $K = XW^{-1} \in \mathbb{R}^{mxn}$, the control law $v = Ke$ is such that the Lyapunov function $V_\ell(e) := e^T P e$, with $P = W^{-1}$, satisfies the decrease conditions*

$$\dot{V}_\ell(e) < 0 \qquad \forall e \in \mathbb{R}^3 \setminus \{0\}, \tag{12}$$

$$V_\ell(e^+) - V_\ell(e) \leq 0 \qquad \forall e \in \mathbb{R}^3, \tag{13}$$

along the linearized dynamics (9). *Moreover, bound* (11) *holds locally around the origin $e = 0$. In particular, the origin of* (9) *is locally asymptotically stable.*

B. Energy-based backstepping design

To enlarge the closed-loop's basin of attraction, we also propose a nonlinear control strategy based on a backstepping approach. This method stabilizes the origin for (8) by first stabilizing the mechanical subsystem with a fictitious control law $e_{3,d} = \frac{s - \sqrt{s^2 + 2k(x_1^\star - p_{\text{rest}})\psi(x_1)}}{\psi(x_1)} - x_3^\star$. Subsequently, the overall system is stabilized using the control input voltage v, which is selected by way of the energy-based Lyapunov function $V(e) = \frac{1}{2} k e_1^2 + \frac{1}{2} m e_2^2 + \frac{1}{2} L(x_1)(e_3 - e_{3,d})^2$.

Theorem 2 *Given any $\alpha > 0$, the control law $v = Re_3 + se_2 + L(x_1)\dot{e}_{3,d} - \alpha(e_3 - e_{3,d})$, ensures local asymptotic stability of the origin of the hybrid system* (8).

Simulation results are not included but can be found in [1].

REFERENCES

[1] B. Zambotti, "Hybrid modeling, identification and simulation of electromagnetic actuators," Master's thesis, Università di Trento, 2024.

[2] B. Zambotti, Y. Ariba, F. Gouaisbaut, and L. Zaccarian, "Modeling and control of an impacting electromagnetic actuator via hybrid lyapunov techniques." [Online]. Available: https://homepages.laas.fr/lzaccari/ZambottiTCST.pdf

[3] F. Deschaux, F. Gouaisbaut, and Y. Ariba, "Nonlinear control for an uncertain electromagnetic actuator," in *2018 IEEE Conference on Decision and Control (CDC)*, 2018, pp. 2316–2321.

PWM-Based Energy-Efficient Adaptive Control for Multi-Chamber Hydraulic Servo Actuators

Augusto Bozza[1], Graziana Cavone[2], Raffaele Carli[1], and Mariagrazia Dotoli[1] .

***Abstract*—Pulse Width Modulation (PWM)-based multi-chamber Hydraulic Servo Actuators (HSAs) are highly efficient actuators for which it is possible a precise control of flow-rates and pressures. However, their modeling and control is not trivial due to the complexity introduced by the exponential increase in force combinations and their hybrid behaviour. This research work [1], on the one hand, extends the Average Equivalent Discrete-time Model (AEDM) of [2] to the mechanical dynamics, relating the valves duty-cycle with chamber pressures and piston force. On the other hand, it presents an adaptive control, combining a Decoupled Proportional-Integral (DPI) controller with a Model Reference Adaptive Control (MRAC) for an effective force tracking and pressure control, offering a better-performing alternative to existing methods.**

I. INTRODUCTION

PWM-based HSAs are widely popular in industrial applications (e.g., hydraulic machines [3]) for their high force and torque with a compact size-to-power ratio, having a reduced number of switching valves. Multi-chamber HSAs enhance the force resolution by using cylinders with more than two chambers, offering n^N force modes based on the number of chambers N and pressure lines n [4]. However, their complex structure, sensitivity, high costs, and hybrid nature pose challenges for advanced modelling and control approaches [5]. In contrast to analogical systems, few examples of adaptive and robust control techniques are given for digital HSAs in the related literature. Conversely, in this research work [1], we first extend the AEDM proposed in [2] also to mechanics. Second, we propose a two-level adaptive control architecture, involving an outer DPI controller for the force tracking, and an inner nonlinear discrete-time MRAC for the pressure control of each chamber.

II. RESEARCH CONTRIBUTIONS

The extended AEDM [2] proposed here to represent the PWM-based multi-chamber HSA is formulated as follows:

$$\begin{cases} \overline{v}_{k+1} = \overline{v}_k + \dfrac{1}{\mathrm{M}}\Big(-\mathrm{b_m}\overline{v}_k - \displaystyle\sum_{i\,=\,1}^{\mathrm{N}}(-1)^i \mathrm{A}_{c_i}\overline{p}_{i,k}\Big)\mathrm{T} & \text{(1a)} \\ \overline{y}_{k+1} = \overline{y}_k - \Big(\mathrm{b_m}\overline{v}_k - \displaystyle\sum_{i=1}^{\mathrm{N}}(-1)^i \mathrm{A}_{c_i}\overline{p}_{i,k}\Big)\mathrm{T} & \text{(1b)} \\ \overline{p}_{i,k+1} = a_{i,k}\ f_{i,d}(\overline{p}_{i,k}) + b_{i,k}\ g_{i,d}(\overline{p}_{i,k})d^{+}_{i,k} + \omega_{i,k} & \text{(1c)} \end{cases}$$

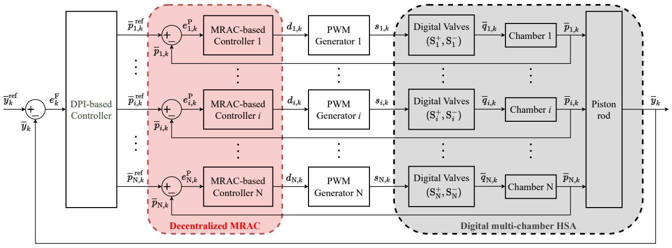

Fig. 1. Block diagram of the proposed adaptive control architecture. In gray the digital multi-chamber HSA, while in red the decentralized MRAC-based low-level controller.

with:

$$f_{i,d}(\overline{p}_{i,k}) = -\sqrt{|\overline{p}_{i,k} - \mathrm{P_t}|} \tag{2a}$$

$$g_{i,d}(\overline{p}_{i,k}) = \sqrt{|\mathrm{P_s} - \overline{p}_{i,k}|} + \sqrt{|\overline{p}_{i,k} - \mathrm{P_t}|} \tag{2b}$$

$$a_{i,k} = b_{i,k} = \frac{\mathrm{E}\Phi_i}{\overline{V}_{i,k}} \tag{2c}$$

$$\Phi_i = \mathrm{A}_{s_i}\mathrm{C}_{\mathrm{d},i}\sqrt{\frac{2}{\rho}} \tag{2d}$$

$$\omega_{i,k} = (-1)^i \mathrm{A}_{c_i}\overline{v}_k \tag{2e}$$

where eqs. (1c) and (2a)-(2e) are valid $\forall i = 1, \dots, \mathrm{N}$. Eqs. (1a)-(1b) describe the mechanical behavior of the piston rod, while (1c) represents the hydraulic dynamics, where the duty-cycle $d^{+}_{i,k}$ acts as input, $f_{i,d}(\cdot)$ and $g_{i,d}(\cdot)$ respectively stand for the nonlinear state and input functions, $\overline{v}$ and $\overline{y}$ respectively for the rod velocity and force, and $\overline{p}_i$ for the i-th chamber pressure. Parameters such as mass piston (M), total rod length (L), chamber area (A_{c_i}), valve cross-sectional area (A_{s_i}), valve discharge coefficient ($\mathrm{C}_{\mathrm{d},i}$), viscous coefficient ($\mathrm{b_m}$), oil density ($\rho$), fluid compressibility (E), sampling time T, supply pressure $\mathrm{P_s}$, and venting pressure $\mathrm{P_t}$ are constant. Chamber volume $V_{i,k}$, the unknown parameters $a_{i,k}$ and $b_{i,k}$, and disturbance $\omega_{i,k}$ change over time.

The control framework (Fig. 1) uses a DPI-based controller to decouple the force error into N components, determining the reference pressure signals for each chamber. Then, the N MRAC-based controllers provide the valves' duty-cycle to correctly track these pressures in each chamber.

The MRAC designed for the i-th plant eqs. (1c)-(2), considers the parameters $a_{i,k}$ and $b_{i,k}$ as unknown, and uses the following reference model for tracking the pressure:

$$\overline{p}_{i,k+1}^{\,\mathrm{m}} = -a_i^{\mathrm{m}}\overline{p}_{i,k}^{\,\mathrm{m}} + b_i^{\mathrm{m}} p_{i,k}^{\,\mathrm{ref}}, \quad \forall i = 1, \dots, \mathrm{N}$$

where $\overline{p}_{i,k}^{\,\mathrm{m}}$, a_i^{m}, and b_i^{m} are respectively the model reference pressure, and the model state and input parameters, while $p_{i,k}^{\,\mathrm{ref}}$

[1] A. Bozza, R. Carli, and M. Dotoli are with the Department of Electrical and Information Engineering of the Polytechnic of Bari, Italy (e-mail: {augusto.bozza, raffaele.carli, mariagrazia.dotoli}@poliba.it).

[2] G. Cavone is with the Department of Civil, Computer Science, and Aeronautical Technologies Engineering of the University Roma Tre, Rome, Italy (e-mail: graziana.cavone@uniroma3.it).

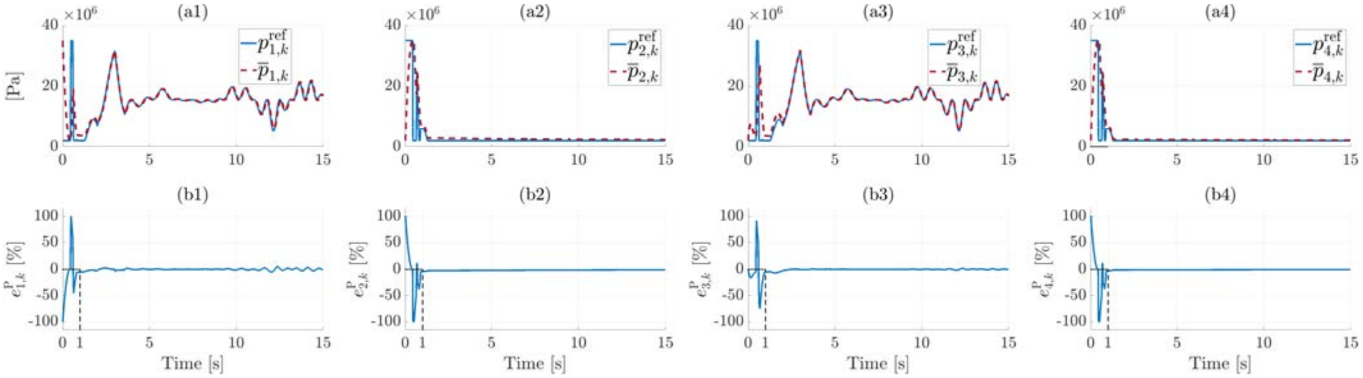

Fig. 2. Closed-loop simulation - Pressure tracking for chamber 1 (a1), chamber 2 (a2), chamber 3 (a3), and chamber 4 (a4) and corresponding relative percentage error respectively obtained for chamber 1 (b1), chamber 2 (b2), chamber 3 (b3), and chamber 4 (b4) over 15 s of simulation time window.

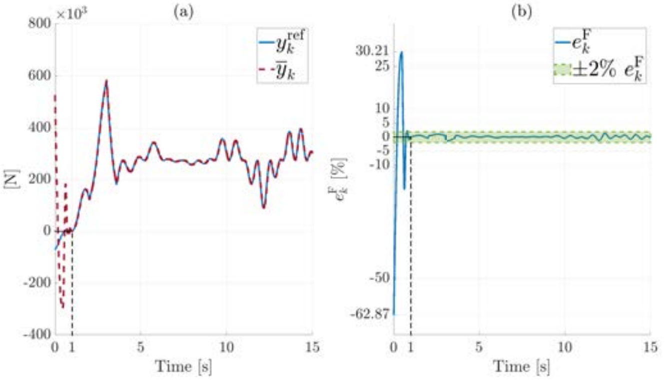

Fig. 3. Closed-loop simulation - Force tracking (a) and corresponding relative percentage error (b) over 15 s of simulation time window.

is the desired pressure for the relative chamber. The proposed control law is:

$$u_{i,k} = \tfrac{1}{g_{i,d}(\overline{p}_{i,k})} \boldsymbol{\phi}_{i,k}^{\top} \hat{\boldsymbol{\theta}}_{i,k}, \quad \forall i = 1, \ldots, \mathrm{N} \tag{3}$$

where $\boldsymbol{\phi}_{i,k}$ is the regressors vector and $\hat{\boldsymbol{\theta}}_{i,k}$ is the estimated parameters vector of the unknown controller gains vector $\boldsymbol{\theta}_{i,k}^{*}$:

$$\left.\begin{aligned} \boldsymbol{\phi}_{i,k} &= \Big(f_{i,d}(\overline{p}_{i,k}),\ \overline{p}_{i,k},\ p_{i,k}^{\mathrm{ref}},\ \omega_{i,k}\Big)^{\top} \\ \hat{\boldsymbol{\theta}}_{i,k} &= \Big(\hat{\theta}_{i_1,k},\ \hat{\theta}_{i_2,k},\ \hat{\theta}_{i_3,k},\ \hat{\theta}_{i_4,k}\Big)^{\top} \end{aligned}\right., \quad \forall i = 1, \ldots, \mathrm{N}.$$

Thus, the following Lyapunov-based discrete-time adaptive law is proposed to estimate $\hat{\boldsymbol{\theta}}_{i,k}$:

$$\hat{\boldsymbol{\theta}}_{i,k+1} = \hat{\boldsymbol{\theta}}_{i,k} - \boldsymbol{\gamma}_i \boldsymbol{\phi}_{i,k}^{\top} e_{i,k}^{\mathrm{P}} \mathrm{T}, \quad \forall i = 1, \ldots, \mathrm{N}, \tag{4}$$

where $e_{i,k}^{\mathrm{P}} = \overline{p}_{i,k} - \overline{p}_{i,k}^{*}$ is the pressure tracking error at time t_k and $\boldsymbol{\gamma}_i$ is the adaptive gains vector, defined as follows:

$$\boldsymbol{\gamma}_i = \Big(\gamma_{i_1}, \gamma_{i_2}, \gamma_{i_3}, \gamma_{i_4}\Big)^{\top}, \quad \text{with } \gamma_{i_l} > 0$$

$\forall i = 1, \ldots, \mathrm{N}, \forall l = 1, \ldots, 4$, with $l \in \mathbb{N}$.

Finally, the i-th control law (3), updated via (4), is normalized as follows to achieve the related duty-cycle $d_{i,k}^{+}$:

$$d_{i,k}^{+} = \frac{u_{i,k} - q_{i,\min}}{q_{i,\max} - q_{i,\min}}, \quad \forall i = 1, \ldots, \mathrm{N}, \tag{5}$$

where $q_{i,\min}$ and $q_{i,\max}$ are respectively the minimum and the maximum allowable flow-rates for the i-th chamber.

III. CASE STUDY

The proposed approach is applied to a four-chamber digital HSA with eight ON-OFF valves used as the core part of a real excavator presented in [6], the most recent and innovative paper in this field, where Model Predictive Control is applied for the system control. The results for the pressure and force tracking are respectively shown in Fig.s 2 and 3. Compared to the results in [6], our approach improves the energy efficiency by 7.6%, albeit the force peak error goes beyond by 0.45%. Notably, our control approach significantly streamlines the cascaded control-loop proposed by the benchmark, reducing the computational time required for evaluating the control law.

IV. CONCLUSIONS AND FUTURE WORKS

In this work, we extend the AEDM for PWM-based multi-chamber HSAs of [2] also to their mechanics. Then, we introduce a novel adaptive control architecture for tracking the force and pressure, using a decentralized MRAC scheme that addresses the HSA nonlinearities and uncertainties. Albeit the force peak error is comparable to [6], we significantly improve the energy efficiency and we streamline the control architecture. Future works will regard multi-pressure HSAs and robust MRAC schemes.

REFERENCES

[1] A. Bozza, G. Cavone, R. Carli, and M. Dotoli, “Pwm-based energy-efficient adaptive control for multi-chamber hydraulic servo actuators,” *IEEE Transactions on Control Systems Technology*, (Under submission).

[2] ——, “A power electronic converters-inspired approach for modeling pwm switched-based nonlinear hydraulic servo actuators,” in *2023 IEEE International Conference on Systems, Man, and Cybernetics (SMC)*. IEEE, 2023, pp. 2477–2482.

[3] G. Cavone, A. Bozza, R. Carli, and M. Dotoli, “Mpc-based process control of deep drawing: An industry 4.0 case study in automotive,” *IEEE Transactions on Automation Science and Engineering*, vol. 19, no. 3, pp. 1586–1598, 2022.

[4] O. Niemi-Pynttäri, M. Linjama, A. Laamanen, and K. Huhtala, “Parallel pump-controlled multi-chamber cylinder,” in *Fluid Power Systems Technology*, vol. 45974. American Society of Mechanical Engineers, 2014, p. V001T01A014.

[5] V. H. Donkov, T. Andersen, M. Linjama, and M. Ebbesen, “Digital hydraulic technology for linear actuation: A state of the art review,” *International Journal of Fluid Power*, pp. 263–304, 2020.

[6] K. Heybroek and J. Sjöberg, “Model predictive control of a hydraulic multichamber actuator: A feasibility study,” *IEEE/ASME Transactions on Mechatronics*, vol. 23, no. 3, pp. 1393–1403, 2018.

Session 7A: Energy management in vehicles

Exploiting the potential of hybrid batteries in racing: optimal sizing and energy management

Stefano Radrizzani, Giorgio Riva, Giulio Panzani, Matteo Corno, Sergio M. Savaresi

***Abstract*—The electrification trend is spreading not only in the field of traditional vehicles, but also in the racing one, pushing towards the design of dedicated energy storage systems to cope with high demanding requirements, as witnessed by the next generation of Formula E that will increase power up to 600 kW. In this scenario, Hybrid Battery Packs (HBPs) raise up to an interesting solution thanks to their combined high-power and high-energy features. In this report, firstly, we showcase the potential benefits of hybrid battery packs, compared to single chemistry ones, when employed in a racing scenario. To this aim, we formulate a co-design optimization problem (Co-OP) to find the optimal hybrid battery pack configuration minimizing the race time. As a byproduct of the solution, the optimal power split between the two energy sources is obtained as an implicit control law. From this result, we address the problem of designing a real-time, explicit, energy management strategy (EMS) for the application. In this respect, we devise a modified co-design optimization problem, where explicit power split logic can be directly included, allowing to compare and rank them with respect to the optimal implicit one, considering as a case study the Formula E Gen 3 car in the 2021 Rome Formula E ePrix.**

I. INTRODUCTION

VEHICLE electrification is one of the most important trends not only in the mass-market automotive, as witnessed by the growth of the full-electric Formula E racing competition. For electric racing vehicles, the performance is intimately related to the architecture and size of the powertrain, especially regarding the battery pack. Toward this aim, in our first work [1], a co-design approach has been applied to the full-electric racing scenario with a traditional battery pack. With respect to sizing problems for traditional vehicles, the driving-cycle is not known a priori, and, therefore, the minimum race time (MRT) framework represents the building block to formulate a co-design optimization problem (Co-OP). The Co-OP proposed in [1] chooses, through an external layer, the optimal cell technology and the battery pack size; while an internal layer optimizes both battery usage and mechanical braking, while being compliant with the battery power limits. The mathematical structure and properties of the Co-OP, as a function of the battery model, are deeply discussed in [2].

Given the ambitious goal of Formula E to deliver power requests up to 600 kW, we delved into the analysis of a promising architecture, i.e., hybrid battery packs (H-BPs). Indeed, they are made up of two different cell chemistries sharing complementary characteristics, which cannot be simultaneously matched by a single cell technology, allowing to potentially satisfy both the high power and mileage requirements of incoming racing competitions. In order to analyze the potential of H-BPs in this scenario, we extended in [3] the two-layered Co-OP formulated in [1] to a three-layered solution where also the couple of Li-ion cells is optimized, showing that H-BPs can be a promising concept for the racing scenario. Leveraging this result, in [4] we shifted the focus to the design of suitable energy management strategies (EMS) for the H-BP, which can be implemented in real-time applications [4] to split the power between the two sources. To this purpose, we build upon the optimization framework in [3] to account for explicit power split strategies, showing that the well-known Equivalent Consumption Minimization Strategy (ECMS) represents the best solution also in this scenario.

In the following, the optimal sizing and energy management is recalled in Section II, before showing the results in Section III, considering as a case study the Formula E Gen 3 car in the 2021 Rome Formula E ePrix.

II. OPTIMAL SIZING AND ENERGY MANAGEMENT

The optimal sizing Co-OP employs a space-reformulation of vehicle and battery dynamics to optimize the overall race time along a circuit. Reminding that a rigorous and complete formulation is available in [3], we report here a lighter version to enhance readability for the upcoming discussion:

$$\begin{aligned} \min \quad & \text{race time} \\ \text{s.t.} \quad & \text{vehicle dynamics \& friction limits} \\ & \text{batteries dynamics \& limits} \\ & \text{battery pack-vehicle coupling.} \end{aligned} \tag{1}$$

In more detail, batteries and vehicle dynamics are modeled respectively through a static Equivalent Circuit Model (ECM) and a point-mass model moving on a fixed raceline, where the friction limit allows for linking and constraining longitudinal and lateral dynamics. Given the objective of the work, the coupling between the battery pack and vehicle is simplified via a constant average efficiency including electric motors and power-electronics devices. Finally, the batteries limits prevent State-of-Charge (SoC), current, and voltage from overcoming safety boundaries, and constrain the total power at the terminals to comply with possible limitations enforced by racing regulations. Moreover, the battery cell technology must belong to the dataset in [3], which associates for any energy density the most power dense technology.

In such a formulation, as in [3], no explicit EMS has been imposed, yet, meaning that an implicit control law for the optimal power split between the two sources in the battery pack is derived as a byproduct of the Co-OP.

The authors are with Dipartimento di Elettronica, Informazionee Bioingegneria, Politecnico di Milano, Via G. Ponzio 34/5, 20133, Milan, Italy.

The EMS is introduced in [4] as an additional constraint in the optimization problem (1), imposing one of the two battery powers, e.g., $P_{\mathrm{b},1}$, to satisfy the explicit EMS policy f_{EMS}:

$$P_{\mathrm{b},1} = f_{\mathrm{EMS}}\left(P_{\mathrm{b}}, \dots\right), \tag{2}$$

where P_{b} is the delivered battery power, and $P_{\mathrm{b},2}$ is constrained to satisfy $P_{\mathrm{b},2} = P_{\mathrm{b}} - P_{\mathrm{b},1}$.

Specifically, two different energy management strategies have been tested: the first one is an heuristics based on a complementary filter (CF) strategy, and the other one is optimization-based, employing the equivalent consumption minimization strategy (ECMS).

CF. In [4] we consider a first-order low-pass filter parameterized by a fixed filter frequency f_{lp}. Given the dynamic nature of the low-pass filter, an additional state variable is added to the optimization dynamical model. We define $P_{\mathrm{b,lp}}$ as the low-pass filtered version of the total battery power P_{b}, whose dynamic equation in space-domain, i.e., along the path-abscissa s, is obtained:

$$\frac{\mathrm{d}P_{\mathrm{b,lp}}}{\mathrm{d}s} = \frac{1}{v}\left(-2\pi f_{\mathrm{lp}} P_{\mathrm{b,lp}} + 2\pi f_{\mathrm{lp}} P_{\mathrm{b}}\right) \text{ and } P_{\mathrm{b},1} = P_{\mathrm{b,lp}}, \tag{3}$$

where v is the vehicle speed, and recalling that the battery operating limits are already included in (1), and f_{lp} is another optimization variable.

ECMS. In the ECMS framework, the power split is the result of an optimization problem, aiming at minimizing the weighted (through the equivalence factor λ) sum of the current power consumption $P_{\mathrm{bc},i}$ of each battery $i = 1, 2$:

$$P_{\mathrm{b},1} = \arg\min P_{\mathrm{bc},1} + \lambda P_{\mathrm{bc},2}, \tag{4}$$

while satisfying the driver's power request P_{b} and subject to the battery operating limits. The outcome of this problem is not an explicit function, hence, to be included as a constraint in the optimization problem (1), the solution is approximated in [4] by a Feed-Forward Neural Network (FFNN):

$$P_{\mathrm{b},1} = f_{\mathrm{ffnn}}\left(P_{\mathrm{b}}, \mathrm{SoC}_1, \mathrm{SoC}_2, \lambda\right). \tag{5}$$

III. CASE STUDY: GEN3 FORMULA E

The case study in this section considers the Gen3 Formula E and the 23 laps Rome 2021 ePrix, which is common to both reported works [3] and [4]. First of all, the best chemistry selection has been found in [3] without imposing any specific EMS. Results, in Fig. 1, show that to fully exploit the potential of H-BPs, the most energy dense technology (Kokam SLPB065) is coupled with the most power dense one (Saft VL5U). Instead, in single chemistry battery packs, the power-energy trade-off is handled placing somewhere in between (Sony Murata VTC5A). Focusing on the race time, reported in TABLE I, a significant advantage of 2.22 seconds per lap is visible. One of the main reasons of this results is the lightness of the H-BP, which weights 151 kg less than the optimal single chemistry one. Fixing the cell technologies, the optimal tuning of the EMS has been carried out in [4]. As shown in Fig. 2, **ECMS** reaches results close to the optimal implicit solution, in terms of battery weight and race time, gaining 2.17 seconds per lap. The optimal tuning of the ECMS is $\lambda = 0.98$, meaning that the two battery power consumption are equally weighted in (4). **CF**, instead, stands as a viable simple heuristic approach, paying with a heavier battery pack and slower solutions, but still gaining 1.74 seconds per lap. The optimal tuning of the CF is $f_{\mathrm{lp}} = 10^{-5}$ Hz, meaning that the high-energy battery drains a power current during the race and the high-power one handles the power peaks requests.

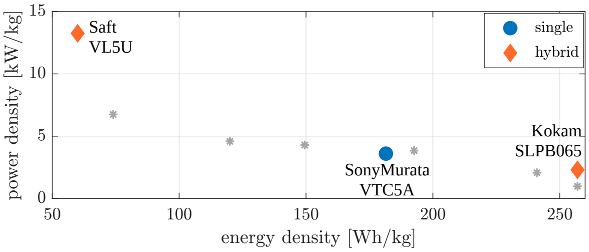

Fig. 1: Optimal cell technology selection for single and hybrid battery packs.

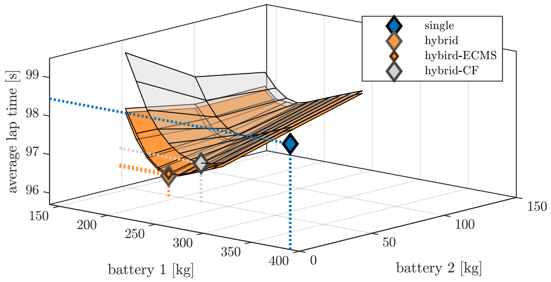

Fig. 2: Comparison of single and hybrid solutions with different EMSs.

TABLE I: Results

cell technology	EMS	weight	average lap time	gain per lap
single	-	390.6 kg	98.46 s	-
hybrid	-	239.6 kg	96.24 s	2.22 s
hybrid	ECMS ($\lambda = 0.98$)	239.6 kg	96.29 s	2.17 s
hybrid	CF ($f_{\mathrm{lp}} = 10^{-5}$)	273.4 kg	96.72 s	1.74 s

IV. FUTURE WORKS

In these report, the potential advantages of hybrid battery packs in electric racing car have been shown. To further going on with a real employment of such a solution, further analyses on the electrical connections and consequences on the sizing and EMS will be investigated.

REFERENCES

[1] G. Riva, S. Radrizzani, G. Panzani, M. Corno, and S. M. Savaresi, “An optimal battery sizing co-design approach for electric racing cars,” *IEEE Control Systems Letters*, vol. 6, pp. 3074–3079, 2022.

[2] G. Riva, S. Radrizzani, and G. Panzani, “Battery model impact on time-optimal co-design for electric racing cars: review and application,” *IEEE Transactions on Transportation Electrification*, 2024, (early access).

[3] S. Radrizzani, G. Riva, G. Panzani, M. Corno, and S. M. Savaresi, “Optimal sizing and analysis of hybrid battery packs for electric racing cars,” *IEEE Transactions on Transportation Electrification*, vol. 9, no. 4, pp. 5182–5193, 2023.

[4] ——, “Time-optimal real-time energy management strategies for hybrid battery packs in electric racing cars,” in *2024 European Control Conference (ECC)*, 2024, (in press).

EXTENDED ABSTRACT
Energy Management System Based on Model Predictive Control for Battery-Powered Trains Under Catenary-Free Conditions

Alessio La Bella, Gian Paolo Incremona, Aline Cristiane Buzzi and Patrizio Colaneri

***Abstract*—This work contributes to the railway field by proposing a novel energy management approach based on model predictive control (MPC) to provide a more efficient govern of the electric equipment inside trains. Specifically, the proposed MPC is capable of addressing the challenging scenario of partially catenary-free tracks for trains equipped with batteries. In particular, the MPC optimizes the current flows to supply the traction motors and the parallel-connected auxiliary loads, while reducing the amount of losses over the electric lines.**

I. INTRODUCTION

Railway systems are nowadays recognized as highly efficient means of transportation due to their limited environmental impact. Furthermore, over the years different sustainable solutions have been proposed for energy management and losses reduction [1].

In fact, apart from eco-driving solutions (see e.g., [2]), another instrumental aspect for train energy efficiency is the power control to supply auxiliary services (e.g., heating, cooling or lightning). Centralized converter architectures are typically used, although they are not very efficient, often requiring expensive and bulky voltage source converters (VSCs). An efficient alternative is therefore that of parallel-connected converters to power distribution in railway vehicles in order to minimize the current through the auxiliary services and traction motors, hence achieving load sharing and losses reduction. In the literature, conventional control solutions in this context adopt droop-control strategies [3], [4], but the recent paradigm consisting of catenary-free scenarios makes the introduction of optimal control approaches more suitable.

The main goal of this work is to propose a novel optimal-based energy management system for regulating the train internal electric resources, thus maximizing its efficiency. Specifically, a MPC is designed taking into account the time-varying catenary supply, and thus coordinating in advance the battery charge based on the knowledge of the future track characteristics. The proposed MPC plays the role of a high-level controller to provide voltage and current references tracked by suitable low-level controllers. As a beneficial effect, the proposed MPC enables high energy savings in terms of active power losses reduction, and a proper management of the batteries state of charge, e.g., exploiting regenerative braking. The proposed strategy is finally applied to a realistic case study relying on data provided by Alstom rail transport.

II. MODELLING AND PROBLEM STATEMENT

The schematic representation of the electric components of the ith train carriage is that in Fig. 1.

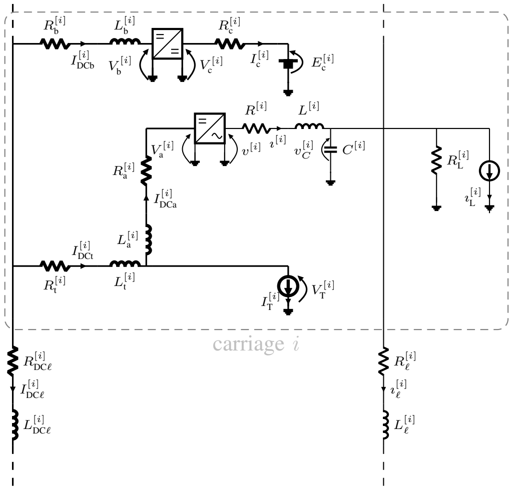

Fig. 1: Single line electric diagram for a single carriage with battery and traction motor on the DC-network, and auxiliary load on the AC-network.

The dynamic model of the system, omitted for the sake of brevity, can be achieved by applying the Kirchhoff's voltage and current laws to the illustrated electrical scheme (see [5] for the details) and it consists of the DC-network, drive-train, auxiliary loads AC-networks and batteries, whose state of charge is given by

$$\mathrm{SoC}^{[i]}(t) = \mathrm{SoC}^{[i]}(0) + E_{\rm c}^{[i]} \int_0^t \frac{I_{\rm c}^{[i]}(z)}{c_{\rm c}^{[i]}}\,\mathrm{d}z$$

with $c_c^{[i]}$ being the battery capacity. As described in [5], a DC/DC converter interfaces the DC-link with the battery internal circuit, as well as a VSC does the same for the AC auxiliary loads, while the traction circuit is simplified as a current generator capable of sending current through the DC-link if the train brakes. All the carriages are then connected to the following and preceding ones via DC- and AC network impedances. Moreover, we assume to have some "buggy" carriage i.e., without traction motors.

Now, considering variables in Fig. 1 and all the dynamic equations and algebraic equations of the system, letting

$$x^{[i]} = [I_{\rm DCb}^{[i]}, I_{\rm DCa}^{[i]}, I_{\rm DCt}^{[i]}, I_{{\rm DC}\ell}^{[i]}, I_d^{[i]}, I_q^{[i]}, V_{Cd}^{[i]}, V_{Cq}^{[i]}, I_{\ell d}^{[i]}, I_{\ell q}^{[i]}]',$$

$$u^{[i]} = [V_{\rm b}^{[i]}, V_{\rm a}^{[i]}, V_{\rm t}^{[i]}, V_{\rm DC}^{[i]}, V_{\rm c}^{[i]}, I_{\rm c}^{[i]}, V_d^{[i]}, V_q^{[i]}]',$$

$$d^{[i]} = [V_0, I_{\rm T}^{[i]}, I_{{\rm L}d}^{[i]}, I_{{\rm L}q}^{[i]}]',$$

Alessio La Bella, Gian Paolo Incremona and Patrizio Colaneri are with Dipartimento di Elettronica, Informazione e Bioingegneria, Politecnico di Milano, Piazza Leonardo da Vinci 32, 20133 Milan, Italy ({`alessio.labella`, `gianpaolo.incremona`, `patrizio.colaneri`}`@polimi.it`). Aline Cristiane Buzzi is with Alstom SESTO, Via Fosse Ardeatine, 120, 20099 Sesto San Giovanni, Milan, Italy (e-mail: `aline-cristiane.buzzi@alstomgroup.com`).

one can write the model in a compact way as

$$\dot{x}^{[i]} = f(x^{[i]}, u^{[i]}, d^{[i]}), \tag{1a}$$

$$g(x^{[i]}, u^{[i]}, d^{[i]}) = 0\,, \tag{1b}$$

where $f(\cdot)$ and $g(\cdot)$ are properly defined vector functions. Moreover, all train electric variables must be constrained within their physical limits, implying that

$$\underline{x}^{[i]} \leq x^{[i]} \leq \bar{x}^{[i]}, \tag{2a}$$

$$\underline{u}^{[i]} \leq u^{[i]} \leq \bar{u}^{[i]}. \tag{2b}$$

The control objective is to design an MPC-based management system for the electric devices of the train. Such an MPC will play the role of a high-level controller capable of generating voltage or current references to low-level regulators.

III. MPC-BASED ENERGY MANAGEMENT SYSTEM

Considering an MPC running at slower rate, and, given the train circuit dynamics, the latter is included as static in the MPC problem formulation, since electric transients are typically much faster than the MPC sampling time, namely $\tau_\text{s} \in \mathbb{R}$. Hence, (1a) is included in the MPC at its equilibrium, i.e., $f(x^{[i]}, u^{[i]}, d^{[i]}) = 0$.

Then, suitably discretizing the model, with $t = k\tau_\text{s} \in \mathbb{R}$, where $k \in \mathbb{N}_{\geq 0}$, let the prediction horizon be $\mathcal{T}_k := \{k, \dots, k+N-1)$, with the integer $N \geq 1$ being the horizon length, while the ith SoC dynamics becomes

$$\text{SoC}^{[i]}(k+1) \;=\; \text{SoC}^{[i]}(k) \;+\; \frac{E_\text{c}^{[i]} I_\text{c}^{[i]}(k)}{c_\text{c}^{[i]}}\,\tau_\text{s}$$

subject to

$$\underline{\text{SoC}}^{[i]} \leq \text{SoC}^{[i]}(k) \leq \overline{\text{SoC}}^{[i]},$$

where $0 \leq \underline{\text{SoC}}^{[i]} < \overline{\text{SoC}}^{[i]} \leq 1$. Moreover the MPC is designed to accomplish the following goals:

1) batteries should work with SoC higher than a predefined threshold SoC^th (e.g., 50%) so as to ensure that a sufficient charge is available in case of catenary-free sections of the track, i.e., $\text{SoC}^{[i]}(k) \geq \text{SoC}^\text{th} - \Delta s^{[i]}(k)$, where $\Delta s^{[i]} \geq 0$ is a slack variable;
2) when the traction current $I_\text{T}^{[i]} < 0$, i.e., in case of regenerative braking, the recovered energy must be charged in batteries instead of being injected in the catenary grid. Therefore, it is imposed that $I_{\text{DC}\ell}^{[0]}(k) \geq -\Delta I_\text{cat}(k)$, where $I_{\text{DC}\ell}^{[0]}$ is the current absorbed by the catenary, whereas $\Delta I_\text{cat} \geq 0$ is a slack variable;
3) power losses, compactly indicated as

$$P_\text{loss}(k) \;=\; \sum_{i=1}^{n} \mathcal{I}^{[i]}(k)' \,\mathcal{R}^{[i]}\, \mathcal{I}^{[i]}(k)\,,$$

must be minimized, while transferring energy from/to batteries to/from carriages.

Hence, given the previous objectives, the following MPC optimization problem is solved at each $t = k\tau_\text{s}$, i.e.,

$$\min_{u(\cdot)} \sum_{h=k}^{k+N-1} P_\text{loss}(h) + \gamma_\text{cat} \Delta I_\text{cat}(h)^2 + \gamma_s \sum_{i=1}^{n} \Delta s^{[i]}(h)^2,$$

subject to (1), (2), $\forall h \in \mathcal{T}_k$,

with $\gamma_\text{cat} > 0$ and $\gamma_s > 0$ being properly defined weights.

IV. CASE STUDY

The proposal has been assessed in simulation making reference to a regional train with $n = 4$ carriages moving over a track with two stops. The first and the fourth carriages are equipped with both batteries and traction motors, while the other two are "buggy" carriages. In the considered scenario we assume that the train crosses a catenary-free section of the track in the interval $t \in [80,\, 140]\,\text{min}$. The train parameters and motor current required by the train or regenerated during braking have been provided by Alstom rail transport, while all the MPC setting can be found in [5].

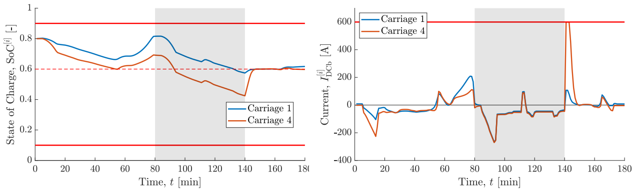

Fig. 2: SoC profiles for the batteries on carriages 1 and 4 (left) and profiles of battery current $I_\text{DCb}^{[i]}$, $i = 1, 4$ (right)

Fig. 2 shows that from an initial SoC equal to 0.8, both SoCs ($i = 1, 4$) decrease but with different rate by virtue of the minimization of losses operated by the MPC, and at $50\,\text{min}$, both batteries are charged since the MPC foresees a catenary-free section of the track. The same figure shows the time evolution of the battery currents $I_\text{DCb}^{[i]}$, $i = 1, 4$, where one can observe that, in order to minimize losses, MPC makes the batteries supply part of the traction and load, while they are charged when the train brakes. The computation of the total energy losses amounts to $0.78\,\text{kW h}$, compared with an heuristic control strategy for which losses are $1.58\,\text{kW h}$, i.e., a 50.7% power saving is obtained using the proposal.

V. CONCLUSIONS

In this work, a novel MPC strategy to address the energy-management problem for trains, equipped with parallel-connected auxiliary loads, traction motors and batteries, is proposed. We have designed a promising sustainable solution for real time implementation, also capable of efficiently governing the batteries in the case of partial catenary-free scenarios.

REFERENCES

[1] G. M. Scheepmaker, R. M. Goverde, and L. G. Kroon, "Review of energy-efficient train control and timetabling," *European Journal of Operational Research*, vol. 257, no. 2, pp. 355–376, 2017.
[2] H. Farooqi, "Design of collaborative eco-drive control algorithms for train networks," Ph.D. dissertation, Politecnico di Milano, 2019.
[3] J. Kim, J. M. Guerrero, P. Rodriguez, R. Teodorescu, and K. Nam, "Mode adaptive droop control with virtual output impedances for an inverter-based flexible ac microgrid," *IEEE Transactions on Power Electronics*, vol. 26, no. 3, pp. 689–701, 2011.
[4] M. Li, Y. Gui, Z. Jin, Y. Guan, and J. M. Guerrero, "A synchronous-reference-frame I-V droop control method for parallel-connected inverters," in *International Power Electronics Conference*, Niigata, Japan, May 2018, pp. 2668–2672.
[5] A. La Bella, G. P. Incremona, A. C. Buzzi, and P. Colaneri, "Model predictive control of battery-powered trains for catenary-free operation," *IFAC-PapersOnLine*, vol. 56, no. 2, pp. 1964–1969, 2023, 22nd IFAC World Congress.

Optimizing electric vehicles charging through smart energy allocation and cost-saving

Luca Ambrosino[1], Giuseppe Calafiore[1,2], Khai Manh Nguyen[2],
Riadh Zorgati[4], Doanh Nguyen-Ngoc[2,3], Laurent El Ghaoui[2,3]

[1]Dipartimento di Elettronica e Telecomunicazioni (DET), Politecnico di Torino, Torino, Italy
[2]College of Engineering and Computer Science (CECS), Vin University, Hanoi, Vietnam
[3]College of Environmental Intelligence (CEI), Vin University, Hanoi, Vietnam
[4]R&D Department, Électricité de France (EDF), Paris, France

In light of the pressing need for sustainable energy solutions to combat the environmental crisis, this paper addresses the challenges associated with integrating electric vehicles (EVs) into daily life, specifically focusing on the optimization of EV charging stations. While much of the existing literature emphasizes the impact of EVs on the power grid and the importance of reducing grid strain through data-driven models and off-peak charging strategies [1], our approach diverges by concentrating on optimizing a single charging station in a business perspective. Smart Charging, which employs advanced technologies and algorithms to optimize charging station usage, is central to our study, aiming to enhance efficiency, reduce costs, and minimize grid strain [2].

Our research[1] introduces a mathematical optimization model formulated as a Linear Programming problem to optimize the decision-making processes within a charging station from a business perspective. This model seeks to maximize operational efficiency and minimize costs by determining which vehicles to charge, for how long, and the power allocation for each EV. Differently to other optimization frameworks [3], we also incorporate a Robust Optimization approach to manage real-world uncertainties, such as fluctuating electricity prices and varying energy demands [4]. The significant cost-saving potential of our model, particularly as the number of EVs increases, is demonstrated in our results, highlighting the contribution of this innovative approach to the development of Smart Charging solutions for the future of transportation.

$$\begin{aligned} p^* = \min_{Y} : & \sum_{t=1}^{T} \pi_t \left(\left(1 + y_t^0\right) \cdot \sum_{i: t \in [a_i, d_i]} Y_{ti} \right) \\ \text{s.t. } & \sum_{t=a_i}^{d_i} Y_{ti} \geq L_i, \quad i = 1, \ldots, N \\ & \sum_{i=1}^{N} Y_{ti} \leq C_t, \quad t = 1, \ldots, T \\ & 0 \leq Y_{ti} \leq s_t, \quad t = 1, \ldots, T, i = 1, \ldots, N. \end{aligned}$$

The optimization model considers the following variables and parameters: π_t (linear energy cost at time t), y_0 (a T-dimensional vector representing systematic energy waste during the charging process), L (load vector representing required energy demand for each vehicle divided by the time step length Δ), (a_i, d_i) (arrival and departure times for each vehicle), C_t (maximum power generated by the station at time t), and s_t (maximum power generated by a single charging socket), assuming reasonably fixed

---

[1] This paper has been presented at ESCC 2024 - 11th International Conference on Energy, Sustainability and Climate Crisis, August 26 - 30, 2024, Corfu, Greece. This paper is based upon work supported by Vin University under Grant No. VUNI.2223.FT08. Furthermore, Luca Ambrosino is supported by the he FAIR - Future Artificial Intelligence Research and received funding from the European Union Next-Generation EU (PIANO NAZIONALE DI RIPRESA E RESILIENZA (PNRR) – MISSIONE 4 COMPONENTE 2, INVESTIMENTO 1.3 – D.D. 1555 11/10/2022, PE00000013).

values for C and s in simulations. The mathematical optimization model has been tested across 730 scenarios demonstrated an average cost saving of 9% compared to a standard algorithm. The model also offers flexibility for robust optimization, handling uncertainties in input parameters effectively.

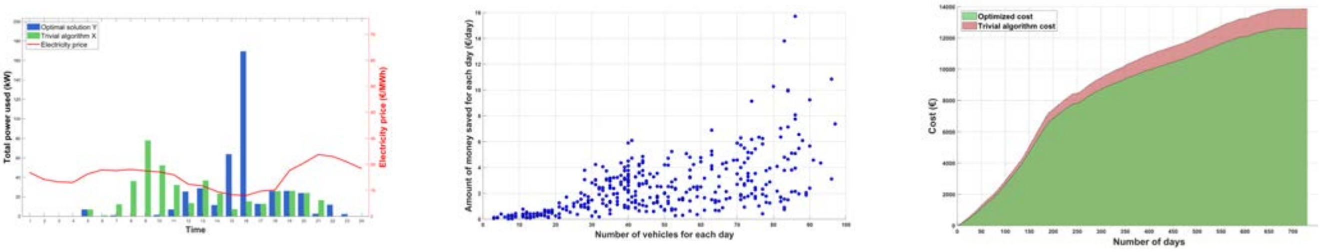

Figure 1: Three different ways to visualize the results

Furthermore, we adopted a robust strategy with respect to the electricity prices and the load vector uncertainties. The first idea to deal with energy demand is to implement the interval uncertainty, by substituting in the constraint the L_i with its worst case/upper bound $\bar{L}_i$. For what concerns the electricity prices, we implement the norm-bounded uncertainty in the objective functions by assuming that π is known up to a sphere $||\pi - \hat{\pi}||_2 \leq \rho$, where the nominal cost $\pi \in \mathbf{R}^T$ and the uncertainty level $\rho \geq 0$ are known. In matrix form, the robust counterpart of the mathematical optimization model becomes a Second Order Cone Programming problem (SOCP) of the form:

$$
\begin{aligned}
p^* = \min_{Y} :& \pi_t \left(diag(AY^T) + y_t^0 \cdot diag(AY^T) \right) + \rho \cdot ||diag(AY^T) + y_t^0 \cdot diag(AY^T)||_2 \\
\text{s.t. } & diag(A^T Y) \geq \bar{L} \\
& diag(AY^T) \leq C \\
& 0 \leq Y \leq s.
\end{aligned}
$$

Future improvements include incorporating profitability into the objective function to handle variable electricity prices and extended charging discounts. As the EV market grows, adding constraints on the solution's cardinality and using constraint relaxation techniques could manage computational complexity. Additionally, considering a network of charging stations instead of focusing only to one can surely improve the scalability of our approach. Developing more advanced models based on this framework will be crucial for advancing Smart Charging optimization and supporting sustainable energy solutions.

References

[1] S. Powell, G. Cezar, L. Min, I. Azevedo, and R. Rajagopal, "Charging infrastructure access and operation to reduce the grid impacts of deep electric vehicle adoption," *Nature Energy*, vol. 7, pp. 1–14, 09 2022.

[2] D. A. Hussien, W. A. Omran, and R. M. Sharkawy, "Smart charging of electric vehicles in charging stations," in *2023 5th International Youth Conference on Radio Electronics, Electrical and Power Engineering (REEPE)*, vol. 5, 2023, pp. 1–5.

[3] J. Liu, G. Lin, S. Huang, Y. Zhou, Y. Li, and C. Rehtanz, "Optimal EV charging scheduling by considering the limited number of chargers," *IEEE Trans. Transp. Electrif.*, vol. 7, no. 3, pp. 1112–1122, Sep. 2021.

[4] G. Benetti, M. Delfanti, T. Facchinetti, D. Falabretti, and M. Merlo, "Real-time modeling and control of electric vehicles charging processes," *IEEE Transactions on Smart Grid*, vol. 6, 2015.

Predictive Models for Vehicle-to-Grid Available Aggregated Capacity Prediction

Luca Patanè*, Francesca Sapuppo*§, Marco Calapristi *, Antonino Maio*,
Antonino Comi†, Giuseppe Napoli‡, Riccardo Caponetto* and Maria Gabriella Xibilia*
**Dipartimento di Ingegneria*, *Università degli Studi di Messina*, Messina, Italy
†*Istituto di Tecnologie Avanzate per l'Energia (ITAE)*, *Consiglio Nazionale delle Ricerche (CNR)*, Messina, Italy
‡*Dipartimento di Ingegneria dell'Impresa*, *Università degli Studi di Roma "Tor Vergata"*, Rome, Italy

***Abstract*—Vehicle-to-grid (V2G) technology has proven to be a promising solution for integrating electric vehicles (EVs) into the electricity grid, offering benefits such as grid stabilization and demand response. Predicting the aggregated available capacity (AAC) of EVs is crucial for the effective utilization of their energy storage capabilities. A comprehensive framework for predicting AAC in V2G systems is presented here. It includes methods for data pre-processing and feature selection tailored to managing complex datasets with multiple data sources such as GPS, weather, vehicle characteristics, historical data, and calendar information. Different predictive models based on machine learning, such as Neural Networks, Long Short-Term Memory networks, Tree Ensembles, and Gaussian Process Regressors were implemented. The application of such models on different multidimensional datasets seeks to enhance the accuracy of AAC predictions, explaining and modeling the complex dependencies within the input data and the target available capacity, ultimately improving the efficiency and reliability of V2G systems.**

***Index Terms*—Vehicle-to-Grid, data-driven predictive model, time-series prediction, machine learning, aggregator hub planning**

I. INTRODUCTION

Vehicle-to-Grid (V2G) allows the flow of energy between electric vehicles (EVs) and the power grid, making EVs mobile energy storage units that enhance grid stability. With EVs expected to reach 60% market penetration by 2030 [1], efficient V2G integration is vital. Predicting aggregated available capacity (AAC) at hubs is essential for V2G reliability and economic viability. This prediction relies on EV availability, influenced by user behavior, charging infrastructure location, vehicle characteristics, meteorological data, and calendar information, as weather and travel habits on weekends and holidays affect EV usage. Machine Learning (ML) models, including Persistence models, Generalized Linear Models, Artificial Neural Networks (ANNs), Long-Short-Term-Memory networks (LSTM), K-Means Clustering, and Convolutional Neural Networks (CNN), have been used to predict AAC [2], [3]. from various data sources: limited EV fleets, charging point data, historical vehicle information, and calendars [2], [4], [5]. This work aims to combine diverse data sources and apply them to ML prediction algorithms, using real-world mobility data, meteorological information, and weekend and holiday data to predict AAC for V2G applications.

II. DATA COLLECTION AND PRE-PROCESSING

1) The Open-Access Vehicle Energy Dataset (VED): The Vehicle Energy Dataset (VED) [6] is a freely accessible dataset that was used for this study. The dataset covers a wide range of geolocalized vehicles: 264 internal combustion engines (ICEs), 92 hybrid electric vehicles (HEVs), and 27 plug-in hybrid electric vehicles/electric vehicles (PHEV/EVs), operating in real-world conditions from November 2017 to November 2018 in Ann Arbor, Michigan, USA. The HV Battery State of Charge (SoC[%]) is provided for the PHEVs and EVs, while it is calculated as an indirect measure of distance traveled and charging stop intervals according to [3] for ICEs and HEVs. Figure 1 shows the density of stops during different intervals of the day and integrated over the entire year of data. The color scale represents the duration of the stops in hours. A point of interest, referred to as Hub_1, in the city center was chosen as the best candidate for a V2G infrastructure.The real or simulated SoC_v is used to determine the Available Capacity of a vehicle (AC_v) defined as the capacity of the available vehicles (within a specific distance from the hub) to provide energy to the grid in a half-hour (hh) period. Additional considered aggregated time series are the following: Mean Hub Distance ($MHD^{hh}_{hub^C}$) and Stop Duration Integral ($SDI^{hh}_{hub^r}$).

A. Meteo Dataset

The meteorological data (precipitation, temperature, wind speed, humidity, overcast percentage, etc) are extracted from the MeteoStat database using the Python API [7] based on GPS coordinates of the geographical area under study.

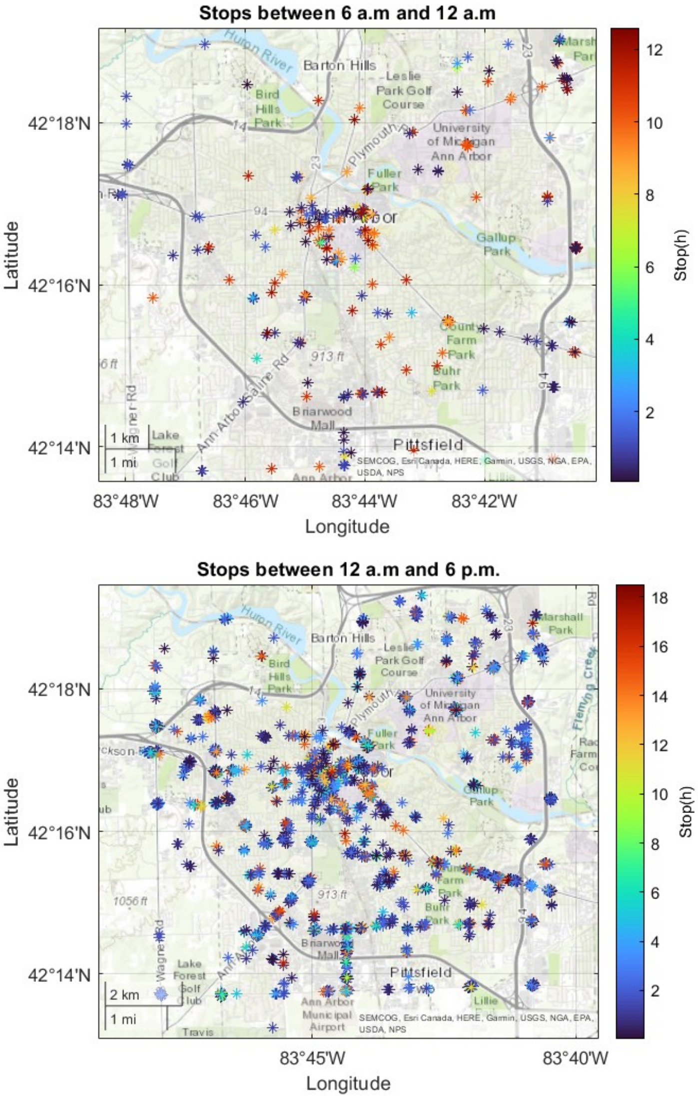

Fig. 1. Stop maps in different time intervals of the day, integrated over the entire year. The stop events have started in the time window: (a) from 6AM to 12 AM (b) from 12 AM to 6 PM

B. National Holidays Dataset

The information about holidays and weekends is represented by a discontinuous time series, which is not suitable for the identification of dynamic models. The goal of fuzzifying such inputs is to obtain a continuous time series, with hh time interval, that contains both weekend and holiday information. Fuzzy membership functions were developed to account for the effects that weekends and holidays might have on drivers' habits on the days before and after these periods. The weekend and holiday membership functions, shown graphically in Figures 2(a) and (b), respectively, were applied to the time series of calendar dates. When the weekend membership function is applied to a calendar day, it outputs a degree of truth, ranging from 0 to 1, indicating the likelihood of the day being a weekend. Similarly, applying the holiday membership function to a calendar day results in a continuous value between 0 and 1, representing the degree of truth for the day being a holiday. To create a single continuous dynamic feature that integrates both weekend and holiday information, the maximum value of these membership functions was taken.

III. RESULTS

Different models have been adopted and compared: Neural Networks (NNs), Long Short-Term Memory (LSTM) Networks, Ensemble of Trees (TE), Gaussian Process Regression (GPR), and Trees. Identification and prediction were performed for three different input selections: Input Set 1 (*IS1*): AAC_{hub_r}, Input Set 2 (*IS2*):

This work was funded by the MASE - Consiglio Nazionale delle Ricerche within the project RICERCA DI SISTEMA 22-24 -21.2 Progetto Integrato Tecnologie di accumulo elettrochimico e termico. CUP Master: B53C22008540001, UNIME-DI-RdS22-24:J43C23000670001 Linea 13

[§] Corresponding Author

TABLE I

MODELS PERFORMANCE COMPARISON FOR DIFFERENT INPUT SETS (IS1, IS2, IS3)

Inputs	**Model**	**RMSE(Test)**	**R^2(Test)**
IS1: AAC_{hub_r}	NN, 2 Layers (122,2)	**3.6918**	**0.83**
	LSTM,2 Layers (233,233)	4.68798	0.51
IS2: AAC_{hub_r}, MHD_{hub_C},SDI_{hub_r}	NN, 3 Layer (298,54,6)	**3.3004**	**0.86**
	LSTM, 3 Layers (278,278,278)	4.6262	0.58
IS3: Meteo, Holidays, AAC_{hub_r}, MHD_{hub_C}, SDI_{hub_r}	NN, 3 Layers (50,100,100)	**3.2745**	**0.87**
	LSTM, 2 Layers (299,299)	3.8875	0.68
	TE (LSBoost, n.learners=257)	3.2819	0.86
	GPR (Linear,Non Isotr.Rat.Quadratic)	3.3093	0.86
	Tree (Min Leaf Size: 15)	3.5102	0.84

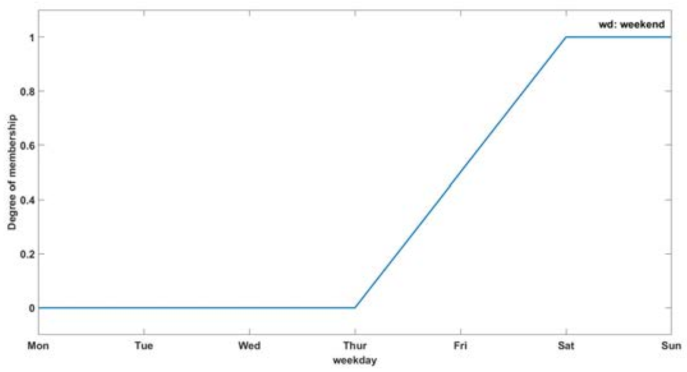

(a) Weekend

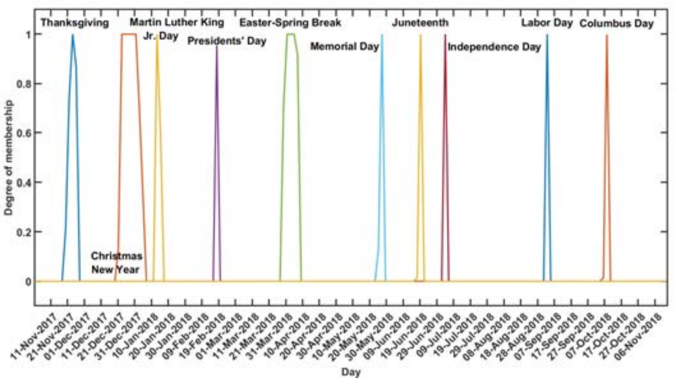

(b) National Holidays

Fig. 2. Membership function for the fuzzification of the holiday rate. (a) Weekend membership. (b) National holiday membership functions.

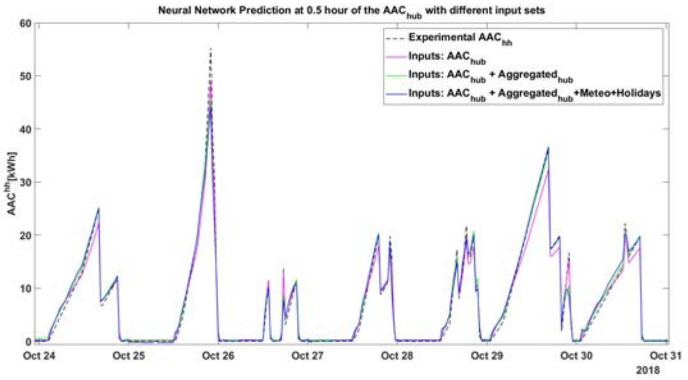

(a) Neural Networks

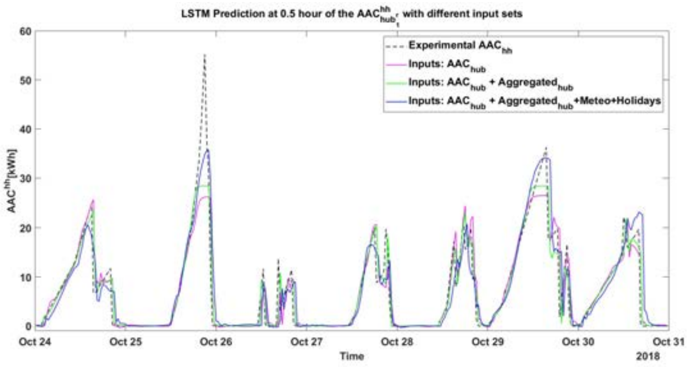

(b) LSTM

Fig. 3. 30-minute ahead prediction for AAC_{hub1_r} using different input sets to the optimized models for the week in the test dataset Oct. 24th to Oct. 31st, 2018. (a) Neural Networks and (b) LSTM.

AAC_{hub_r}, MHD_{hub_C}, SDI_{hub_r}, Input Set 3 ($IS3$): AAC_{hub_r}, MHD_{hub_C}, SDI_{hub_r}, meteo information (precipitation, temperature, wind speed), holiday rate.

Data was divided into training and validation (75%) and testing (25%) datasets. In particular, to avoid seasonal bias and unbalanced datasets, 3 weeks per month were chosen as training/validation, 1 week as test. The model optimization for hyperparameter determination was implemented via a Bayesian algorithm. The optimization metric was based on the minimization of the root mean square error (RMSE). The optimal hyperparameters and associated model performances are shown in Table I in terms of RMSE and correlation coefficient (R^2) for both the test datasets.

The NN and LSTM models were applied to all three input sets, while the TE, the GPR, and the Tree were only applied to the complete input set $IS3$, which resulted in being the most promising. The best-performing model in the validation dataset is the LSTM using the $IS2$. The best-performing model in the test dataset is the NN using the full input dataset $IS3$. This suggest that that the dynamics of the system are affected by the exogenous inputs, thus confirming the validity of the proposed holistic methodological framework.

Figure 3 shows the 30-minute ahead prediction of AAC in the same week with (a) NNs and (b) LSTMs. The performance of NNs is marginally superior to that of LSTM models, which frequently underestimate the actual value of AAC. Nonetheless, the primary objective of this paper is to demonstrate that, irrespective of the model employed, integrating the full input set $IS3$ enhances model prediction accuracy.

IV. CONCLUSIONS

A key contribution of this work to the existing literature is the comprehensive integration of geographical, meteorological, and temporal factors, particularly through the use of a fuzzy input set that accounts for both national holidays and weekends. Future research can expand on this approach by employing data-driven linear state-space representation techniques and comparing them with nonlinear black-box models, leveraging their ability to extract relationships between exogenous inputs and target variables. The application of our forecasting framework can be adapted to general mobility data to support the strategic placement of aggregator hubs and optimize their distribution to effectively manage and utilize the available capacity of geographically dispersed EVs. This strategic planning contributes to the overall scalability and adaptability of the V2G infrastructure. These innovations not only extend the applicability of our method to generic data, but also highlight its versatility in predicting available capacity and demonstrate that it can be adapted for various EV applications beyond V2G.

REFERENCES

[1] I. E. Agency, "By 2030 evs represent more than 60% of vehicles sold globally, and require an adequate surge in chargers installed in buildings," in *IEA, Paris*, 2022.

[2] J. Graham and F. Teng, "Vehicle-to-grid plug-in forecasting for participation in ancillary services markets," in *2023 IEEE Belgrade PowerTech*. IEEE, jun 2023.

[3] R. Shipman, R. Roberts, J. Waldron, S. Naylor, J. Pinchin, L. Rodrigues, and M. Gillott, "We got the power: Predicting available capacity for vehicle-to-grid services using a deep recurrent neural network," *Energy*, vol. 221, p. 119813, 2021.

[4] L. Patanè, F. Sapuppo, M. G. Xibilia, and G. Napoli, "A comprehensive data analysis for aggregate capacity forecasting in vehicle-to-grid applications," in *2024 International Conference on Control, Automation and Diagnosis (ICCAD)*, 2024, pp. 1–6.

[5] L. Patanè, F. Sapuppo, A. Comi, G. Napoli, and M. G. Xibilia, "An explainable model framework for vehicle-to-grid available aggregated capacity prediction," in *2024 IEEE International Conference on Metrology for eXtended Reality, Artificial Intelligence and Neural Engineering*, 2024, pp. 1–6.

[6] G. Oh, D. J. Leblanc, and H. Peng, "Vehicle energy dataset (VED), a large-scale dataset for vehicle energy consumption research," *IEEE Trans Intel Trans Sys*, vol. 23, no. 4, pp. 3302–3312, 2022.

[7] "Meteo stat phyton api," https://dev.meteostat.net/python/.

Infrastructure-less UWB-based Relative Localization: an Active Approach

Valerio Brunacci, Alberto Dionigi, Alessio De Angelis, and Gabriele Costante

***Abstract*— In multi-robot systems, relative localization is crucial in many tasks, such as leader following, target tracking, or cooperative maneuvering. Current approaches either rely on infrastructure-based or on infrastructure-less setups. The former typically achieve high localization accuracy but require fixed external structures. The latter provide more flexibility, but often requires Line-of-Sight (LoS) devices like cameras or lidars. Ultra Wide Band (UWB) devices are emerging as a viable alternative to build infrastructure-less solutions that do not require LoS. These approaches directly deploy the UWB sensors on the robots. However, they require that at least one of the platforms is static, limiting the advantages of an infrastructure-less setup. In this work, we remove this constraint and introduce an active method for infrastructure-less relative localization. Our approach allows the robot to adapt its position to minimize the relative localization error of the other platform.**

I. INTRODUCTION

Localization is a longstanding goal in robotics and is certainly one of the most crucial components of every robotic platform. At a high level, localization can be achieved by relying either on a fixed infrastructure or solely on onboard robot sensors. The former setup is implemented by coupling external sensors with onboard markers or receivers. Infrastructure-less solutions, on the other hand, do not require external structure at fixed known positions.

Relative localization between platforms can be exploited to refine their respective global pose estimate, or used for tasks where platforms are mainly interested in their relative pose with respect to another robot. Relative localization can be achieved with various sensor setups, among which the most popular are based on cameras, lasers, and lidars. Despite the impressive results achieved, these approaches suffer from two important limitations: i) relative pose information needs to be inferred from data through perception algorithms; ii) they require Line-of-Sight (LoS) to operate.

Ultra Wide Band (UWB) technology is currently flourishing as a viable alternative to achieve relative localization. UWB systems are cost-effective, can be used to directly access distance information between entities, and can work in Non-Line-of-Sight (NLoS) conditions. Most of the UWB-based solutions are infrastructure-based, *i.e.*, they use fixed UWB sensors with known positions (namely the *anchors*) to localize the platform equipped with another UWB device (often referred to as *tag*) [1].

Recently, UWB sensors have been also employed in infrastructure-less configurations to achieve relative localization between robots [2], [3]. In this case, also the anchors are mounted on a mobile platform that estimates the relative position of the robot with the tag UWB. However, most of the State-of-the-Art (SotA) approaches keep the robot with anchors in a fixed position, limiting the advantages of an infrastructure-less setup. Additionally, in infrastructure-less setups the tag moves outside the convex hull delimited by the anchors. In practice, this translates in a worse Geometric Dilution Of Precision (GDOP) [4], a metric that models the localization errors depending on the anchor-tag arrangement. In some configurations, particularly those where the tag is outside the anchor hull, small measurement errors might result in large relative position errors.

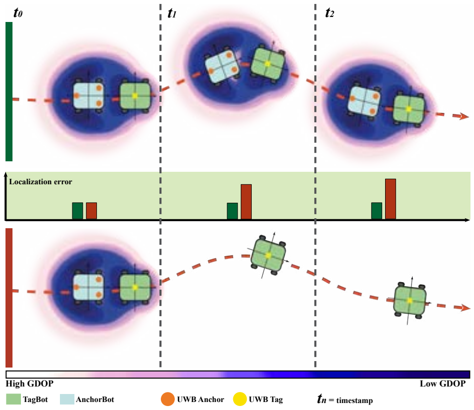

Fig. 1: Overview of the proposed approach. Contrary to the SotA approaches (bottom figure with red bar), we develop an active method (top figure with green bar) that exploits the movement of the robot to enhance the localization performance.

Driven by the aforementioned considerations, the purpose of this research is to build an infrastructure-less UWB-based relative localization approach that overcomes the drawbacks of SotA solutions. In particular, we develop an *active* localization method that enables the robot with the anchors to adapt its position to reduce the relative localization error of the tag robot, see Fig 1. This is achieved by training a Deep Reinforcement Learning (DRL) agent that controls the platform to minimize a loss function based on the GDOP metric and on a measurement model tailored to the specific problem we consider. Differently from other solutions, we do not assume that the robot with the anchors is static.

II. METHODOLOGY AND TASK DETAILS

The objective of the proposed active relative localization method is to provide a robotic platform with a suitable control policy so that to obtain the best possible estimation of another robot position. In this research, we consider an infrastructure-less context with two distinct robotic plat-

---

All the authors are with the Department of Engineering, University of Perugia, 06125 Perugia, Italy `valerio.brunacci@dottorandi.unipg.it`, `{alberto.dionigi, alessio.deangelis, gabriele.costante}@unipg.it`. This work was in part supported by Fondazione Cassa di Risparmio di Perugia - Project: DEIMOS - “droni ecologici intelligenti per il monitorag- gio di oliveti sostenibili”.

TABLE I: Results of the simulation experiments. From top to bottom we consider different *AnchorBot* - *TagBot* initialization distances: 70 cm, 100 cm and 200 cm. The mean μ and the standard deviation σ of the localization RMSE in cm are reported.

Method	Static *TagBot*						Dynamic *TagBot*					
	Front Spawn		Side Spawn		Behind Spawn		Straight Line		Circle		Square	
	μ	σ	μ	σ	μ	σ	μ	σ	μ	σ	μ	σ
SUL-EQ [5]	11.0	7.8	12.9	9.6	16.0	13.9	28.2	24.9	13.3	10.4	21.6	18.2
SUL-IS	10.3	7.1	12.9	9.7	21.6	30.7	26.0	22.8	13.5	14.1	20.2	16.9
AUL-EQ	11.5	8.1	11.7	8.3	11.5	**9.3**	12.7	9.1	11.4	8.0	11.9	8.5
AUL-IS (Our)	**10.7**	**7.5**	**11.0**	**7.8**	**11.3**	9.7	**11.7**	**8.3**	**10.6**	**7.4**	**11.1**	**7.8**
SUL-EQ [5]	15.9	11.7	18.2	13.7	20.7	15.7	33.3	28.3	18.3	13.7	26.2	21.6
SUL-IS	14.9	10.7	18.0	13.6	20.2	19.5	31.0	26.2	17.7	14.1	24.4	20.0
AUL-EQ	12.0	8.7	12.6	9.5	12.9	**9.8**	13.1	9.5	12.2	8.7	12.3	9.0
AUL-IS (Our)	**11.2**	**8.0**	**11.9**	**9.0**	**12.3**	**9.8**	**12.1**	**8.7**	**11.3**	**7.9**	**12.1**	**8.7**
SUL-EQ [5]	33.2	25.2	35.6	27.1	37.9	29.0	50.7	41.0	35.6	27.1	42.8	33.9
SUL-IS	30.8	23.1	35.6	27.1	35.3	27.4	47.0	37.7	34.3	26.2	39.7	31.3
AUL-EQ	21.0	17.9	**22.7**	**19.5**	24.5	20.6	25.4	20.1	13.3	10.3	17.5	16.6
AUL-IS (Our)	**19.5**	**16.6**	23.9	20.4	**22.5**	**19.3**	**23.8**	**18.6**	**12.2**	**9.4**	**15.9**	**15.1**

TABLE II: Results of the real-world experiments. The mean μ the standard deviation σ of the localization RMSE in cm are reported.

Method	Static TagBot						Dynamic TagBot					
	Front Spawn		Side Spawn		Behind Spawn		Straight Line		Circle		Square	
	μ	σ	μ	σ	μ	σ	μ	σ	μ	σ	μ	σ
SUL-IS	5.6	3.7	9.0	6.3	7.6	9.7	32.5	22.2	13.2	8.8	26.6	22.9
AUL-IS (Our)	**4.9**	**3.3**	**7.1**	**4.9**	**5.9**	**4.2**	**12.7**	**8.1**	**12.2**	**7.2**	**14.7**	**7.8**

forms: the first one, named *AnchorBot*, is equipped with three UWB anchor nodes, and its function is to localize with respect to its body frame the second one, referred to as the *TagBot*, which is equipped with a single UWB tag. The *AnchorBot* have access only to the relative distances between the anchors and the tag, and the goal is to adapt its position in order to minimize the *TagBot* localization error.

To this aim, we propose a new framework that i) study and design an anchor arrangement to adapt the GDOP to the relative localization task in mobile robot scenarios and ii) exploits this design through an active localization strategy.

a) Anchors Displacement Analysis: we conduct an in-depth anchor placement analysis to identify suitable configuration for the active localization task. When the *AnchorBot* is static and the *TagBot* moves freely, the best strategy is to keep the GDOP as low as possible at all points surrounding the AnchorBot. [5] finds out that the equilateral triangle arrangement comes closest to achieving this goal. However, a uniformly distributed GDOP results in a higher minimum value compared to configurations tailored for localizing the robot within specific areas. Consequently, through an extensive Monte Carlo simulation campaign over a set of possible configurations, we select an isoscele triangle configuration for the anchors. The trade-off is that the *AnchorBot*'s front region hosts the GDOP minimum, requiring precise localization of the *TagBot* in that zone.

b) UWB Relative Localization Loss: In an UWB-based localization context, directly using the GDOP as the loss function might seem a reasonable choice since, by definition, it is a performance metric for positioning. However, this is impractical since, in an infrastructure-less scenario, the GDOP minimum falls in the AnchorBot footprint area. Furthermore, another aspect that influences localization performance is distance: UWB sensors are not able to provide a reliable measurement for short distances. Consequently, we develop a novel *UWB Relative Localization Loss* that combines the GDOP metric with a suitable measurement model for the anchors that takes into consideration the UWB performance degradation for short ranges.

c) Deep Reinforcement Learning controller: for the implementation of the control policy we employ a DRL strategy that leverages Deep Neural Network (DNN) approximators. In particular, we design two DNN architectures: the *actor* one learns the optimal policy and only leverages range measurements coming from UWB-devices, while the *critic* counterpart is fed with more privileged information and used only during training phase to evaluate such a policy. For the optimization, we design a suitable reward function based on the UWB Relative Localization Loss.

III. EXPERIMENTS

The proposed **AUL-IS** (**A**ctive **U**WB-**L**ocalization - **IS**oscele triangle configuration) approach is tested through an extensive simulation campaign and validated with real-world experiments on a wheeled robotic platform. More specifically, we perform two distinct types of experiments. In the first one, the *TagBot* remains stationary and assumes three different positions: in front of, to the side, and behind the *AnchorBot*. The second set of tests is, instead, aimed at assessing the capability of the proposed active method to localize a moving platform. As a comparison baseline, we employ (i) the method proposed in [5] where the *AnchorBot* is kept stationary and the anchors have an equilateral triangle configuration (**SUL-EQ**), (ii) a stationary *AnchorBot* with our isosceles triangle configuration (**SUL-IS**) and (iii) an active version of [5] (**AUL-EQ**).

The results of the simulated experimental campaign are reported in Table I. A first key finding is that the active approaches **AUL-EQ** and **AUL-IS** outperform their static counterparts **SUL-EQ** and **SUL-IS** in every situation. This result is a direct consequence of the control policy developed by the DRL agent, which is able to effectively move and orient the *AnchorBot* so as to maintain the *TagBot* in low GDOP areas. Moreover, it can be observed that the specialized anchor configuration exploited by **AUL-IS** can further enhance the localization performance.

Real-world experiments are carried out to validate the results obtained in the simulation campaign and to demonstrate the transferability of the DRL controller on a real platform. The trained DRL policy is directly deployed on the real *AnchorBot* without any fine-tuning, and the results against the static baseline are reported in Table II. The learned controller demonstrates strong generalization capabilities as it achieves remarkable localization performance when real robotic platforms and UWB sensors are involved. The numerical experiments show that **AUL-IS** outperforms **SUL-IS** in each considered scenario, confirming what we observe in the simulations experiments.

REFERENCES

[1] F. Zafari *et al.*, "A survey of indoor localization systems and technologies," *IEEE Commun. Surveys Tuts.*, vol. 21, pp. 2568–2599, 2019.

[2] X. S. Zhou *et al.*, "Robot-to-robot relative pose estimation from range measurements," *IEEE Trans. Robot.*, vol. 24, pp. 1379–1393, 2008.

[3] Z. Cao *et al.*, "Relative localization of mobile robots with multiple ultra-wideband ranging measurements," *IEEE IROS*, 2021.

[4] N. Levanon, "Lowest gdop in 2-d scenarios," *IEE Proceedings: Radar, Sonar and Navigation*, vol. 147, pp. 149–155, 2000.

[5] Q. Gao *et al.*, "Infrastructure-free relative localization: System modeling, algorithm design, performance analysis, and field tests," *Authorea Preprints*, 1 2024.

Session 7B: Computer vision and control

Decentralized Control of UAV Swarms for Bandwidth-aware Video Surveillance using NMPC

Mohammad Amin Rezaei, Gioacchino Manfredi, Vito Andrea Racanelli, Luca De Cicco, and Saverio Mascolo

I. INTRODUCTION

Unmanned Aerial Vehicles (UAVs), such as multi-rotor drones, are increasingly being employed as mobile flying platforms to carry out several tasks such as photogrammetry, remote sensing, etc. To perform such tasks, UAVs are equipped with a variety of sensors that produce data to be either stored on the UAVs or sent in real-time through a wireless network connection to a Ground Control Station (GCS). A *UAV swarm* is a system of coordinated UAVs designed to carry out a common task collaboratively. On the one hand, swarms improve data acquisition efficiency and accuracy, increase coverage, and ensure operational resilience. On the other hand, swarming requires both (i) providing the UAVs with autonomous capabilities such as path planning and obstacle avoidance and (ii) the design of control strategies to coordinate the UAVs to perform a given task. Specific tasks such as surveillance, object detection, and patrolling, often require to stream in real-time the videos captured by the onboard cameras to a GCS.

In this work, we propose a distributed multi-agent control framework to track a certain path while both trying to maximize the area covered by the cameras and the quality of the videos sent by each agent to the base station according to the available bandwidth. For this purpose, each drone has the possibility of changing its altitude at each time step.

The control methodology adopted to tackle the aforementioned issues is a partially distributed NMPC framework. Moreover, to implement a realistic scenario, each drone is subject to limited control inputs and limited changes in the control inputs.

II. SCENARIO DEFINITION

Consider a swarm of drones equipped with cameras that are required to track a predefined path and monitor an area for a specific purpose. The camera on each drone points vertically to the ground and scans a square area whose width depends on the drone's altitude. The video content captured by the cameras is then sent to a Ground Control Station (GCS) using a network connection such as f.i., a 5G link. Such a station is in charge of receiving in real-time the video flows sent by all the agents and stitching together the frames to obtain a unique video composing the single videos. When a high available bandwidth is measured, the agents can increase their altitude to increase coverage. On the contrary, when the available bandwidth is scarce, they reduce the altitudes to improve the visual quality.

In the described scenario, each drone has two contrasting goals: i) provide a good percentage of overlap among the videos and the best visual quality for each video captured, and ii) increase coverage of the region of interest. To achieve the first goal, each drone would keep a relatively low altitude, consequently implying a decrease in the GSD and increased visual quality. On the other hand, the coverage is improved when the altitude is increased since the cameras mounted on the drones can capture a wider region.

Moreover, to survey the area, a leader drone is chosen to track a predefined path. The other agents are required to catch up with it while keeping a safe distance both from the leader and from the other agents. Notice that the altitude of each drone changes as it moves according to the measured available network bandwidth [1].

A. Problem definition

Let us now introduce the NMPC run at each drone. In particular, a two-state algorithm has been designed to avoid detachments.

The discrete-time dynamics describing the evolution of the state for each drone is assumed to be a simple integrator for simplicity.

$$s_i(k+1) = s_i(k) + T_s u_i(k), \qquad i = 1, \ldots, N \tag{1}$$

where N is the number of agents, $s_i = (x_i, y_i, z_i)^T$ is the vector of the spatial coordinates of agent i, T_s is sampling time, and $u_i = (u_{x,i}, u_{y,i}, u_{z,i})$ is the control input for agent i. Equipped with this notation, the general optimization is in the following form:

$$\begin{aligned}
\underset{u_i}{\text{Minimize}} \quad & \mathcal{J}_i && (2)\\
\text{subject to} \quad & s_i(k+1) = s_i(k) + T_s u_i(k) && (3)\\
& h_{\min} \leq h_i \leq h_{\max} && (4)\\
& \|X_i(t) - X_j(t)\|_2 \geq 2R_{\text{safe}} && (5)\\
& |u_i| \leq u_{\max} && (6)\\
& |\Delta u_i| \leq \Delta u_{\max} && (7)
\end{aligned}$$

where $X_i = (x_i, y_i)^T$ is the 2-D position of the i-th agent, h_i is the drone's altitude, and Δu_i denotes the variation in the input signal.

In the Tracking state (T), there is no risk of detachment and the leader tracks the predefined path. Conversely, when in the Recovery state (S), there is a high risk of detachment, thus the cost function in the NMPC of each agent changes. In this state, the leader does not move. Only when the adequate overlap is reestablished will the system transition back to the Tracking State. In the Tracking state, the cost functions for the leader and the agents are as follows:

TABLE I: Values of the weights in the cost functions of the NMPCs

	w_l	w_p	w_f	w_h	w_u	$w_{\Delta u}$
$\mathcal{J}_{1,T}$	-	1.5	-	5	0.001	0.001
$\mathcal{J}_{i,T}$	0.5	-	-	1.5	0.001	0.001
$\mathcal{J}_{1,S}$	-	-	-	0.5	0.001	0.001
$\mathcal{J}_{i,S}$	1.5	-	0.3	1.5	-	-

$$\mathcal{J}_{1,T} = w_p J_p + w_h J_h + w_u J_u + w_{\Delta u} J_{\Delta u}, \tag{8}$$

$$\mathcal{J}_{i,T} = w_l J_l + w_h J_h + w_u J_u + w_{\Delta u} J_{\Delta u}, \tag{9}$$

J_p is the cost for the path tracking and J_h is the cost for altitude tracking. J_u and $J_{\Delta u}$ are the costs to limit the control effort and the variation in the control input. The cost function $\mathcal{J}_{i,T}$, for $i = 2, \ldots, N$ is related to the other agents for the state T. J_l is the cost to encourage agent i to follow the leader (X_1).

In the Recovery state, the cost functions for the leader and the other agents are as follows:

$$\mathcal{J}_{1,S} = w_h J_h + w_u J_u + w_{\Delta u} J_{\Delta u} \tag{10}$$

$$\mathcal{J}_{i,S} = w_l J_l + w_h J_h + w_f J_f \tag{11}$$

where, $w_p, w_l, w_f, w_h, w_u, w_{\Delta u}$ are weights to be properly tuned, and J_f encurages the agents to keep close to each other. Using simple geometrical arguments, the relationship between R_i and h_i is given by $R_i = h_i \tan(\phi/2)$, where ϕ is the angular aperture of the video camera [2]. Note that the actual communication graph is a complete directed graph since every agent can communicate with any other agent through the Internet connection. Only for J_f, a subgraph with fewer edges is employed to solve issues related to the agents stuck at the lowest altitude and to avoid redundant communication among the agents

To determine the reference height for each agent, we use the following relationship:

$$\bar{h}_i(b) = \begin{cases} h_{\text{min}} & b < b_{\text{min}} \\ S \cdot b + h_{\text{max}} - S \cdot b_{\text{max}} & b_{\text{min}} \leq b \leq b_{\text{max}} \\ h_{\text{max}} & b > b_{\text{max}} \end{cases} \tag{12}$$

where S is defined as $S = (h_{\text{max}} - h_{\text{min}})/(b_{\text{max}} - b_{\text{min}})$.

III. SIMULATIONS

To run the NMPC, we set $N_p = 5$, $N_c = 2$, $R_{\text{safe}} = 2$, $h_{\text{min}} = 4$, and $h_{\text{max}} = 10$. The upper and lower bounds for Δu have been set to 0.1 for all agents. The maximum control signal u in the x and y direction is set to 1 for all the agents except the leader, which is 0.7, whereas in the z direction it has been set to 0.1. Concerning the network available bandwidth, we set it by drawing from a uniform random distribution of bandwidth values over the area to be scanned. Such values are then variable in space but assumed to be constant in time and altitude. We chose to generate random bandwidth between a minimum value of 500 kbit/s and a maximum value of 5000 kbit/s to have a realistic bandwidth profile due to its unpredictability.

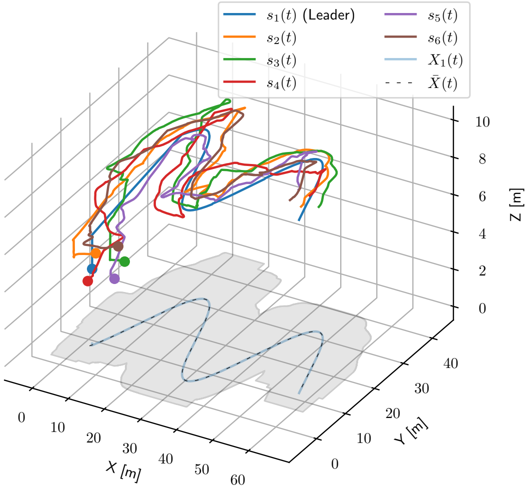

Fig. 1: Drones' trajectories and area covered for $N = 6$

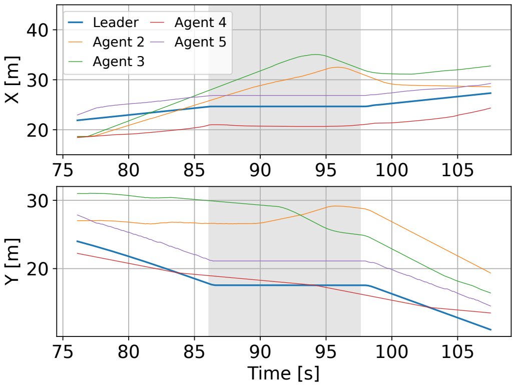

Fig. 2: Agents' coordinates dynamics in the case of a switch between *Tracking* and *Recovery* state

Let us start by considering the case $N = 6$, where the leader is required to track a sine-like path. The drones' trajectories and the area covered by their cameras are shown in Figure 1. It can be seen that the drones, whose initial position is denoted with round markers, strive to follow the leader in the space while sticking together. On the x, y-plane, the reference path for the leader (black dashed line) and the leader's trajectory projection on this plane (light blue line) are depicted. The z-axis represents the altitude of the drones, which is shown to change along the path due to its dependence on the bandwidth.

The switches between the Tracking and Recovery state and their effects on the positions of the agents are illustrated in Figure 2. As one can observe, in the Recovery state (grey area), the lines representing the x and y coordinates of the agents are far from each other. Moreover, the coordinates associated with the leader (blue lines) are constant. After obtaining enough overlap, the system switches to the Tracking state (white areas) as these positions become close to each other.

REFERENCES

[1] G. Carlucci, L. De Cicco, S. Holmer, and S. Mascolo, "Congestion control for web real-time communication," *IEEE/ACM Transactions on Networking*, vol. 25, no. 5, pp. 2629–2642, 2017.

[2] H. Huang, A. V. Savkin, and C. Huang, "Decentralized autonomous navigation of a uav network for road traffic monitoring," *IEEE Transactions on Aerospace and Electronic Systems*, vol. 57, no. 4, pp. 2558–2564, 2021.

Online Minimization of Robot Obstruction in Eye-to-Hand Camera View

G. Cortigiani[1], B. Brogi[1], A. Villani[1], N. D'Aurizio[1,2], D. Prattichizzo[1,2], T. Lisini Baldi[1,2]

***Abstract*— Redundant robots have the potential to perform internal joints motion without modifying the pose of the end-effector by exploiting the null-space of the Jacobian matrix. Capitalizing on that feature, we developed a control technique for minimizing the robot visual appearance when observed from an eye-to-hand camera. Such algorithm is instrumental in contexts where quickly adjusting the perspective to see objects obstructed by the robot is impractical (e.g., teleoperation in narrow environment). Diminished reality techniques are frequently employed in these cases to mitigate the robot intrusion into the environment, although these techniques may sometimes compromise the perceived realism. The experimental evaluation confirmed the effectiveness of our control algorithm, demonstrating an average reduction of 4.67% of the area covered by the robot within the frame when compared to the case without the optimization action.**

I. INTRODUCTION

The challenge of reducing the visual encumbrance of robots is critical in several domains. In teleoperation within unstructured environments, visual encumbrance can hinder performance [1]. Additionally, in visual servoing applications, vision occlusions can result in control failures [2]. Other scenarios include individuals with disabilities who rely on robots to mitigate their limitations [3]. Indeed, visual perception is one of the most fundamental aspects that affects the quality and accomplishment of teleoperation tasks [4].

This work aims at dynamically reducing the impact of the robot in the user's field of view proposing a control algorithm that minimizes the robot silhouette in a eye-to-hand configuration. In particular, achieving this objective involves leveraging the manipulator redundancy to optimize the robot pose while maintaining the desired pose of the end-effector. The null space of the Jacobian matrix is exploited to minimize the number of pixels in the camera framing that contains portions of the robot silhouette, and, at the same time, maximize the distance from the joint limits to keep the primary task (i.e., accomplish a desired trajectory) feasible. Fig. 1 visually summarizes this concept, whereas a more detailed description can be found in [5].

II. ROBOT CONTROL ALGORITHM

The algorithm developed with this work approximates the area of the robot to the cumulative length of the links projected onto the camera plane. More precisely, the distances between the consecutive projected joints are summed, leading to the following function:

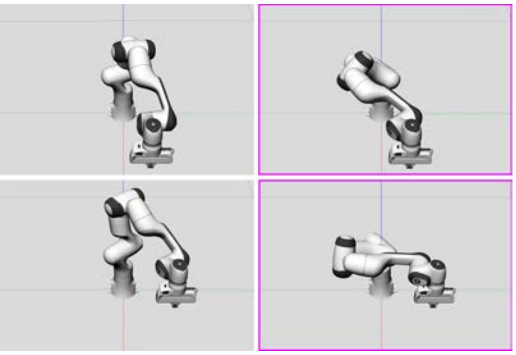

Fig. 1: Two key time instants taken from the execution of a representative end-effector trajectory performed with (right column) and without (left column) the action of the control algorithm minimizing the robot silhouette in the eye-to-hand camera framing. Throughout the trajectory execution, the algorithm actively reduces the robot visibility while maintaining the end-effector pose along the desired path.

$$F_l(\boldsymbol{q}) = \sum_{i=1}^{n-1} \sqrt{(\hat{x}_{i+1} - \hat{x}_i)^2 + (\hat{y}_{i+1} - \hat{y}_i)^2},$$

where $(\hat{x}_i, \hat{y}_i)$ is the position of joint i projected on the camera plane. In a more practical interpretation, this method minimizes the lengths of the link projections, encouraging the links to be oriented along the direction in which the camera is pointing. Starting from this, we can define the cost function $C_l(\boldsymbol{q})$:

$$C_l(\boldsymbol{q}) = \alpha_l F_l(\boldsymbol{q}) + \beta L(\boldsymbol{q})$$

where α_l and β are scaling factors that appropriately weigh each contribution to the overall cost. The term $L(\boldsymbol{q})$ is added to the cost function to prevent the robot from reaching the joint limits during its movement, and it is defined as:

$$L(\boldsymbol{q}) = \sum_{i=1}^{n} \left(\frac{1}{w_M - w(q_i)} - \frac{1}{w_M} \right).$$

Following the approach described in [6], we define the normalized distance from the mechanical joint limits as:

$$w(q_i) = \left(\frac{q_i - \bar{q}_i}{q_{iM} - q_{im}} \right)^2 \tag{1}$$

where q_{iM} and q_{im} represent the upper and lower joint limits, respectively, while $\bar{q}_i$ denotes the midpoint of the joint range. The term $w_M = \frac{1}{4}$ is the maximum value that Eq. (1) can assume. Consequently, maximizing the distance of the joints from the limits guarantees that the robot motion is feasible. The resulting cost C_l is meant to be a differentiable function that approximates the characteristics of the projected robot area, while also adjusting potential joint limit violations.

The robot is then controlled according to the following equation:

$$\dot{\boldsymbol{q}} = \boldsymbol{J}^{\dagger}(\dot{\boldsymbol{r}}_d + \boldsymbol{K}\boldsymbol{e}) - (\boldsymbol{I} - \boldsymbol{J}^{\dagger}\boldsymbol{J})\nabla_{\boldsymbol{q}} C_l(\boldsymbol{q})$$

The research leading to these results has received funding from the European Union's Horizon Europe programme under grant agreement No. 101070292 of the project "HARIA - Human-Robot Sensorimotor Augmentation". This work was also supported by the Leonardo S.p.A. under Grant LDO/CTI/P/0025793/22.

[1] are with the Department of Information Engineering and Mathematics, University of Siena, Via Roma 56, 53100 Siena, Italy. {cortigiani, brogi, villani, lisini, ndaurizio, prattichizzo}@diism.unisi.it

[2] are with the department of Humanoids and Human Centered Mechatronics, Istituto Italiano di Tecnologia, Genova, Italy.

where $\dot{\boldsymbol{q}}$ are the desired joint velocities, $\dot{\boldsymbol{r}}_d$ is the vector containing the desired end-effector linear and angular velocities, $\boldsymbol{J}$ is the Jacobian matrix of the robot, $(\cdot)^\dagger$ is the pseudo-inverse operator, $\boldsymbol{e}$ is the error of the end-effector pose, $\boldsymbol{K}$ is a positive definite matrix that ensures the error convergence, and $(\boldsymbol{I}-\boldsymbol{J}^\dagger\boldsymbol{J})$ is the projector on the null space of the Jacobian matrix. The projected joint velocities do not contribute to the end-effector motion. Therefore, they can be utilized to accomplish a secondary task while guaranteeing the accurate execution of the primary task, i.e., tracking the desired end-effector trajectory.

III. EXPERIMENTAL EVALUATION

A. Correlation Analysis

As a first step, we experimentally assessed if the cost function is suitable for approximating the area of the robot projected onto the camera image plane. To this end, we performed a correlation analysis to determine whether there exists a monotonic relation between the output of the candidate functions $F_l(\boldsymbol{q})$ and the area of the robot silhouette in the framing (expressed as number of pixels). A virtual environment was used to collect data for the correlation analysis. The virtual scene comprised a digital Franka Emika Research 3 Robot and a virtual camera. We tested the correlation by collecting data from three different points of view (Camera 1, Camera 2, and Camera 3). For each condition, we moved the robot in approximately 1.2×10^7 different poses, and, for each pose, we computed the number of pixels projected onto the camera image plane following the methodology described in [7]. For each virtual camera, a Spearman's rank-order correlation test was run to assess the relationship between number of pixels of the robot on the camera image plane and the output of the function $F_l(\boldsymbol{q})$. Resulting correlation factors ($\rho_1 = 0.743$, $\rho_2 = 0.763$, and $\rho_3 = 0.643$) showed a strong correlation for Camera 1 and Camera 2, and a moderate correlation for Camera 3.

B. Minimization Analysis

To test the effectiveness of the control algorithm that minimizes the robot silhouette in the framing by exploiting the cost function based on the link-based method, we simulated four different trajectories using Gazebo and ROS. More precisely, the four trajectories are:

- **T1:** Planar Lissajous Path in the x-y plane with a duration of 20 seconds.
- **T2:** Planar Lissajous Path in the x-y plane with a duration of 30 seconds.
- **T3:** Pouring Trajectory with a duration of 23 seconds.
- **T4:** Pick and Place Trajectory with a duration of 14 seconds.

T1 and T2 delineate paths challenging to be followed due to the differences in curvature and velocity at every point, while T3 and T4 were selected to exemplify real world tasks of a teleoperation scenario. Each trajectory was executed four times: once without the minimization algorithm, and three times with the scene recorded from each of the three different points of view mentioned in Sect. III-A.

Outcomes of the experiments reveal an average reduction of 4.67% in the robot area visible from the camera, with significant variability contingent upon the camera configuration. Specifically, we observe an average reduction of 4.21%, 1.00%, and 8.8% considering Camera 1, Camera 2, and Camera 3, respectively. Concerning T1 and T2, it is worth noting how, on average, T2 presents a more substantial reduction, even though T1 and T2 describe the same path. This is attributed to the longer duration of T2, which gives the robot ample time for reconfiguration into a more advantageous pose.

The influence of the camera configuration on the minimization performance can be attributed to a combination of factors, including the robot task space location and the extrinsic camera parameters. For instance, Camera 2 was positioned laterally and orthogonally to the task space of the robot. Hence, its pose made the achievement of effective minimization along the trajectory challenging. Furthermore, in such configuration, the link section dimensions could also be less negligible.

In the specific case T3 with Camera 2, we observed a negligible average increase in the exposed robot area (+0.16%) compared to the baseline. This lack of improvement can be attributed to the nature of the algorithm as an online optimization method, which tries to optimize the robot pose in a real-time manner without knowledge of future desired positions. Consequently, it initiated a reconfiguration that minimized the area during the first time intervals. However, this subsequently resulted in the robot assuming a less advantageous posture, with no further improvements afterwards. Additionally, the method discourages the robot from operating too close to its joint limits. Therefore, in scenarios where the desired trajectory approaches these limits, the algorithm encourages the robot to exploit its null space to move away from the limits rather than prioritizing the reduction of the robot area.

IV. CONCLUSIONS AND FUTURE WORK

We presented a novel methodology aimed at minimizing the visual footprint of a robotic arm as captured by a camera.

In contrast to approaches based on multiple or controllable cameras, the proposed method only relies on the kinematic control of the robotic arm, thus it can be easily adapted to various setups and scenarios. Additionally, the cost function explicitly depends on the camera pose, which allows for minimization even when the camera moves during the trajectory. In forthcoming studies, we intend to explore an objective function that incorporates the three-dimensional characteristics of the links and considers the boundaries of the image plane. We will also thoroughly analyse how the variation of camera and robot workspace influence the minimization algorithm. Moreover, we will focus on selecting regions or objects within the image that should experience minimal occlusion.

REFERENCES

[1] M. Kamezaki *et al.*, "Visibility enhancement using autonomous multicamera controls with situational role assignment for teleoperated work machines," *Journal of Field Robotics*, vol. 33, no. 6, pp. 802–824, 2016.

[2] D. Nicolis *et al.*, "Occlusion-free visual servoing for the shared autonomy teleoperation of dual-arm robots," *IEEE Robotics and Automation Letters*, vol. 3, no. 2, pp. 796–803, 2018.

[3] C.-S. Chung *et al.*, "Functional assessment and performance evaluation for assistive robotic manipulators: Literature review," *The journal of spinal cord medicine*, vol. 36, no. 4, pp. 273–289, 2013.

[4] L. Almeida *et al.*, "Interface transparency issues in teleoperation," *Applied Sciences*, vol. 10, no. 18, p. 6232, 2020.

[5] G. Cortigiani *et al.*, "Online minimization of the robot silhouette viewed from eye-to-hand camera," in *2024 IEEE International Conference on Robotics and Automation (ICRA)*, 2024, pp. 17 793–17 799.

[6] B. Siciliano *et al.*, *Robotics: Modelling, Planning and Control*. Springer Publishing Company, Incorporated, 2010.

[7] A. Villani *et al.*, "Avatarm: an avatar with manipulation capabilities for the physical metaverse," in *2023 IEEE International Conference on Robotics and Automation (ICRA)*, 2023, pp. 11 626–11 632.

Homography-Based Sampled-Data Visual Servoing

Marco Costanzo, Giuseppe De Maria, and Ciro Natale

◆

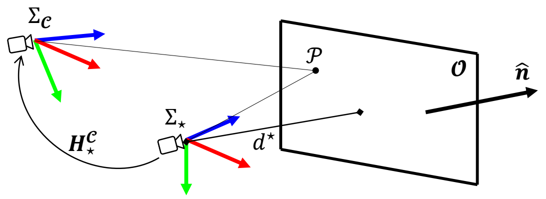

Fig. 1. Current $\Sigma_{\mathcal{C}}$ and desired $\Sigma_{\star}$ camera frames in standard RGB notation. $\mathcal{P}$ is the generic point on the planar object $\mathcal{O}$.

1 INTRODUCTION

Position-Based Visual Servoing (PBVS) and Image-Based Visual Servoing (IBVS) are well-established strategies for visual control [1], [2]. Most of visual servoing schemes use a redundant number of features, and thus their convergence cannot be global [1]. To overcome these drawbacks an approach based on the estimation of the camera displacement between the current and the desired views of a scene has been introduced in [3]. The approach is based on the homography matrix, which contains the Euclidean information between two views of a planar scene. The main results on homography-based control schemes are formulated in the continuous time domain. Due to the limited camera frame rate, actuation delay, and computation time, the intrinsic sampled-data nature of such control schemes should be taken into account. This abstract shows the main result of our recent work [4], where we propose an exact sampled-data model of the homography dynamics and an adaptive visual controller that directly uses the homography matrix and explicitly takes into account camera velocity limits ensuring global asymptotic stability at the same time.

2 SAMPLED DATA MODEL

With reference to Fig. 1, consider a planar object $\mathcal{O}$ and a moving camera identified by the frame $\Sigma_{\mathcal{C}}$. Let $\widehat{\boldsymbol{n}}$ be the unit vector perpendicular to $\mathcal{O}$, $\Sigma_{\star}$ the desired camera frame, and $d^{\star}$ the distance between the origin of $\Sigma_{\star}$ and $\mathcal{O}$. The Homography $\boldsymbol{H}_{\star}^{\mathcal{C}}$ relates the displacement between the view of the camera located in $\Sigma_{\star}$ with the one of the camera located in $\Sigma_{\mathcal{C}}$. Since all the object points belong to the plane with equation $\widehat{\boldsymbol{n}}^{\star\top}\left[x^{\star} y^{\star} z^{\star}\right]^{\top} = d^{\star}$, it holds that

$$\begin{bmatrix} x^{\mathcal{C}} & y^{\mathcal{C}} & z^{\mathcal{C}} \end{bmatrix}^{\top} = \boldsymbol{H}_{\star}^{\mathcal{C}} \begin{bmatrix} x^{\star} & y^{\star} & z^{\star} \end{bmatrix}^{\top}, \tag{1}$$

where $\begin{bmatrix} x^{\mathcal{C}} & y^{\mathcal{C}} & z^{\mathcal{C}} \end{bmatrix}^{\top}$ and $\begin{bmatrix} x^{\star} & y^{\star} & z^{\star} \end{bmatrix}^{\top}$ are the coordinates of the generic point $\mathcal{P}$ referred to the frame $\Sigma_{\mathcal{C}}$ and $\Sigma_{\star}$, respectively, and being $\boldsymbol{H}_{\star}^{\mathcal{C}}$ the well-known homography matrix, [5], which, in view of the plane equation above, can be related to the rotation $\boldsymbol{R}_{\star}^{\mathcal{C}}$ and translation $\boldsymbol{t}_{\star,\mathcal{C}}^{\mathcal{C}}$ of $\Sigma_{\star}$ with respect to $\Sigma_{\mathcal{C}}$ as

$$\boldsymbol{H}_{\star}^{\mathcal{C}}(t) = \boldsymbol{R}_{\star}^{\mathcal{C}}(t) + \boldsymbol{t}_{\star,\mathcal{C}}^{\mathcal{C}}(t)\boldsymbol{n}^{\star\top}, \tag{2}$$

where, by denoting with $\widehat{\boldsymbol{n}}^{\star}$ the vector $\widehat{\boldsymbol{n}}$ expressed in the frame $\Sigma_{\star}$, $\boldsymbol{n}^{\star} = \widehat{\boldsymbol{n}}^{\star}/d^{\star}$.

By assuming to control the velocity of the camera by means of an ideal Cartesian velocity generator, we can obtain the relation between the camera velocity and the homography matrix by deriving (2) with respect to the time t

$$\dot{\boldsymbol{H}}_{\star}^{\mathcal{C}}(t) = \boldsymbol{S}^{\top}(\boldsymbol{\omega}_{\mathcal{C},\star}^{\mathcal{C}}(t))\boldsymbol{H}_{\star}^{\mathcal{C}} - \mathbf{v}_{\mathcal{C},\star}^{\mathcal{C}}(t)\boldsymbol{n}^{\star\top}, \tag{3}$$

where $\boldsymbol{S}(\cdot)$ is the 3D skew-symmetric matrix operator such that $\boldsymbol{S}(\boldsymbol{x})\boldsymbol{y} = \boldsymbol{x} \times \boldsymbol{y}$, and $\mathbf{v}_{\mathcal{C},\star}^{\mathcal{C}}$ ($\boldsymbol{\omega}_{\mathcal{C},\star}^{\mathcal{C}}$) is the linear (angular) velocity of the frame $\Sigma_{\mathcal{C}}$ with respect to the frame $\Sigma_{\star}$ expressed in the frame $\Sigma_{\mathcal{C}}$.

In this work, we explicitly consider the sampled-data nature of the control scheme. To this aim, it is interesting to note that, with reference to the sampling time interval $[kT, (k+1)T)$, the nonlinear system (3) can be written as

$$\dot{\boldsymbol{H}}(t) = \boldsymbol{S}^{\top}(\boldsymbol{\omega}_k)\boldsymbol{H}(t) - \mathbf{v}_k\boldsymbol{n}^{\top}, \ \boldsymbol{H}(kT) = \boldsymbol{H}_k \tag{4}$$

where the control input $\boldsymbol{v}_k = \begin{bmatrix} \mathbf{v}_k^{\top} & \boldsymbol{\omega}_k^{\top} \end{bmatrix}^{\top}$ is kept constant, and $\boldsymbol{H}_k$ is the initial condition at $t = kT$. Defining the function

$$\boldsymbol{P}(\boldsymbol{\omega}, t) = \int_0^t \boldsymbol{e}^{\boldsymbol{S}^{\top}(\boldsymbol{\omega})\sigma}\,\mathrm{d}\sigma, \tag{5}$$

and expanding the exponential matrices in power series, it is possible to write the homography time evolution

$$\boldsymbol{H}(t) = \boldsymbol{H}_k + \boldsymbol{P}(\boldsymbol{\omega}_k, t-kT)\left[\boldsymbol{S}^{\top}(\boldsymbol{\omega}_k)\boldsymbol{H}_k - \mathbf{v}_k\boldsymbol{n}^{\top}\right], \tag{6}$$

which is the homography matrix time evolution, within the sampling interval $[kT, (k+1)T)$, starting from the initial condition $\boldsymbol{H}_k$ and subject to a constant input $\boldsymbol{v}_k$. In order to study the visual servoing problem, it is useful to refer, instead of the homography state space, to the homography error space, i.e. $\boldsymbol{E} = \boldsymbol{H} - \boldsymbol{I}_3$. This way the desired equilibrium point is $\boldsymbol{E} = \boldsymbol{0}_3$, being $\boldsymbol{0}_3$ the 3×3 zero matrix.

Within the sampling interval, it holds that

$$\dot{\boldsymbol{E}}(t) = \boldsymbol{S}^{\top}(\boldsymbol{\omega}_k)(\boldsymbol{E}(t) - \boldsymbol{I}_3) - \mathbf{v}_k\boldsymbol{n}^{\top} \tag{7}$$

$$\boldsymbol{E}(t) = \boldsymbol{E}_k + \boldsymbol{P}(\boldsymbol{\omega}_k, t-kT)\left[\boldsymbol{S}^{\top}(\boldsymbol{\omega}_k)(\boldsymbol{E}_k + \boldsymbol{I}_3) - \mathbf{v}_k\boldsymbol{n}^{\top}\right] \tag{8}$$

where the initial condition is $\boldsymbol{E}(kT) = \boldsymbol{E}_k = \boldsymbol{H}_k - \boldsymbol{I}_3$.

3 CLOSED-LOOP CONTROL SCHEME

The proposed control law has the same structure as in [5]

$$\mathbf{v}_k = \mathrm{k}_{pk}\boldsymbol{E}_k\boldsymbol{n}, \quad \boldsymbol{\omega}_k = \mathrm{k}_{rk}\boldsymbol{\omega}_k^1, \ \text{with} \tag{9}$$

$$\boldsymbol{\omega}_k^1 = \mathrm{vex}(\boldsymbol{A}_k), \ \boldsymbol{A}_k = \boldsymbol{E}_k - \boldsymbol{E}_k^{\top}. \tag{10}$$

The main difference with the procedures already proposed in the literature is that the control gains k_{pk} and k_{rk} are adapted at each sampling instant kT in order to guarantee asymptotic stability.

The authors are with the Dipartimento di Ingegneria, Università degli Studi della Campania Luigi Vanvitelli, 81031 Aversa (CE), Italy e-mail: {marco.costanzo, giuseppe.demaria, ciro.natale}@unicampania.it.

In order to study the time evolution of the error within $[kT,(k+1)T)$, let $\boldsymbol{P}_k(\cdot)=\boldsymbol{P}(\boldsymbol{\omega}_k^1,\cdot)$, we can write the closed-loop error system as

$$\boldsymbol{E}(t)=\boldsymbol{E}_k-\boldsymbol{P}_k(\mathrm{k}_{rk}(t-kT))\left[\boldsymbol{A}_k(\boldsymbol{E}_k+\boldsymbol{I}_3)+\frac{\mathrm{k}_{pk}}{\mathrm{k}_{rk}}\boldsymbol{E}_k\boldsymbol{n}\boldsymbol{n}^\top\right]. \tag{11}$$

Note that, in (11), the time t is multiplied by the rotational gain k_{rk}, thus the system trajectory in the error space depends only on the initial condition $\boldsymbol{E}_k$ and the gain ratio $\frac{\mathrm{k}_{pk}}{\mathrm{k}_{rk}}$, while the time axis is just scaled by k_{rk}. Given this reasoning, we propose the following change of variables

$$\gamma_k=\mathrm{k}_{rk}(t-kT), \quad \alpha_k=\frac{\mathrm{k}_{pk}}{\mathrm{k}_{rk}}. \tag{12}$$

With this choice γ_k is the new time variable, it is a scaled time with the coefficient k_{rk}. Thus, we can define the function

$$\tilde{\boldsymbol{E}}(\gamma)=\boldsymbol{E}(\gamma/\mathrm{k}_{rk}+kT) \tag{13}$$

which is the error evolution in the scaled time γ. It holds that

$$\left.\frac{\mathrm{d}}{\mathrm{d}\gamma}\tilde{\boldsymbol{E}}(\gamma)\right|_{\gamma=\mathrm{k}_{rk}(t-kT)}=\dot{\boldsymbol{E}}(t)/\mathrm{k}_{rk} \tag{14}$$

$$\left.\frac{\mathrm{d}}{\mathrm{d}\gamma}\tilde{\boldsymbol{E}}(\gamma)\right|_{\gamma=\gamma_k}=\boldsymbol{A}_k^\top(\tilde{\boldsymbol{E}}(\gamma_k)-\boldsymbol{I}_3)-\alpha_k\boldsymbol{E}_k\boldsymbol{n}\boldsymbol{n}^\top \tag{15}$$

$$\tilde{\boldsymbol{E}}(\gamma_k)=\boldsymbol{E}_k-\boldsymbol{P}_k(\gamma_k)\left[\boldsymbol{A}_k(\boldsymbol{E}_k+\boldsymbol{I}_3)+\alpha_k\boldsymbol{E}_k\boldsymbol{n}\boldsymbol{n}^\top\right]. \tag{16}$$

We want to prove that the error norm time derivative is negative in the sampling time interval $(kT,(k+1)T)$. In the new variables γ_k and α_k, this is equivalent to the following condition

$$\mathcal{F}(\gamma_k,\alpha_k)=\frac{1}{2}\left.\frac{\mathrm{d}}{\mathrm{d}\gamma}\left\|\tilde{\boldsymbol{E}}(\gamma)\right\|_{\mathrm{F}}^2\right|_{\gamma=\gamma_k}<0,\ \forall\gamma_k\in(0,\mathrm{k}_{rk}T). \tag{17}$$

The following lemma holds.

Lemma 1. Consider $\mathcal{F}(\gamma_k,\alpha_k)$ in (17), it holds that $\forall\boldsymbol{E}_k\neq\boldsymbol{0}_3,\ \forall\alpha_k>0,\ \exists\bar{\gamma}_k>0\mid\mathcal{F}(\gamma_k,\alpha_k)<0,\ \forall\gamma_k\in(0,\bar{\gamma}_k)$

We are now ready to state the main result of this work.

Theorem 1. Consider the system (3) where the control $\boldsymbol{v}(t)=\begin{bmatrix}\mathbf{v}^\top(t) & \boldsymbol{\omega}^\top(t)\end{bmatrix}^\top$ is kept constant for $t\in[kT,(k+1)T)$ at the values in (9). Select $\gamma_k^\star$, $\alpha_k^\star$ satisfying Lemma 1, i.e.

$$\mathcal{F}(\gamma_k^\star,\alpha_k^\star)\leq 0, \tag{18}$$

if the control gains $\mathrm{k}_{pk},\mathrm{k}_{rk}>0$ are selected to satisfy

$$\gamma_k^\star=\mathrm{k}_{rk}T, \quad \alpha_k^\star=\mathrm{k}_{pk}/\mathrm{k}_{rk}, \tag{19}$$

then the equilibrium $\boldsymbol{H}=\boldsymbol{I}_3$ is globally asymptotically stable.

Theorem 1 provides sufficient conditions for the global asymptotic stability of the visual control scheme, but the performances in terms of rate of convergence and camera velocity constraints are not taken into account. This can be done by selecting the control parameters $\gamma_k^\star$ and $\alpha_k^\star$ in order to maximize the performances of the closed-loop system. This can be pursued by solving the following optimization problem at each sampling instant $t=kT$:

$$\underset{\gamma_k,\,\alpha_k}{\arg\min}\ \left[\Delta V(\gamma_k,\alpha_k)+\beta(\gamma_k^2+\alpha_k^2)\right] \tag{20a}$$

$$\text{s.t. } \mathcal{F}(\gamma_k,\alpha_k)\leq 0 \tag{20b}$$

$$0<\gamma_k\leq\frac{\omega_M T}{\|\boldsymbol{A}_k\|_2}, \quad 0<\alpha_k\gamma_k\leq\frac{\mathrm{v}_M T}{\|\boldsymbol{E}_k\boldsymbol{n}\|} \tag{20c}$$

where

$$\Delta V(\gamma_k,\alpha_k)=\left\|\tilde{\boldsymbol{E}}(\gamma_k)\right\|_{\mathrm{F}}^2-\|\boldsymbol{E}_k\|_{\mathrm{F}}^2. \tag{21}$$

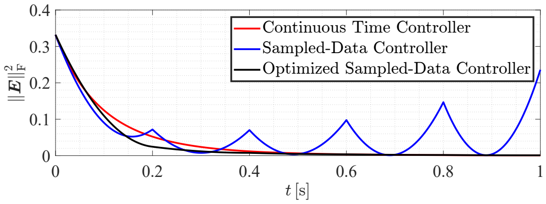

Fig. 2. Error norm trajectory obtained by using a continuous-time controller (red), a constant gains sampled-data controller (blue), and the proposed optimized sampled-data controller (black).

4 NUMERICAL EXPERIMENTS

Fig. 2 shows the results of three simulations carried out by selecting the initial condition $\boldsymbol{R}_\star^{\mathcal{C}}=\boldsymbol{R}_y(6^\circ)\boldsymbol{R}_z(20^\circ)$, and $\boldsymbol{t}_{\star,\mathcal{C}}^{\mathcal{C}}=\begin{bmatrix}-0.15 & 0 & -0.1\end{bmatrix}^\top$ m. The regularization term is set with $\beta=0.5\cdot 10^{-4}$. The red curves show the results carried out by adopting a continuous-time controller with constant gains $\mathrm{k}_p=4.23$ and $\mathrm{k}_r=2.28$, selected such that the resulting velocities are below the imposed camera velocity limits $\mathrm{v}_M=1.2\,\mathrm{m/s}$ and $\omega_M=\pi/2\,\mathrm{rad/s}$. By utilizing the same constant gains selected in the continuous-time controller, the simulation has been repeated by considering the realistic sample-data scenario with a sampling frequency of 5 Hz (blue curve). Note that with such a choice the equilibrium point $\boldsymbol{E}=\boldsymbol{0}_3$ is unstable and the velocity increases above the desired limits. Finally, the black curves show the results obtained with the proposed sampled-data adaptive controller. The performance si better than the continuous-time controller design, in terms of manoeuvre execution speed while satisfying stability and velocity constraints.

5 CONCLUSION

This abstract presented an HBVS control scheme that explicitly uses the homography matrix in the controller design and considers the intrinsic sampled-data nature of the visual control system. By solving a constrained optimization problem, the proposed controller can automatically select the control gains, at each sampling instant, that ensure the global asymptotic stability of the closed-loop system. This is possible since, in each sampling interval, the sampled-data system is linear and the homography dynamics time evolution can be written explicitly. Thus, the stability constraint can be written in terms of the time evolution of the Frobenius norm of the homography error. We proved that translational and rotational control gains always exist that ensure global asymptotic stability. The optimization algorithm, demonstrated to be feasible, finds the best control gains that maximize the execution speed of the approaching manoeuvre to the target pose while satisfying the camera velocity constraints.

REFERENCES

[1] F. Chaumette and S. Hutchinson, “Visual servo control, Part I: Basic approaches,” *IEEE Robotics and Automation Magazine*, vol. 13, no. 4, pp. 82–90, 2006.

[2] F. Chaumette and S. Hutchinson, “Visual servo control, Part II: Advanced approaches,” *IEEE Robotics and Automation Magazine*, vol. 14, no. 1, pp. 109–118, 2007.

[3] E. Malis, F. Chaumette, and S. Boudet, “2 1/2 d visual servoing,” *IEEE Trans. Robot. Autom.*, vol. 15, no. 2, pp. 238–250, 1999.

[4] M. Costanzo, G. D. Maria, and C. Natale, “Homography-based sampled-data visual servoing,” *IEEE Control Systems Letters*, vol. 8, pp. 754–759, 2024.

[5] S. Benhimane and E. Malis, “Homography-based 2d visual tracking and servoing,” *The International Journal of Robotics Research*, vol. 26, no. 7, pp. 661–676, 2007.

Session 7C: Education

Deep Learning-Based Feature Extraction for Robust Visual SLAM in Challenging Indoor Environments

Marco Legittimo[1], Francesco Crocetti[1], Giuseppe Mollica[2], Mario Luca Fravolini[1],
Gabriele Costante[1], Paolo Valigi[1]

***Abstract*— Autonomous robot navigation relies on its ability to understand its environment for localization, typically using a Visual Simultaneous Localization And Mapping (V-SLAM) algorithm that processes image sequences. In this work, we propose LF^{2}SLAM, "Learned Features For SLAM", a hybrid method for navigation in challenging indoor scenarios, like low-light conditions. It integrates a robust data-driven feature extraction within a classic geometric VO estimation pipeline. In particular, we train a deep neural network for feature extraction and integrate it into one of the most used state-of-the-art algorithms: ORBSLAM3. We developed a novel loss function employing a binary mask for filtering the informative features. The experimental evaluation shows that our approach has remarkable generalization capabilities in scenarios that differ from those used for training.**

SUPPLEMENTARY MATERIAL

Code: github.com/isarlab-department-engineering/LFFS

I. INTRODUCTION

Vision-based algorithms like VSLAM and VO have gained traction in robotics due to decreasing sensor costs and size [1], [2]. While state-of-the-art methods like ORB-SLAM3 and DSO demonstrate effectiveness, their hand-crafted feature extractors lack robustness in non-ideal conditions [3], [4], [5]. Hybrid methods, combining CNN feature extraction with geometric models, have addressed this issue [6], [7], [8], [9]. However, their potential in challenging environments is still underexplored. We propose LF^{2}SLAM, a novel approach leveraging the Superpoint feature extractor and Monodepth2's image warping framework [10]. An image reconstruction loss is introduced to promote learning of pose-specific sparse features. The learned extractor then replaces ORB in ORBSLAM3.

II. METHODOLOGY

Our algorithm leverages the Superpoint algorithm (SP) [11], adapting it to extract sparse keypoints and descriptors within an image for pose estimation purposes. Specifically, we combine the Superpoint network with the Monodepth2 [10] (MD2) framework: SP is a CNN that extracts sparse features in an image. It consists of an Encoder-Decoder architecture in which only the Encoder layers have learnable parameters. To train the SP network to estimate features suitable for VO purposes, we integrate it within the MD2 training framework. This is achieved by modifying the original photometric loss used in MD2 as the sum of three components:

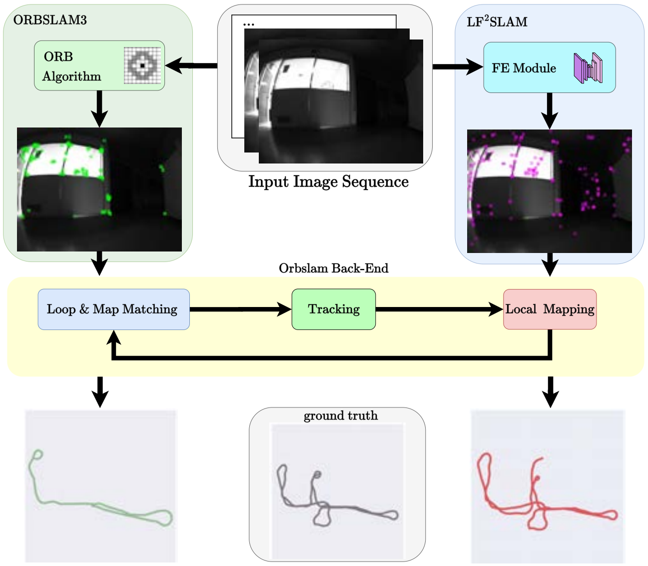

Fig. 1: Comparison between the hybrid LF^{2}SLAM and the state-of-the-art ORBSLAM3 approaches: LF^{2}SLAM achieves better performances than the ORB geometric algorithm in low light environments.

$$\mathcal{L} = \alpha\mathcal{L}_{SP} + \beta\mathcal{L}_{sparse} + \gamma\mathcal{L}_{SPconst} \ , \tag{1}$$

where $\mathcal{L}_{SP}$ embeds the original photometric loss including the keypoints masks computed from the SP network, $\mathcal{L}_{sparse}$ and $\gamma\mathcal{L}_{SPconst}$ are two regularization terms for forcing the training to select a number of feature points close to an assigned desired value and for imposing that the extracted keypoints should not excessively deviate from those computed by the original SP model [11]. After optimization, the learned sparse feature extractor is integrated into ORB-SLAM3, replacing the ORB algorithm and leveraging the monocular configuration.

III. EXPERIMENTAL SETUP

To assess the accuracy of the estimates of the two algorithms, we employ a summary metric S defined as:

$$S = \begin{cases} \frac{ATE+ARE}{R_{traj}^2}, \ if \ \ 0 < R_{traj} < 1 \\ R_{traj}^2(ATE + ARE), \ if \ \ R_{traj} \geq 1 \end{cases} \tag{2}$$

---

[1] The authors are with the Department of Engineering, University of Perugia, 06125 Perugia, Italy. `email:{francesco.crocetti, gabriele.costante, marco.legittimo, mario.fravolini, paolo.valigi}@unipg.it`.

[2] The author is with ART Spa, Voc. Pischiello, 20 - 06065 Passignano sul Trasimeno. `email:giuseppe.mollica@artgroup-spa.com`

This work was in part supported by Fondazione Cassa di Risparmio di Perugia - Project: DEIMOS - "droni ecologici intelligenti per il monitoraggio di oliveti sostenibili"

Fig. 2: **UNILAB dataset**: examples of challenging sequences acquired with a ground robot in low-light and poor-texture environments.

that relies on the Absolute Translation Error (ATE), Absolute Position Error (APE), and the trajectory length ratio R_{traj} between the estimated and the ground truth trajectories. We selected EuRoC [12] and the KITTI [13] as reference datasets, and we collected four challenging indoor sequences X1, X2, B1, and C1 with non-ideal lighting conditions using a ground robot in three different indoor areas of the University Department. Figure 2 shows some frames extracted from the experimental dataset dataset.

IV. RESULTS AND DISCUSSIONS

In Table I, the experiments on the sequences are performed with the best hyperparameter combination found in each dataset. The analysis of the results highlights that LF^{2}SLAM outperforms OS3 in the KITTI/09 sequence and the UNILAB more challenging sequences. Conversely, our approach shows comparable performances on the EuRoC dataset. While the LF^{2}SLAM better performance on the KITTI dataset is expected since our feature extractor is trained with images from sequences of the same scenario, more interesting considerations can be drawn by observing the results on EuRoC. Despite our approach being tested on a scenario different from that used for training, it exhibits comparable performance to OS3, which proves its generalization capabilities. The quantitative performance on the UNILAB dataset, instead, demonstrates that the proposed LF^{2}SLAM achieves considerably higher scores compared to the OS3 baseline. These results are remarkable considering the more challenging sequences of this dataset, characterized by sudden light changes and texture-less scenarios. While our approach exploits the convolutional feature extraction to achieve robustness against these conditions, OS3 frequently loses track due to the poor extracted keypoints.

V. CONCLUSIONS AND FUTURE DIRECTION

This paper introduces LF^{2}SLAM, a hybrid framework for VSLAM. It uses a unique training method to extract features for image-based pose estimation. Once trained, it was integrated into the OS3 pipeline. The approach shows excellent generalization across various environments and outperforms the OS3 baseline in challenging conditions. Future work will focus on improving binary descriptor estimation and optimizing for extreme conditions.

TABLE I: Results on KITTI, EuRoC, and UNILAB.

Dataset	Sequence	ORBSLAM3	LF^{2}SLAM
KITTI	09	43.32	**9.62**
EuRoC	MH_02	**1.845**	1.944
	MH_03	**1.729**	1.836
	MH_04	**1.523**	2.369
	MH_05	**1.942**	1.983
	V1_01	**5.923**	7.767
	V1_02	**1.429**	1.904
	V1_03	**2.241**	4.005
	V2_01	13.77	**2.702**
	V2_02	**1.284**	1.702
	V2_03	**3.730**	13.02
UNILAB	B1	5.651	**2.627**
	C1	7.356	**3.989**
	X2	58.18	**4.151**

REFERENCES

[1] K. Yousif, A. Bab-Hadiashar, and R. Hoseinnezhad, “An overview to visual odometry and visual slam: Applications to mobile robotics,” *Intelligent Industrial Systems*, vol. 1, no. 4, pp. 289–311, 2015.

[2] L. R. Agostinho, N. M. Ricardo, M. I. Pereira, A. Hiolle, and A. M. Pinto, “A practical survey on visual odometry for autonomous driving in challenging scenarios and conditions,” *IEEE Access*, vol. 10, pp. 72 182–72 205, 2022.

[3] C. Campos, R. Elvira, J. J. G. Rodríguez, J. M. Montiel, and J. D. Tardós, “Orb-slam3: An accurate open-source library for visual, visual–inertial, and multimap slam,” *IEEE Transactions on Robotics*, vol. 37, no. 6, pp. 1874–1890, 2021.

[4] J. Engel, V. Koltun, and D. Cremers, “Direct sparse odometry,” *IEEE transactions on pattern analysis and machine intelligence*, vol. 40, no. 3, pp. 611–625, 2017.

[5] N. Yang, R. Wang, and D. Cremers, “Feature-based or direct: An evaluation of monocular visual odometry,” *arXiv preprint arXiv:1705.04300*, pp. 1–12, 2017.

[6] E. Parisotto, D. Singh Chaplot, J. Zhang, and R. Salakhutdinov, “Global pose estimation with an attention-based recurrent network,” in *Proceedings of the ieee conference on computer vision and pattern recognition workshops*, 2018, pp. 237–246.

[7] L. Sun, W. Yin, E. Xie, Z. Li, C. Sun, and C. Shen, “Improving monocular visual odometry using learned depth,” *IEEE Transactions on Robotics*, vol. 38, no. 5, pp. 3173–3186, 2022.

[8] H. M. S. Bruno and E. L. Colombini, “Lift-slam: A deep-learning feature-based monocular visual slam method,” *Neurocomputing*, vol. 455, pp. 97–110, 2021.

[9] S. Milz, G. Arbeiter, C. Witt, B. Abdallah, and S. Yogamani, “Visual slam for automated driving: Exploring the applications of deep learning,” in *Proceedings of the IEEE Conference on Computer Vision and Pattern Recognition Workshops*, 2018, pp. 247–257.

[10] C. Godard, O. Mac Aodha, M. Firman, and G. J. Brostow, “Digging into self-supervised monocular depth prediction,” October 2019.

[11] D. DeTone, T. Malisiewicz, and A. Rabinovich, “Superpoint: Self-supervised interest point detection and description,” in *Proceedings of the IEEE conference on computer vision and pattern recognition workshops*, 2018, pp. 224–236.

[12] M. Burri, J. Nikolic, P. Gohl, T. Schneider, J. Rehder, S. Omari, M. W. Achtelik, and R. Siegwart, “The euroc micro aerial vehicle datasets,” *The International Journal of Robotics Research*, 2016.

[13] A. Geiger, P. Lenz, C. Stiller, and R. Urtasun, “Vision meets robotics: The kitti dataset,” *International Journal of Robotics Research (IJRR)*, 2013.

Recent Developments in Dynamical-System Analysis (Self-Similarity and Time-Harmonic Structures) and Educational Activities (*Kids in Control*)

Cristiano Maria Verrelli

University of Rome Tor Vergata, Electronic Engineering Department,
Rome, Italy, `verrelli@ing.uniroma2.it`.

Abstract: This extended Abstract hints at some recent developments in the analysis of dynamical systems, including both an innovative result and an educational fall-out. *Analysis.* Starting from the most recent findings, by the author, regarding self-similarity in walking and swimming (in its simple and enhanced nature), a new research direction – involving the tennis framework and, in particular, relying on experimental results on the forehand – has been originally defined and highlighted, with the theoretical derivations and the experimental results being in line with all the previous research carried out by the author within different frameworks. *Education. Kids in Control* is a control-centered workshop that has been conceived to promote STEM (Science, Technology, Engineering, and Mathematics) skills and inclusion for kids from 8 to 10 years old. It includes activities and devices developed to improve the learning process while fostering the creation of a new teaching and learning style, based on the most advanced digital technologies (allowing for the aforementioned self-similarity analysis). It also aims to be firmly rooted in the foundations of pedagogy and in the interaction between teacher and learner, especially in its International School (IS) version.

1. CYCLIC HUMAN MOVEMENTS AND TIME-HARMONIC STRUCTURES

It is well-known that the golden ratio $\phi = (1+\sqrt{5})/2 \approx 1.618$ is (the positive) solution to the equation $x^2 = 1 + x$, [4]). It is related to Euclid's problem of cutting self-proportionally a given segment and exhibits a host of geometric and aesthetic properties, making it a subject of fascination in art, architecture, and design [3]. Furthermore, the Fibonacci sequence exhibits numerous intriguing properties related to its divisibility, modular arithmetic, and continued fractions, which have implications in number theory and algebraic geometry, as well as in cryptography and digital signal processing [5]. From the arrangement of petals in flowers and the spirals of nautilus shells to the branching patterns of trees and the proportions of human anatomy, the Fibonacci sequence is deeply ingrained in the fabric of the natural world, extending its ubiquity far beyond the realm of mathematics. In addition, in computer algorithms, Fibonacci numbers are widely utilized in optimization problems and dynamic programming, while in music, composers employ Fibonacci-inspired rhythms and structures to create harmonious compositions [2].

Now, very recent research efforts by the author (see all the references within [8]) – starting from [1] experimentally characterizing the walking gait –, have been dedicated to theoretically explaining the experimental occurrence of time-harmonic motor patterns in human repetitive movements. The resulting discoveries by the author have found out that such patterns: i) are implicitly defined by the golden ratio when it occurs as the ratio [1] of movement sub-phases durations composing a generalized Fibonacci sequence of finite length [6]; ii) also meaningfully exist in running and swimming. Indeed, the golden ratio is related to a Fibonacci sequence of finite length (namely, $a, b, c, d, \ldots$), through the explicit solution to the discrete-time, second-order auto-regressive scalar system:

$$y(k+2) = y(k+1) + y(k),\ k = 0, 1, \ldots,$$

with $y(0) = a$, $y(1) = b$ and $y(2) = c$, $y(3) = d$, $\ldots$, or its state-space representation:

$$\xi(k+1) = \mathcal{M}\xi(k),\ k = 0, 1, \ldots,$$

with $\xi(l)$ representing the vector $[y(l), y(l+1)]^{\mathrm{T}}$, $l = 0, 1, 2\ldots$, and $\mathcal{M}$ denoting the square 2×2 matrix $[0, 1; 1, 1]$. On the other hand, neurophysiological analyses have suggested that smooth and efficient locomotor movements might be generated by the strict relationship between cortical input, sensory feedback, and neuron networks named *central pattern generators* CPGs: the nervous system seems to reduce the complexity of controlling the redundant degrees of freedom associated with the bilateral multi-joint limbs, while dictating timing and coordination of muscle activation patterns. Even though swimming does not appear to belong to CPG-based instinctive patterns, front crawl swimming apparently possesses a rhythmicity similar to walking and running: it is induced by repetitive training for a long enough time, with technique automatizing learning of complex movements.

In the latest [8], just after reviewing the different scenarios of walking and swimming, in which time-harmonicity has been proven to occur, and stitching them together on a common logical platform, a new research direction is defined, and transposition arguments are adopted. Such a new research scenario involves the tennis framework. The

---

[1] Just accounting for the ratio between the consecutive phase durations allows the gait cycle duration to be a parameter freely characterizing the individual subject's walking.

self-similarity analysis (in its simple nature and enhanced – namely, stronger – variant) is originally extended to find surprising time-harmonic patterns in the forehand [2] executions that are illustrated by experimental results. Such experimental results are thus in line with the ones obtained in the previous papers concerning different frameworks in terms of self-similarity and enhanced self-similarity. This might confirm that, differently from walking and analogously to swimming, tennis technique is crucial: to become an expert player, subjects must undergo a considerable amount of practice and instruction that makes the player move from non-self-similarity to self-similarity up to enhanced self-similarity.

2. *KIDS IN CONTROL*: EDUCATIONAL ACTIVITY AND DEVICES FOR IS STUDENTS

With advances in science and technology, studies have been devoted to figuring out the main issues regarding children's learning. Indeed, interactive learning tools facilitate the possibility for students to develop an intuitive feel and understanding. Relevant examples can be mentioned (see [9] for some of them). Within this framework, *Kids in Control* is a control-centered workshop that has been conceived to promote STEM skills and inclusion for kids from 8 to 10 years old. It has been sponsored by the IFAC Activity Fund action and supported by the IFAC Technical Committee 9.2. *Systems and Control for Societal Impact* whose Chair is Mariana Netto, from Université Gustave Eiffel. *Kids in Control* aims at complementing the successful experience of *Girls in Control* [7] [GIC, Workshop and Material - (ifac-control.org)] within an age in which gender differences are not as marked as during puberty and background & foreknowledge are almost uniform. Helping kids of a young age (8-10) with a pretty positive attitude towards STEM actually choose STEM in higher education, while, in particular, early rooting out related skills and capabilities, constitutes an important part of the teacher's role. With respect to this, the goal of *Kids in Control* is to help kids of 8-10 years achieve self-efficacy towards technology. The most beautiful ideas lying at the root of the design of control strategies are presented before the kids' eyes, with a simple language that aims at being also emotionally- and intellectually-involving. A tasting of beauty in unveiling certain beautiful aspects of mathematics that lie at the root of the design of control algorithms and strategies is provided. Special emphasis is devoted to the psychological processes driving the expression. Videos are further included in order to render the kid more pleasant.

In the latest [9], the developments of such a project are presented with reference to its version specifically dedicated to ISs, Responsible: C.M. Verrelli. ISs allow for the use of a uniform language (English) world-wide while exploiting the ability of the elaboration of the human mind through distributed knowledge and enabling technologies. A 3-hour experience (by C.M. Verrelli, M. El Arayshi, M. Tiberti) is envisioned, in which the kids:

i) experience the research-world-taste and are made familiar with intuitively understandable applications of dynamic systems analysis & automatic control in various fields of life, including recognition of the golden ratio occurrence in temporal analysis of walking gaits & swimming strokes % tennis forehand through wearable sensors/video devices, besides high-performance control of elevators, automotive control, control of robots;
ii) are made familiar with intuitively understandable ideas of analysis & control strategies (involving sensors, actuators, feedback, dynamic evolution);
iii) are made familiar with https://scratch.mit.edu/, a visual coding platform, to learn, subconsciously, in a playful way, how to create programs, and, this way, increase their self-efficacy towards using computer languages to describe reality;
iv) look at the use of https://www.microbit.org/, a low-cost educational board that can be programmed through https://scratch.mit.edu/, as hardware-in-the-loop to learn the potential of electronics subconsciously, and, this way, increase their self-efficacy towards managing hardware;
v) understand, from a mathematical point of view, the design of control algorithms for electric motors and see their experimental application to DC motors, as well as to an autonomous electric vehicle with 2 in-wheel motors (scale 1:10) [3].

REFERENCES

[1] Iosa, M., Fusco, A., Marchetti, F., Morone, G., Caltagirone, C., Paolucci, S., Peppe, A.: The golden ratio of gait harmony: Repetitive proportions of repetitive gait phases. BioMed Research International, 1-7 (2013).

[2] Lima, M.: Visual Complexity: Mapping Patterns of Information. Princeton Architectural Press (2019).

[3] Livio, M.: The golden ratio: The story of phi, the world's most astonishing number. Crown (2008).

[4] Marino, R., Verrelli, C.M., Gnucci, M.: Synchronicity rectangle for temporal gait analysis: Application to Parkinson's Disease. Biomedical Signal Processing and Control, 62 (2020).

[5] Vajda, S.: Fibonacci and Lucas numbers, and the golden section: theory and applications. Courier Corporation (2008).

[6] Verrelli, C.M., Iosa, M., Roselli, P., Pisani, A., Giannini, F., Saggio, G.: Generalized Finite-Length Fibonacci Sequences in Healthy and Pathological Human Walking: Comprehensively Assessing Recursivity, Asymmetry, Consistency, Self-Similarity, and Variability of Gaits. Frontiers in Human Neuroscience, Special Issue: Motor Neuroscience (2021).

[7] M.D. Di Benedetto, S. Knorn, R. Jackson, D. Varagnolo, Girls in Control: Reaching out with control, *IEEE Control Systems Magazine*, 41(4): 16-18, 2021.

[8] B7) C.M. Verrelli, L. Caprioli, V. Bonaiuto, Cyclic Human Movements and Time-Harmonic Structures: Role of the Golden Ratio in the Tennis Forehand, Engineering Methodologies for Medicine and Sport, Rome, February 7-9 2024,*in R. Montanari et al. (Eds.): EMMS 2024*, MMS 162, pp. 1–21, 2024.

[9] C.M. Verrelli, M. El Arayshi, M. Tiberti, Kids in Control: Educational Activity and Devices for International School Students, *IFAC 2023.*

---

[2] For a right-handed player, the forehand is a stroke that starts on the right side of the player's body, continues across the body as the impact with the ball occurs, and ends up on the left side of the body. It is considered the easiest and most natural shot to master.

[3] An autonomous electric vehicle with two in-wheel motors is used to make kids familiar with a relevant application of motor controls. In the presented application, the references for the two motor speeds are provided within a cruise control scenario by a supervisor control that modifies the longitudinal velocity of the vehicle (and the yaw rate) when a change in the tire-road adhesion coefficient occurs.

System Identification at University with Blended Learning Techniques and Advanced Assessment Strategies

Laura Screpanti[*], Martina Morano[*], David Scaradozzi[*]

[*] *Dipartimento di Ingegneria dell'Informazione, Università Politecnica delle Marche, Italy*

I. INTRODUCTION

Technology and society have experienced significant changes, affecting the skills and knowledge required by engineering students. The job market prompts universities to update their programs accordingly. Innovative teaching practices and technology-enhanced resources help foster a dynamic and inclusive learning environment, aiding students in mastering linear systems identification [1], - [3]. So far, few experiences describe undergraduate courses on dynamical systems identification, with only one integrating a BL framework and summative assessment [5], [6]. None combine both summative and formative assessments with automated personalized feedback. This paper draws from the international control community's discussions, supported by IFAC and IEEE Technical Committees, to presents a structured approach to teaching linear system identification at an undergraduate level within a blended learning (BL) environment incorporating automated personalized feedback [4].

II. CONTEXT

BL combines online and in-person education, creating a dynamic and interactive environment that enhances student engagement and personalizes the learning experience [7]. A key feature of BL is its flexibility, allowing students to learn at their own pace while maintaining essential interactions with instructors and course materials. Furthermore, BL integrates various instructional strategies and resources to accommodate diverse learning preferences and schedules. Incorporating educational technology into traditional courses enables automated assessments and timely feedback, thus improving the quality of learning [11], [12], [13]. Shared resources in BL include e-books, videos, quizzes, forums, and interactive assignments with personalized feedback. These digital tools support data-driven evaluation, aiding student self-regulation and teacher assessments [13]. In engineering courses, MathWorks MATLAB is a popular tool for practical simulations and theoretical demonstrations [8]. MATLAB is also valuable for automating student and teacher feedback processes in BL settings. When combined with tools like MATLAB Grader [9], BL has shown positive effects on student engagement and satisfaction [10].

III. DEVELOPMENT OF A BL COURSE ON MODELLING AND IDENTIFICATION OF LINEAR SYSTEM

A. *Requirements*

The course is designed for undergraduate students, and its syllabus specifies that 72 hours (equivalent to 9 CFU) are allocated for instructional activities planned by the lecturer. The total duration is divided into 51 hours of classroom lectures and 21 hours of laboratory activities. The course was selected to be part of the "e-learning blended" initiative, which supports lecturers in integrating digital tools to enhance student access to learning. Specifically, the Università Politecnica delle Marche, while reaffirming its commitment to in-person teaching, promotes the adoption of e-learning methodologies to improve learning outcomes, facilitate skill acquisition, ease access to studies, and foster the integration and dissemination of knowledge. The courses "Modelling and Identification of Dynamical Systems" in the Automation and Computer Science Engineering degree and "Modeling and Optimization for Industrial Processes" in the Management degree were selected for the initiative and, thus, included 10 hours of online activities out of the 72 total hours.

Instructional themes in the courses were:

- Introduction to the problem of system identification
- Recalling the basics of system theory
- Nonparametric system identification
- White Noise characteristics and whiteness tests
- Parametric identification: the black-box approach
- Models' families(OE, AR/ARX, ARMA/ARMAX)
- The predictive approach
- The least squares method
- The maximum likelihood method
- Recursive identification
- Persistent excitation
- The validation procedure
- Introduction to Neural Networks for identification

B. *Tools*

The lecturers developed both the physical and online components of the BL course. The structure of the course is represented in Figure 1. Traditional face-to-face lessons were held at the university facilities according to the regular timetable, except for the 10 hours of online learning. Laboratory activities were conducted in a hybrid manner [14]. Students were assigned tasks using laboratory equipment and they were required to upload MATLAB LiveScript reports on Moodle, which were graded asynchronously by the lecturer via the online platform. The course's online infrastructure relied on the Moodle LMS, which integrated various preinstalled resources and activities. To enhance the delivery of course content, instructors created short video lessons as introductory materials for each module thanks to the university's lightboard recording system and multimedia facility. These videos elucidated key topics and emphasized critical points, thus complementing face-to-face learning both as multimedia learning aids and as flipped learning resources. Lecturers also incorporated supplementary activities like MATLAB Academy's online courses to enhance students'

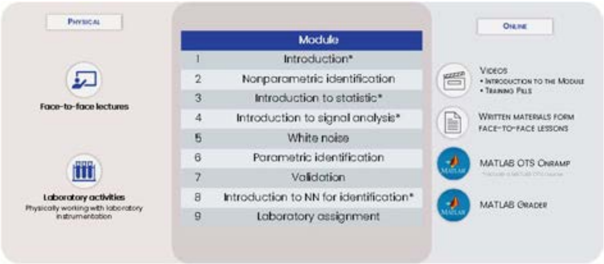

	Module
1	Introduction*
2	Nonparametric identification
3	Introduction to statistic*
4	Introduction to signal analysis*
5	White noise
6	Parametric identification
7	Validation
8	Introduction to NN for identification*
9	Laboratory assignment

Figure 1: the organization of modules

proficiency in MATLAB programming, statistics, signal processing, and machine learning. These resources strategically reinforced students' understanding of key concepts, which they could use to build more efficiently new, elaborated concepts. The MATLAB Grader tool was also used for formative assessments, supporting students' learning by providing timely and personalized feedback crafted by lecturers. The online infrastructure enabled teachers to monitor students' performance throughout the course, utilizing data from students' interactions with online materials and Moodle's gradebook. Additionally, pre- and post-course questionnaires gathered information on students' interests, future value expectations, self-efficacy, and perceived usefulness of the teaching methods. Figure 2 shows the entire structure of the design of the evaluation.

IV. DISCUSSION AND CONCLUSION

Implementing the BL approach to a course on modeling and identification of dynamical systems showed several benefits along with potential areas for improvement. Integrating physical and online components, the course established a dynamic and interactive learning environment that enhanced student engagement and personalized the learning experience. Incorporating supplementary resources from MATLAB Academy's online courses and using the MATLAB Grader tool for formative assessments proved to be effective strategies. Students reported great appreciation for these tools as they received immediate feedback from the platform and improvement suggestions crafted by the instructor during tool setup. Furthermore, integrating these tools encouraged students to engage in discussions with lecturers, mainly when reporting supposed system bugs, which helped uncover misconceptions in their knowledge. Future enhancements will explore additional features, especially those aimed at bridging gaps in prerequisite knowledge to ensure a more inclusive learning environment.

In conclusion, the BL approach showed promising results in enhancing student engagement, learning outcomes, and skill acquisition. Future iterations of the course could benefit from addressing challenges related to the allocation of time for online resources and further refining the balance between physical and online components to optimize the learning experience.

ACKNOWLEDGMENT

The authors acknowledge Università Politecnica delle Marche for the support to the projects "Modellistica e Ottimizzazione per i Processi Industriali" (n. 2606638) e "Modellistica e Identificazione dei Processi Dinamici" (n. 2614233). The authors thank MathWorks Italia for the support received and for the ongoing cooperation in the improvement of the evaluation process. Research was supported also by RoboPisces (2019-1-IT02-KA201-063073), RoboAquaria (2022-1-IT02-KA220-SCH-000089578), E-tech (2020-1-PL01- KA226-HE-096375) projects under the Erasmus+ programme. The research is also part of the work conducted under PNRR program - Mission 4 Component 2 Investment 3.3 (DM 117/2023), grant number 39-033-01-DOT1301942-9176.

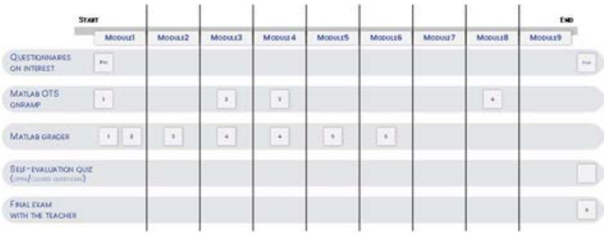

Figure 2: structure of the course evaluation

REFERENCES

[1] A. Visioli, "Control Education: TC 9.4 Developments and Vision," *IFAC-PapersOnLine*, vol. 56, no. 2, pp. 332-335. 2023.

[2] J. A. Rossiter, "Future Trends for a First Course in Control Engineering," *Frontiers in Control Engineering*, vol. 3, 956665, 2022. doi: 10.3389/fcteg.2022.956665

[3] D. Y. Abramovitch, "Thoughts on Furthering the Control Education of Practicing Engineers [Focus on Education]," *IEEE Control Systems Magazine*, vol. 43, no. 1, pp. 64-88. 2023.

[4] L. Screpanti, M. Morano, and D. Scaradozzi. "Designing Courses in Modeling and Identification of Dynamic Systems for Real-Time Assessment." *2024 32nd Mediterranean Conference on Control and Automation (MED)*. IEEE, 2024.

[5] V. Makarov, "Fundamental Scientific Discipline "Identification of Systems" and Fundamental Education,", in *2023 16th International Conference Management of large-scale system development (MLSD)*, Sep. 2023, pp. 1–4. doi: 10.1109/MLSD58227.2023.10303984.

[6] Z. Lei, H. Zhou, W. Hu, and G.-P. Liu, "Teaching and Comprehensive Learning With Remote Laboratories and MATLAB for an Undergraduate System Identification Course," *IEEE Transactions on Education*, vol. 65, no. 3, pp. 402–408, Aug. 2022, doi: 10.1109/TE.2021.3123302.

[7] A. D. Ekawati, L. Sugandi, and D. L. Kusumastuti, "Blended learning in higher education: Does gender influence the student satisfaction on blended learning?," in *2017 International Conference on Information Management and Technology (ICIMTech)*, Nov. 2017, pp. 160–164. doi: 10.1109/ICIMTech.2017.8273530.

[8] Matlab. https://www.mathworks.com/products/matlab.html. Last accessed 16/02/2024.

[9] Matlab Grader. https://grader.mathworks.com. Last accessed 16/02/2024.

[10] L. Ni, and K. Hekman, "Improving Student Learning Experience with MATLAB Grader and Live Scripts," in *2022 ASEE Annual Conference & Exposition*, August 2022.

[11] L. Screpanti, B. Miotti, and A. Monteriù, "Robotics in education: A smart and innovative approach to the challenges of the 21st century". In Makers at School, Educational Robotics and Innovative Learning Environments: Research and Experiences from FabLearn Italy 2019, in the Italian Schools and Beyond, 2021, pp. 17-26. Cham: Springer International Publishing.

[12] L. Screpanti, D. Scaradozzi, R. N. Gulesin, and N. Ciuccoli, "Control Engineering and Robotics since Primary School: an Infrastructure for creating the Digital Twin model of the Learning Class". *IFAC-PapersOnLine*, vol. *55, no.* 17, pp. 267-272, 2022.

[13] D. Scaradozzi, L. Cesaretti, L. Screpanti and E. Mangina, "Identification and assessment of educational experiences: Utilizing data mining with robotics". *IEEE Robotics & Automation Magazine*, *28*(4), 103-113, 2021.

[14] L. Screpanti, V. Bartolucci, D. Scaradozzi, and E. Zattoni, "A Max-plus Algebra approach to model laboratories experiences in blended Control Engineering education". In *proceedings of the 4th Workshop on Internet Based Control Education (IBCE2024)*, 18-20 September 2024, Ghent Belgium.

Innovative Solutions for Collaborative Teaching in Automatic Control: Insights from IFAC TC 9.4

Laura Screpanti[1], David Scaradozzi[1], Damiano Varagnolo[2,3], Adriano Fagiolini[4]

[1] Dipartimento di Ingegneria dell'Informazione, Univeristà Politecnica delle Marche, 60131 Ancona, Italy
[2] Department of Information Engineering, University of Padova, Padova, Italy
[3] Department of Engineering Cybernetics, Norwegian University of Science and Technology, Trondheim, Norway
[4] Department of Engineering, Università degli Studi di Palermo, 90128 Palermo, Italy

I. INTRODUCTION

Control engineering education is widely debated among professionals and academics in the field. On the one hand, there is the need to transmit the rigorous notions of control theory. On the other hand, there is the need to adapt curricula to the skill demand of the industry. The ongoing discussion highlights how control engineering education has been evolving both in terms of curriculum content [1], [2], design [3], and delivery [4], and in terms of technological tools that can enhance learning [1], [2], [3]. The issue of restructuring the first course in control engineering at university is widely debated and many proposals arouse to align the pathway of the course educational contents [5], [6], as well as the assessment of the learning outcomes [7], [8].

The evolution of teaching methodologies in automatic control has revealed significant challenges and opportunities for collaboration among educators. Two main issues that influence workflows are: 1) **the systematic difficulty in exchanging instructional materials with colleagues**, and 2) **the complexity of establishing commonalities in the courses' programs across different institutions and nations**. These challenges are interconnected, impacting both the efficiency of teaching and the enrichment of student experiences. IFAC's Technical Committee (TC) 9.4 is investigating solutions to these problems that rely on open databases of instructional materials as enhancers of teaching and learning. Such databases offer valuable content for teaching activities, scaffolding, and self-assessment provided that robust taxonomies are identified and used to index the instructional materials to avoid the subjective biases. This contribution provides an overview of the solution being investigated by this TC and how it may improve collaborative teaching and learning in automatic control.

II. CONTEXT

Control engineering education faces the challenge of meeting several demands, including increasing its attractiveness, incorporating relevant and rapidly evolving content, and fulfilling the growing need for teaching skills beyond technical competency. Addressing these needs effectively can be achieved by fostering the sharing of high-quality resources and facilitating collaboration in higher education. Although some initiatives and bureaucratic infrastructures supporting collaboration and resource sharing already exists, specific needs must be addressed to optimize these efforts. Many groups worldwide put a lot of effort in creating, adjusting and delivering effective and engaging educational resources in control engineering. Usually, each lecturer creates or adapts the educational material intended for the course. Unfortunately, this wealth of materials and knowledge about didactics of control engineering is usually not shared and cannot be exploited for further refinements, testing or optimization, thus hampering the creation of efficient methodologies to teach control systems. The creation of validated methodologies and resources for control engineering could eventually lead to improve teaching quality, decreasing the workload of lecturers, and also establishing benchmarks across control engineering curriculum.

To fill the gap the present paper introduces a platform based on a community of practice (CoP) approach [9], [10]. CoP members share a common interest and focus on sharing best practices and generating new knowledge to advance their professional field. Ongoing interaction is crucial, often facilitated through face-to-face meetings, e.g., conferences, and web-based collaborative platforms to communicate, connect, and carry out community activities. The present work aims at describing a collaborative platform to find and share effective and validated open educational resources (OERs) in control engineering.

III. THE PLATFORM

The database, hosted at https://faceittools.com, is actually a portal that enables users to:

1) create mindmaps of the contents of the own courses,
2) upload or create assessment material,
3) share their own assessment material and mindmaps with selectable groups of colleagues and students,
4) find and reuse assessment material and mindmaps from other colleagues,
5) organize such assessment material in quizzes,
6) associate such quizzes to the mindmaps of the own courses, or specific parts of them,
7) administer these quizzes to students,
8) collect and analyse the performance of such students on such quizzes.

The current available resources are materials indexed by contents (prerequisite and developed knowledge) and by complexity (through the using-explaining taxonomy, [7]).

To prepare such teaching and assessment resources in control engineering several underlying issues are considered:

1. Establishing a universal method to describe the difficulty and complexity of instructional material to facilitate easy comparison, searching, and communication among educators, as well as enabling joint teaching.
2. Agreeing on a common notation for standard items in control education (e.g., transfer functions, signal names) to allow for direct sharing of materials without the need for adaptations or defining a set of notation standards and translation lookup tables to enable convenient switching of notations.

3. Creating a universal system to organize and categorize instructional material in control engineering to facilitate easy comparison, recognition of courses taken abroad, and joint teaching.

4. Setting up an efficient method for the technical sharing of teaching materials with minimal administrative effort.

We note that the taxonomy used to index the material (actually to label the nominal difficulty of exam or test questions in control engineering, see more details in [7]), measures the complexity of the *solutions* of such questions, and this through a two-dimensional approach (complexity of the explanations given in the solution, complexity of the formulas used in the solution). This two-dimensional approach proved effective and consistent among experts. Moreover, A graphical representations of courses allow for the visualization of content flows and hierarchical structures of the material. These graphs can help automate the validation of student exchanges and provide a common language between students and teachers, enhancing the understanding of course content and knowledge levels.

IV. DISCUSSION

Lecturers globally spend significant time creating new instructional materials, which often remain within local networks and are not widely accessible. Storing and indexing this material in a computer-accessible database would benefit the entire control community for several reasons:

- peer reviewed materials increase the validity of the OERs
- OERs indexed using a recognized taxonomy ensures a standard categorization and description of educational content. This consistency helps educators and students understand and compare resources more easily, improving searchability of educational resources.
- it can help align educational resources with curriculum standards and learning objectives. This alignment ensures that the materials support the intended learning outcomes and educational goals.
- it improves communication among educators, students, and other stakeholders. It provides a shared language for discussing educational content, instructional strategies, and assessment criteria.
- it can support differentiated instruction by clearly identifying the complexity and skills addressed by each resource. This allows educators to select materials that match the diverse needs and abilities of their students.
- educators can map student achievements to specific levels, providing a clear picture of the students' learning journey across a standard benchmark.
- when developing new educational courses, referring to an existing wealth of resources ensures that the resources are comprehensive and cover all necessary aspects of the subject matter. It also helps identify gaps that need to be addressed.
- when different curricula are involved, the repository may highlight connections between different subject areas promoting a more integrated and holistic approach to control engineering education.
- the taxonomy-based indexing of educational resources allows for more effective data analytics. Educators and researchers can analyze patterns, effectiveness, and usage of resources, leading to data-driven improvements in teaching and learning.
- authorship tracking, which ensures proper attribution to authors, is recognized and should account for the professionalism of the author.

Despite the many benefits of the proposed tool and the full support of the IFAC community, the platform still faces several challenges, both in technological development and user adoption. Technologically, the ability to edit content requires robust mechanisms to maintain the validity and usability of the material, ensuring precision and correctness. Regarding user adoption, some issues remain unresolved. The platform must demonstrate its full operational capacity to encourage users to transition from traditional paper textbooks to the new system.

V. CONCLUSION

Due to rapid technological advancements and the resulting increased demands on control engineering educators, sharing materials and joint teaching have become increasingly critical. This challenge can be addressed by enhancing the final domain of the community of practice in control engineering: building a shared repertoire of resources and ideas that sustain a core of collective knowledge about control engineering education. To this end, a platform designed as a database and sharing hub is introduced to overcome barriers that discourage collaborative teaching among educators. Several challenges remain, including (i) establishing a common notation for easier material sharing, (ii) developing mechanisms for fair and well-founded decisions on module acceptance for students returning from abroad, and (iii) creating structures for joint teaching of modules by participating educators, both onsite and digitally.

REFERENCES

[1] Visioli, A., "Control Education: TC 9.4 Developments and Vision," IFAC-PapersOnLine, 2023, 56(2), 332-335.

[2] Rossiter, J. A., "Future Trends for a First Course in Control Engineering". Frontiers in Control Engineering, 2020, 3.

[3] Screpanti, L., Morano, M. & Scaradozzi, D., "Designing Courses in Modeling and Identification of Dynamic Systems for Real-Time Assessment" In the 32nd Mediterranean Conference on Control and Automation Book of Abstracts, 2024 (pp. 304-309).

[4] Screpanti, L. & Scaradozzi, D. "Control Systems Engineering and Robotics Education since Primary School". In Proceedings of the 2024 European Control Conferences, 2024.

[5] Serbezov, A., Zakova, K., Visioli, A., Rossiter, J. A., Douglas, B., & Hedengren, J. (2022). Open access resources to support the first course in feedback, dynamics and control. IFAC-PapersOnLine, 55(17), 1-6.

[6] Knorn, S., Topalovic, D., & Varagnolo, D. (2022). Redesigning a classic control course using constructive alignment, student centred teaching and continuous assessment. IFAC-PapersOnLine, 55(17), 180-185.

[7] Liotino, M., Garone, A., Knorn, S., Varagnolo, D., Garone, E., & Fedeli, M. "Assessing engineering exercises: a novel taxonomy". IFAC-PapersOnLine, 2022, 55(17), 49-54.

[8] Mohammadi, A., Fagiolini, A., Cirrincione, M., Garone, E., Garone, A., & Varagnolo, D., "Towards an open database of assessment material for STEM subjects: requirements and recommendations from early field trials", 2023, IFAC-PapersOnLine, 55(17), 7-12.

[9] Lave, J., & Wenger, E., "Situated learning: Legitimate peripheral participation". Cambridge university press, 1991.

[10] Townley, A. L., "Leveraging communities of practice as professional learning communities in science, technology, engineering, math (STEM) education". Education Sciences, 2020, 10(8), 190.

Session 7D: Applications

EEG Data-Driven Control and Risk Prediction in Roundabout Maneuvers

Enrico Zero[1], Alessandro Bozzi[1], Simone Graffione[1], Roberto Sacile[1]

I. INTRODUCTION

Continuous technological advancements are enhancing life quality across domains, with biomedical devices like Electroencephalogram (EEG) widely used in clinical settings for diagnosing neurological disorders and researching brain function. EEG also powers Brain-Computer Interfaces (BCIs), enabling control over devices [1] and robotic arms by decoding EEG signals [2]. It's increasingly applied in biomedical and robotic control theory [3], and emerging interest focuses on using EEG for vehicle control, enhancing safety and driving experiences. Emotions like fear and anxiety are studied in driving simulations [4], and risk-taking behavior is predicted successfully [5]. This research employs a Support Vector Machine (SVM) to predict driver-perceived risk in roundabout maneuvers. Roundabouts challenge autonomous vehicles, requiring coordination with human-driven vehicles (HDVs) [6]. Integrating EEG with vehicle control systems allows vehicles to respond to the driver's mental state, potentially reducing collisions. For example, detecting distraction or drowsiness prompts alerts or adjusts speed and lane position. This fusion of automotive technology and neuroscience aims to enhance road safety by making driving more responsive and adaptable.

II. METHODS

A. System Architecture

In vehicle safety and control, understanding the driver's risk perception is crucial for preventing potential road hazards. Drivers constantly assess traffic, road conditions, and environmental factors to gauge risk, influencing their behavior and decision-making, which impacts overall road safety. Fig. 1 illustrates the system architecture. The setup integrates the SCANeR Studio simulator with a display interface, creating a realistic driving environment and providing real-time feedback to the driver, including driving style and dashboard information. Communication between the driving setup and the simulator is facilitated via a serial bus interface. Additionally, the Unicorn Hybrid Black EEG cap with eight electrodes captures the driver's brain activity. This data is used to train a SVM model to identify patterns indicating different levels of driver risk.

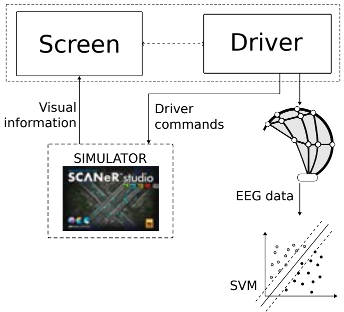

Fig. 1: System design for network testing.

B. Data acquisition, synchronisation and normalisation

During the data acquisition phase, the volunteers engaged in a three-minute simulation within a roundabout environment. Electrodes were strategically placed over the sensorimotor cortex for motor imagery-based BCIs, and over central, parietal, and occipital areas for P300 paradigms. Additional electrodes targeted parietal regions for steady-state visual evoked potential (SSVEP) and code-based VEP paradigms. Participants had real-time decision-making capabilities mirroring actual driving scenarios, allowing them to select paths and maneuvers. A custom application integrated into the simulator software captured comprehensive data about surrounding vehicles within the roundabout, including their position, speed, orientation, and location. This data facilitated manual assessment of driver risk, categorized into three levels: 1 - low risk, 2 - moderate risk with increased attention needed, and 3 - high risk indicating proximity to other vehicles with collision risk. Synchronizing vehicle data with EEG readings posed challenges due to differing collection frequencies: 250 Hz for EEG and 20 Hz for the simulator. To bridge this gap, an oversampling technique was employed to align ScanerStudio data with EEG data, ensuring consistent samples between successive EEG readings. Each EEG signal underwent filtering to eliminate specific frequencies and normalization to enhance data quality for SVM processing. EEG signals were normalized relative to a baseline 'resting state', EEG_c^i, captured while candidates were seated but not actively driving. For each candidate i, the final EEG dataset, denoted as EEG_{final}^i, is derived as follows:

$$EEG_{\text{final}}^i = \frac{EEG^i - EEG_c^i}{EEG_c^i} \tag{1}$$

C. Predictive Model

In the SVM model design, the choice of the kernel function is crucial. In this research, the Gaussian kernel function is utilized due to its ability to capture complex nonlinear relationships present in the EEG data, thereby enhancing the

---

[1] Enrico Zero, Simone Graffione, Alessandro Bozzi, and Roberto Sacile are with the Department of Informatics, Bioengineering, Robotics and Systems Engineering (DIBRIS) University of Genoa, 16145 Genoa, Italy.
Corresponding author: enrico.zero@dibris.unige.it

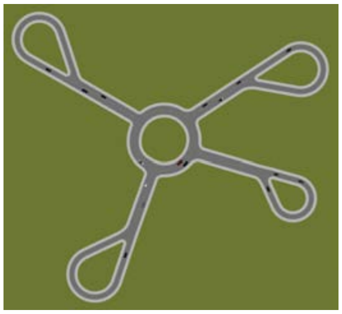

Fig. 2: Scenario designed for the driving sessions and tests.

model's capacity to discern subtle patterns indicative of different risk levels. When assessing the accuracy of the results, especially in scenarios with unbalanced classes, the Matthews correlation coefficient (2) serves as a valuable metric. This coefficient is commonly employed in biomedical applications [7] and is widely used in machine learning contexts to assess the effectiveness of binary classifications. Furthermore, its extension to multiclass scenarios is also widespread.

$$MCC = \frac{\sum_k \sum_l \sum_m C_{kk} C_{lm} - C_{kl} C_{mk}}{\sqrt{\sum_k (\sum_l C_{kl})(\sum_{k'|k' \neq k} \sum_{l'} C_{k'l'})}}$$

$$\frac{1}{\sqrt{\sum_k (\sum_l C_{lk})(\sum_{k'|k' \neq k} \sum_{l'} C_{l'k'})}} \qquad (2)$$

III. CASE STUDY

The experiment was performed by three men between 28 and 33 years old with driving licenses. The driving scenario shown in Fig. 2 is a simulation that features a dynamic environment with a two-lane roundabout, which differs from the usual single-lane configurations found in other road segments. The inclusion of a two-lane roundabout inherently increases driver attention by accommodating a higher volume of vehicles travelling through the roundabout simultaneously. In order to achieve realistic traffic dynamics, the roundabout is populated with a diverse mix of vehicles controlled by SCANeR Studio. It is important to note that the software exercises complete control over these vehicles, directing their trajectories within the roundabout in a randomized manner. The deliberate introduction of variability in vehicle movements enhances the authenticity of the simulation, providing a comprehensive and true-to-life representation of the obstacles that drivers may encounter.

IV. RESULTS

This study investigates the correlation between brain activity and road risk. The data from multiple driving sessions are preprocessed as explained previously. The dataset was split into two subsets: one for training (50% of the data) and one for independent testing. The confusion matrices in Fig. 3 show the results. The precision was 86.9% for the validation set and 87.1% for the test set, with positive predictive values exceeding 80% for all samples. This highlights a significant correlation between brain activities and the risk levels associated with navigating roundabouts. The Matthews Correlation Coefficient (MCC), calculated from the confusion matrix in Fig. 3, was 75.6%, indicating good prediction accuracy. Additionally, a Pattern Recognition Neural Network (PRNN) model with ten hidden layers was evaluated. It achieved 80% performance on the initial test set and comparable performance on another test set, with an MCC of 62.5%.

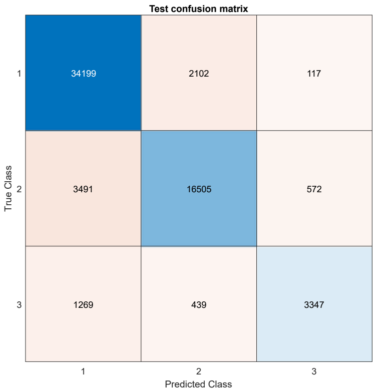

Fig. 3: Test confusion matrix showing an accuracy of 87.1%

V. CONCLUSION

This study introduces a novel method using EEG signals from the Unicorn Hybrid Black EEG cap to estimate risk levels. Employing a SVM with a fine Gaussian kernel, the research achieves high accuracy in classifying EEG data into three risk categories. The SVM outperforms the PRNN, underscoring its superior classification capabilities and reliability for risk assessment in diverse scenarios. Future research aims to enhance this model's applicability by extending it to dynamic speed trend assessments and testing across varied real-world conditions.

REFERENCES

[1] E. Zero, A. Bozzi, S. Graffione, and R. Sacile, "Controlling decisions by head electrical signals," in *International Conference on System-Integrated Intelligence*. Springer, 2022, pp. 425–436.

[2] A. Schwarz, M. K. Höller, J. Pereira, P. Ofner, and G. R. Müller-Putz, "Decoding hand movements from human eeg to control a robotic arm in a simulation environment," *Journal of neural engineering*, vol. 17, no. 3, p. 036010, 2020.

[3] S. Y. Gordleeva, S. A. Lobov, N. A. Grigorev, A. O. Savosenkov, M. O. Shamshin, M. V. Lukoyanov, M. A. Khoruzhko, and V. B. Kazantsev, "Real-time eeg–emg human–machine interface-based control system for a lower-limb exoskeleton," *IEEE Access*, vol. 8, pp. 84 070–84 081, 2020.

[4] E. Zero, C. Bersani, L. Zero, and R. Sacile, "Towards real-time monitoring of fear in driving sessions," *IFAC-PapersOnLine*, vol. 52, no. 19, pp. 299–304, 2019.

[5] A. Vance, B. B. Anderson, C. B. Kirwan, and D. Eargle, "Using measures of risk perception to predict information security behavior: Insights from electroencephalography (eeg)," *Journal of the Association for Information Systems*, vol. 15, no. 10, p. 2, 2014.

[6] R. Mohebifard and A. Hajbabaie, "Trajectory control in roundabouts with a mixed fleet of automated and human-driven vehicles," *Computer-Aided Civil and Infrastructure Engineering*, vol. 37, no. 15, pp. 1959–1977, 2022.

[7] S. Boughorbel, F. Jarray, and M. El-Anbari, "Optimal classifier for imbalanced data using matthews correlation coefficient metric," *PloS one*, vol. 12, no. 6, p. e0177678, 2017.

A Lightweight Encryption Approach for Data Confidentiality in Critical Infrastructures

Camilla Fioravanti[1], Luca Faramondi[1], Gabriele Oliva[1], and Roberto Setola[1]

***Abstract*— Guaranteeing data confidentiality while allowing agents to reach an agreement on some shared variables is an essential feature to foster the adoption of distributed protocols. In this submission, we take a geometrical perspective to implement a novel encryption methodology via coordinate shifts. This choice guarantees, on one side, the existence of an uncountable infinity of possible vectors and, on the other side, provides a control-theoretical viewpoint on encryption that naturally blends with a dynamical system. Leveraging vector coordinate shifts, our method excels in efficiency and speed of implementation, ensuring compliance with the stringent time constraints of real-time protocols. This makes our method easily applicable to a wide range of critical infrastructures, including the GOOSE protocol for digital substations communication in power grids. Indeed, the adherence to the IEC 62351 standard, governing security requirements for the GOOSE protocol, has always been an open challenge as it presents practical issues due to the conflict between time requirements imposed by operations and traditional cryptographic procedures.**

***Index Terms*— Cyber-Physical Systems, Cryptography, Networked Systems, Security.**

I. INTRODUCTION

The growing need to provide resilience and privacy guarantees in the context of distributed algorithms and, in particular, in applications to distributed consensus has led to researchers' attention being directed in this regard in recent years. A class of methods endows the network with *privacy-preservation* features against honest but curious nodes, i.e., each agent in the network tries to hide its initial condition from the others [1], [2], while other works focus on *eavesdropping resistance*, i.e., the need to protect the state of each agent, thus including both the initial and consensus values, from malicious third parties [3]. A powerful tool to enforce data confidentiality is *cryptography*; however, traditional encryption methodologies (e.g., RSA) are difficult to apply on networks working in real time as they usually are computationally intensive and time-consuming. In [1] authors propose homomorphic encryption, which enables a class of mathematical operations to be performed on encrypted data but can operate exclusively with states that are integers and introduces quantization errors. Another popular approach for privacy preservation in a distributed averaging process relies on the idea of differential privacy [4], which masks state variables by injecting carefully designed noises; however, these approaches often result in a trade-off between accuracy and privacy.

In this submission, we present a new geometric-based methodology [5] for lightweight encryption, that can be applied to distributed continuous-time consensus algorithm; the method provides resistance against eavesdroppers over a directed and strongly connected graph topology (thus, allowing the handling of asymmetric situations, such as the case of wireless nodes or mobile agents equipped with directional emitters/receivers), without introducing quantization or approximation errors. The proposed scheme also extends to enforce privacy, by assuming each agent's hidden state is influenced by a disturbance signal for a finite amount of time. Interestingly, by resorting to coordinate shifts, our geometrical approach does not have a combinatorial nature, as there is an uncountable infinity of possible choices for the constant weight vector, which makes it more robust to brute-force attacks. In addition, we show how the application of a geometric-based cryptographic methodology can be the blueprint for addressing a security problem within the GOOSE protocol for digital substations in power grids [6].

II. A GEOMETRICAL APPROACH FOR CONSENSUS

In [5] we consider a network of n agents, interconnected by a graph $G = \{V, E\}$, each holding a scalar initial condition $w_i(0)$. We evaluate a scenario where the legitimate nodes are willing to collaborate in order to reach the weighted average consensus value, i.e., each agent i aims to reach a steady state that satisfies $\lim_{t\to\infty} w_i(t) = \boldsymbol{\xi}^T \boldsymbol{w}(0)$, where $\boldsymbol{\xi}^T$ is the left eigenvector of the Laplacian matrix L corresponding to the zero eigenvalue, suitably scaled so that $\mathbf{1}_n^T \boldsymbol{\xi} = 1$. However, the agents do not want unintended third parties (or eavesdroppers) to become aware of their states. To this aim, each agent maintains an augmented state with m state variables $\boldsymbol{x}_i(t) = [x_{i1}(t), \ldots, x_{im}(t)]^T \in \mathbb{R}^m$. In this view, the agents exchange their vectorial states $\boldsymbol{x}_i(t)$ instead of the hidden scalar states $w_i(t)$. Moreover, each agent i selects an initial condition $\boldsymbol{x}_i(0) \in \mathbb{R}^m$ so that $\boldsymbol{q}^T \boldsymbol{x}_i(0) = w_i(0)$. At this point, each agent i selects an $(m-1) \times m$ matrix Q_i such that the $m \times m$ matrix

$$T_i = \begin{bmatrix} \boldsymbol{q}^T \\ Q_i \end{bmatrix}$$

is invertible; matrix T_i represents a coordinate shift such that

$$T_i \boldsymbol{x}_i(t) = \begin{bmatrix} \boldsymbol{q}^T \boldsymbol{x}_i(t) \\ Q_i \boldsymbol{x}_i(t) \end{bmatrix} = \begin{bmatrix} w_i(t) \\ * \end{bmatrix}, \quad (1)$$

i.e., the coordinate shift allows to obtain $w_i(t)$ from $\boldsymbol{x}_i(t)$. In this way, the agents can interact protecting their states from third parties while being able to reconstruct the state of their

---

[1] Department of Engineering, University Campus Bio-Medico of Rome, Via Alvaro del Portillo, 21 - 00128 Roma, Italy. E-mails: {c.fioravanti, l.faramondi, g.oliva, r.setola}@unicampus.it.

This work was supported by the Italian National Project INAIL BRIC 2023 ID 44 "Industrial Cyber Shield (ICS)" under CUP C83C22001460001.

neighbors based on $\boldsymbol{q}$, which is known to each agent (e.g., because it has been securely pre-deployed). Moreover, let us consider a scenario in which agents also want to enforce the privacy of their initial conditions against honest but curious neighbors. To this aim, we modify the dynamics as follows

$$\dot{\boldsymbol{x}}_i(t) = \sum_{j\in\mathcal{N}_i^{\mathtt{in}}} \left(\boldsymbol{x}_j(t)-\boldsymbol{x}_i(t)\right) + T_i^{-1}\begin{bmatrix}u_i(t)\\ \mathbf{0}_{m-1}\end{bmatrix}, \tag{2}$$

where $u_i(t)$ is such that

$$\int_0^{t_i^*} u_i(\tau)d\tau = 0, \quad u_i(t) = 0 \text{ for } t > t_i^* \tag{3}$$

and $t_i^* \geq 0$. In other words, each agent selects a time instant t_i^* and designs the noise $u_i(t)$ so that the cumulative effect is zero at time t_i^*, while $u_i(t)$ becomes zero afterward. In a compact form, the proposed dynamics for the agents read as follows $\dot{\boldsymbol{x}}(t) = -\left(L\otimes I_m\right)\boldsymbol{x}(t) + \mathcal{T}^{-1}\boldsymbol{z}(t)$, where

$$\mathcal{T} = \begin{bmatrix}T_1 & & \\ & \ddots & \\ & & T_n\end{bmatrix}, \ \boldsymbol{x}(t) = \begin{bmatrix}\boldsymbol{x}_1(t)\\ \cdots \\ \boldsymbol{x}_n(t)\end{bmatrix}, \ \boldsymbol{z}(t) = \begin{bmatrix}u_1(t)\\ \mathbf{0}_{m-1}\\ \cdots \\ u_n(t)\\ \mathbf{0}_{m-1}\end{bmatrix}.$$

The following theorem shows that, in spite of the presence of nonzero values $u_i(t)$, the hidden dynamics converges to the intended consensus value.

Theorem 1: Under the assumptions that the agents are interconnected by a strongly connected graph and that $u_i(t)$ satisfies Eq. (3), the proposed dynamics is such that

$$\lim_{t\to\infty} \boldsymbol{q}^T\boldsymbol{x}_i(t) = \boldsymbol{\xi}^T\boldsymbol{w}(0), \tag{4}$$

where $\boldsymbol{\xi}$ is the left eigenvector of L corresponding to the zero eigenvalue, with $\mathbf{1}_n^T\boldsymbol{\xi} = 1$.

In order to mitigate the requirement of a secure pre-deployment of the vector $\boldsymbol{q}$, we discuss an extension where each agent i relies on a different and locally established vector $\boldsymbol{q}_i \in \mathbb{R}^m$. In particular, let us assume that each agent i selects $\boldsymbol{q}_i \in \mathbb{R}^m$ and $\overline{\boldsymbol{x}}_i(0) \in \mathbb{R}^m$ such that $\boldsymbol{q}_i^T\overline{\boldsymbol{x}}_i(0) = w_i(0)$. Moreover, each agent chooses $Q_i \in \mathbb{R}^{(m-1)\times m}$ such that $\overline{T}_i = \left[\boldsymbol{q}_i, Q_i^T\right]^T$ is invertible. In this view, each agent i maintains an augmented state $\overline{\boldsymbol{x}}_i(t) \in \mathbb{R}^m$, which is updated as follows

$$\dot{\overline{\boldsymbol{x}}}_i(t) = \overline{T}_i^{-1}\sum_{j\in\mathcal{N}_i^{\mathtt{in}}}\left(\overline{T}_j^{(i)}\overline{\boldsymbol{x}}_j(t) - \overline{T}_i\overline{\boldsymbol{x}}_i(t)\right) + \overline{T}_i^{-1}\begin{bmatrix}u_i(t)\\ \mathbf{0}_{m-1}\end{bmatrix}, \tag{5}$$

where $\overline{T}_j^{(i)} = \left[\boldsymbol{q}_j, *\right]^T$, and is not required to be invertible. In particular, the lowermost block of $\overline{T}_j^{(i)}$ is chosen locally by agent i (for the sake of simplicity, in the following we will consider it equal to Q_i^T). The main improvement of this variation is that, to be able to compute $w_i(t)$ each node just needs the vectors $\boldsymbol{q}_i$ of its in-neighbors, which can be shared locally via a single transmission without the requirement to provide them to the whole network.

III. Application to Digital Substations

In recent years, increasing attention has been paid to security issues affecting critical infrastructures such as power grids, on both network and physical layers. With the progressive development of cyber threats, some recommendations have been provided in the new IEC 62351 standard to secure the GOOSE protocol [7]. Specifically, the IEC 62351 standard requires an authentication approach for protecting the integrity and authenticity of the GOOSE messages, while it recommends encryption for protecting data confidentiality. Although the recommendations imposed by the IEC 62351 standard are mandatory to remedy the security gaps in the GOOSE protocol, their actual application clashes with the operational speed requirement of the IEC 61850 standard, which specifies that GOOSE messages must be generated, transmitted, and processed in less than 3 milliseconds [8].

To fill this gap, we propose in [6] the application of the geometric approach to develop an encryption and authentication methodology that can be particularly fast and easy to implement, while preserving the integrity and confidentiality characteristics of the messages. The main strengths of the proposed approach are summarized below.

(i) The proposed authentication and encryption algorithms, based on a geometric-cryptographic mechanism, have execution times that prove to be well below the 3-millisecond constraint. Furthermore, by using such algorithms, the integrity and confidentiality of GOOSE messages are provided without changing the format structure of the messages.

(ii) The implementation of the authentication and encryption algorithm can reduce the processing time required to detect data manipulation in GOOSE messages.

(iii) The proposed algorithms can be applied to GOOSE messages of any length and are effective in several infrastructures without requiring the use or addition of specific hardware components.

References

[1] C. N. Hadjicostis and A. D. Domínguez-García, "Privacy-preserving distributed averaging via homomorphically encrypted ratio consensus," *IEEE Transactions on Automatic Control*, vol. 65, no. 9, pp. 3887–3894, 2020.

[2] M. Kishida, "Encrypted average consensus with quantized control law," in *2018 IEEE Conference on Decision and Control (CDC)*. IEEE, 2018, pp. 5850–5856.

[3] W. Abbas, A. Laszka, and X. Koutsoukos, "Improving network connectivity and robustness using trusted nodes with application to resilient consensus," *IEEE Transactions on Control of Network Systems*, vol. 5, no. 4, pp. 2036–2048, 2017.

[4] D. Fiore and G. Russo, "Resilient consensus for multi-agent systems subject to differential privacy requirements," *Automatica*, vol. 106, pp. 18–26, 2019.

[5] C. Fioravanti, L. Faramondi, G. Oliva, and C. Hadjicostis, "A geometrical approach for consensus security," *Systems & Control Letters*, vol. 185, p. 105717, 2024.

[6] M. F. Elrawy, C. Fioravanti, G. Oliva, M. K. Michael, and R. Setola, "A geometrical approach to enhance security against cyber attacks in digital substations," *IEEE Access*, 2024.

[7] M. A. Aftab, S. S. Hussain, I. Ali, and T. S. Ustun, "IEC 61850 based substation automation system: A survey," *International Journal of Electrical Power & Energy Systems*, vol. 120, pp. 1–16, 2020.

[8] S. M. S. Hussain, T. S. Ustun, and A. Kalam, "A review of IEC 62351 security mechanisms for IEC 61850 message exchanges," *IEEE Trans. Industrial Informatics*, vol. 16, no. 9, pp. 5643–5654, 2020.

MUSAPOEM: Multi Satellite Proximity Operations for Rendezvous and Docking Missions in Earth and Moon Orbits

Giordana Bucchioni [1], **Lorenzo Pollini** [1]
University of Pisa, Department of Information Engineering.[1]
E-mail: giordana.bucchioni@unipi.it, lorenzo.pollini@unipi.it

MUSAPOEM (Multi Satellite Proximity Operations for Rendezvous and Docking Missions in Earth and Moon Orbits) is a project co-funded by the Italian Space Agency, which aims at advancing autonomous multi-agent proximity operations in space. The project is a collaborative effort involving the Polytechnic of Turin, the University of Pisa, Argotec, and Kurs Orbital. Its objective is to advance the state-of-the-art in modelling, guidance, navigation, control, and identification algorithms for multi-vehicle autonomous proximity operations in space, defined as operations where the relative distance among the satellites is less than a few tens of kilometres. The project's reference scenario involves four satellites in orbits around Earth or the Moon (see Figure 1):

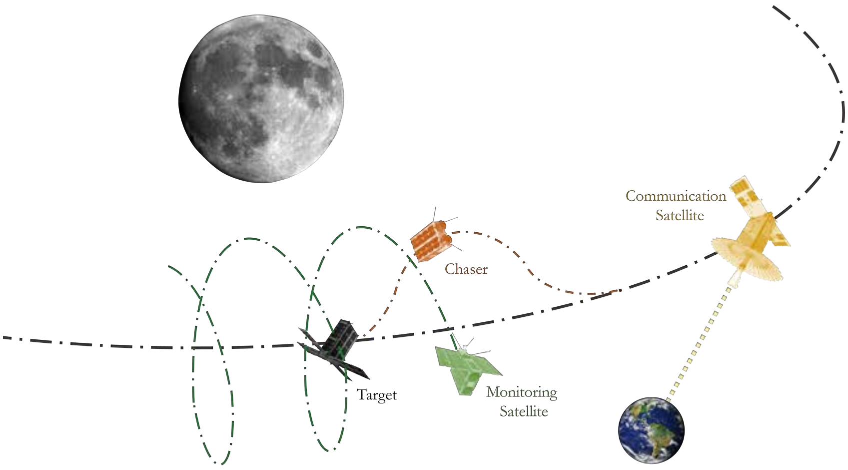

Figure 1: Concept of operation Musapoem

- **Target vehicle:** A passive satellite in a Kepleian (Earth case) or non-Keplerian (Moon case) orbit with some uncertainty. This satellite is the mission's focus and shall be observed, monitored, and approached by the formation.

- **Chaser:** An active vehicle aiming to approach the target through a rendezvous sequence. The chaser, equipped with a limited number of sensors (radar, lidar, laser) and power, performs rendezvous and docking with the target. It can communicate and collaborate with other satellites to support the rendezvous operations.

- **Observer Satellite:** Equipped with cameras and radar to support navigation during the rendezvous operation, it is positioned on a trajectory that maximizes visibility and minimizes station-keeping control expenses.

- **Communication Satellite:** This satellite maintains the link between the formation and Earth. Its trajectory is chosen to maximize visibility with other satellites and Earth while minimizing station-keeping control costs.

During the project, it is expected that a digital twin will be implemented using Python and MATLAB, Hardware-in-the-Loop (HIL) simulations to model the complex relative dynamics of the formation, and the GNC algorithms on a flying onboard computer.

The presented work focuses on the tasks carried out by the University of Pisa on designing Guidance, Navigation, Control (GNC), mission management and orbit identification algorithms for multi-agent proximity operations in lunar space. Operations in the vicinity of the Moon are characterized by highly non-linear non-Keplerian dynamics, significant perturbations, communication delays with Earth, the absence of GPS/GNSS, and potential lunar eclipses and communication losses.

Although the project began in December 2023 and has a duration of two years, some preliminary results are already available:

- **Model Selection and Implementation**: The first result is the selection and implementation of the most suitable model for Earth-Moon dynamics, which is highly non-linear. Several models have been identified for designing the GNC loop. According to the literature [1], the restricted three-body ephemeris with environmental perturbations (solar radiation pressure, higher-order gravitational harmonics) is an effective model for describing the complex environment. For GNC design, simpler models are selected to compute guidance, control inputs, navigation outputs, and target orbit estimates. These models include the Circular Restricted Three-Body Problem [1], which ensures the existence of equilibrium points around which marginally stable trajectories (non-Keplerian periodic orbits) and stable/unstable modes can be found. Another simplified model used for orbit identification is the Virtual Primary Encke's method [2], which uses a two-body approximation of the dynamics, allowing the use of well-established techniques.

- **Autonomous Mission Management Strategy**: A preliminary study has been conducted to address the limited literature on autonomous mission management in space, particularly in cislunar space. This study explores natural dynamics to save fuel. The proposed solution involves a genetic algorithm [3] to select the best rendezvous sequence for the chaser satellite and quasi-halo orbits for the other two vehicles, minimizing fuel expenses and maximizing the connectivity and safety of the formation.

- **Shared Rendezvous Standard**: Another innovative result is the formulation of a shared rendezvous standard to define the sequence of operations a chaser shall perform to approach a passive target.

Currently, an autonomous determination algorithm is being developed based on an innovative approach combining a particle filter and the Virtual Primary Encke (VPE) method to locally identify the partially unknown target orbit. Future work will focus on selecting and implementing robust control algorithms for rendezvous and station-keeping and improving the state-of-the-art in performing relative and inertial navigation for each satellite without using GPS/GNSS.

Aknowledgements

This work is supported by the Italian Space Agency for "GiORNATE DELLA RICERCA ACCADEMICA SPAZIALE" (RESEARCH DAY) ASI 2020 afferente al Tavolo Tematico “Proximity Operations”, Area Tematica “Proximity operations for orbital and/or surface activities in planetary exploration”

References

[1] Wang Sang Koon, Martin W Lo, Jerrold E Marsden, and Shane D Ross. Dynamical systems, the three-body problem and space mission design. World Scientific, 2000.

[2] Catello Leonardo Matonti, Giordana Bucchioni, Armando Vittorio Atzori, and Marcello Romano. A new form of osculating keplerian approximation of n-body non-keplerian motion for the design of gnc algorithms. 2023.

[3] Fabrizio Pilone, Giordana Bucchioni, Bone Spencer, and Stèphanie Lizy-Destrez. Autonomous mission planning for multi-agent lunar mission. 2024.